transactions of the ASME

Published Quarterly by
The American Society of
Mechanical Engineers

Volume 92 • Series C • Number 3
AUGUST 1970

journal of heat transfer

EDITORIAL OFFICES are at ASME Headquarters, United Engineering Center, 345 East 47th Street, New York, N. Y. 10017. Cable address, "Mechaneer," New York.
PUBLISHED QUARTERLY at 20th and Northampton Streets, Easton, Pa. 18042. Second-class postage paid at Easton.
CHANGES OF ADDRESS must be received at Society headquarters seven weeks before they are to be effective. Please send old label and new address.
PRICES: to members, $2.25 a copy, $7.50 annually; to nonmembers, $4.50 a copy, $15.00 annually.
Add 50 cents for postage to countries outside the U. S. and Canada.

INDEXED by the Engineering Index, Inc.

(Contents Continued on page 568)

CONTENTS

(CONTINUED)

FRANK KREITH
Professor of Engineering,
University of Colorado,
and Consultant,
National Center for Atmospheric Research,
Boulder, Colo.
Mem. ASME

Thermal Design of High-Altitude Balloons and Instrument Packages

The vertical motion of balloon systems depends critically on the heat transfer to and from the gas inside because the temperature and pressure of the gas determines the lift of the balloon and its payload. In the past the thermal design of high-altitude balloons has largely been based on a combination of experience, empirical data, and approximate calculations. Recent advances in heat-transfer research have made it possible, however, to calculate the temperature of the lifting gas as a function of altitude and to predict the vertical motion with the aid of high-speed computers. This review presents the results of heat-transfer experiments and theory pertinent to the processes which affect the calculations of balloon performance and the thermal design of their instrument packages.

When a body is completely immersed in a fluid at rest or in two stationary fluids one of which lies above the other, the body is buoyed up by a vertical force equal in magnitude to the weight of fluid displaced.

Archimedes

Introduction

The history of ballooning goes back to the days of Leonardo da Vinci who is said to have filled wafer-thin wax figures with hot air and made them fly for the coronation of Pope Leo X in 1513 [1].[1] But the first men who really made a balloon were the French brothers Joseph and Etienne Montgolfier, papermakers in a small town near Lyons. Inspired by Priestley's "Treatise on Air," the Montgolfier brothers began in 1782 experiments with paper bags held upside down over a kitchen fire. They discovered from these experiments that bags filled with hot air rose to the ceiling. They decided then to make bigger and better bags which eventually led to the beginning of the air age when they launched a hot-air balloon on June 5, 1783 from the marketplace of their hometown, Annonay.

The French Academy heard about these experiments and commissioned one of its members, the renowned Professor Charles, to look into them. Professor Charles incorrectly assumed that the inventors of the balloon had utilized Cavendish's discovery of hydrogen, which was at that time known as the inflammable air, to make an object which could fly, and he designed and built a hydrogen balloon from scratch. On August 27, 1783, he successfully launched a 13-ft diameter sphere filled with hydrogen before astonished spectators on the Champ de Mars.

As with many spectacular inventions, once the breakthrough is made, events move rapidly. On September 12, 1783, the Montgolfier brothers launched another hot-air balloon, and a week later they sent up a balloon carrying a sheep, a duck, and a cock. On November 21 of the same year, the young physicist Pilâtre de Rozier persuaded the king of France to allow him to ascend with the Marquis d'Arlandes, and the two men made the first aerial voyage in history. They flew a distance of 5½ miles in 25 min from the Château de la Muette in the Bois de Boulogne and landed safely.

Professor Charles, in the meantime, designed a rubberized-fabric hydrogen balloon, complete with a net to support the gondola, a control valve, ballast, and a barometer to record the altitude. With this almost-modern balloon he ascended with his helper from the Tuileries on December 1, 1783, and landed safely at Nerle, 27 miles away. This event was the birth of modern ballooning [2].

Current Status of Scientific Ballooning

Scientific ballooning, since its beginnings late in the eighteenth century, has made innumerable contributions to science and technology, and despite the development of aircraft, rockets, and satellites, balloons are still widely used for atmospheric studies. The number of scientific balloon flights, the sizes of the balloons, and their payloads have increased steadily over the past few years. The average size of stratospheric balloons flown today is 10 million cu ft, but balloons with a volume of 30 million cu ft have been flown. Balloons of this size can fly far above the weather at altitudes between 120,000 and 160,000 ft, but they can also be flown at lower altitudes. Thus balloons provide very stable platforms within the atmosphere at altitudes up to 180,000 feet, whereas satellites generally cannot remain for long in orbits below 100 miles altitude. The swing of a package suspended from a balloon is less than 1 deg of arc, and the period of this swing is, depending upon the length of the supporting line, 5 to 15 sec. Balloon rotation rates rarely exceed 20 deg per min and are frequently nearly zero for as long as an hour. A balloon can

[1] Numbers in brackets designate References at end of paper.

Contributed by the Heat Transfer Division and presented as an invited lecture at the 1969 Winter Annual Meeting, Los Angeles, Calif., November 16–20, 1969, of The American Society of Mechanical Engineers. Revised manuscript received by Heat Transfer Division, April 30, 1970.

float at a given altitude for considerable time although it will generally rise during the day when the temperature of the gas in the balloon increases and sink at night when the gas temperature drops.

Two types of balloons are in common use for scientific research and meteorological observations: zero-pressure and superpressure. Zero-pressure balloons, usually made of polyethylene skin with a thickness of 1 mil or less, are the most common aerostats used to lift heavy loads to the highest altitudes. They are nonextensible vented balloons made of a gas-tight material and are usually spherical or inverted-onion shaped. These balloons are inflated to only a small fraction of their capacity, and as they rise the relatively small bubble of helium at the top expands to several hundred times its initial volume and fills the balloon, as shown in Fig. 1.

Flights as long as a week have been successful with zero-pressure balloons. However, if the system is to remain at altitude when the balloon cools at night, the contraction of gas and loss of lift must be compensated for by lightening the system. This is done by dropping ballast, which for each day of flight may amount to as much as 10 percent of the entire system weight. Because of this, a flight of 3 days is generally considered maximum. Loads of 10,000 lb have been flown at 80,000 ft; 2200 lb at 130,000 ft; and 450 lb at 161,500 ft with zero-pressure balloons. Development of reliable systems for carrying 650 lb to 180,000 ft is now under way.

Fig. 2 shows the approximate cost of lifting various payloads to desired altitudes with zero-pressure balloons. A balloon costs roughly $1000 per million cu ft of volume at float altitude. This cost is a little higher for smaller balloons and a little lower for very large balloons (30 million cu ft). A launch from a fixed base costs approximately $5000, which covers the launching operation, tracking, and payload recovery. When balloons are launched from remote sites, as during the 1965 expedition to India, the cost per launch increases to about $10,000. In addition to the balloon and launch costs, the cost of helium, approximately $1.00 per lb of weight lifted into the air, must be added. This lift must include the weight of the skin of the balloon, the rigging, and the parachute used for recovering the payload.

Superpressure balloons are nonextensible balloons which are unvented, i.e., sealed to prevent gas release. At float level the free lift gas in these balloons exerts a pressure on the balloon walls greater (about 20 percent) than the ambient atmospheric pressure—hence the term superpressure. Variations in heat transfer will produce changes in the superpressure but not in the balloon volume. Consequently, as long as the balloon is pressurized, it continues to float at a constant-density level and does not require release of ballast at sunset to maintain altitude. Robot weathermen, e.g., GHOST balloons, are examples of this type of aerostat [3]. Superpressure balloons flown by V. E. Lally of NCAR have stayed aloft as long as 14 months. In a recent series of such balloon flights Lally and his group have charted for the first time the global atmospheric currents in the Southern Hemisphere [4]. Superpressure balloons (5 to 50 ft in diameter) are generally smaller than zero-pressure balloons (50 to 500 ft in diameter) and usually carry payloads of less than 100 pounds. They can, however, easily fly "in the weather" and gather atmospheric data effectively. Leakage of gas, excessive heat transfer, and icing are their most pressing problems.

In comparing the advantages and disadvantages of balloons with those of satellites, several factors must be considered. One

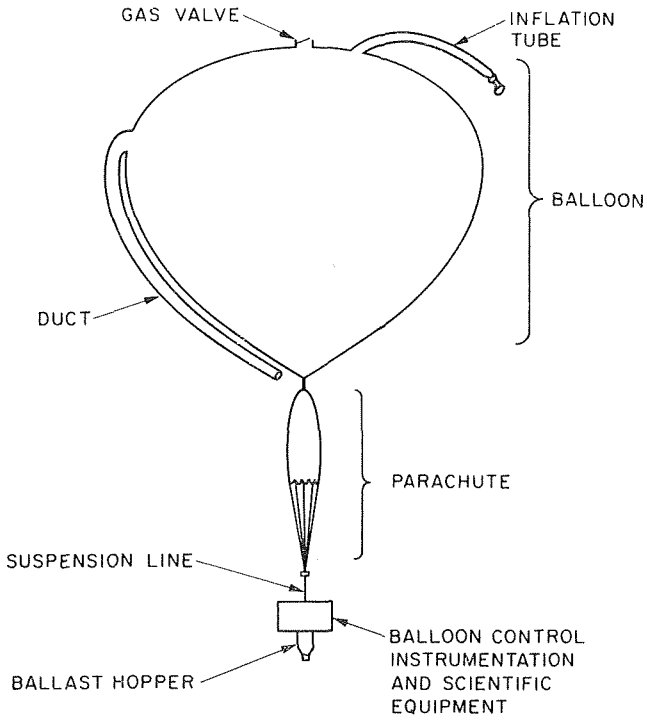

Fig. 1 Schematic sketch of zero-pressure balloon

Nomenclature

A = area
a = absorptance
b = thickness of fabric
C_D = drag coefficient
C_M = virtual displacement coefficient
c_v = specific heat at constant volume
D = diameter
$\dot{E}$ = exhaust rate of balloon gas through expulsion duct and valve
e = emittance
F = force
G = rate of radiation incident on surface
g = gravitational constant
h = heat-transfer coefficient
I = intensity of radiation
L_F = free lift, see equation (2)
L_G = gross lift = $\rho_a V_g - m_g$
M = molecular weight
m = mass
P = pressure
q = rate of heat transfer
R = universal gas constant
r = reflectance or radial distance
S = surface area
T = temperature
t = time
U = velocity
V = volume
v = specific volume
z = altitude or geopotential height
ζ = zenith angle
γ = lapse rate of atmosphere
λ = wave length of radiation or latitude
θ = polar angle or supertemperature, see equation (3)
π = superpressure, see equation (3)
ρ = mass density
σ = Stefan-Boltzmann constant
τ = tilt angle
ψ = azimuth angle
ϕ = longitude

Subscripts

a = atmospheric air
B = ballast
b = balloon system
c = convections
D = drag
d = ducting
f = balloon skin fabric
g = balloon gas
i = infrared
0 = zero altitude
p = payload
s = solar
v = valve

Dimensionless numbers

Gr = Grashof number
Nu = Nusselt number
Pr = Prandtl number
Ra = Rayleigh number
Re = Reynolds number
Re* = equivalent Reynolds number
Sc = Schmidt number

advantage of satellites over balloons is that satellites can remain aloft much longer. To date, large balloons have flown for only a few days. But a number of ideas are being tried at present to maintain big balloons aloft for much longer periods, and for the long-range view there exists the possibility of keeping large balloons in flight for as long as a month or even a year. A rather unfortunate political problem arises with balloon flights at the present time. Balloons are not allowed, without permission, to fly over other countries, whereas satellites may, by international agreement, fly over any country. Satellites, however, cannot directly measure or sample the atmosphere. They can photograph the weather from great distances and give, thereby, a global weather picture, but the distributions of pressure, temperature, moisture, and wind speeds is difficult to determine by means of satellites. Balloons, however, can be used to measure these atmospheric variables directly.

Another point on the credit side of satellites is that their positions can be predicted, whereas balloon positions are largely dependent upon the weather. The position of a balloon when it transmits information back to earth must, therefore, be determined before such information can be interpreted. Determining the global weather picture with balloons would require many balloons and could be as expensive as using satellites. However, a single satellite launch costs about $5 million, and the advantages of obtaining local information quickly and cheaply with balloons are obvious. Moreover, balloons can carry delicate instruments such as telescopes because they are not subject to the vibration and abrupt acceleration of a rocket launch.

About 400 stratospheric balloons with payloads in excess of 50 lb were launched last year in the United States alone and many more of the smaller variety known as GHOST weather balloons were launched and circled the globe continuously. Balloons can make significant contributions in the quest to predict and control the weather, but in order to take full advantage of the opportunities that balloons present as data-taking vehicles, it is necessary to understand the thermal characteristics of the balloon and its paraphernalia.

Equations of Vertical Motion

The total mass of a balloon system which must be accelerated during ascent and descent, including a virtual mass term $C_M\rho_a V_g$ to account for the air mass displaced by the motion of the balloon [5, 6], is

$$\Sigma m_i = m_g + m_f + m_B + m_p + C_M\rho_a V_g \tag{1}$$

where $m_g + m_f + m_B + m_p = m_b$, is the physical mass of the balloon system. The sum of the forces acting on the balloon system, see Fig. 3, is

$$\Sigma F_i = g[\rho_a V_g - m_g - m_f - m_B - m_p] - {}^1/_2 C_D\rho_a|U_b|U_b A_b \tag{2}$$

The sum of the five terms in the bracket times g is usually called the "free lift" L_F and the last term represents the aerodynamic drag force F_D.

For a spherical shape in the Reynolds number range of large-balloon flights, i.e., above 6×10^5, the drag coefficient C_D is equal to 0.1 [7], but no data for actual balloon shapes have been published. In reference [8] a value of 0.3 for C_D was used as an average for computational purposes.

In balloon terminology $g(\rho_a V_b - m_g)$ is called the "gross lift" L_G. Using the perfect gas law as the equation of state for the atmospheric air and the balloon gas, L_G is given by the expression

$$L_G = gm_g\left[\frac{M_a}{M_g}\,\frac{P_a}{P_a + \pi}\,\frac{T_a + \theta}{T_a} - 1\right] \tag{3}$$

where $\theta = (T_g - T_a)$ is often called the gas superheat (although it is actually a supertemperature), and $\pi = (P_g - P_a)$ is called the gas superpressure.

The quantities θ and π are usually quite small compared to T_a and P_a, respectively. The ratio of π/P_a is of the order of 0.0015 in zero-pressure balloons, but may be as large as 0.25 in superpressure balloons. The ratio θ/T_a depends on the heat-transfer characteristics of the system, as discussed in detail in subsequent sections of this paper. By expanding the fraction in equation (3) one can deduce the widely used approximate relation

$$L_G = gm_g\left[\frac{M_a}{M_g} - 1 + \frac{M_a}{M_g}\left(\frac{\theta}{T_a} - \frac{\pi}{P_a}\right)\right] \tag{4}$$

Substituting equations (1) and (2) in Newton's second law of motion gives

$$L_F - {}^1/_2 C_D\rho_a\left|\frac{dz}{dt}\right|\frac{dz}{dt}A_b = [m_g + m_f + m_B + m_p + C_M\rho_a V_g]\,\frac{d^2z}{dt^2} \tag{5}$$

In applying the above equations it is possible to relate the balloon pressure to the height z through the hydrostatic balance and the equation of state of the atmosphere, because there is generally only a very slight superpressure in a balloon. In zero-pressure balloons this superpressure is limited by the automatic exhaustion of gas through the expulsion duct just before float altitude is reached. This gas release keeps the balloon from bursting and prevents "high-altitude bounce." Gas is also released through an exhaust valve controlled from the ground ("valving") to reduce the free lift when the balloon ascends too rapidly and to initiate descent from float altitude.

Atmospheric Property Variations. In hydrostatic equilibrium the variation of pressure in the atmosphere with altitude is given by the relation

$$\frac{dP_a}{dz} = -g\rho_a \tag{6}$$

If it is assumed that the atmospheric air obeys the perfect gas law, the pressure as a function of altitude is expressed by

$$\frac{dP_a}{P_a} = -g\,\frac{M_a}{RT_a}\,dz \tag{7}$$

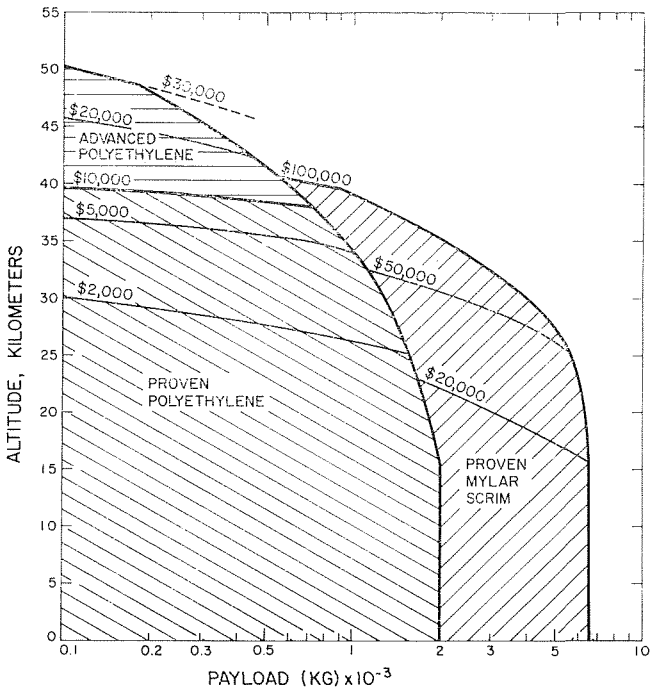

Fig. 2 Cost of lifting payloads to desired altitudes with zero-pressure balloons

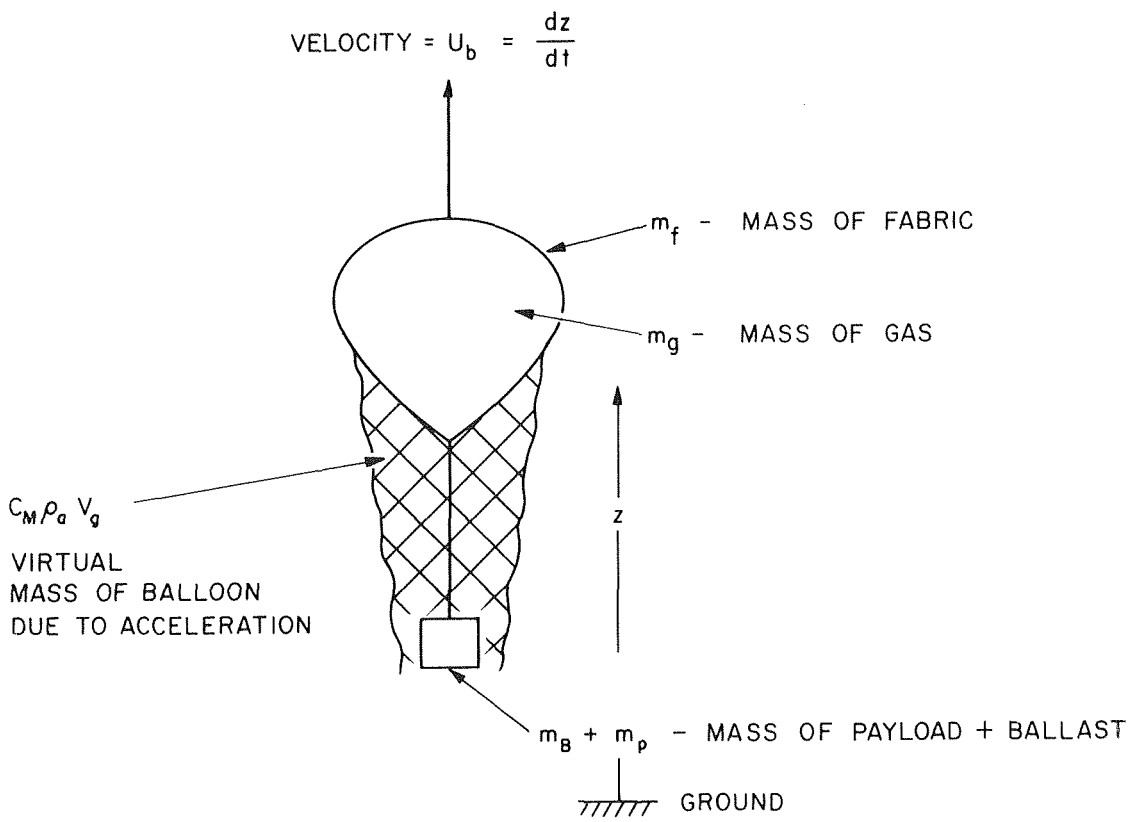

$$\Sigma F_z = \text{MASS} \times \text{ACCELERATION}$$

$$g\left[(\rho_a V_g - m_g - m_f - m_B - m_p) - C_D \rho_a U_B^2 A_b\right]$$

$$= (m_g + m_f + m_B + m_p + C_M \rho_a V_g) \cdot \frac{d^2 z}{dt^2}$$

Fig. 3 Schematic sketch illustrating force balance for vertical balloon motion

or

$$\ln \frac{P_a}{P_{a0}} = -\frac{gM_a}{R} \int_{z_0}^{z} \frac{dz}{T_a}$$

Over limited ranges in altitude the variation of the atmospheric air temperature with altitude is often approximated by the linear relation

$$T_a = T_{a0} + \gamma(z - z_0) \tag{8}$$

where

$$\gamma \text{ is the lapse rate} = \left(\frac{dT_a}{dz}\bigg|_{\text{at } z}\right)$$

Fig. 4 shows the temperature distribution up to 100 km as a function of altitude according to various models of the atmosphere proposed during the past 15 years [9].

If the atmospheric air temperature profile is known (or taken for purposes of calculations from Fig. 4), the pressure and density variations over an altitude change between z_1 and z_2 for which the lapse rate is a constant can be written in the form

$$\frac{P_{a1}}{P_{a2}} = \left(\frac{T_{a2}}{T_{a1}}\right)^{\frac{gM_a}{R\gamma}} \quad \text{and} \quad \frac{\rho_{a1}}{\rho_{a2}} = \left(\frac{T_{a2}}{T_{a1}}\right)^{\frac{gM_a + R\gamma}{R\gamma}} \tag{9}$$

Balloon Gas Expansion. The variation of the gas volume in the balloon with time is

$$\frac{dV_g}{dt} = \frac{d}{dt}\left(\frac{Rm_g T_g}{M_g P_g}\right) = \frac{Rm_g}{M_g P_g}\frac{dT_g}{dt} + \frac{RT_g}{M_g P_g}\frac{dm_g}{dt} - \frac{Rm_g T_g}{M_g P_g^2}\frac{dP_g}{dt} \tag{10}$$

If the relation between atmospheric pressure and altitude from equation (7) is used and superpressure is neglected, the above equation can be written in the form

$$\frac{dV_g}{dt} = \frac{R}{M_g P_a}\left(m_g \frac{dT_g}{dt} + T_g \frac{dm_g}{dt} + \frac{gm_g T_g M_a}{RT_a}\frac{dz}{dt}\right) \tag{11}$$

Lift and Load Adjustments. As was mentioned earlier, the lift of a balloon system can be reduced by exhausting helium automatically through the gas expulsion duct, when float altitude is reached, or by valving to maintain float altitude or to cause the balloon to descend. If $\dot{E}_d$ is the volumetric gas flow rate through the expulsion duct (required to stabilize the balloon at ceiling) and $\dot{E}_v$ is the flow rate through the exhaust valve, the net change in balloon mass due to loss of gas is

$$\frac{dm_g}{dt} = \rho_{gd}\dot{E}_d + \rho_{gv}\dot{E}_v \tag{12}$$

The mass of the balloon system can be reduced by dropping ballast or part of the payload. The total change in mass of the balloon system during a time increment $\Delta t = t_2 - t_1$ is

$$\int_{t_1}^{t_2} \frac{dm_b}{dt} = \int_{t_1}^{t_2} \frac{dm_B}{dt} + \Delta m_p \tag{13}$$

where Δm_p represents the amount of mass dropped during the time interval Δt.

Energy Equations. The conservation equation for the gas inside the skin of the balloon can be obtained by applying the first law of thermodynamics. The rate of change of the internal energy of the gas equals the rate at which heat is transferred to the gas (q_1) minus both the rate at which net work is done by the gas and the rate at which internal energy is lost by valving. Assuming that the equation of state of the gas can be approximated by the ideal gas law and that the temperature and pressure of the gas inside the balloon are uniform, one obtains

$$\frac{d}{dt}(c_v m \bar{T})_g = q_1 + \frac{RT_g}{M_g}\frac{dm_g}{dt} - P_a\frac{dV_g}{dt} + (c_v\bar{T})_g\frac{dm_g}{dt} \tag{14}$$

where the term on the left-hand side of equation (14) is the rate of change in internal energy of the balloon gas, the first term on the right hand represents the rate of heat transfer by free convection from the interior surface of the balloon skin to the gas, the second term the flow work done during gas release, the third term the work done on the external pressure when the balloon volume changes due to a change in temperature of the gas or resulting from valving, and the last term the loss of internal energy by valving. If the pressure inside the balloon is uniform and equal to the atmospheric pressure, the flow work done during valving in the absence of heat transfer equals the work done by the atmosphere on the balloon, and the second and third terms cancel.

The assumption that the temperature of the gas inside the balloon is uniform may lead to serious error when short-term transients occur and the gas adjacent to the balloon skin undergoes temperature variations while the gas in the interior does not. When this situation prevails, the first term in the energy equation should be replaced by $\frac{d}{dt}\left[\iiint_{V_g} c_{v_g}\rho_g T_g dV_g\right]$.

A similar analysis can be performed on the balloon skin. The internal energy of the skin will change only because of heat transfer to and from its surfaces. The skin is so thin that one can neglect the temperature drop across it at any location, but since the heat transfer over the skin is not uniform its temperature will vary. This variation cannot, however, be expressed analytically, but when it becomes important a numerical analysis will yield a satisfactory approximation of the internal energy of the skin.

To simplify the thermodynamic analysis it will be assumed that an averaged skin temperature can be used. A first-law analysis then gives

$$\frac{d}{dt}\iint_{S_f} c_f\rho_f l_f T_f dS_f = c_f m_f\frac{d\bar{T}_f}{dt} = q_2 + q_3 + q_4 - q_5 - q_6 \tag{15}$$

where

c_f = specific heat of skin
ρ_v = density of the skin

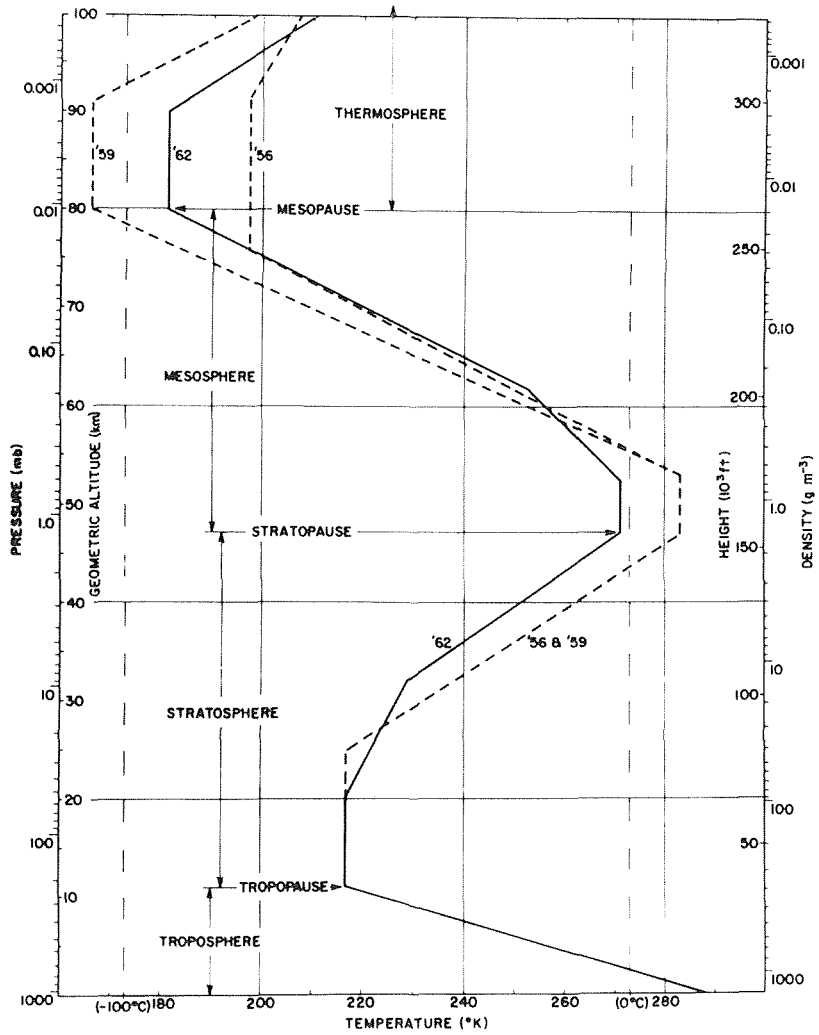

Fig. 4 Temperature distribution in the atmosphere up to 100 km; reference [9]

m_f = mass of skin
S_f = surface area of balloon skin
t_f = thickness of skin
$\bar{T}_f$ = average skin temperature
q_1 = rate of heat transfer by convection from the skin to the lift gas
q_2 = rate of absorption of solar radiation = ($q_{2\,\text{direct}} + q_{2\,\text{reflected}}$)
q_3 = rate of absorption of infrared radiation
q_4 = rate of heat transfer by convection from the atmosphere to the skin
q_5 = rate of radiant heat transfer from the skin

Equations (14) and (15) are the two energy equations which must be combined with equation (5) to determine the vertical position and the motion of the balloon. The energy equations for the balloon gas and the skin fabric can be treated analytically if one assumes that all of the gas and the entire skin are at uniform, but not equal, temperatures. This assumption is quite good at night but can introduce appreciable errors during the day, when solar energy heats the skin unevenly. Modifications for nonuniform heating could be made in the analysis [10] for the exterior of the fabric skin by numerical means, but the convection process inside a nonuniformly heated, balloon-shaped container is very complex. At this time the process is not well enough understood to be modeled analytically, and thus an accurate calculation of the heat transfer in the interior is not possible. Fortunately, during normal flight balloons rotate so that all parts of their skins are exposed equally (on the average) to the sun and the balloon gas is mixed. This makes the assumption of uniform gas and skin temperatures valid for thermal analyses performed for times ranging from intermediate to long, i.e., hours to days.

In the following two sections the heat-transfer phenomena of balloon systems will be examined in the light of recent advances in heat-transfer research. The next section will deal with convection and the following section with radiation phenomena. The final objective will be the evaluation of the five heat-transfer terms in equation (15).

Convection Between the Atmosphere and the Balloon System; q_4 in Equation (15)

Convective heat transfer between balloon systems and the atmosphere occurs over wide ranges of the convectional parameters used to describe the process. Heat is transferred between the atmosphere and the balloon by forced convection or free convection, or both, at Reynolds numbers from 0 to 10^7 and Grashof numbers from 0 to 10^{11}. Depending on the circumstances, the flow can be laminar or turbulent. The shape of a superpressure balloon resembles a sphere, that of a zero-pressure balloon resembles an onion, but instrument packages come in a variety of shapes, such as boxes, cylinders, and plates. Balloon diameters range from 10 to 400 ft, ascent velocities from 0 to 40 ft/sec, and temperature differences (between the skin and gas) from 0 to 50 deg F.

Although convective heat transfer to and from an object in air has been studied extensively, few investigations extend into the extreme Reynolds and Grashof number ranges encountered by balloons and none has specifically treated the onion shape typical of zero-pressure balloons. Approximations and extrapolation of existing data are, therefore, unavoidable.

Heat transfer from spherical shapes in forced convection has recently been investigated experimentally by Yuge [11] and by Vliet and Leppert [12]. Local values of the heat-transfer coefficient in flow over a sphere in the neighborhood of the stagnation point have been calculated by Merk [13]. The pressure distribution for flow over spheres has been investigated by Fage [14], who also measured the separation point. He found that at a Reynolds number of 1.6×10^6 separation occurred at a polar angle ϕ of 70 deg (see Fig. 6) and that it moved toward the rear with increasing Reynolds number. At the highest Reynolds number of his tests, $\text{Re}_D = 4.2 \times 10^6$, separation occurred at a polar angle of 100 deg.

Extensive correlations of experimental data indicate that in forced convection the average Nusselt number of the entire surface of the sphere in air can be obtained from the relation

$$\text{Nu}_m = \frac{\bar{h}_c D}{k_a} = 2 + 0.30\,\text{Re}_{D,m}^{0.57} \tag{16}$$

for Reynolds numbers between 1.8×10^3 and 1.4×10^5 [11] or from the relation

$$\text{Nu}_m = \frac{\bar{h}_c D}{k_a} = 2 + 0.41\,\text{Re}_{D,m}^{0.55} \tag{17}$$

for Reynolds numbers between 0.4 and 2×10^5 [12]. In both of the above equations, the subscript m indicates that all physical properties should be evaluated at the mean temperature between the skin and the atmospheric temperatures.

Using equation (17), the rate of heat transfer by convection to or from the surface of a spherical balloon skin during ascent or descent can be written in the form

$$q_4 = 3.9 V_g^{1/3} k_a (T_a - \bar{T}_f)\left[2 + 0.472 V_g^{0.183}\left(\rho_a \frac{dz}{dt}\Big/ \mu_a\right)^{0.55}\right] \tag{18}$$

Krause and Schenck [15] investigated thermal free convection from a warmer surrounding fluid to a cooler spherical body at uniform surface temperature in the range of Rayleigh numbers between 6×10^8 and 5×10^9. As shown in Fig. 6, the experimental results for the local heat-transfer coefficient agree reasonably well with a theoretical analysis of Merk [16] up to the hydrodynamic separation point, which for the narrow Grashof number range of this investigation occurred at a polar angle of about 145 deg from the vertical axis. Since Merk's theory applies equally well for

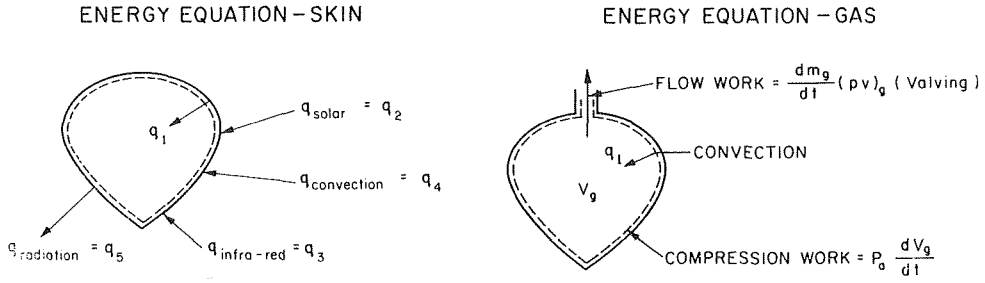

Fig. 5 Schematic sketch illustrating energy balance for lifting gas and balloon skin

○ $\Delta T = 15{,}5°C$; ● $\Delta T = 19{,}5°C$.

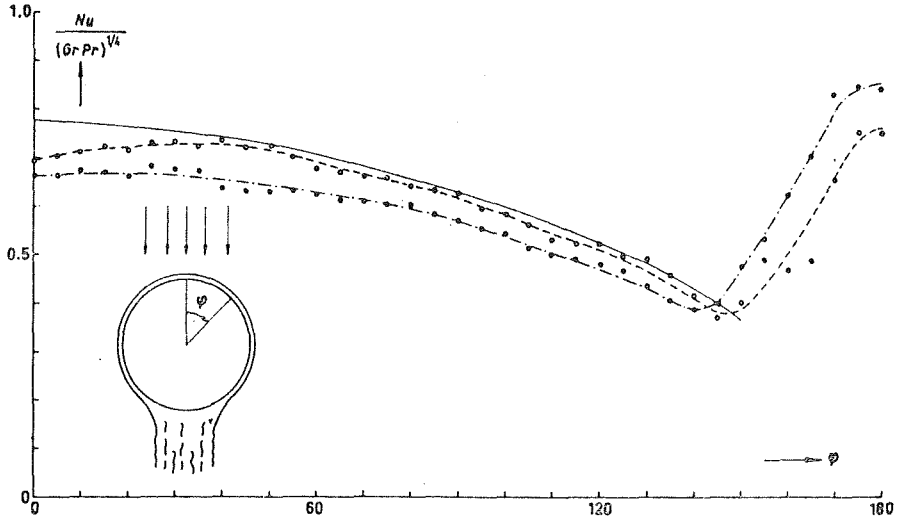

Fig. 6 Local free convection heat transfer over sphere—comparison of theory and experiments; reference [15]

laminar convection from a heated sphere, it also seems reasonable to apply the data in Fig. 6 to calculate heat transfer from the upper hemispherical surface of heated balloons. No data or theory exist at present, however, to predict the influence of the nonuniform azimuthal temperature distribution, which is always present when a balloon is heated by the sun.

Experimental evidence is contradictory regarding the influence of the Grashof number on the separation point in laminar free convection to or from a sphere. Garner, et al. [17, 18] found a shift in separation point from 155 deg to 100 deg between mass transfer Rayleigh numbers (Gr·Sc) from 1.5×10^8 to 5.5×10^8 for different fluids with $800 < Sc < 2200$, whereas Schütz [19] found a much weaker dependency in the region $2 \times 10^8 < Gr \cdot Sc < 2 \times 10^{10}$ (170 deg to 135 deg) for a fluid with Sc = 1800. According to conventional boundary-layer theory the separation point should shift toward the stagnation point with increasing Grashof numbers and the heat-transfer coefficient in the region of the free convection plume, where the flow is turbulent, will be larger than in the laminar flow regions, as shown in Fig. 6. The results agree qualitatively with observations of free convection about a horizontal cylinder.

The point of transition from laminar to turbulent flow in the free convection regime is not presently known. Schlieren patterns [15] show that purely laminar flow prevails over a sphere between the stagnation point and the equator at Grashof numbers as high as 6×10^8 and that some disturbances exist between 100 deg and separation (190 deg to 150 deg), but real turbulence was observed only in the plume at a Grashof number of about 10^9. Perhaps the stability analysis of Gebhart [20] could be applied to natural convection over a balloonshaped body (idealized as a sphere) in order to predict the point of transition analytically. Gebhart's analysis for a flat plate predicts that turbulent instabilities could amplify at local Grashof numbers of the same order of magnitude as have been observed on balloons.

If the designer can use averaged values of the heat-transfer coefficient over the entire spherical surface, available data can be correlated [15] by a relation of the type

$$\overline{Nu}_m = \frac{D\bar{h}_c}{k} = 2 + 0.6(Gr\ Pr)_m^{1/4} \qquad (19)$$

for Rayleigh numbers between 10^5 and 2×10^{10}. The constant value of 2 applies in the limit as the Grashof number approaches zero and the heat-transfer mechanism approaches pure conduction. The theoretical convergence of the Nusselt number at small Grashof numbers has recently been elegantly verified by Fendall [21].

The influence of vibration on the heat transfer from spheres has been investigated in free and forced convection [22], and the influence of rotation about a vertical axis has been studied experimentally for free convection [23, 24]. The results of these investigations indicate that under flight conditions neither vibration nor rotation will influence balloon heat-transfer characteristics.

Using equation (19), the rate of heat transfer by free convection to or from a balloon at float altitude can be written in the form

$$q_4 = 7.8 V_y^{1/3} k_a (T_a - \bar{T}_f) \left\{ 1 + 0.322 \left[\frac{\rho_a^2 g (T_a - \bar{T}_f) V_y}{T_a \mu_a^2} \right]^{1/4} \right\} \qquad (20)$$

For computational purposes a very convenient correlation of averaged experimental convection data has recently been provided by Börner [25], who reviewed seventy previous investigations of heat and mass transfer by free convection or forced convection or both in flow over single bodies and who also conducted additional tests. One convenience of Börner's correlation is that data for bodies of different shapes can be handled [26] by choosing a pertinent length dimension, l', defined in Table 1 for several shapes.

Table 1

Shape of Body	Equivalent Length l'
Very wide plate with surface parallel to the flow in forced convection with length l in direction of flow.	$l' = l$
Sphere or long cylinder of diameter D with axis perpendicular to the flow in forced and free convection	$l' = (\pi/2)D$
Long rectangular bar of width a^*, height b^*, with its long axis perpendicular to the flow in forced convection	$l' = a^* + b^*$
Vertical plate (surface parallel to gravity) of height l in free convection	$l' = l$
Long horizontal plate (surface perpendicular to gravity) of width l in free convection	$l' = l/2$

Reference [25] presents correlations of free convection data for plates (horizontal and vertical), spheres, and cylinders (horizontal and vertical) as plots of $\overline{Nu}_{l'} = \bar{h}_c l'/k$ versus $[Gr_{l'} \cdot Pr] = [(g\rho^2\beta\Delta T l'^3/\mu^2) \cdot (c_p\mu/k)]$ and of forced convection data in the form $\overline{Nu}_{l'}$ versus $Re_{l'}$. A combined free and forced convection

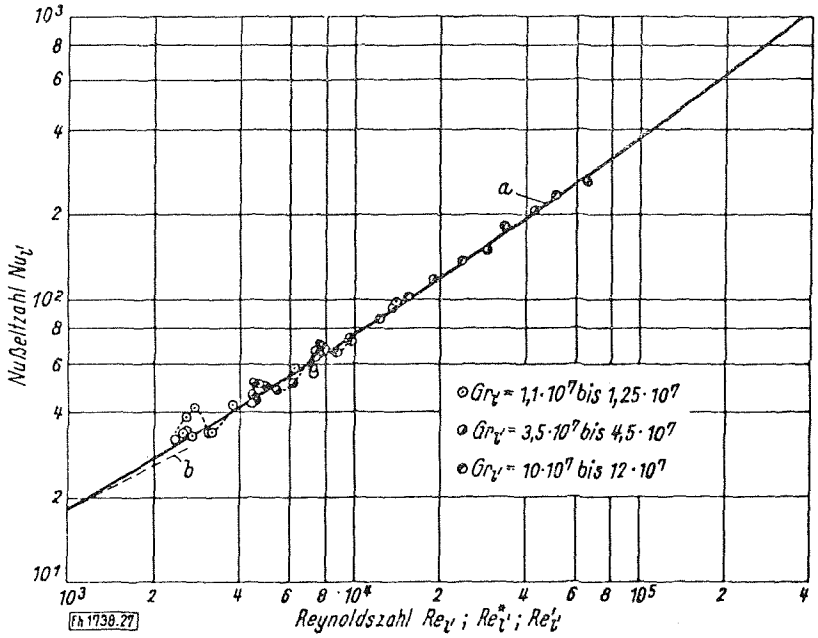

Fig. 7 Average Nusselt number for sphere in combined free and forced convection flow; reference [25]

correlation was obtained by defining an equivalent Reynolds number for free convection $Re_{l'}^*$

$$Re_{l'}^* = f(Pr)(Gr_{l'})^{1/2} \tag{21}$$

where the function $f(Pr)$ for air, which is dependent upon the Prandtl number, should be taken equal to $\sqrt{1/2}$ for "a best fit correlation," compared to 0.64 predicted by analysis. With the *definition of an equivalent Reynolds number for free convection* given in equation (21), free convection dominates when $Re_{l'} < 2.4\ Re_{l'}^*$ and forced convection dominates when $Re_{l'}^* < 2.4\ Re_{l'}$. A transition region, where both free and forced convection are appreciable, exists between these limits. It has been shown that in this transition regime free convection aids the forced convection transfer when the motion due to buoyancy is in the same direction as the forced flow and retards it [27, 28] when buoyancy opposes the flow. In order to bridge the gap between forced and free convection, Börner [25] defines a third Reynolds number $Re'_{l'}$ according to

$$Re'_{l'} = \sqrt{Re_{l'}^2 + (Gr_{l'}/2)} \tag{22}$$

and then plots $Nu_{l'}$ versus $Re'_{l'}$. Fig. 7 shows the results of this *correlation for a sphere with downward forced convection*, the situation of an ascending balloon. Under these circumstances free convection will oppose the forced convection flow, but visualization studies for this condition [25] have shown that the existence of a free convection field will produce turbulence at low velocities and also cause separation of the boundary layer. These effects tend to offset any decrease in the heat transfer, as predicted for purely laminar flow [27]. The correlation function shown in Fig. 7 was found to be also applicable for upward flow, the condition of a descending balloon. Experimental results recently published by Sharma, et al. [29] *on the interaction between* free and forced convection in flow over a horizontal cylinder for Reynolds numbers from 10 to 5000 and Grashof numbers from 3×10^3 to 7×10^6 indicate that the Reynolds number exponent n in the parameter Gr/Re^n is affected by turbulence and separation phenomena and that a value of 3.25 is most suitable when free convection dominates, whereas a value of 1.8 is more suitable at the forced convection end. An average value of 2.5 was found to give a reasonably good correlation in the transition region.

Börner's correlation does not give insight into local variations of the heat-transfer coefficient, but it is very convenient. By computing $Re_{l'}$ and $Re_{l'}^*$ simultaneously and continuously from the launch until the balloon has reached the float condition, a smooth transition between the forced and free convection regime can be made, and the influence of radiation can be superimposed directly.

In general only the equilibrium temperature at float altitude is important to the thermal design of balloon instrument packages. During ascent forced convective heat transfer is quite effective [30] in maintaining a small instrument package at a temperature close to that of the ambient air, but when the balloon has reached its float altitude, only free convection can transfer heat directly between the package and the surrounding air. The relative magnitude of the radiation to and from the surfaces of the package dominates the thermal transfer during the day, but convection enters prominently at night.

In certain specialized instrument packages, in addition to the averaged heat-transfer coefficient, local values at the top and bottom surfaces are also sometimes of interest. Some insight into the flow and temperature field in the vicinity of a heated horizontal square plate has been provided at small Rayleigh numbers by the numerical study of Suriano and Yang [31]. Table 2 shows averaged Nusselt numbers obtained by their calculations for both the top and bottom surfaces. The temperature field over a horizontal plate at a Rayleigh number of 50 (see Fig. 8) suggests boundary-layer behavior on the lower surface but not on the upper. The analysis of Stewartson [32], as modified by Gill, et al. [33], indicates, however, that a boundary layer forms also over the upper surface of a heated horizontal strip and that the average Nusselt number for a strip of width L in air can be predicted from the relation

$$\overline{Nu} = \frac{\bar{h}_c L}{k_a} = 0.79\,(Gr_L)^{1/5} \tag{23}$$

in the laminar flow regime. This result is not in complete agreement with experimental data for the upper surface of a heated square plate of side L in air [34]. This data gave larger heat-transfer coefficients that are correlated empirically by the relations

$$\overline{Nu} = 0.50\,(Gr_L)^{1/4} \quad (10^5 < Gr_L < 2 \times 10^7, \text{ laminar}) \tag{24}$$

$$\overline{Nu} = 0.125\,(Gr_L)^{1/3} \quad (2 \times 10^7 < Gr_L < 3 \times 10^9, \text{ turbulent}) \tag{25}$$

Table 2 Average Nusselt numbers for horizontal plate

N_{Ra}	$N_{Pr} = 0.72$			
	$x = 0-$	$x = 0+$	average	Buznik and Bezlomtsev*
0	1.049	1.047	1.048	1.00
0.01	1.050	1.047	1.049	1.16
0.10	1.052	1.045	1.048	1.28
1.0	1.104	1.041	1.073	1.51
5.0	1.201	0.946	1.074	1.77
10.0	1.406	0.932	1.169	1.91
50.0	2.879	1.259	2.069	2.38
100.0	4.041	1.330	2.685	2.64
200.0	6.166	1.492	3.829	2.96
300.0	7.620	1.678	4.469	3.03

* Buznik, V. M., and Bezlomtsev, K. A., "A Generalized Equation for the Heat Exchange of Natural and Forced Convection During External Flow About Bodies," *Izv. Uyssh. Uchcb. Zaved.*, Vol. 2, pp. 68–74, 1960; *Ref. Zh. Meckl.*, Vol. 6, Rev. 6V506, 1961.

Heat transfer by free convection from the lower surface of finite heated plates (or to the upper surface of cooled plates) has recently been studied by Singh, et al. [35] for square and circular plates and a long strip. Local heat-transfer coefficients are lowest in the center and increase toward the edges. For a square plate of side L, the local Nusselt number at a distance x from the center is

$$\frac{h(x)L}{k_a} = 0.58\,\mathrm{Ra}_L^{1/5} \Bigg/ \left\{ \left[1 - \left(\frac{2x}{L} \right)^2 \right] + 0.271 \left[1 - \left(\frac{2x}{L} \right)^2 \right]^4 + \ldots \right\}^{1/4} \tag{26}$$

The average Nusselt number is given by

$$\overline{\mathrm{Nu}}_L = \frac{\bar{h}_c L}{k_a} = C\,\mathrm{Gr}_L^{\,n} \tag{27}$$

where the constants C and n are given in Table 3.

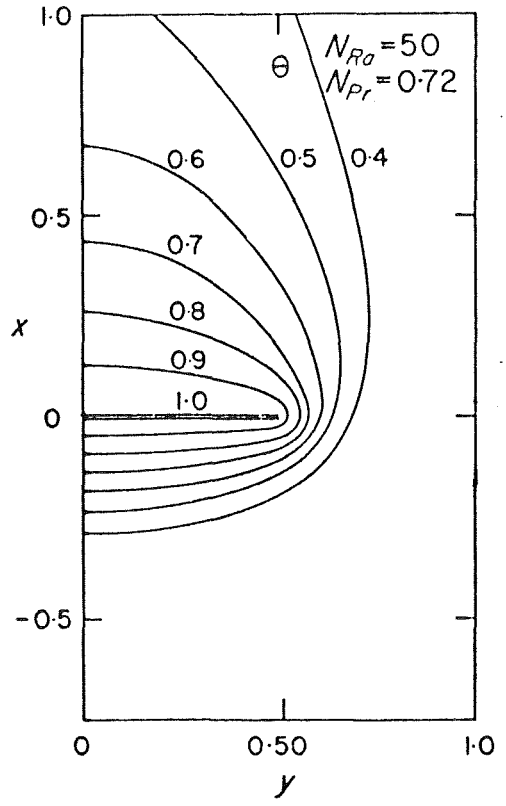

Fig. 8 Temperature field about a heated horizontal flat plate at a Rayleigh number of 50; reference [31]

Table 3 Constants for free convection; equation (27)

	Square Plate*	
	C	n
reference [35] (analytical)	0.89	0.2
reference [34] (experimental)	1.00	0.2
	Circular Plate*	
reference [35] (analytical)	0.79	0.2
reference [36] (experimental)	1.0	0.2
	Infinite Strip*	
references [32] and [33] (analytical)	0.80	0.2

* Heated surface facing downward, influence of side walls neglected.

Flow-visualization experiments with a number of other shapes, with heated surface facing upward, have been reported by Sparrow and Husar [37], but information regarding the interaction between the boundary-layer flow over vertical surfaces and the flow developing over horizontal surfaces, i.e., the top and bottom of boxes or vertical cylinders, is still lacking.

Convection Inside the Balloon; q_i in Equations (14) and (15)

The convection process inside the balloon is important because it determines the temperature, the pressure, and the volume of the lift gas (usually helium). Very little research has been done on convection inside a sphere [39], and none has been done on convection inside cavities resembling the shapes of high-altitude balloons.

The heat-transfer process is free convection. S. W. Churchill showed as early as 1961 [40, 41] that the partial differential equations for the conservation of mass, momentum, and energy can be solved for laminar, natural convection under many different conditions, but so far no solution for the heat transfer inside a balloon has been obtained. Investigations of natural convection in annuli [42] suggest that several types of flow patterns will exist as the temperature difference between the surface and the gas changes during a 24-hr period. It seems likely that in the daytime when the balloon skin is warmer than the gas inside, there would be upward flow near the balloon skin and downward flow in the interior. The reverse would be expected at night. But there could also be situations during the day when gas ascends on the side heated by the sun and descends on the cooler side. As a first approximation, one could use existing solutions for flow in a rectangular cavity heated on two sides as long as the flow is *laminar. But the tremendous size of a balloon makes it very* likely that the flow will be turbulent, except at very small temperature differences.

A semi-empirical analysis [43] suggests that for turbulent free convection over a vertical plate the Nusselt number fits the relation

$$\frac{\bar{h}_c L}{k} = 0.021(\mathrm{Gr}_L\,\mathrm{Pr})^{2/5}$$

at Grashof numbers of the order of 10^{12}, but Clark [44] suggests using a relation of the type

$$\frac{D_g \bar{h}_c}{k_g} = C \left[\frac{\rho_g^2 g(\bar{T}_f - \bar{T}_g) D_g^{\,3}}{T_g \mu_g^2}\,\mathrm{Pr}_g \right]^n \tag{28}$$

with the constants C and n selected from Table 4 and with all physical properties of the gas evaluated at the skin temperature.

Table 4 Free convection inside a sphere; constant C and exponent n for equation (28)

Gr·Pr	C	n	Type of Flow
10^4–10^9	0.59	1/4	laminar
10^9–10^{12}	0.13	1/3	turbulent

In the absence of more concrete information, Dingwell, et al.

[45] used equation (28) for their balloon study, with C and n equal to 0.13 and $^1/_3$, respectively. Equation (28) can then be used to write the rate of heat transfer from the fabric to the gas in the form

$$q_1 = \iint_{S_f} h_i(T_f - T_g)dS_f = \bar{h}_i \pi D_g^2 (T_f - T_g)_{\text{ave}}$$

$$= \bar{h}_i 4.83 V_g^{2/3}(T_f - T_g)_{\text{ave}}$$

$$= 0.628 V_g^{2/3} k_g (\bar{T}_f - \bar{T}_g)\left[\frac{\rho_g^2 g(\bar{T}_f - \bar{T}_g)}{\mu_g^2 T_g}\,\text{Pr}_g\right]^{1/3} \quad (29)$$

Experimental data supporting the form of equation (28) have recently been reported by Ulrich, et al. [46] for the transient condition encountered in filling a cylindrical tank with air at Grashof numbers between 10^8 and 10^{13}. The length-to-diameter ratio of their tanks varied between 0.5 and 2.0 so that their results should indicate what might occur inside a sphere. The experiments showed that during the initial stages of the process the heat-transfer, coefficients were significantly higher than those predicted by turbulent free convection, but after a few seconds agreement with the heat-transfer rate predicted by equation (28) was achieved. Available information on the transient free convection heat-transfer characteristics of vertical surfaces has been summarized by Gebhart in the laminar regime [47].

Radiation Heat Transfer

The radiation heat transfer to and from balloons is important for their performance and determines their short term response and stability. Balloon skins absorb direct and reflected radiation from the sun and radiation emitted by the earth and the atmosphere. Over 99 percent of the solar radiation is in the wavelength range between 0.2 and 4.0 microns, whereas the earth and atmospheric radiation is in the infrared range between 6 and 100 μ, with about 70 percent below 20 μ. Balloon skins are at temperatures of about 480 deg R and thus emit infrared radiation. For approximate calculations the sun and the earth can be considered to be black bodies at 10,000 deg R and 540 deg R, respectively. The direct radiation from the earth and the clouds can be as high as 150 Btu/ft^2-hr [3]. However, the direct solar radiation is collimated and, therefore, the effective receiving area is the projected area, which in the case of a 1-million-cu-ft balloon (equivalent to a 124-ft-dia sphere) would be about 12,100 ft^2. Reflected solar radiation, on the other hand, impinges on the lower half of the total surface area of the balloon, which is about 24,000 ft^2. Earth radiation impinges on the total area of the balloon (about 48,000 ft^2) during ascent through the atmosphere but impinges on only the lower half of the balloon surface after it has risen to an altitude of 70,000 ft, where less than 5 percent of the total air mass remains above. The total direct solar radiation is thus about 5.4×10^6 Btu/hr, and the reflected radiation is about 3.6×10^6 Btu/hr. Infrared irradiation from the earth and the atmosphere can be as much as 7.2×10^6 Btu/hr but at float altitude will be of the order of 2×10^6 Btu/hr. The balloon emits radiation at a rate of $4.8 \times \bar{e}_f \times 10^6$ Btu/hr, where the effective emittance $\bar{e}_f$ may vary between 0.2 and 0.7 for different skin materials. In comparison, convection contributes only about 2×10^5 Btu/hr to the heat transfer over the exterior balloon surface, but it is the only heat-transfer mechanism in the interior because helium is transparent to radiation.

Since the actual amount of radiation absorbed depends critically on the radiation properties of the receiving and emitting surfaces, a knowledge of these properties is very important to the designer. The two most common materials for balloon skins are polyethylene and Mylar, which have (according to available data [48]) an effective absorptance to infrared earth radiation of about 0.12 and 0.17, respectively. The absorptance to infrared earth radiation, which is almost approximately the emittance of the skin, is 0.21 for polyethylene and 0.63 for scrim Mylar (0.5-mil Mylar on dacron scrim). A Mylar balloon absorbs, therefore, a much smaller percentage of its total radiation load from the sun than does a polyethylene balloon, and since it also emits more radiation by virtue of its higher emittance, a Mylar balloon will be cooler than a polyethylene balloon. At the same time, however, because of its high emittance, a change in environmental conditions, e.g., setting of the sun, will reduce the gas temperature in a Mylar balloon more quickly than in a polyethylene balloon and thereby reduce its altitude stability.

In the evaluation of the radiant contribution to the total heat load on balloons and their instrument packages, engineers are faced with a lack of experimental data for the pertinent surface radiation characteristics of the materials used for balloon systems. To calculate accurately the percent of direct solar incident radiation absorbed by a surface, one must know its monochromatic absorptance for radiation of wavelengths between 0.2 and 4.0 μ at various angles of incident radiation [49]. The absorptance of thin films has a strong angular variation; radiation perpendicular to the surface passes through more readily than does radiation at a grazing angle. This angular variation can become particularly important in a balloon system where the radiation incidence angle is zero at sunrise, rises to a maximum at noon, and then decreases again to zero at sunset. For passive temperature control, i.e., the use of surfaces with very different solar absorptances and infrared emittances, the influence of the average incident angle of radiation cannot be ignored.

The difficulty of determining radiation properties for balloon skins is exacerbated by the transparency of these skins, and the transmittance has to be considered [50]. As will be shown, to calculate accurately the radiation heat load on a balloon, one needs to know the total hemispherical emittance of the skin at its temperature, the directional and the angular hemispherical absorptance in the solar spectrum (since surfaces are irradiated directly and indirectly by the sun), the directional reflectances of clouds and terrestrial surfaces in the solar spectrum, and the hemispherical absorptance in the infrared (for the surfaces exposed to the earth or clouds). In 1968 D. K. Edwards summarized the knowledge of the radiative transfer characteristics of materials [51] and surveyed techniques available to measure surface properties [52].

It does not seem feasible to measure spectral-angular surface properties for all potentially useful materials. The amount of data would be unmanageable, and the cost with present equipment would be unreasonably high. It would, therefore, be desirable to classify materials according to their physical surface properties and to develop working relationships to estimate "effective" angular properties from measurements of a few select properties. One should also know the influence on the radiation surface properties of launch procedures, aging, solar radiation, and atmospheric phenomena so thermal predictions can be made not only for idealized laboratory samples but also for actual operational systems.

The life of a balloon depends critically on the relationship between the amount of radiant energy absorbed during the day and the amount of radiant energy lost at night. In the morning the balloon is usually at the lowest float altitude because the gas is at its lowest temperature. After sunrise the gas is warmed by transient free convection from the skin, after the skin has been warmed by the absorption of solar radiation. The part of the skin exposed to the sun transfers heat by transmission and internal emission to the rest of the skin. As the temperature of the gas increases, the buoyancy of the balloon also increases and the system begins to rise. This rise will continue until shortly after sunset, whereupon the net loss of energy exceeds the net input of energy, and the balloon begins to sink. Presently the total balloon heat balance over a 24-hr period shows a small loss in internal energy.

One of the long-range objectives of balloon designers is a system which will passively maintain its average float altitude, i.e., for which the net change in lifting gas internal energy over a 24-hr

period is zero. Various schemes to achieve a zero net change have been tried without success. But even if a "permanent balloon" is not possible, increased balloon lifetime and altitude stability would materially contribute to programs aimed at permitting long-term weather prediction and eventual weather control.

At altitudes below 70,000 ft the radiation incident on a balloon is subject to considerable variation, and quantitative estimates are uncertain. The amounts of infrared irradiation from below and from above will differ and will both depend on the weather and the cloudcover. The incident solar radiation will also depend on the altitude and the clouds. At altitudes over 70,000 ft a balloon is above the weather and receives nearly all of its infrared radiation from below. Under these conditions the infrared radiation heat load can be estimated with considerably more confidence. Fortunately, large balloons are generally launched in good weather so that changes in cloud cover during ascent are minimized.

Although measurements of upward and downward radiation in the atmosphere have been made for many years, accurate evaluation of rapid changes in radiation flux are unreliable because it is not possible to predict local weather changes in advance. One could, however, coordinate weather observations and particular types of clouds and their altitude, with radiation heat flux calculations. Calculations based on recent observations made at ESSA by Dr. P. M. Kuhn [53] clearly correlate changes in the radiation flux with cloud cover. Application of available knowledge of atmospheric radiation to balloon performance will, however, require close cooperation between meteorologists, cloud physicists, and engineers.

For small packages used on superpressure balloons at intermediate altitudes, an engineering analysis of the thermal control problem and a summary of the experience gained in several flights by NCAR have been presented by Litchfield and Carlson [30]. The basic problems of temperature control at float altitude are quite similar to those encountered in spacecraft. In space, where only radiation can transfer heat, the equilibrium temperature T developed by an opaque body subjected only to direct solar radiation at the rate G_s over a projected surface area S_s normal to the sun, having an averaged directional absorptance per unit projected area $\bar{a}_{s,\text{ave}}$ and a surface area S with an average hemispherical emittance in the infrared $\bar{e}_{H,i}$ is $T = (\bar{a}_{s,\text{ave}} G_s S_s / \sigma \bar{e}_{H,i} S)^{1/4}$, which shows that the ratio of the absorptance in the solar spectrum to the emittance in the infrared controls the equilibrium temperature.

In the balloon packages the heat-transfer problem is more complicated than for spacecraft because of the addition of reflected solar radiation, convection, and the influence of the atmospheric radiation, all of which depend strongly on the cloud cover and the weather. In daytime flights, the temperature can be controlled by proper treatment of the surface of the package. The properties of a number of materials and surface coatings for such use are presented in references [54–57]; Table 5 presents a typical selection. Silver sulfide, which has an average infrared emittance of only 0.03 and an average solar absorptance of 0.60, has been used successfully in balloon packages for which a temperature of from 44–60 deg F was desirable. A further increase in temperature during the day was achieved by covering the package with a thin film of material such as Mylar which is transparent to radiation only in the solar spectrum between 0.2 and 3.0 μ but has a large reflectance for infrared radiation. This method of trapping the radiation, sometimes called the greenhouse effect, should be used with caution because it can easily result in an excessive temperature rise during the middle of the day.

For nighttime balloon flights, energy must be stored to maintain the internal temperature of the flight package. A simple energy reservoir is water; 42 watt-hr of energy per pound of water is released when it freezes. In addition, as water is cooled to its freezing point, 0.3 watt-hr of energy is released for each pound of water cooled 1 deg F. Table 6 compares the energy-storage capacity of water with that of zinc-air and silver-zinc batteries. The batteries have greater energy-storage capacity than water, but zinc-air batteries require more oxygen at balloon float altitudes, and water is cheaper and easier to handle.

Table 5 Radiative characteristics of surfaces

Material	IR Emittance	Solar Absorptance	$\bar{a}_s/\bar{e}_i$ Ratio
Silver (polished)	0.02	0.07	0.28
Platinum	0.05	0.10	0.50
Aluminum	0.08	0.15	0.53
Nickel	0.12	0.15	0.80
Stellite	0.18	0.30	0.60
Aluminum paint	0.55	0.55	1.00
White lead paint	0.95	0.25	3.80
Zinc oxide paint	0.95	0.30	3.20
Gray paint	0.95	0.75	1.26
Black paint	0.95	0.95	1.00
Lamp black	0.95	0.97	0.98
Silver sulfide*	0.03	0.60	0.05
Nickel black*,[1]	0.10	0.90	0.11
Cupric oxide*,[1]	0.15	0.90	0.16

* These are special surfaces where a metal is covered with a very thin layer of absorbing material. The layer is so thin that it is a fraction of a wavelength thick in the infrared and is, therefore, almost transparent to IR. The result is that the IR emissivity is nearly that of the underlying metal. However, the thickness is large compared to the wavelength of the maximum solar spectrum so the absorptivity is large for solar radiation.

[1] H. Tabor, *Solar Energy*, September, 1961.

Table 6 Energy storage capabilities of water and batteries

	w-hr/lb	w-hr/kg	w-hr/in.
Water (heat of fusion)	50	110	1.7
Water (per °C)	0.63	1.38	0.0225
Zinc-air	80	176	5
Lead-acid	11	24.2	1.2
Nickel-cadmium	8	17.6	0.4
Silver-cadmium	35	77.0	3.5
Silver-zinc	55	121	4.5

For flights lasting several days, the package must be able to absorb as much heat during the day as it loses during the night. With suitable black paint daytime surface temperatures of +6 to 10 deg F can be attained; but since a typical nighttime surface temperature is −67 deg F, it is necessary to achieve a daytime surface temperature of about 130 deg F to maintain temperature equilibrium in the water. This requires the use of special coatings, such as silver sulfide, or the use of one or more greenhouse covers. One can also use solar cells to generate energy within the package during the day, but this adds weight and complicates the system.

Emitted Radiation; q_5 in Equation (15)

The balloon fabric, polyethylene or Mylar, transfers heat to the atmosphere by infrared radiation. A typical Mylar balloon fabric (0.35-mil-thick Mylar with Dacron scrim, 4 × 6 strands per inch) has an average transmittance of about 0.55 at its operating temperature, an average reflectance of about 0.20, and an average absorptance of about 0.25. A typical polyethylene film has an average absorptance of 0.20, an average reflectance of only 0.05, and an average transmittance of 0.75. However, the monochromatic properties of fabric materials vary considerably. Mylar, for example, has radiation windows with transmittances as high as 0.80 for wavelengths between 3 and 6 μ and opaque ranges with transmittances as low as 0.10 for wavelengths between 13 to 15 μ [59].

To calculate the emitted radiation it is necessary to know the spectrally averaged hemispherical emittance in the infrared region. The evaluation of an average hemispherical emittance for

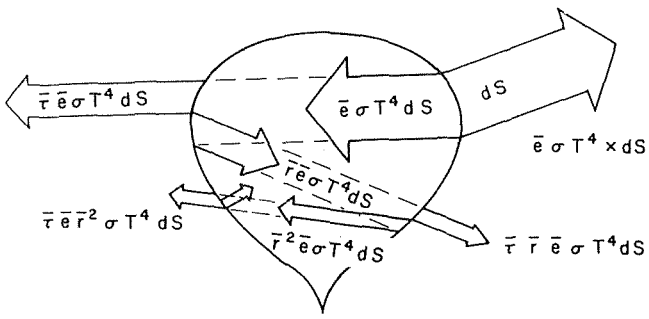

$$E_f = \int_S \int_0^\infty e_H(\lambda)\,\sigma\,T^4\,dS\,d\lambda \simeq \bar{e}_H\,\pi D_g^2\,\sigma\,T_f^4$$

$$Q_{total} \simeq \bar{e}_H\,\pi\,D_g\,\sigma\,T_f^4\left[1+\bar{e}\,\bar{\tau}(1+\bar{r}+r^2+\ldots\ldots)\right]$$

Fig. 9 Emission of radiation from a balloon skin—the effective emittance

a given wavelength range or a given temperature offers no difficulties for an opaque surface [51, 55, 58]. As shown in Fig. 9, however, a surface element of a balloon skin dS radiates not only directly into space, but also into the interior where radiation can pass through the fabric into space, can be reflected from the interior surface of the balloon fabric, or can be absorbed by the fabric. To calculate accurately the "effective emittance" of a balloon from data on the surface radiation properties of its fabric skin, bidirectional values of the monochromatic emittance, absorptance, and reflectance of the interior surface would have to be known for the infrared wavelengths between 6 and 100 μ [51]. Such measurements are difficult and are generally too expensive. For balloon design it would actually be much more desirable to measure the actual emittance of a spherical sample of the fabric material filled with helium. However, no such data have as yet been taken, and calculations have been based on a model proposed by Germeles [8]. This model assumes that the inner fabric surface obeys Lambert's law, i.e., it emits and reflects diffusely. It also assumes that average values can replace the spectrum of values for the emittance, absorptance, and reflectance of the inner surface over the wavelength range (between 6 and 20 μ) for which data are available [59]. The net rate of emission from the entire balloon is then equal to the radiation directly emitted from the outer surface, $\bar{e}_i\pi D_b^2\sigma T_f^4$, plus that portion of the radiation emitted by the interior surface which eventually passes through the fabric, $\bar{e}_i\bar{\tau}_i\pi D_b^2\sigma T_f^4(1+\bar{r}_i+\bar{r}_i^2+\ldots)$. By summing these series, one obtains the effective emittance of the fabric

$$\bar{e}_{effective} = \bar{e}_i[1+\bar{\tau}_i(1+\bar{r}_i+\bar{r}_i^2\ldots)$$

$$= \bar{e}_i\left(1+\frac{\bar{\tau}_i}{1-\bar{r}_i}\right) = \bar{e}_i\left(2-\frac{\bar{a}_i}{1-\bar{r}_i}\right) \quad (30)$$

where

$$\bar{a}_i = \int_6^{100} a(\lambda)I(\lambda)d\lambda \Big/ \int_6^{100} I(\lambda)d\lambda \quad (31a)$$

$$\bar{r}_i = \int_6^{100} r(\lambda)I(\lambda)d\lambda \Big/ \int_6^{100} I(\lambda)d\lambda \quad (31b)$$

$$\bar{\tau}_i = 1-\bar{r}_i-\bar{a}_i \quad (31c)$$

$$\bar{e}_i(T_f) = \bar{a}_i(T_f) \quad (31d)$$

Use of the effective emittance gives the rate of heat transfer from the balloon fabric in the form

$$q_5 = 4.83\bar{e}_{eff}V_g^{2/3}\sigma\bar{T}_f^4 \quad (32)$$

where $\bar{T}_f^4$ is the average of the fourth power of the absolute temperature of the balloon fabric.

The infrared hemispherical emittance of the surface of an opaque body can be measured easily so that the determination of the radiation emitted by the surface of a balloon instrument package generally offers no problem.

Direct Solar Radiation; $q_{2,d}$ in Equation (15)

The solar radiation spectrum has been investigated in great detail, and summaries of the current state of knowledge are presented in references [9, 54]. Fig. 10 shows the solar spectrum at the outer fringes of the atmosphere and at the surface of the earth after attenuation and absorption by the atmosphere. Over 99 percent of the solar energy is contained within a narrow wavelength band between 0.2 and 4 μ, and for most engineering heat-transfer calculations the sun's spectrum can be approximated by that of a black body at 10,600 deg R. The solar constant, i.e., the radiation received by a surface placed perpendicular to the rays

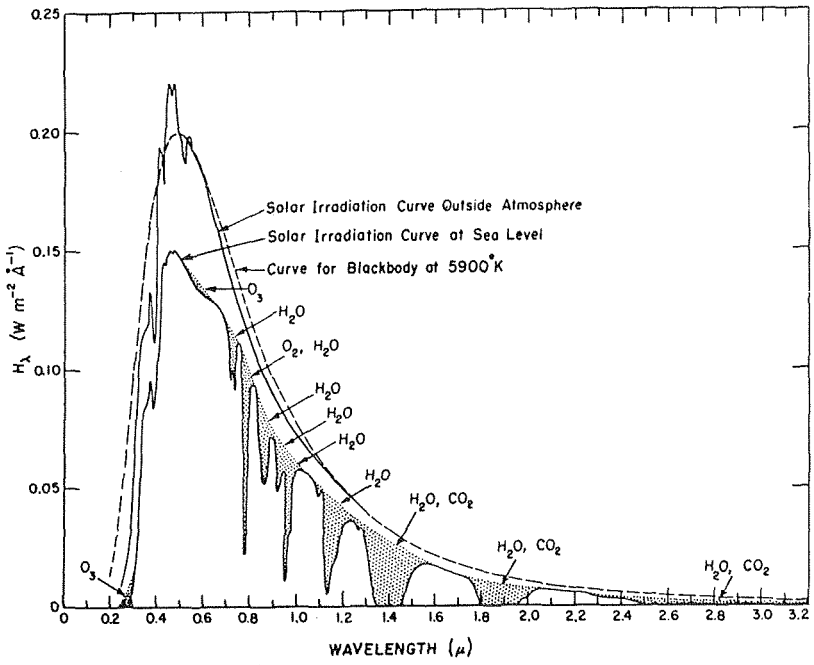

Fig. 10 Spectral distribution of solar radiation in space and at sea level; reference [9]

of the sun outside the earth's atmosphere, is 2.0 cal/cm²-min, or 442 Btu/ft²-hr. The solar radiation per unit area on a horizontal surface outside the earth's atmosphere depends only on the zenith angle, i.e., the angle between the normal to the surface and the rays of the sun. This angle can be determined from the relation

$$\cos \zeta = \sin \lambda \sin \sigma_s + \cos \lambda \cos \sigma_s \cos h \tag{33}$$

As shown in detail in references [58, 60], the radiation per unit area on a surface which is tilted at an angle τ to the horizontal is

$$\bar{G} = \bar{G}_s \cos \zeta \cos \phi \tag{34}$$

where

τ = angle between the surface and the horizontal
α = westward declination (measured from the south meridian) of the projection on the earth's surface of the normal to the surface
$\cos \phi = \cos (A_z - \alpha) \cos (90 - \zeta) \sin \tau + \sin (90 - \zeta) \cos \tau$
λ = latitude
σ_s = solar declination
h = local hour angle
A_z = azimuth of the sun, measured westward from the south meridian
$\bar{G}_s$ = average incident solar radiation

Once the angle between the sun and the surface, i.e., $(\zeta - \tau)$, is known the solar radiation absorbed by a surface outside the atmosphere is simply $\bar{a}_s(\zeta - \tau)G_i$, where $\bar{a}_s(\zeta - \tau)$ is the effective directional absorptance for that angle.

In passing through the atmosphere, the intensity and spectrum of the solar energy are altered by absorption and scattering [61]. Therefore, the radiation on an object is strongly dependent on the atmospheric path length of the solar rays, usually expressed in terms of the "optical air mass." Exact calculations of the attenuated spectrum are quite cumbersome [61, 62], and for engineering purposes such calculations are only useful when the directional absorptances of the receiving surfaces are known [63, 64]. Fig. 11 shows the distribution of direct solar radiation incident at sea level on a horizontal surface, as a function of wavelength, for several short paths corresponding to optical air masses between 1.0 and 8.0. The optical air mass is unity when the sun is directly overhead and the body receiving radiation is on the earth's surface. Under these conditions only 70.2 percent of the solar constant is received. For other values of optical air mass (m), the fraction of solar radiation received is expressed to within 3 percent accuracy [8] by the empirical relation

$$\frac{\bar{G}_{s,z}}{\bar{G}_{s,0}} = 0.5(e^{-0.65m} + e^{-0.095m}) \tag{35}$$

where the optical air mass depends on the altitude and the sun's zenith angle ζ. The variation of the optical air mass at sea level with zenith angle, $m(0, \zeta)$, is given in Table 16–18 of reference [9] and can be closely approximated [8] by the relation

$$m(0, \zeta) = [1229 + (614 \cos \zeta)^2]^{1/2} - 614 \cos \zeta \tag{36}$$

for $0 < \zeta < 90$ deg. Since the attenuation is proportional to the number of air molecules in the path, for a given zenith angle the optical air mass at altitude z can be related approximately to the air mass at sea level by the relation

$$m(z) = m(0)[\rho(z)/\rho(0)] \tag{37}$$

Using equations (33)–(37) one can determine radiation on a surface at any altitude, geographical location, and time between sunset and sunrise. There are two short periods

$$90 \text{ deg} < \zeta \leq 90 \text{ deg} + \cos^{-1}\left[\frac{D_{\text{earth}}}{D_{\text{earth}} + 2z}\right]$$

before sea-level sunrise and after sea-level sunset during which a balloon also receives solar radiation. A method for determining the air mass during these periods is presented in reference [8], but for most purposes it is sufficiently accurate to double the value of the air mass calculated at sea-level sunrise or sunset.

The portion of the solar radiation absorbed at the surface of an opaque body, such as an instrument package, can be calculated once the relative position between the sun and the surface is

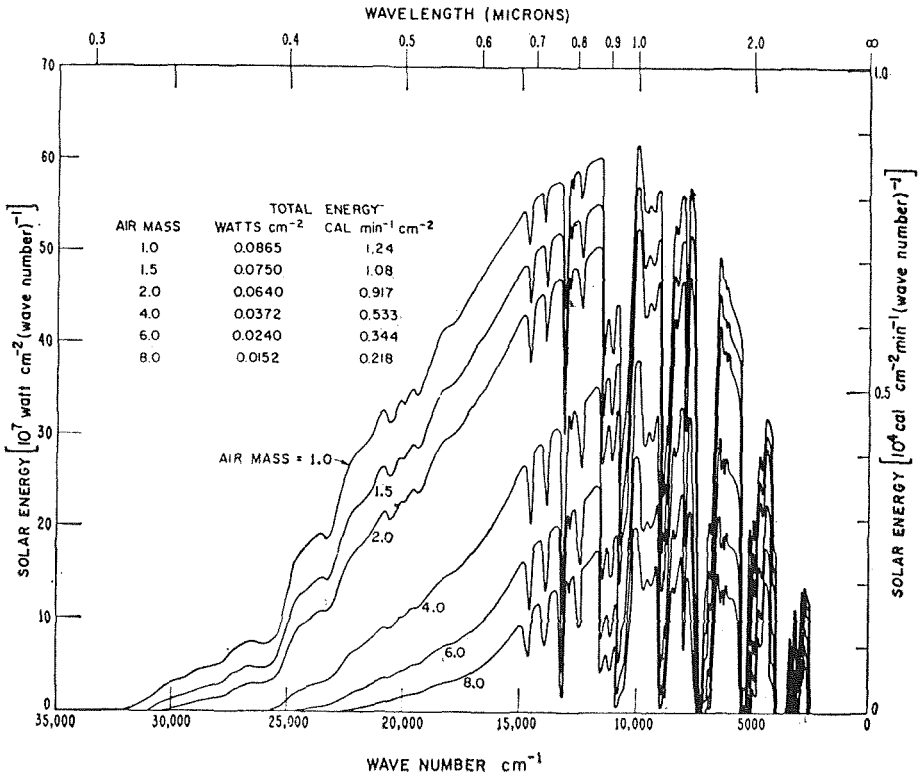

Fig. 11 Spectral distribution of solar radiation incident at sea level for air masses 1.0 to 8.0; reference [61]

known. The amount of the incident radiation absorbed per unit area is

$$q_{\text{absorbed}} = \int_{0.2}^{4} a(\zeta - \tau, \lambda)G(\lambda, z)d\lambda = \bar{a}_s(\zeta - \tau)\bar{G}(z) \quad (38)$$

However, as mentioned previously, the problem is more complicated for the balloon because the skin is transparent, and a portion of the incident solar radiation is absorbed, a portion reflected, and the rest transmitted into the interior where some of the radiation transmitted on the first pass will be absorbed as a result of internal reflection and absorption.

Except for occasional measurements in connection with basic investigation of radiation [51, 63], only Dingwell [59] has attempted to make systematic measurements of the radiation properties of balloon fabrics. Since balloon skins are transparent, absorptances are difficult to measure directly. Dingwell measured, therefore, the monochromatic transmittance of solar radiation using a Beckman D.K. spectrophotometer. The reflectance was then estimated by observing interference fringes caused by internal reflections and applying Fresnel's formula for normal incidence. Finally, the monochromatic absorptance for incident radiation, presumably normal to the surface, was calculated from the relation

$$a(\lambda) = 1 - r(\lambda) - \tau(\lambda) \quad (39)$$

and the integrated normal absorptance of the fabric over the solar spectrum was determined by numerical integration of the relation

$$\bar{a}_s \text{ (normal)} = \int_{0.2}^{4.0} a(\lambda)I(\lambda)d\lambda \Big/ \int_{0.2}^{4.0} I(\lambda)d\lambda \quad (40)$$

No measurements have yet been made of the effect of the angle of incidence of solar radiation on the radiation properties of balloon films. D. K. Edwards [64] has shown, however, that predicted equilibrium temperatures can be as much as 40 deg F in error if the angular dependence of radiation characteristics is neglected, and it would be desirable to measure the directional absorptance, $a(\theta, \phi, \lambda, T)$, for some typical materials.

To estimate from available information the percent of the solar radiation actually absorbed by the skin of a balloon, it will be assumed that the absorptance of the skin is independent of the angle of incidence and that radiation transmitted through the skin emerges diffusely from the interior surface. Furthermore, the shape of the balloon will be idealized as a sphere so that the projected area is $\pi D_g^2/4$. The fraction of the incident solar energy absorbed on the first pass is $\bar{\alpha}_s G(z)\pi D_g^2/4$, and the fraction transmitted is $\bar{\tau}_s G(z)\pi D_g^2/4$. Of the fraction transmitted, $\bar{\alpha}_s$ will be absorbed by the fabric and $\bar{r}_s$ will again be reflected. The total amount of the incident solar radiation eventually absorbed, obtained by summing this series of inter-reflections, will be

$$q_{2,d} = G(z)(\pi D_g^2/4)\bar{a}_s\left[1 + \frac{\bar{\tau}_s}{1 - \bar{r}_s}\right] \quad (41)$$

or in terms of the gas volume in the balloon

$$q_{2,d} = G(z)1.21V_g^{2/3}\bar{a}_s\left[1 + \frac{\bar{\tau}_s}{1 - \bar{r}_s}\right] \quad (42)$$

The zenith angle ζ can be defined in a time coordinate system related to the flight of the balloon. If at time of launch the Greenwich hour angle is GHA, then at any subsequent time t the hour angle is

$$\delta_h = \text{GHA} - \lambda + (t/240) \quad (43)$$

where GHA and the latitude λ are in degrees and t is in seconds.

Reflected Solar Radiation; $q_{2,r}$ in Equation (15)

Until recently, the heat load of greatest uncertainty in equation (15) was the reflected solar radiation. It was known from an overall heat balance that the portion of the solar radiation reflected by the earth and its atmosphere, the albedo, when averaged over time and space, was about 34 percent [65]. It was also known from balloon and aircraft observations that the albedo can vary widely, but no accurate long-term measurements could be made without an observation station outside the atmosphere. The early measurements of Explorer VII and several Tiros satellites resulted in data for only a portion of the globe because these satellites were not in polar orbits. In 1967 and 1968, however, the meteorological satellite Nimbus II measured the incoming and outgoing radiation over the entire globe for several weeks, and Dr. E. Raschke of the Goddard Space Flight Center correlated the results and presented them in convenient graphs [65][2]. These results are very useful for estimating the reflected solar radiation above the atmosphere at the geographic locations

[2] According to a private communication all the curves in reference [65] are shifted by 2.5 deg due to a drafting error.

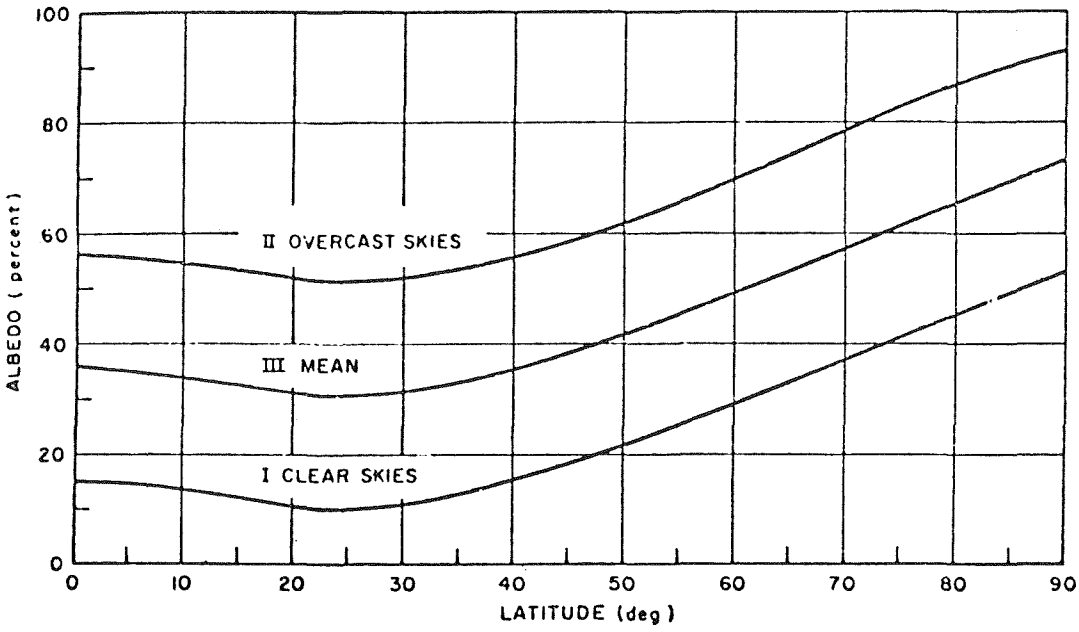

Fig. 12 Albedo as a function of latitude under various sky conditions; reference [54]

Table 7 Relative spectral distribution of albedo radiation under various sky conditions

λ (μ)	R_λ* Clear Skies	Mean	Overcast Skies	λ (μ)	R_λ* Clear Skies	Mean	Overcast Skies
0.29	0	0	0	0.53	0.378	0.668	0.807
0.30	0.882	0.721	0.477	0.54	0.252	0.663	0.812
0.31	0.892	0.761	0.534	0.55	0.333	0.637	0.795
0.32	0.848	0.749	0.553	0.56	0.312	0.615	0.770
0.33	1.000	0.920	0.705	0.57	0.288	0.590	0.752
0.34	0.858	0.813	0.648	0.58	0.276	0.581	0.748
0.35	0.815	0.802	0.661	0.59	0.262	0.563	0.734
0.36	0.744	0.746	0.634	0.60	0.241	0.541	0.717
0.37	0.768	0.796	0.700	0.70	0.134	0.396	0.554
0.38	0.671	0.714	0.632	0.80	0.084	0.293	0.425
0.39	0.575	0.624	0.570	0.90	0.057	0.224	0.331
0.40	0.758	0.840	0.772	1.00	0.042	0.179	0.266
0.41	0.781	1.000	0.950	1.10	0.028	0.149	0.219
0.42	0.790	0.937	0.925	1.20	0.019	0.118	0.181
0.43	0.675	0.835	0.835	1.30	0.017	0.095	0.145
0.44	0.708	0.908	0.934	1.40	0.015	0.076	0.115
0.45	0.734	0.958	1.000	1.50	0.013	0.063	0.093
0.46	0.649	0.892	0.960	1.60	0.010	0.051	0.078
0.47	0.713	0.864	0.954	1.70	0.008	0.042	0.063
0.48	0.563	0.834	0.935	1.80	0.006	0.034	0.052
0.49	0.487	0.749	0.853	1.90	0.005	0.029	0.045
0.50	0.452	0.727	0.840	2.00	0.005	0.025	0.037
0.51	0.422	0.697	0.825	4.00	0.000	0.002	0.028
0.52	0.378	0.650	0.780				

* R_λ = the ratio of the spectral irradiance at wavelength λ to the spectral irradiance at the wavelength of maximum intensity.

scanned by Nimbus II, but they cover only a limited period and do not indicate variations with weather or with direction.

The works of Houghton [66] and Fritz [67] are, therefore, still very useful for engineering design. The former established a convenient graph for the approximate albedo as a function of latitude for clear, partially overcast, and completely overcast skies (see Fig. 12). Although these curves were designed for conditions above the atmosphere, they also will give approximate results for balloons in the atmosphere as long as the sky above is not completely overcast. The accuracy of the method, which is very good for altitudes above 50,000 ft, depends upon the altitude and the amount of cloud cover. From the work of Fritz [67] and Coulson [68] an estimate of the spectrum of the reflected solar radiation can be made. Table 7 presents the results [54] as the ratio of the solar radiation received from below at a wavelength λ to the radiation at the wavelength of maximum intensity for three sky conditions. The reflected solar radiation incident on a satellite or a balloon from a surface element of the earth-atmosphere dS_e (see Fig. 13) is

$$dG_s = (\pi D_b^2/4) G_s r_s(\theta, \zeta) \cos\theta \cos\zeta dS_e / l_{s-b}^2 \qquad (44)$$

where

G_s = solar radiation incident on dS_e
$r_s(\theta, \zeta)$ = the bidirectional reflectance of dS_e for a zenith angle ζ in the direction of the balloon, θ
l_{s-b} = the distance between the balloon and dS_e

For a known geographical distribution of $r_s(\theta, \zeta)$, the reflected radiation can be calculated numerically. If one assumes that the earth-atmosphere system reflects uniformly and diffusely, equation (44) can be approximately integrated [72] over the portion of the earth visible from the balloon, and the radiation heat load due to albedo reflection $q_{2,r}$ becomes

$$q_{2,r} = (\pi D_g^2/4) \bar{a}_s G_{\text{solar}} [2\bar{r}_{s,a}(1 - \sqrt{z/D_e}) \cos\theta_s] \qquad (45)$$

where

G_{solar} = solar constant (442 Btu/ft²-hr)
$\bar{a}_s$ = average effective absorptance of the skin in the solar spectrum
$\bar{r}_{s,a}$ = average hemispherical albedo of the earth atmosphere for a given zenith angle

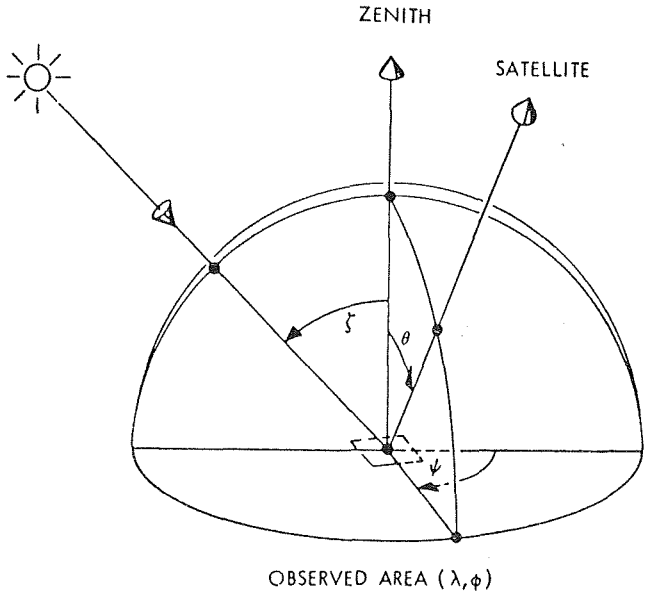

Fig. 13 Satellite or balloon to earth geometric configuration

z = altitude of the balloon
D_e = earth diameter (7920 miles)
θ_s = angle between a vertical line through the balloon and the earth's center and a line through the earth's center and the sun.

When a part of the atmosphere below a balloon is covered by clouds and the rest is clear, the reflection from below will not be uniform. In such a situation one can improve the accuracy of the calculations by dividing the visible earth-atmosphere system into areas of uniform, but not equal, reflection. Assuming that each area reflects diffusely, one can approach this problem by means of shape-factor algebra [58, 69, 70] just as in calculations of radiation between two diffuse surfaces.

Although the atmospheric layers are curved, one can approximate the atmosphere and the clouds below the balloon by a flat surface without introducing an appreciable error. The shape factor between a small sphere dA_1 and a plane rectangle A_2 with the

Table 8 (Adopted from reference [77]) Mean values of thickness, albedo reflectance, and absorptance as well as constants b_1 and b_2 for various cloud types

	Mean albedo reflectance $\bar{r}_t$	Mean absorptance $\bar{a}_t$	Mean thickness t (meters)	b_1 ($\times 10^{-4}$m^{-1})	b_2 ($\times 10^{-4}$m^{-1})
Low cloud	0.60	0.07	450	21.9	4.5
Middle cloud	0.48	0.04	600	10.5	1.8
High cloud	0.21	0.01	1700	1.2	0.15
Nimbostratus	0.70	0.10	4000	4.2	0.78
Cumulonimbus	0.70	0.10	6000	2.8	0.52
Stratus	0.69	0.06	100	155	16.8

$\bar{r}_t = r_\infty (1 - e^{-b_1 t})$
Value of $\bar{r}_t$ corresponds to mean thickness
$\bar{a}_t = a_\infty (1 - e^{-b_2 t})$
Value of $\bar{a}_t$ corresponds to mean thickness

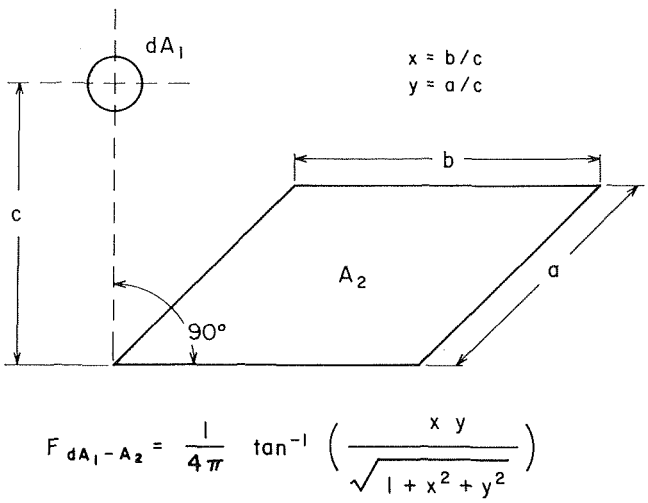

Fig. 14 Shape factor for small sphere and rectangular area

sphere located at one corner of a rectangle that has a common side with A_2 (see Fig. 14) is

$$F_{dA_1 - A_2} = \frac{1}{4\pi} \tan^{-1} \frac{xy}{\sqrt{1 + x^2 + y^2}} \tag{46}$$

where $x = b/c$ and $y = a/c$.

The reflectance of various types of clouds can be estimated from Table 8 in conjunction with the relation [79]

$$r_t = r_\infty (1 - e^{-b_1 t}) \tag{47}$$

where

r_t = reflectance of cloud of thickness t
r_∞ = reflectance of cloud of infinite depth
t = cloud thickness in meters
b_1 = constant whose value depends on liquid water content or cloud type

An approximate method, sufficiently accurate for most purposes, is to assume that (1) the atmosphere ends at the intersection of a straight line between the balloon and the horizon and (2) the atmospheric surface below the balloon is flat.

As x and y approach infinity, the shape factor for radiation between a sphere and an infinitely large plane approaches $\pi D_g^2/2$, which is larger by a factor of $(1 - \sqrt{4z/D_{\text{earth}}})$ than the correct value between a small and a large sphere. At an altitude of 20 miles the error would be about 10 percent. A calculation taking the curvature into account is presented by Cunningham [69].

Data from which the geographic distribution of reflected solar radiation above the atmosphere can be calculated were gathered

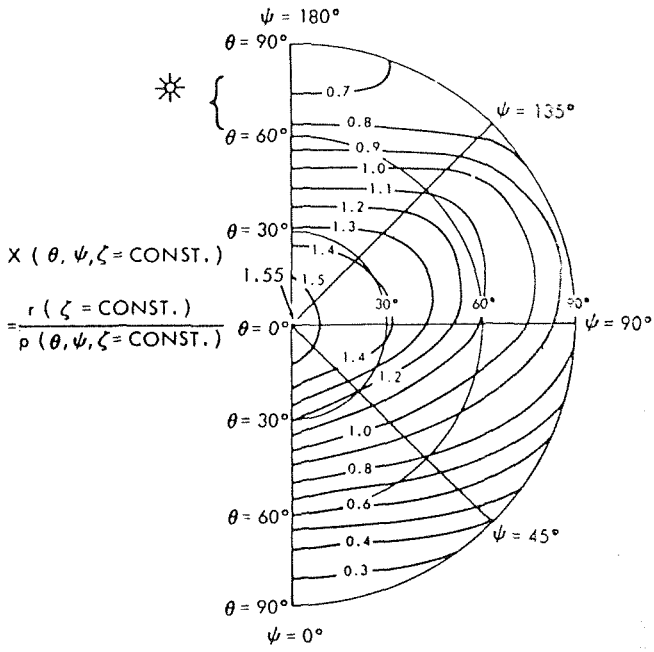

Fig. 15 Variation of directional solar reflectance with position of receiver at low sun angles; reference [65]

by the Nimbus II meteorological satellite, which was launched May 16, 1966, and remained in a polar, synchronous, circular orbit at a mean altitude of 1140 km until July 28, 1966. Its orbital period was 108.6 min, and during its 13 daily orbits the entire globe could be observed day and night. Reflected solar radiation in the wavelength range between 0.2 and 4 microns and the earth-emitted long-wave radiation between 5 and 30 microns were measured with a radiometer. Details of the data reduction and instrumentation are presented by Raschke [65]. In the following, only the application of the averaged data to the evaluation of the reflected solar radiation will be discussed.

Using the parameters defined in Fig. 13, the solar radiation reflected from a surface element dS_e depends on the location of dS_e on the globe, the time of year, the weather conditions (primarily the cloud cover and the zenith angle of the sun). The total hemispherical radiation reflected from dS_e will be

$$q_{\text{reflected}} = \int_0^{2\pi} \int_0^{\pi/2} I_s^-(\theta, \psi) \sin\theta \cos\theta d\theta d\psi \tag{48}$$

where I_s^- is the intensity of the reflected solar radiation and θ and ψ are the polar and azimuthal angles of measurement, respectively. Since the intensity of radiation reflected from the earth-atmosphere system depends on θ, ψ, and ζ[1] (the instantaneous

zenith angle of the sun), ρ^1, the *instantaneous bi-directional* reflectance of the area element dS_e at latitude λ and longitude Φ, can be defined as

$$\rho^1(\theta, \psi, \zeta^1, \lambda, \phi) = \frac{I_s^-(\lambda, \phi)}{\cos \zeta^1 I_s^+} \tag{49}$$

where I_s is the instantaneous direct intensity of the direct solar radiation incident on dS_e.

The hemispherical directional reflectance $r(\zeta)$ is the ratio of the total reflected solar radiation (as would be received by a black hemisphere placed over dS_e) to the incoming solar radiation. It depends only on the zenith angle ζ and the time of year. From airplane and balloon measurements Raschke prepared diagrams relating the ratio between the directional hemispherical reflectance (r) and the bi-directional reflectance ($\rho^1 = \rho/\pi$) at various azimuthal angles within relatively narrow ranges of the zenith angle. Fig. 15 shows one of these diagrams in which isolines of $x = r/\rho$ are drawn as functions of θ and ψ for a range of solar zenith angles between 60 and 80 deg. With the aid of these intermediate approximations Raschke calculated the hemispherical directional reflectance from the Nimbus II data and presented his results as maps of the average albedo of the earth-atmosphere system during a two-week period [65]. Fig. 16 shows such a map for the Northern Hemisphere during the period July 16–28, 1966. The albedo varies from 20–30 percent over coastal parts of the North American continent to 60 percent over Greenland and the Sahara Desert.

In addition to the albedo maps, Raschke also presented a correlation of available data showing the variation of the directional hemispherical reflectance with zenith angle (Fig. 17) and the ratio between the directional hemispherical reflectance and the bi-directional reflectance at various azimuth angles for snow, stratocumulus clouds, and cloudless ocean areas. With the aid of these diagrams one can make predictions of the reflection at altitudes above 50,000 ft. Such predictions are quite accurate except when there are changes in cloud cover. For engineering design it is usually satisfactory, however, to use equation (45) in combination with the graph in Fig. 17 relating the average hemispherical reflectance to the zenith angle, which can be calculated using equation (43) in a time coordinate system related to a balloon flight.

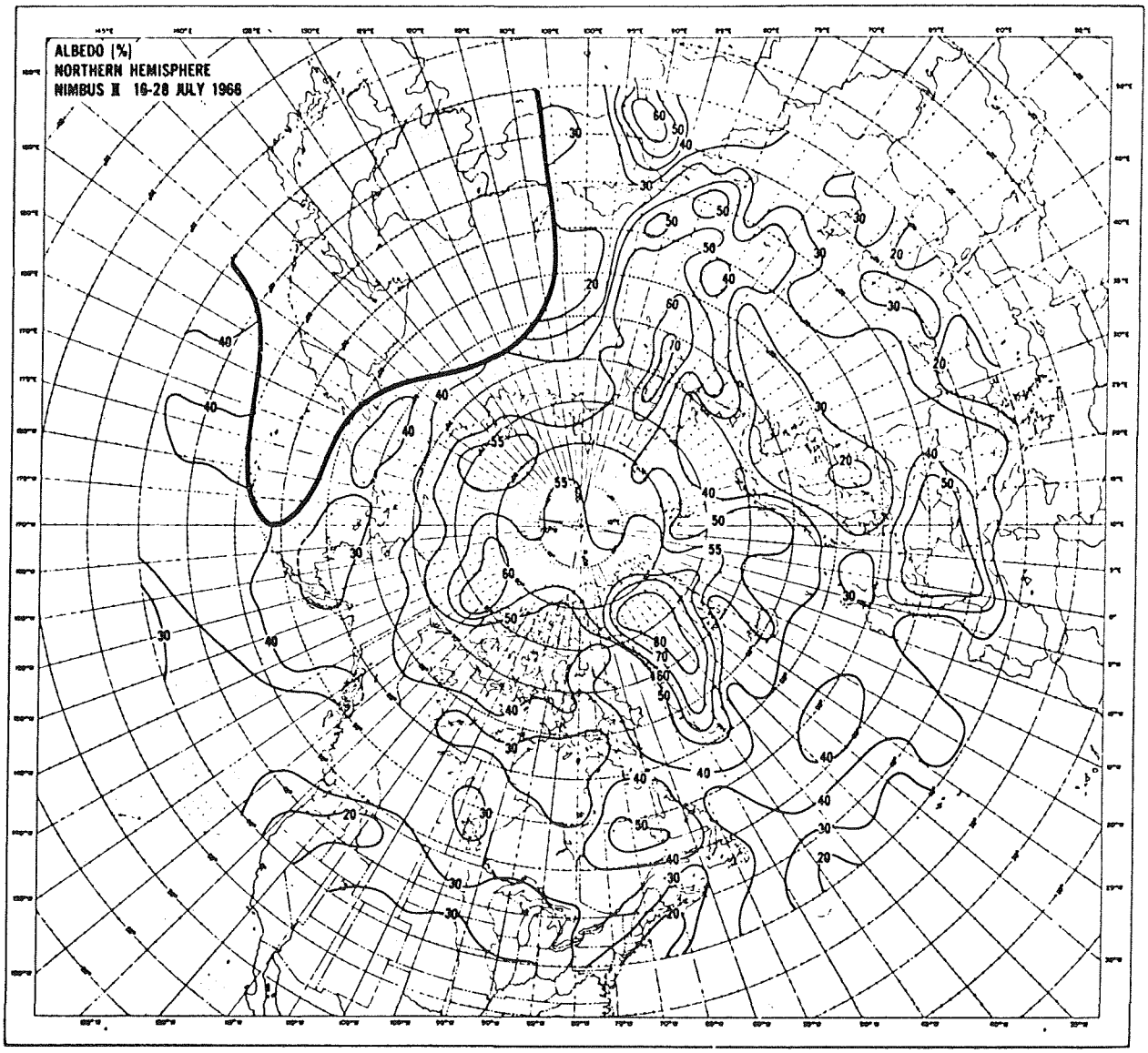

Fig. 16 Albedo map for the Northern Hemisphere during July 16–28, 1966; reference [65]

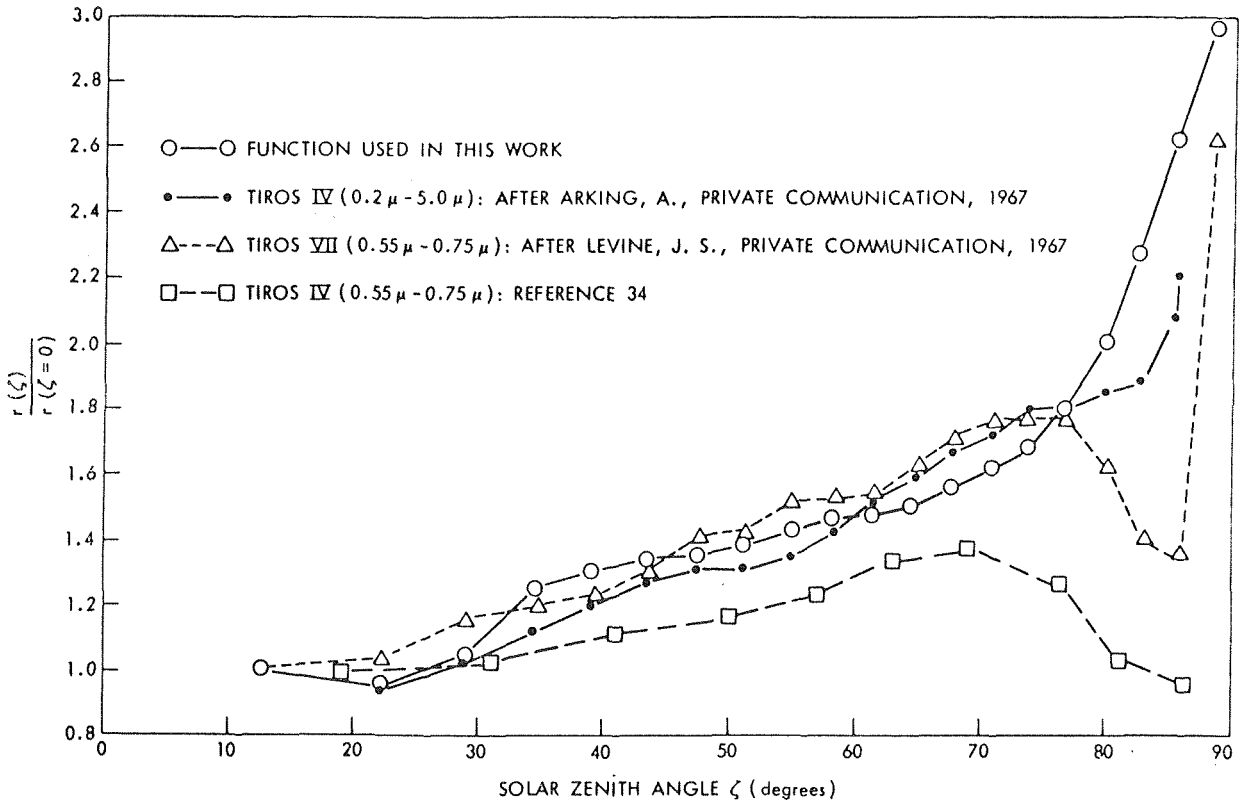

Fig. 17 Variation of directional solar reflectance with zenith angle; reference [65]

Infrared Radiation From the Earth and the Atmosphere; q_3 in Equation (15)

The contribution to the total heat load on a balloon by the radiation from the earth and the atmosphere is an important variable in the energy balance formulated by equation (15). Unfortunately, the quantitative prediction of this portion of the total heat load is subject to some uncertainty because it depends on several factors which are difficult to specify.

The infrared radiation from the earth and the atmosphere varies as the balloon ascends. Immediately after its launch, the balloon receives radiation from the atmosphere over its entire surface, but as it ascends the amount of air above the balloon continuously decreases. Eventually, only the lower part of the balloon receives radiation from the atmosphere. This infrared radiation is, of course, dependent on the altitude and the cloud cover. Since the cloud cover often changes rapidly, a balloon can experience unexpected and unpredictable fluctuations in the radiation from the earth-atmosphere. The situation improves considerably, however, as the balloon ascends; once it has risen above the clouds and the weather to an altitude of about 60,000 ft, the contribution of radiation from the earth and the atmosphere can be predicted with a considerable degree of accuracy.

Radiation of the earth and the atmosphere is of considerable interest to meteorologists. Comprehensive treatises on the radiation characteristics of the atmosphere have been published during the past decade by outstanding meteorologists such as Goody [13], Feigelson [62], Budyko [74], and Kondratyev [75]. The radiation characteristics have been investigated and reduced to convenient graphs and charts by Simpson [76], Yamamoto [77], and Elsasser and Culbertson [78]. Using Nimbus II data Raschke also prepared infrared radiation maps. Fig. 18 shows the infrared radiation emitted from the earth and the atmosphere into space over the Northern Hemisphere during the period July 16–28, 1966.

In connection with efforts to construct a general circulation model of the atmosphere, several researchers including Houghton [66], London, [79], Manabe and Möller [80], and Davis [81] have studied theoretical aspects of atmospheric radiation, but most of them calculated the meridional distribution and seasonal variation of the radiation balance and not its global distribution. From a practical point of view, Simpson's simple model [76, 82] is still very useful for estimating radiation heat loads, although Budyko [74] presents more accurate heat-balance calculations at the earth's surface. Neither of them, however, considers the radiation within the atmosphere. Recently A. Katayama [83] has made valuable calculations of the radiation budget of the troposphere over the Northern Hemisphere, and Sasamori [84] has developed a method for calculating the upward and downward radiation flux in a cloudless atmosphere. Sasamori's calculations are based on empirical formulas for the spectral variations of the absorptances of water vapor, carbon dioxide, and ozone (the constituents of the atmosphere with absorption bands in the infrared range), and on the assumption that the surface of the earth is perfectly black. A summary of his results is shown for different latitudes in Fig. 19, where the upward radiation flux and the downward radiation flux are plotted as a function of altitude. The spectral characteristics of the radiation are not shown but can be calculated from the empirical relations in reference [84].

It should be noted that the atmosphere is almost transparent to wavelengths between 8 and 12 microns so that a balloon will receive such radiation directly from the earth. At longer and shorter wavelengths the atmospheric water vapor and carbon dioxide have strong absorption bands so that the infrared radiation in that part of the spectrum received by a balloon is emitted by the atmosphere, usually at a temperature lower than that of the earth. Some balloon materials exhibit considerable variations in the monochromatic absorptance in the infrared, and to estimate reliably the infrared radiation absorbed by the skin, integrations over the spectrum between 6 and 100 microns, as

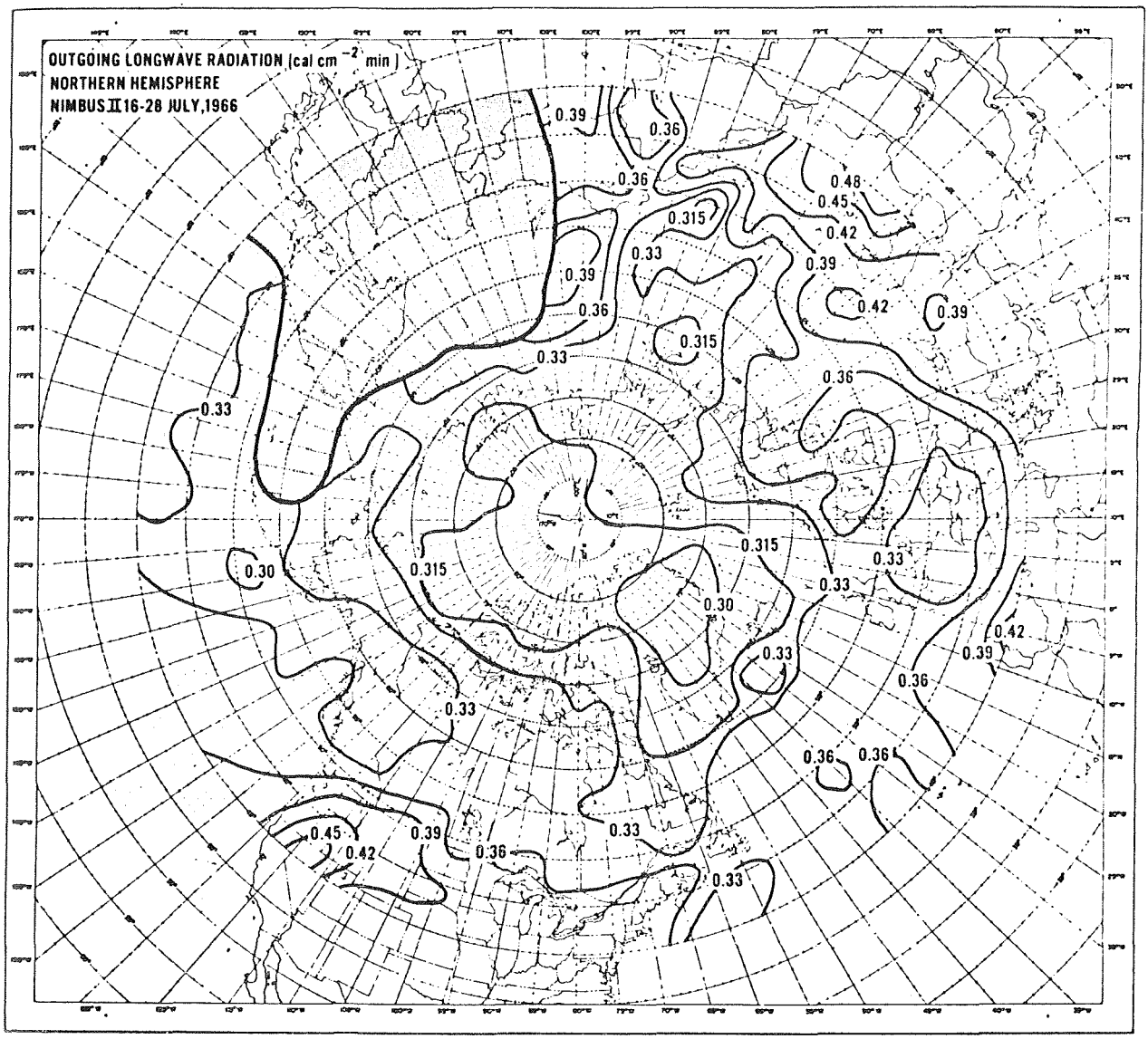

Fig. 18 Infrared radiation map for the Northern Hemisphere during July 16–28, 1966; reference [65]

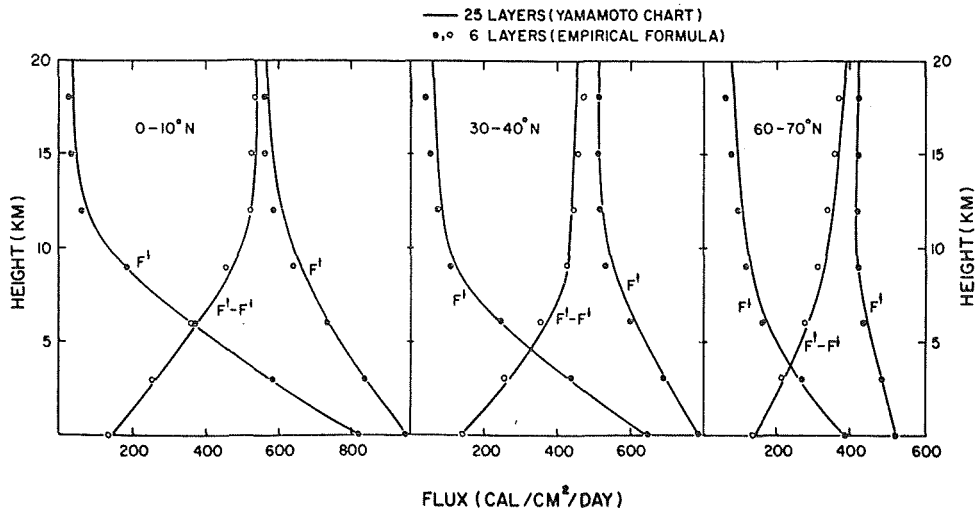

Fig. 19 Upward and downward radiation flux as a function of altitude; reference [84]

Table 9 Radiation environment for superpressure balloon (reference [3])

Altitude	Season	Air temperature, °C	Average nighttime clear sky balloon super temperature		Mylar balloon ($\alpha_0 = 0.05$)		
			Mylar balloon, °C	Metallized top balloon, °C	Temperature increase per w/m² increment, °C	Maximum added solar flux w/m²	Maximum daytime temperature increase, °C
	Temperate, winter	−10	0	+5	0.24	35	8
3 km	Temperate, summer	5	−3	+2	0.21	35	8
(700 mb)	Tropic	10	−5	0	0.20	35	8
	Temperate, winter	−30	0	+8	0.30	35	10
6 km	Temperate, summer	−15	−5	+5	0.27	35	9
(500 mb)	Tropic	−5	−10	+2	0.25	35	9
	Temperate, winter	−50	+5	+15	0.36	40	14
9 km	Temperate, summer	−35	−5	+7	0.34	40	13
(300 mb)	Tropic	−30	−10	+2	0.34	40	13
	Temperate, winter	−55	+10	+20	0.36	45	16
12 km	Temperate, summer	−55	+10	+20	0.36	45	16
(200 mb)	Tropic	−50	+5	+15	0.36	45	16
	Temperate, winter	−60	+5		0.42	45	19
16 km	Temperate, summer	−65	+10		0.42	45	19
(100 mb)	Tropic	−80	+15		0.47	45	21
	Temperate, winter	−55	−5		0.45	45	20
24 km	Temperate, summer	−55	−5		0.45	45	20
(30 mb)	Tropic	−55	−5		0.45	45	20

shown by equation (31), are necessary [58, 85]. For these integrations, simplified models of the variations in the monochromatic radiation of the atmosphere, such as those given in references [9, 58], are quite satisfactory.

In view of these complicated conditions it is not surprising that several different approaches have been taken to calculate the radiation from the earth and its atmosphere which is absorbed by a balloon. Lally [3], dealing only with superpressure balloons, divided the incoming infrared radiation into four parts: from below, from above, and from two sides, each illuminating an area of $(\pi D_g^2/4)$. The radiation environment is then estimated using the following simplified assumptions:

1 Downward radiation

(*a*) If clouds above, the downward flux equals black-body radiation from a source the temperature of the cloud base.

(*b*) If clear above: balloon above 15 km—10 w/m²; balloon between 10–15 km—20 w/m²; balloon below 10 km—40 w/m².

2 Upward radiation

(*a*) If clouds below, the upward flux equals black-body radiation from a source the temperature of the cloud-tops.

(*b*) If clear below, the upward radiation will vary from 150 w/m²–450 w/m², depending on altitude and air mass. Table 9 provides estimates of upward flux for several altitudes and air masses.

3 The radiation from the sides can be estimated as equal to black-body radiation from a source the temperature of the air at balloon altitude.

London [85] considered only the upward and the downward fluxes. The advantage of this approach is that theoretical analyses and measurements of atmospheric radiation usually provide only the upward and the downward, but not horizontal, radiation fluxes. An instrument which has been used widely at ESSA to obtain measurements of the upward and downward atmospheric radiation was developed by Suomi and Kuhn [86]. This instrument, shown in Fig. 20, is basically a double-faced, hemispherical bolometer with broad-response, blackened sensing surfaces shielded from convection currents by thin membranes of polyethylene. The radiation flux up and down can be calculated from the temperature, measured with tiny thermistors, of the sensor surfaces and the air. An experimental flight verification

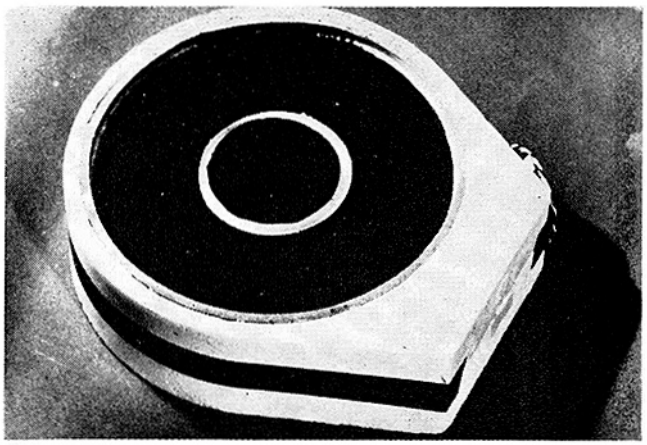

Fig. 20 Suomi-Kuhn flat plate radiometer (courtesy of Dr. P. Kuhn and ESSA)

of this instrument, also called an "economical net-radiometer," is presented in reference [87]. Data taken during several balloon flights have been published, e.g. [88, 89, 90, 91], and data from other flights are being processed at ESSA [53]. Whenever the spectrum of the upward and downward infrared radiation is known, the rate at which infrared radiation is transferred to the balloon skin can be calculated from the relation

$$q_3 = (\pi D_g^2/2) \int_4^{100} [\tilde{a}_{\text{eff}}(\lambda) G_{i,\text{up}}(\lambda) + \tilde{a}_{\text{eff}}(\lambda) G_{i,\text{down}}(\lambda)] d\lambda \tag{50}$$

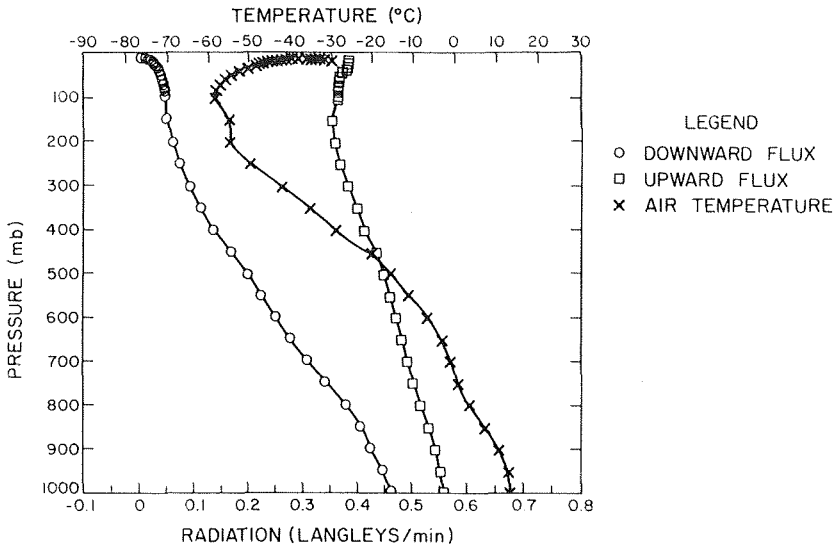

Fig. 21 Radiation environment at Green Bay, Wisc., in the summer; reference [53]

where $\bar{a}_{\text{eff}}(\lambda)$ is the effective monochromatic absorptance of the balloon film, which can be approximated from equation (30) by

$$a(\lambda)\left[1 + \frac{1 - a(\lambda) - r(\lambda)}{1 - r(\lambda)}\right]$$

$G_{i,\text{up}}(\lambda)$ is the upward monochromatic radiation as measured by a hemispherical flat surface radiometer, and $G_{i,\text{down}}(\lambda)$ is the downward monochromatic radiation, likewise measured.

Unfortunately, however, only the total average radiation over all wavelengths is usually measured. Typical data from meteorological measurements are illustrated in Fig. 21 where the air temperature and the total radiation on a horizontal surface from above and from below are plotted as a function of altitude at Green Bay, Wisconsin, during the summer. Also shown are the net radiation flux, i.e., the difference between the radiation from above and from below and the atmospheric cooling rate, quantities which are of meteorological interest only.

A third method of estimating the infrared heat load has been proposed by Germeles [8]. It uses the measurements obtained by a "black ball" radiometer, an instrument widely used by meteorologists to measure the radiation in the atmosphere. The instrument, developed by Gergen [92], consists essentially of a small balsa-wood dodecahedron painted black and surrounded by a convection shield, Fig. 22. A thermistor imbedded in the center is used to measure T_r, the "equilibrium radiation temperature" of the device. From this measurement, the radiation is then calculated from the relation [92]

$$G_i = \sigma T_r^4 \tag{51}$$

Measurements with this device are carried out during the night so the detector is not affected by the sun. It is claimed that the temperature recorded by the black ball is representative of the total radiation field to which it is exposed. Black-ball equilibrium temperatures have been recorded as a function of altitude at different geographical locations, and it has been observed that large changes in the black-ball temperature profile occur at the same location within days. The results of these measurements support the following approximate, simple, general rule. At ground level, the radiation temperature is usually less than the air temperature, but the deviation is no more than about 10 deg F. The equivalent radiation temperature decreases almost linearly with altitude up to the tropopause, where it approaches about 30 percent of its ground value. From there to higher altitudes the radiation temperature remains approximately constant, indicating that most of the radiation is received from below.

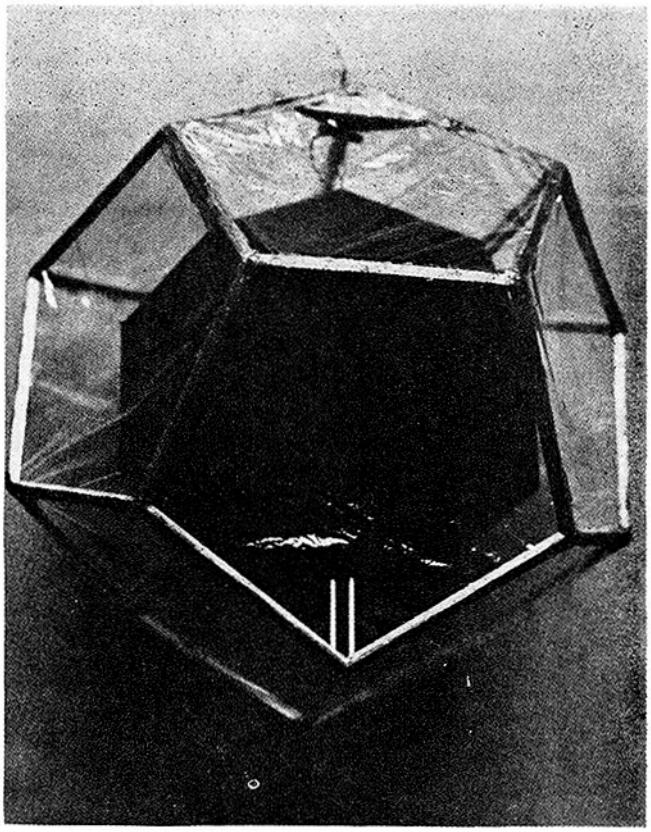

Fig. 22 Gergen "black-ball" radiometer; reference [92]

Germeles [8] used data obtained by means of a black-ball radiometer to calculate the infrared radiation on a balloon. He assumed that the black-ball temperature profile is known. Since the black ball has a shape similar to that of a balloon, the radiation absorbed by the balloon can be obtained from the relation

$$q_3 = 4.83\bar{a}_{\text{eff}}\sigma V_g^{2/3}T_r^4 \quad (52)$$

It is apparent that the estimates of radiation emitted by the atmosphere and the earth require considerable improvement and elaboration. It may well be that such improvement has not been made because the properties of balloon fabrics are only known approximately, so that even if the heat load could be calculated with considerably higher accuracy, the uncertainty in the absorption load would remain.

At this juncture I would recommend calculating the heat load from above and below, making use of measurements obtained with an instrument such as the Suomi-Kuhn radiometer and calculating the actual amount of radiation with a simple model of the atmosphere such as that proposed by Simpson [76], which considers only water and carbon dioxide absorption. This approach, described in reference [58] for use in spacecraft design, is also directly applicable to calculations on balloon and instrument packages. For calculations of heat loads in areas where the Kuhn-Suomi instrument has not been flown, I suggest use of the Nimbus II data, which are similar to albedo data, in that they include the total radiation flux emitted by the earth's atmosphere. This approach, of course, will only be useful for altitudes above 60,000 ft since satellite data are taken far outside the atmosphere. *An aid to further improvement of the calculation of the heat load would be to fly several balloons instrumented to measure gas temperatures, the radiation heat load, and the air temperature simultaneously.* Although such measurements have not been made, they are feasible with existing instrumentation.

Experimental Results

Coordinated measurements of the thermal and aerodynamic characteristics of large balloons have been published for only two flights conducted with 250,000-cu-ft balloons designed to float at 80,000 ft. The skins of both balloons were 1.5-mil polyethylene. During both flights the atmospheric temperature, the altitude, and the balloon helium temperature were measured continuously. During one flight the temperature of the balloon fabric was also measured at two locations, and the black-ball radiation temperature 300 ft below the balloon was determined. These flights were conducted by NCAR from its launch site in Page, Arizona in, October, 1966, and January, 1968. A third flight has been made, but the results are not yet available.

During the first flight, two of the five thermistors inside the balloon failed during launch, and the telemetering system measuring the air temperature malfunctioned after the balloon reached its ceiling. The thermistors used inside the balloon have a diameter of 9 mils, roughly 20 times the mean free path of helium at its pressure at 80,000 ft. Such small thermistors were used to maximize the ratio of q_c/q_r of heat loss by conduction or convection to heat loss by radiation. As shown by Ney, et al. [96], for a spherical sensor this ratio is

$$q_c/q_r = 2k_g/eD\sigma T^3 \quad (53)$$

The error because of incident radiation and self-heating is given by the equation

$$T - T_g = (D\bar{a}_i G/k_g) + (\dot{P}/2\pi Dk_g) \quad (54)$$

where T is sensor temperature, T_g the true gas temperature, D the sensor diameter, k_g the gas conductivity, a the absorptance for incidence radiation, G the incident radiation flux per unit surface area, and $\dot{P}$ the internal power dissipation. The estimated temperature error in the tests is less than 0.2 deg F.

Uncertainties in the data reduction resulted from the difference between the value of the air temperature measured by a standard radiosonde and the value indicated by the thermistor suspended 300 ft below the payload. Approximately 1.5 hr after launch, at an altitude of about 65,000 ft, the air temperature indicated by

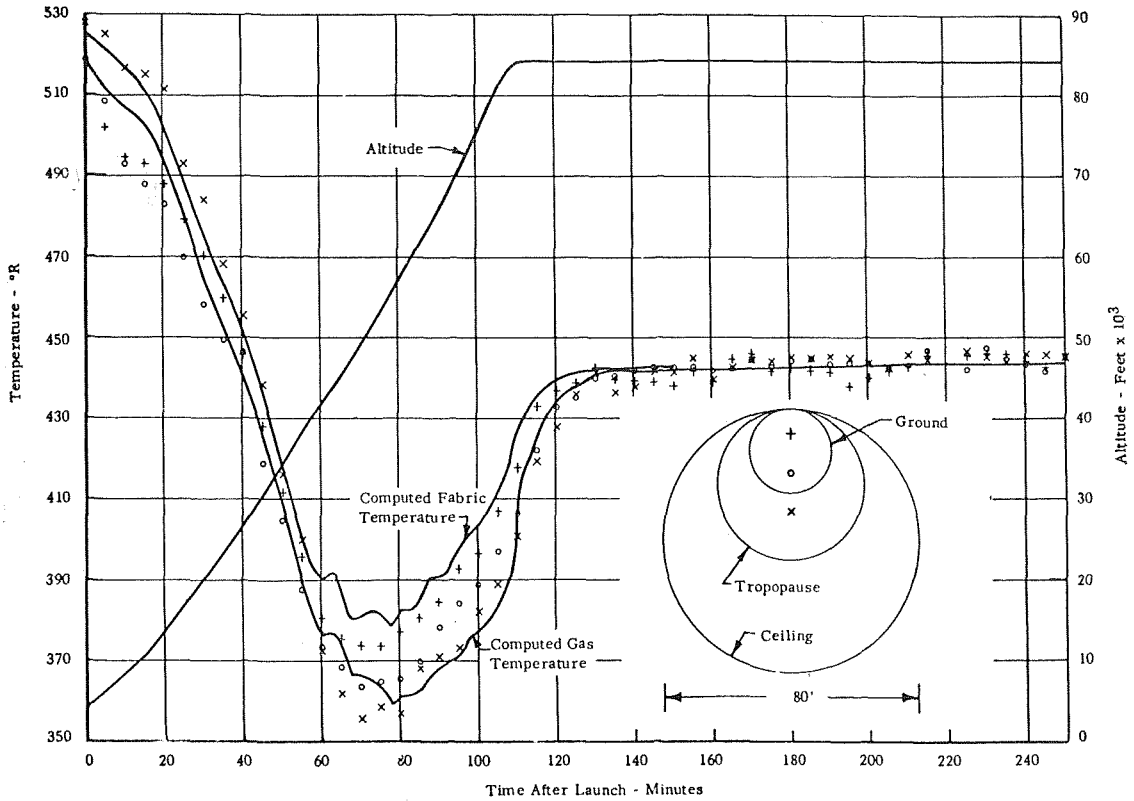

Fig. 23 Comparison of predicted and measured balloon gas temperatures; reference [93]

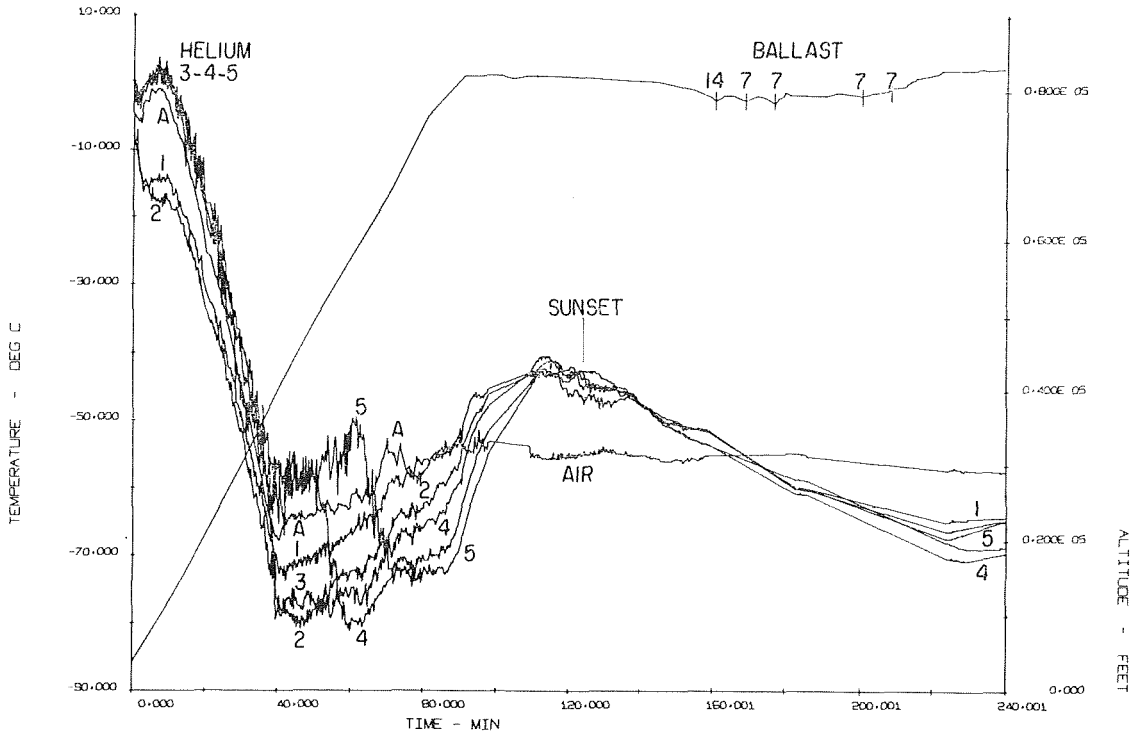

Fig. 24 Internal balloon temperature distribution measured during flight; reference [94]

the radiosonde was 40 deg F higher than the air temperature indicated by the thermistor.

The internal balloon temperatures measured during the flight were compared with the temperature computed using equations very similar to those representing the simplest model presented in this paper. The results of this comparison between the computed and measured temperatures are shown in Fig. 23 for the first flight. The relationship between the temperature of each thermistor and the average temperature of the gas and fabric depends on the position of the thermistor in the balloon. The rough position of each thermistor during the flight is indicated on the sketch on the lower right of Fig. 23, in which the balloon is approximated by a sphere. The diameter of the balloon was about 26, 46, and 80 ft at ground, tropopause, and ceiling, respectively. The lowest thermistor was buried in the loose fabric at ground level and became exposed to the helium only after the tropopause was reached.

An examination of the experimental data shows that there was considerable temperature stratification in the helium, but the averaged gas temperature followed closely the prediction of the idealized model. The computed gas temperature initially followed the upper thermistor, but just before reaching the tropopause it approached more closely the temperature record of the middle thermistor. At float altitude, the thermistor in the center of the balloon agreed most closely with the average temperature prediction. After about an hour, the temperature of the top thermistor followed closely the temperature predicted for the fabric of the balloon.

All five internal thermistors operated throughout the January, 1968, flight, and the temperatures they measured are shown in Fig. 24. Just after launch, thermistors 1 and 2 were cooled by expansion of the helium, but thermistors 3, 4, and 5 were still inside the fabric and measured a fabric temperature. Near tropopause, i.e., at 40,000 ft, thermistor 3 was exposed to the helium and its temperature dropped to -112 deg F. At 50,000 ft, thermistor 4 and, at 60,000 ft, thermistor 5 cooled rapidly from 77 to -112 deg F.

Fig. 25 shows the relative temperature of fabric, air, and helium during the flight as well as the black-ball radiation temperature. Dingwell and Lucas [94] attempted to predict the temperature-time history and compare it with the measured results. They found that to obtain reasonable agreement between the experimental data and those predicted by analysis, they had to increase the coefficient of heat transfer for natural convection. But, so far, no suitable heat-transfer model from which appropriate calculations could be made had been chosen. According to Dingwell and Lucas, conventional estimates of air and helium heat-transfer coefficients were reasonably accurate during stable portions of the flight but were not appropriate during sunset.

Summary

There are three general problem areas in which thermal design can improve balloon operation. The first involves rapid variations in internal energy which occur when clouds suddenly change the radiation incident on the balloon. This type of change in heat-transfer rate is usually sensed only after the altimeter registers a change, and it is compensated for by dropping ballast or valving gas in order to maintain altitude. If one could control altitude by reacting rapidly to a change in radiation, the loss of ballast or gas could be reduced. The second type of thermal-design problem is concerned with changes in heat loss during a complete day and night period. More accurate predictions of heat loss and gain, coupled with the use of appropriate materials or surface coatings, could increase the payload or the float altitude for a given balloon system. The third kind of thermal-design problem arises in long-range planning for balloon flights over new routes such as those currently envisioned in the equatorial zone.

In this lecture I have reviewed recent advances in heat-transfer experiments and theory pertinent to the heat-transfer processes which affect the calculations of balloon performance and the thermal design of their instrument packages. I hope that

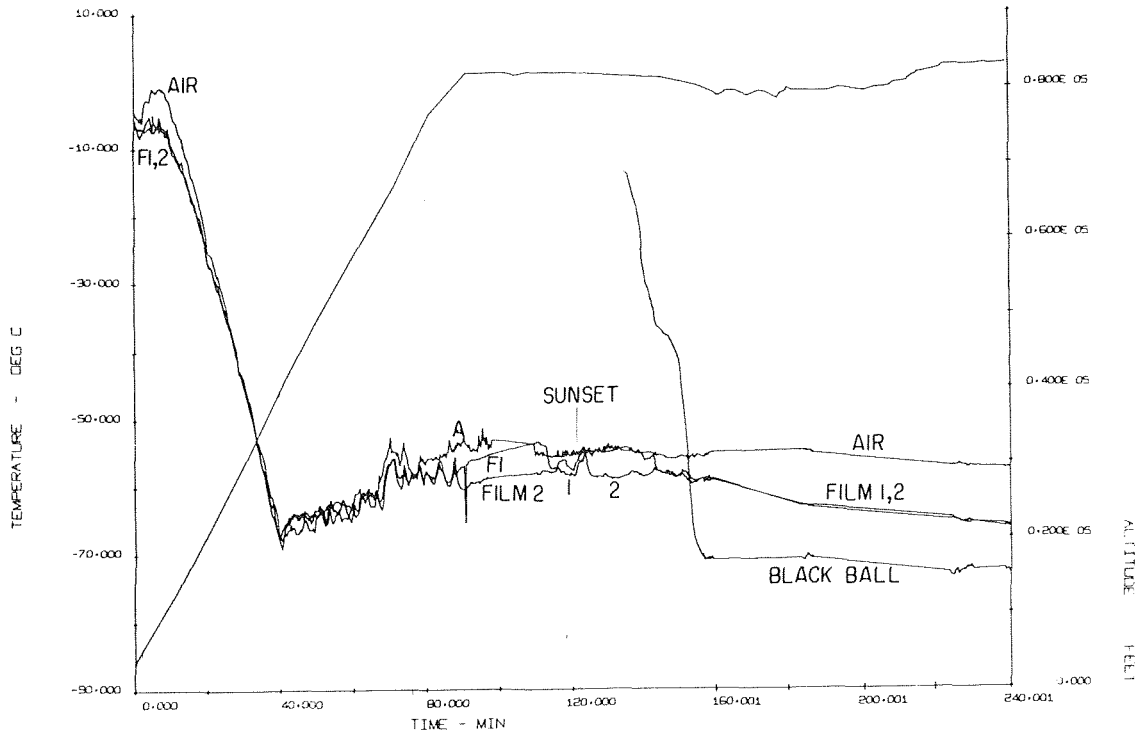

Fig. 25 Air, skin, and black-ball temperatures measured during flight; reference [94]

this review will help to improve the accuracy of the predictions of the performance characteristics of balloons and eventually lead also to an understanding of certain factors which contribute to balloon failure, such as thermal stresses and flight instabilities caused by unexpected atmospheric conditions.

On the basis of available evidence it appears that the basic method outlined in this lecture can, with some additional measurements, be refined to the point where it can be used with confidence for the thermal design of high-altitude balloon and instrument packages. The current rapid pace of research in heat transfer, meteorology, and atmospheric physics insures that those areas where knowledge is insufficient will be studied and that the information needed for reliable thermal design will become available in the near future. Close cooperation between researcher and designer will be necessary, however, to interpret and relate the results of research so they will be accessible to the people designing and operating scientific balloons.

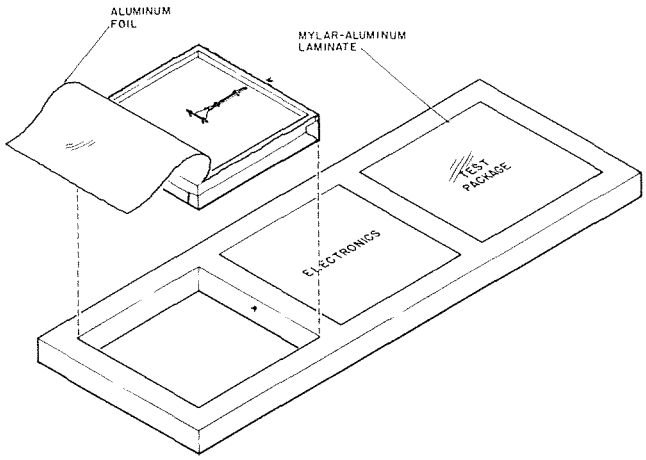

Fig. 26 Schematic diagram of experimental balloon instrument package; reference [97]

Acknowledgment

In the thermal design of high-altitude balloons and instrument packages one encounters not only all the problems involved in the thermal design of satellites, but also problems associated with thermal convection from sea level to the maximum float altitude. In preparing this lecture I have, therefore, drawn on work done in connection with predicting the heat transfer to and from satellites, on research done by astro-geophysicists and meteorologists, and on the experience gained by a group of individuals who can best be described as the artisan-engineers of balloon launch and flight control. I have tried to give credit to all of these sources in the bibliography, but I would like in particular to thank A. L. Morris and K. Stefan of the NCAR Scientific Balloon Facility, for their help and encouragement in the preparation of this lecture and Dr. T. Sasamori for reviewing the manuscript and making suggestions for improving the presentation. I would also like to thank the National Center for Atmospheric Research for typing the manuscript and preparing the illustrations.

References

1 Gibbs-Smith, C. H., *Ballooning*, Penguin Books, Loudon, 1948.
2 Dollfus, C., *Balloons*, Orion Press, New York, 1961.
3 Lally, V. E., "Superpressure Balloons for Horizontal Soundings of the Atmosphere," NCAR TN-28, June 1967, Boulder, Colo.
4 Lear, S., "Forecasting the Solar Wind," *Saturday Review of Literature*, July 6, 1968, p. 41.
5 Iversen, H. W., and Balent, R., "A Correlation Modulus for Fluid Resistances in Accelerated Motion," *Journal of Applied Physics*, Vol. 22, 1951, p. 324.
6 Robertson, J. M., *Hydrodynamics in Theory and Application*. Prentice-Hall, Englewood Cliffs, N. J., 1965.
7 Schlichting, H., *Boundary Layer Theory*, 4th ed., McGraw-Hill. New York, 1960.
8 Germeles, A. E., "Vertical Motion of High Altitude Balloons," Tech. Rep. IV to ONR, A.D. Little, Inc., July 1966.
9 Valley, S. L., ed., *Handbook of Geophysics and Space Environments*, revised ed., Macmillan, New York, 1965.
10 Kreith, F., *Principles of Heat Transfer*, 2nd ed., International Textbook Co., Scranton, Pa., 1965.
11 Yuge, T., "Experiments on Heat Transfer From Spheres In-

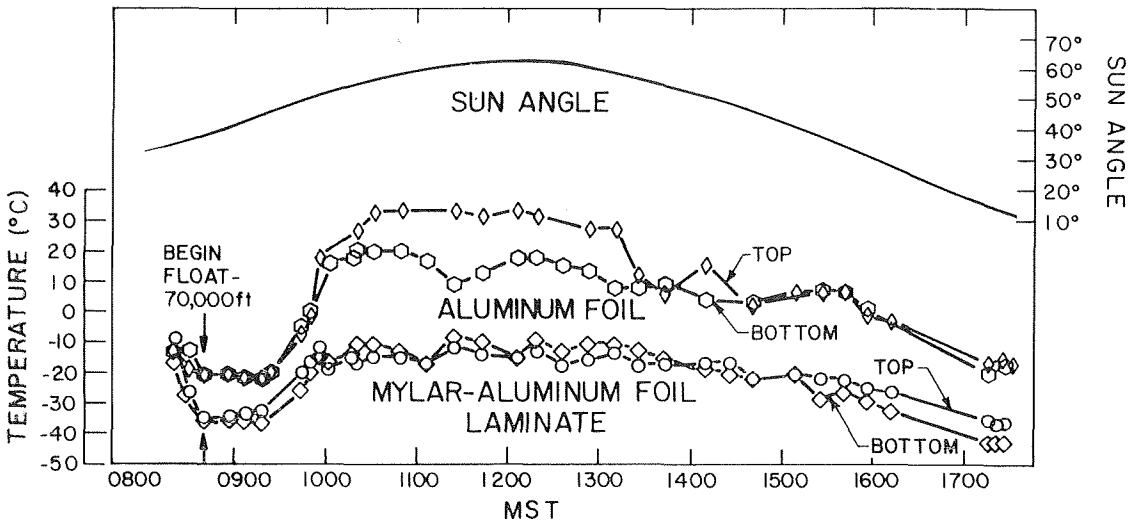

Fig. 27 Measured temperatures of instrument package during flight; reference [97]

cluding Combined Natural and Forced Convection," JOURNAL OF HEAT TRANSFER, TRANS. ASME, Series C, Vol. 82, No. 3, Aug. 1960, pp. 214–220.

12 Vliet, G. C., and Leppert, G., "Forced Convection Heat Transfer From an Isothermal Sphere to Water," JOURNAL OF HEAT TRANSFER, TRANS. ASME, Series C, Vol. 83, No. 2, May 1961, pp. 163–175. (see also discussions by R. M. Drake, J. Kestin, and P. D. Richardson) JOURNAL OF HEAT TRANSFER, *Trans.* ASME, Series C, Vol. 83, No. 2, May 1961, pp. 163–175.

13 Merk, H. J., "Rapid Calculation for Boundary Layer Transfer Using Wedge Solution and Asymptotic Expansions," *Journal of Fluid Mechanics*, Vol. 5, 1959, p. 460.

14 Fage, A., "Pressure Distribution for Flow Past Spheres," Brit. Aeronaut. Res. Com. R. & M. 1766, 1937.

15 Krause, A. A., and Schenk, J., "Thermal Free Convection From a Solid Sphere," *Applied Scientific Research, A-15*, 1965, p. 397.

16 Merk, H. J., and Prins, J. A., "Thermal Convection in Laminar Boundary Layers," (Parts I, II, and III), *Applied Scientific Research, A-4*, 1954, pp. 195, 207.

17 Garner, F. H., and Keey, R. B., "Mass Transfer From Single Solid Spheres," Parts I and II, *Chemical Engineering Science*, Vol. 9, 1958–59, pp. 119, 218.

18 Garner, F. H., and Hoffman, J. M., "Mass Transfer from Single Solid Spheres by Free Convection," *Journal of the American Institute of Chemical Engineers*, Vol. 7, 1961, p. 198.

19 Schütz, G., "Natural Convection Mass-Transfer Measurements on Spheres and Horizontal Cylinders by an Electro-chemical Method," *International Journal of Heat and Mass Transfer*, Vol. 6, 1963, p. 873.

20 Gebhart, B., "Natural Convection Flow, Instability, and Transition," JOURNAL OF HEAT TRANSFER, TRANS. ASME, Series C, Vol. 91, No. 2, May 1969, p. 293.

21 Fendell, F. F., "Laminar Natural Convection About an Isothermally Heated Sphere at Small Grashof Number," *Journal of Fluid Mechanics*, Vol. 34 (Part 1), 1968, p. 163.

22 Baxi, C. B., and Ramachandran, A., "Effect of Vibration on Heat Transfer From Spheres," JOURNAL OF HEAT TRANSFER, TRANS. ASME, Series C, Vol. 91, No. 3, Aug. 1969, pp. 337–344.

23 Kreith, F., Roberts, G., Sullivan, J. A., and Sinha, S. N., "Convection Heat Transfer and Flow Phenomena of Rotating Spheres," *International Journal of Heat and Mass Transfer*, Vol. 6, 1963, p. 881.

24 Nordlie, R. L., and Kreith, F., "Convection from a Rotating Sphere," *International Developments in Heat Transfer*, ASME, New York, N. Y., 1961, pp. 461–467.

25 Börner, H., "Über den Wärme- und Stoffübergang an umspülten Einzelnkörpen bei Überlagerung von freier und erzwunener Strömung" (Heat and Mass Transfer of Single Bodies by Combined Free and Forced Convection), VDI-Forschungsheft, No. 512, 1965.

26 Krischer, O., and Loos, G., "Wärme and Stoffaustausch bei erzwungener Strömung an Körpern verschiedener Form-Teilung," Chemie-Ing.-Techn., Vol. 30, 1958, p. 31.

27 Acrivos, A., "Combined Laminar Free and Forced Convection Heat Transfer in External Flows," *Journal of the American Institute of Chemical Engineers*, Vol. 4, 1958, p. 285.

28 Mori, Y., "Buoyancy Effects in Forced Laminar Convection Flow Over a Horizontal Flat Plate," JOURNAL OF HEAT TRANSFER, TRANS. ASME, Series C, Vol. 83, No. 4, Nov. 1961, pp. 479–493.

29 Sharma, G. K., and Sukhatme, S. P., "Combined Free and Forced Convection Heat Transfer From a Heated Tube to a Transverse Air Stream," JOURNAL OF HEAT TRANSFER, TRANS. ASME, Series C, Vol. 91, No. 3, Aug. 1969, pp. 457–459.

30 Litchfield, E. W., and Carlson, N. E., "Temperature Control of Balloon Packages," NCAR TN-32, Boulder, Colo., August 1967.

31 Suriano, F. J., and Yang, K-T., "Laminar Free Convection About Vertical and Horizontal Plates at Small and Moderate Grashof Numbers," *International Journal of Heat and Mass Transfer*, Vol. 11, No. 3, 1968, p. 473.

32 Stewartson, K., "Free Convection from a Horizontal Plate," *ZAMP*, Vol. 9U, 1958, p. 276.

33 Gill, W. N., Zeh, D. W., and Casal, E. D., "Free Convection on a Horizontal Plane," *ZAMP*, Vol. 16, 1965, p. 539.

34 Saunders, O., and Fischenden, M., "Some Measurements of Convection by an Optical Method," *Engineering*, 1935, p. 483.

35 Singh, S. N., Birkebak, R. C., and Drake, R. M., "Laminar Free Convection Heat Transfer from Downward Facing Horizontal Surfaces of Finite Dimensions," *International Journal of Heat Transfer*, Vol. 12, 1969, p. 87.

36 Kambadi, V., and Drake, R. M., "Free Surfaces for Prescribed Variations in Surface Temperature and Mass Flow through the Surface," T.R. Mech. Eng. HT-1, Princeton Univ., June 1960.

37 Huser, R. B., and Sparrow, E. M., "Patterns of Free Convection Flow Adjacent to Horizontal Heated Surfaces," *International Journal of Heat and Mass Transfer*, Vol. 11, No. 7, 1968, p. 1206.

38 Tyler, B. J., and Tuck, A. F., "Heat Transfer to a Gas from a Spherical Enclosure: Measurements and Mechanisms," *International Journal of Heat and Mass Transfer*, Vol. 10, No. 21, 1967, p. 251.

39 Sherman, M., and Ostrach, S., "Lower Bounds to the Critical Rayleigh Number in Completely Confined Regions," *Journal of Applied Mechanics*, Vol. 34, No. 2, TRANS. ASME, Vol. 89, Series E, 1967, pp. 308–312.

40 Hellums, J. D., and Churchill, S. W., "Computation of Natural Convection by Finite Difference Methods," *International Developments in Heat Transfer*, Part 4, ASME, New York, 1961, pp. 984–994.

41 Hellums, J. D., and Churchill, S. W., "Transient and Steady State, Free and Natural Convection, Numerical Solutions, Part II, The Region Inside a Horizontal Cylinder," T19, 1962, pp. 690–695.

42 Powe, R. E., Carley, C. T., and Bishop, E. H., "Free Convective Flow Patterns in Cylindrical Annuli," JOURNAL OF HEAT TRANSFER, TRANS. ASME, Series C, Vol. 91, No. 3, Aug. 1969, pp. 310–314.

43 Eckert, E. R. G., and Jackson, T. W., "Analysis of Free Convection Boundary Layer on a Flat Plate," NACA Rep. No. 1015, 1950.

44 Clark, A. J., "Cryogenic Heat Transfer," *Advances in Heat Transfer*, Vol. 5, Academic Press, New York, 1968.

45 Dingwell, J. W., Sepetoski, W. K., and Lucas, R. M., "Vertical Motions of High Altitude Balloons," TR II to ONR, Arthur D. Little, Inc., Dec. 1963.

46 Ulrich, R. D., Wirtz, D. P., and Nunn, R. H., "Transient Heat Transfer in Closed Containers After Gas Injection," JOURNAL OF HEAT TRANSFER, TRANS. ASME, Series C, Vol. 91, No. 3, Aug. 1969, pp. 461–463.

47 Gebhart, B., Dring, R. P., Polymeropoulos, C. E., "Natural Convection From Vertical Surfaces, The Convection Transient Re-

gime," JOURNAL OF HEAT TRANSFER, TRANS. ASME, Series C, Vol. 89, No. 1, Feb. 1967, pp. 53–59.

48 Dingwell, I., "Thermal Radiation Properties of Some Polymer Balloon Fabrics," Tech. Rep. V to ONR, A.D. Little, Inc., 1967.

49 Dunkle, R. V., "Thermal Radiation Characteristics of Surfaces," *Fundamental Research in Heat Transfer*, J. A. Clark, ed., Macmillan, New York, 1963, pp. 1–31.

50 Hartnett, J. P., Eckert, E. R. G., and Birkebak, R., "The Emissivity and Absorptivity of Parachute Fabrics," JOURNAL OF HEAT TRANSFER, TRANS. ASME, Series C, Vol. 81, No. 3, Aug. 1959, pp. 195–201.

51 Edwards, D. K., "Radiative Transfer Characteristics of Materials," JOURNAL OF HEAT TRANSFER, TRANS. ASME, Series C, Vol. 91, No. 1, Feb. 1969, pp. 1–15.

52 Edwards, D. K., "Thermal Radiation Measurements; Measuring Techniques in Heat Transfer," Eckert, E. R. G., and Goldstein, R. J., eds., Advisory Group for Aeronautical Research and Development (AGARD), 1969.

53 Kuhn, P. M., Environmental Science Services Administration, Boulder, Colo., private communication.

54 Goetzel, C. G., Rittenhouse, J. B., Singletary, J. B., eds., *Space Materials Handbook*, 2nd ed., TORML 64-40 Air Force Materials Laboratory, Wright-Patterson Air Force Base, Ohio, 1965.

55 Comack, W. A., and Edwards, D. K., "Effects of Surface Thermal Radiation Characteristics on the Temperature Control Problem in Satellites," *Surface Effects on Spacecraft Materials*, Clauss, F. J., ed., Wiley, New York, 1960.

56 Gaumer, R. C., and McKellar, L. A., "Thermal Radiative Control Surfaces for Spacecraft," Lockheed T.R. LMSD-704D14, March 1961, Lockheed Aircraft Corp., Sunnyvale, Calif.

57 Blau, H. H., Jr., and Fischer, H., eds., *Radiative Transfer From Solid Materials*, Macmillan, New York, 1962.

58 Kreith, F., *Radiation Heat Transfer*, International Textbook Co., Scranton, Pa., 1962.

59 Dingwell, I. W., "Thermal Radiation Properties of Some Polymer Balloon Fabrics," Tech. Rep. VI to ONR, A.D. Little, Inc., June 1967.

60 Zarem, A. M., and Erway, D. D., eds., *Introduction to the Utilization of Solar Energy*, McGraw-Hill, New York, 1963.

61 Gates, D. M., "Spectral Distribution of Solar Radiation at the Earth's Surface," *Science*, Vol. 151, 1966, p. 523.

62 Feigelson, E. M., *Light and Heat Radiation in Stratus Clouds*, U. S. Dept. of Commerce, Springfield, Va., 1966.

63 Dunkle, R. V., Edwards, D. K., Gier, J. T., Nelson, K. E., and Roddick, R. D., "Heated Cavity Reflectometer for Angular Reflectance Measurements," *Proceedings International Heat Transfer Conference*, ASME-AIChE, New York, 1961, pp. 541–562.

64 Edwards, D. K., "Directional Solar Reflectances in the Space Vehicle Temperature Control Problem," Nov. 1961, p. 1548.

65 Raschke, E., "The Radiation Balance of the Earth-Atmosphere System From Radiation Measurements of the Nimbus II Meteorological Satellite," NASA TN D-4589, Washington, D. C., July 1968.

66 Houghton, M. G., "On the Annual Heat Balance of the Northern Hemisphere," *Journal of Meteorology*, Vol. 11, No. 1, 1954.

67 Fritz, S., "The Albedo of the Planet Earth and of Clouds," *M. Meteorol.*, Vol. 6, 1949, p. 277.

68 Coulson, K. L., "Characteristics of the Radiation Emerging From the Top of a Rayleigh Atmosphere: Total Upward Flux and Albedo," *Planetary and Space Science*, Pergamon Press, London, Vol. 1, 1959, p. 277.

69 Cunningham, F. E., "Power Input to a Small Flat Plate From a Diffusely Radiating Sphere," TN D-710, NASA, Washington, D. C. Any. 1961.

70 Hottel, H. C., and Sarofim, A. F., *Radiative Transfer*, McGraw-Hill, New York, 1967.

71 Camack, W. G., and Edwards, D. K., "Effect of Surface Thermal Radiation Characteristics on the Temperature-Control Problem in Satellites," *Surface Effect on Space Craft Material*, Clauss, F. J., ed., Wiley, New York, 1960.

72 Hibbs, A. R., "The Temperature of an Orbiting Missile," Program Rep. No. 20-294, JPL, Pasadena, Calif., 1956.

73 Goody, R. M., *Atmospheric Radiation, Vol. I., Theoretical Basis*, Oxford Mansgr. Meteor., Clarendon Press, Oxford, 1964.

74 Budyko, M. I., "The Heat Balance of the Earth's Surface," Hydrometeorological Publishing House, Leningrad, 1956 (trans. by U. S. Weather Bureau, 1958).

75 Kondratyev, K. Y., *Radiative Heat Exchange in the Atmosphere* (trans. from Russian by O. Tedder), Pergamon Press, Oxford, 1965.

76 Simpson, G. C., "Some Studies in Terrestrial Radiation," *Mem. Roy. Meteor. Soc.*, Vol. 2, 1928, p. 16.

77 Yamamoto, G., "On a Radiation Chart," Sci. Rep. Tohoku Univ., Ser. 5, Geophysics, Vol. 4, 1952, p. 9.

78 Elsasser, W. M., and Culbertson, M. F., "Atmospheric Radiation Tables," *Meteor. Monogr.*, Vol. 4, No. 23, 1960.

79 London, J., "A Study of the Atmospheric Heat Balance," Final Report AF19 (122-165), New York University, 1957.

80 Manabe, F., and Möller, F., "On the Radiative Equilibrium and Heat Balance of the Atmosphere," *Monthly Weather Review*, Vol. 89, 1961, p. 508.

81 Davis, P. A., "An Analysis of the Atmospheric Heat Budget," *Journal of Atmospheric Science*, Vol. 20, 1963, p. 5.

82 Simpson, G. C., "The Distribution of Terrestrial Radiation," *Mem. Roy. Meteor. Soc.*, Vol. 3, 1929, p. 53.

83 Katayama, A., "On the Radiation Budget of the Troposphere Over the Northern Hemisphere," Parts I and II, *Journal of the Meteorological Society of Japan*, Vol. 44, 1966, p. 381, and Vol. 45, 1967, p. 1.

84 Sasamori, T., "The Radiative Cooling Calculations for Application to General Circulation Experiments," *Journal of Applied Meteorology*, Vol. 7, 1968, p. 721.

85 London, J., "The Heat Lost on a Balloon," unpublished notes, 1965.

86 Suomi, V. E., and Kuhn, P. M., "An Economical Net Radiometer," *Tellus*, Vol. 10, 1958, p. 160.

87 Bushnell, R. M., and Suomi, V. E., "Experimental Flight Verification of the Economical Net Radiometer," *Journal of Geophysical Research*, Vol. 66, 1961, p. 2843.

88 Suomi, V. E., Staley, D. O., and Kuhn, P. M., "A Direct Measurement of Infrared Radiation Divergence to 160 mb," *Quarterly Journal of the Royal Meteorological Society*, Vol. 84, 1958, p. 134.

89 Kuhn, P. M., "Measured Effective Longwave Emissivity of Clouds," *Monthly Weather Review*, Oct.-Dec. 1963, pp. 636–640.

90 Kuhn, P. M., and Johnson, D. R., "Improved Radiometersonde Observations of Atmospheric Infrared Irradiance," *Journal of Geophysical Research*, Vol. 71, 1966, p. 367.

91 Kuhn, P. M., Stearns, L. P., and Stremikis, J. R., "Atmospheric Infrared Radiation Over the Antarctic," ESSA TR 1ER 55-1AS2, Boulder, Colo., 1967.

92 Gergen, J. L., "Black Ball: A Device for Measuring Atmospheric Infrared Radiation," *Review of Scientific Instruments*, Vol. 27, 1956, p. 453.

93 Gabon, F., Dingwell, L., Allen, B., Comstock, D., "A Study of Balloon-Borne Instrumentation to Detect Thermal Radiation Transients," NCAR Subcontract 84-68, A. D. Little, Inc., Oct. 1968.

94 Dingwell, I., and Lucas, R., "Recent Theoretical and Experimental Studies of High Altitude Balloon Vertical Trajectories," AIAA Paper 68-940, Sept. 1968.

95 Lucas, R. M., and Hall, G. H., "The Measurement of High Altitude Balloon Gas Temperature," TR V to ONR, A. D. Little, Inc., 1960.

96 Ney, E. P., Maas, R. W., and Huch, W. F., "The Measurement of Atmospheric Temperature," *Journal of Meteorology*, Vol. 18, 1961, p. 60.

97 Kreith, F., and Warren, J. C., "An Analytical and Experimental Thermal Analysis of Balloon-Borne Instrument Packages at 70,000 and 130,000 Feet," NCAR Technical Report No. 45, National Center for Atmospheric Research, Boulder, Colo., 1970.

L. H. BACK
Technical Staff.
Mem. ASME

R. F. CUFFEL
Senior Engineer.
Assoc. Mem. ASME

P. F. MASSIER
Group Supervisor.

Jet Propulsion Laboratory,
California Institute of Technology,
Pasadena, Calif.

Laminarization of a Turbulent Boundary Layer in Nozzle Flow—Boundary Layer and Heat Transfer Measurements With Wall Cooling[1]

Boundary layer and heat transfer measurements are presented for flow through a cooled, conical nozzle with a convergent and divergent half-angle of 10 deg for a wall-to-total-gas temperature ratio of about 0.5. A reduction in heat transfer below values typical of a turbulent boundary layer was found when values of the parameter $K = (\mu_e/\rho_e u_e^2)(du_e/dx)$ *exceeded about 2 to 3* $\times 10^{-6}$. *The boundary layer measurements, when viewed in conjunction with the heat transfer measurements, reveal the complicated nature of the flow and thermal behavior and their interrelationship when laminarization occurs.*

Introduction

Basic information on turbulent flows that experience the kind of flow accelerations and thermal environment found in practice—e.g., cooled rocket engine thrust chambers, heated channels of proposed nuclear rocket engines, and cooled turbine blades—is scarce. One of the important aspects of these flows is the convective heat transfer. A study of the structure of the boundary layer is vital in this regard because the heat transfer to a cooled surface or from a heated surface involves the transport of thermal energy across the boundary layer. Generally, there is interest in relatively high Reynolds number flows, for which the boundary layer is usually assumed to be turbulent. However, although the boundary layer may be initially turbulent, previous investigations of heat transfer from heated air flowing through cooled axisymmetric nozzles have revealed an apparent reduction of turbulent transport of heat along the nozzles even though the throat Reynolds numbers based on diameter were as large as 4×10^5 to 2×10^6 [1–4].[2] This reduction in heat transfer, also apparent in rocket engine tests [5] and observed by others [6–9], is believed to be associated with the effect of flow acceleration on turbulence. A reduction in heat transfer has also been observed in low-speed investigations with small temperature differences and essentially constant properties [10, 11]. From the low-speed, essentially constant-property, boundary layer measurements of [11–13] and the flow observations of [14], a turbulent boundary layer was found to become laminar-like near the wall, presumably due to the loss of turbulent transport in the wall vicinity. This process, which has been referred to as

[1] This work presents the results of one phase of research carried out in the Propulsion Research and Advanced Concepts Section of the Jet Propulsion Laboratory, California Institute of Technology, under Contract No. NAS 7-100, sponsored by the National Aeronautics and Space Administration.

Contributed by the Heat Transfer Division of The American Society of Mechanical Engineers and presented at the ASME-AIChE Heat Transfer Conference, Minneapolis, Minn., August 3–6, 1969. Manuscript received by the Heat Transfer Division, June 9, 1969. Paper No. 69-HT-56.

[2] Numbers in brackets designate References at end of paper.

Nomenclature

c_f = friction coefficient, $c_f/2 = \tau_w/(\rho_e u_e^2)$

c_p = specific heat at constant pressure

c = constant, equation (3)

C = density-viscosity product ratio, $\rho\mu/(\rho_e u_e)$

D = nozzle diameter

F = frequency of sublayer growth

f' = dimensionless velocity, u/u_e

f_w'' = gradient at wall

g = dimensionless enthalpy, $H/H_e = T/T_e$

g_w = wall-to-free-stream enthalpy ratio, $H_w/H_e = T_w/T_e$

g_w' = gradient at wall

G = dimensionless enthalpy difference, $(g - g_w)/(1 - g_w) = (T - T_w)/(T_e - T_w)$

G_w' = gradient at wall

h = convective heat transfer coefficient, $q_w/(T_{aw} - T_w)$

H = enthalpy

K = laminarization parameter, $(\mu_e)/(\rho_e u_e^2)\left(\frac{du_e}{dx}\right)$

M = Mach number

p = pressure

Pr = Prandtl number

(Continued on next page)

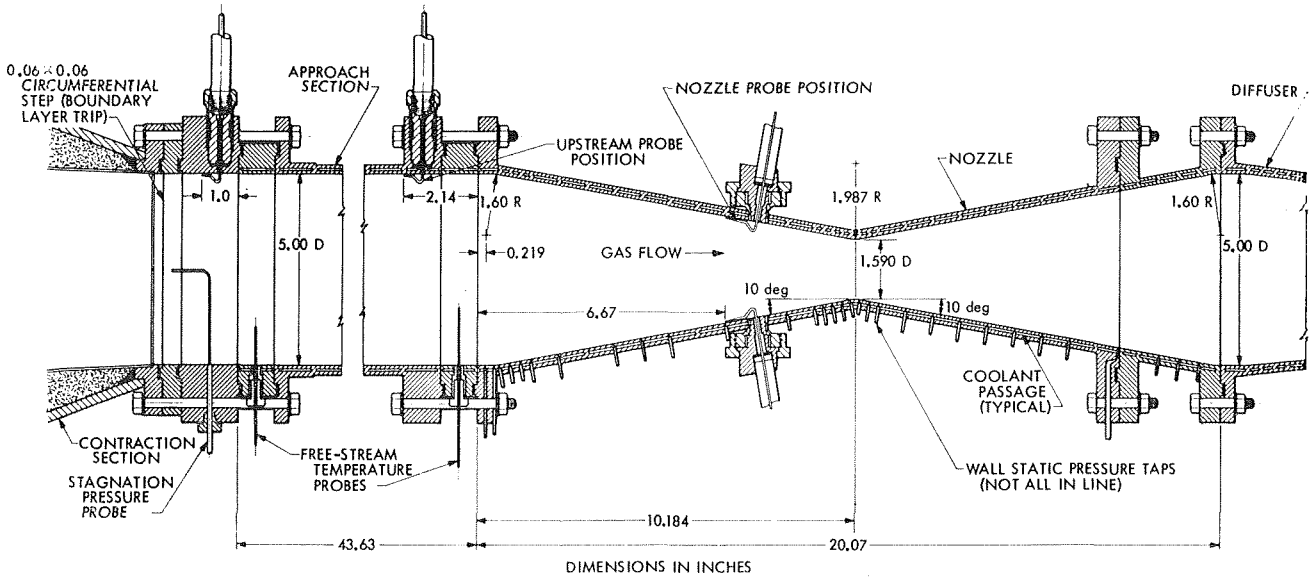

Fig. 1 System investigated

laminarization, apparently occurs when values of a parameter $K = (\mu_e/\rho_e u_e^2)(du_e/dx)$ exceed about 2×10^{-6}.

The purpose of this paper is to present boundary layer and heat transfer measurements along a cooled, conical nozzle with a 10 deg half-angle of convergence and divergence. The nozzle is shown in Fig. 1 and will be referred to as the 10–10 deg nozzle. Of particular interest is the detailed nature of the heat transfer and boundary layer measurements and their interrelationship when laminarization occurs.

The mean structure of the boundary layer is obtained from pitot tube and thermocouple measurements. Heat transfer measurements were made by calorimetry in circumferential coolant passages having passage widths relatively small compared with the nozzle radius. Ambient air was compressed and heated to pressures of 200 psia and temperatures of 1500 deg R at a remote distance upstream of the nozzle. The ratio of the cooled wall temperature to total gas temperature, (T_w/T_{t0}), was about 0.5. The gas side wall temperature was determined from the heat flux measurements and thermocouple measurements on the coolant side wall. The flow at the nozzle entrance was determined by probe measurements near the end of a cooled tube 8.7 diameters long that preceded the nozzle. Conditions at the edge of the boundary layer along the nozzle were obtained from numerous wall static pressure measurements.[3] Additional information is presented in [3, 15] on the test apparatus and measurement technique used in the author's investigations of flows through nozzles that were tested previously but were not instrumented with boundary layer probes. Previous boundary layer measurements at one location in the convergent section of conical nozzles with larger convergent half-angles of 30 deg and 60 deg were reported in [4, 16]. Boundary layer measurements with unheated air flow through the nozzle shown in Fig. 1 appear in [17].

[3] Wall static pressure and heat transfer measurements shown graphically herein are given in tabular form in the authors' Jet Propulsion Laboratory Technical Report 32-1455.

Nomenclature

q_w = wall heat flux
r = nozzle radius
R = gas constant
$\mathcal{R}$ = recovery factor
S = flow speed parameter, equation (13)
St = Stanton number, $h/(\rho_e u_e c_{p_e})$
T = temperature
T_{aw} = adiabatic wall temperature, $\mathcal{R} = \mathrm{Pr}^{1/3} = (T_{aw} - T_e)/(T_{t0} - T_e)$
T^+ = dimensionless temperature, equation (1)
u, v = components of velocity parallel and normal to wall, respectively
u^+ = dimensionless velocity, equation (1)
u_τ = friction velocity, equation (1)
x = distance along wall in flow direction
y = distance normal to wall
y^+ = dimensionless normal distance, equation (1)
$\bar{y}_s^+$ = Coles' sublayer thickness
z = axial distance from nozzle inlet
α = angle between wall and axis
β = acceleration parameter, equation (12)
β_c = cooling parameter, equation (2)
γ = specific heat ratio
δ^* = displacement thickness, $\delta^*\left(r - \frac{\delta^* \cos\alpha}{2}\right) = \int_0^\infty \left(1 - \frac{\rho u}{\rho_e u_e}\right)(r - y\cos\alpha)dy$
ζ = similarity variable in physical plane, equation (16)
η = dimensionless coordinate normal to wall, equation (9)
θ = momentum thickness, $\theta\left(r - \frac{\theta\cos\alpha}{2}\right) = \int_0^\infty \frac{\rho u}{\rho_e u_e}\left(1 - \frac{u}{u_e}\right)(r - y\cos\alpha)dy$
μ = viscosity
ξ = coordinate in x-direction, equation (9)
ρ = density
τ_w = wall shear stress
ϕ = energy thickness, $\phi\left(r - \frac{\phi\cos\alpha}{2}\right) = \int_0^\infty \frac{\rho u}{\rho_e u_e}\left[1 - \left(\frac{T - T_w}{T_e - T_w}\right)\right](r - y\cos\alpha)dy$
χ = parameter, equation (3)
ω = viscosity-temperature exponent

Subscripts

e = condition at free-stream edge of boundary layer
i = condition at nozzle inlet
t = stagnation condition
th = throat condition
0 = reservoir condition
w = wall condition
$\overline{(\ )}$ = constant-property value

Probes and Measurements

Velocity and temperature profiles across the boundary layer in the nozzle were determined by measurements of impact pressure and temperature. The pitot tube was 0.005 in. high and 0.065 in. wide. The temperature probe consisted of an exposed thermocouple about 0.004 in. thick in the direction normal to the wall. The lead wires, embedded in MgO insulating material, extended through a tube that was 0.010 in. high and 0.027 in. wide at the tip. With the probes resting on the wall, the center of the opening of the pitot tube was 0.0025 in. from the wall, and the center of the thermocouple was 0.005 in. from the wall. These distances, very important in establishing the boundary layer profiles in the wall vicinity, were determined by visual observation with a 64-power telescope.

The probes were moved normal to the wall by a micrometer lead screw. The wall location was determined by electrical contact and the probe location from the wall was determined with a helipot. The probes were motor-driven at speeds up to 0.25 in/min in the outer part of the boundary layer, but at slower speeds down to 0.05 in/min near the wall. The pressure difference between the pitot tube and a wall static pressure tap was measured with a transducer. The output signals of the transducer and thermocouple were plotted continuously versus distance from the wall. The length and diameter of the tubes connecting the pitot tube and wall pressure tap to the differential transducer were chosen to minimize the response of a simultaneous step pressure input at the probe tip and wall tap. At the traversing speeds used, no difference was observed between the readings obtained by traversing from the wall to the free stream and then back again to the wall.

Since the density varies across variable-property boundary layers because of temperature changes, measurement of the temperature in addition to the impact pressure is required to obtain the velocity profile. Both velocity and temperature profiles are shown throughout the boundary layer, including the region between the pitot tube and the temperature probe locations, with both probes resting on the wall. In this narrow region of 0.0025 in., the temperature profile was extrapolated toward the wall, guided by the known wall temperature and the known temperature gradient at the wall obtained from the measured wall heat flux. However, when this extrapolation was made, the temperature readings with the probe resting on the wall and at distances to 2 mils from the wall were found to be low, apparently because of heat convection to the cooled wall from the thermocouple surface adjacent to the wall. Consequently, these temperatures were adjusted to be consistent with extrapolation to the temperature gradient at the wall. Errors associated with this extrapolation are expected to be small, especially for the velocity profile, since the velocity depends on the square root of the density or temperature measurement.

Such effects as (1) heat conduction along the thermocouple wires, (2) radiation from the exposed thermocouple, and (3) the exposed thermocouple recovery temperature effect that can lead to errors in temperature measurement are expected to be insignificant: The probe length parallel to the wall was 0.5 in., the ratio of the estimated radiative to convective heat transfer coefficient for the thermocouple was small, and the measurements were made in that portion of the nozzle where the flow speed was relatively low ($M_e < 0.2$).

Thicknesses were calculated from the profile measurements as indicated by the expressions in the Nomenclature. These thicknesses are tabulated in Table 1. The accuracy of these thicknesses in the nozzle is probably no better than 10 to 20 percent because of the uncertainty in determining the edge of the boundary layer.

Table 1 Boundary layer thicknesses

Probe Position	Test	P_t, psia	T_{t0}, °R	$\frac{T_w}{T_{t0}}$	θ, in.	ϕ, in.	$\frac{\delta^*}{\theta}$	$\frac{\phi}{\theta}$	$\frac{\rho_e u_e \theta}{\mu_e}$	$\frac{\rho_e u_e \phi}{\mu_e}$
Upstream	516	15.1	1505	0.41	0.155	0.172	0.54	1.11	1640	1820
z = -2.14 in.	514	20.7	1500	0.42	0.135	0.153	0.52	1.14	2010	2280
	515	30.3	1495	0.43	0.125	0.132	0.59	1.06	2730	2880
	513	45.3	1485	0.44	0.113	0.128	0.55	1.13	3690	4170
	510	75.5	1495	0.45	0.095	0.098	0.62	1.04	5210	5420
	511	100.8	1505	0.47	0.102	0.111	0.58	1.09	7450	8120
	512	149.6	1500	0.47	0.099	0.114	0.56	1.15	10500	12200
	537	200.5	1510	0.48	0.098	0.106	0.63	1.08	14300	15500
Nozzle	516	15.1	1505	0.42	0.041	0.113	-0.56	2.8	1340	3700
z = 6.67 in.	514	20.7	1500	0.42	0.039	0.104	-0.51	2.7	1740	4700
	515	30.3	1495	0.44	0.036	0.098	-0.50	2.7	2350	6500
	517	45.4	1495	0.45	0.036	0.096	-0.46	2.7	3500	9500
	518	75.6	1485	0.47	0.032	0.081	-0.31	2.5	5300	13500
	511	100.8	1505	0.47	0.030	0.078	-0.37	2.6	6500	17000
	523	150.6	1505	0.50	0.029	0.071	-0.19	2.5	9600	23100
	537	200.5	1510	0.50	0.030	0.078	-0.25	2.6	13000	33700

Results

Local heat transfer coefficients are shown in Fig. 2 in a representation that has been found to correlate heat transfer data for turbulent boundary layers for which $St \propto (\rho_e \mu_e / \mu_e)^{-1/5}$. (The subscript i refers to conditions at the nozzle inlet.) Flow conditions were changed by varying the pressure. For higher pressures ($p_t \gtrsim 45$ psia) and correspondingly higher mass fluxes and Reynolds numbers, the Stanton number dependence on Reynolds number is apparently typical of a turbulent boundary layer, as indicated by the merging of the higher Reynolds number results. However, at lower Reynolds numbers (i.e., lower pressures), a reduction in heat transfer occurs along the convergent section. This reduction amounts to as much as about 50 percent along the convergent section and is locally largest in the vicinity of the probe position shown. Farther downstream the reduction is less, but at the throat the magnitude of the reduction is about the same again as it was upstream. Unfortunately the flow was overexpanded at the lower pressures where the reduction in heat transfer occurred, and consequently only a small number of heat transfer data were obtainable in the divergent portion of the nozzle with the nozzle flowing full. Instead, shock-induced flow separation occurred in the divergent section of the nozzle, and, for clarity, heat transfer data are not shown in this region ([18] contains heat transfer data obtained in the shock-induced flow separation region of a different nozzle).

Because of the reduction in heat transfer along the convergent section of the nozzle, the heat transfer is less in the throat vicinity where the heat flux is highest. This desirable situation is shown in Fig. 3, where the reduction in heat transfer at the throat is shown by the local Stanton-Prandtl number group. Also shown in Fig. 3 are other data obtained in a nozzle with a steeper convergent section (larger half-angle of convergence of 45 deg) but with the same inlet radius and throat radius and, therefore, with the same contraction area ratio. The significant influence of convergent half-angle on the Reynolds number, below which a reduction in heat transfer occurs, is apparent [2]. The new information provided by the 10-10 deg nozzle results is the effect of convergent section length on throat heat transfer when a reduction in heat transfer occurs. The laminar boundary layer predictions [19] shown in Fig. 3 for the different nozzles agree with the experimental trend of lower throat heat transfer with increasing convergent section length. These predictions, in which similarity solutions were used on a local basis to predict heat transfer, were initiated at the inlets of the nozzles, and for simplicity the isentropic core flow was assumed to be one-dimensional. It should be mentioned that although the throat heat flux is less with a longer convergent section, the total heat transfer, e.g., up to the throat, is greater for a nozzle with a smaller convergent half-angle but with the same contraction area ratio. This occurs primarily because of the larger heat transfer surface area. In comparison, a negligible effect of convergent section

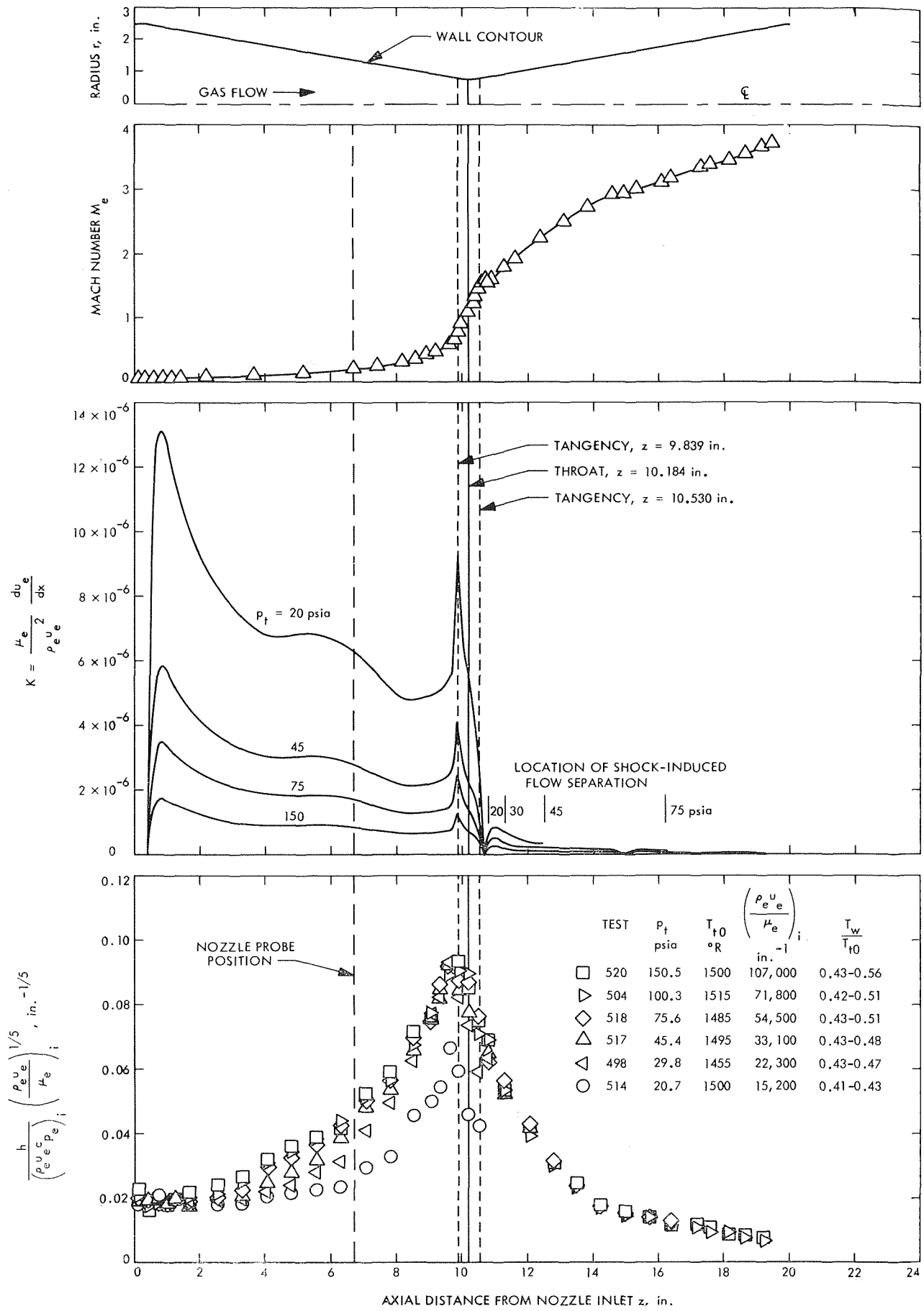

Fig. 2 Variation of the Mach number, parameter *K*, and turbulent boundary layer heat transfer group along the nozzle (Mach number distribution for nozzle flowing full)

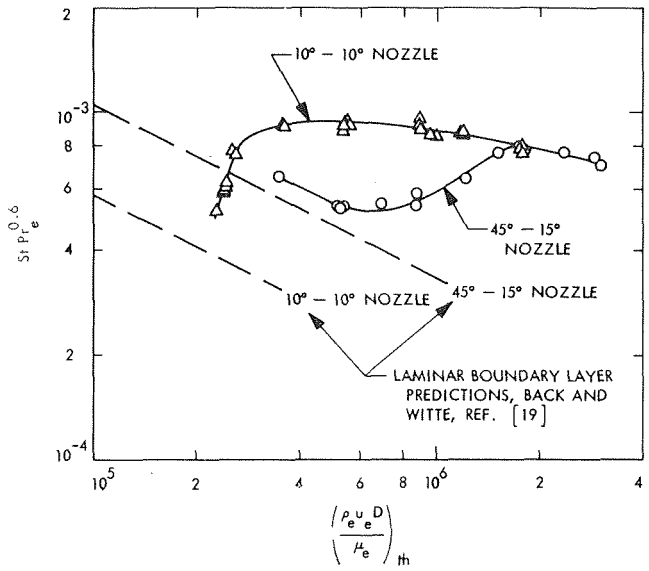

Fig. 3 Variation of the Stanton-Prandtl number group at the nozzle throats

length is indicated by the data in Fig. 3 at the higher Reynolds numbers where the boundary layer remained turbulent.

Actually the heat transfer coefficient is a maximum at a location upstream of the throat, as seen in Fig. 2. In fact, the peak heat transfer coefficient is located upstream of where the mass flux is largest, and corresponds to a location where the Mach number is still only 0.6 for the lower Reynolds number results and 0.8 for the higher Reynolds number results.

The variation of the parameter K, which has emerged from the few theoretical considerations and measurements mentioned in the Introduction as a parameter whose magnitude is indicative of the importance of acceleration on turbulence, is shown in Fig. 2 at different pressures or Reynolds numbers. At a given operating condition, values of K are largest in the inlet region, diminish along the convergent section, and then increase as the gas is locally more rapidly accelerated in flowing from the conical section and into the curved throat section. Values of K decrease through the throat section and actually become negative (i.e., the flow decelerates) as the gas flows into the conical divergent section. This flow deceleration, which was deduced from the measured wall static pressure rise just downstream of the tangency between the curved throat and conical divergent sections, is believed to be associated with a compressive turning of the flow [3]. The test at 30 psia indicates that this pressure rise apparently caused retransition from a partially laminar boundary layer to a turbulent layer similar to that observed in [3]. Farther downstream, values of K increase again and subsequently diminish to lower values as the gas expands to higher supersonic velocities along the divergent section. The dip in K at $z = 14.9$ in. is associated with the incidence of the shock wave generated by the compressive turning of the flow downstream of the throat that is reflected off the centerline before arriving at the wall.

Having observed the rather complicated variation of the parameter K along the nozzle, it is of interest to determine whether there is a connection between K and the reduction in heat transfer that is found. The magnitude of K depends on the operating condition. With decreasing pressure or Reynolds number, K increases, since, for choked nozzle flow, $K \propto 1/p_t$ or

$$K \propto \left(\frac{1}{\frac{\rho_e u_e}{\mu_e}}\right)_i$$

Although there is a difficulty in selecting a particular value of K associated with the observed reduction in heat transfer, the results do indicate that a reduction occurs when values of K exceed about 2 to 3 $\times$ 10^{-6}. However, as also observed by others men-

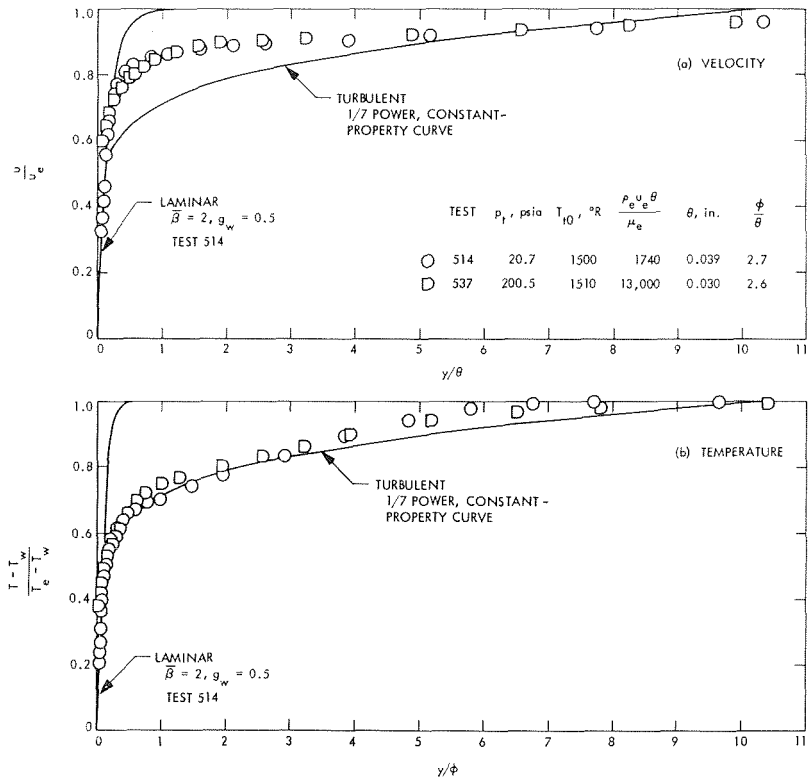

Fig. 4 Velocity and temperature profiles in the nozzle

tioned in the Introduction, the correspondence between larger values of K and a reduction in heat transfer is not direct, e.g., in the inlet region, K is largest, but the reduction in heat transfer occurs farther downstream. This trend is also observable in the throat region downstream of where K again increases locally. A delay between the thermal response and the parameter K is evident, and this perhaps occurs because there is also a delay between the flow response and the parameter K. Increasing values of the parameter $K/(c_f/2)$ apparently can inhibit the production of turbulence as indicated in [1], and this trend has been inferred from the observed decrease in the frequency of turbulent "bursting" of fluid from the wall vicinity [14] in an accelerated flow. For convenience, the parameter K is usually used rather than $K/(c_f/2)$ because the friction coefficient is generally not known. Consequently, from this argument the flow response would not be expected to coincide with the parameter K because, if turbulence production were inhibited, a region of viscous dissipation of the residual turbulence would follow. However, another viewpoint can be offered as well and is discussed in the section Observations.

Boundary layer measurements were obtained in the nozzle over the pressure range investigated at the probe position shown in Fig. 2, a location where the reduction in heat transfer at the lower Reynolds numbers is largest.

Velocity and temperature profiles upstream of the nozzle are similar to those shown in [3] and are not shown again. Both the velocity and temperature profiles could be described by $1/7$ power curves typical of a turbulent boundary layer. Information obtained from the upstream boundary layer traverses is contained in Table 1.

The effect of flow acceleration on the velocity and temperature profiles in the nozzle is shown in Fig. 4 for the relatively low- and high-pressure tests. The velocity profiles become relatively flat in the outer part of the layer and lie above the $1/7$ power relation shown as a reference curve. However, the slope of the velocity profile at the wall is considerably reduced at the lower pressure, where a reduction in heat transfer was observed although this is not that discernible in the scale of Fig. 4. In fact, a laminar boundary layer velocity profile fits the measured profile quite well in the wall vicinity, as indicated. A discussion of the predicted velocity and temperature profiles for accelerated laminar boundary layers with wall cooling appears in the Appendix along with a description of how the friction coefficient is obtained, equation (17). The temperature profiles are still in relatively good agreement with the $1/7$ power relation in the outer part of the layer. However, the slope of the temperature profile at the wall is reduced at the lower pressure and is similar to the slope of the velocity profile. Note that the thickness of the thermal layer is considerably larger than that of the velocity boundary layer implied by the ratio of energy to momentum thicknesses of about 3.

The combined effect of acceleration and cooling on the local mass flux profile across the boundary layer is shown in Fig. 5. The local mass flux can exceed the free-stream value, and for this situation the boundary layer displacement is not outward from the wall, but inward. Values of δ^* are negative for the profiles shown. The observed values of the ratios δ^*/θ and ϕ/θ are in fair agreement with predictions from a turbulent boundary layer analysis [20] involving a solution of the integral form of the momentum and energy equations. For example, at the probe position for the 150-psia test (see Table 1), predicted values of δ^*/θ and ϕ/θ are -0.50 and 3.0, respectively, but the predicted momentum thickness θ is virtually the same as the experimental value.

A more useful representation of the velocity and temperature profiles in the region near the wall, as well as in the outer part of the layer, is shown in Fig. 6 in terms of u^+, T^+, and y^+ as defined by

$$u^+ = \frac{u}{u_\tau}, \qquad T^+ = \frac{T_w - T}{\dfrac{q_w}{\rho_w u_\tau c_{p_w}}}, \qquad y^+ = \frac{\rho_w u_\tau y}{\mu_w} \tag{1}$$

where the friction velocity $u_\tau = (\tau_w/\rho_w)^{1/2}$.

At the higher pressure where the boundary layer apparently remained turbulent, the wall shear stress or friction coefficient was determined by using the predicted velocity profile of van Driest [21] or from Coles' transformation theory [22] as a guide. Either of these predictions was found to be in fair agreement with measurements in nonaccelerating, low-speed, turbulent boundary layers with wall cooling [23] where velocity and temperature profiles were found to lie above the constant-property profiles when viewed on a u^+, T^+, and y^+ basis. The amount of departure was found to be dependent on a parameter β_c [24] defined by

$$\beta_c = \frac{q_w}{T_w \rho_w c_{p_w} u_\tau} \tag{2}$$

For cooling, when $q_w < 0$, then $\beta_c < 0$. Although there is some curvature of the measured velocity profile near the wall, associated with the effect of acceleration, a fair fit is still found to the predicted velocity profiles at the higher pressure. In the outer part of the velocity boundary layer at the higher pressure test shown in Fig. 6, the wake-like behavior [25] found upstream of the nozzle [23] has disappeared. Instead, the velocity profile is relatively flat and lies below the turbulent predictions. The

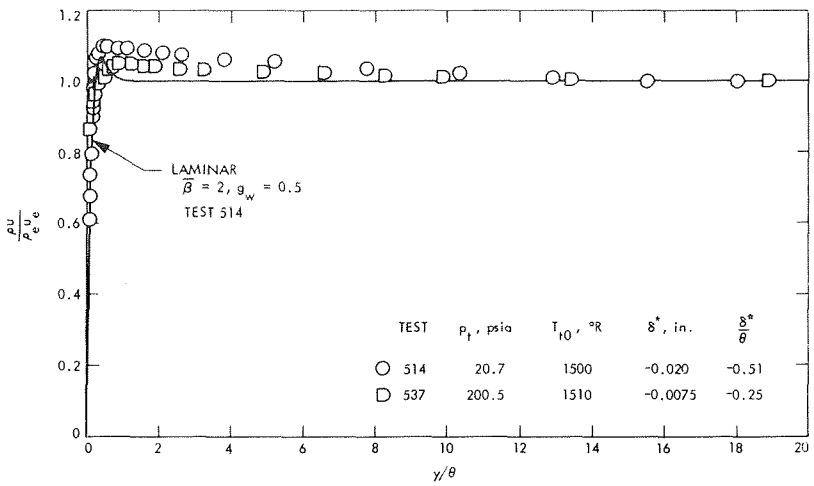

Fig. 5 Mass flux profiles across the boundary layer in the nozzle

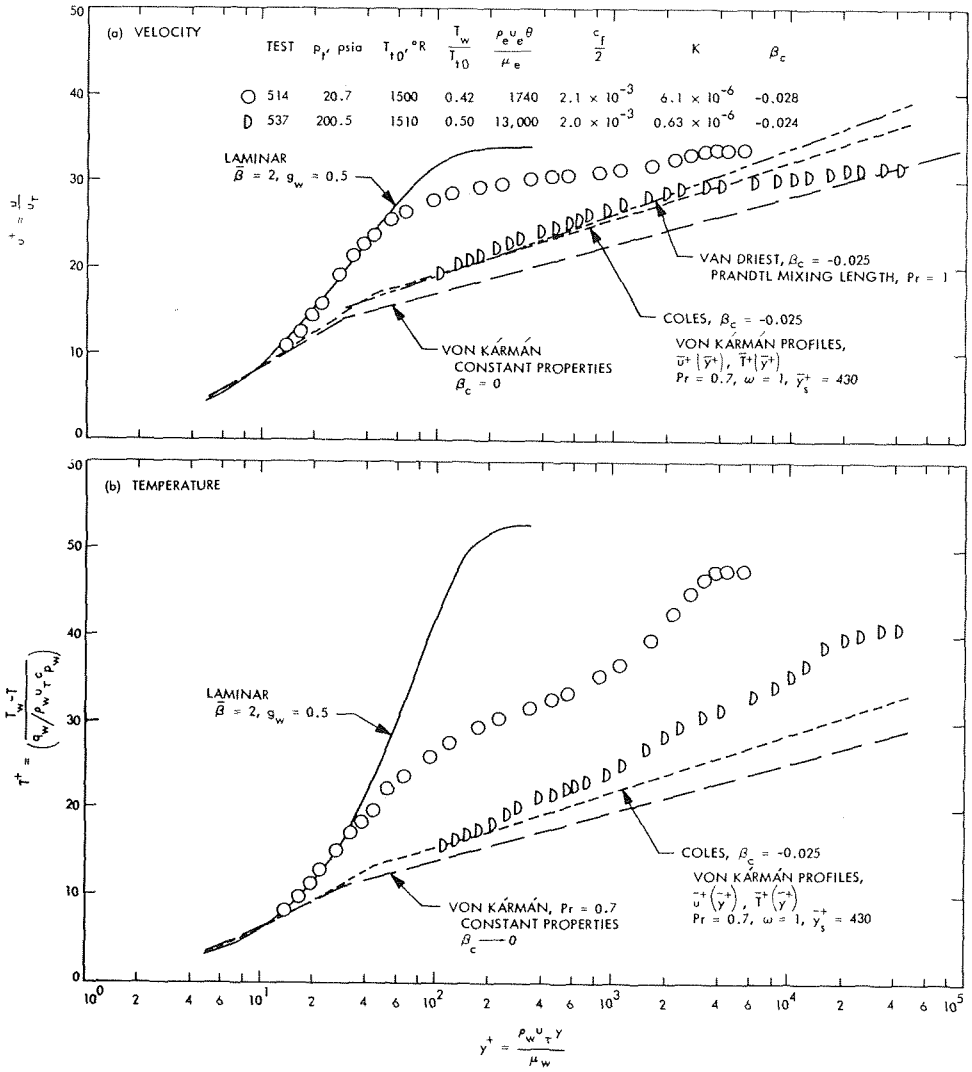

Fig. 6 Velocity profiles in terms of u^+ and y^+ and temperature profiles in terms of T^+ and y^+ in the nozzle

temperature profile at the higher pressure is virtually identical to the profile found upstream of the nozzle [23]. In the outer part of the layer, the temperature profile is not flat like the velocity profile.

At the lower pressure, where a reduction in heat transfer was found, the laminar-like appearance of both the velocity and temperature profiles in the wall vicinity is evident in Fig. 6. Inference from the agreement between the laminar profiles and the measured velocity and temperature profiles suggests that turbulent transport could not have been significant in the wall vicinity where the production of turbulence is largest for a normal turbulent boundary layer. For example, at $y^+ \sim 30$ in a normal turbulent boundary layer, laminar transport is small compared with turbulent transport. However, both the velocity and temperature profiles indicate the influence of turbulent transport farther away from the wall.

More information on the laminarization process and the relationship between the flow and thermal response was obtained by making boundary layer surveys at a number of other pressures in the nozzle. These profiles are shown in Fig. 7. The friction coefficients were obtained for these intermediate tests by observing the slope of the measured velocity profiles in the wall vicinity and using the laminar and turbulent boundary layer predictions in the wall vicinity as bounding guidelines. Although such a method is not precise, it nevertheless yields reasonable estimates of the friction coefficient, a quantity very difficult to obtain directly in accelerated flows such as those investigated here.

There is a significant difference between the velocity and temperature profiles shown in Fig. 7, not only in shape, but also at a given pressure. The temperature profiles at pressures of 45 psia and above collapse on one another, being in good agreement with the turbulent predictions from Coles' analysis. As was observed in Fig. 2, the heat transfer was apparently indicative of a turbulent boundary layer at these higher pressures. At the lower pressures, where the heat transfer was reduced, the thermal resistance was larger, and this effect is consistent with the larger values of T'^+ indicated in Fig. 7. However, the velocity profile at 45 psia (shaded points) lies nowhere near the turbulent profile; instead, it is nearly coincident with the laminar profile in the wall vicinity. In fact, only at the highest pressures is the measured velocity profile near the turbulent profile.

One infers from the comparison in Fig. 7 that acceleration affects the velocity distribution at a given location in a flow undergoing reverse transition more than it affects the temperature distribution. This apparent lag of the thermal response, compared with the flow response, implies that laminarization occurs at larger Reynolds numbers than those indicated by reductions in heat transfer. An important consequence of this lag is that even though the heat transfer may appear to be typical of a turbulent boundary layer, the friction coefficient may be reduced and hence the frictional drag may be less.

The relationship between the friction coefficient and Stanton

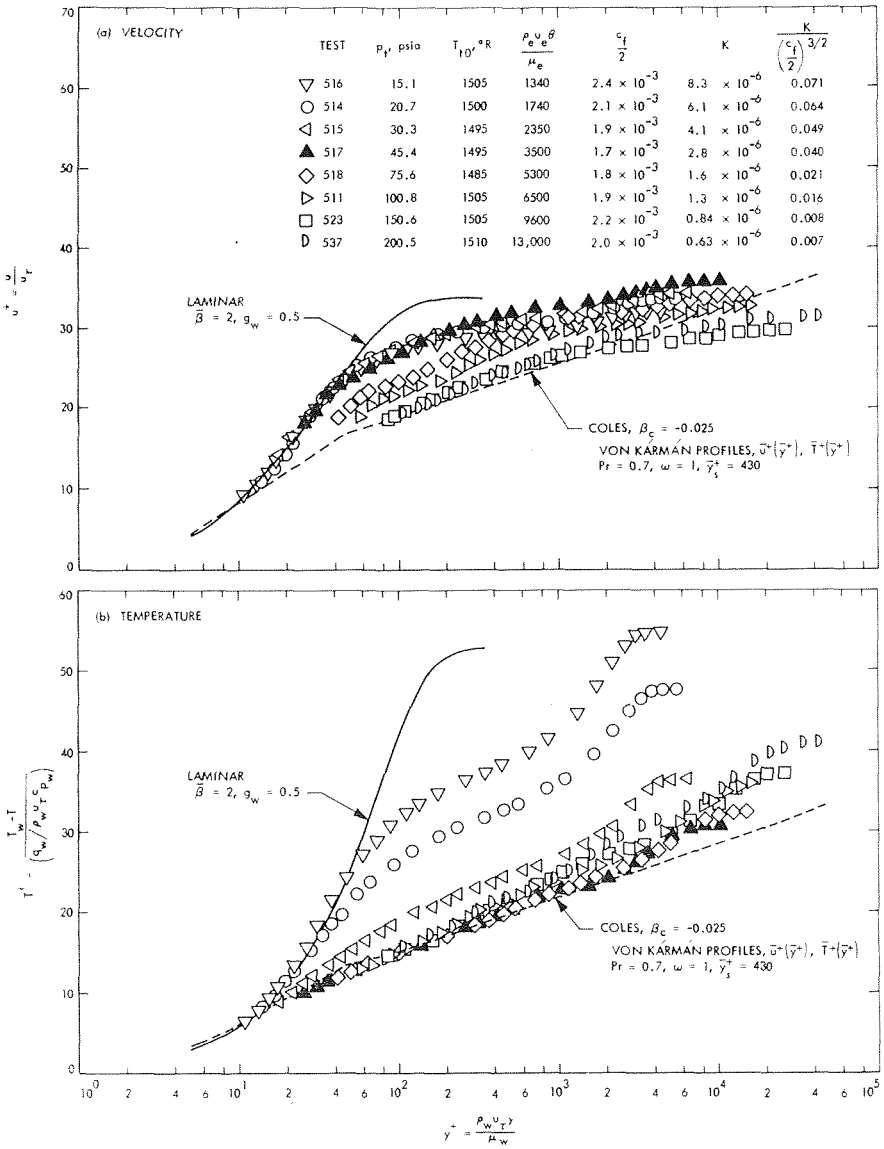

Fig. 7 Reverse transition velocity and temperature profiles in the nozzle

number at the probe position in the nozzle is shown in Fig. 8 over a range of pressures indicated above the points. The Stanton numbers appear to lie in the reverse transition region at pressures below 45 psia, but the friction coefficients lie in the reverse transition region at higher pressures (up to about 150 psia). Of note are the relatively large momentum thickness Reynolds numbers (up to about 8000) associated with the reverse transition process. Aside from the overlapping region where the heat transfer is apparently typical of a turbulent boundary layer while the friction coefficient is typical of a laminarized layer, values of $St/(c_f/2)$ are less than unity. For the lower-pressure test at 20 psia, the predicted value of $St/(c_f/2) = 0.56$ for a laminar boundary layer (Table 2) agrees fairly well with the experimentally deduced value of 0.63. This correspondence implies that the predicted Stanton number, equation (18), consistent with the estimate of the friction coefficient from the laminar profiles, is in fair agreement with the measured value. This relationship is also borne out by the agreement between the predicted laminar and measured temperature profiles in the wall vicinity, shown in Fig. 6 at the lower pressure.

Fig. 8 also indicates that a form of Reynolds analogy, e.g., von Kármán or Colburn, would predict values of $St/(c_f/2)$ that are too high in accelerated turbulent boundary layers that remain turbulent. Instead, values of $St/(c_f/2)$ appear to be less than unity (about 0.7) for the flow under consideration. One of the alternative prediction methods of [20] indicates the same trend. In this method the von Kármán relation is used; however, the friction coefficient is not taken to be the actual friction coefficient, but instead the friction coefficient evaluated at the energy thickness Reynolds number ($n = 0$ in their nomenclature). Since predicted values of the energy thickness exceed the momentum thickness, the predicted fictitious friction coefficients are smaller, and the predicted Stanton number is less than the actual friction coefficient. Although this modification of the von Kármán relation is certainly a different interpretation than that intended in the original derivation by von Kármán, the prediction nevertheless is in good agreement with the experimental data at the higher Reynolds number, as indicated in Fig. 9. In this regard, a more direct relationship between the Stanton number and energy thickness Reynolds number obtained in an analogous manner (but using the Colburn equation and the Blasius friction relation [26]),

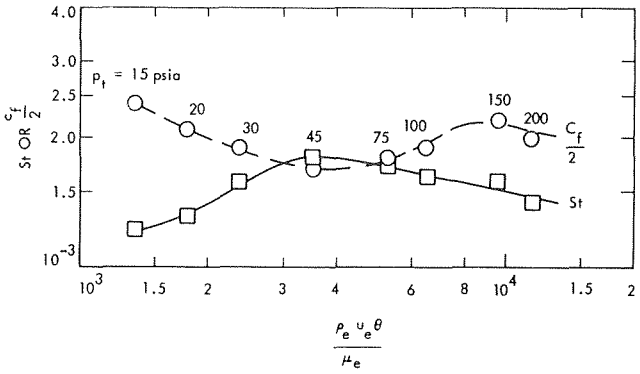

Fig. 8 Friction coefficients and Stanton numbers at the nozzle probe position

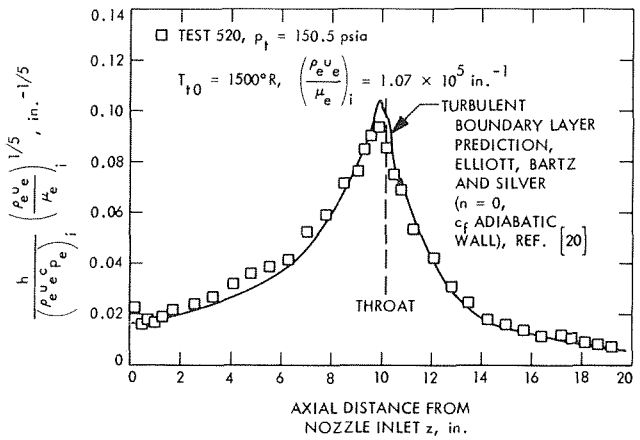

Fig. 9 Heat transfer along the nozzle at the higher Reynolds number

$$\mathrm{St}\,\mathrm{Pr}^{2/3} = \frac{A}{\left(\frac{\rho_e u_e \phi}{\mu_e}\right)^{1/4}}\left(\frac{T_e}{T_{aw}}\right)^{0.6}$$

would agree about as well with the data as the modified von Kármán relation if A is taken to be 0.015, a value slightly higher than the Blasius value of 0.0128.

Observations

Observations have indicated the important role of the wall in the production of turbulence. Experimental studies of turbulent boundary layers [27, 28] indicate the rather violent nature of the fluid in the wall vicinity, which interacts strongly with the fluid in the outer part of the layer and undergoes sudden oscillation, bursting, and ejection processes. Earlier models [29, 30] on the generation of turbulence near the wall have depicted a periodic growth of the sublayer, which then becomes unstable and turns into turbulence itself. This model provides insight to the nature of the flow near the wall, and the predicted mean velocity distribution in the sublayer is in good agreement with measurements. The basic idea of an instability in the sublayer flow has been later pursued in [31].

From the observations on laminarization, the mechanism by which turbulence is produced in the wall vicinity is apparently suppressed in accelerating flows. Consequently, there is merit in extending the ideas set forth in [29, 30] to variable free-stream velocity flows. Such an investigation, currently in progress, is an extension of a prior analysis carried out by Back [32]. The significant feature of the analysis is that the predicted frequency F of sublayer growth before disintegrating decreases in an accelerating flow, as shown in Fig. 10. The parameter on which the frequency of sublayer growth depends is

$$\chi = \left[\frac{8}{3\pi}\left(1 + \frac{4}{3\pi}\right)u_s^+\right]\frac{\mu u_e \frac{du_e}{dx}}{\rho u_\tau^3} = cu_s^+\frac{K}{\left(\frac{c_f}{2}\right)^{3/2}} \qquad (3)$$

where u_s^+ is the nondimensional velocity at the edge of the sublayer u_s/u_τ, and $c = (8/3\pi)[1 + (4/3\pi)]$.

The trend of the prediction is in agreement with observations on the decrease in the frequency of turbulent "bursting" of fluid from the wall vicinity in an accelerated flow [14]. Unfortunately, a direct comparison is not possible, since the results in [14] were shown in terms of the parameter K. If the interpolated curve is used, complete cessation of sublayer growth is predicted where the value of the parameter $K/(c_f/2)^{3/2}$ is

$$\frac{K}{\left(\frac{c_f}{2}\right)^{3/2}} = \frac{\chi_c}{cu_s^+} \cong \frac{0.75}{1.21(15.6)} = 0.040 \qquad (4)$$

This relation was obtained using a value of the sublayer velocity $u_s^+ = 15.6$, found by Einstein and Li [29] to give good agreement with measured mean velocity profiles in turbulent boundary layers with constant free-stream velocity, although a somewhat larger value of u_s^+, perhaps up to about 20, would be needed to provide agreement between predicted and measured velocity profiles in low-speed, constant-property, accelerated turbulent boundary layers when laminarization occurs. This critical value of the parameter $K/(c_f/2)^{3/2}$ is in good agreement with the observed occurrence of laminarization as indicated in the table in Fig. 7. The critical value given by equation (4) is also consistent with observations of the value of the parameter K at which laminarization occurs. For example, for the results presented here, a typical value of the friction coefficient $c_f/2$ is 2×10^{-3} (Fig. 8), and, from equation (4), the critical value of K is

$$K \cong 0.040(2 \times 10^{-3})^{3/2} = 3.6 \times 10^{-6}$$

This value would be somewhat less if a larger value of u_s^+ were used.

Both the parameter $K/(c_f/2)$, mentioned previously, and the

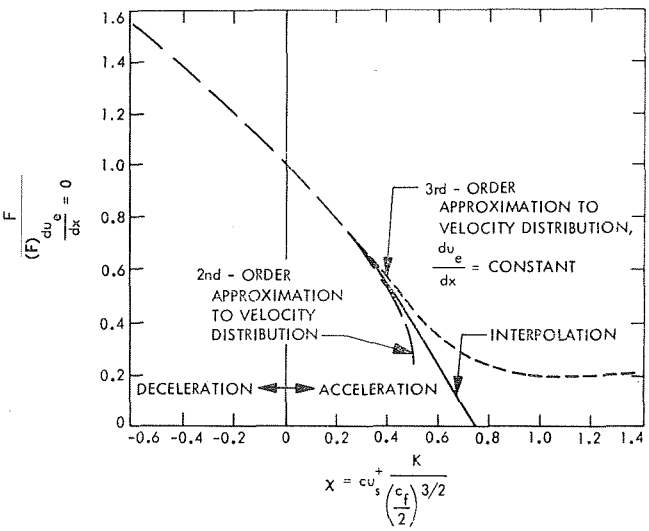

Fig. 10 Predicted frequency of sublayer growth in variable free-stream velocity turbulent boundary layers in a low-speed, constant-property flow

parameter $K/(c_f/2)^{3/2}$ are related to the effect of acceleration on turbulence. The two parameters arise because of different considerations. At this point there does not appear to be a strong basis for choosing one or the other or, for that matter, another parameter [13] as *the* parameter descriptive of the occurrence of laminarization. As mentioned previously, the parameter K is usually quoted because in many investigations the friction coefficient is not measured. However, it is interesting that the predicted magnitude of the parameter $K/(c_f/2)^{3/2}$, arising from the sublayer growth model, is in reasonable agreement with observations of laminarization.

One can also infer a time lag between the flow response and values of the parameter K inherent in the sublayer growth model. Since the fluid flows downstream during the period of sublayer growth, the actual condition along the surface is related to upstream conditions. For nozzle flow in particular, the fluid is subjected to larger values of K upstream than at the location of interest (Fig. 2).

Summary and Conclusions

Heat transfer measurements along the convergent section of a cooled, conical nozzle were found to be below those typical of a turbulent boundary layer when values of the parameter $K = (\mu_e/\rho_e u_e^2)(du_e/dx)$ exceeded about 2 to 3 $\times$ 10^{-6}. The reduction in heat transfer amounted to about 50 percent at the larger values of K or lower Reynolds numbers. The ratio of the cooled wall temperature to total gas temperature was about 0.5. Boundary layer measurements indicated the drastic change in the velocity and temperature profiles in the wall vicinity at the larger values of K. The profiles became laminar-like near the wall. From the observations on laminarization, the mechanism by which turbulence is produced in the wall vicinity is apparently suppressed in accelerating flows, and this view is consistent with observations on the important role of the wall in the production of turbulence.

At intermediate values of K, a different trend was found. Although the velocity profile still became laminar-like near the wall, the temperature profile, like the heat transfer, was typical of a turbulent boundary layer. An important consequence of this apparent thermal lag is that laminarization can occur at higher Reynolds numbers than those indicated by reductions in heat transfer. The friction coefficient can be reduced similarly to that found at the larger values of K, even though the heat transfer was relatively unaffected. Hence the frictional drag would be less.

The values of K at which laminarization was found to occur were in reasonable agreement with those predicted by considering the effect of acceleration on the periodic growth and decay of the sublayer, a model previously proposed for the production of turbulence near a wall in a nonaccelerating flow

Other findings were as follows:

1 Values of the ratio of $St/(c_f/2)$ for a laminarized layer and a turbulent boundary layer were found to be less than unity in the accelerated flow investigated.

2 The effect of increasing the convergent section length was found to reduce the throat heat transfer when laminarization occurred, but hardly to affect the results when the boundary layer remained turbulent.

3 The combined effect of acceleration and cooling was to cause the displacement thickness to become negative and the energy thickness to exceed the momentum thickness.

Acknowledgment

The authors express their gratitude to J. J. Godley for operation of the system and data acquisition; to P. Breckheimer, who carried out the numerical solutions of the laminar boundary layer equations on an IBM 7094 computer; and to others for their contribution to the investigation.

APPENDIX

Laminar Boundary Layer With Acceleration and Cooling

The laminar boundary layer equations for flow of a perfect gas over a surface are as follows when (1) both the velocity and thermal layer thicknesses are small compared with either the body radius r for an external flow or the channel radius for an internal flow and (2) the effect of longitudinal curvature of the surface is small:

Continuity:

$$\frac{\partial}{\partial x}(\rho u r^j) + r^j \frac{\partial}{\partial y}(\rho v) = 0 \tag{6}$$

Momentum:

$$\rho u \frac{\partial u}{\partial x} + \rho v \frac{\partial u}{\partial y} = -\frac{dp}{dx} + \frac{\partial}{\partial y}\left(\mu \frac{\partial u}{\partial y}\right) \tag{7}$$

Energy:

$$\rho u \frac{\partial H_t}{\partial x} + \rho v \frac{\partial H_t}{\partial y} = \frac{\partial}{\partial y}\left[\frac{\mu}{\mathrm{Pr}} \frac{\partial H_t}{\partial y} + \mu\left(1 - \frac{1}{\mathrm{Pr}}\right)\frac{\partial}{\partial y}\left(\frac{u^2}{2}\right)\right] \tag{8}$$

The equations apply to axisymmetric flow with $j = 1$ and to flow over a plane surface with $j = 0$.

Application of the combined Levy-Mangler transformation

$$\eta = \frac{r^j \rho_e u_e}{(2\xi)^{1/2}} \int_0^y \frac{\rho}{\rho_e}\, dy; \qquad \xi = \int_0^x \rho_e \mu_e u_e r^{2j} dx \tag{9}$$

and the introduction of the stream function to satisfy the continuity equation give the following transformed momentum and energy equations:

$$(Cf'')' + ff'' + \bar{\beta}[g - (f')^2] = 0 \tag{10}$$

$$\left(\frac{C}{\mathrm{Pr}}\, g'\right)' + fg' + S\left[2C\left(1 - \frac{1}{\mathrm{Pr}}\right) f'f''\right]' = 0 \tag{11}$$

In these equations the velocity component u in the flow direction x is normalized to its variable free-stream value, i.e., $u/u_e = f'$, and the total enthalpy H_t is normalized to its uniform free-stream value, i.e., $H_t/H_{t0} = g$. Implied in these equations is that both f' and g depend on the transformed coordinate η, not ξ, and this dependence is the similarity assumption. The primes denote differentiation with respect to η. The other terms that appear in equations (10) and (11) are the dimensionless density viscosity product $C = (\rho\mu)/(\rho_e\mu_e)$ and the acceleration parameter $\bar{\beta}$ which can be written either in terms of the variation of free-stream velocity or Mach number M_e for a perfect gas ($p = \rho RT$) with a constant specific heat ($H = c_p T$) as

$$\bar{\beta} = \beta \frac{T_{t0}}{T_e} = \frac{2\xi}{\mathsf{M}_e} \frac{d\mathsf{M}_e}{d\xi} \qquad \text{where } \beta = \frac{2\xi}{u_e} \frac{du_e}{d\xi} \tag{12}$$

The flow speed parameter S, the ratio of kinetic energy to total enthalpy in the free stream, is

$$S = \frac{u_e^2}{2H_{t0}} = \frac{\gamma - 1}{2} \frac{\mathsf{M}_e^2}{\left(1 + \dfrac{\gamma - 1}{2}\mathsf{M}_e^2\right)} \qquad \gamma = \text{const} \tag{13}$$

The form of equations (10) and (11) considered herein pertains to a low-speed flow $S \to 0$ of a gas with viscosity-temperature relation $\mu \propto T^\omega$ and a constant Prandtl number and are given as follows:

$$(Cf'')' + ff'' + \bar{\beta}[G(1 - g_w) + g_w - (f')^2] = 0 \tag{14}$$

$$(CG')' + (\mathrm{Pr})fG' = 0 \tag{15}$$

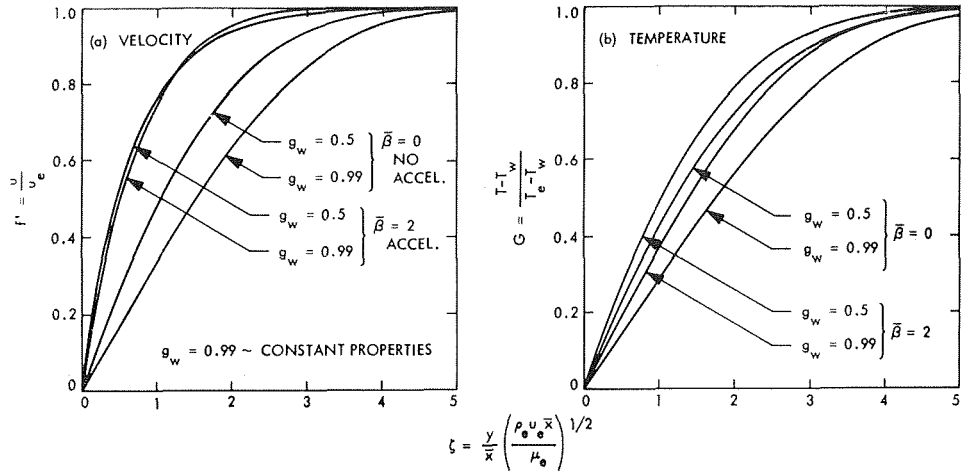

Fig. 11 Predicted laminar boundary layer velocity and temperature profiles with acceleration and cooling (Pr = 0.7, ω = 0.7)

where

$$C = \left[\frac{1}{G(1 - g_w) + g_w}\right]^{1-\omega}$$

For convenience, g has been replaced by $G = (g - g_w)/(1 - g_w)$, so that the boundary conditions for flow over an impervious surface at a specified temperature or enthalpy $g_w = (H_w/H_e) = (T_w/T_e)$ are as follows:

1 At the wall, $\eta = 0$: $f(0) = 0$, $f'(0) = 0$, and $G(0) = 0$.

2 Asymptotic condition in free-stream as $\eta \to \infty$: $f'(\eta) \to 1$ and $G(\eta) \to 1$.

The parameters in equations (14) and (15) are $\bar{\beta}$, g_w, Pr, and ω.

Solutions of the coupled, nonlinear equations (14) and (15) were obtained on a digital computer for values of Pr = 0.7, ω = 0.7 (a good approximation of the actual variation of viscosity with temperature for air over the temperature range of interest), and two values of $\bar{\beta}$ and g_w. The solution method is discussed in [33], and some predicted values that were obtained are shown in Table 2. The predicted velocity and temperature profiles are shown in Fig. 11. The effect of acceleration and cooling is to steepen the profiles near the wall and to increase their curvature. Since the actual effect of cooling on the profiles in the physical plane is opposite to that in the transformed plane, the profiles are shown in terms of the coordinate ζ, related to the physical plane. This coordinate was obtained by inverting the transformation relation, equation (9), and is

$$\zeta = \frac{y}{\bar{x}}\left(\frac{\rho_e u_e \bar{x}}{\mu_e}\right)^{1/2} = 2^{1/2}\int_0^\eta \frac{\rho_e}{\rho}\,d\eta = 2^{1/2} \times \int_0^\eta [G(1 - g_w) + g_w]d\eta \quad (16)$$

Table 2 Effect of acceleration and cooling on a low-speed variable-property laminar boundary layer flow over an isothermal wall, Pr = 0.7, ω = 0.7

$\bar{\beta}$	$g_w = \frac{T_w}{T_e}$	G'_w	f''_w	$\frac{\delta^*}{\theta}$	$\frac{\Phi}{\theta}$	$St/(c_f/2)$
0	0.5	0.35220	0.40053	1.165	1.248	1.256
0	0.99	0.41331	0.46861	2.56	1.254	1.260
2	0.5	0.41905	1.0663	0.350	2.077	0.561
2	0.99	0.52194	1.6753	0.210	3.204	0.445

where

$$\bar{x} = \frac{\xi}{\rho_e \mu_e u_e r^{2j}} = \frac{\int_0^x \rho_e \mu_e u_e r^{2j} dx}{\rho_e \mu_e u_e r^{2j}}$$

The predicted velocity profile f' for $\bar{\beta} = 2$ and $g_w = 1/2$ was fitted to the measured velocity profile near the wall when laminarization occurred, as shown in Figs. 4 and 6. The fit specifies ζ in terms of the experimental value of y/θ, and the friction coefficient is then determined from the slope of the exact solution f_w'' at the wall and the measured value of $(\rho_e u_e \theta)/\mu_e$ from the relationship

$$\frac{c_f}{2} = \frac{\tau_w}{\rho_e u_e^2} = \frac{\mu_w}{\rho_e u_e^2}(u_e f_w'')\left(\frac{d\eta}{d\zeta}\right)_w \left(\frac{d\zeta}{dy/\theta}\right)\frac{1}{\theta} = \frac{1}{(2)^{1/2}} \frac{f_w''}{\left(\frac{\rho_e u_e \theta}{\mu_e}\right)} \left(\frac{T_w}{T_e}\right)^{\omega-1} \left(\frac{d\zeta}{dy/\theta}\right) \quad (17)$$

It should be noted that the selection of a laminar profile for $\bar{\beta} = 2$, in particular, rather than another value of $\bar{\beta}$ is not necessarily arbitrary, since once ζ is determined in terms of y/θ, $\bar{\beta}$ is specified:

$$\bar{\beta} = 2\left(\frac{T_{t0}}{T_e}\right) K \frac{\left(\frac{\rho_e u_e \theta}{\mu_e}\right)^2}{\left(\frac{d\zeta}{dy/\theta}\right)^2}$$

A back calculation for the test shown in Figs. 4 and 6 yields a value of $\bar{\beta} = 1.97$, a value differing slightly from $\bar{\beta} = 2$.

In an analogous manner, the Stanton number is also specified by this fit in terms of the slope of the exact solution G_w' at the wall:

$$St = \frac{q_w}{(H_e - H_w)\,\rho_e u_e} = \frac{1}{(2)^{1/2}} \frac{G_w'}{\left(\frac{\rho_e u_e \theta}{\mu_e}\right)} \left(\frac{T_w}{T_e}\right)^{\omega-1} \left(\frac{d\zeta}{dy/\theta}\right)\frac{1}{\mathrm{Pr}} \quad (18)$$

Other quantities associated with the calculation of the velocity and temperature profiles as they are shown in Figs. 6 and 7 are as follows:

$$y^+ = \left(\frac{\rho_e u_e \theta}{\mu_e}\right)\left(\frac{c_f}{2}\right)^{1/2} \frac{1}{\left(\frac{T_w}{T_e}\right)^{\omega+1/2}} \left[\frac{\zeta}{\left(\frac{d\zeta}{dy/\theta}\right)}\right],$$

$$u^+ = \frac{f'}{\left(\frac{c_f}{2}\right)^{1/2}\left(\frac{T_w}{T_e}\right)^{1/2}}$$

$$T^+ = \frac{\left(\frac{c_f}{2}\right)^{1/2}}{\left(\frac{T_w}{T_e}\right)^{1/2}} \frac{G}{\mathrm{St}}$$

References

1 Back, L. H., Massier, P. F., and Gier, H. L., "Convective Heat Transfer in a Convergent-Divergent Nozzle," *International Journal of Heat and Mass Transfer*, Vol. 7, May 1964, pp. 549–568.

2 Back, L. H., Massier, P. F., and Cuffel, R. F., "Some Observations on Reduction of Turbulent Boundary Layer Heat Transfer in Nozzles," *American Institute of Aeronautics and Astronautics Journal*, Vol. 4, 1966, pp. 2226–2229.

3 Back, L. H., Massier, P. F., and Cuffel, R. F., "Flow Phenomena and Convective Heat Transfer in a Conical Supersonic Nozzle," *Journal of Spacecraft and Rockets*, Vol. 4, No. 8, Aug. 1967, pp. 1040–1047.

4 Boldman, D. R., Schmidt, J. F., and Gallagher, A. K., "Laminarization of a Turbulent Boundary Layer as Observed From Heat-Transfer and Boundary-Layer Measurements in Conical Nozzles," NASA TN D-4788, National Aeronautics and Space Administration, Washington, Sept. 1968.

5 Witte, A. B., and Harper, E. Y., "Experimental Investigation of Heat Transfer Rates in Rocket Thrust Chambers," *American Institute of Aeronautics and Astronautics Journal*, Vol. 1, Feb. 1963, pp. 443–451.

6 Deich, M. E., and Lazarev, L. Y., "Study of the Transition of a Turbulent Boundary Layer Into a Laminar One," Applied Physics Laboratory, Johns Hopkins University, March 1966, translated from Russian *Journal of Engineering Physics*, Vol. 7, No. 4, 1964, pp. 18–24.

7 O'Brien, R. L., "Laminarization of Nozzle Wall Boundary Layers as a Means of Reducing Heat Flux," AFRPL-TR-65-40, United Aircraft Research Laboratories, East Hartford, Conn., Feb. 1965.

8 Talmor, E., and Weber, N., "Heat Transfer From Boundary Layers Undergoing an Acceleration-Induced Reverse Transition," to be published in the *American Institute of Chemical Engineers Journal*.

9 McEligot, D. M., Coon, C. W., and Perkins, H. D., "Relaminarization in Tubes," *International Journal of Heat and Mass Transfer*, Vol. 13, Feb. 1970, pp. 431–433.

10 Moretti, P. M., and Kays, W. M., "Heat Transfer to a Turbulent Boundary Layer With Varying Free-Stream Velocity and Varying Surface Temperature, an Experimental Study," *International Journal of Heat and Mass Transfer*, Vol. 8, 1965, pp. 1187–1202.

11 Back, L. H., and Seban, R. A., "Flow and Heat Transfer in a Turbulent Boundary Layer With Large Acceleration Parameter," *Proceedings Heat Transfer Fluid Mechanics Institute*, 1967, pp. 410–426.

12 Launder, B. E., "Laminarization of the Turbulent Boundary Layer by Acceleration," Report No. 77, 1964, Massachusetts Institute of Technology, Gas Turbine Laboratory, Cambridge, Mass.

13 Patel, V. C., and Head, M. R., "Reversion of Turbulent to Laminar Flow," *Journal of Fluid Mechanics*, Vol. 34, Part 2, Nov. 1968, pp. 371–392.

14 Kline, S. J., "Observed Structure Features in Turbulent and Transitional Boundary Layers," *Fluid Mechanics of Internal Flow*, edited by G. Sovran, Elsevier Publishing Co., Amsterdam, 1967.

15 Back, L. H., Massier, P. F., and Gier, H. L., "Comparison of Measured and Predicted Flows Through Conical Supersonic Nozzles, With Emphasis on the Transonic Region," *American Institute of Aeronautics and Astronautics Journal*, Vol. 3, 1965, pp. 1606–1614.

16 Boldman, D. R., Schmidt, J. F., and Ehlers, R. C., "Effect of Uncooled Inlet Length and Nozzle Convergence Angle on the Turbulent Boundary Layer and Heat Transfer in Conical Nozzles Operating With Air," JOURNAL OF HEAT TRANSFER, TRANS. ASME, Series C, Vol. 89, No. 4, Nov. 1967, pp. 341–350.

17 Back, L. H., Cuffel, R. F., and Massier, P. F., "Laminarization of a Turbulent Boundary Layer in Nozzle Flow," *American Institute of Aeronautics and Astronautics Journal*, Vol. 7, No. 4, April 1969, pp. 730–733.

18 Back, L. H., Massier, P. F., and Cuffel, R. F., "Heat Transfer Measurements in the Shock-Induced Flow Separation Region in a Supersonic Nozzle," *American Institute of Aeronautics and Astronautics Journal*, Vol. 6, May 1968, pp. 923–925.

19 Back, L. H., and Witte, A. B., "Prediction of Heat Transfer From Laminar Boundary Layers, With Emphasis on Large Free-Stream Velocity Gradients and Highly Cooled Walls," JOURNAL OF HEAT TRANSFER, TRANS. ASME, Series C, Vol. 88, Aug. 1966, pp. 249–256.

20 Elliott, D. G., Bartz, D. R., and Silver, S., "Calculation of Turbulent Boundary-Layer Growth and Heat Transfer in Axisymmetric Nozzles," TR 32-387, Jet Propulsion Laboratory, Pasadena, Calif., Feb. 1963.

21 van Driest, E. R., "Turbulent Boundary Layer in Compressible Fluids," *Journal of Aeronautical Science*, Vol. 18, No. 3, March 1951, pp. 145–160.

22 Coles, D., "The Turbulent Boundary Layer in a Compressible Fluid," *Physics of Fluids*, Vol. 7, No. 9, Sept. 1964, pp. 1403–1423.

23 Back, L. H., Cuffel, R. F., and Massier, P. F., "Effect of Wall Cooling on the Mean Structure of a Turbulent Boundary Layer in Low-Speed Gas Flow," to be published in *International Journal of Heat and Mass Transfer*.

24 Deissler, R. G., "Turbulent Heat Transfer and Friction in the Entrance Regions of Smooth Passages," TRANS. ASME, Vol. 77, 1955, pp. 1221–1233.

25 Coles, D., "The Law of the Wake in the Turbulent Boundary Layer," *Journal of Fluid Mechanics*, Vol. 1, 1956, pp. 191–226.

26 Bartz, D. R., "Turbulent Boundary-Layer Heat Transfer From Rapidly Accelerating Flow of Rocket Combustion Gases and of Heated Air," *Advances in Heat Transfer*, Vol. 2, edited by T. F. Irvine and J. P. Hartnett, Academic Press, New York, 1965.

27 Kline, S. J., Reynolds, W. C., Schraub, F. A., and Runstadler, P. W., "The Structure of Turbulent Boundary Layers," *Journal of Fluid Mechanics*, Vol. 30, Part 4, Dec. 1967, pp. 741–773.

28 Kim, H. T., Kline, S. J., and Reynolds, W. C., "An Experimental Study of Turbulence Production Near a Smooth Wall in a Turbulent Boundary Layer With Zero Pressure Gradient," Report MD-20, Thermosciences Division, Mechanical Engineering Department, Stanford University, Jan. 1968.

29 Einstein, H. A., and Li, H., "The Viscous Sublayer Along a Smooth Boundary," *Journal of American Society of Civil Engineers*, Vol. 123, 1958, pp. 293–317.

30 Hanratty, R. J., "Turbulent Exchange of Mass and Momentum With a Boundary," *Journal of American Institute of Chemical Engineers*, Vol. 2, No. 3, 1956, pp. 359–362.

31 Black, T. J., "Some Practical Applications of a New Theory of Wall Turbulence," *Proceedings of the Heat Transfer Fluid Mechanics Institute*, 1966, pp. 366–386.

32 Back, L. H., "Heat Transfer to Turbulent Boundary Layers With a Variable Free-Stream Velocity," PhD thesis, University of California, Berkeley, Calif., June 1962, p. 72.

33 Back, L. H., "Acceleration and Cooling Effects in Laminar Boundary Layers—Subsonic, Transonic, and Supersonic Speeds," *American Institute of Aeronautics and Astronautics Journal*, Vol. 8, April 1970, pp. 794–802.

E. S. NOWAK
Professor,
Faculty of Engineering Science.
Mem. ASME

A. K. KONANUR
Graduate Student.

The University of Western Ontario,
London, Ontario, Canada

An Analytical Investigation of Free Convection Heat Transfer to Supercritical Water

Heat transfer to supercritical water (at 3400 psia in the pseudocritical region) by stable laminar free convection from an isothermal, vertical flat plate was analytically investigated. The actual variations with temperature of all or some of the thermophysical properties of supercritical water were taken into consideration. Fair agreement was found between the analytical values of this paper and existing experimental data.

Introduction

THE GROWING trend toward modern power systems operating in the supercritical region of water necessitates the accurate analytical prediction of heat transfer coefficients. The marked variations in the thermophysical properties of water in the supercritical region not only complicate the analysis of heat transfer but also indicate that high rates of free convection heat transfer may be anticipated. Experimental investigations in this region confirmed the anticipated high rates of heat transfer [1, 2, 3, 4].[1]

Fritsch and Grosh [5] found that the constant property analysis of Ostrach [6] yielded values which were in poor agreement with the experimental results of heat transfer in the supercritical region of water [3]. They therefore conducted an analytical investigation in which variations of the thermodynamic properties with temperature were taken into account and with the variations in the transport properties neglected (partial variable property analysis). The results from their partial variable property analysis were about 20 percent lower than the available experimental results.

Fritsch and Grosh concluded that better agreement would have been obtained if account were taken of the variations with temperature of the transport properties as well as the thermodynamic properties. The purpose of this paper, therefore, was to extend their analytical investigations by considering the variations with temperature of the transport properties as well as the thermodynamic properties (i.e., the general variable property case). Also investigated were the cases where some of the property values were assumed to be constant. More specifically, the following three different cases were investigated in this paper:

Case 1. Compressible flow with variable constant pressure specific heat, variable thermal conductivity, and variable dynamic viscosity, i.e., the general variable property case.

Case 2. Compressible flow with variable constant pressure

[1] Numbers in brackets designate References at end of paper.

Contributed by the Heat Transfer Division for presentation at the Winter Annual Meeting, New York, N. Y., November 29–December 3, 1970, of THE AMERICAN SOCIETY OF MECHANICAL ENGINEERS. Manuscript received at ASME Headquarters, March 9, 1970. Paper No. 70-WA/HT-6.

Nomenclature

C = C_1 for case 1 and C_2 for cases 2 and 3
C_1, C_2 = dimensional constant defined in Table 1
C_p = constant pressure specific heat
F = dimensionless velocity related similarity variable
F_x = body force in the x direction
g = acceleration due to gravity
G = dimensionless temperature variable defined in Table 1
h_x = local heat transfer coefficient
k = thermal conductivity
p = pressure
q_x'' = local heat flux
T = temperature
ΔT = temperature difference, $T_w - T_\infty$
u = velocity component in the x direction
v = velocity component in the y direction
x = coordinate along the plate
y = coordinate perpendicular to the plate
β = volumetric coefficient of expansion
$\bar{\beta}$ = $\beta\Delta T$
δ = boundary layer thickness
γ = density variation at constant pressure, $\frac{1}{\rho}\frac{\partial^2\rho}{\partial T^2}$
$\bar{\gamma}$ = $\gamma(\Delta T)^2$
η = similarity coordinate defined in Table 1
μ = dynamic viscosity
ρ = density
ψ = stream function

Subscripts

m = mean value
p = at constant pressure
r = reference
w = value at wall
x = local value
∞ = value at ambient (bulk fluid)

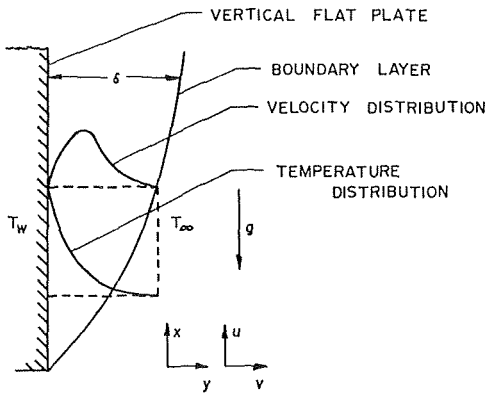

Fig. 1 Physical model and coordinate system

specific heat, constant thermal conductivity, and constant dynamic vicosity, i.e., the partial variable property case.

Case 3. Variable constant pressure specific heat and density variations considered only in the evaluation of the buoyancy force, *i.e., the simplified partial variable property case.*

Case 1 is the most complex, whereas case 3 is the simplest of the previously mentioned analyses. Prior to the research of this paper no information existed for cases 1 or 3 in the supercritical region of water. It should be mentioned that Fritsch and Grosh [5] obtained solutions for case 2 by considering mean temperature as the reference temperature to evaluate the transport properties. In this paper solutions for cases 2 and 3 were obtained for three reference temperatures, i.e., wall temperature, mean temperature, and ambient temperature.

In all the cases supercritical water at 3400 psia was considered, and the ranges of variables investigated were:

Ambient temperature, T_∞ = 714 deg F,[2] 715 deg F

Temperature difference, $\Delta T = T_w - T_\infty$ = 0.5 deg F–24 deg F.

Physical Model and Fundamental Equations

A semiinfinite vertical flat plate as shown in Fig. 1 was chosen as the physical model. The plate was assumed to be isothermal and situated in an unbounded domain. Steady, two-dimensional, stable laminar boundary layer flow conditions were assumed.

After the usual boundary layer approximations, the fundamental equations of conservation of mass, momentum, and energy may be written in the following form:

$$\frac{\partial}{\partial x}(\rho u) + \frac{\partial}{\partial y}(\rho v) = 0 \tag{1}$$

$$\rho u \frac{\partial u}{\partial x} + \rho v \frac{\partial u}{\partial y} = -\frac{\partial p}{\partial x} + F_x + \frac{\partial}{\partial y}\left(\mu \frac{\partial u}{\partial y}\right) \tag{2}$$

$$\rho C_p \left(u \frac{\partial T}{\partial y} + v \frac{\partial T}{\partial y}\right) = \frac{\partial}{\partial y}\left(k \frac{\partial T}{\partial y}\right) \tag{3}$$

with the boundary conditions:

$$\begin{aligned} u = v = 0,\ T = T_w, \quad &\text{at} \quad y = 0 \\ u = 0,\ T = T_\infty, \quad &\text{at} \quad y = \infty \end{aligned} \tag{4}$$

The body force F_x and the pressure gradient $\dfrac{\partial p}{\partial x}$ in equation (2) were replaced by $g(\rho_\infty - \rho)$.

Thermophysical Properties of Supercritical Water at 3400 psia

The values for the thermophysical properties used in this research are presented in Fig. 2. The specific volume data used was based essentially on the data given by Nowak [7]. This data was further interpolated numerically and graphically at 0.125 deg F intervals [9]. Values for the coefficient of volume expansion β and the density variation γ were obtained by graphical and numerical differentiation of the previously mentioned specific volume data.

For values of C_p greater than 10 the empirical correlation

$$C_p = \beta T/4.81 + 1 \tag{5}$$

given by Nowak [8] was utilized, whereas for values of C_p less than 10, the enthalpy data given in [10] were utilized. The transport properties (k and μ) were computed by utilizing the formulations given in [11] and [12]. The reader will find further details of all the tabulations and correlations of the property values in [9].

Reduction of Equations and Numerical Solutions

Equations (1), (2), and (3) describing free convection heat transfer are a set of nonlinear, simultaneous partial differential equations with variable coefficients. In each case, by defining a proper stream function, the conservation of mass equation was eliminated. The similarity variable transformations, along with the similarity variables listed in Table 1, were used to reduce equations (2) and (3) to ordinary nonlinear differential equations.

At any given pressure the property values were assumed to be temperature-dependent only. Substituting the variables listed in Table 1 into equations (2) and (3), the following pairs of reduced differential equations for the three cases were obtained:

Case 1 General variable property analysis

$$\frac{\mu}{\mu_\infty} F''' + F''\left[3F + \frac{G'}{\mu_\infty}\left(\frac{\partial \mu}{\partial T}\Delta T + 2\mu\bar{\beta}\right)\right] + F'\left[3\bar{\beta}G'F - 2F' + \frac{1}{\mu_\infty}\left\{\mu[G'^2(2\bar{\beta}^2 - \bar{\gamma}) + \bar{\beta}G''] + \frac{\partial \mu}{\partial T}\Delta T\ \bar{\beta}G'^2\right\}\right] + \frac{\rho(\rho_\infty - \rho)}{\rho_\infty(\rho_\infty - \rho_w)} = 0 \tag{6}[3]$$

$$kG'' + G'\left[3C_p\mu_\infty F + \frac{\partial k}{\partial T}\Delta T G'\right] = 0 \tag{7}$$

Case 2 Partial variable property analysis

The reduced equations of this case are identical to those of Fritsch and Grosh [5]:

$$F''' + 3FF'' - 2F'^2 + \bar{\beta}G'(3FF' + 2F'') - F'G'^2(\bar{\gamma} - 2\bar{\beta}^2) + \bar{\beta}F'G'' + \frac{\rho(\rho_\infty - \rho)}{\rho_\infty(\rho_\infty - \rho_w)} = 0 \tag{8}$$

$$G'' + \frac{3\mu}{k} C_p F G' = 0 \tag{9}[4]$$

Case 3 Simplified partial variable property analysis

$$F''' + 3FF'' - 2F'^2 + \frac{\rho(\rho_\infty - \rho)}{\rho_\infty(\rho_\infty - \rho_w)} = 0 \tag{10}$$

$$G'' + \frac{3\mu}{k} C_p F G' = 0 \tag{11}[4]$$

The boundary conditions for all the cases in terms of new variables were:

[2] This temperature corresponds to the pseudocritical point at which both β and C_p are maximum.

[3] The primes in equations (6)–(13) represent differentiation with respect to η.

[4] The thermal conductivity and the dynamic viscosity were evaluated at the reference temperature.

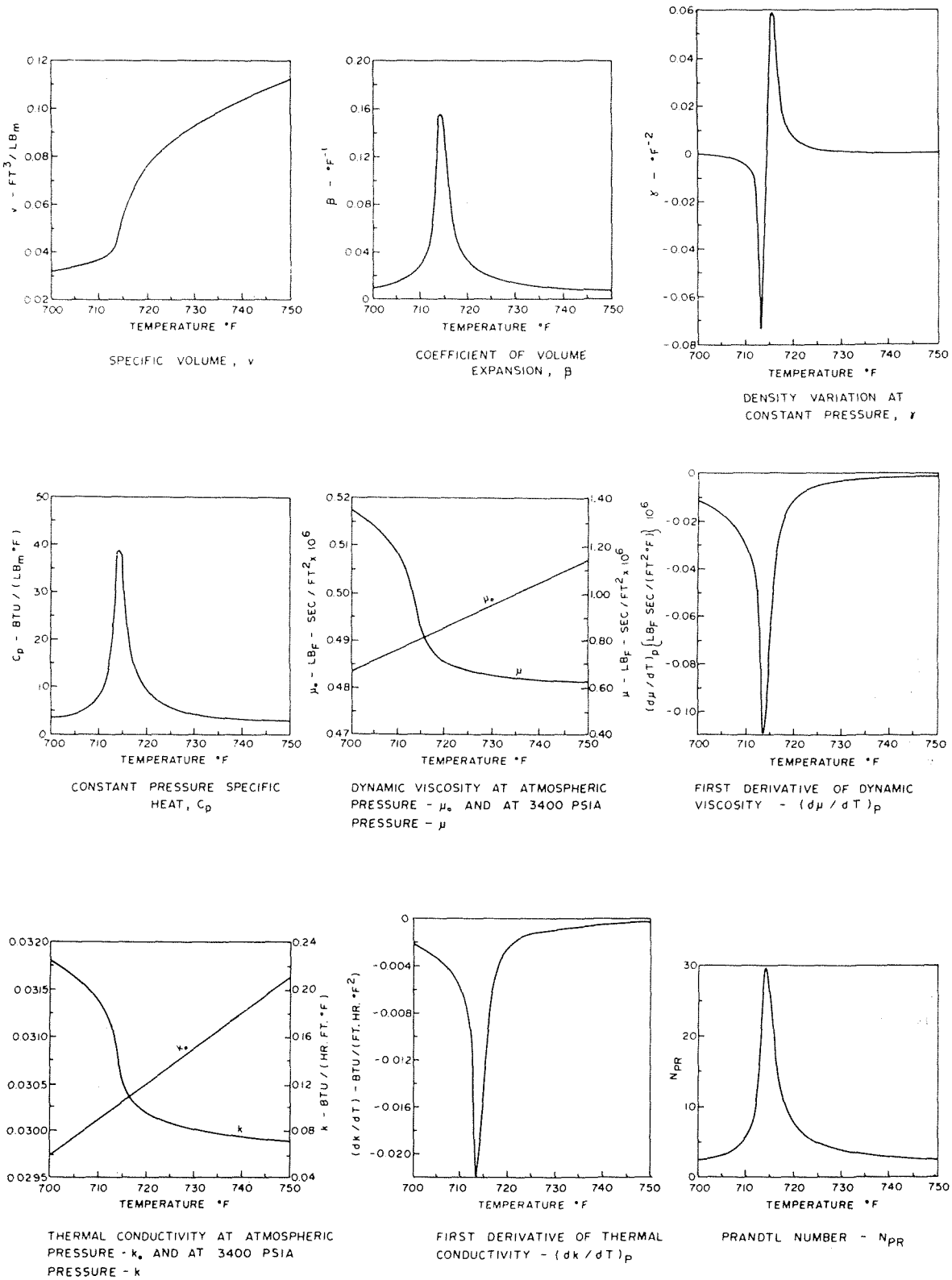

Fig. 2 Thermophysical properties of water at 3400 psia

$$F = F' = 0, G = 1 \quad \text{at} \quad \eta = 0$$
$$F' = 0, G = 0 \quad \text{at} \quad \eta = \infty \tag{12}$$

The local heat flux q_x'' and the local heat transfer coefficient h_x were computed as:

$$q_x'' = -k\Delta TCG'(0)x^{-1/4}$$
$$h_x = q_x''/\Delta T = -kCG'(0)x^{-1/4} \tag{13}$$

For a given ambient temperature and plate temperature, the sets of differential equations were integrated on a computer by using the classical fourth-order Runge-Kutta method. The unknown initial values $F''(0)$ and $G'(0)$ required to start the integration were estimated and improved continuously to satisfy the conditions for F' and G at the second boundary (which varied up to η equal to 10 in some cases) within 10^{-6}. The description and results of numerical solutions are given in [9].

In Figs. 3 and 4 some of the plots of F' and G obtained by numerical integration are presented. It should be noted that F' is a measure of u, the tangential component of velocity along the plate, whereas G is a measure of the temperature distribution in the boundary layer next to the plate.

Case	Stream Function ψ	Similarity Variable η	New Dependent Variables $F(\eta)$	$G(\eta)$
1	$u = \frac{\rho_\infty}{\rho}\frac{\partial \psi}{\partial y}$	$C_1 y/x^{1/4}$ where $C_1 = \{\frac{g(\rho_\infty - \rho_w)\rho_\infty}{4\mu_\infty^2}\}^{1/4}$	$\frac{\psi \rho_\infty}{x^{3/4} 4\mu_\infty C_1}$	$\frac{T - T_\infty}{T_w - T_\infty}$
2	$v = -\frac{\rho_\infty}{\rho}\frac{\partial \psi}{\partial x}$	$C_2 y/x^{1/4}$ where $C_2 = \{\frac{g(\rho_\infty - \rho_w)\rho_\infty}{4\mu^2}\}^{1/4}$	$\frac{\psi \rho_\infty}{x^{3/4} 4\mu C_2}$	
3	$u = \frac{\partial \psi}{\partial y}$ $v = -\frac{\partial \psi}{\partial x}$			

Table 1 Stream functions and similarity variables

Discussion of Results

A total of 182 solutions were obtained including the separate solutions obtained for different reference temperatures in cases 2 and 3. Values for the local heat flux, q_x'', and the local heat transfer coefficient, h_x, for a location $x = 1$ ft are presented in Figs. 5–8 for ambient temperatures of 714 and 715 deg F.

It is evident that the general variable property analysis is an improvement over the partial variable property analysis when the mean temperature was used as a reference temperature. However, complete agreement between the results of the general variable property analysis and existing experimental heat transfer data was not obtained. The lack of complete agreement may, in part, be attributed to the fact that the Fritsch and Grosh experimental heat transfer data was obtained from a surface more closely resembling constant heat flux conditions than one at a uniform temperature. A constant heat flux surface gives higher heat fluxes and heat transfer coefficients than those from a corresponding isothermal heat transfer surface.

The lack of complete agreement between the general variable property case and the existing experimental data might also be attributable to (*a*) errors in the thermophysical properties and to (*b*) the fact that viscous dissipation which was neglected in the analysis may be significant in the supercritical region.

It is evident, from Figs. 5–8, that the heat transfer results of cases 2 and 3 are significantly influenced by the choice of reference temperature. The analytical results are highest in value when the transport properties are evaluated at the ambient fluid temperature, whereas they are the lowest when evaluated at the

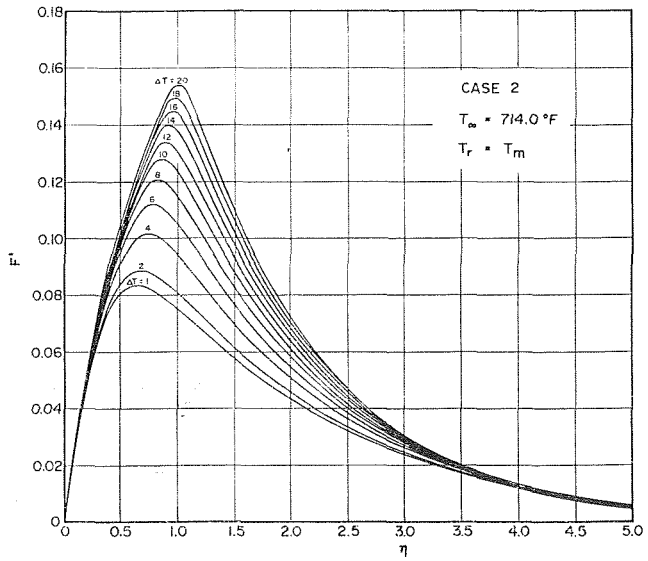

Fig. 3 Dimensionless velocity distribution, F'

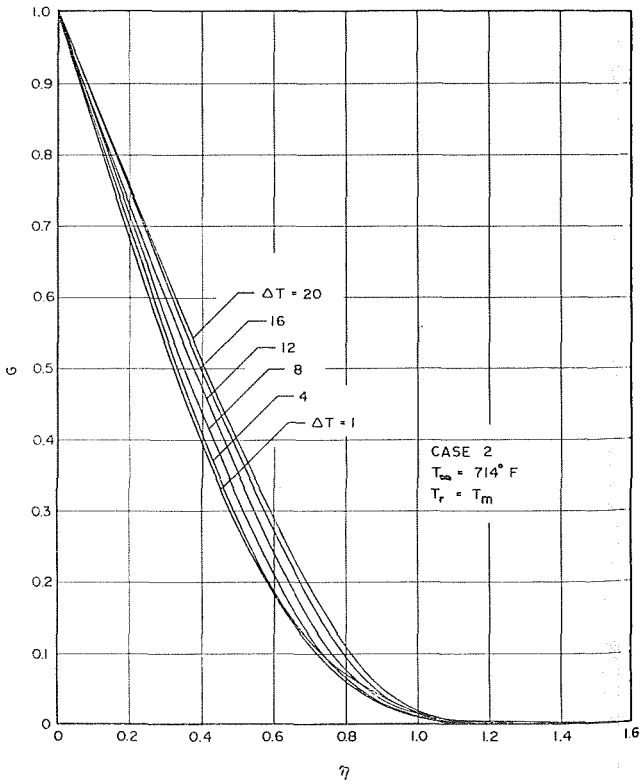

Fig. 4 Dimensionless temperature distribution, G

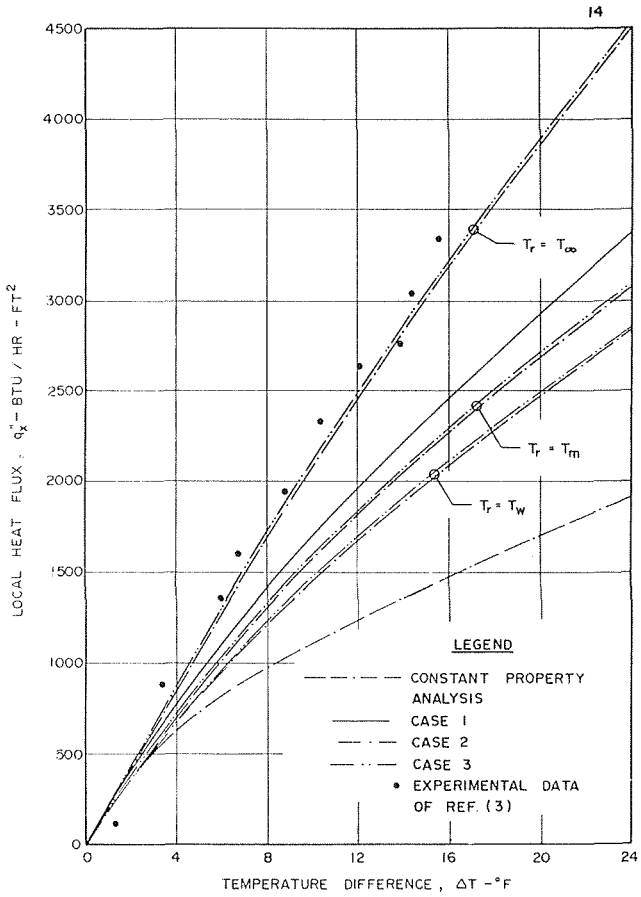

Fig. 5 Local heat flux versus temperature difference for $T_\infty = 714$ deg F

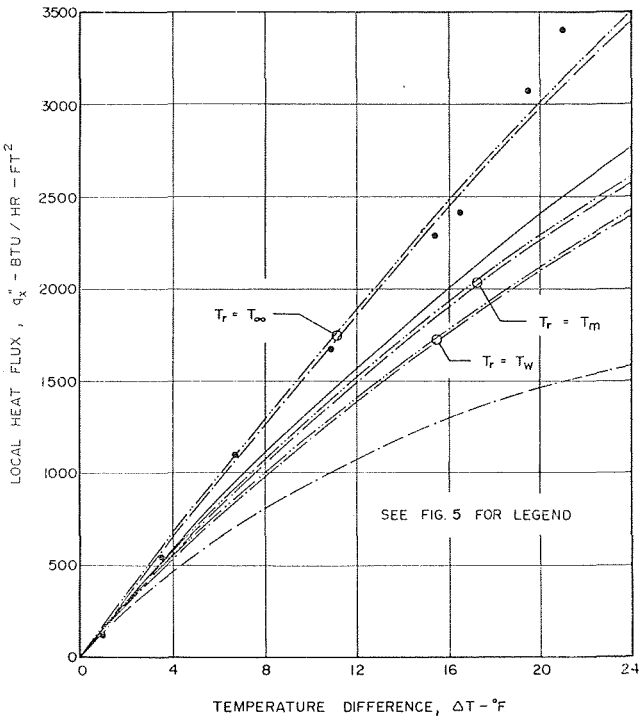

Fig. 6 Local heat flux versus temperature difference for $T_\infty = 715$ deg F

wall temperature. The authors consider the excellent agreement between the experimental data and the results from cases 2 and 3 as being fortuitous when using ambient temperature as the reference temperature due to the fact that they are simplifications and are not as comprehensive as case 1.

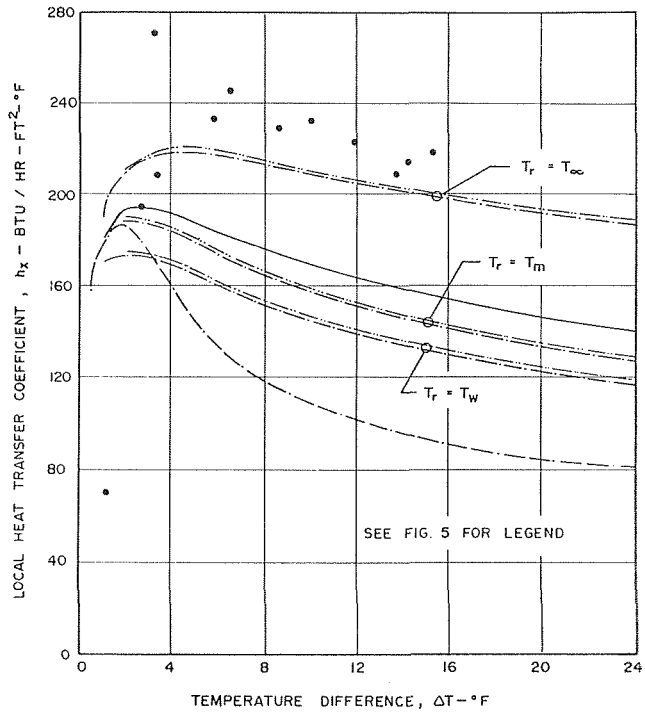

Fig. 7 Local heat transfer coefficient versus temperature difference for $T_\infty = 714$ deg F

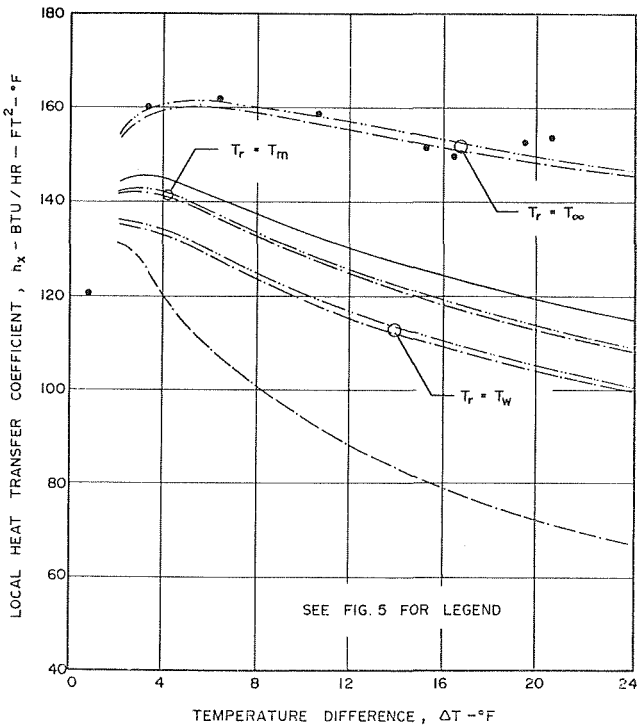

Fig. 8 Local heat transfer coefficient versus temperature difference for $T_\infty = 715$ deg F

The heat transfer results of case 2 of the present study for T_r equal to T_m are found to be lower than the analytical results of Fritsch and Grosh [5]. This is due to the use of somewhat different thermophysical property values and particularly to the fact that the thermal conductivity values used in this paper were approximately 8 percent lower than the thermal conductivity values used by Fritsch and Grosh.

The results from the simplified partial variable property analysis, case 3, are almost identical to the partial variable property analysis, case 2. Not only is case 3 simpler in anal-

ysis than case 2, but also the errors introduced in the computation of the first and second derivatives of density (β and γ) are eliminated. It is apparent from the results of cases 2 and 3 and the constant property analysis that the influence of the density variations with temperature is extremely small in comparison to that of the variations with temperature of the constant pressure specific heat.

The present analytical results confirm the trends found experimentally [3]. It is evident that local heat transfer coefficients reach a maximum corresponding to temperature differences of approximately 4 deg F. It would also appear that the heat transfer coefficient approaches zero as ΔT approaches zero.

Conclusions and Recommendations

The analytical heat transfer results obtained from the general variable property-type analysis of this paper were found to be lower than existing experimental data of free convection heat transfer in the supercritical region. The reasons for this lack of complete agreement are (*a*) deficiencies in the existing experimental heat transfer data, (*b*) errors in the thermophysical properties of water in the supercritical region, and (*c*) viscous dissipation which was neglected in the present analysis but may be significant in the supercritical region.

In view of the foregoing, it is recommended that new experimental data be obtained for free convection heat transfer in the supercritical region of water. Moreover, the general variable property analysis should be extended by considering viscous dissipation. In view of the marked effect caused by the choice of reference temperatures when evaluating thermophysical properties, the effect of uncertainties in the thermophysical properties on heat transfer should be systematically evaluated.

Acknowledgments

The senior author wishes to acknowledge the support received from the Faculty of Engineering Science of the University of Western Ontario and the Grants-in-Aid received from the National Research Council of Canada.

References

1 Schmidt, E., Eckert, E. R. G., and Grigull, V., "Heat Transfer to Liquids Near the Critical State," A.A.F. Translation, No. 527, Air Material Command, Dayton, Ohio, 1946.

2 Doughty, D. L., and Drake, R. M., Jr., "Free Convection Heat Transfer From a Horizontal Right Circular Cylinder to Freon 12 Near the Critical State," TRANS. ASME, Vol. 78, 1956, pp. 1843–1850.

3 Fritsch, C. A., and Grosh, R. J., "Free Convection Heat Transfer to Supercritical Water Experimental Measurements," JOURNAL OF HEAT TRANSFER, TRANS. ASME, Vol. 85, No. 2, 1963, pp. 289–294.

4 Hahne, E. W. P., "Wärmetransport durch natürliche Konvektion in Medien nahe Ihrem kritischen Zustand," *International Journal of Heat and Mass Transfer*, Vol. 8, 1965.

5 Fritsch, C. A., and Grosh, R. J., "An Analytical Investigation of Free Convection Heat Transfer to a Supercritical Fluid," *Proceedings of the 1961 International Heat Transfer Conference*, Part V, Paper 121, 1961.

6 Ostrach, S., "An Analysis of Laminar Free Convection Flow and Heat Transfer About a Flat Plate Parallel to the Direction of the Generating Body Force," NACA TR 1111, 1953.

7 Nowak, E. S., Grosh, R. J., and Liley, P. E., "Smoothed Pressure-Volume-Temperature Data for Water in the Critical Region Derived From Experimental Measurements," JOURNAL OF HEAT TRANSFER, TRANS. ASME, Vol. 83, No. 2, 1961, pp. 14–26.

8 Nowak, E. S., and Grosh, R. J., "An Analysis of the Specific Heat Data for Water Vapor in the Critical Region," Technical Report No. 8, Purdue University.

9 Konanur, A. K., "An Analytical Investigation of Free Convection Heat Transfer to a Supercritical Fluid," M.E.Sc. thesis, The University of Western Ontario, London, Canada, 1967.

10 Nowak, E. S., personal communication, Faculty of Engineering Science, The University of Western Ontario, London, Canada.

11 Fritsch, G. A., and Grosh, R. J., "A Description of Thermal Conductivity and Dynamic Viscosity of Water in the Critical Region," ANL-6238, Oct. 1960.

12 Haywood, R. W., "Supplementary Release on Transport Properties," *Sixth International Conference on Properties of Steam*, issued by ASME, 1964.

WALTER R. DEBLER
Professor,
University of Michigan,
Ann Arbor, Mich.
Assoc. Mem. ASME

LOUIS W. WOLF
Associate Professor,
University of Michigan,
Dearborn Campus, Dearborn, Mich.

The Effects of Gravity and Surface Tension Gradients on Cellular Convection in Fluid Layers With Parabolic Temperature Profiles

The effects of surface tension and buoyancy on the convection stability of fluid layers with a mean parabolic temperature distribution is examined. A variety of free-surface, thermal boundary conditions are used. Quantitative values for the effect on the critical Rayleigh number of the free-surface boundary condition, fluid depth, and physical properties are given. The role of the mean temperature profile is also discussed. The results should be of value in judging experiments where a free surface is used to enhance the flow visualization. The numerical procedure used to find the eigenvalues was effective and easily altered to obtain results for similar stability problems.

Introduction

A NUMBER of convection experiments with thin fluid layers possessing a free surface have been performed. The layers were warmer at the lower, solid boundary, and previously it was thought that the convection cells were due to buoyancy effects caused by the vertical temperature gradient. The analysis of Pearson [1][1] showed that cells induced by surface-tension gradients can occur in the absence of gravity. It was suggested that surface tension, and not buoyancy, was the mechanism inducing convection in many of the experiments that had been conducted. Scriven and Sternling [2] extended Pearson's work by including the effects of surface viscosity and surface displacement. These authors were able to show that in surface-tension-driven convection there is upflow beneath depressions in the free surface. This fact cast additional doubt upon the conclusions for the cause of instability in some of the previously performed experiments. To date, all of the analyses dealing with surface tension have concentrated upon fluid layers with the constant temperature gradient associated with the conduction state.

It is the purpose of this study to determine quantitatively the contributions of gravity and surface tension on the onset of convection in fluid layers with a parabolic temperature distribution. Such a situation is associated with internal heat generation in the layer and may be due to exothermic chemical reactions or Joule heating, for example. The results of this work may be used as a guide by experimenters in assessing their data for experiments where a free surface is present.

[1] Numbers in brackets designate References at end of paper.

Contributed by the Heat Transfer Division for publication (without presentation) in the JOURNAL OF HEAT TRANSFER. Original manuscript received by Heat Transfer Division, January 19, 1970. Paper No. 70-HT-K.

Problem Statement and Results

By the familiar process of pertubing the momentum, continu-

Nomenclature

A = matrix for the coefficients of the differential system
a = wave number
B = matrix for the coefficients in the boundary conditions
b = matrix obtained from boundary conditions
C = matrix formed from the b matrices
c = specific heat
D = first derivative with respect to vertical coordinate, also a determinant
D^2 = second derivative with respect to vertical coordinate, other superscripts indicate order of derivative
d = depth of fluid layer
g = gravitational constant
k = thermal conductivity
K = any linear initial value technique for solving differential equations
N_M = Marangoni number = $\sigma(\Theta_B - \Theta_T)d/\mu\kappa$
N_N = Nusselt number = qd/k
N_R = Rayleigh number = $g\alpha(\Theta_B - \Theta_T)d^3/\nu\kappa$
q = rate of change with temperature of heat loss per unit area from the upper surface to the fluid about it
R = Rayleigh number, same as N_R
R_0, R_1, etc. = terms in a power series for N_R
S = a matrix function of B and K

(Continued on next page)

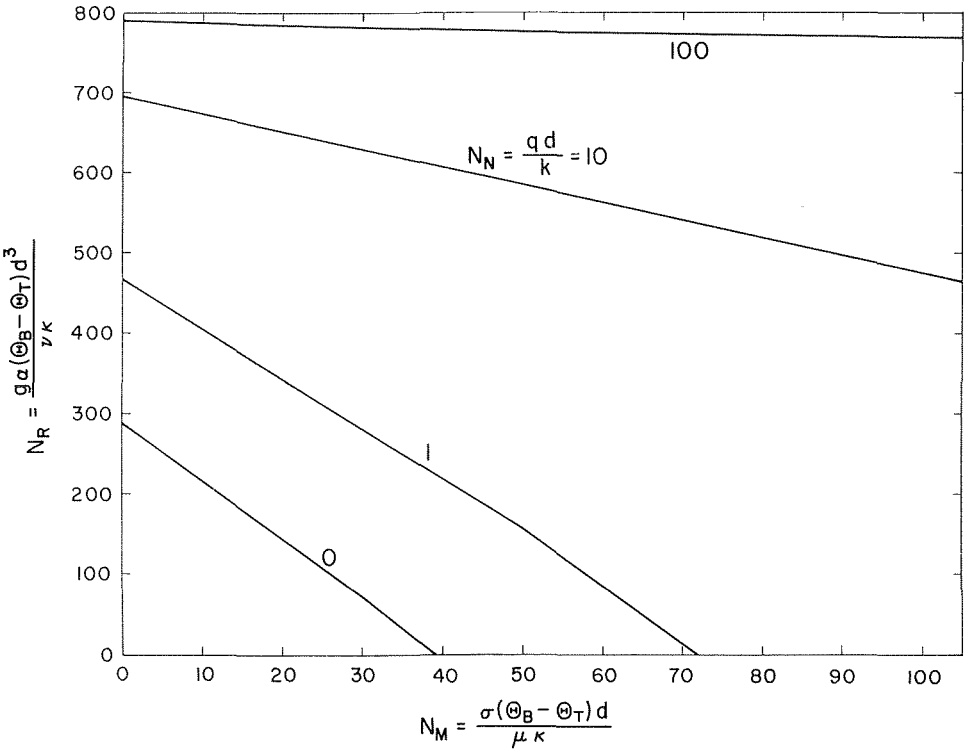

Fig. 1 Relationship between critical Rayleigh and Marangoni number for a parabolic temperature distribution in layer; *DT* is zero at lower surface and various free-surface Nusselt numbers are displayed

ity, and state equation, the following differential equation is obtained (cf. Debler [3]).

$$(D^2 - a^2)^2 w = a^2 N_R T. \tag{1}$$

In this equation D^2 denotes the second derivative with respect to the vertical coordinate, z; a is a wave number; w is the velocity component in the vertical direction; N_R is a Rayleigh number; T is the perturbation temperature. All of the variables are dimensionless. In the same way the energy equation can be written

$$(D^2 - a^2)T = wD\bar{T}. \tag{2}$$

Here the term $D\bar{T}$ is the first derivative of the temperature distribution that exists during the conducting state just prior to the onset of convection.

The surface at $z = 0$ is considered for all cases to be an insulating rigid plate. Thus the mean temperature derivative taken normal to the plate, $D\bar{T}$, is zero there. Unless it is noted to the contrary, it will be assumed in this paper that the insulation at the plate is sufficiently good that the perturbation temperature gradient also is constrained to be zero there. The boundary conditions at $z = 0$ can then be written as

$$w = 0,\ Dw = 0 \text{ and } DT = 0. \tag{3}$$

The surface at $z = 1$ is considered to be free (i.e., in contact with a nonrestricting fluid). The surface-tension effects are included to the extent that local shear stresses are generated by the variations of the surface tension due to the thermal gradients in the liquid surface. A wide range of thermal conditions at the surface is considered. The surface varies from perfectly insulating to very conducting. Unlike Scriven and Sternling [2], who did not include buoyancy, the amplitude of surface deflection is not included. Thus the boundary conditions at $z = 1$ are

$$w = 0,\ (D^2 + a^2)w = -N_M a^2 T \text{ and } DT = N_N T, \tag{4}$$

in which N_M and N_N are the Marangoni and Nusselt numbers, respectively.

Equations (1)–(4) were solved by three methods. The approach of Chandrasekhar (Debler [3]) was used for the limiting case when $N_M = 0$. An analysis similar to that of Pearson [1] was used for the extreme case when $N_R = 0$. All other combinations of Marangoni and Rayleigh numbers were solved by an initial value, Runge-Kutta technique on a digital computer. A detailed discussion of this method is given in the next section.

Nomenclature

T = dimensionless vertical temperature perturbation, also the transpose of a matrix

T = mean temperature, dimensionless = $\Theta/(\Theta_B - \Theta_T)$

T_0, T_1, etc. = terms in a power series for T

w = dimensionless vertical perturbation velocity component

w_0, w_1, etc. = terms in a power series for w

y = the unknown functions in the differential system

z = dimensionless vertical coordinate

Θ = mean temperature in fluid layer

Θ_B = mean temperature of lower plate

Θ_T = mean temperature of upper free surface

α = coefficient of thermal expansion

κ = thermal diffusivity = $k/\rho c$

ρ = mass density

μ = absolute viscosity

ν = kinematic viscosity

σ = the negative of the variations of surface tension with temperature, evaluated at the local mean temperature of the surface

Subscripts

1, 2, etc. = elements of a row or column matrix

11, 12, etc. = elements of a matrix with row-column designations

Superscripts

f = final values

s = starting values

The major results of the calculations are shown in Fig. 1. The minimum, or critical, Rayleigh number is given as a function of the Marangoni number for various values of the Nusselt number. The curves clearly show how surface tension decreases the convection stability of the fluid layer. One could extend the curves for constant Nusselt number across the horizontal axis. The points on the curves in this quadrant would correspond to a case in which the Rayleigh number is negative due to a choice of the coordinate system that requires the gravitational constant, g, to be negative. This would be the case for a fluid film with the free surface below the solid one, as on a ceiling and the z axis chosen to be positive downward. In such a situation the buoyancy effects would tend to stabilize the layer and the surface tension to destabilize it. Fig. 2 extends the range of the surface-tension parameter shown in Fig. 1.

The information in Figs. 1 and 2 can be presented as in Fig. 3, in which the abscissa is taken as the ratio $(N_R/N_M)^{1/2}$. This parameter is linear in the film thickness. It can be seen that as the fluid layer becomes sufficiently thick, the gravity effects dominate and surface tension has little or no effect. However, surface tension is the controlling factor when the liquid film is quite thin. This conclusion was pointed out qualitatively by Pearson [1] who used the same ratio, $(N_R/N_M)^{1/2}$, in his argument. Fig. 3 does show that the fluid layer must become quite thick before the effect of surface tension is very negligible. This is demonstrated by using the physical constants for water. With these values $(N_R/N_M)^{1/2}$ is $2.89d$, in which d is the fluid depth in inches. A depth of 1 in. would make $(N_R/N_M)^{1/2}$ about 3, a value for which there is a significant reduction in the critical Rayleigh number over a wide range of Nusselt numbers. It is expected, in view of these remarks, that most free-surface experiments with parabolic temperature distributions will encounter the influence of surface tension.

The role of the initial, or mean, temperature distribution was examined by solving the stability problem for a constant temperature gradient in addition to the linear one discussed heretofore. The boundary conditions given by equations (3) and (4) were used. This means that an "insulating" condition was imposed on the perturbation boundary condition. This might be appropriate if the lower surface was a relatively poor thermal conductor. The differential system that was solved is akin to that given by equations (1) and (2), but in the present situation the term $D\bar{T}$ in equation (2) is a constant. The results of the calculations are shown in Figs. 4 and 5 which point out, when compared with Figs. 1 and 2, that there is little difference between the stability characteristics for the linear and parabolic temperature profiles. The linear temperature distribution proves to be the more stable one. Fig. 6 is a presentation of the information in the previous two figures to show the effect of fluid depth on the stability of these layers.

Because of the ease with which the computation procedure could be adjusted to deal with different temperature profiles and boundary conditions, a series of computations were made to see how the solutions compared with those obtained by others for the selected test problem. In this way the validity of the computer program could be assessed. A linear temperature profile was selected with a "conducting" condition on the perturbation temperature (i.e., $T(0) = 0$). A free surface was employed but the Marangoni number set to 0.01, almost zero. Nusselt numbers of 0, 1, 10, 100, 10000 were used. The critical Rayleigh numbers that were obtained are also plotted in Fig. 4 to show the effect of the lower themal boundary condition. The Rayleigh number for the highly conducting free surface was 1100.54 at a wave number of 2.7. The agreement with the solution of Jeffries [4] is more than adequate. Finally, the problem of a fluid layer with a linear temperature distribution that is contained between two rigid, conducting boundaries was tried. The minimum eigenvalue was 1707.9 with a equal to 3.1. The agreement with the well-known solution was satisfactory (cf. Jeffries). The information given in Figs. 4 and 5 differs from that presented by Nield [5] because of the different boundary conditions that were treated. Nield's results along with those presented in this paper form a fairly complete picture of the stability of horizontal liquid layers with a free surface, provided surface deflection is not considered and only infinitesimal disturbances are allowed (cf. Davis [6]).

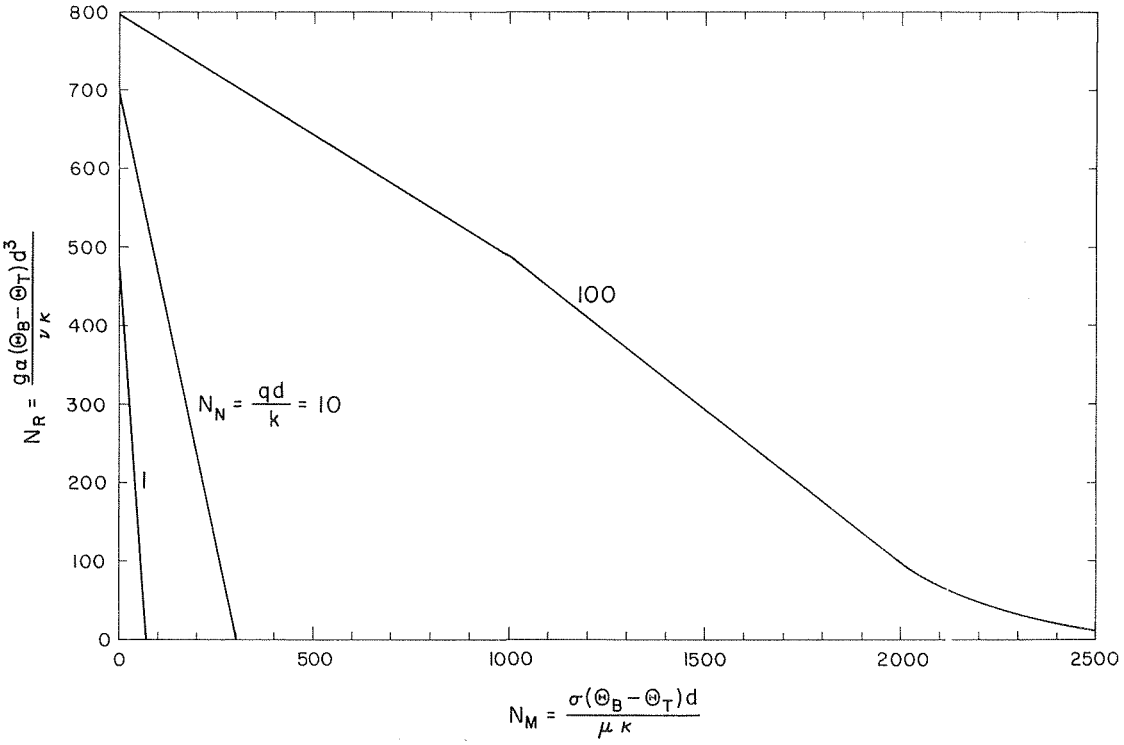

Fig. 2 Extended range of Marangoni number for conditions shown in Fig. 1

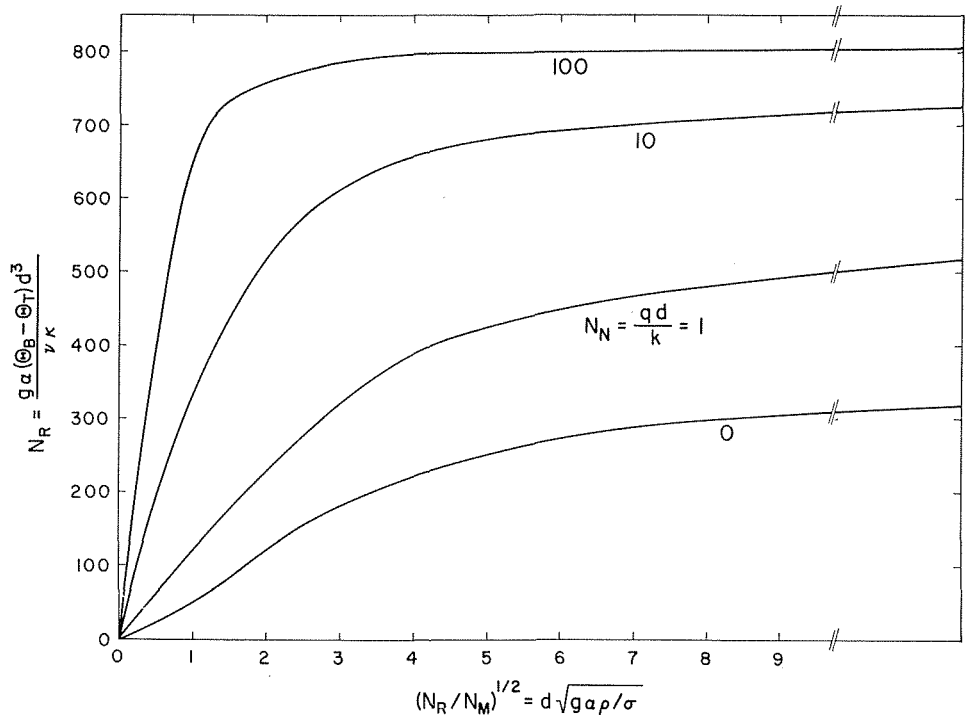

Fig. 3 Explicit dependency of critical Rayleigh number upon depth for parabolic temperature distribution in layer; *DT* is zero at lower surface and various free-surface Nusselt numbers are displayed

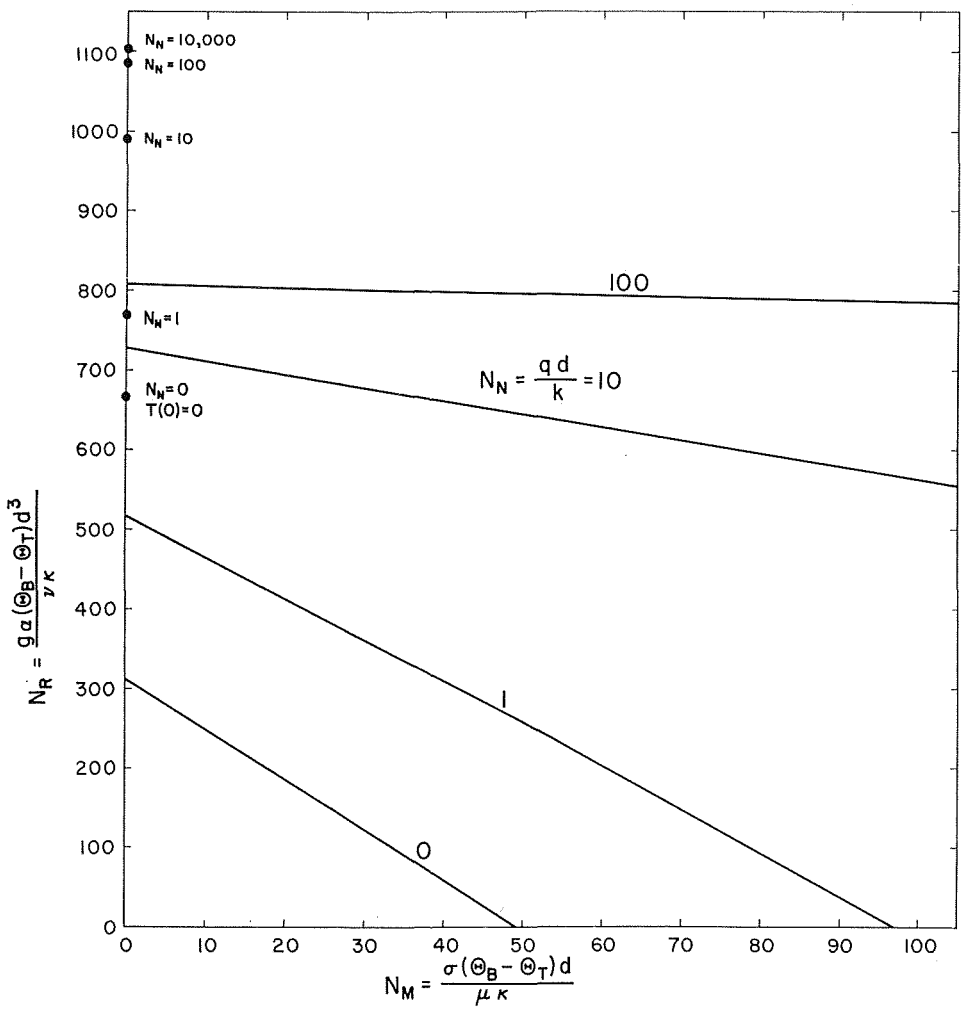

Fig. 4 Relationship between critical Rayleigh and Marangoni numbers for a linear temperature distribution in layer; *DT* is zero at lower surface and various free-surface Nusselt numbers are displayed (Points on ordinate axis show critical Rayleigh numbers for $T(0) = 0$ for comparison)

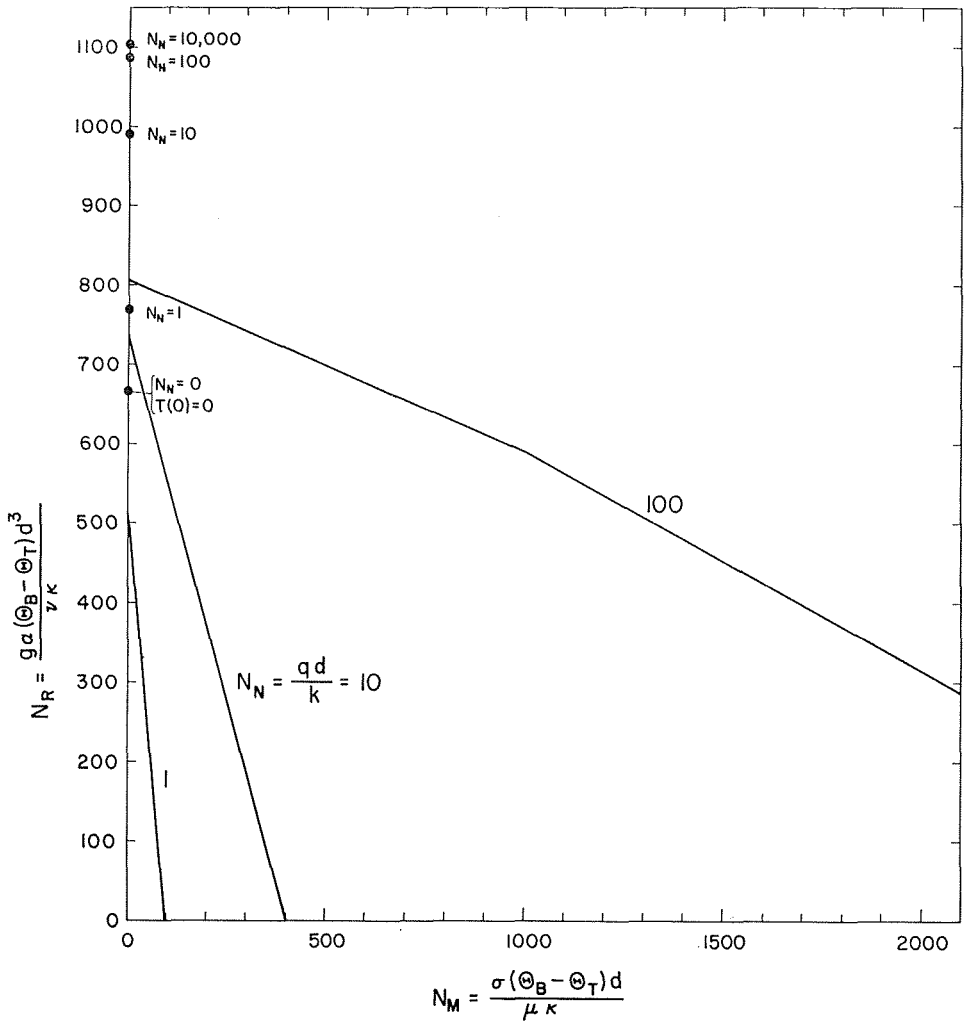

Fig. 5 Extended range of Marangoni number for conditions shown in Fig. 4

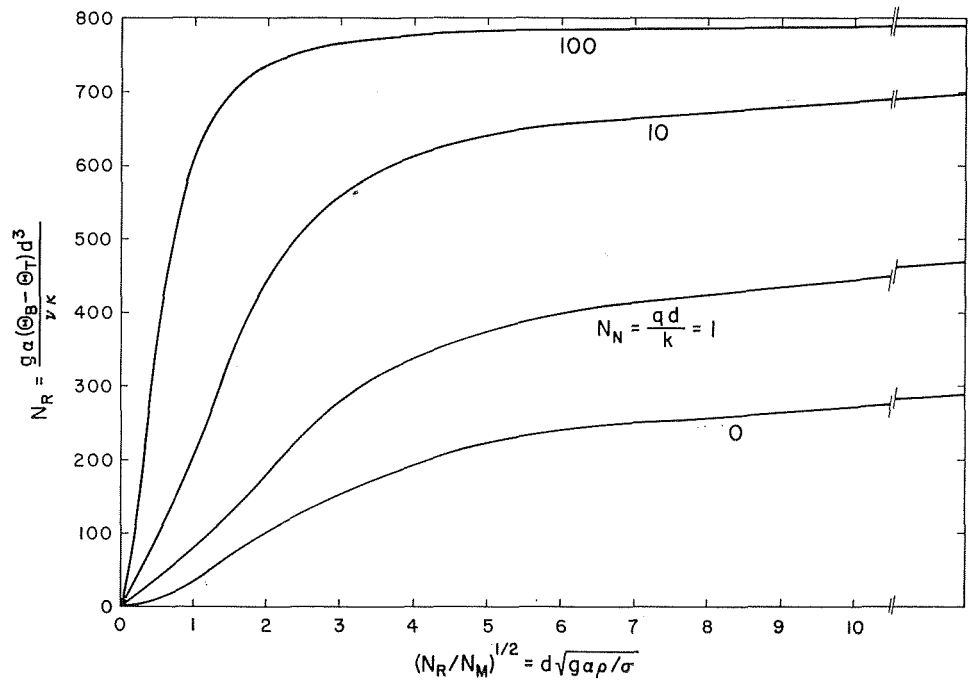

Fig. 6 Explicit dependency of critical Rayleigh number upon depth for linear temperature distribution in layer; *DT* is zero at lower surface and various free-surface Nusselt numbers are displayed

The computational procedure gave solutions in concert with those using Chandrasekhar's method (cf. Debler [3]) for the parabolic temperature distributions with N_M equal to zero and for the limiting cases of zero and infinite Nusselt number. For these problems the infinite series for the temperature perturbation that was assumed was $\Sigma A_n \cos(n\pi z)$ with $n = 0, 1, 2$, etc. for a Nusselt number of zero, and $\Sigma A_n \cos(n\pi z/2)$ with n taking on the values of the odd integers when the Nusselt number is infinite.

The variation of the wave number at which the minimum Rayleigh number occurred for various values of Nusselt and Marangoni number is presented in Fig. 7. It can be seen that the critical wave number is almost independent of Marangoni number. Thus, observed values of a would not be expected to give an indication of the extent of the surface-tension effects.

No actual calculations were performed for the case of $N_N = 0$. Instead, values near zero, 0.01–0.10, were used. The fact that the minimum Rayleigh number occurs at $a = 0$ when $N_N = 0$, regardless of the value of N_M, can be easily demonstrated. Because the parameter a occurs in the differential equations and boundary conditions only as a^2, it is reasonable to expand the solution, w and T, as well as N_R, in a power series of a^2. In this way the following terms will be substituted into equations (1) and (2).

$$w = w_0 + a^2 w_1 + a^4 w_2 + \ldots\ldots;$$
$$T = T_0 + a^2 T_1 + a^4 T_2 + \ldots\ldots;$$

and

$$N_R = R_0 + a^2 R_1 + a^4 R_2 + \ldots\ldots;$$

If the terms in a^0, a^2, a^4, etc. are collected together the equations which must be solved are

$$D^4 w_0 = 0,$$
$$D^4 w_1 - 2D^2 w_0 = R_0 T_0,$$
$$D^4 w_2 - 2D^2 w_1 + w_0 = R_0 T_1 + R_1 T_0, \text{ etc.}$$

as well as

$$D^2 T_0 = w_0(D\bar{T}),$$
$$D^2 T_1 - T_0 = w_1(D\bar{T}),$$
$$D^2 T_2 - T_1 = w_2(D\bar{T}), \text{ etc.}$$

The boundary conditions must be satisfied independently of a^2 so one has at $z = 0$

$$w_i = 0 = DT_i = DW_i$$

in which $i = 0, 1, 2$, etc. At $z = 1$ the boundary conditions are

$$w_i = 0 = DT_i$$

for all values of the index i and

$$D^2 w_0 = 0, \; D^2 w_i + w_{i-1} = -N_M T_{i-1}.$$

Such a formulation of the eigenvalue problem gives for the case of a linear mean-temperature profile (i.e., $D\bar{T} = -1$)

$$R_0 = 320 - 6.66\, N_M \tag{5}$$

and for the parabolic profiles, $D\bar{T} = -2z$,

$$R_0 = 288 - 7.20 N_M. \tag{6}$$

These are the values of N_R for $a = 0$. Since a finite value of R_0 was achieved, it is to be expected that the critical value of the Rayleigh number is realized at $a = 0$, where $dN_R/da = 0$, regardless of the value of N_M. Thus the fact that the calculations indicated a maximum in the N_R versus a curve was to be expected near $a = 0$ has been independently substantiated. Also equations (5) and (6) point out the existence of the linear eigenvalue relationship between N_R and N_M for $N_N = 0$, as shown in Figs. 1 and 4.

Method of Solution

In order to be able to apply the Runge-Kutta technique to this eigenvalue problem, the equations were handled in the following way. The foregoing differential equations (1)–(4) may be decomposed into a set of N (N equals six in this case) simultaneous first-order equations. These may be represented in matrix form by

$$y' = Ay$$

in which A, an $N \times N$ matrix, is the matrix of the coefficients and y is a column matrix of the independent variables. The matrix A is a function of the parameter $R = N_R$, a, and z. In this case

$$y_1 = T, \; y_2 = DT \quad y_3 = w, \; y_4 = Dw, \quad y_5 = D^2 w, \quad y_6 = D^3 w$$

and thus the matrix can be written as

$$A = \begin{bmatrix} 0 & 1 & 0 & 0 & 0 & 0 \\ a^2 & 0 & D\bar{T} & 0 & 0 & 0 \\ 0 & 0 & 0 & 1 & 0 & 0 \\ 0 & 0 & 0 & 0 & 1 & 0 \\ 0 & 0 & 0 & 0 & 0 & 1 \\ a^2 R & 0 & -a^4 & 0 & 2a^2 & 0 \end{bmatrix}$$

The starting values of y are denoted as y^s (at the value of $z = 0$ for this problem). Let y^f be the final values of y (at the value $z = 1$ for this problem). The Runge-Kutta process, or for any linear initial-value technique, for a linear set of equations represents a linear transformation between y^s and y^f of the following form

$$y^f = Ky^s \tag{7}$$

in which K is a function of the matrix A, the specific initial-value technique being used, and the grid spacing.

In order to get a solution to the problem it is necessary to select for a specific wave number, a, a set of values for y^s and the proper

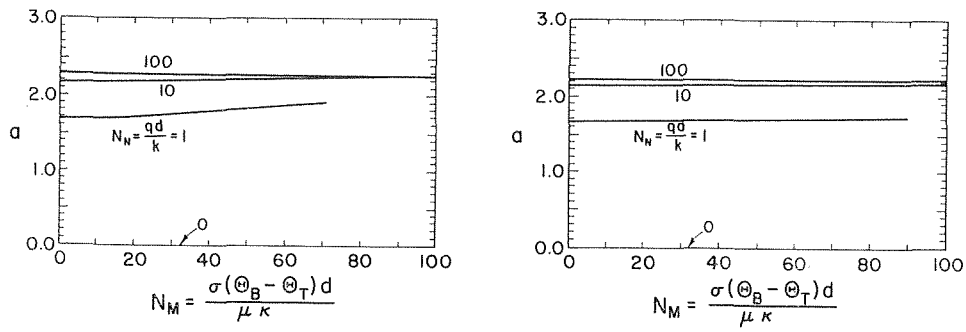

Fig. 7 Wave number a, at the critical Rayleigh number, as a function of Marangoni and Nusselt numbers; (a) left, parabolic mean-temperature distribution; (b) right, linear mean-temperature distribution

value of R. The known starting conditions must be satisfied and the correct values for y^f must be realized ultimately at the end of the interval.

The boundary conditions at either end involve a mixture of the various y's. It is convenient not to select the y values but to transform the y^s and y^f into another space to facilitate subsequent selection of independent solutions. Let

$$b^s = B^s y^s \tag{8}$$

and

$$b^f = B^f y^f \tag{9}$$

The values for B^s, B^f, b^s, b^f are chosen to satisfy the boundary conditions and to make B^s and B^f nonsingular. The equations (8) or (9) can be represented by

$$b = By \tag{10}$$

If this equation set is partitioned

$$b = [b_1, b_2]^T$$

$$B = \begin{bmatrix} B_{11}B_{12} \\ B_{21}B_{22} \end{bmatrix}$$

and

$$y = [y_1, y_2]^T;$$

the partitioning takes place in such a way that b_1 has n entries where n is the number of boundary conditions specified at that point (in the present problem n is 3). For eigenvalue problems b_1 is constructed to be always null, and B_{11} and B_{12} are the coefficients of y in those boundary conditions. The values of b_2 are not specified and can be determined only as a part of the solution procedure. B_{21} and B_{22} may be chosen arbitrarily subject to the constraint that these lower rows must be independent of the upper rows. It is desirable from the point of view of error control to have these lower rows as nearly orthogonal as possible; that is, the B matrix should be as close to an orthogonal matrix as possible. Thus B^s, B^f, $b_1{}^s$, and $b_1{}^f$ are determined a priori with $b_2{}^s$ and $b_2{}^f$ undetermined.

If equations (1), (2), and (3) are combined

$$b^f = B^f y^f = B^f K y^s = B^f K (B^s)^{-1} b^s$$

or

$$b^f = S b^s$$

in which

$$S = B^f K (B^s)^{-1}.$$

By partitioning this equation in the same manner as (10) the following equations result,

$$b_1{}^f = S_{11} b_1{}^s + S_{12} b_2{}^s$$

and

$$b_2{}^f = S_{21} b_1{}^s + S_{22} b_2{}^s.$$

These reduce in the eigenvalue problem to

$$S_{12} b_2{}^s = 0 \tag{11}$$

and

$$S_{22} b_2{}^s = b_2{}^f \tag{12}$$

since $b_1{}^s$ and $b_1{}^f$ are null.

In order that (11) not be trivial the determinant of S_{12} must be zero. S_{12} for a given wave number, a, is a function of the parameter R only. The vanishing of the determinant represents the criterion for judging whether or not one has selected the proper value of R.

The solution to the eigenvalue problem now involves the calculation of S_{12} as a function of R. This is done by selecting an $N \times N$ matrix, C^s, such that the first, n rows are null and the remaining rows are arbitrarily chosen to be independent vectors. A matrix C^f is calculated from C^s by

$$C^f = SC^s. \tag{13}$$

These two C matrices are square and consist of N columns of the appropriate b matrices. The C^s matrix is partitioned in the manner of the S matrix. The multiplications are performed, noting that $C_{11}{}^s$ and $C_{12}{}^s$ are null, with the result that

$$C^f = \begin{bmatrix} S_{12}C_{21}{}^s & S_{12}C_{22}{}^s \\ S_{22}C_{21}{}^s & S_{22}C_{22}{}^s \end{bmatrix}. \tag{14}$$

Since $C_{21}{}^s$ and $C_{22}{}^s$ can be chosen arbitrarily, they can be chosen to have $C_{22}{}^s$ null and $C_{21}{}^s$ nonsingular and easily invertable. In many cases this can simply be the $n \times n$ identity matrix. Then equation (14) reduces to

$$C_{11}{}^f = S_{12}C_{21}{}^s \tag{15}$$

and

$$C_{21}{}^f = S_{22}C_{21}{}^s. \tag{16}$$

Consequently, S_{12} and S_{22} may be determined by

$$S_{12} = C_{11}{}^f (C_{21}{}^s)^{-1} \tag{17}$$

and

$$S_{22} = C_{21}{}^f (C_{21}{}^s)^{-1}. \tag{18}$$

Inasmuch as only the determinant of S_{12} is necessary for determination of the eigenvalue, the determinant of $C_{21}{}^s$ can be precalculated (it is unity if $C_{21}{}^s$ is the identity matrix) and

$$\det (S_{12}) = \det (C_{11}{}^f) \, [\det (C_{21}{}^s)]^{-1}. \tag{19}$$

For the problem under consideration in this paper the following were chosen:

$$B^s = \begin{bmatrix} 0 & 1 & 0 & 0 & 0 & 0 \\ 0 & 0 & 1 & 0 & 0 & 0 \\ 0 & 0 & 0 & 1 & 0 & 0 \\ 1 & 0 & 0 & 0 & 0 & 0 \\ 0 & 0 & 0 & 0 & 1 & 0 \\ 0 & 0 & 0 & 0 & 0 & 1 \end{bmatrix}$$

$$B^f = \begin{bmatrix} 0 & 0 & 1 & 0 & 0 & 0 \\ a^2 N_M & 0 & 0 & 0 & 1 & 0 \\ N_N & 1 & 0 & 0 & 0 & 0 \\ 0 & 0 & 0 & 1 & 0 & 0 \\ 0 & 0 & 0 & 0 & 1 & 0 \\ 0 & 0 & 0 & 0 & 0 & 1 \end{bmatrix}$$

$$b^s = [0 \quad 0 \quad 0 \quad b_4{}^s \quad b_5{}^s \quad b_6{}^s]^T$$

$$b^f = [0 \quad 0 \quad 0 \quad b_4{}^f \quad b_5{}^f \quad b_6{}^f]^T$$

$$C^s = \begin{bmatrix} 0 & 0 & 0 & 0 & 0 & 0 \\ 0 & 0 & 0 & 0 & 0 & 0 \\ 0 & 0 & 0 & 0 & 0 & 0 \\ 1 & 0 & 0 & 0 & 0 & 0 \\ 0 & 1 & 0 & 0 & 0 & 0 \\ 0 & 0 & 1 & 0 & 0 & 0 \end{bmatrix}$$

Because $C_{21}{}^s$ is an order-3 identity matrix its determinant is unity. This is clearly an advantage in solving equation (19). A fourth-order Runge-Kutta-Gill process was used to determine K from which S, and consequently S_{12}, is determined.

A simple half-interval searching technique was used to find the value of R that gave a null value for the determinant of $C_{11}{}^f$. Initial bounds were chosen for R on the basis of past experience; rapid convergence was obtained.

The parameter a is implicit in matrix A and hence in K and S,

but N_N and N_M appear only linearly in the matrix B^i. In view of this B^i can be decomposed in the following way:

$$B^i = B_N{}^i \quad N_N + B_M{}^i \quad N_M + B_1{}^i,$$

in which $B_N{}^i$, $B_M{}^i$, and $B_1{}^i$ are those matrices which are the coefficients of N_N, N_M, and unity in matrix B^i. For selected values of a and R, S is a linear function of N_N and N_M. Thus $C_{11}{}^i$ is also a linear function of N_N and N_M, and can be written

$$C_{11}{}^i = C_N{}^i \quad N_N + C_M{}^i \quad N_M + C_1{}^i,$$

in which the coefficients are defined in a similar matter to those for B^i. The determinant of $C_{11}{}^i$ also is linear in N_N and N_M for the problem under examination, but it generally involves a cross-product term such as

$$D = D_N N_N + D_M N_M + D_{NM} N_N N_M + D_1.$$

The determinants D_N, D_M, D_{NM}, and D_1, the coefficients of the dimensionless parameters, are usually nonlinear functions of a and R. The fact that D is linear in N_M and independently linear in N_N makes the task of finding the D which gives a minimum value of R considerably simpler. Although the exact value of a which give a minimum R cannot be determined a priori, the region of the correct a can be quickly delimited. By selecting values of a and R in a range known to contain the solution and plotting the results, the values of a and R causing the determinant D to equal zero were estimated by simple interpolation. These refined values of a and R then were validated as being the required solution by direct calculation of the determinant to see if it was within the prescribed limits of being zero. The entire process went quickly.

Conclusions

The method for solving the eigenvalue problem associated with equations (1), (2), (3), and (4) is easy to use and has the desired precision. It is also extremely flexible, and by adjusting $D\bar{T}$ and the various boundary conditions in the appropriate matrices a variety of other stability problems can be solved. The computations show a nearly linear relationship between the critical Rayleigh and Marangoni numbers for the problem studied. The work shows the influences of the free-surface heat transfer condition, the boundary condition assumed at the lower surface for the perturbation temperature, and the minor effect on the stability due to the mean-temperature profile. One may infer from the results that as the mean-temperature distribution becomes increasingly nonlinear, the stability of the layer is lessened. The extent of the decrease in the critical Rayleigh number for fluid layers of various depths is given. This presentation suggests that surface-tension effects can influence the observed critical Rayleigh number for many laboratory configurations. The critical wave number proves to be almost independent of the Marangoni number.

References

1 Pearson, J. R. A., "On Convection Cells Induced by Surface Tension," *Journal of Fluid Mechanics*, Vol. 4, 1958, p. 81.

2 Scriven, L. E., and Sternling, C. V., "On Cellular Convection Driven by Surface Tension Gradients: Effects of Mean Surface Tension and Surface Viscosity," *Journal of Fluid Mechanics*, Vol. 19, 1964, p. 321.

3 Debler, W. R., "On the Analogy Between Thermal and Rotational Hydrodynamical Stability," *Journal of Fluid Mechanics*, Vol. 24, 1966, p. 165.

4 Jeffries, H., and Jeffries, B. S., *Methods of Mathematical Physics*, 3rd ed., Cambridge Press, 1956, pp. 442–444.

5 Nield, D. A., "Surface Tension and Buoyancy Effects in Cellular Convection," *Journal of Fluid Mechanics*, Vol. 19, 1964, p. 341.

6 Davis, S. H., "Buoyancy—Surface Tension Instability by the Method of Energy," *Journal of Fluid Mechanics*, Vol. 39, 1969, p. 347.

7 Sparrow, E. M., Munro, W. D., and Jonsson, V. K., "Instability of the Flow Between Rotating Cylinders: The Wide Gap Problem," *Journal of Fluid Mechanics*, Vol. 20, 1964, p. 35.

Note Added in Proof

Professor Sparrow has pointed out to the authors that a Runge-Kutta method was used to solve a stability problem in reference [7]. The approach adopted by him and his co-authors is similar to that employed in the present paper. The formal construction and use of the B, C, and S matrices on the previous page appears to be the most obvious variation.

STANLEY J. WILCOX
Engineer,
E. I. duPont de Nemours & Co. Inc.,
Wilmington, Del.
Assoc. Mem. ASME

WARREN M. ROHSENOW
Professor of Mechanical Engineering,
Massachusetts Institute of Technology,
Cambridge, Mass.
Fellow ASME

Film Condensation of Potassium Using Copper Condensing Block for Precise Wall-Temperature Measurement

Major differences exist in results published by investigators of film condensation of liquid metal vapors. In particular, the reported dependence of the condensation coefficient on pressure has raised questions about both the precision of the reported data and the validity of the basic interphase mass transfer analysis. An error analysis presented in this investigation indicates that the reported pressure dependence of the condensation coefficient at higher pressures is due to an inherent limitation in the precision of the condensing wall temperature measurement. The magnitude of this limitation in precision is different for the various test systems used. The analysis shows, however, that the primary variable affecting the precision of the wall temperature measurement is the thermal conductivity of the condensing block. To verify the analysis, potassium was condensed on a vertical surface of a copper condensing block. The copper block was protected from the potassium with nickel plating. Condensation coefficients near unity were obtained up to higher pressures than those previously reported for potassium condensed with stainless steel or nickel condensing blocks. These experimental results agree with the prediction of the error analysis. In addition, a discussion of the precautions used to eliminate the undesirable effects of both noncondensable gas and improper thermocouple technique is included. It is concluded from the experimental data and the error analysis that the condensation coefficient is equal to unity and that the pressure dependence reported by others is due to experimental error.

Introduction

Condensation heat transfer has been studied since the original work of Nusselt in 1916 [1].[1] Recent measurements for condensation of liquid metals disagreed with the simple Nusselt theory. Although part of the discrepancy may be due to the presence of noncondensable gases, most of the experimenters seriously attempted to eliminate even traces of such gases. It has become clear for liquid metals that the resistance to heat transfer at the liquid-vapor interface is significant, particularly at low pressures. The analysis of this interphase resistance as given by Schrage [2] has been applied to many condensation experiments. The resulting condensation (or accommodation) coefficient is unity at very low pressures but is reported to decrease as pressure increases above some threshold value. This reported dependence of the condensation coefficient on pressure has raised questions about both the accuracy of the reported data and the validity of the basic interphase mass transfer analysis.

Measurements of condensation and evaporation coefficients suggest that as the system becomes successively cleaner, the magnitudes of the coefficients rise toward unity. In the condensation process, the liquid surface is continually being formed from clean condensing vapor. This clean interface, therefore, could also have a condensation coefficient of unity. The results of an error analysis presented here suggest that the condensation coefficient is indeed unity and independent of pressure. Data obtained in this investigation using a copper condensing block for increased precision of measurement substantiate this finding. The previously reported decrease of the condensation coefficient at higher pressure is explained on the basis of precision of measurement.

Theory

Fig. 1 shows schematically saturated vapor condensing on a surface. From experiment, the temperatures of the cold wall (T_w), the temperature of the saturated vapor far from the condensate (T_v), and the heat flux (q/A) are determined. From these measured quantities, the temperature at the free surface of the condensate (T_s), the temperature of the subcooled vapor (T_i), and the condensation coefficient (σ) can be calculated.

[1] Numbers in brackets designate References at end of paper.

Contributed by the Heat Transfer Division and presented at the Winter Annual Meeting, Los Angeles, Calif., November 16–20, 1969, of The American Society of Mechanical Engineers. Manuscript received by the Heat Transfer Division, July 7, 1969. Paper No. 69-WA/HT-29.

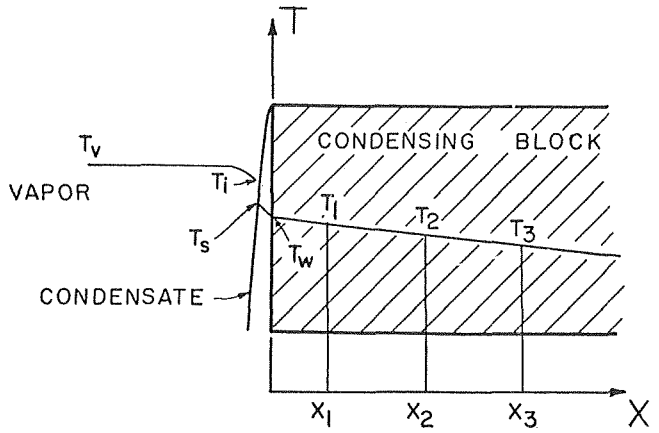

Fig. 1 Fundamental diagram for film condensation

For vertical plates, T_s is obtained from a modified Nusselt analysis as presented in [3]:

$$q/A = 0.943 \sqrt[4]{\frac{\rho_l g(\rho_l - \rho_v)(k_l)^3 h_{fg}'}{L(\mu_l)}} (T_s - T_w)^{0.75} \quad (1)$$

This analysis neglects momentum effects, shear stress on the liquid surface assuming a stagnant vapor, and the curvature in the actual temperature distribution through the film. Since consideration of these effects would change the calculated value of $(T_s - T_w)$ by less than 1 percent, equation (1) was used without correction.

In addition to the heat transfer resistance through the film, there is an interphase mass transfer resistance. The interphase mass transfer resistance is the predominant resistance in the experiments performed in this investigation. A kinetic theory analysis of this resistance is presented by Schrage [2] and leads to the following equation for the net mass flux toward the interface:

$$W/A = \frac{2\sigma}{2 - \sigma} \sqrt{\frac{M}{2\pi R}} \left[\frac{P_v}{\sqrt{T_i}} - \frac{P_s}{\sqrt{T_s}} \right] \quad (2)$$

The derivation of this equation is based on a kinetic theory estimation of both the mass flow of vapor at pressure P_v and temperature T_i toward the interface and also the mass flow due to evaporation from the liquid surface at T_s. Under equilibrium conditions the evaporation rate from the surface is calculated using the saturation pressure P_s corresponding to T_s. It is assumed in the Schrage analysis that this same rate of evaporation does occur from the liquid at T_s even when the vapor is at P_v and T_i.

The theory allows for the possibility of some of the molecules being reflected; therefore, the mass of vapor which condenses is equal to the mass of molecules which strike the surface multiplied by the condensation (or accommodation) coefficient σ. The mass of liquid which evaporates is the amount estimated from kinetic theory multiplied by the evaporation coefficient σ_E. At equilibrium $\sigma = \sigma_E$. It is further assumed that at nonequilibrium, when net condensation occurs, σ is also equal to σ_E. These assumptions lead to equation (2).

A number of investigators [4–7] have reviewed the interphase mass transfer process, and some have attempted to eliminate the simplifying assumptions embodied in the Schrage equation. The results of these studies produce only small corrections and lead to the conclusion that equation (2) adequately describes the process for condensation problems. The results of the present investigation suggest that σ, calculated from equation (2), equals unity at all pressures during condensation.

By defining $\Delta P = P_v - P_s$ and $\Delta T = T_i - T_s$, the "driving force" term in equation (2) may be rewritten as follows:

$$\left[\frac{P_v}{\sqrt{T_i}} - \frac{P_s}{\sqrt{T_s}} \right] = \frac{P_s}{\sqrt{T_i}} \left[1 + \frac{\Delta P}{P_s} - \left(1 + \frac{\Delta T}{T_s} \right)^{1/2} \right]$$

By expanding $\left(1 + \frac{\Delta T}{T_s} \right)^{1/2}$ in a binomial series and setting higher-order terms equal to zero, the following expression results:

$$\left[\frac{P_v}{\sqrt{T_i}} - \frac{P_s}{\sqrt{T_s}} \right] = \frac{P_s}{\sqrt{T_i}} \left[\frac{\Delta P}{P_s} - \frac{\Delta T}{2T_s} \right]$$

For most fluids and for liquid metals in particular, $\Delta T/2T_s$ is small compared with $\Delta P/P_s$ and hence may be neglected.

	$\frac{\Delta T/2T_s}{\Delta P/P_s}$	p_v(atm)
Potassium	0.03–0.05	0.001–1.0
Sodium	0.03–0.05	0.001–1.0
Mercury	0.03–0.04	0.001–1.0
Water	0.03–0.04	0.006–1.0

In the above calculation, ΔT was taken as $(T_v - T_s)$ which is greater than $(T_i - T_s)$; hence, the significance of $\Delta T/2T_s$ is even less than shown above. Realizing that $T_i \simeq T_s \simeq T_v$, $\sqrt{T_i}$ in equation (2) may be replaced with either $\sqrt{T_s}$ or $\sqrt{T_v}$ as an excellent approximation.

The above simplification permits equation (2) to be written as:

$$W/A = \frac{2\sigma}{2 - \sigma} \sqrt{\frac{M}{2\pi R T_v}} (P_v - P_s) \quad (3)$$

A simple heat balance yields the relation between (W/A) and (q/A):

$$q/A = (W/A)(h_{fg}') \quad (4)$$

Nomenclature

A = area
c = heat capacity
$E(z)$ = expected value of z
$f(z)$ = density function for variable z
g = gravitational acceleration
h_{fg} = latent heat of vaporization
h_{fg}' = latent heat which includes change of enthalpy due to the subcooling of the liquid $= h_{fg} + 0.68c_l(T_s - T_w)$
k = thermal conductivity of condensing block
k_l = thermal conductivity of liquid
L = condenser plate length
M = molecular weight
P_v = bulk saturation pressure of the vapor
P_s = saturation pressure which corresponds to liquid surface temperature T_s
q/A = measured heat flux for test condenser
r = radius of thermocouple hole in condensing block
R = universal gas constant
S = standard deviation
T = temperature (identified by subscripts)
W/A = mass flux
x = coordinate, normal-to-the-wall
z = dummy variable
ρ = density
σ = condensation coefficient
μ = average distance of thermocouple holes from wall
μ_l = dynamic viscosity

Subscripts

cu-ni = copper-nickel boundary
i = interface
s = condensate surface
v = vapor
w = wall
l = liquid
1, 2, . . . n = thermocouple hole relative to condensing surface (1 is hole closest to surface)

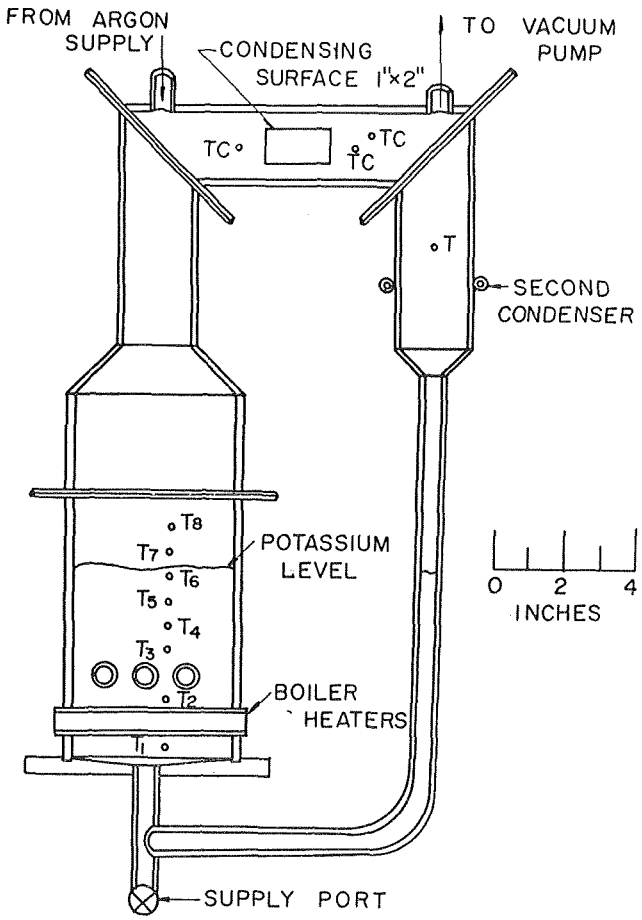

Fig. 2 Schematic of natural convection loop

Since the saturation pressures P_v and P_s are functions of T_v and T_s, respectively, equation (3) can be handled as a heat transfer resistance by eliminating (W/A) using equation (4). The heat transfer resistance is then the sum of the two series resistances represented by equation (1) and equations (3) and (4).

Experimental Apparatus

The natural convection loop (Fig. 2), containing 2.5 lb of potassium, consists of a boiler, test condenser, second condenser, and return line. The basic loop was fabricated from seamless type 304 stainless steel tubing.

Test Condenser. The test condenser is the most critical element in the system. The ability to measure with precision the temperature of the cold condenser wall is critical and is a function of the test condenser design. The test condenser consists of copper and stainless steel elements as shown in Fig. 3. After the elements were brazed together, the condensing surface was ground to a finish of 16AA and then plated with 0.0017 in of nickel. This thickness of nickel plating was measured with a Magne-Gage to a tolerance of ±10 percent. The six thermocouple holes (Fig. 3) of 0.023-in. radius were drilled through the 2-in-wide copper condenser. The positions of these holes were measured on a traversing microscope.

In operation, the test condenser was cooled by passing silicone oil through a $^1/_4$-in. copper tube which was welded to the 0.5-in. copper block (Fig. 3). This copper block insured that the stainless steel resistance block would see a heat sink of uniform temperature.

Second Condenser. The apparatus also included a second condenser (Fig. 2) with which net velocities of various magnitudes could be generated over the test surface. This second condenser consisted of a stainless steel tube welded to the far leg of the loop. By varying the velocity over the test surface as described in [8], one can determine whether noncondensable gas is accumulating at the test surface and affecting the experimental results. By measuring both the flow rate of silicone oil to the condenser as well as the inlet and outlet oil temperatures, the net heat extracted by the second condenser was determined. The mass of potassium vapor condensed was then determined by dividing the net heat extracted by the latent heat. Since the vapor which condensed at this condenser traveled through the test section region on its way from the boiler to the second condenser, a net velocity was generated over the test surface.

Thermocouples. All temperatures were measured with chromel-alumel thermocouples. All thermocouples were made from 28-gage wire from the same spool and heat treated at 750 deg F for 1 hr to remove inhomogeneity due to cold working of the wire. (Cold working recovery temperature range for chromel-alumel is 500–1000 deg F.) The thermocouple wire was continuous from the hot junction (chromel-alumel) to the cold junctions

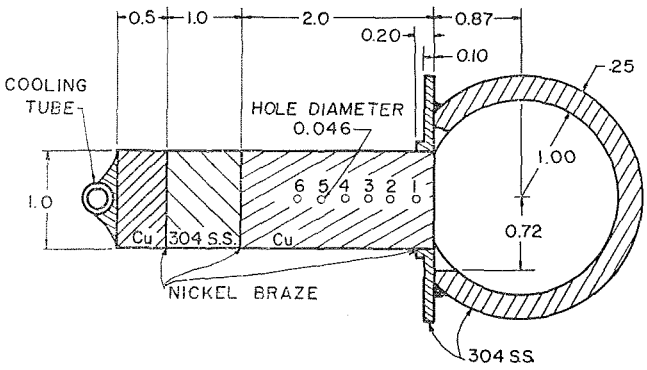

Fig. 3 Sectional view of test condenser

(chromel-copper and alumel-copper). From the cold junctions, which were in an ice bath, copper leads ran by means of a selector switch to a Leeds and Northrup K-2 potentiometer which is capable of reading to ±2 microvolts.

Vapor temperature was obtained by inserting a thermocouple into a well which protruded into the vapor. The reported vapor temperature (T_v) was obtained by averaging the temperatures from the thermocouple wells near the test section. Three thermocouple wells were used during Series 1 and 2. Three additional wells were installed after Series 2; therefore, six wells were used to obtain T_v in Series 3. Temperature readings from all wells generally were within ±0.30 deg F.

The temperature of the vertical condensing wall (T_w) was obtained indirectly by measuring the temperature at six locations in the condensing block. Tests showed that cooling of the chromel-alumel junction by conduction along the thermocouple leads was negligible as long as the junction was inserted at least 0.50 in. into the block. The six thermocouples were inserted 1.1 in. for all experiments. Using the position of the center line of each hole and the temperature of the thermocouple junction in each hole, a straight line was fit to these data by the method of least squares. From this line, the temperature of the copper-nickel boundary was obtained, and then by considering the thickness and conductivity of the nickel plating, the temperature of the condensing wall was calculated. The temperature of the condensate at the liquid-vapor interface was then calculated from equation (1).

From the slope of the line and the conductivity of copper, the heat flux (q/A) was obtained. Heat leakage into the copper block from the stainless steel mount was calculated using a conduction node method and found to be negligible.

Operating Procedure

While the boiler was being brought up to temperature, the argon atmosphere in the loop was evacuated by a mechanical vacuum pump. Boiling occurred at approximately 600 deg F. Since the vacuum pump was connected via an external condenser to the loop, potassium vapor was initially permitted to exit from the loop. After approximately 20 min of boiling, the valve which isolated the loop from the vacuum system was closed. After the system reached equilibrium, data were taken. When two successive readings of the vapor and block temperatures agreed within 3 microvolts, the data qualified as an acceptable "run." This is equivalent to less than 3 microvolts change in 2 min. Once a run had been recorded, the boiler voltage was increased and another test condition approached. Each run took an average of 1.5 hr.

Sample Data and Calculated Results

Fig. 4 and Fig. 5 are graphical presentations of both experimental data and calculated results for run 3 and run 18, respectively. The calculations were performed using the properties of [9] and the following saturation pressure-temperature relationship for potassium from [10]:

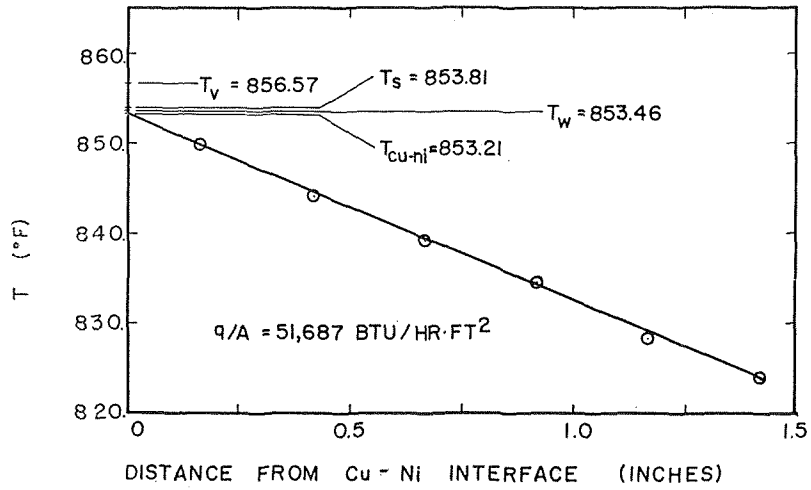

Fig. 4 Data and results; run 3, Series 1

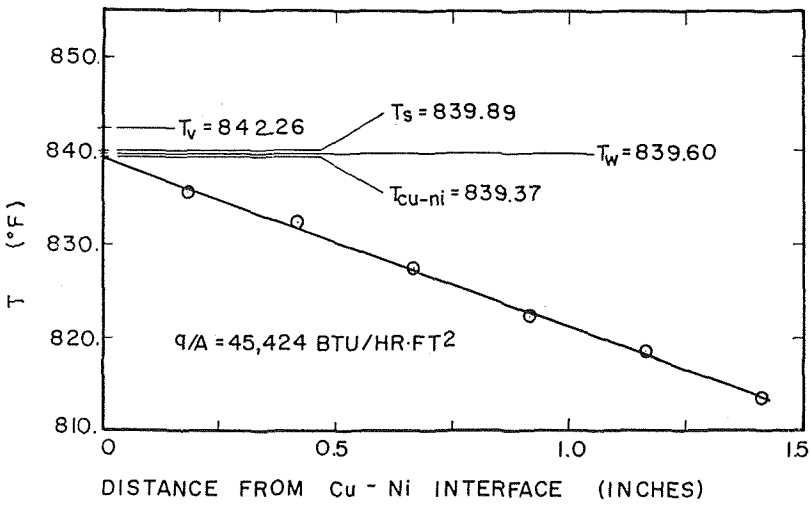

Fig. 5 Data and results; run 18, Series 3

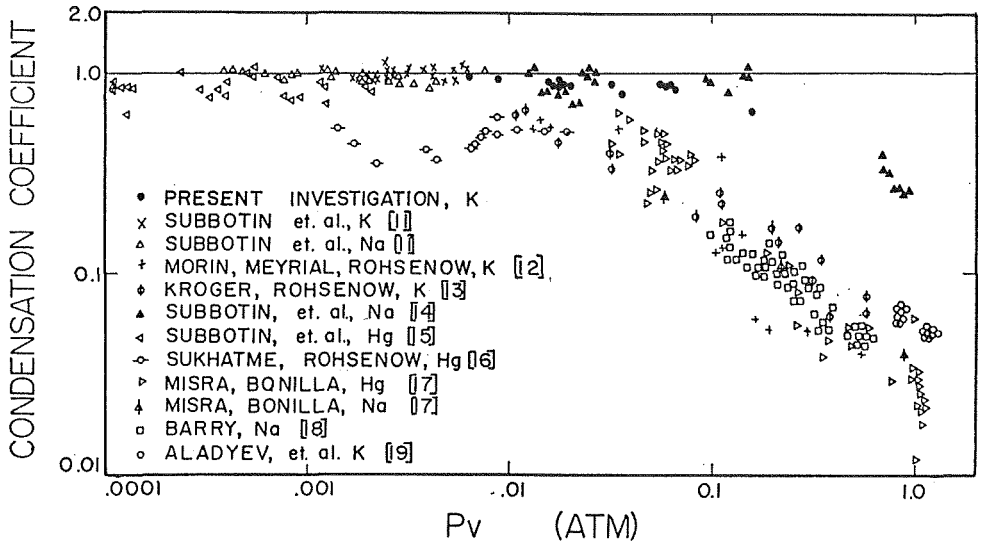

Fig. 6 Survey of condensation coefficient data

$$\log_{10} P(\text{atm}) = 4.185 - \frac{7797.6}{T(\text{deg R})}$$

One can note that both the temperature drop across the nickel plating and the potassium film are small. Under the conditions shown, the main temperature drop is associated with the interphase mass transfer resistance. Since the overall temperature drop $(T_v - T_w)$ is small, precision in the determination of T_w is essential. Although a quantitative error analysis will be presented toward the end of this paper, one should note qualitatively the improved accuracy in the determination of T_w due to the shallow slope of the line shown. If one used stainless steel instead of copper, the slope would be approximately twenty times steeper for the same heat flux. In addition, the number of thermocouples used in determining the line as well as both the position and size of hole into which these thermocouples are placed affect the precision of T_w.

General Data and Calculated Results

Table 1 contains data and calculated results from this investigation. Fig. 6 is a plot of condensation coefficient versus saturation pressure for these data and the data of others [11–19]. All results were calculated using the properties found in [9]. One can note that at low pressure the data is distributed around a condensation coefficient of unity, whereas at high pressure there is not only a great deal of scatter but also a general decrease in most data with increasing pressure. A closer analysis of Fig. 6 shows an effect of experimental accuracy. Specifically, the condensation coefficients obtained both by Subbotin [14] and in the present experiments maintain a value closer to unity up to a higher pressure than do the data of others. Subbotin used a copper block protected from sodium by a thin layer of stainless steel; the present experiments were run with a copper block protected with nickel plating. Others used condensing blocks or condensing tubes made of nickel or stainless steel. The error analysis presented in the next section predicts the pressure dependence shown in Fig. 6 and demonstrates, a posteriori, that the condensation coefficient is actually unity at all pressures.

When the interphase resistance is small compared to the Nusselt film resistance, inaccuracies in the analysis of the film resistance will have a very large effect on the calculated condensation coefficient. For example, if condensate from the area immediately above the test surface flows onto the test condenser, the film resistance will be larger than predicted by the Nusselt analysis, and therefore the calculated condensation coefficient will be smaller than the actual coefficient. To avoid concern over the effect of inaccuracies in the analysis of the film resistance, experiments were curtailed in the present investigation when the interphase and Nusselt resistances were of approximately equal magnitude. However, the data of Subbotin [14] at $P_v \simeq 0.8$ atm were obtained under conditions where the magnitude of the interphase resistance is only $^1/_4$ of the size of the Nusselt film resistance. Although his calculated condensation coefficients at $P_v \simeq 0.8$ atm are significantly higher than those obtained using nickel or stainless steel condensing blocks, a precise study of the interphase resistance under such conditions is not possible. Although this limitation applies to all the data at $P_v \simeq 0.8$ atm, precise determination of the condensation coefficient using nickel or stainless steel condensing blocks is limited to much lower pressures as will be discussed in the next section. The relative size of the interphase and film resistance does, however, represent a limitation to the experimental determination of the condensation coefficient from film condensation experiments performed on apparatus designed for high precision.

Error Analysis

Although three quantities T_v, T_w, q/A are obtained from experiment and are subject to measurement error, this error analysis considers only errors in measurement of T_w. Unlike T_v which is measured directly, T_w is obtained indirectly and is, therefore, subject to cumulative inaccuracies. Errors in q/A have comparatively little effect on the deduced magnitude of the condensation coefficient.

Sensitivity of σ to Errors in $(T_v - T_s)$. Since the temperature at the surface of the condensate T_s is obtained from T_w via equation (1), any error in T_w is reflected as an error in T_s. The effect on the calculated condensation coefficient from an error in T_s can be realized using Fig. 7. The three curves shown in Fig. 7 represent three different pressure levels for potassium. As the pressure increases from 0.0055 atm to 0.22 atm, the value of $(T_v - T_s)$ which gives a calculated value of $\sigma = 1.0$ decreases from 6.5–0.3 deg F for the example shown. In addition, a comparison of the slopes of the three curves shows that the effect on the deduced condensation coefficient from a given temperature measurement error increases with increasing pressure. Associated with each experimental apparatus is a possible experimental error in the determination of $(T_v - T_s)$. Note that a 1 deg F error has little effect at low pressure. At high pressure a 1 deg F error not only has a tremendous effect on the value of the condensation coefficient but also injects the possibility of obtaining *negative* value of $(T_v - T_s)$. Although it is possible to obtain $T_s > T_v$, all would recognize that such a result is due to experimental error.

Table 1 Tabulated results

Series No.	Run No.	T_v (°F)	T_s (°F)	T_w (°F)	$T_{cu\text{-}ni}$ (°F)	q/A Btu/hr-ft²	σ	P_v (atm)	P_s (atm)	$q_{2nd\ cond}$ (Btu/hr)
1	1	853.76	851.66	851.41	851.21	39,941	0.873	0.0178	0.0174	0
	2	843.01	841.01	840.77	840.58	38,185	0.920	0.0159	0.0155	818
	3	856.57	853.81	853.46	853.21	51,687	0.855	0.0183	0.0178	959
	4	988.32	987.15	986.68	986.39	62,915	0.882	0.0633	0.0626	0
	5	963.94	962.87	962.44	962.16	59,388	0.981	0.0512	0.0507	940
	6	981.19	979.98	979.54	979.26	59,754	0.864	0.0595	0.0589	0
	7	977.61	976.60	976.16	975.88	59,602	0.964	0.0577	0.0572	1523
	8	864.23	861.99	861.67	861.43	48,799	0.897	0.0198	0.0193	0
2	9	846.02	843.57	843.28	843.06	44,633	0.885	0.0164	0.0160	0
	10	852.45	850.09	849.82	849.61	43,100	0.859	0.0175	0.0171	752
	11	850.71	848.56	848.28	848.07	43,084	0.912	0.0172	0.0168	1010
	12	853.04	850.38	850.00	849.73	54,884	0.917	0.0176	0.0172	0
	13	789.11	785.18	784.85	784.60	49,431	0.959	0.0088	0.0084	0
	14	761.31	756.55	756.25	756.01	47,017	0.975	0.0063	0.0060	0
	15	915.53	913.65	913.21	912.93	59,815	0.882	0.0328	0.0322	0
	16	973.07	971.71	971.23	970.93	63,917	0.867	0.0554	0.0548	0
	17	854.57	852.35	852.07	851.85	44,301	0.894	0.0179	0.0175	0
3	18	842.26	839.89	839.60	839.37	45,424	0.926	0.0157	0.0154	0
	19	922.60	920.83	920.51	920.27	48,654	0.785	0.0351	0.0345	0
	20	990.94	989.88	989.52	989.28	51,719	0.825	0.0647	0.0641	0
	21	989.38	988.56	988.20	987.96	51,725	0.957	0.0638	0.0634	1091
	22	1098.18	1097.30	1096.87	1096.61	57,992	0.655	0.1516	0.1506	0

The following analysis is based on the assumption that any data which measures $T_s > T_v$ will remain unreported. Who could get such data published?

Constant Error for Each Assembly of a System. When a thermocouple is inserted into a condensing block, the exact location and, therefore, the exact temperature of the junction is unknown. It is reasonable to assume that the location of the junction will not change once the thermocouple has been inserted. If a junction of a homogeneous thermocouple is located such that its temperature is greater than the undisturbed temperature at the center line of the hole, it will always read high. When a new set of thermocouples is inserted, a different set of errors in readings results.

As shown in Table 1, the experiments were divided into three series. Between each series, all thermocouples were replaced. For any series, the positions of the thermocouple readings relative to the line obtained using the least-square method remained virtually unchanged. For example, in Series 1 (Fig. 4), thermocouples 2, 3, and 5 always read below the line and thermocouple 4 always reads above the line at all heat fluxes and pressures.

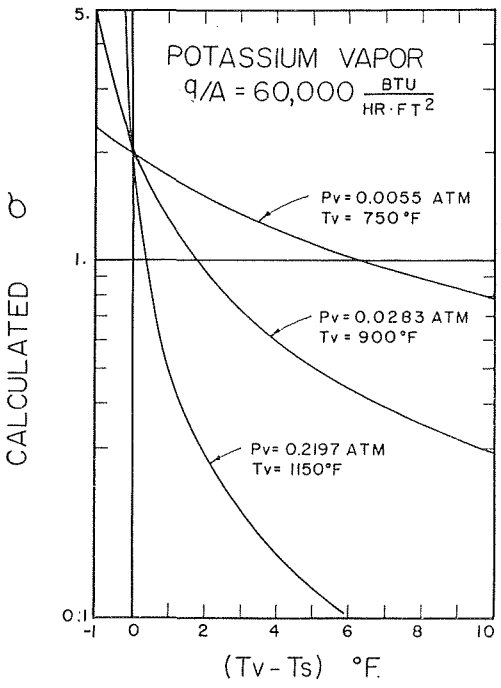

Fig. 7 Condensation coefficient versus ($T_v - T_s$)

When all of the thermocouples were removed and new ones assembled for the data in Fig. 5, a different system characteristic is observed. Here thermocouples 1 and 4 are below and thermocouple 2 is above the least-square line.

Since at high temperatures the effect of thermocouple inhomogeneity is always present to a small degree even if the thermocouples have been heat treated, both position and inhomogeneity effects are present in Fig. 4 and Fig. 5. For the copper block, both effects are estimated as being of the same order of magnitude; however, the effect of position for nickel and stainless steel blocks will be one to two orders of magnitude larger than the effect of inhomogeneity. Since in general inhomogeneity represents a small effect, all thermocouples are assumed to be homogeneous in the following analysis. To analyze both the magnitude of the possible experimental error in the wall temperature and the effect of this error on the condensation coefficient, the following steps will be performed:

1 Estimate the distribution of possible thermocouple temperature readings in a hole.

2 Obtain the distribution of possible values of wall temperatures obtained from these readings.

3 Exclude data which indicate $T_s > T_v$ and then obtain the expected value of T_w and expected value of σ.

Distribution of Measured Temperatures in Thermocouple Hole. A typical hole of radius r is shown in Fig. 8*a* with an assumed linear temperature gradient (Fig. 8*b*) impressed across the hole. The actual position of the hole center line is $\bar{x}_1$ and the undisturbed temperature at the center line is $\bar{T}_1$. The bar over any symbol indicates the actual value instead of a measured value. Using the linear temperature gradient (Fig. 8*b*), the temperature may be related, for purpose of discussion, to position in the hole by the Fourier conduction equation:

$$\bar{x} - \bar{x}_1 = \frac{\bar{T} - \bar{T}_1}{\frac{q/A}{k}} \tag{5}$$

Although the thermocouple reading must lie between the temperatures at $+r$ and $-r$, its exact magnitude is not known. Each experimenter assumes, however, that the thermocouple junction lies on the centerline $\bar{x}_1$ and is, therefore, at the temperature $\bar{T}_1$. The error resulting from this assumption is determined by noting that the measured temperature T_1 may assume any of the values shown as $\bar{T}$ in Fig. 8*b*. The quantity $(T_1 - \bar{T}_1)$ is experimental error in the temperature reading at hole 1. It follows that x_1 is the position corresponding to the measured temperature T_1. After inserting T_1, x_1, and after making equation (5) dimension-

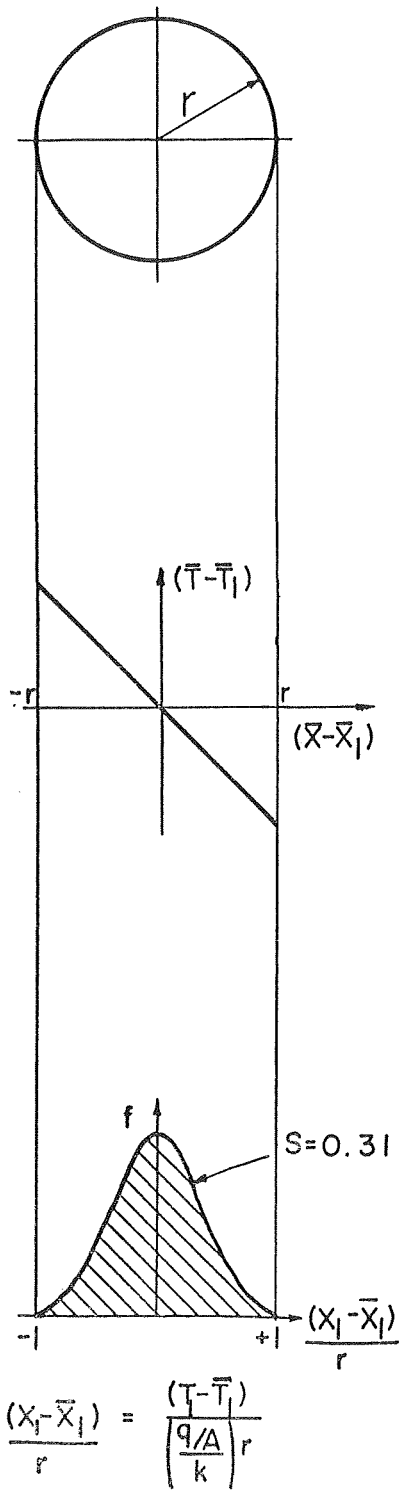

Fig. 8 *(a)* **Top, typical hole of radius** r; *(b)* **center, simplified linear temperature drop impressed across hole; (c) bottom, Gaussian distribution of temperature measurements in hole**

less by dividing both sides by r, one obtains:

$$\frac{x_1 - \bar{x}_1}{r} = \frac{T_1 - \bar{T}_1}{\frac{q/A}{k} r} \tag{6}$$

It follows that the limits on $\frac{x_1 - \bar{x}_1}{r}$ are:

$$-1 \leq \frac{x_1 - \bar{x}_1}{r} \leq 1$$

In order to specify a distribution of measured temperatures at any hole, a density function representing possible thermocouple locations within the hole is first chosen. By definition, the integral of a density function $f(z)$ between any two limits (a, b) yields the probability that the variable z lies in the interval (a, b). For example,

$$P\left(a \leq \left(\frac{x_1 - \bar{x}_1}{r}\right) \leq b\right) = \int_a^b f\left(\frac{x_1 - \bar{x}_1}{r}\right) d\left(\frac{x_1 - \bar{x}_1}{r}\right)$$

may be interpreted as the probability that the thermocouple lies between dimensionless positions a and b within thermocouple hole 1. With equation (6), $P\left(a \leq \frac{x_1 - \bar{x}_1}{r} \leq b\right)$ may also be interpreted as the probability that the temperature reading lies between T_a and T_b.

Since the exact distribution of possible locations is not known, a Gaussian density function $f(z)$ was chosen (Fig. 8*c*) with 99.9 percent of its area falling between the dimensionless positions $+1$ and -1. The Gaussian density function is given by:

$$f\left(\frac{x_1 - \bar{x}_1}{r}\right) = \frac{1}{S\sqrt{2\pi}} e^{-\left(\frac{x_1 - \bar{x}_1}{r}\right)^2 \frac{1}{2S^2}}$$

where S is the standard deviation obtained from:

$$\int_{-1}^{+1} f\left(\frac{x_1 - \bar{x}_1}{r}\right) d\left(\frac{x_1 - \bar{x}_1}{r}\right) = 0.999$$

This integral is tabulated in terms of S [20] and yields $S = 0.31$. The interpretation of this standard deviation is as follows: 68 percent of all possible measurements lie in the range $(x_1 - \bar{x}_1)/r = \pm 0.31$.

Distribution of Possible Wall Temperature Measurements. The distribution of temperature measurement errors at each hole and the distribution of error resulting around $\bar{T}_w$ are shown schematically in Fig. 9. The actual temperature profile in the block is known from the Fourier conduction equation. Both in the holes and at the wall, the experimental errors are symmetrical about the *actual* temperature existing at that location. Using the same grouping of variables as given in Fig. 8*c*, the distribution of $\left(\frac{T_w - \bar{T}_w}{\frac{q/A}{k} r}\right)$ is, according to [21], Gaussian with a mean value of zero and a standard deviation (S_w) given by:

$$S_w = S\sqrt{\frac{1}{n} + \frac{\mu^2}{\sum_{i=1}^{n} (\bar{x}_i - \mu)^2}} \tag{7}$$

where

$$\mu = \frac{1}{n} \sum_{i=1}^{n} \bar{x}_i$$

n = number of thermocouple holes

$\bar{x}_i$ = distance of ith hole from wall

The following data were used to evaluate the distribution of wall temperature measurements for three typical systems. The "effective radius" shown is taken equal to twice the actual radius; this larger radius was assumed in an attempt to account conservatively for the distortion of isotherms around a hole. For a hole across which no heat is transferred, the distortion of isotherms causes a temperature difference across the hole equal to twice the difference which would exist if no distortion occurred. The "effective radius" is used in all of the following calculations.

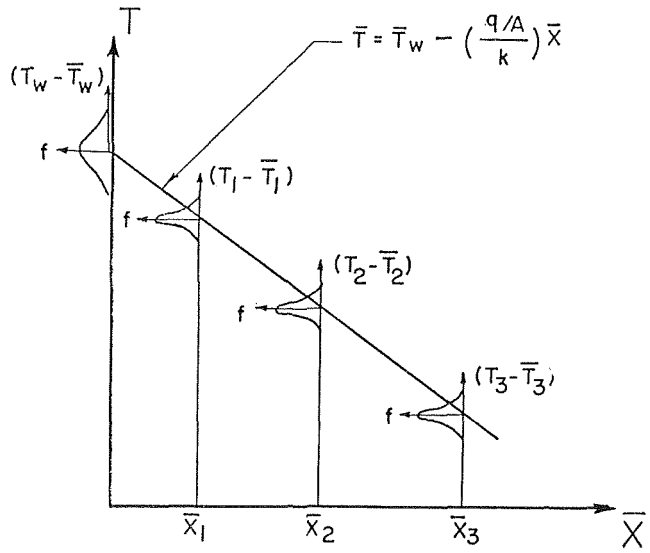

Fig. 9 Schematic representation of distributions in holes and at wall

System (Material: k)	Hole	Distance to Wall, in.	Effective Radius, in.
Present (copper: 210)	1	0.1675	0.046
	2	0.4169	
	3	0.6670	
	4	0.9176	
	5	1.1670	
	6	1.4183	
Kroger [13] (nickel: 28)	1	0.0625	0.062
	2	0.3750	
	3	0.6875	
Meyrial [12] (st. steel: 12)	1	0.125	0.062
	2	0.375	
	3	0.625	

The standard deviation for $\left(\frac{T_i - \bar{T}_i}{\frac{q/A}{k}\,r}\right)$ is equal to the standard deviation for $\frac{x_i - \bar{x}_i}{r}$, namely S. Both S_w, the standard deviation of $\left(\frac{T_w - \bar{T}_w}{\frac{q/A}{k}\,r}\right)$, and S are given below for the three systems:

System	At Each Hole S	At the Wall S_w; equation (7)
Present	0.31	0.26
Kroger [13]	0.31	0.31
Meyrial [12]	0.31	0.37

With the present system of 6 thermocouple holes the possible temperature measurement error at the wall is less than the temperature measurement error in any hole; however, the opposite is true for Meyrial's [12] system of three thermocouple holes. As one would expect, a large number of holes spaced far apart reduces the possible error in the extrapolated temperature at the wall. The comparison shows less than a 50 percent difference between the three systems from the effects of number and position of holes. The variable $\left(\frac{T_w - \bar{T}_w}{q/A}\right)$ is, however, the meaningful comparison of the three systems. The standard deviation for the variable $\left(\frac{T_w - \bar{T}_w}{q/A}\right)$ is shown below:

System	Standard Deviation of $\left(\frac{T_w - \bar{T}_w}{q/A}\right)$
Present	4.8×10^{-6}(deg F)/(Btu/hr-ft^2)
Kroger [13]	5.8×10^{-5}
Meyrial [12]	1.6×10^{-4}

Fig. 10 shows the resulting distributions for the three systems. The profound differences between the systems are primarily due to the conductivities of the material used in the condensing block. The present system used copper ($k = 210$); Kroger used nickel ($k = 28$); Meyrial used stainless steel ($k = 12$).

Fig. 11 shows that the drop across the condensate $(\bar{T}_s - \bar{T}_w)$ is a very weak function of pressure; therefore, the distribution of temperature errors at the surface of the condensate is identical to the distribution at the wall.

As the pressure increases, the magnitude of $(\bar{T}_s - \bar{T}_s)/(q/A)$ decreases (Fig. 11). Clearly when the probable error in the determination of $(T_w - \bar{T}_w)/(q/A)$ and hence in $(T_s - \bar{T}_s)/(q/A)$ is

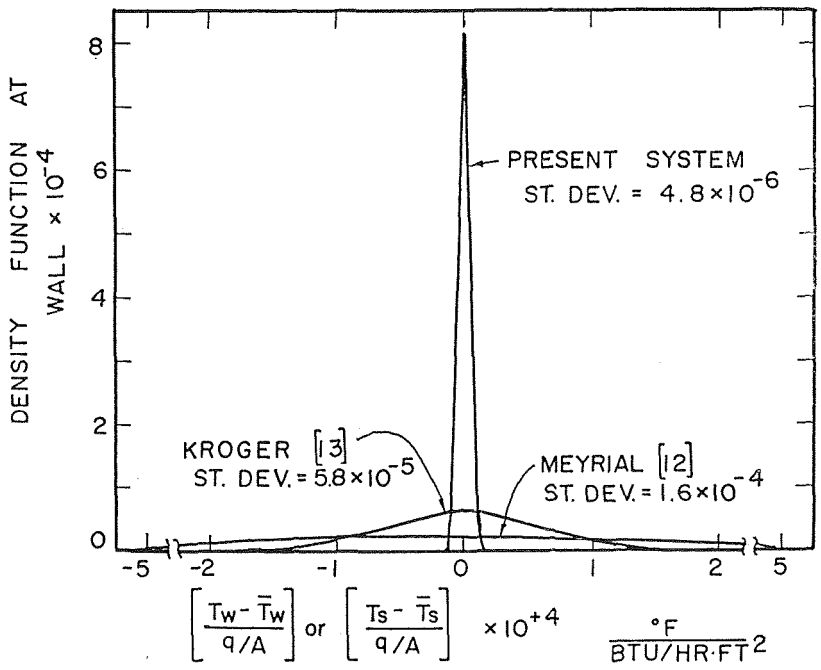

Fig. 10 Probability density function at wall

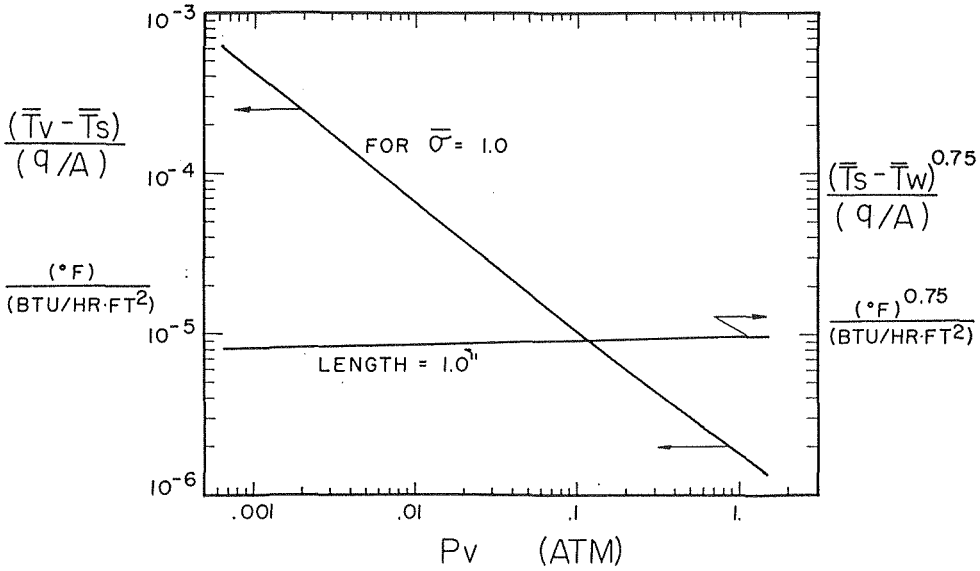

Fig. 11 Effect of P_v on $(\bar{T}_v - \bar{T}_s)$ and $(\bar{T}_s - \bar{T}_w)$ for potassium

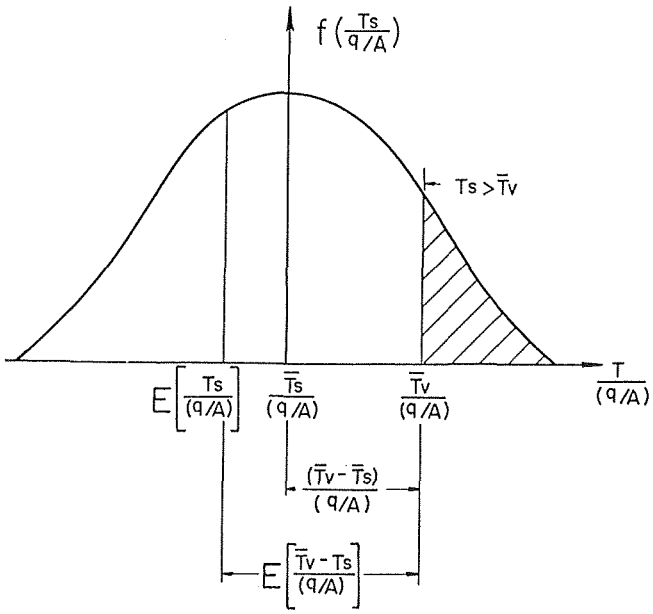

Fig. 12 Distribution of condensate surface temperature

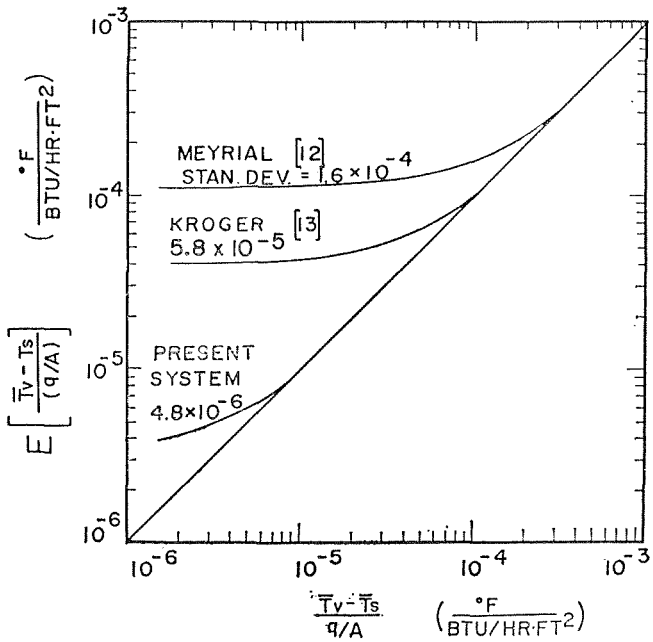

Fig. 13 $E[(\bar{T}_v - T_s)/(q/A)]$ versus $(\bar{T}_v - \bar{T}_s)/(q/A)$

equal to the magnitude of $(\bar{T}_v - \bar{T}_s)/(q/A)$, the limit of meaningful measurement has certainly been reached. Taking the standard deviation from Fig. 10 as the measure of probable error in $(T_s - \bar{T}_s)/(q/A)$ and equating this to the magnitude of $(\bar{T}_v - \bar{T}_s)/(q/A)$, the upper limit of P_v where meaningful measurements can be made is read from Fig. 11. For the three sets of experiments discussed, this limit is as follows:

Experimenter	"Probable" Error (Fig. 10)	Corresponding P_v (Fig. 11)
Wilcox	4.8×10^{-6}(deg F)/(Btu/hr-ft^2)	0.27 atm
Kroger	5.8×10^{-5}	0.011
Meyrial	1.6×10^{-4}	0.0034

Since Kroger's [13] and Meyrial's [12] data fall above 0.01 atm, the accuracy of their data as well as any other data which were obtained without exceptional concern with the measurement of T_w is very questionable.

Exclusion of Data Indicating $T_s > T_v$; Calculation of $E(T_w)$, $E(\sigma)$. A value of unity is now assigned to the actual condensation coefficient ($\bar{\sigma}$). This will be justified a posteriori. One could argue that the possible experimental error shown in Fig. 10 should simply cause scatter in the data points around a condensation coefficient of unity. However, if all data for which $T_s > T_v$ is assumed to remain unreported, the reported data will yield magnitudes of σ which scatter around a number less than unity. This is shown in Fig. 12 where the magnitude of $\bar{T}_v$ lies within the range of possible magnitudes of T_s. Then the expected value of T_s, $E(T_s)$, is not $\bar{T}_s$ but a value somewhat less than $\bar{T}_s$. $E(T_s)$ is determined by dividing the remaining area of the density function below $\bar{T}_v$ in two equal parts as indicated by the vertical line labeled $E[T_s/(q/A)]$ in Fig. 12. Associated with $E(T_s)$ and $\bar{T}_v$ is an expected value of the condensation coefficient $E(\sigma)$. It follows that the published data should scatter about $E(\sigma)$ even though $\bar{\sigma} = 1$.

Fig. 13 was formulated for the variables in Fig. 12 by using the tabulated properties of a Gaussian density function. Note in Fig. 13 that the higher the precision of one's system (lower magnitude of standard deviation), the closer $E(T_s)$ is to $\bar{T}_s$.

As pressure increases, $(\bar{T}_v - \bar{T}_s)/(q/A)$ decreases rapidly. In general at low pressure $T_v \gg T_s$, and it is not possible to measure $T_s > T_v$.

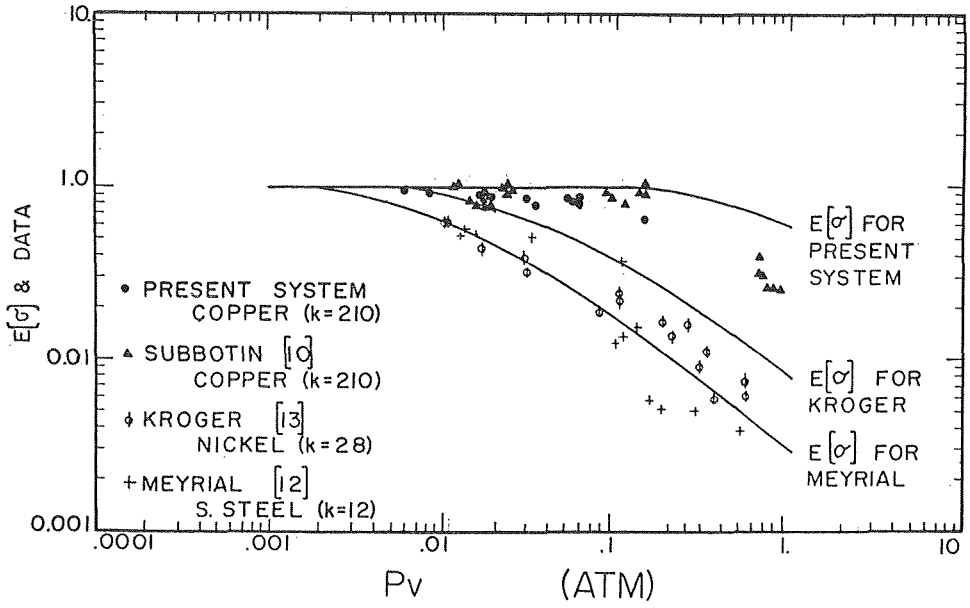

Fig. 14 $E[\sigma]$ and data versus P_v

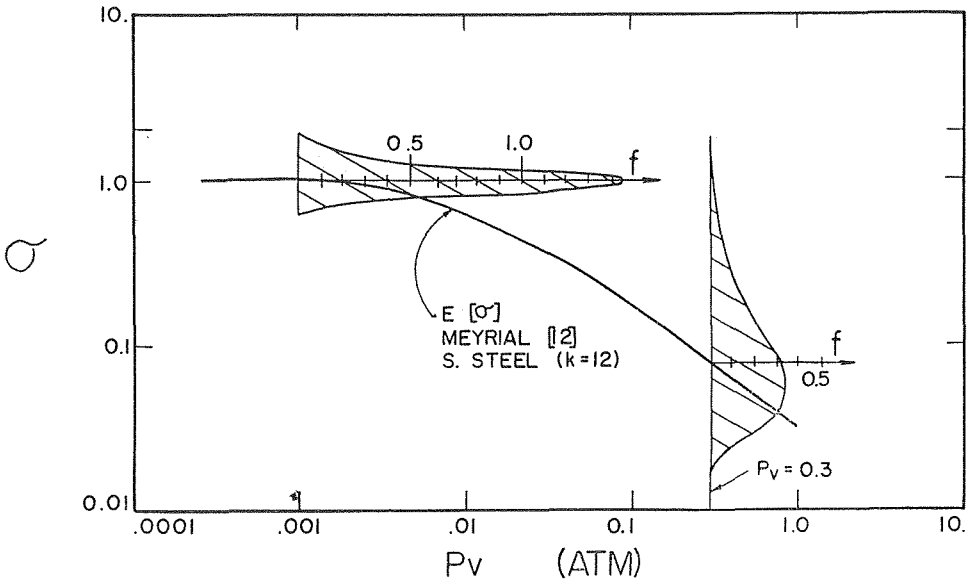

Fig. 15 Predicted distribution of data

The curves of Fig. 14 present the curves of Fig. 13 in terms of the predicted expected value of σ, $E(\sigma)$, for the three test systems. $E(\sigma)$ is obtained by evaluating and equating the right-hand side of equation (3) for the following two sets of conditions: $\sigma = 1$ at $(\bar{P}_v - \bar{P}_s)$ and $\sigma = E(\sigma)$ at $E(\bar{P}_v - P_s)$. This yields:

$$\frac{2E(\sigma)}{2 - E(\sigma)} E(\bar{P}_v - P_s) = \frac{2}{2 - 1} (\bar{P}_v - \bar{P}_s)$$

For small differences of $(T_s - \bar{T}_s)$

$$\frac{\bar{P}_v - \bar{P}_s}{\bar{P}_v - P_s} = \frac{\bar{T}_v - \bar{T}_s}{\bar{T}_v - T_s}$$

then

$$\frac{E(\sigma)}{2 - E(\sigma)} = \frac{\bar{T}_v - \bar{T}_s}{E(\bar{T}_v - T_s)} = \frac{\left(\frac{\bar{T}_v - \bar{T}_s}{q/A}\right)}{E\left(\frac{\bar{T}_v - T_s}{q/A}\right)}$$

The curves in Fig. 14 show a strong effect of pressure on $E(\sigma)$ resulting simply from the assumption that data indicating $T_s > T_v$ remain unreported. It is interesting to note that the arguments which have led to $E(\sigma)$ are essentially equivalent to claiming a fixed error in $(\bar{T}_v - T_s)/(q/A)$ for an experimenter. This is readily seen from the approximately horizontal lines shown for [12] and [13] in Fig. 13.

By considering both the distribution of possible wall temperature measurements that remain after the area (Fig. 12) where $T_s > T_v$ is eliminated and the relationship between σ and $(\bar{T}_v - T_s)$, one can estimate where the condensation coefficient data should be concentrated. Fig. 15 shows this result for Meyrial's [12] system at two pressures. The probability that data will fall between any two given values of the condensation coefficient is given by the area under the curve between the two values of interest. It follows that the total area under the curve must equal unity. A unit area results for the curves shown if a unit distance on the abscissa is taken as the linear distance between $\sigma = 1$ and $\sigma = 2$. Note that at high pressures one should not expect the remaining data to yield a condensation coefficient close to unity. For example, the curve shown at $P_v = 0.3$ atm has only 10 percent of its area in the range of $0.35 \leq \sigma \leq 2.0$. A comparison shows

that Meyrial's data (Fig. 14) in the vicinity of $P_v = 0.3$ atm appear to be concentrated as one would expect using the distribution of Fig. 15.

Effect of Condensing Fluid

A similar error analysis leading to $E(\sigma)$ versus P_v curves (Fig. 16) for various liquid metals was made for the condensing-block geometry and material of Fig. 3 and those of Kroger [13] and of Meyrial [12]. It is observed that the differences between the liquid metals are not very great. Note also that the curves for nickel and stainless steel for the various liquid metals group together as do the data in Fig. 6 taken with stainless steel and nickel blocks. The effect of the hole size and spacing used by the various experimenters would move the predicted curves somewhat; however, the effect of variation in hole size and spacing used by various experimenters would probably not be large compared with the effect of block conductivity.

Since many experimenters are interested in the condensation coefficient of water, this analysis was also run for water. Even with a copper condensing block, Fig. 17 shows the available precision to be marginal. Considering the fact that with water the Nusselt film resistance is approximately 10–100 times greater than the interphase resistance for the range and systems shown in Fig. 16, meaningful measurements of the condensation coefficient for water using a standard film condensation experiment appear to be almost impossible to obtain.

Experiments Using Second Condenser

It has been shown (Kroger [22]) that traces of noncondensable gas in a condensing test system tend to collect at the cold surface and drastically reduce the heat transfer at the condensing surface. Experiments were run to determine whether minute quantities of noncondensable gas were accumulating at the test surface and affecting the experimental results. In these experiments, the second condenser (Fig. 2) was cooled with silicone oil and the net heat extracted was calculated. Since this vapor passed through the test section on its way from the boiler to the second condenser, a net velocity was generated over the test surface. This velocity would tend to sweep away the noncondensable gas and minimize its accumulation at the test surface. If the results with and without this net vapor flow are the same, one may conclude that there is probably no noncondensable gas collected at the test surface.

A similar method of preventing accumulation of noncondensable gas was used successfully by Citakoglu and Rose [8] in the study of drop condensation. In the present investigation, data were taken at a P_v of approximately 0.02 atm as shown in Fig. 18. For the data shown at approximately 900 Btu/hr, the "average"

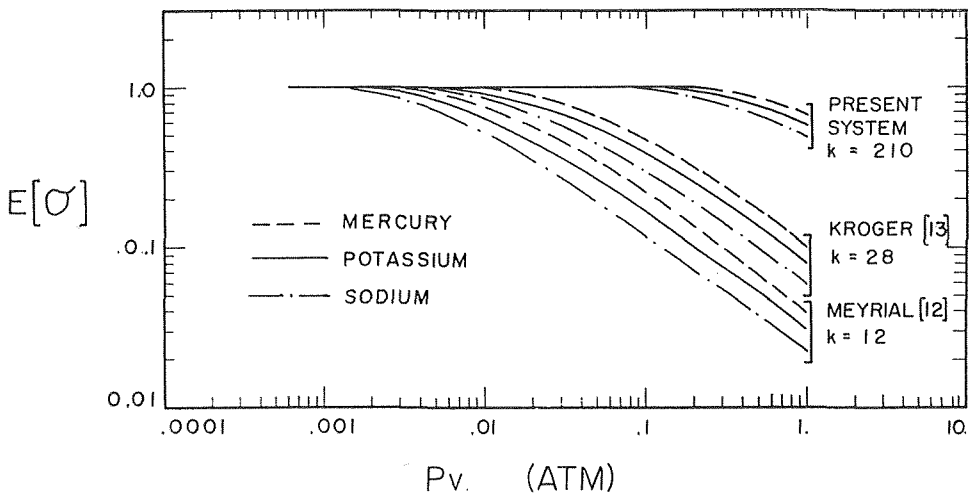

Fig. 16 Effect of fluid on $E[\sigma]$

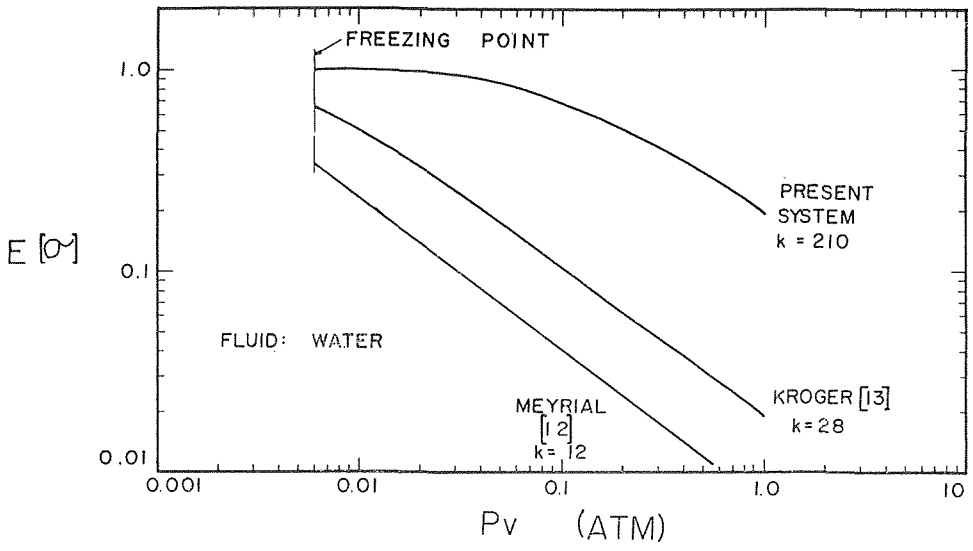

Fig. 17 $E[\sigma]$ versus P_v for water

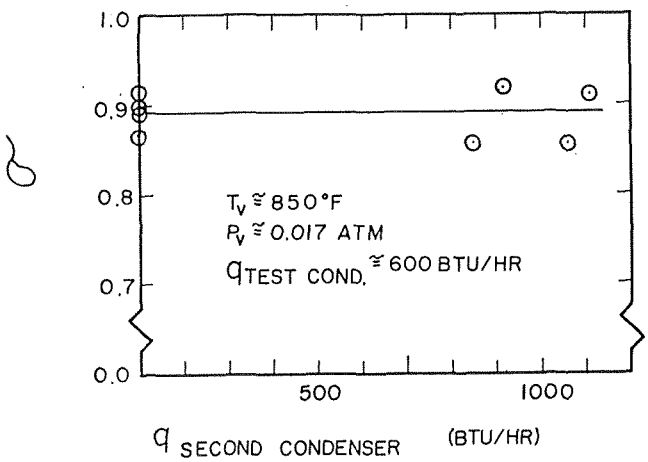

Fig. 18 Effect of second condenser at ~0.02 atm

velocity through the test section is calculated to be approximately 15 ft/sec. No measured effect of vapor flow and hence of noncondensable gas was observed.

Discussion

The error analysis presented here is limited to errors resulting in the determination of T_w (and hence T_s and $(T_v - T_s)$) deduced from extrapolation of the readings of thermocouples placed in the cold block at various distances from the condensing surface. It shows clearly the requirement for high precision in the determination of T_s at higher pressures. As pressure is increased the actual magnitude of $\bar{T}_v - \bar{T}_s$ decreases and above some limiting pressure for any system becomes less than the measuring precision of the particular system. The magnitude of this measuring precision is affected by the thermal conductivity of the condensing-block material and the thermocouple hole size and spacing. Since hole size and spacing do not vary greatly among test systems, the major effect is that of thermal conductivity.

The analysis shows that above the precision-limited pressure, it is possible that T_s can be determined from the measurements to be greater than $\bar{T}_v$. Assuming that such data would not be reported, the expected value of σ, $E(\sigma)$, should be less than unity even though the actual value $\bar{\sigma} = 1.0$. Reliance, therefore, should be placed only on those data obtained below the precision-limited pressure.

It is interesting to note that the actual magnitude of the heat flux has practically no effect on the precision of the determination of σ. Since for small differences $(P_v - P_s)$ is approximately linear with $(T_v - T_s)$, then from equation (3) and equation (4) $(T_v - T_s)$ varies linearly with (q/A). In the subsection on Distribution of Possible Wall Temperature Measurements, it is shown that the error $(T_s - \bar{T}_s)/(q/A)$ is a function of only the condenser-block design; therefore, the error $(T_s - \bar{T}_s)$ is linear in (q/A) for a given design. The ratio of $(T_s - \bar{T}_s)/(T_v - T_s)$ is, therefore, independent of q/A. It follows that $E(\sigma)$ is independent of q/A for this analysis.

Although all of the experimenters of Fig. 6 did not determine the wall or condensate surface temperature by placing thermocouples in holes drilled in a condensing block, the requirement of high precision in the determination of the temperature T_s and hence T_w are just as stringent. While the details of the error analysis would differ for the various systems, the results would all suggest curves for $E(\sigma)$ versus P_v similar to those of Fig. 14.

Conclusions

1 An error analysis suggests that for each condensing test system there exists an upper limit of pressure above which the precision of measurement required to determine the condensation coefficient (σ) exceeds that of the apparatus.

2 For systems in which the wall surface temperature is determined from measurements within the condensing block, such as in Fig. 3, the precision of measurement depends on the thermal conductivity of the block and the thermocouple hole size and spacing. For the various test systems used, the strongest effect on precision is the thermal conductivity of the test block with high precision resulting from the use of a high-thermal-conductivity material.

3 Assuming that the actual value of the condensation coefficient is unity ($\bar{\sigma} = 1.0$) and assuming that any data indicating the condensate surface temperature to be higher than the vapor temperature would not be reported, an error analysis of any condensing system would lead to a curve of expected value of σ versus vapor pressure (P_v) which would be unity at low pressures and decreasing below unity at increasing pressures.

4 Experimental data for potassium presented here for a copper condensing block and data previously obtained for a stainless steel block [12] and a nickel block [13] scatter around the curves of $E(\sigma)$ versus P_v (Fig. 14) predicted by the error analysis which uses an actual value of the condensation coefficient of unity at all pressures.

5 The actual value of the condensation coefficient equals unity for liquid metals at all pressures.

References

1 Nusselt, W., *Zeitsch. d. Ver. deutsch. Ing.*, Vol. 60, 1916, p. 541.

2 Schrage, R. W., *A Theoretical Study of Interphase Mass Transfer*, Columbia University Press, New York, 1953.

3 Rohsenow, W. M., and Choi, H. Y., *Heat, Mass and Momentum Transfer*, Prentice-Hall, Englewood Cliffs, N. J., 1961.

4 Adt, R. R., "A Study of the Liquid-Vapor Phase Change of Mercury Based on Irreversible Thermodynamics," PhD dissertation, Massachusetts Institute of Technology, Cambridge, Mass., 1967.

5 Bornhorst, W. J., and Hatsopoulos, G. N., "Analysis of a Liquid Vapor Phase Change by the Methods of Irreversible Thermodynamics," *Journal of Applied Mechanics*, TRANS. ASME, Vol. 34, Series E, No. 4, Dec. 1967, pp. 840–846.

6 Wilhelm, D. J., "Condensation of Metal Vapors: Mercury and the Kinetic Theory of Condensation," Argonne National Report #6948, 1964.

7 Mills, A. F., "The Condensation of Steam at Low Pressures," PhD dissertation, Technical Report Series No. 6, Issue No. 39, Space Science Laboratory, University of California, Berkeley, 1965.

8 Citakoglu, E., and Rose, J. W., "Dropwise Condensation Some Factors Influencing the Validity of Heat-Transfer Measurements," *International Journal of Heat and Mass Transfer*, Vol. 2, 1968, p. 523.

9 Weatherford, W. D., Tyler, J. C., Ku, P. M., *Properties of Inorganic Energy-Conversion and Heat-Transfer Fluids for Space Applications*, Wadd Technical Report 61-96, 1961.

10 Lemmon, A. W., Deem, H. W., Hall, E. H., and Walling, J. P., "The Thermodynamic and Transport Properties of Potassium," Battelle Memorial Institute.

11 Subbotin, V. I., Ivanovskii, M. N., Sorokin, V. P., and Chulkov, V. A., *Teplophizika Vysokih Temperatur*, No. 4, 1964, p. 616.

12 Meyrial, P. M., Morin, M. L., and Rohsenow, W. M., "Heat Transfer During Film Condensation of Potassium Vapor on a Horizontal Plate," Report No. 70008-52, Engineering Projects Laboratory, Massachusetts Institute of Technology, Cambridge, Mass., 1968.

13 Kroger, D. G., and Rohsenow, W. M., "Film Condensation of Saturated Potassium Vapor," *International Journal of Heat and Mass Transfer*, Vol. 10, Dec., 1967.

14 Subbotin, V. I., Bakulin, N. V., Ivanovskii, M. N., and Sorokin, V. P., *Teplofizika Vysokih Temperatur*, Vol. 5, 1967.

15 Subbotin, V. I., Ivanovskii, M. N., and Milovanov, A. I., "Condensation Coefficient for Mercury," *Atomnaya Energia*, Vol. 24, No. 2, 1968.

16 Sukhatme, S., and Rohsenow, W. M., "Heat Transfer During Film Condensation of a Liquid Metal Vapor," JOURNAL OF HEAT TRANSFER, TRANS. ASME, Series C, Vol. 88, 1966, pp. 19–29.

17 Misra, B., and Bonilla, C. F., "Heat Transfer in the Condensation of Metal Vapors: Mercury and Sodium Up to Atmospheric Pressure," *Chem. Engr. Prog. Sym.*, Ser. 18 52(7), 1965.

18 Barry, R. E., and Balzhiser, R. E., "Condensation of Sodium at High Heat Fluxes," *Proceedings of 3rd International Heat Transfer Conference*, Vol. 2, p. 318, Chicago, Illinois, 1966.
19 Aladyev, I. T., Kondratyev, N. S., Mukhin, V. A., Mukhin, M. E., Kipshidze, M. E., Parfentyev, I., and Kisselev, J. V., "Film Condensation of Sodium and Potassium Vapor," *3rd International Heat Transfer Conference*, Chicago, Illinois, Vol. 2, 1966, p. 313.
20 *C.R.C. Standard Mathematical Tables*, Chemical Rubber Publishing Company, 1961.
21 Hald, A., *Statistical Theory With Engineering Application*, Wiley, New York, 1952, p. 536.
22 Kroger, D. G., and Rohsenow, W. M., "Condensation Heat Transfer in the Presence of a Non-Condensable Gas," *International Journal of Heat and Mass Transfer*, Vol. 10, 1967.

ARTHUR F. OKUNO
Research Scientist.

CHUL PARK
Research Scientist.

NASA, Ames Research Center, Moffett Field, Calif.

Stagnation-Point Heat-Transfer Rate in Nitrogen Plasma Flows: Theory and Experiment

A theory for the heat transfer to the stagnation point of a hemisphere in a supersonic, high-enthalpy, low-density nitrogen plasma flow was developed. The theory assumed a flow that is frozen with respect to molecular dissociation and relaxing with respect to ionization. The calculations for this partially frozen flow yielded heat-transfer rates that were generally lower than predicted by other theories for both frozen and equilibrium flows. Experimental heat-transfer rates from measurements in a high-enthalpy constricted-arc tunnel agreed with the theoretical value within 10 percent in the mean.

1. Introduction

Prolonged tests in a high-enthalpy supersonic stream are necessary to evaluate the thermal performance of ablating materials for reentry bodies. To attain the enthalpies corresponding to super-orbital speeds, a continuous, constricted electric-arc tunnel [1, 2][1] can be employed. One important diagnostic measurement required in such a tunnel is the heat-transfer rate to the stagnation point of a hemisphere located on the test-stream center line. Preliminary test data [3] taken in arc tunnels at relatively low densities and high enthalpies indicate that the heat-transfer rates in the ionized flow regime may be lower than those taken in a shock tube or predicted by the available theories [4, 5]. The purposes of this paper are to present additional experimental data and to develop a theory that explains the lower heat-transfer measurements.

In contrast to the equilibrium flow in a high-velocity shock tube, typical high-enthalpy arc-heated flow has relatively low density and generally is believed to be frozen with respect to molecular dissociation and to be relaxing with respect to ionization throughout the flow field. Fig. 1 compares the enthalpy regimes and corresponding pressures of the present measurements with those of shock-tube experiments [6]. As seen in Fig. 1, the pressures produced in the arc tunnel are as much as two decades lower than those in shock tubes and, so, are more likely to produce nonequilibrium flows.

In the present work the experimental heat-transfer rate to the stagnation point is determined by a thermal inertia-type copper calorimeter coated with nickel or tungsten. The stream enthalpy, which was the major uncertainty of the data in reference [3], was determined by a spectroscopic technique.

The theoretical heat-transfer rate is calculated by considering

[1] Numbers in brackets designate References at end of paper.

Contributed by the Heat Transfer Division and presented at the Winter Annual Meeting, Los Angeles, Calif., November 16–20, 1969, of The American Society of Mechanical Engineers. Manuscript received by the Heat Transfer Division, December 10, 1969. Paper No. 69-WA/HT-49.

Nomenclature

C = α or β, (12)
C_{pf} = frozen specific heat at constant pressure for un-ionized gas, (A2)
D = effective binary diffusion coefficient, (A6)
E_d, E_i = dissociation and ionization energy, respectively
e = electronic charge
f = dimensionless normal velocity, (6)
H = total enthalpy
H_{av} = total mass-averaged enthalpy
H_j = partial static enthalpy of j-species
h = Planck's constant
k = Boltzmann's constant
K_e = partial thermal conductivity of electron gas, (A14a)
K_h = partial thermal conductivity of heavy-particle gas, (A14b)
K_L = Spitzer's thermal conductivity, (A15)
K_u = thermal conductivity of un-ionized gas, (A1)
k_w = surface catalytic recombination rate coefficient for atomic recombination
L = Lewis number for frozen flow of un-ionized gas, (A7)
m_j = mass of j-species
m_{jk} = equivalent mass in collision between j- and k-species, (B2)
n_j = number density of j-species
P_r = Prandtl number of un-ionized gas, (A3)

(*Continued on next page*)

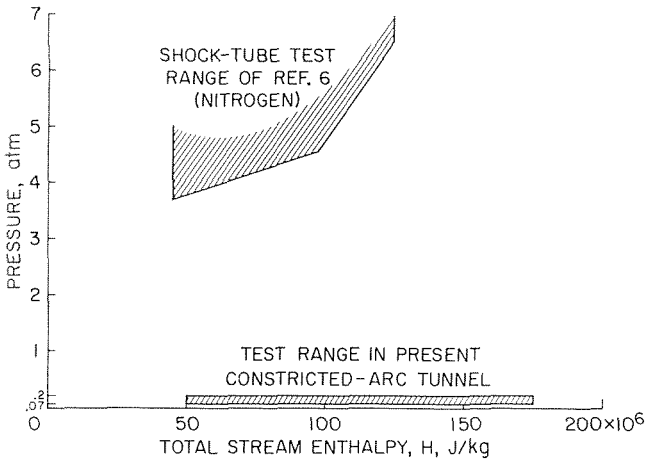

Fig. 1 Comparison of stagnation-point simulation

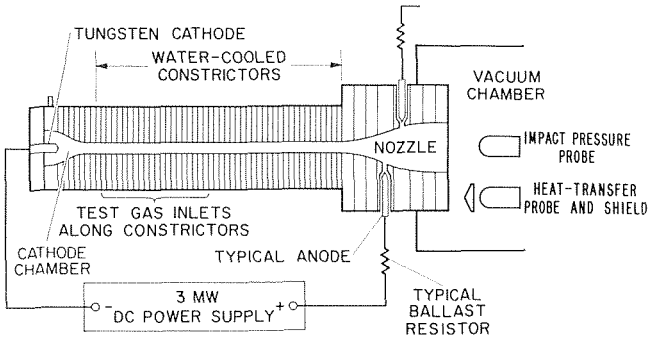

Fig. 2 Schematic drawing of constricted-arc tunnel

the effect of thermochemical relaxation because recent theories for weakly ionized flows [7–9] indicate that this effect can appreciably affect the heat-transfer rate. The theory developed herein combines three concepts: the viscous shock-layer concept [10–13]; the multi-species, highly ionized boundary-layer concept [4]; and the two-temperature, thermochemically relaxing, ionized boundary-layer concept [7–9]. The boundary conditions are chosen to represent the conditions of the present arc-tunnel experiments. Solution is obtained by machine computation employing an implicit integrating scheme developed for inviscid nozzle flows [14], which circumvents the usual difficulties [15] associated with integrating the chemical rate equations (see, e.g., reference [16]).

II. Theory

II.1. Arc-Tunnel Flow

To calculate the stagnation-point heat transfer in the nonequilibrium flow of the arc tunnel (Fig. 2), the properties ahead of the shock wave must be known approximately. These properties of the stream have been previously calculated [17–19]. The calculations show that at the exit of the constrictor the flow is fully dissociated and is in ionization equilibrium [17, 18]. For the expansion region of the arc tunnel, a computer program has been developed [19] to calculate the gas properties, assuming nitrogen to be monatomic.

A typical result of such a calculation is shown in Fig. 3 where α, β, T, T_e, and v are plotted against the distance along the nozzle. The mass fractions, α for ionized species and β for dissociated species, are defined, respectively, as [4]

$$\alpha \equiv \frac{m_i n_i}{\rho} = \frac{n_i}{2n_m + n_a + n_i} \tag{1}$$

$$\beta \equiv \frac{m_a n_a + m_i n_i}{\rho} = \frac{n_a + n_i}{2n_m + n_a + n_i} \tag{2}$$

The nitrogen flowing through the nozzle is fully dissociated and remains so. The ionized-species fraction in the test-section stream is approximately 30 percent of the equilibrium value behind a fictitious normal shock wave for this case and varies between 25 percent and 70 percent throughout the present test range. Also, for the present test range, the test-section electron temperature is within ±20 percent of 8000 deg K. The velocity approaches 9.5×10^5 cm/sec in the test section for the condition given in Fig. 3. Further calculations for the complete experimental range showed that the kinetic energy of the stream is a fixed function of the total enthalpy and that the velocity of the stream in the test section is approximately

$$v_\infty = 90\sqrt{H} \text{ cm/sec} \tag{3}$$

where the unit of H is J/kg.

Nomenclature

p = pressure
p_j = partial pressure of j-species
q = heat-transfer rate
R = nose radius of the hemisphere
R_n = Reynolds number, (4)
R_s = radius of curvature of bow shock wave
$\dot{R}$ = radiation power loss per unit volume
Sc = Schmidt number of un-ionized gas, (A9)
T = heavy-particle temperature
T_e = electron temperature
u, v = velocity component in x and y directions, respectively
V_j = diffusion velocity of j-species
v_∞ = free-stream (i.e., test-section) velocity
W_C = rate of production of species C by chemical reaction
$W_{\alpha 1}$, $W_{\alpha 2}$ = rate of production of ions by collisional and radiative processes, respectively, (C1) and (C5)
X_j = body force acting on j-species
x, y = coordinate along and normal to wall (Fig. 4), respectively
Z_a, Z_i = partition function for atom and ion, respectively
α, β = mass fraction of ionized and dissociated species, respectively, (1) and (2)
γ = ionic recombination rate coefficient, (C3)
ξ, η = dimensionless coordinates in x and y directions, respectively, (6)
μ = viscosity
μ_u = viscosity of un-ionized gas
ν_{jk} = collision frequency between j- and k-species
θ, θ_e = normalized heavy-particle and electron temperatures, respectively, (14) and (15)
ρ = density
ϕ = plasma sheath potential
χ_e, χ_i = fraction of electrons and ions reflected at surface, respectively

Subscripts

a = neutral atom
C = α or β
c = edge of plasma sheath (i.e., $\eta \to 0$ in continuum regime)
E = equilibrium
e = electron
h = heavy particle
i = ion
j, k = dummy variable indicating species; j, k = 1, 2, 3, and 4 correspond to m, a, i, and e, respectively
m = molecule
s = immediately behind shock wave
u = un-ionized gas
w = wall
∞ = free stream (i.e., test section)

II.2. Stagnation-Point Flow

II.2.1. Mass and Momentum Equations. The flow model is shown in Fig. 4. The equations of conservation of mass and momentum for the flow around a blunt body in a hypersonic stream take different forms depending on the Knudsen and Reynolds numbers. In a low-density ionized flow characterized by charge-charge collisions with large Coulomb cross sections, the mean free path and the Knudsen number are very small even though the mass density is relatively low. Thus the continuum approach with the assumption of zero shock-wave thickness for heavy particles, which is consistent with small Knudsen number, is adopted. The characteristic Reynolds number R_n is defined as

$$R_n = \frac{\rho_s R_s v_\infty}{\mu_s} \tag{4}$$

Since R_n in the present experiment is less than approximately 1000 but larger than 100, the viscous shock-layer approximation [10–13] was employed. The conservation equations for these conditions can be written approximately within the stagnation region [13]

$$(\text{mass})\ \frac{\partial}{\partial x}(\rho u x) + \frac{\partial}{\partial y}(\rho v x) + \frac{\rho v x}{R} = 0 \tag{5a}$$

$$(\text{momentum})\rho\left(\frac{u\partial u}{\partial x} + \frac{v\partial u}{\partial y}\right) = \frac{\partial}{\partial y}\left(\mu\frac{\partial u}{\partial y}\right) - \frac{\partial p}{\partial x} \tag{5b}$$

Equations (5*a*) and (5*b*) are reduced to dimensionless form through the following transformation of variables:

$$\xi = \int_0^x \rho_s\mu_s u_s x^2 dx, \qquad \eta = \frac{u_s}{\sqrt{2\xi}}\int_0^y \rho x dy$$
$$\frac{\partial\psi}{\partial y} = \rho u x, \qquad \frac{\partial\psi}{\partial x} = -\rho v x, \qquad \psi = \sqrt{2\xi} f(\eta) \tag{6}$$

where $u_s = (du_s/dx)_{\xi=0}\, x$. When $\xi^2 \ll 1$, equations (5*a*) and (5*b*) combine into the single dimensionless equation [13]

$$\left(\frac{\rho\mu}{\rho_s\mu_s} f''\right)' + ff'' + \frac{1}{2}\left[2\frac{\rho_\infty}{\rho} - (f')^2\right] = 0 \tag{7}$$

where the prime denotes the differentiation with respect to η. The boundary conditions are [13]

$$f(0) = f'(0) = 0 \tag{8}$$

$$f'(\eta_s) = 1 \tag{9}$$

From the definition of (6), and from the Newtonian hypersonic approximation

$$\left(\frac{du_s}{dx}\right)_{\xi=0} = \frac{v_\infty}{R_s} \tag{10}$$

f_s can be written as [13]

$$f_s \equiv f(\eta_s) = \frac{\rho_\infty}{\rho_s}\sqrt{\frac{R_n}{2}} \tag{10a}$$

The density ratio across the shock wave is taken as $^1/_4$ to be consistent with the assumption of frozen molecular dissociation and ionization across the shock wave (see II.2.2.). Expressions for the factors $\rho\mu/\rho_s\mu_s$ and ρ_∞/ρ in (7) are derived in Appendix A.

II.2.2. Species Equation. Four different species are considered in the present problem: the molecule, neutral atom, atomic ion, and electron. A possible additional species, the molecular ion, was not considered because its concentration found from the spectroscopic observation was negligibly small. The condition of charge neutrality requires that the number density of positive and negative charge be equal, i.e.,

$$n_i = n_e \tag{11}$$

With the addition of (11), the fractions of all four species are specified completely if those of any two species are given.

To derive the governing equations for the species fractions α and β, the expressions for the flux $\rho\alpha V_\alpha$ and $\rho\beta V_\beta$ caused by the diffusion of the species concerned must be derived. Expressions for these fluxes are derived in Appendix B. The general equation for the conservation of α and β has the form [4, 20]

$$\rho\left(u\frac{\partial C}{\partial x} + v\frac{\partial C}{\partial y}\right) = -\frac{\partial}{\partial y}(\rho C V_C) + m_a W_C \tag{12}$$

in which C stands either for α or β, and W_C is the rate of production of species C per unit volume by chemical reaction.

For the present flow regime the dissociation process is considered to be frozen because of the low density. Neglecting the species-production term in (12), substituting (B8) of Appendix B into the right-hand side (RHS) of (12), and transforming the coordinate by (6), the following is obtained:

$$\left(\frac{\rho\mu_u}{\rho_s\mu_{us}}\cdot\frac{\beta}{\mathrm{Sc}}\right) + f\beta' = \left[\frac{\rho\mu_u}{\rho_s\mu_{us}}\cdot\frac{1-\beta}{\mathrm{Sc}}\cdot\frac{(\beta + 2\alpha\theta_e/\theta)'}{1+\beta+2\alpha\theta_e/\theta}\right]' \tag{13}$$

Expressions for μ_u and Sc are derived in Appendix A. Also, θ

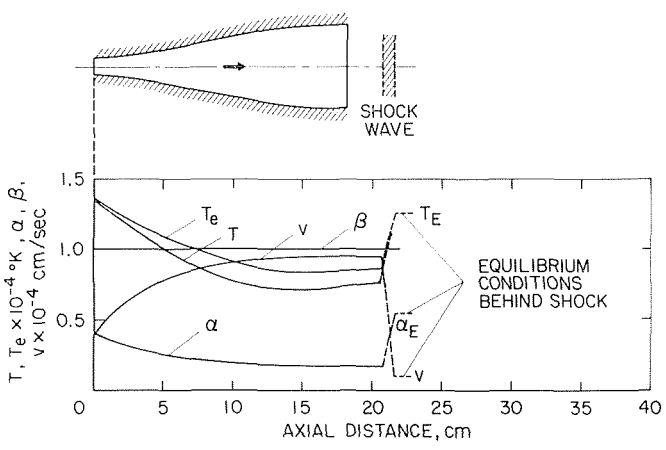

Fig. 3 Typical theoretical variation of flow properties along center line of a diverging nozzle; initial enthalpy $H = 1.18 \times 10^8$ J/kg; pressure at throat = 0.551 atm

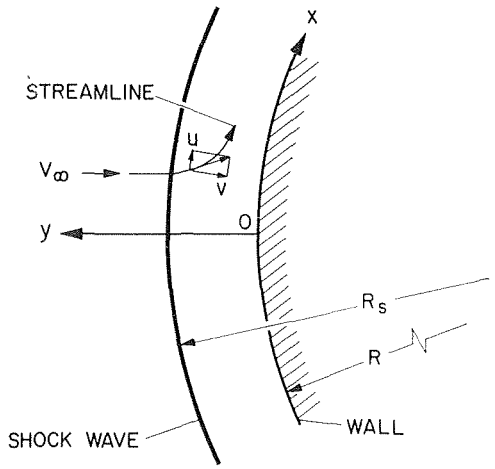

Fig. 4 Sketch of flow field in the stagnation region of an axisymmetric hypersonic shock layer

and θ_e are heavy-particle and electron temperatures normalized by E_i/k

$$\theta \equiv \frac{T}{(E_i/k)} = \frac{T(°\mathrm{K})}{168{,}600} \tag{14}$$

$$\theta_e \equiv \frac{T_e}{(E_i/k)} = \frac{T_e(°\mathrm{K})}{168{,}600} \tag{15}$$

The boundary condition for (13) at the wall is derived from the assumption of first-order surface reaction [21]

$$\left(\rho D \frac{\partial \beta}{\partial y}\right)_w = \rho_w D_w k_w \beta_w \tag{16}$$

Applying the transformation (6) to (16), the surface condition for the dissociation equation becomes

$$\beta_w' = \mathrm{Sc} \frac{\mu_{us}}{\mu_{uw}} \frac{k_w}{v_\infty} \sqrt{\frac{R_n}{2}}\, \beta_w \tag{17}$$

The flow immediately behind the shock wave can be assumed to be fully dissociated [12] because the test stream is fully dissociated and because the Reynolds number is not less than approximately 100. Thus the boundary condition behind the shock is

$$\beta(\eta_s) = 1 \tag{18}$$

There are two non-negligible ionizing reactions occurring in the gas. These are the collisional reaction

$$N + e \rightleftarrows N^+ + e + e \tag{19}$$

and the radiative reaction

$$N + h\nu \rightleftarrows N^+ + e \tag{20}$$

The net rate of change W_α in (12) is the sum of the rate of change by collisional reaction (19), $W_{\alpha 1}$, and that by radiative reaction (20), $W_{\alpha 2}$, i.e.,

$$W_\alpha = W_{\alpha 1} + W_{\alpha 2} \tag{21}$$

The expressions for $W_{\alpha 1}$ and $W_{\alpha 2}$ are given in Appendix C. By substituting $\rho\alpha V_\alpha$ from (B9) into (12) and transforming the coordinate by (6), the conservation equation for ionized species becomes

$$\left(\frac{\rho\mu_u}{\rho_s\mu_{us}} \cdot \frac{2}{\mathrm{Sc}}\right)\left\{\left[\alpha\left(1 + \frac{\theta_e}{\theta}\right)\right]' - \alpha\left(1 + \frac{\theta_e}{\theta}\right)\frac{(\beta + 2\alpha\theta_e/\theta)'}{1 + \beta + 2\alpha\theta_e/\theta}\right\}' + f\alpha' = -\frac{R_s m_a}{2v_\infty \rho}\,(W_{\alpha 1} + W_{\alpha 2}) \tag{22}$$

The boundary condition at the wall for equation (22) is determined from the consideration of plasma-sheath phenomena and will be discussed separately in II.2.5. Immediately behind the shock wave, the ionization-species fraction is approximately the same as it is in the free stream [7]. As mentioned in II.1. the free-stream ionized-species fraction falls within 25–70 percent of the equilibrium ionized fraction behind the shock. In the present computation, therefore, the boundary condition at $\eta = \eta_s$ is within the following range (see II.3.2. and Appendix E):

$$0.25\alpha_E \leqslant \alpha(\eta_s) \leqslant 0.7\alpha_E \tag{23}$$

II.2.3. Electron Energy Equation. The general equation of conservation of electron energy in a thermochemical nonequilibrium plasma has been derived in references [22, 23]. Solutions have been obtained for boundary-layer flows in references [7–9]. In the present work, where the electrical current is assumed zero everywhere, the electron energy equation becomes [8]

$$\rho\left(u\frac{\partial}{\partial x} + v\frac{\partial}{\partial y}\right)\left[\alpha\left(\frac{3}{2}kT_e + E_i\right)\right] - m_e n_e k T_e\left(u\frac{\partial}{\partial x} + v\frac{\partial}{\partial y}\right)\ln\rho = \frac{\partial}{\partial y}\left(K_e\frac{\partial T_e}{\partial y}\right) + 3m_a n_e k(T - T_e)\sum_{j=1}^{3}\frac{m_e}{m_j}\nu_{ej} - m_a\dot{R} \tag{24}$$

The expression for K_e is given in Appendix A. The electron-heavy-particle-energy-transfer term on the RHS of (24) is derived in Appendix D. In the nearly optically thin gas under consideration (see Appendix C, and note that the resonance line radiations are assumed to be fully absorbed), the radiative loss consists mainly of the radiative recombinations into the low-lying states of the nitrogen atom. Therefore $\dot{R}$ was approximated by $E_i W_{\alpha 2}$. After transforming variables by (6), there results

$$\left(\frac{\rho\mu_u}{\rho_s\mu_{us}}\frac{1}{\mathrm{P}_r}\frac{K_e}{K_u}\theta_e'\right)' + f\left\{\left[\alpha\left(1 + \frac{3}{2}\theta_e\right)\right]' + \frac{2\alpha\theta_e}{(1+\beta)\theta + 2\alpha\theta_e}\left(\frac{1 + \alpha + \beta}{2} + \alpha\theta_e\right)'\right\} = -\frac{3R_s}{5v_\infty}\alpha(\theta - \theta_e)\sum_{j=1}^{3}\frac{m_e}{m_j}\nu_{ej} - \frac{R_s m_a W_{\alpha 2}}{5v_\infty\rho} \tag{25}$$

where K_u and P_r are given in Appendix A. The quantities on the RHS of (25) are derived explicitly in Appendices C and D. The high thermal conductivity of the electron gas allows the electron energy to be conducted through the shock wave [7], and therefore the boundary condition for the electron temperature immediately behind the shock wave is given by the free-stream electron temperature. As mentioned in II.1., the free-stream electron temperature is within approximately ±20 percent of 8000 deg K for all calculations. In terms of the dimensionless electron temperature, therefore, the boundary condition at $\eta = \eta_s$ lies in the range (see II.3.2. and Appendix E)

$$0.04 \leqslant \theta_e(\eta_s) \leqslant 0.06 \tag{26}$$

The second boundary condition is given at the wall from the consideration of the plasma-sheath behavior and is discussed separately in II.2.5.

II.2.4. Total Energy Equation. The vibrational mode of the molecules is assumed to be fully excited and the vibrational energy is approximated by kT per particle. The partial static enthalpies of each species can then be written as follows:

$$(\text{molecule})H_m = \frac{4.5kT}{m_m} \tag{27}$$

$$(\text{atom})H_a = \frac{2.5kT + 0.5E_d}{m_a} \tag{28}$$

$$(\text{ion-electron pair})\,H_{ie} = \frac{2.5k(T + T_e) + 0.5E_d + E_i}{m_a} \tag{29}$$

The total enthalpy of the mixture is the sum of the above plus the kinetic energy. Using the dimensionless quantities, the mixture enthalpy becomes

$$H = \frac{E_i}{m_a}\left\{\frac{9 + \beta}{4}\theta + 0.386\beta + \left(1 + \frac{5}{2}\theta_e\right)\alpha\right\} + \frac{1}{2}(u^2 + v^2) \tag{30}$$

in which the factor 0.386 represents the ratio $0.5E_d/E_i$. The kinetic energy is neglected later in the actual calculations because it is small compared to the other energy components in the shock layer. The total energy conservation equation is [4]

$$\rho\left(u\frac{\partial H}{\partial x}+v\frac{\partial H}{\partial y}\right)=-\frac{\partial q}{\partial y}-m_a\dot{R} \tag{31}$$

where q is [4]

$$q\equiv -K_h\frac{\partial T}{\partial y}-K_e\frac{\partial T_e}{\partial y}+m_a\sum_j n_jV_jH_j \tag{32}$$

The radiation loss $\dot{R}$ in (31) can be taken as $E_iW_{\alpha 2}$ as in the preceding section. Expressions for the species flux n_jV_j (derived in Appendix B) are substituted into (31), and the coordinate transformation (6) is applied. The dissociated species equation (13) is then subtracted from the resulting dimensionless energy equation to simplify the energy equation because the Schmidt number is unity (see (A9)). The resulting dimensionless form of the energy equation is

$$\left(\frac{\rho\mu_u}{\rho_s\mu_{us}}\frac{1}{\mathrm{P}_r}\left\{\frac{K_h}{K_u}\theta'+\frac{K_e}{K_u}\theta_e'+\frac{4L}{5}\left[\alpha\left(1+\frac{\theta_e}{\theta}\right)\right]'-\frac{4L}{5}\cdot\frac{\alpha(1+\theta_e/\theta)(\beta+2\alpha\theta_e/\theta)'}{1+\beta+2\alpha\theta_e/\theta}\right\}\right)'+\frac{2}{5}f\left[\frac{9+\beta}{4}\theta+\left(1+\frac{5}{2}\theta_e\right)\alpha'+\frac{5}{2}\alpha\theta_e'\right]=-\frac{R_sm_aW_{\alpha 2}}{5v_\infty\rho} \tag{33}$$

One boundary condition for the energy equation (33) is specified at the wall where the heavy-particle temperature must equal the wall-surface temperature, taken as 500 deg K in the present work, i.e.,

$$\theta(0)=\theta_w=500/(E_i/k)=0.00297 \tag{34}$$

Immediately behind the shock wave, the heavy-particle temperature is given as

$$\theta(\eta_s)=\theta_s \tag{35}$$

The boundary condition (35) is not used explicitly in the computation, however, as explained in Appendix E.

II.2.5. Wall Conditions for Electrons. The continuum analysis of the present work is not valid near the wall, i.e., within one mean free path from the surface. Near the wall, the inequality in the mobility of electrons and ions generally creates a region of charge separation. The fundamental physics of this phenomenon is well understood and is incorporated into the boundary-layer analysis by Sherman and Reshotko [8] and Knight [9]. In the present work, the results of such analyses are used to derive the boundary conditions for the conservation equations for electrons.

According to the plasma-sheath theory, the heavy particles are not affected by the electrical field produced in the sheath because of their large inertia and they experience no change in temperature across the charged sheath. For electrons, however, both the density and temperature change appreciably across the sheath; therefore, the boundary condition for the continuum electron equations (22) and (25) must be derived using plasma-sheath theory. With regard to the electrons, the interface between the sheath and the outside flow is identified by the subscript c in this section. It should be noted that the continuum analysis cannot distinguish the sheath-boundary-layer interface from the wall, and therefore the subscript c can be replaced by the subscript w.

Defining χ_i and χ_e as ion and electron reflection coefficients [9], the combination of conservation of electron flux and Poisson's equation results in the following relation [9]

$$(1-\chi_e)\frac{n_{ec}}{4}\sqrt{\frac{8}{\pi}\frac{kT_{ec}}{m_e}}\exp\left(\frac{e\varphi}{kT_{ec}}\right)=(1-\chi_i)\frac{n_{iw}}{4}\sqrt{\frac{8}{\pi}\frac{kT_w}{m_i}} \tag{36}$$

By equating the ion flux n_iV_i of (B7) in Appendix B in the continuum regime with that reaching the surface (i.e., the RHS of (36), see reference [9]), and transforming the coordinate by (6), and using the condition $\alpha_{ec}\ll 1$,

$$\left(\frac{\rho\mu_u}{\rho_s\mu_{us}}\frac{2}{\mathrm{Sc}}\right)_w\left[\alpha\left(1+\frac{\theta_e}{\theta}\right)\right]_c'=\frac{\alpha_c}{4\sqrt{2}}\frac{\rho_w}{\rho_s}\sqrt{\frac{E_i}{v_\infty{}^2m_a}\frac{8}{\pi}\theta_w\mathrm{R}_n}\,(1-\chi_i) \tag{37}$$

Likewise, the balance of electron energy across the sheath [9] gives the dimensionless relationship

$$\left(\frac{\rho\mu_u}{\rho_s\mu_{us}}\frac{1}{\mathrm{P}_r}\frac{K_e}{K_u}\right)_w\theta_{ec}'=\frac{1}{10\sqrt{2}}\sqrt{\frac{8}{\pi}\frac{m_a}{m_e}}\frac{\rho_w}{\rho_s}\sqrt{\frac{E_i}{m_av_\infty{}^2}\theta_{ec}\mathrm{R}_n}\times\exp\left(\frac{e\varphi}{kT_{ec}}\right)\alpha_c\left\{\chi_e\left(2\theta_{ec}-\frac{3}{2}\theta_w\right)+(1-\chi_e)\left(\frac{|e\varphi|}{E_i}-\frac{\theta_{ec}}{2}\right)\right\} \tag{38}$$

Equations (37) and (38) specify two boundary conditions for electron equations (22) and (25), i.e., α and θ_e must equal α_c and θ_{ec} in the limit of $\eta\to 0$.

From equations (37) and (38) it is seen that χ_i, χ_e, and φ control the boundary conditions for the electrons. Therefore, χ_i, χ_e, and φ are examined to determine these boundary conditions. Metal surfaces are fully catalytic for ionic recombination, i.e., $\chi_i=\chi_e=0$. The sheath potential φ for this case becomes maximum, so from equation (36)

$$e\varphi=e\varphi_{\max}\equiv kT_{ec}\ln\left(\sqrt{\frac{m_e}{m_i}\frac{T_w}{T_{ec}}}\right)\quad(\chi_i=\chi_e=0) \tag{39}$$

For the ionically noncatalytic surface (i.e., $\chi_i\to 1$, $\chi_e\to 1$), φ is determined by the limiting value of the ratio $(1-\chi_i)/(1-\chi_e)$ from equation (36). To the author's knowledge, no data or theory is available at present to evaluate φ for the ionically noncatalytic surface. It is believed, however, that the sheath potential is either nonexistent or is very small if it exists, i.e.,

$$e\varphi\simeq 0\qquad(\chi_i\to 1,\ \chi_e\to 1) \tag{40}$$

because all electrons are allowed to come into contact with the surface, and thereby the incoming electrons are not decelerated to cause a space-charging. For comparison, however, the hypothetical case where $\varphi=\varphi_{\max}$, $\chi_i\to 1$, $\chi_e\to 1$ has also been considered in the computation.

II.2.6. Heat-Transfer Rates. The rate of heat transfer to the wall, q_w, is the value of q in equation (32) evaluated in the limit of $\eta\to 0$ in the continuum regime. In terms of the dimensionless quantities, the heat-transfer rate can be written as

$$q_w=74\left[\frac{\theta^{0.81}(1+\beta/9)}{(1+\beta)\theta+2\alpha\theta_e}\cdot\frac{0.72+1.28\beta}{1+\beta}\cdot\frac{p_sv_\infty}{R_s}\right]^{1/2}\times\left(\frac{\rho_s\mu_s}{\rho\mu_u}\right)^{1/2}\left(\frac{\rho\mu_u}{\rho_s\mu_s}\frac{1}{\mathrm{P}_r}\right)\cdot\left\{\frac{K_h}{K_u}\theta'+\frac{K_e}{K_u}\theta_e'+\frac{2}{5}\left(\frac{\theta}{4}+0.386\right)\times\left[\beta'+(1-\beta)\frac{(\beta+2\alpha\theta_e/\theta)'}{1+\beta+2\alpha\theta_e/\theta}\right]+\frac{4}{5}L\left[\alpha+\left(1+\frac{\theta_e}{\theta}\right)\right]'-\frac{4}{5}L\alpha\left(1+\frac{\theta_e}{\theta}\right)\frac{(\beta+2\alpha\theta_e/\theta)'}{1+\beta+2\alpha\theta_e/\theta}\right\}_{\eta=0} \tag{41}$$

in W/cm² when p_s is in atm, v_∞ in cm/sec, and R_s in cm. In (41), the values of electron temperature and ionized species fraction at $\eta=0$ refer to the values at the edge of the plasma sheath which are identified by subscript c in II.2.5.

In the present calculation the electron recombination term is found to be as much as 40 percent of the total heat-transfer rate to a noncatalytic surface.

II.3. Results of Calculations

II.3.1. Method of Solution. The solutions to the set of differential equations (7), (13), (22), (25), and (33) satisfying the boundary conditions (8), (9), (17), (18), (23), (26), (34), (35), (37), and (38) are obtained numerically using the "shooting" method with an implicit integration scheme [14]. With a set of estimated wall values of dependent variables, the differential equations were integrated numerically starting from the wall, $\eta = 0$, to the shock wave, $\eta = \eta_s$, along the stagnation streamline. At the shock wave, the variables of the differential equations were compared with the given boundary values. If they did not agree, a new set of wall values was estimated and the integration was repeated. This trial and error procedure was continued until the shock boundary conditions were satisfied. Further details of the computational procedures are described in Appendix E.

The computations described above were carried out for the following range of conditions:

$$\chi_i = \chi_e = 0, \qquad \chi_i = \chi_e = 1$$
$$k_w = 0,\ 550,\ \text{and}\ \infty\ \text{cm/sec}$$
$$p_s = 0.01\ \text{and}\ 0.1\ \text{atm}$$
$$R = 1.27\ \text{cm}$$
$$50 \times 10^6 < H < 200 \times 10^6\ \text{J/kg}$$

II.3.2. General Features of the Solutions. A typical solution is shown in Fig. 5, where α, β, T, and T_e are plotted against η. At the wall the value of α approaches zero and T_e is about 7000 deg K. These values agree closely with those calculated by Knight [9] for a weakly ionized gas. However, β (which was taken equal to unity in Knight's calculation) is a variable in the present calculation. The main difference between the present theory and that of Knight occurs near the shock wave. In the present work the properties do not reach equilibrium anywhere in the shock layer, whereas Knight assumed equilibrium at the edge of the boundary layer.

As seen in Fig. 5, α and T_e reach maxima at almost the same intermediate point within the shock layer. This feature provides the basis for the spectroscopic diagnosis of the shock-layer flow described in III.1. Theoretically, the electron temperature can be determined exactly at the maximum α point by a spectroscopic technique (see III.1.1.), but this point is difficult to determine experimentally. Therefore, the maximum electron temperature was measured assuming that the peaks of α and T_e occurred at the same location (see III.1.2.). Fig. 5 also shows that the peak electron temperature is approximately equal to the equilibrium temperature. Thus the enthalpy calculated from the peak electron temperature, assuming equilibrium, is close to the true enthalpy.

For all the numerical solutions performed it was found that the calculated heat-transfer rate was insensitive to the values of α_s and θ_{es} (see equations (23) and (26)). This is probably because the heat-transfer rate is dependent mainly on the total enthalpy and is relatively independent of the detailed partitioning of the enthalpy among different species and modes.

II.3.3. Effect of Surface Atomic Recombination. Calculated heat-transfer rates multiplied by $(R/p_s)^{1/2}$ are shown in Fig. 6. As seen from the figure, surface atomic recombination increases the heat-transfer rate; that is, the heat-transfer rate to the wall for $k_w = \infty$ (fully atomically catalytic) is greater than that for $k_w = 0$ (atomically noncatalytic). This phenomenon is the same as observed in an un-ionized, dissociated gas [21]. Quantitatively, however, the effect of surface catalysis for atomic recombination is surprisingly large. From Goulard's theory [21], one would expect that the fractional contribution of surface atomic recombination to total heat-transfer rate should be proportional to the ratio of dissociation energy to total enthalpy, i.e.,

$$\frac{q(k_w = \infty) - q(k_w = 0)}{q(k_w = \infty)} \simeq \frac{E_d/m_m}{H}$$
$$\simeq 0.22 \text{ at } H = 150 \times 10^6\ \text{J/kg}$$

Fig. 6 indicates that the actual contribution by the surface atomic recombination is much larger, probably due to the coupling between the ionization and molecular diffusion. As seen from equation (C4), the ionization reaction rate W_{α_1} is affected by β, and therefore a change in the profile of β would affect the profile of α and hence alter the magnitude of energy flux contained in the ionized species.

Also shown in Fig. 6 is the heat-transfer rate to a nickel surface ($k_w = 550$ cm/sec) because most of the data were taken with a nickel-coated calorimeter. Only in the region of low ionization is there an appreciable difference in the heat-transfer rate between a nickel surface and noncatalytic surface ($k_w = 0$, $\chi_i = \chi_e = 0$) for the selected pressure and nose radius. The effect of varying k_w on the heat-transfer rate is treated in Appendix F. The heat-transfer rate for an arbitrary, finite value of k_w can be determined by combining the results shown in Fig. 6 with those in Appendix F.

II.3.4. Effect of Surface Ionic Recombination.

For $k_w = 0$, two extreme solutions are obtained by varying χ_i and χ_e between 0 and 1, corresponding respectively to a metallic surface and to an assumed ionically noncatalytic surface (see II.2.5.). For the ionically noncatalytic surface, φ is considered

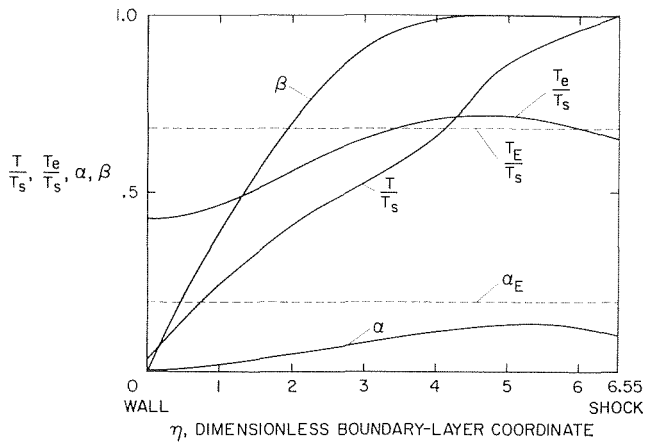

Fig. 5 Typical variation of α, β, T, and T_e in the boundary layer; fully catalytic surface for atoms, ions, and electrons ($k_w = \infty$, $\chi_i = \chi_e = 0$), $p_s = 0.1$ atm, and $H = 72.5 \times 10^6$ J/kg

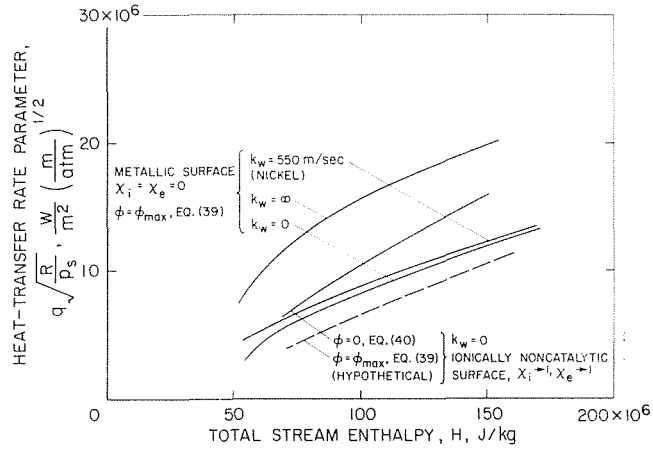

Fig. 6 Calculated stagnation-point heat-transfer rate in dissociated and ionized flows of nitrogen

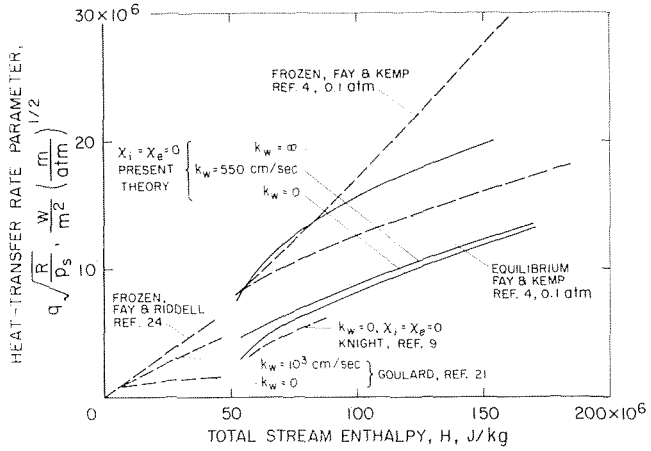

Fig. 7 Comparison of calculations for stagnation-point heat-transfer rate in dissociated and ionized nitrogen

to be zero (equation 40)), but the hypothetical case of $\varphi = \varphi_{max}$ (equation (39)) is also computed and shown for comparison. As seen from Fig. 6, for $\chi_i, \chi_e \rightarrow 1$ the heat-transfer rate for $\varphi = 0$ is greater than for $\varphi = \varphi_{max}$. This occurs because, in the absence of the sheath, the electrons are not inhibited from bombarding the surface, and a large flux of energy is carried to the solid surface through the kinetic energy of the bombarding electrons.

It is interesting to note that the heat-transfer rate to the ionically noncatalytic wall (with $\varphi = 0$ and $k_w = 0$) is greater than that to the ionically catalytic wall ($k_w = 0$). Evidently the ion-electron recombination energy released at the ionically catalytic surface is less than the total energy flux carried by the impinging electrons to the ionically noncatalytic surface. For the ionically catalytic surface, the energy transmission due to electron impact is negligible because most electrons are repelled from the surface by the sheath.

II.3.5. Comparison With Other Theories. In Fig. 7, the present heat-transfer rate calculations (solid curves) are compared with other theories. At low degrees of ionization, $H = 50 \times 10^6$ J/kg, the present theory appears to be in reasonable agreement with the theories of Fay and Riddell [24] and Goulard [21], which apply at lower enthalpies. For the weakly ionized region, $50 \times 10^6 < H < 70 \times 10^6$ J/kg, the present theory gives slightly higher nonequilibrium heating rates than those predicted by Knight [9], probably because the present theory includes vorticity interaction effects [10–13]. At the higher ionization levels the present nonequilibrium theory is compared with the equilibrium and frozen flow (with fully catalytic surface) theories of Fay and Kemp [4] because no nonequilibrium theory is available for comparison. For $k_w = 0$, $\chi_i = \chi_e = 0$, the present calculation shows lower heat-transfer rate than given by the equilibrium theory [4], probably because the energy of dissociation is not recovered at the surface. For $k_w = \infty$, the present calculations agree with the frozen-flow solution of reference [4] in the weakly ionized region and fall between the results of the frozen and equilibrium theories of reference [4] in the highly ionized region.

II.3.6. Effect of Body Size and Pressure. The heat-transfer rate is commonly compared in terms of the parameter $q\sqrt{p_s/R_s}$. However, the factor $\sqrt{p_s/R_s}$ does not account for all of the effects of p_s and R_s on the heat-transfer rate. There are, in addition, (i) the effect of surface atomic recombination and (ii) the influence of p_s and R_s on the profiles of energy and species through the terms representing the chemical reaction rates (Appendix C) and thermalization (Appendix D) in the basic differential equations. Effect (i) is discussed in Appendix F, where it is shown that the heat-transfer rate is controlled by the factor $k_w\sqrt{p_s R}$. To investigate effect (ii), one calculation was performed at $p_s = 0.01$ atm, and the resulting heat-transfer rate was only 2.5 percent higher than the corresponding case of $p_s = 0.1$ atm. From this calculation and from the results of Knight [9], effect (ii) is concluded to be negligible for nonequilibrium flow. Therefore, the curves plotted in Figs. 6 and 7 can be extended to other pressures and nose radii if account is taken of the effect of surface atomic recombination.

III. Experiment

III.1. Determination of Enthalpy

III.1.1. Basis of Spectroscopic Technique. To evaluate the heat-transfer rate to a blunt body it is essential to know the enthalpy of the test stream, and this was determined in the present experiment by a spectroscopic technique. The basic principles of spectroscopy for plasma are well known (see, e.g., reference [25]). The following two conditions must be met in order to obtain an exact value of enthalpy through spectroscopic measurements: (i) the bound electronic states are populated according to the steady-state distribution [26], and (ii) a relationship must be known which gives the enthalpy from the measured electron temperature. The present spectroscopic technique is based on the results of the shock-layer calculations. Calculations of the shock-layer flow show that condition (i) is met exactly at one point and condition (ii) is met approximately in the shock layer; i.e., the enthalpy calculated from the peak electron temperature assuming equilibrium is approximately equal to the true enthalpy of the nonequilibrium flow (see II.3.2.). In the present experiment, therefore, the enthalpy was determined spectroscopically from the measured peak electron temperature using the approximate relationship between the peak electron temperature and enthalpy.

The theoretical calculations of shock-layer flow, and hence the spectroscopic technique, depend weakly on the boundary conditions (23) and (26). These boundary conditions are substantiated to the degree of accuracy required by the experimental results of references [19, 27, 28] together with other unpublished spectroscopic data.

III.1.2. Method of Spectroscopic Diagnosis. To measure the peak electron temperature, a 2.25-m Ebert Jarrell-Ash spectroscope was focussed on a point in the stagnation region. Two blunt body shapes were used for this purpose, i.e., a hemisphere and a flat circular disk, both of 2.54 cm diameter. The hemisphere was used in the medium-to-high-enthalpy region where the peak electron temperature does not differ greatly from the equilibrium temperature according to theoretical calculations such as the one shown in Fig. 5. In the low-enthalpy regime (i.e., less than 8×10^7 J/kg), however, the calculated nonequilibrium electron temperature in the shock layer of the hemisphere was appreciably different from the equilibrium value. Therefore a flat disk was used to provide a larger shock standoff distance and hence a larger flow residence time to enable the nonequilibrium electron temperature to approach the equilibrium value in the low-enthalpy regime. The width of entrance slit of the spectroscope was kept below 100 μ and the aperture of the optics on the object side was approximately f/50. These optical arrangements enabled one to observe the shock layer with spatial resolution of less than 200 μ. The maximum in the electron temperature distribution was found by scanning the focal point across the shock layer and selecting the point where the ratio of the intensities of the lines selected gave the maximum value.

Electron temperature was determined by three different techniques depending on the regime of enthalpy. For temperatures above approximately 14,000 deg K, the electron temperature was determined by an ion-atom line ratio method, i.e., by comparing the intensities of the 5680NII line with those of 4935NI and 7468NI. For this measurement, EMI 9558 photomultiplier tubes with S-20 spectral response were applied. This method is believed to give the electron temperature to within ±3 percent of the true value [27].

For temperatures below approximately 14,000 deg K but above 10,000 deg K, the intensities of the 5680NII line were too weak to be measured, and therefore only the intensities of 6008NI

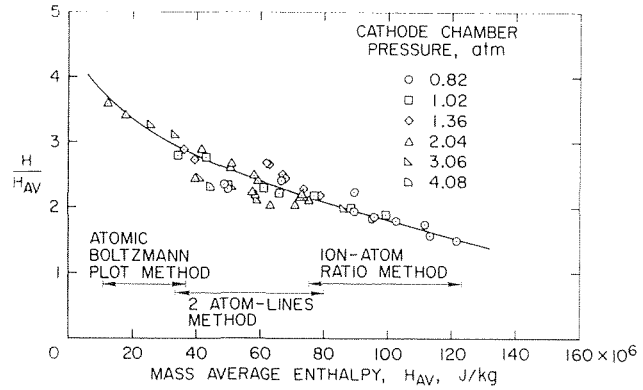

Fig. 8 Enthalpy ratio versus mass-average enthalpy

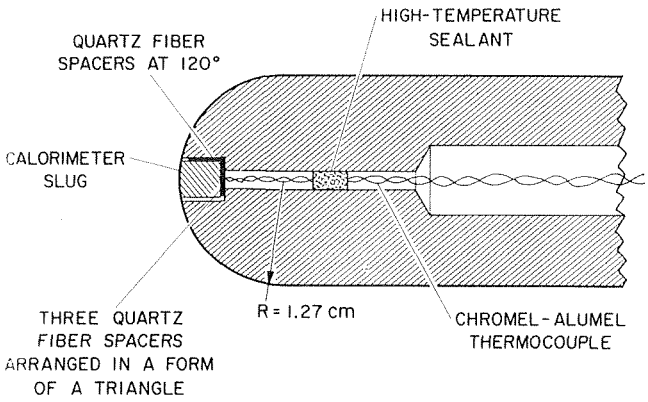

Fig. 9 Schematic drawing of a calorimeter

and 7468NI lines were compared [19], i.e., 2-atom line method. S-20 phototubes were used for this method, also. Here the accuracy is believed to be within ±15 percent in temperature. For the above two methods, the line intensity from the shock layer of the hemispherical model was observed.

For temperatures below approximately 10,000 deg K, more careful measurement was necessary because the existence of excitation equilibrium was in doubt. For this low-enthalpy regime, therefore, the shock layer of the flat disk was observed instead of that of the hemisphere, and the entire spectrum within the wavelength range 4000 Å–11,500 Å was used to determine the electron temperature. All of the atomic line radiations were measured with photomultiplier tubes of S-20 and S-1 (EMI 9684) spectral responses and analyzed to form atomic Boltzmann plots. The transition probabilities of the spectral lines required for this procedure were obtained from reference [29]. The result showed that excitation equilibrium existed in the low-ionization regime, and therefore it was possible to determine the electron temperature.

III.1.3. Result of Enthalpy Measurements. The enthalpy H was calculated assuming equilibrium exists at the measured electron temperature. In Fig. 8 the spectroscopically determined enthalpy is compared with the mass-averaged enthalpy H_{av} [1, 2], the quotient of the net power input into the arc tunnel (i.e., electrical power minus cooling loss), and the gas mass flow rate. The approximate ranges of enthalpies for the three spectroscopic methods described in III.1.2. are indicated in Fig. 8. The spectroscopically determined enthalpies correlate well in the high and low-enthalpy regimes, but a relatively larger experimental scatter in the intermediate range appears when the temperature is determined from only two lines. The spectroscopically determined enthalpy H is greater than the mass-averaged enthalpy H_{av} because the spectroscopic measurement determines the enthalpy along the axis of the arc-tunnel flow whereas the mass-averaged enthalpy is a bulk value for the entire stream that includes the cold boundary layer near the nozzle wall. Fig. 8 also shows that the ratio of center-line enthalpy to the mass-averaged enthalpy is not strongly affected by the cathode-chamber pressure of the arc tunnel.

III.2. Heat-Transfer Measurements

The experimental investigation was performed in a constricted-arc plasma jet [1, 2] which had a constrictor 1.27 cm in diameter and 30.5 cm long, followed by a diverging-contoured nozzle of area ratio 22 (Fig. 2).

Test calorimeters were mounted on a support system that could insert them into the stream center line for prescribed times. The calorimeters were shielded from the hot gas during insertion and retraction from the stream.

The heat-transfer rates to the stagnation region of the hemisphere cylinder were measured with a heat-sink transient-type calorimeter (Fig. 9). The copper calorimeter slug was 0.475 cm in diameter and 0.5 cm long. Both calorimeter and shroud were either electroplated with a thin layer of nickel or vacuum-deposited with tungsten. Heat-transfer rates were determined from the temperature variation of the calorimeter slug by the method of reference [30].

The stagnation-point pressures were measured with a 2.54-cm-dia water-cooled hemisphere-cylinder probe which had a 0.318-cm-dia orifice at the stagnation region connected to a strain-gage-type pressure transducer. The range of measured stagnation pressures was 0.07–0.20 atm.

III.3. Results of Experiments

Measured heat-transfer rates multiplied by $(R/p_s)^{1/2}$ for various values of total stream enthalpy are shown in Fig. 10. Also shown are the experimental results of Rose and Stankevics [6] and Pope [3]. As seen in Fig. 10, the present measurements for a nickel surface agree well with Pope's data. Compared with the measurements of Rose and Stankevics [6], the present data and those of Pope [3] are lower, especially in the high-enthalpy region where the difference is almost 40 percent. This discrepancy can be partially explained by the difference in boundary-layer chemistry between the two types of experiments. In the shock-tube experiment of Rose and Stankevics [6], the stagnation-region pressure was greater than 7 atm so that the flow was in equilibrium for both ionization and dissociation. As seen from Fig. 7, one would expect a higher heat-transfer rate from a completely equilibrium flow than from the nonequilibrium flow of the arc-

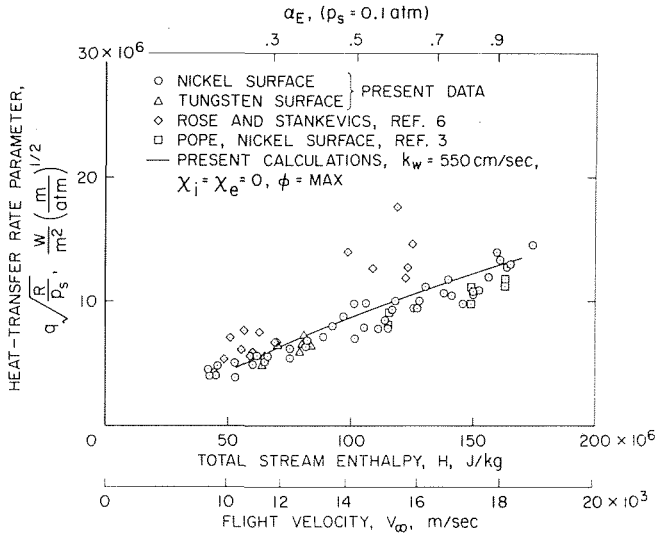

Fig. 10 Heat-transfer rate in dissociated and ionized flows of nitrogen

heated tunnel for $k_w = 550$ cm/sec. The present theory with $k_w = 550$ cm/sec and ionically catalytic wall agrees with the experiment to within 10 percent in the mean throughout most of the ionized region, suggesting that the theory developed in II is valid.

Fig. 10 also shows that there is little difference between heat-transfer rates measured with a nickel or a tungsten-coated calorimeter. This is not unexpected because calculated curves in Fig. 7 indicate a difference in heat-transfer rate of only about 10 percent between a noncatalytic surface and a surface having $k_w = 550$ cm/sec. Tests with tungsten-coated calorimeters were not conducted in the higher-enthalpy region because the calculated curves in Fig. 7 indicated that the difference in heat-transfer rate between tungsten and nickel surfaces would be greatest in the lower-enthalpy regime. The present result differs from that of Pope [3] who found a significant difference (of 30 percent or more) between the heat-transfer rates for solid tungsten-slug calorimeters and nickel-coated copper calorimeters under similar test pressures. The reason for this discrepancy is not known at present.

IV. Summary and Conclusions

A theory for the heat transfer at the stagnation point of a hemisphere in a stream frozen with respect to molecular dissociation and relaxing with respect to ionization was developed for highly ionized nitrogen. As seen from Fig. 10, the heat-transfer rate to the stagnation point of a nickel surface measured in an arc tunnel agrees to within ± 10 percent in the mean with the calculations based on the assumption $\chi_i = \chi_e = 0$ and $k_w = 550$ cm/sec. The agreement between theory and experiment lends support to the validity of the theory so that the heat-transfer rate can be calculated with a fair degree of confidence. However, the machine computation is difficult. The procedure for finding the solutions, as indicated in Appendix E, is extremely tedious and time-consuming, mainly because the implicit integration method is incompatible with piecewise-linearization techniques. The present theoretical and experimental heat-transfer rates are significantly lower than those calculated by equilibrium theory or those measured in a shock tube.

The physical phenomena in an ionized boundary layer are different both quantitatively and qualitatively from those in an un-ionized, dissociated boundary layer for the following reasons: (i) transport coefficients are greatly altered by the ionization, (ii) electrons have a high thermal speed and are capable of transporting a large fraction of the total energy, and (iii) a charged plasma sheath develops adjacent to the wall. Thus the classical concept of dissociated boundary layer should not be extended into the regime of ionized boundary layers without considering these factors. The present theoretical calculation shows that, contrary to expectations, the heat-transfer rate would likely be larger for an ionically noncatalytic wall than for an ionically catalytic wall. On the other hand, the atomically noncatalytic wall reduces the heat transfer, as occurs in an un-ionized flow. The lowest heat-transfer rate would most likely occur, therefore, with an atomically noncatalytic ($k_w = 0$), ionically fully catalytic wall ($\chi_i = \chi_e = 0$).

Appendix A. Transport Properties

A.1. Un-ionized Nitrogen

When nitrogen is not ionized, its thermal conductivity K_u can be approximated by [4]

$$K_u = 3.52 \times 10^{-6} T^{0.81} \frac{0.72 + 1.28\beta}{1 + \beta}, \qquad \text{W/cm-deg K} \quad \text{(A1)}$$

Because the vibrational mode of molecular nitrogen is assumed to be fully excited (see equation (27)), the frozen specific heat at constant pressure for the un-ionized nitrogen, C_{pf}, can be written approximately as

$$C_{pf} = \frac{4.5K}{m_m}(1 - \beta) + \frac{2.5K}{m_a}\beta = 1.34\left(1 + \frac{\beta}{9}\right), \qquad \text{J/g-deg K} \quad \text{(A2)}$$

Frozen Prandtl number of an un-ionized gas is approximately constant (see, e.g., Hansen [31]), which is taken to be 0.6 as in reference [4], i.e.,

$$\mathrm{P}_r \equiv \frac{\mu_u C_{pf}}{K_u} = 0.6 \quad \text{(A3)}$$

From (A1)–(A3), the viscosity of the un-ionized nitrogen becomes, assuming $\beta/9 \ll 1$,

$$\mu_u = 1.58 \times 10^{-6} T^{0.81} \frac{0.72 + 1.28\beta}{1 + \beta}, \qquad \text{poise} \quad \text{(A4)}$$

Although the un-ionized viscosity μ_u varies at $T^{0.81}$ explicitly in (A4), the change in β makes the overall dependence of μ_u on T roughly linear, i.e.,

$$\mu_u \sim T \quad \text{(A5)}$$

The effective binary diffusion coefficient D is defined in the present work as in reference [4], i.e.,

$$D \equiv \frac{n_a kT}{(n_m + n_a + n_i) m_{ma} \nu_{ma}} \quad \text{(A6)}$$

The Lewis number of the un-ionized gas is defined as

$$L \equiv \frac{(n_m + n_a + n_i) D m_a C_{pf}}{K_u} \quad \text{(A7)}$$

Reference [4] defines the Lewis number in the same manner as above, except that C_{pf}/K_u of (A7) refers to the fully dissociated gas. The difference is considered negligible because the ratio C_{pf}/K_u changes only by 20 percent in the transition from molecular to atomic state. Thus, as was done by Fay and Kemp [4], the Lewis number is taken to be 0.6, i.e.,

$$L = 0.6 \quad \text{(A8)}$$

From (A3) and (A8), the Schmidt number becomes

$$\mathrm{Sc} = \frac{L}{\mathrm{P}_r} = 1 \quad \text{(A9)}$$

A.2. Ionized Nitrogen

The nitrogen plasma is considered to be a binary mixture of heavy-particle gas and electron gas. The viscosity can be written in the form [32]

$$\mu = \mu_u \left\{ \sqrt{\frac{m_e}{m_h}\frac{T_e}{T}}\, \alpha \left[\alpha \frac{\Omega_{ee}}{\Omega_{hh}} + (1 - \alpha)\sqrt{2}\,\frac{\Omega_{eh}}{\Omega_{hh}} \right]^{-1} + \left[\frac{\alpha}{1 - \alpha} \sqrt{\frac{2m_e T}{m_h T_e}}\,\frac{\Omega_{eh}}{\Omega_{hh}} + 1 \right]^{-1} \right\} \quad \text{(A10)}$$

In (A10), m_h is the average mass of the heavy-particle species, and Ω_{ee}, Ω_{eh}, and Ω_{hh} are collision integrals [32] that are weak functions of temperature alone. Assuming Ω_{ee}, Ω_{eh}, and Ω_{hh} are constant, the ratio μ/μ_u becomes a function only of the parameter $\alpha\sqrt{T_e/T}$ in a weakly ionized regime, i.e.,

$$\frac{\mu}{\mu_u} \simeq F(\alpha\sqrt{T_e/T}) \quad \text{(A11)}$$

Combining with (A5), one obtains

$$\frac{\mu}{T} \simeq F(\alpha\sqrt{T_e/T}) \quad \text{(A12)}$$

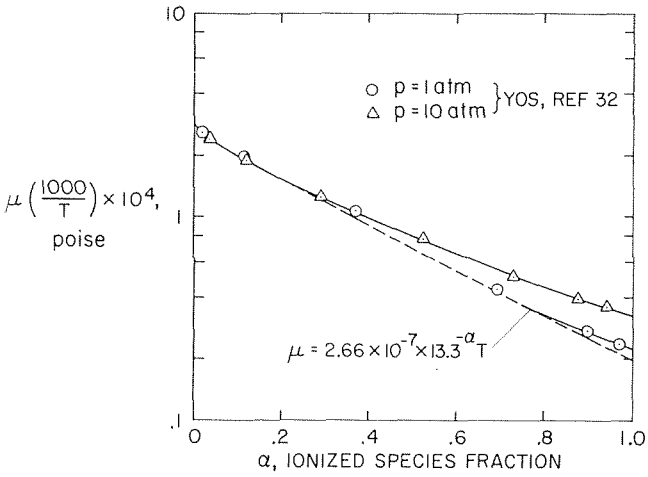

Fig. 11 Viscosity of equilibrium nitrogen

The functional relation (A12) for the special case where $T = T_e$ is shown in Fig. 11 for the experimental work of reference [33] as summarized by DeRienzo and Pallone [5]. As seen from Fig. 11, the viscosity can be approximated by

$$\mu \simeq 2.66 \times 10^{-7} \times 13.3^{-\alpha T}, \qquad \text{poise} \qquad (A12a)$$

when $T_e = T$ for $p \simeq 1$ atm. By generalizing to the nonequilibrium ($T_e \neq T$) case according to (A11), the viscosity of nonequilibrium nitrogen is obtained from

$$\mu = 13.3^{-\alpha\sqrt{T_e/T}}\mu_u \qquad (A13)$$

where μ_u is given by (A4). In view of the fact that (A12a) describes the viscosity of equilibrium nitrogen over a wide range of α as shown in Fig. 11, (A13) is assumed to hold even in a highly ionized regime.

The present concept of binary mixture of heavy-particle and electron gas is the basis also for deriving the energy equations (24) and (32). The partial thermal conductivities K_e and K_h of equations (24) and (32) are [34]

$$\frac{K_e}{K_L} = \left[1 + \sqrt{2}\,\frac{1-\alpha}{\alpha}\,\frac{K_L}{K_u}\,\frac{\sigma_{eh}}{\sigma_{hh}}\sqrt{\frac{m_e T}{m_h T_e}}\right]^{-1} \qquad (A14a)$$

$$\frac{K_h}{K_u} = \left(1 + \frac{\alpha}{1-\alpha}\,\frac{\sigma_{hi}}{\sigma_{hh}}\right)^{-1} \qquad (A14b)$$

Here σ_{eh} and σ_{hh} are collision cross sections between the species indicated, and σ_{hi} is the cross section for heavy-particle ion collision. K_L is the thermal conductivity as given by Spitzer [35]

$$K_L = \frac{1.84 \times 10^{-12} T_e^{2.5}}{\ln(\Lambda)}, \qquad \frac{\text{W}}{\text{cm-deg K}} \qquad (A15)$$

where

$$\Lambda = 1.24 \times 10^4 T_e^{1.5} n_e^{-0.5} \qquad (A15a)$$

A further simplification is introduced in (A14a) and (A14b) by assuming [32]

$$2\sigma_{eh} = \sigma_{hi} = \sigma_{hh}$$

which is valid within the degree of uncertainty [32] in these values involved. Then equations (A14a) and (A14b) can be written as

$$\frac{K_e}{K_u} = \frac{K_L}{K_u}\,\alpha\left[\alpha + 0.0044(1-\alpha)\,\frac{K_L}{K_u}\sqrt{\frac{\theta}{\theta_e}}\right]^{-1} \qquad (A16)$$

$$\frac{K_h}{K_u} = 1 - \alpha \qquad (A17)$$

A.3. Approximations for $\rho\mu$ and ρ_∞/ρ

It is known [24] that the solutions of the boundary-layer equations are only weakly dependent on $\rho\mu$ parameters. If these parameters are evaluated correctly at two extreme points of integration, i.e., $\eta = 0$ and $\eta = \eta_s$, the details of the shape in the variation of these parameters do not affect the solution appreciably [24]. Therefore, the following arbitrary approximations are made

$$\frac{\rho\mu}{\rho_s\mu_s} = \left\{\left(\frac{\rho_s\mu_s}{\rho_w\mu_w}\right)^4 + \left[1 - \left(\frac{\rho_s\mu_s}{\rho_w\mu_w}\right)^4\right]f'\right\}^{-1/4} \qquad (A18)$$

$$\frac{\rho\mu_u}{\rho_s\mu_{us}} = \left\{\left(\frac{\rho_s\mu_{us}}{\rho_w\mu_{uw}}\right)^4 + \left[1 - \left(\frac{\rho_s\mu_{us}}{\rho_w\mu_{uw}}\right)^4\right]f'\right\}^{-1/4} \qquad (A19)$$

The parameters $\rho_w\mu_w/(\rho_s\mu_s)$ and $\rho_w\mu_{uw}/(\rho_s\mu_{us})$ in (A18) and (A19) are evaluated from the wall and shock conditions through the use of (A4) and (A13).

The density ratio ρ_∞/ρ appearing in equation (7) is approximated by

$$\frac{\rho_\infty}{\rho} = \frac{\rho_\infty}{\rho_s}\left[\frac{\rho_s}{\rho_w} + \left(1 - \frac{\rho_s}{\rho_w}\right)f'\right] \qquad (A20)$$

Appendix B. Expressions for Diffusion Flux

The diffusion velocities V_j for the four species concerned are related by the following set of equations [20]:

$$\sum_{k=1}^{4} m_{jk} n_j \nu_{jk}(V_k - V_j) = \frac{\partial p_j}{\partial y} + n_j X_j \qquad (B1)$$

where m_{jk} is the equivalent mass

$$m_{jk} \equiv \frac{m_j m_k}{m_j + m_k} \qquad (B2)$$

In order to simplify the analysis, the cross sections are assumed to be related by

$$\frac{3}{2}\,\sigma_{ia} = \sigma_{im} \qquad (B3)$$

$$\sigma_{mi} = \sigma_{ma} \qquad (B4)$$

The Coulomb body forces, X_i for ions and X_e for electrons, are equal in magnitude but opposite in sign. With the use of (B3) and (B4), $n_j V_j$ are then determined from (B1) as follows:

$$n_m V_m = -\frac{n_a m_a}{\rho m_{ma}\nu_{ma}}\,\frac{\partial p_m}{\partial y} \qquad (B5)$$

$$n_a V_a = -\frac{n_a m_m}{\rho m_{ma}\nu_{ma}}\,\frac{\partial p_a}{\partial y} \qquad (B6)$$

$$n_j V_j = n_e V_e = -\frac{n_a m_m}{\rho m_{ma}\nu_{ma}}\,\frac{\partial}{\partial y}(p_i + p_e) \qquad (B7)$$

The diffusion coefficient D is related to ν_{ma} through (A6). Therefore, ν_{ma} in (B5)–(B7) can be eliminated so the resuting expression will contain the diffusion coefficient D instead. The diffusion flux of dissociated species (i.e., neutral atoms and atomic ions) and the diffusion flux of ionized species can now be written as

$$\rho\beta V_\beta \equiv m_a n_a V_a + m_i n_i V_i = \rho D\left(1 + \beta + 2\alpha\,\frac{\theta_e}{\theta}\right)\frac{1+\beta}{2}\,\frac{\partial}{\partial y}\left(\frac{p_m}{p}\right) \qquad (B8)$$

$$\rho\alpha V_\alpha \equiv m_i n_i V_i + m_e n_e V_e =$$

$$= -\rho D \left(1 + \beta + 2\alpha \frac{\theta_e}{\theta}\right) \frac{1+\beta}{2} \frac{\partial}{\partial y}\left(\frac{p_i + p_e}{p}\right) \quad \text{(B9)}$$

Appendix C. Ionizing Reactions

In equation (21), the rate of change of ion density by the ionizing reaction W_α is expressed intuitively as consisting of two components W_{α_1} and W_{α_2} representing the collisional rate and radiative rate, respectively. A careful examination reveals [36] that such a division is possible only if (i) the plasma is optically thin, and (ii) all the excited bound electronic states are populated according to a quasi-steady-state nonequilibrium distribution [26]. These two assumptions are made on the ground that (i) because of low pressure, all radiation, both line and continuum, is approximately optically thin except for the resonant lines which can be assumed to be fully absorbed and hence do not contribute to the collisional-radiative process, and (ii) the process behind the shock wave is slow compared with the time required to establish the quasi-steady-state bound-state distribution.

Under the assumption of quasi-steady-state excitation, the effective forward and reverse rates in a collisional process are related [37] by the equilibrium constant, i.e., the Saha function. Therefore, it is justifiable to write the collisional rate W_{α_1} as

$$W_{\alpha_1} = \gamma n_e^3 \left(\frac{n_a}{n_{ae}} - 1\right), \qquad \text{cm}^{-3}\,\text{sec}^{-1} \quad \text{(C1)}$$

where γ is the recombination rate coefficient and n_{ae} is the equilibrium-atom density defined by the local electron density and temperature through Saha equation

$$n_{ae} = \frac{n_e^2}{2} \frac{Z_a}{Z_i} \left(\frac{h^2}{2\pi m_e k T_e}\right)^{1.5} e^{\left(\frac{Ei}{kT_e}\right)} \quad \text{(C2)}$$

In the range of conditions concerned, $p \simeq 0.1$ atm and $3000 < T_e < 16{,}000$ deg K, the ratio Z_a/Z_i is a weak function of electron temperature. It is approximated by the constant 1.88 which is the value at $p = 0.1$ atm and $T_e = 12{,}000$ deg K. The rate coefficient γ is shown by Park [27, 37] to be approximately

$$\gamma = 1.15 \times 10^{-26} \left(\frac{T_e}{10{,}000}\right)^{-5.27}, \qquad \text{cm}^6\,\text{sec}^{-1} \quad \text{(C3)}$$

When (C2) and (C3) are substituted into (C1), and when the dimensionless quantities α, β, θ, and θ_e are introduced, the first term on the RHS of (22) becomes

$$\frac{R_s m_a W_{\alpha_1}}{2 v_\infty \rho} = 15.1 \frac{R_s}{v_\infty} \theta_e^{-5.27} \alpha \left[\frac{p\ (\text{atm})}{(1+\beta)\theta + 2\alpha\theta_e}\right]^2 \times \left\{(\beta - \alpha) \frac{(1+\beta)\theta + 2\alpha\theta_e}{p_s\ (\text{atm})} \times 0.727 \times 10^7 \theta_e^{1.5} e^{-1/\theta_e} - \alpha^2\right\} \quad \text{(C4)}$$

The radiative recombination rate for optically thin nitrogen is derived from references [38] and [39] and approximated by

$$W_{\alpha_2} = \frac{5.69 \times 10^{-11}}{\sqrt{T_e}} n_e^2, \qquad \text{cm}^6\,\text{sec}^{-1} \quad \text{(C5)}$$

In terms of the dimensionless quantities, the second term on the RHS of (22) can be written therefore as

$$\frac{R_s m_a W_{\alpha_2}}{2 v_\infty \rho} = -\frac{6.07 \times 10^3\ p_s\ (\text{atm})\ \alpha^2 R_s}{\sqrt{\theta_e}\, v_\infty [(1+\beta)\theta + 2\alpha\theta_e]} \quad \text{(C6)}$$

The sum of the two terms (C4) and (C6) is much smaller than the diffusion term in equation (22) for the weakly ionized regime but is of the same order or greater for the highly ionized region.

Appendix D. Energy Transfer Between Electron and Heavy Particle (Thermalization)

In the RHS of equation (24), the second term represents the rate of energy transfer from heavy particles to electrons. Its summation extends over all three heavy species, i.e., molecule, atom, and ion. The collision frequency between electron and atom ν_{ea} is calculated from the work of Yos [32] as in reference [40]. The electron-ion collision frequency, ν_{ei}, is calculated by Spitzer's formula [35]. The electron-molecule collision frequency is deduced from references [41] and [42]. These references show that the effective electron-molecule collision frequency is one order greater than that for electron-atom collisions. Consequently σ_{em} is assumed to be equal to $10\sigma_{ea}$. The first term on the RHS of (25) can be written as

$$\frac{3}{5} \frac{R_s}{v_\infty} \alpha(\theta - \theta_e) \sum_{j=1}^{3} \frac{m_e}{m_j} \nu_{ej} = 0.435 \times 10^5\, p_s\,(\text{atm})\, \alpha \frac{\theta - \theta_e}{\theta} \times \frac{R_s}{v_\infty} \times \left\{1.27 \sqrt{\theta_e}\,(2.5 - \alpha - 1.5\beta) + 0.362 \frac{\ln \Lambda}{\theta_e^{1.5}}\right\} \quad \text{(D1)}$$

in which Λ is defined in equation (A15a).

Appendix E. Computational Procedures

The solutions to the set of differential equations (7), (13), (22), (25), and (33) satisfying the boundary conditions (8), (9), (17), (18), (23), (26), (34), (35), (37), and (38) are obtained numerically through four steps. From the initially assumed value of free-stream enthalpy, v_∞ is determined by (3). The Rankine-Hugoniot relationship gives the heavy-particle temperature behind the shock corresponding to the assumed free-stream condition. From the heavy-particle temperature and the enthalpy the transport properties behind the shock wave are calculated. From these, the values of f_s is determined by (10a).

As the first step, the momentum equation (7) is integrated. A Newton-Raphson iteration technique is applied and the integration is repeated until (9) is satisfied. The value of η where (9) is satisfied is then defined as η_s.

In the second step, the first approximation to the dissociation equation (13) is obtained by neglecting the RHS of (13).

In the third step the solutions for α, θ_e, and θ are found by integrating (22), (25), and (33) along with (7) and (13). The values of α_w, θ_{ew}, and θ_w' are first estimated, from which α_w' and θ_{ew}' are determined through (37) and (38). With these wall values, the numerical integration is started. At $\eta = \eta_s$, the enthalpy of the gas is calculated from the local values of α_s, β_s, θ_{e_s}, and θ_s, using equation (30). α_E is calculated from the enthalpy and pressure, which is then compared with the computed local value of α_s. If α_s and α_E do not satisfy condition (23), or if θ_{e_s} does not satisfy (26), the iteration continues. When both (23) and (26) are satisfied, the values of μ_s and μ_{us} used in the computation are compared with the more realistic values based on the newly computed values of α_s, θ_{es}, and θ_s. If they are different by more than 5 percent, a new set of values of μ_s and μ_{us} are computed from the values of α_s, θ_{es}, θ_s, and calculation continues.

In the fourth step, the more exact solution of the dissociation equation (13) is obtained by including the RHS of (13). The RHS of (13) is calculated from the solutions obtained from the previous three steps. When the solution is found from the above four steps, v_∞ is recalculated from the final enthalpy value and the heat-transfer rate is calculated from equation (41).

The numerical integration of the differential equations in steps 1–3 is accomplished by the use of an implicit scheme [14]. The implicit method was necessary because of the "stiffness" [14] of the ionization equation (22). The stiffness of the equation precludes [15] the solution of the problem by conventional methods such as that by Fay and Kaye [16]. The strong nonlinearity of the ionization equation (22) presents another formidable difficulty.

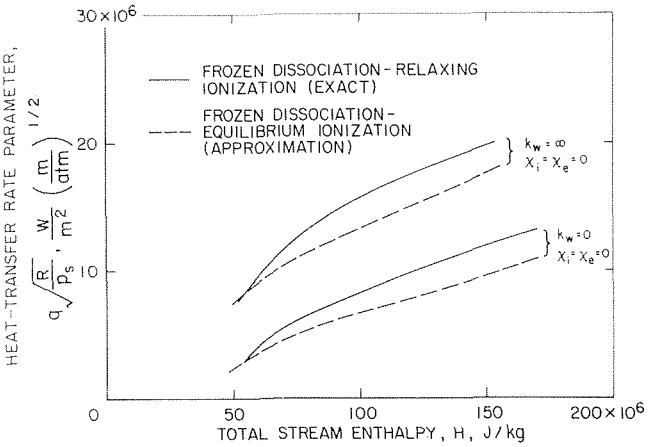

Fig. 12 Comparison of exact and approximate methods for 0.1 atm

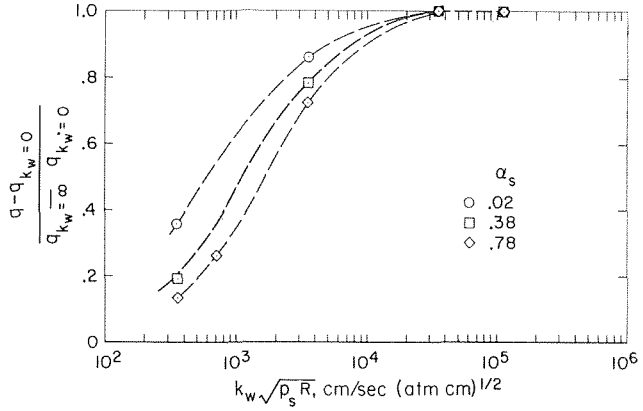

Fig. 13 Effect of catalycity, body size, and pressure on recombination heat-transfer rate

In the present computation, the degree of nonlinearity is approximately equal to $1/\theta_e$ and has values between 10 and 100. Unless the selected wall values are within close proximity to the correct values, the integration would not reach $\eta = \eta_s$ before the dependent variables diverged to $\pm\infty$. That is, the "corridor" of the solution is very narrow. Because of the narrow corridor, it was extremely difficult to provide an iteration scheme (e.g., for an IBM 360) that would improve the necessary wall values systematically. Therefore, the solutions were obtained by a conversational time-sharing computing system. The advantage of a conversational computing system is that the iteration procedure need not be programmed because the operator can select a new, more realistic set of wall conditions judiciously by inspecting the old results.

Appendix F. Effect of Varying Surface Atomic Recombination Rate Coefficient, k_w

The effect of varying k_w on heat-transfer rate is calculated approximately assuming the ionization to be in equilibrium, $T = T_e$, and dissociation to be frozen. The solution of such an equilibrium-ionization, frozen-dissociation model can be easily machine-computed by the Runge-Kutta integration method and thereby eliminate the need to solve the stiff rate equation. With this simplified model, values of q_w were computed for various stagnation pressures and nose radii.

Fig. 12 compares the result of the equilibrium-ionization, frozen-dissociation calculations with that of the exact solution described in the main text for $k_w = 0$ and $k_w = \infty$. The simple model yields correct heat-transfer values in the weakly ionized regime, but somewhat lower values in the highly ionized regime. The difference between the two extremes, $q(k_w = \infty) - q(k_w = 0)$, given by the simple model agrees approximately with the exact calculations. Therefore, despite the fact that the ionization thermochemical nonequilibrium effects are ignored, the simple model can be used to calculate the contribution of surface atomic recombination approximately.

The results of the simplified computation are shown in Fig. 13. The contribution of surface atomic recombination to the total heat-transfer rate is determined mainly by the parameter $k_w\sqrt{p_s R}$ as for un-ionized, dissociated gas, so that

$$\frac{q - q(k_w = 0)}{q(k_w = \infty) - q(k_w = 0)} \simeq F(k_w\sqrt{p_s R})$$

References

1 Shepard, C. E., Watson, V. R., and Stine, H. A., "Evaluation of a Constricted Arc Supersonic Jet," NASA TN D-2066, 1964.

2 Shepard, C. E., Ketner, D. M., and Vorreiter, J. W., "A High Enthalpy Plasma Generator for Entry Heating Simulation," NASA TN D-4583, 1968.

3 Pope, R. B., "Stagnation-Point Convective Heat Transfer in Frozen Boundary Layers," *Journal of the American Institute of Aeronautics and Astronautics*, Vol. 6, 1968, pp. 619–626.

4 Fay, J. A., and Kemp, N. H., "Theory of Stagnation-Point Heat Transfer in a Partially Ionized Diatomic Gas," *Journal of the American Institute of Aeronautics and Astronautics*, Vol. 1, 1963, pp. 2741–2751.

5 DeRienzo, P., and Pallone, A. J., "Convective Stagnation-Point Heating for Re-entry Speeds up to 70,000 fps Including Effects of Large Blowing Rates," *Journal of the American Institute of Aeronautics and Astronautics*, Vol. 5, 1967, pp. 193–200.

6 Rose, P. H., and Stankevics, J. O., "Stagnation-Point Heat-Transfer Measurements in Partially Ionized Air," *Journal of the American Institute of Aeronautics and Astronautics*, Vol. 1, 1963, pp. 2752–2763.

7 Chung, P. M., "Weakly Ionized Nonequilibrium Viscous Shock Layer and Electrostatic Probe Characteristics," *Journal of the American Institute of Aeronautics and Astronautics*, Vol. 3, 1965, pp. 817–825.

8 Sherman, A., and Reshotko, E., "The Nonequilibrium Boundary Layer Along an Insulator Wall," *Journal of the American Institute of Aeronautics and Astronautics*, Vol. 7, 1969, pp. 610–615.

9 Knight, D. D., "Electron Thermochemical Nonequilibrium Effects in Re-entry Boundary Layers," AIAA Paper No. 69-82, 1969.

10 Chung, P. M., "Hypersonic Viscous Shock Layer of Nonequilibrium Dissociating Gas," NASA TR R-109, 1961.

11 Howe, J. T., and Viegas, J. R., "Solutions of the Ionized Radiating Shock Layer, Including Reabsorption and Foreign Species Effects and Stagnation Region Heat Transfer," NASA TR R-159, 1963.

12 Cheng, H. K., "The Blunt-Body Problem in Hypersonic Flow at Low Reynolds Number," IAS Paper No. 63-92, 1963.

13 Park, C., "Dissociative Relaxation in Viscous Hypersonic Shock Layers," *Journal of the American Association of Aeronautics and Astronautics*, Vol. 2, 1964, pp. 1202–1207.

14 Lomax, H., "Stable Implicit and Explicit Numerical Methods for Integrating Quasi-Linear Differential Equations with Parasitic-Stiff and Parasitic-Saddle Eigenvalues," NASA TN D-4703, July 1968.

15 Kaye, H., "Numerical Solution of Near-Equilibrium Boundary Layers," *Journal of the American Association of Aeronautics and Astronautics*, Vol. 7, No. 1, 1969, pp. 172–173.

16 Fay, J. A., and Kaye, H., "A Finite-Difference Solution of Similar Nonequilibrium Boundary Layers," *Journal of the American Association of Aeronautics and Astronautics*, Vol. 5, 1967, pp. 1949–1954.

17 Stine, H. A., and Watson, V. R., "The Theoretical Enthalpy Distribution of Air in Steady Flow Along the Axis of a Direct-Current Arc," NASA TN D-1331, 1962.

18 Watson, V. R., and Pegot, E. B., "Numerical Calculations for the Characteristics of a Gas Flowing Axially Through a Constricted Arc," NASA TN-4042, 1967.

19 Park, C., "Relaxation of Electronic State Populations in Expanding Flows of Ionized Nitrogen," AIAA Paper 68-734, 1968.

20 Hirschfelder, J. O., Curtis, C. F., and Bird, R. B., *Molecular Theory of Gases and Liquids*, Wiley New York, ch. 8, 1954.

21 Goulard, R., "On Catalytic Recombination Rates in Hypersonic Stagnation Heat Transfer," *Jet Propulsion*, Vol. 28, 1958, pp. 737–745.

22 Appleton, J. P., and Bray, K. N. C., "The Conservation Equation for a Nonequilibrium Plasma," *Journal of Fluid Mechanics*," Vol. 20, Pt. 4, 1964, pp. 659–672.

23 Kruger, C. H., and Mitchner, M., "Kinetic Theory of Two-Temperature Plasmas," *Physics of Fluids*, Vol. 10, No. 9, 1967, pp. 1953–1961.

24 Fay, J. A., and Riddell, F. R., "Theory of Stagnation Point Heat Transfer in Dissociated Air," *Journal of Aerospace Science*, Vol. 25, 1958, pp. 73–85.

25 Griem, H. R., *Plasma Spectroscopy*, McGraw-Hill, New York, 1964.

26 Park, C., "Spectral Line Intensities of Nonequilibrium Nitrogen Plasma," *Journal of Quantitative Spectroscopy and Radiative Transfer*, Vol. 8, No. 10, 1968, pp. 1633–1654.

27 Park, C., and Okuno, A. F., "Diagnosis of High-Density Highly Ionized Nitrogen Wind Tunnel Flows," *Proceedings of Second International Congress on Instrumentation in Aerospace Simulation Facilities*, Stanford University, August 1966.

28 Park, C., "Measurement of Ionic Recombination Rate of Nitrogen," *Journal of the American Institute of Aeronautics and Astronautics*, Vol. 6, 1968, pp. 2090–2094.

29 Wiese, W. L., Smith, M. W., and Glennon, B. M., *Atomic Transition Probabilities*, Vol. 1, Hydrogen Through Neon, NSRDS-NBS 4, National Bureau of Standards, May 1966.

30 Hiester, N. K., and Clark, C. F., "Feasibility of Standard Evaluation Procedures for Ablating Materials," NASA CR-379, 1966.

31 Hansen, C. F., "Approximations for the Thermodynamic and Transport Properties of High-Temperature Air," NASA TR R-50, 1959.

32 Yos, J. M., "Transport Properties of Nitrogen, Hydrogen, Oxygen and Air to 30,000 deg K," AVCO/RAD-TM-63-7, March 1963.

33 Bennett, A., Yos, J. M., Knopp, C. F., Morris, J., and Bade, W. L., "Theoretical and Experimental Studies of High-Temperature Gas Transport Properties," final report, AVCO/RAD-TR-65-7, May 1965; also AVCO/RAD-SR-65-35, Feb. 1965.

34 Camac, M., and Kemp, N. H., "A Multitemperature Boundary Layer," AVCO Everett Research Lab., RR-184, 1964.

35 Spitzer, L., Jr., *Physics of Fully Ionized Gases*, Interscience Publishers, New York, ch. 5, 1956.

36 Bates, D. R., Kingston, A. E., and McWhirter, R. W. P., "Recombination Between Electrons and Atomic Ions. I. Optically Thin Gas," *Proceedings of the Royal Society*, Series A., Vol. 267, 1962, pp. 297–312.

37 Park, C., "Collisional Ionization and Recombination Rates of Atomic Nitrogen," *Journal of the American Institute of Aeronautics and Astronautics*, Vol. 7, 1969, p. 1653.

38 Bates, D. R., and Dalgarno, A., "Electronic Recombination," *Atomic and Molecular Processes*, Academic Press, New York and London, 1962, pp. 245–271.

39 Hahne, G. E., "The Vacuum Ultraviolet Radiation from N^+ and O^+ Electron Recombination in High Temperature Air," NASA TN D-2794, 1965.

40 Bently, S. B., "Shock Ionization Kinetics of Pure Nitrogen," *Physics of Fluids*, Vol. 12, 1969, p. 1939.

41 Engelhardt, A. G., Phelps, A. V., and Risk, C. G., "Determination of Momentum Transfer and Inelastic Collision Cross Sections for Electrons in Nitrogen Using Transport Coefficients," *Physics Review*, Vol. 135, No. 6, 1964, pp. A 1566–1574.

42 Demetriades, S. T., "Determination of Electron Energy-Loss Factors in Hot Gases," Progress Report No. 31 on Contract NAS 2-3580, Technical Report STD 004-65-31, Jan. 1969.

W. R. WOLFRAM, JR.
NASA Trainee.

W. F. WALKER
Associate Professor of Aerospace Engineering.

Department of Mechanical and Aerospace Engineering, Rice University, Houston, Texas

The Effects of Upstream Mass Injection on Downstream Heat Transfer

The present study was performed in order to determine the effects of upstream mass injection on downstream heat transfer in a reacting laminar boundary layer. The study differs from numerous previous investigations in that no similarity assumptions have been made. The complete set of coupled reacting laminar boundary layer equations with discontinuous mass injection was solved for this problem using an integral-matrix technique. The effects of mass injection on heat transfer to both sharp and blunt-nosed isothermal flat plates were studied for a Mach 2 freestream. The amount of injection and the length of the injected region were varied for each body. Heat transfer rates were found to decrease markedly in the injected region. A sharp rise in heat transfer was found immediately downstream of the region of injection followed by an asymptotic approach to the heat transfer rates calculated for the case of no injection. An insulating effect was found to persist for a considerable distance downstream from the injection region. The distance required for this insulating effect to die out was found to depend on the length of the injection region as well as the rate of injection.

Introduction

THE present investigation was undertaken in order to determine the effects of upstream mass injection on the downstream heat transfer in a supersonic laminar boundary layer. High velocity lifting entry vehicles require considerable ablation or mass injection cooling in the stagnation region in order to overcome the large heat transfer rates produced by the severe thermal environment during entry. This injected mass remains in the boundary layer as the flow accelerates around the body. However, additional mass injection or even thermal sampling may be taking place on the afterbody of the vehicle. Therefore, it is desirable to determine to what extent the insulating properties of the upstream injection persist downstream in the boundary layer flow.

The laminar boundary layer with mass injection has been the subject of numerous investigations in the past. Most of these studies have treated flow in the region of injection and flow over an impermeable surface downstream from the injection region as two separate problems. The solutions obtained required matching solutions at the interface between the injection region and the impermeable region.

Solutions for the injected region have usually been of the similarity type. Such a solution was obtained by Low [1],[1] who performed a classical similarity analysis for the compressible

Contributed by the Heat Transfer Division for publication (without presentation) in the JOURNAL OF HEAT TRANSFER. Manuscript received by the Heat Transfer Division, July 17, 1969; revised manuscript received March 25, 1970. Paper No. 70-HT-L.

[1] Numbers in brackets designate References at end of paper.

Nomenclature

c = product of density and viscosity normalized by their freestream values
C_p = heat capacity
d_0, d_1, d_2 = finite difference coefficients defined in reference [7]
D_{12} = binary diffusion coefficient
f = stream function
G = dummy variable
g = the velocity ratio specified at a control node
h = static enthalpy
H_t = total enthalpy defined by $H_t = h + u^2/2$
k = thermal conductivity
K_i = mass fraction of the ith species
$\dot{m}_w$ = $\rho_w v_w$ = mass rate of injection
N = number of nodal points across the boundary layer
N_{pr} = Prandtl number = $C_p\mu/k$
N_{sc} = Schmidt number = $\mu/\rho D_{12}$
p = static pressure
$\dot{q}_{nb}$ = local heat transfer rate for the zero injection case (Btu/sec-ft^2)
$\dot{q}_{st}$ = stagnation point heat transfer rate
$\dot{q}_w$ = local wall heat transfer rate
r_c = local radius of curvature of the surface
s = streamwise distance measured along the body

(*Continued on next page*)

laminar boundary layer with continuous fluid injection. This solution has often been cited as the "exact" solution and has usually formed the starting point for studies of flow downstream from an injection region. However, similarity requires the rather restrictive assumption that the rate of coolant injection, $\dot{m}_w$, be proportional to some power of the distance from the leading edge. Otherwise, boundary conditions cannot be transformed properly. In the case of reference [1], the power was $(-1/2)$. This assumption is obviously questionable in many physically realistic cases.

The downstream region has been studied mainly by use of the Karman-Pohlhausen integral approach. Rubesin and Inouye [2] used this method with a seventh-degree polynomial approximation to the velocity and temperature profiles. They matched their profiles to Low's solution at the interface by assuming the shear stress and boundary layer thickness to be continuous at the junction. Libby and Pallone [3] used sixth-degree polynomials but introduced additional parameters to insure continuity of mass, momentum, and energy at the interface. The profiles were allowed to change discontinuously at the interface but the parameters were not made functions of distance. The solution is, therefore, valid only for a short distance downstream from the injection region.

Howe [4] used a finite difference scheme in the downstream region but again matched to Low's solution at the junction. In comparing results with those of Rubesin and Inouye as well as Libby and Pallone, significant differences were found among the solutions. All three of the above investigations studied the rise in wall temperature along an insulated plate. Howe's results fell in between the optimistic results of Libby and Pallone and the more conservative findings of Rubesin and Inouye.

Libby [5] took a somewhat different approach by treating the effect of mass transfer as a perturbation of the Blasius solution. The resulting eigenvalue problem yields closed form solutions once the eigenvalues and eigenfunctions have been obtained. Several calculations using this method have been compared with the results of the current study and will be discussed later.

Pallone [6] has also studied wall temperature rise along an insulated plate, using Low's similarity solution in the porous region. The analysis is significant in that it more nearly follows the method of integral relations used in the present investigation. Instead of integrating across the whole boundary layer, as is done in the Karman-Pohlhausen approach, the boundary layer was divided into N separate strips. Integration of the governing equations was then performed across each strip, using a polynomial to represent the integrand over each individual strip. This resulted in far greater accuracy than is possible with the more gross momentum-integral approach. The resulting ordinary differential equations were integrated numerically and the results compared well with Howe's finite difference results.

The present investigation differs from the previous studies in several respects. First of all, many of the restrictive assumptions of previous investigations have been relaxed. No similarity has been assumed for the region of injection, thus allowing specification of arbitrary distributions of mass injection. For the cases considered, mass injection was taken to be constant over the first portion of a planar body, followed by a region of no injection. The complete nonsimilar, compressible laminar boundary layer equations have been solved for both the injection and impermeable downstream regions by use of the integral-matrix technique [7]. This method is a recent outgrowth of the method of integral relations [8]. The effects of mass injection on heat transfer to an isothermal plate were studied. Both sharp and blunt-nosed configurations were considered and the results compared.

Analysis

The equations that govern the physical system under consideration are the two-dimensional, steady-state, reacting, laminar boundary layer equations as follows:

Continuity

$$\frac{\partial}{\partial s}(\rho u) + \frac{\partial}{\partial y}(\rho v) = 0 \tag{1}$$

Streamwise Momentum

$$\rho u \frac{\partial u}{\partial s} + \rho v \frac{\partial u}{\partial y} + \frac{\partial p}{\partial s} = \frac{\partial}{\partial y}\left(\mu \frac{\partial u}{\partial y}\right) \tag{2}$$

Normal Momentum

$$\left(\frac{\partial p}{\partial y}\right)_s = \frac{\rho u^2}{r_c} \tag{3}$$

Species Conservation

$$\rho u \frac{\partial K_i}{\partial s} + \rho v \frac{\partial K_i}{\partial y} = \frac{\partial}{\partial y}\left(\rho D_{12} \frac{\partial K_i}{\partial y}\right) \tag{4}$$

Energy

$$\rho u \frac{\partial H_t}{\partial s} + \rho v \frac{\partial H_t}{\partial y} = \frac{\partial}{\partial y}\left(\mu \frac{\partial (u^2/2)}{\partial y} + k \frac{\partial T}{\partial y}\right) + \frac{\partial}{\partial y}\left(\rho D_{12}(h_1 - h_2) \frac{\partial K_1}{\partial y}\right) \tag{5}$$

where K_i is the mass fraction of the ith species, D_{12} is the binary diffusion coefficient, μ is the mixture viscosity, k is the thermal conductivity, and H_t is the total enthalpy.

Thermal diffusion has been neglected and no internal generation of species has been assumed. The radius of curvature, r_c, is assumed to be large compared with the boundary layer thickness. Therefore the pressure gradient term appearing in equation (3) is approximately equal to zero. It may then be concluded that there is no normal pressure gradient, and the pressure becomes a function of streamwise distance only. In all cases of interest in the present study the system was assumed to be air, a mixture of 78.8 percent N_2 and 21.2 percent O_2 by volume. The species

Nomenclature

s_L = distance from leading edge (feet)
T = static temperature
u = velocity component in the streamwise direction
v = velocity component normal to the surface
X_1, X_2, X_3, X_4 = coefficients involving truncated Taylor series defined in reference [7]
y = distance measured normal to the body
Z_1, Z_2, Z_3, Z_4 = coefficients involving truncated Taylor series defined in reference [7]
α_H = normalizing parameter
β = pressure gradient parameter defined by equation (13)
η = transformed coordinate normal to the surface
μ = viscosity
ρ = density
θ = local surface angle of leading edge
ξ = transformed streamwise coordinate

Superscripts

$'$ = 'denotes partial differentiation with respect to η

Subscripts

∞ = boundary layer edge
i = ith chemical species
g = subsurface gas
l = lth streamwise station
n = nth nodal point from the surface
w = wall

equation has been included for completeness. However, for the temperatures of interest here, there is no significant dissociation and the effects of diffusion are small.

The boundary conditions for the governing equations are as follows:

(i) $u_w = 0$
(ii) $\dot{m}_w = \rho_w v_w$, a given function of s
(iii) T_w = a given function of s
(iv) $u_\infty' = T_\infty' = K_{i\infty}' = 0$
(v) Edge conditions are specified functions of s, i.e.: $u_\infty(s)$, $P_\infty(s)$, $T_\infty(s)$, $K_{i\infty}(s)$
(vi) The boundary condition on the diffusion equation is determined from a mass balance at the wall, i.e.:

$$\dot{m}_w(K_{iw} - K_{ig}) + \left(\rho D_{12} \frac{\partial K_i}{\partial y}\right)_w = 0$$

where subscript "w" denotes the wall (i.e., $y = 0$) and subscript "g" denotes the injected (or generated) subsurface gas. In boundary condition (vi) the quantity K_{ig} is the mass fraction of the subsurface gas and is specified. The transport properties are treated by the method of reference [9] with slight modifications reported in reference [7].

Transformations. A modified Levy-Lees similarity transformation is used with nonsimilar terms being retained in the equations. The transformed variables, η and ξ, are given by [7]:

$$\eta = \frac{u_\infty(\xi)}{\alpha_H(\xi)(2\xi)^{1/2}} \int_0^y \rho(y)dy$$
$$\xi = \int_0^s u_\infty(s)\rho_\infty(s)\mu_\infty(s)ds \tag{6}$$

The quantity $\alpha_H(\xi)$ is a stretching parameter the value of which is determined during numerical integration. It is used to keep the boundary layer thickness relatively uniform in the transformed plane. The use of this parameter is a numerical convenience in that a uniform placement of nodal points across the boundary layer may be set a priori for all problems. The quantity $\alpha_H(\xi)$ is determined by specifying the velocity ratio at a certain nodal point, η_c, in the boundary layer.

$$f'|_{\eta_c} = gf'|_{\eta_\infty} \tag{7}$$

where $f' = \alpha_H u/u_\infty$

A good choice has been $g = 0.80$ at the 5th of seven nodes.

A stream function is also defined and is given by:

$$f - f_w = \alpha_H \int_0^\eta \frac{u}{u_\infty}\, d\eta \tag{8}$$

Applying these transformations to equations (2), (4), and (5) yields the transformed equations:

Momentum

$$ff'' + \left[\frac{cf''}{\alpha_H}\right]' + \beta\left(\alpha_H{}^2 \frac{\rho_\infty}{\rho} - f'^2\right) = 2\left(f' \frac{\partial f'}{\partial \ln \xi} - f'' \frac{\partial f}{\partial \ln \xi} - f'^2 \frac{d \ln \alpha_H}{d \ln \xi}\right) \tag{9}$$

Species

$$fK_i' + \left[\frac{c}{\alpha_H N_{sc}} K_i'\right]' = 2\xi\left[f' \frac{\partial K_i}{\partial \xi} - K_i' \frac{\partial f}{\partial \xi}\right] \tag{10}$$

Energy

$$fH_t' + \left\{\frac{c}{\alpha_H}\left[\frac{f'f''}{\alpha_H{}^2} u_\infty{}^2 + \frac{C_p}{N_{pr}} T' + \frac{h'}{N_{sc}} - \frac{C_p T'}{N_{sc}}\right]\right\}' = 2\xi\left[f' \frac{\partial H_t}{\partial \xi} - H_t' \frac{\partial f}{\partial \xi}\right] \tag{11}$$

where $'$ denotes $\dfrac{\partial}{\partial \eta}$

$$c = \rho\mu/\rho_\infty\mu_\infty \tag{12}$$

and

$$\beta = 2 \frac{d(\ln u_\infty)}{d(\ln \xi)} \tag{13}$$

The quantity β therefore is a pressure gradient parameter. The boundary conditions are likewise transformed to give:

$$f_w = -(2\xi)^{-1/2} \int_0^\xi \frac{\rho_w v_w d\xi}{\rho_\infty u_\infty \mu_\infty} \tag{14}$$

$$f_w' = 0; \quad f_\infty' = \alpha_H; \quad f_\infty'' = 0; \quad H_{t\infty}' = K_{i\infty}' = 0$$

$$\frac{\dot{m}_w(2\xi)^{1/2}}{\rho_\infty u_\infty \mu_\infty}(K_{iw} - K_{ig}) - \frac{c}{\alpha_H N_{sc}} K_{iw}' = 0$$

The quantities H_{tw}, $H_{t\infty}$, and $K_{i\infty}$, are specified functions of ξ.

Integral Matrix Procedure. The method of integral matrix analysis is discussed in detail in reference [7]. Only the essentials of the method are presented here. First the transformed equations are put into integral matrix form. The details of this procedure are presented only for the momentum equation. The handling of the species concentration and energy equations is completely analogous and is therefore omitted. The transformed momentum equation is:

$$ff'' + \left[\frac{cf''}{\alpha_H}\right]' + \beta\left(\alpha_H{}^2 \frac{\rho_\infty}{\rho} - f'^2\right) = 2f'\left(\frac{\partial f'}{\partial \ln \xi} - f'' \frac{\partial f}{\partial \ln \xi} - f'^2 \frac{d \ln \alpha_H}{d \ln \xi}\right) \tag{18}$$

The boundary layer is divided into N-1 strips at each streamwise station, s. These strips are bounded by N nodal points. In the final numerical solution $N = 7$ has been used. The points are designated η_n where $n = 1$ at the wall and $n = N$ on the boundary layer edge.

Let G_n represent any of the quantities $f(\eta_n)$, $f'(\eta_n)$, $f''(\eta_n)$, or $f'''(\eta_n)$. Then G_{n+1} can be related to G_n by means of a Taylor series expansion about η_n:

$$G_{n+1} = G_n + G_n'\delta\eta + G_n'' \frac{(\delta\eta)^2}{2!} + G_n''' \frac{(\delta\eta)^3}{3!} + G_n'''' \frac{(\delta\eta)^4}{4!} + \ldots \tag{19}$$

where $\delta\eta = \eta_{n+1} - \eta_n$

The highest order derivative of the dependent variable f which appears in the boundary layer equations is f'''. Therefore, the series is truncated at the next highest derivative, f''''. The quantity f'''' is considered to be constant between η_n and η_{n+1}.

$$f'''' = \frac{f_{n+1}''' - f_n'''}{\delta\eta} \tag{20}$$

Thus truncated Taylor series expansions for f_n, f_n', f_n'', can be obtained as an implicit set of relations giving f_{n+1}, f_{n+1}', f_{n+1}'', and f_{n+1}''' as functions of η. This is known as a "spline fit" and serves the same purpose as finite difference relations in usual numerical analyses. However, in this case the functions join in a continuous manner at the nodal points, thus requiring fewer nodes for the same relative accuracy. The variables H_t and K_i are treated in the same manner.

Derivatives in the streamwise direction are represented by conventional three-point backward difference relations.

The momentum equation can be integrated at constant ξ across each strip to obtain equations of the form:

$$\int_{n-1}^{n} ff''d\eta + \left[\frac{cf''}{\alpha_H}\right]_{n-1}^{n} + \beta{\alpha_H}^2 \int_{n-1}^{n} \frac{\rho_\infty}{\rho}\, d\eta - \beta \int_{n-1}^{n} f'^2 d\eta = \int_{n-1}^{n} 2\left(f' \frac{\partial f'}{\partial \ln \xi} - f'' \frac{\partial f}{\partial \ln \xi}\right) d\eta - 2\int_{n-1}^{n} f'^2 \frac{d \ln \alpha_H}{d \ln \xi}\, d\eta \quad (21)$$

The integrals are then integrated by parts and the remaining integrals expanded in Taylor series. For example:

$$\int_{n-1}^{n} f'G d\eta = f_n'G\delta\eta - (f_n'G' + f_n''G)\frac{(\delta\eta)^2}{2!} + (f_n'G'' + 2f_n''G' + f_n'''G)\frac{(\delta\eta)^3}{3!} - (f_n'G''' + 3f_n''G'' + 3f_n'''G' + f_n''''G)\frac{(\delta\eta)^4}{4!} + (4f_n''G''' + 6f_n'''G'' + 4f_n''''G')\frac{(\delta\eta)^5}{5!} - (10f_n'''G''' + 10f_n''''G'')\frac{(\delta\eta)^6}{6!} + 20f_n''''G'''\frac{(\delta\eta)^7}{7!} \quad (22)$$

where G may be any dependent variable. The same truncation criterion has been applied as in previous Taylor series expansions. An analogous procedure can be applied to the integrals of the streamwise derivatives by incorporating the finite difference approximation.

It remains to evaluate $\int_{n-1}^{n} \frac{\rho_\infty}{\rho}\, d\eta$. This is done by approximating ρ_∞/ρ as a cubic between $n-1$ and n. The four coefficients are evaluated by matching the cubic approximation to the value of ρ_∞/ρ and $(\rho_\infty/\rho)'$ at adjacent nodal points. The function can then be integrated exactly across the strip to give:

$$\int_{n-1}^{n} \frac{\rho_\infty}{\rho}\, d\eta = \left(\frac{\rho_\infty}{\rho} + \frac{\rho_\infty}{\rho_{n-1}}\right)\frac{\delta\eta}{2} + \left(\frac{\rho_\infty {\rho_n}'}{{\rho_n}^2} - \frac{\rho_\infty {\rho_{n-1}}'}{{\rho_{n-1}}^2}\right)\frac{(\delta\eta)^2}{12} \quad (23)$$

This approximation will not be quite as accurate as the preceding ones since the derivatives are not necessarily continuous at each node.

Substituting all these relations into the momentum equation yields:

$$\left[\frac{cf''}{\alpha_H} + f'((1+d_0)f + d_1 f_{l-1} + d_2 f_{l-2})\right]_{n-1}^{n} + \beta{\alpha_H}^2\left[\left(\frac{\rho_\infty}{\rho_n} + \frac{\rho_\infty}{\rho_{n-1}}\right)\frac{\delta\eta}{2} + \left(\frac{\rho_\infty {\rho_n}'}{{\rho_n}^2} - \frac{\rho_\infty {\rho_{n-1}}'}{{\rho_{n-1}}^2}\right)\frac{(\delta\eta)^2}{12}\right] - \left(1 + \beta + d_0 - \frac{d_1\alpha_{H_{l-1}} + d_2\alpha_{H_{l-2}}}{\alpha_H}\right) \times [f_n'X_1 + f_n''X_2 + f_n'''X_3 + f_{n-1}'''X_4] - 2[f_n'Z_1 + f_n''Z_2 + f_n'''Z_3 + f_{n-1}'''Z_4] = 0 \quad (24)$$

The X's and Z's are defined in reference [7] and are convenient groupings of the coefficients in the Taylor series expansions.

Matrix Solutions Procedure. A procedure analogous to that above is applied to the species conservation and energy equations. The resulting matrix of equations for a binary mixture contains $3(N-1)$ conservation equations over the $N-1$ intervals, $7(N-1)$ Taylor series expansions, 10 boundary conditions, and the α_H constraint. These contain $10N+1$ variables, i.e., the primary variables f, H_t, and K_i and their derivatives at each nodal point, and α_H. These equations are solved through use of a generalized Newton-Raphson iteration procedure. The linearized momentum equation becomes:

$$\left[\frac{cf''}{\alpha_H}\left(\frac{\Delta f''}{f''} + \frac{\Delta c}{c} - \frac{\Delta\alpha_H}{\alpha_H}\right) + ((1+d_0)f + d_1 f_{l-1} + d_2 f_{l-2})\Delta f' + f'(1+d_0)\Delta f\right]_{n-1}^{n} + \beta\alpha_H\left[\left(\frac{\rho_\infty}{\rho_n} + \frac{\rho_\infty}{\rho_{n-1}}\right)\delta\eta + \left(\frac{\rho_\infty {\rho_n}'}{{\rho_n}^2} - \frac{\rho_\infty {\rho_{n-1}}'}{{\rho_{n-1}}^2}\right)\frac{(\delta\eta)^2}{6}\right]\Delta\alpha_H - \beta{\alpha_H}^2\frac{\rho_\infty}{{\rho_n}^2}\frac{\delta\eta}{2}\left(1 + \frac{\delta\eta}{3}\frac{{\rho_n}'}{\rho_n}\right)\Delta\rho_n - \beta{\alpha_H}^2\frac{\rho_\infty}{{\rho_{n-1}}^2}\frac{\delta\eta}{2} \times \left(1 - \frac{\delta\eta}{3}\frac{{\rho_{n-1}}'}{\rho_{n-1}}\right)\Delta\rho_{n-1} + \beta{\alpha_H}^2\rho_\infty\frac{(\delta\eta)^2}{12}\left(\frac{\Delta{\rho_n}'}{{\rho_n}^2} - \frac{\Delta{\rho_{n-1}}'}{{\rho_{n-1}}^2}\right) - 2\left[1 + \beta + d_0 - \frac{d_1\alpha_{H_{l-1}} + d_2\alpha_{H_{l-2}}}{\alpha_H}\right] \times [X_1\Delta f_n' + X_2\Delta f_n'' + X_3\Delta f_n''' + X_4\Delta f_{n-1}'''] - \left(\frac{d_1\alpha_{H_{l-1}} + d_2\alpha_{H_{l-2}}}{{\alpha_H}^2}\right)[f_n'X_1 + f_n''X_2 + f_n'''X_3 + f_{n-1}'''X_4]\Delta\alpha_H - 2[Z_1\Delta f_n' + Z_2\Delta f_n'' + Z_3\Delta f_n''' + Z_4\Delta f_{n-1}'''] = -\text{error} \quad (25)$$

The quantity "error" is simply the momentum equation (24) evaluated after the previous iteration. Similar expressions may be derived for the species and energy equations.

The solution for this set of equations has been programmed for digital computations [10]. Convergence has been found to be very rapid, usually in three to four iterations for the first streamwise station. Downstream stations converge in one or two iterations since the upstream solution is used as a first guess for the next point downstream.

Results and Discussion

Calculations have been performed for several planar bodies with air into air injection. Plates of one and five-foot lengths with both sharp and blunt leading edges have been considered. Free-stream conditions were held constant for all cases with $M_\infty = 2.0$, $P_\infty = 0.0428$ atm, and $T_\infty = 1442$ deg R. Furthermore, only isothermal surfaces at 750 deg R were considered. Results are presented in graphical form with $\dot{q}_w/\dot{q}_{st}$ as the ordinate, where $\dot{q}_w$ the local heat transfer rate at the wall, is given by

$$\dot{q}_w = \left[k\frac{\partial T}{\partial y} + \rho D_{12}\sum_i h_i\frac{\partial K_i}{\partial y}\right]_w - \dot{m}_w h_w + \dot{m}_w h_g \quad (26)$$

where h_w is the enthalpy of the gas at the wall temperature, T_w and h_g is the enthalpy of the gas injected beneath the surface. For the purposes of this investigation h_g was taken to be zero at the reference temperature T_g of 298 deg K.

The quantity $\dot{q}_w$ is the amount of heat which would have to be removed internally in order to maintain a constant T_w of 750 deg R. The quantity $\dot{q}_{st}$ is the heat transfer rate at the stagnation point for the case of no injection. In cases of plates with sharp leading edges, $\dot{q}_{st}$ is the stagnation point heat transfer for a geometrically similar body with a blunt leading edge. For the problem at hand $\dot{q}_{st}$ has been computed to be 24.55 Btu/sec-ft² for the 1-ft plate and 10.98 Btu/sec-ft² for the 5-ft plate. These values compare well with those of 23.87 Btu/sec-ft² and 10.68 Btu/sec-ft², respectively obtained by using Fay and Riddell's [11] correlation. In both cases the stagnation point velocity gradient was computed by a curve fit of pressure data as explained later. The corresponding nose radii were 0.1 and 0.5 ft, respectively.

Figs. 1 through 3 present the results for 1 and 5 ft plates with sharp leading edges. In each case, the injection is distributed over the first 10, 20, and 40 percent of the plate length

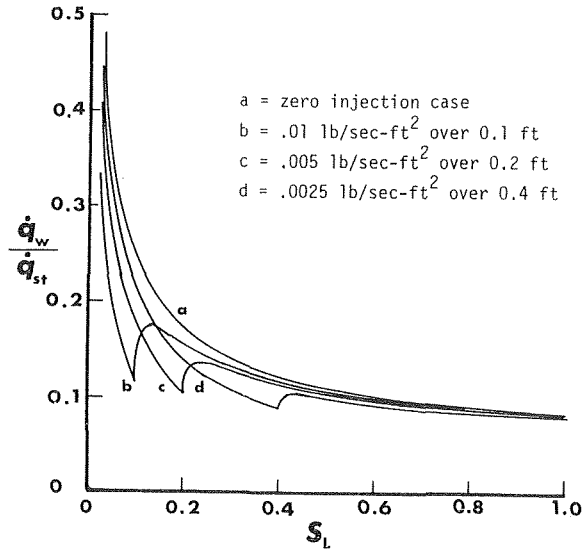

Fig. 1 Heat transfer to a 1-ft sharp plate with large rates of injection

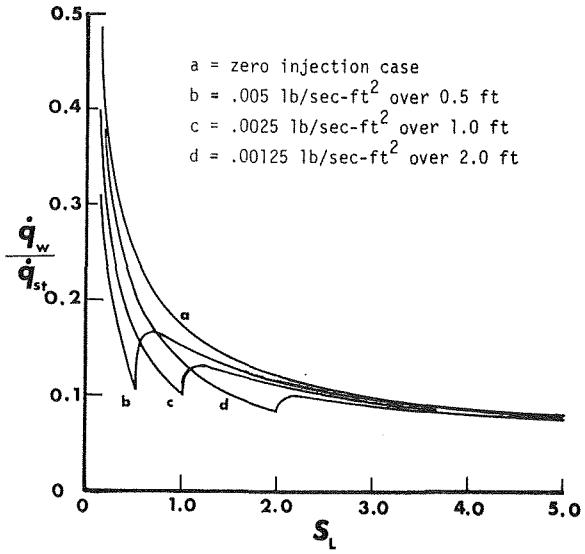

Fig. 2 Heat transfer to a 5-ft sharp plate with moderate rates of injection

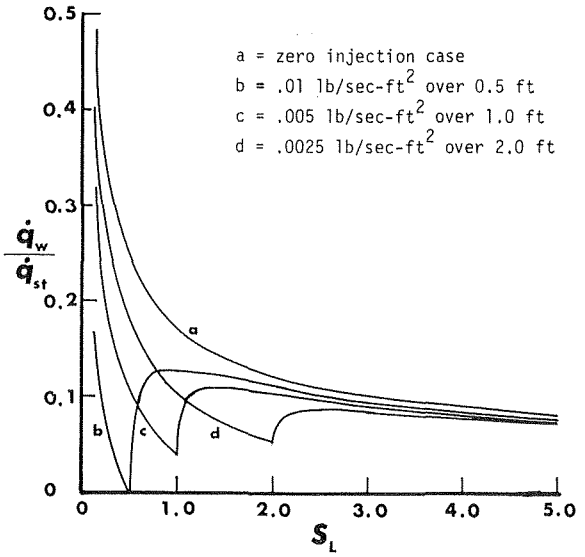

Fig. 3 Heat transfer to a 5-ft sharp plate with large rates of injection

while holding the total mass of injectant constant. It is observed that increasing the total mass of coolant injected in successive cases decreases the heat transfer but leaves the shape of the curves relatively unchanged. In the injection region, the heat transfer is observed to decrease relative to the no injection case as the distance from the leading edge increases. This is followed by a sharp rise in heat transfer immediately downstream from the point where injection stops. The mathematical model actually predicts a discontinuous jump in heat transfer at the termination of injection. This is due to the fact that no internal heat conduction is permitted in the isothermal wall. In reality, such conduction would occur and the wall could not be held exactly at a constant temperature. The curves have been drawn smoothly to a cusp as a compromise at this point.

It can be observed that the length needed for recovery to the zero injection heat transfer rate depends on the length of the injection region as well as the coolant injection rate. As the length of the injection region increases, so the distance required for recovery increases. The physical reasoning behind this fact is as follows: the persistence of any insulating effect downstream from injection is due to the presence of extra mass in the boundary layer. This mass causes both a thickening of the boundary layer and an increase in the total heat capacity of the boundary layer. Furthermore, the boundary layer naturally grows with distance from the leading edge at a rate roughly proportional to $s_L^{1/2}$, where s_L is the distance from the leading edge. Thus, at points downstream from injection cutoff, the boundary layer will be thicker and grow more slowly than at points upstream. Therefore, the extra thickening due to injection dies out more slowly at downstream points than at points near the leading edge. In this way, the heat blockage due to injection can persist for greater distances when the injection region is longer.

Comparison of results for the 1 and 5-ft plates shows the lack of any direct scaling. This is due to the highly nonlinear equations that describe the system. The boundary layer thickness does not scale directly with the geometric dimensions. Thus the 5-ft plate is more strongly affected by proportionately equal mass injection than is the 1-foot plate. Fig. 4 presents the same results as Fig. 3 but in the form of a ratio of heat transfer with injection to heat transfer with no injection.

Figs. 5 and 6 show typical velocity and temperature profiles. The profiles in the injection region show a basic difference from those downstream in that the injection region profiles exhibit a reverse curvature near the wall. Injection rates large enough to

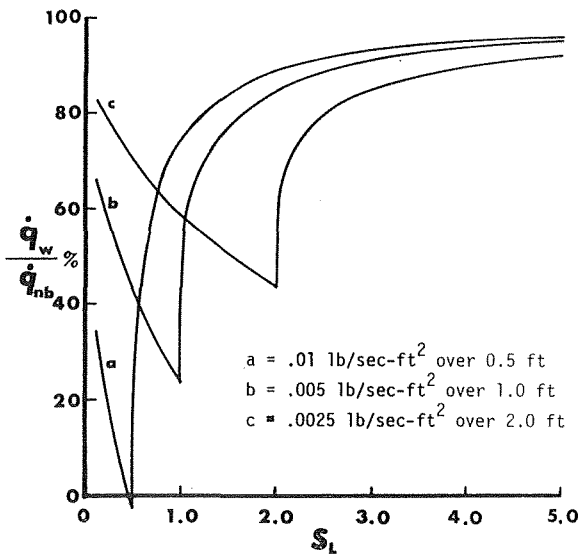

Fig. 4 Reduction in heat transfer to a 5-ft sharp plate with large rates of injection

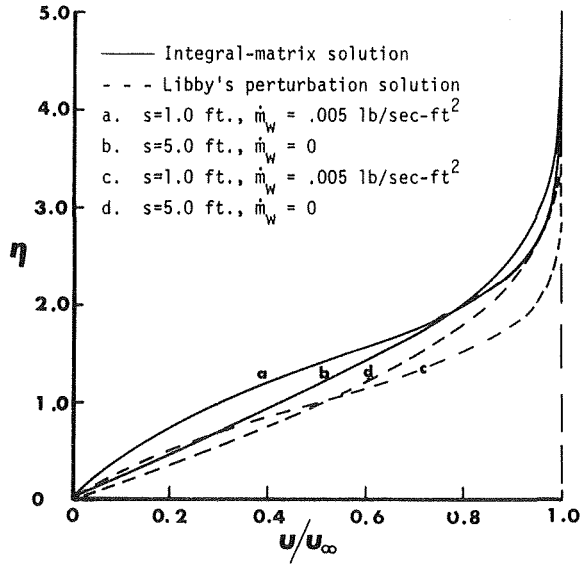

Fig. 5 Velocity profiles along a 5-ft sharp plate with injection $M_\infty = 2.0$; $v_\infty = 3660$ ft/sec; $p_\infty = 0.0428$ atm. Injection cutoff at $s = 1.0$ ft.

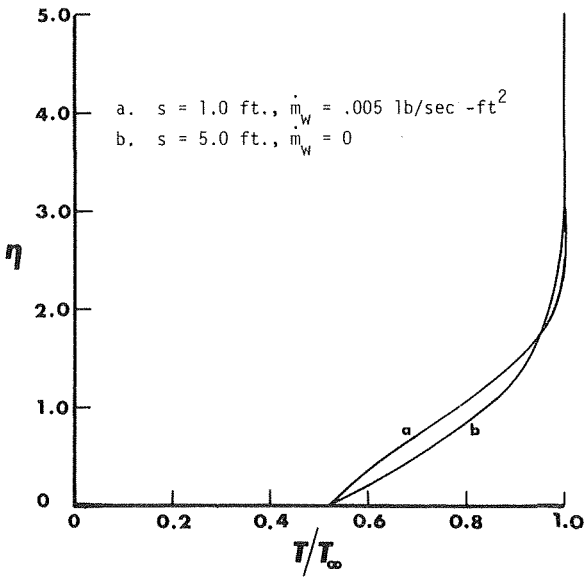

Fig. 6 Temperature profiles along 5-ft sharp plate with injection $M_\infty = 2.0$; $T_\infty = 1442$ deg R; $T_w = 750$ deg R. Injectio n cutoff at $s = 1.0$ ft.

cause negative heat transfer rates usually caused the numerical solution to become unstable as profiles became nearly vertical at the wall. The actual prediction of boundary layer blowoff is not possible however since one of the basic assumptions of the laminar boundary layer equations is violated under blowoff conditions. The profiles recover their characteristic laminar shape a short distance downstream from the end of injection as the slow injected air is accelerated in the boundary layer.

Several comparisons have been made between the results obtained using the integral matrix method and the results of previous studies. In particular, Libby's [5] perturbation method has been applied to the present problem to produce both the velocity profiles and heat transfer rates over the injected and downstream regions. A set of eigenfunctions was generated from the published eigenvalues using a standard Runge-Kutta procedure. The velocity profiles were then computed according to the given series solutions.

The results are shown in Fig. 5 where u/u_e is plotted against η. At $s = 1.0$ ft the agreement is fair. The difference is due to a substantial thickening of the boundary layer caused by the injection. Libby's method contains no provision for stretching η to account for this as the Blasius profile is perturbed at constant η only. The calculated value of α_H at this point is 1.604 which implies that the boundary layer is roughly 60 percent thicker at this point than the Blasius solution would indicate. Agreement is much better at $s = 5.0$ ft ($\alpha_H = 1.081$) where the boundary layer more nearly approaches the classical configuration. Therefore the perturbation approach is best applied when mass injection rates are relatively small.

The corresponding heat transfer rates have been computed from skin-friction results by use of Reynold's analogy. The results are presented in Fig. 7. The lack of close agreement is again due to the influence of boundary layer thickening on the heat transfer. Also, the perturbation solution forces the effects of injection to diminish exponentially with distance downstream. Thus the rapid increase in heat transfer just downstream from injection cutoff cannot be closely approximated.

Heat transfer rates have also been plotted based on Rubesin and Inouye's [2] Karman-Pohlhausen integral method. The data was again taken from skin-friction results using Reynold's analogy. However, the method assumed an inverse-root distribution of mass transfer. Therefore the comparison is based only on equal total amounts of injected mass. These results are shown also in Fig. 7. The curve is observed to deviate substantially in the region immediately downstream from injection cutoff. This shows that the distribution of the injection has considerable influence on downstream heat transfer. The effect is observed to diminish with increasing distance downstream though it does not disappear entirely.

Figs. 8 and 9 depict the heat transfer rates over the leading edge and downstream sections of a one foot blunt plate. The pressure distribution over the leading edge was taken from the experimental results of Gowen and Perkins [12]. Injection was limited to the first 75 deg of the circular arc. The qualitative nature of the results is the same as the sharp plate cases.

The increase in the heat transfer rate over the stagnation point heat transfer at about 5 deg appears also in the results of Kemp, et al. [13], whose correlation is also plotted for comparison. They have observed this phenomenon experimentally as well. It is perhaps due to a slight thinning of the boundary layer as it undergoes high acceleration rates. It should be noted that the shape of the curves over the first 30 deg is an approximation because the solution is extremely sensitive to the pressure gradient parameter in this region. The stagnation point pressure gradient parameter was computed from a curve fit of the input pressure data. This was felt to be more accurate than using the Newtonian flow approximation at the relatively low Mach number under consideration.

Fig. 10 shows the percentage reduction in downstream heat transfer for the one foot blunt plate. At the end of the plate, for the largest rate of mass injection, the heat transfer is seen to be about 18 percent lower than the zero injection case.

Conclusions

The effect of upstream mass injection on downstream heat transfer in a laminar boundary layer has been investigated for supersonic flow over flat plates with both sharp and blunt leading edges. The complete set of nonsimilar boundary layer equations was solved using the integral matrix technique. In cases with large mass injection rates, an insulating effect has been found to persist for a considerable distance downstream from injection cutoff. Furthermore, the length of the injection region has also been found to have substantial effect on the distance required for the heat blockage effects due to injection to die out. For a given total coolant mass, longer injection regions were found to require proportionally longer distances for the local heat transfer rate to

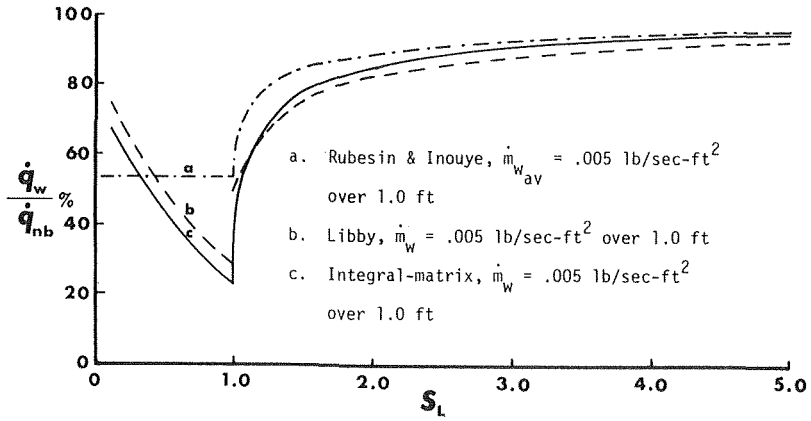

Fig. 7 Comparison of three methods for calculating the reduction in heat transfer to a 5-ft sharp plate with mass injection

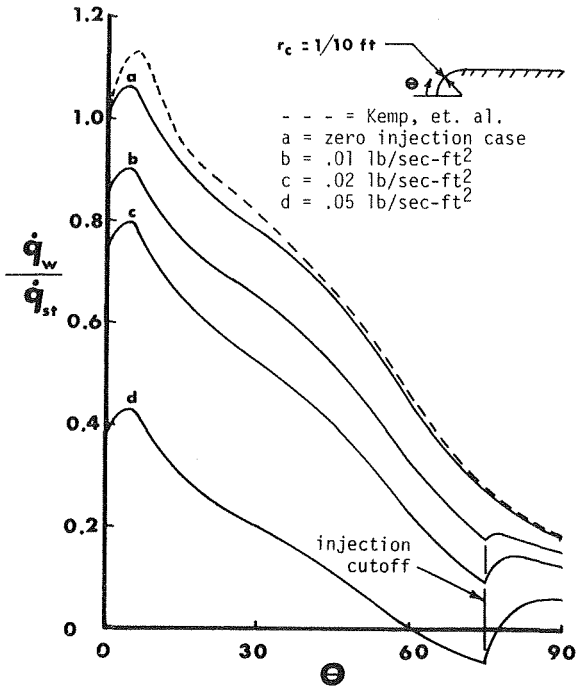

Fig. 8 Heat transfer to the leading edge of a 1-ft blunt plate

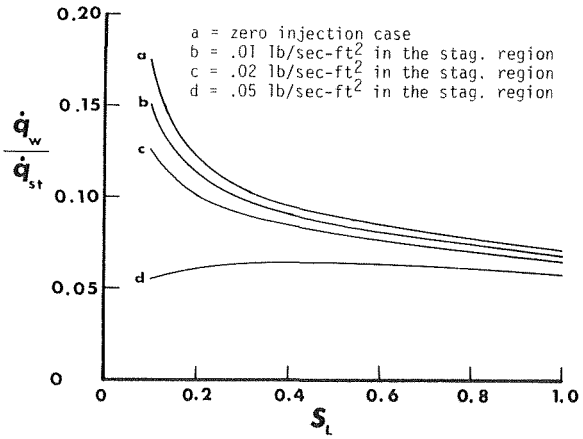

Fig. 10 Reduction in heat transfer downstream on a 1-ft blunt plate with injection in the stagnation region

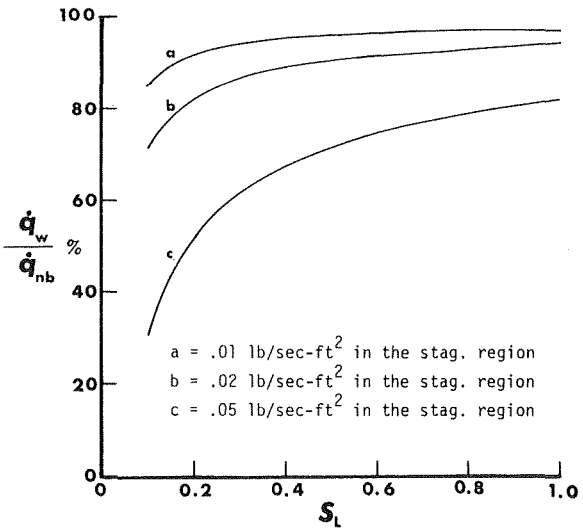

Fig. 9 Heat transfer downstream on a 1-ft blunt plate

approach a given percentage of the local zero injection heat transfer rate.

Acknowledgment

The work reported herein was supported in part by the National Aeronautics and Space Administration under grant number NGR-44-006-033.

References

1 Low, George M., "The Compressible Laminar Boundary Layer With Fluid Injection," NACA TN 3404, 1955.

2 Rubesin, Morris W., and Inouye, Mamoru, "A Theoretical Study of the Effect of Upstream Transpiration Cooling on the Heat-Transfer and Skin-Friction Characteristics of a Compressible, Laminar Boundary Layer," NACA TN 3969, 1957.

3 Libby, Paul A., and Pallone, Adrian, "A Method for Analyzing the Heat Insulating Properties of the Laminar Compressible Boundary Layer," *Journal of the Aeronautical Sciences*, Vol. 21, No. 12, Dec. 1954.

4 Howe, John T., "Some Finite Difference Solutions of the Laminar Compressible Boundary Layer Showing the Effects of Upstream Transpiration Cooling," NASA MEMO 2-26-59A, Feb. 1959.

5 Libby, Paul, "The Laminar Boundary Layer With Arbitrarily Distributed Mass Transfer," *The International Journal of Heat and Mass Transfer*, Vol. 9, 1966, pp. 1109–1123.

6 Pallone, Adrian, "Nonsimilar Solutions of the Compressible-Laminar Boundary-Layer Equations With Applications to the Upstream-Transpiration Cooling Problem," *Journal of the Aerospace Sciences*, Vol. 28, No. 6, June 1961.

7 Kendall, R. M., and Bartlett, E. P., "Nonsimilar Solution of the Multicomponent Laminar Boundary Layer by an Integral-Matrix Method," *AIAA Journal*, Vol. 6, No. 6, June 1968.

8 Dorodnitsyn, A. A., "General Method of Integral Relations and Its Application to Boundary Layer Theory," *Advances in Aeronautical Sciences*, Vol. 3, 1960, pp. 207–219.

9 Hirschfelder, J. O., Curtis, C. F., and Bird, R. B., *Molecular Theory of Gases and Liquids*, 2nd printing, corrected, with notes added, Wiley, New York, 1964.

10 Bartlett, Eugene P., and Deblaye, Christian, "User's Manual—Boundary Layer Integral Matrix Procedure (BLIMP)," Aerotherm Report No. 68-42, October 15, 1968.

11 Fay, J. A., and Riddell, F. R., "Theory of Stagnation Point Heat Transfer in Dissociated Air," *Journal of the Aeronautical Sciences*, Vol. 25, No. 2, Feb. 1958, pp. 73–85.

12 Gowen, Forrest E., and Perkins, Edward W., "Drag of Circular Cylinders for a Wide Range of Reynolds Numbers and Mach Numbers," NACA TN 2960, 1953.

13 Kemp, Nelson H., Rose, Peter H., and Detra, Ralph W., "Laminar Heat Transfer Around Blunt Bodies in Dissociated Air," *Journal of the Aero/Space Sciences*, Vol. 26, No. 7, July 1959, pp. 421–430.

G. R. LING
Graduate Student in Bioengineering.

C. L. TIEN
Professor. Mem. ASME

Department of Mechanical Engineering,
University of California, Berkeley, Calif.

An Analysis of Cell Freezing and Dehydration

A quantitative picture of the effect of low-temperature exposure on the survival of living cells is presented through discussion of solutions to a differential equation relating the volume of intracellular water to the temperature, the cooling rate, and various cell parameters. It is found that for a given cell, a single parameter which depends on the cooling rate governs the behavior of the cell when it is exposed to low temperatures. The analysis develops relationships between solutions to the differential equation and the phenomena affecting cell survival, namely, intracellular freezing and cell dehydration. Theoretical predictions are found to agree well with existing experimental observations.

Introduction

Cryobiology is concerned with the preservation of biological systems at low temperatures. One fundamental problem in cryobiology is the effect of low temperature on the survival of a highly complex system, the living cell. Prior to 1940 there had been little research with the primary goal of studying the basic questions of biological freezing [1].[1] With the discovery of the protective effect of glycerin in 1949 [2], the subject of cryobiology experienced a surge in interest. However, as Meryman [3] has pointed out, enormous amounts of very carefully determined experimental data are often relevant only to the particular system from which these data were obtained and cannot be extrapolated to other similar systems of interest. This circumstance has largely resulted from the lack of theoretical analyses of the basic physical phenomena involved. Consequently, the physical and chemical factors underlying the observed effects of low temperature on living cells are not well understood.

Different kinds of cells may differ greatly in size, shape, and structure but it is useful to put together a representative cell for the purpose of examining the basic features shared in varying degrees by all cells. Such a cell is shown in Fig. 1. Here we see the basic cell constituents: the cell membrane, the cytoplasm containing various organelles such as mitochondria, endoplasmic reticulum, Golgi bodies, centrosomes, and finally a central nucleus. The functions of the various elements composing the cell are profoundly affected by the dehydration which accompanies biological freezing [4–6] as well as by the freezing itself. Because this dehydration can have disastrous effects on the survival of living cells, it would be desirable to have some quantitative description of the relationship between the amount of water remaining in a cell and the temperature. The formation of intracellular ice crystals can also prove lethal to a cell exposed to low temperatures [4–8] and it is, therefore, important to determine the circumstances under which this phenomenon can occur. Once we have developed a clearer picture of the physical and chemical factors underlying the phenomena of intracellular freezing and

[1] Numbers in brackets designate References at end of paper.

Contributed by the Heat Transfer Division and presented at the Winter Annual Meeting, Los Angeles, Calif., November 16–20, 1969, of The American Society of Mechanical Engineers. Revised manuscript received by the Heat Transfer Division, March 17, 1970. Paper No. 69-WA/HT-31.

Nomenclature

A = area of cell membrane
a = membrane pore radius
B = cooling rate
b = coefficient defined in the expression for permeability constant
k = permeability constant
k_g = permeability constant at a reference temperature T_g
L_f = molar heat of fusion of water
n = number of moles of solutes within the cell
R = gas constant
r = radius of spherical ice-water interface
T = temperature
T_c = freezing point of water in membrane pore
T_f = freezing point of protoplasm
V = volume of intracellular water
V_i = initial volume of intracellular water
v = molar volume of water
α = parameter defined in equations (4)
β = parameter defined in equation (9)
γ = constant defined in equations (4)
δ = parameter defined in equation (15)
ϵ = parameter defined in equations (4)
η = parameter defined in equations (4)
θ = dimensionless temperature defined in equations (3)
θ_c = critical temperature defined by equation (14)
θ_e = temperature at which cooling is ceased
θ_v = critical temperature given by equation (16)
σ = interfacial tension at the ice-water interface
ϕ = contact angle between ice and capillary wall
ψ = dimensionless volume defined in equations (3)
ψ_c = critical volume
ψ_e = equilibrium volume

cell dehydration, we will be able to predict the effect of a given freezing experiment on the survival of a living cell.

Fundamental Equation

By making certain simplifying assumptions, Mazur [6] has developed a differential equation relating the volume of intracellular water to the temperature, the cooling rate, and various cell parameters. A detailed discussion of these assumptions and their limitations can be found in Mazur's paper. The system under consideration consists of a cell like that in Fig. 1 and its immediate environment. The cell is assumed to be in the so-called "unprotected state," i.e., no protective additives are present. Initially the whole system is assumed at a temperature T_f, the freezing point of protoplasm. Externally the cell is surrounded by ice, and internally it contains supercooled water. A mass balance for the intracellular water, combined with other thermodynamic and transport considerations, yields Mazur's equation

$$Ve^{b(T_g-T)}\frac{d^2V}{dT^2} - \left[(bT + 1)e^{b(T_g-T)} - \frac{ARk_g n}{L_f(V + nv)}\frac{T^2}{V}\right]\frac{dV}{dT} = \frac{L_f A k_g}{Be} \quad (1)$$

where T is the temperature; V the volume of intracellular water; k_g and b are related to the permeability constant, k, by the empirical relation $k = k_g \exp[b(T - T_g)]$; A is the area of the cell membrane; R the gas constant; n the number of moles of solutes within the cell; v the molar volume of water; L_f the molar heat of fusion of water; and B the cooling rate. The equation is subject to the following initial conditions:

$$T = T_f,\ V = V_i \text{ and } T = T_f,\ \frac{dV}{dT} = 0 \quad (2)$$

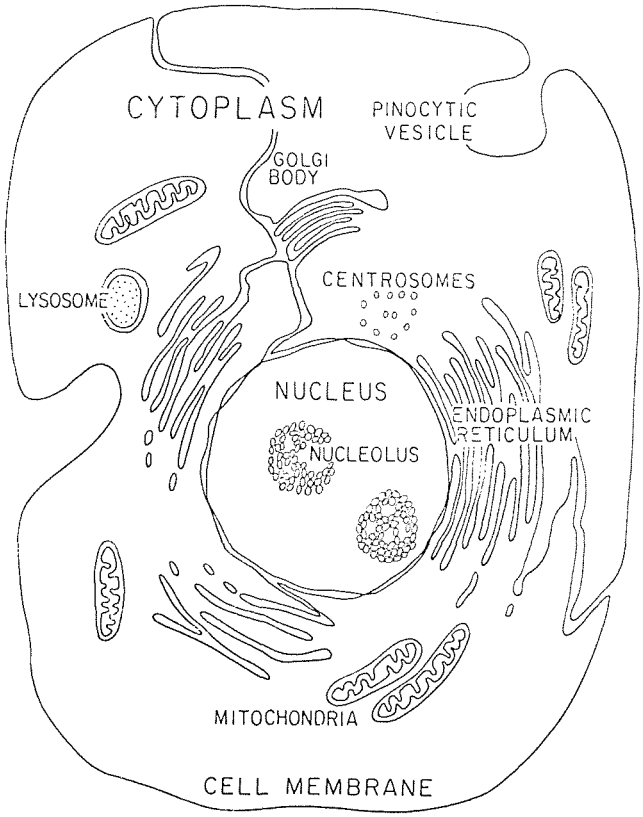

Fig. 1 Diagram of a representative cell

where T_f is the freezing point of protoplasm and V_i the initial volume of intracellular water.

The governing equation is of such a form that no simple analytical solution can be obtained. Mazur [6] has attempted a numerical solution of the equation. Unfortunately, due to the large number of physical parameters in the equation, his solution is limited to a few special cases, which were supposed to represent typical cells. It is found, however, that by grouping various physical parameters into dimensionless groups, the number of variables in equation (1) can be reduced and the resulting equation becomes much easier to analyze and discuss on both mathematical and physical grounds. Indeed, under certain limiting physical conditions, simple analytical solutions can be obtained and the associated physical phenomena can be analyzed in a quantitative manner.

If we employ the dimensionless temperature and volume defined by

$$\theta = \frac{T_f - T}{T_f}, \qquad \psi = \frac{V_i - V}{V_i} \quad (3)$$

and rewrite equation (1) in terms of these variables, we find that the various constants and cell parameters can be arranged into the four dimensionless groups given by

$$\alpha = bT_f, \qquad \gamma = \frac{L_f}{RT_f}, \qquad \epsilon = -\left(\frac{ARk_g T_f^2}{BvV_i}\right) \times \exp[b(T_f - T_g)], \qquad \eta = \frac{nv}{V_i} \quad (4)$$

Furthermore, since cells in the unprotected state are rarely cooled below -10 deg C (if survival is important), nearly all physically realistic cases correspond to small values of θ. For $\theta \ll 1$, we have

$$\frac{d^2\psi}{d\theta^2} + \left\{(\alpha + 1) + \frac{\epsilon\eta}{[(1 - \psi) + n](1 - \psi)}\right\}\frac{d\psi}{d\theta} = \epsilon\gamma e^{-\alpha\theta} \quad (5)$$

From equations (2), the initial conditions are

$$\theta = 0, \qquad \psi = 0 \quad \text{and} \quad \theta = 0, \qquad \frac{d\psi}{d\theta} = 0 \quad (6)$$

Limiting Solutions

Under certain limiting conditions it is possible to obtain analytic solutions to equation (5). We will now consider four such limiting conditions: $\eta = 0$, $\psi \ll 1$, $\epsilon \ll 1$, and $\epsilon \to \infty$.

Case 1: Solutions for $\eta = 0$. The simplest case is when the cell contains only water and no solutes. Then $\eta = 0$, the nonlinear term in equation (5) vanishes, and the solution is straightforward

$$\psi = \frac{\epsilon\gamma}{(\alpha^2 + \alpha)}[1 + \alpha e^{-(\alpha+1)\theta} - (\alpha + 1)e^{-\alpha\theta}] \quad (7)$$

Case 2: Solutions for $\psi \ll 1$. If we assume that the cell dehydration resulting from the freezing process is small (i.e., $\psi \ll 1$), then we can write $(1 - \psi) \approx 1$ in equation (5), and the solution is again straightforward

$$\psi = \frac{\epsilon\gamma}{\alpha\beta(\beta - \alpha)}[(\beta - \alpha) + \alpha e^{-\beta\theta} - \beta e^{-\alpha\theta}] \quad (8)$$

where

$$\beta = (\alpha + 1) + \frac{\epsilon\eta}{(1 + \eta)} \quad (9)$$

Noting that equation (8) reduces to equation (7) in the limit as $\eta \to 0$, we can see that the presence of intracellular solutes affects the volume of water remaining in the cell as a function of temperature in a quantitative way but leaves the qualitative picture unchanged. Equation (8) agrees well with Mazur's

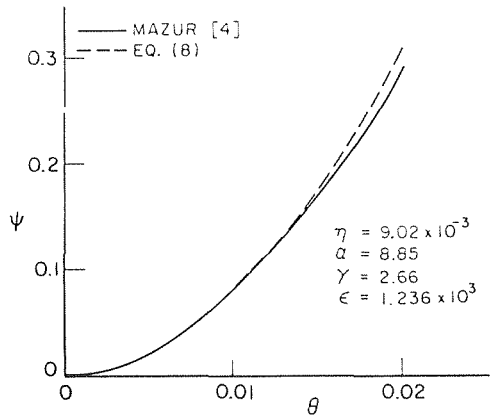

Fig. 2 Comparison between asymptotic ($\psi \ll 1$) and exact solutions

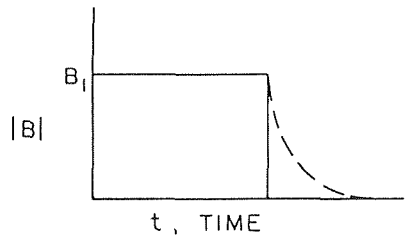

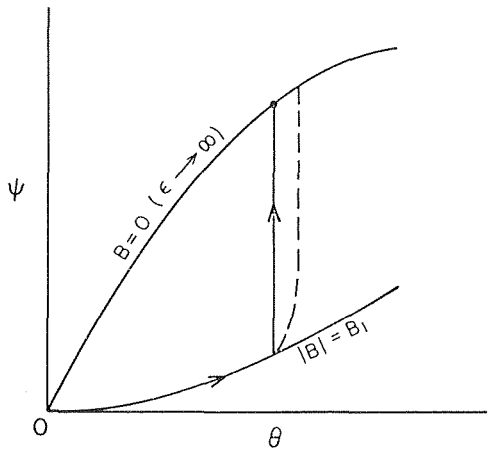

Fig. 3 System behavior when cooling is ceased

numerical solutions [6] within the stated limits $\theta \ll 1$, $\psi \ll 1$. Fig. 2 shows the deviation of equation (8) from Mazur's numerical solution for a typical cell with a value of $\epsilon = 1.236 \times 10^3$. Similar results can be found for other cells and for different values of ϵ.

Case 3: Solutions for $\epsilon \ll 1$. For high cooling rates ϵ is small, and equation (5) can be solved by perturbation methods where

$$\psi = \psi_0 + \epsilon\psi_1 + \epsilon^2\psi_2 + \ldots \tag{10}$$

The zeroth order term is found to be $\psi_0 = 0$. That this result is physically reasonable can be seen by noting that for an infinite cooling rate (i.e., $\epsilon \to 0$) the water within the cell will freeze instantaneously before any dehydration can occur. Thus, $V = V_i$ for all T, and, hence, $\psi = 0$ for all θ.

The first-order approximation is

$$\psi = \psi_0 + \epsilon\psi_1 = \frac{\epsilon\psi}{(\alpha^2 + \alpha)}\left[1 + \alpha\epsilon^{-(\alpha+1)\theta} - (\alpha + 1)e^{-\alpha\theta}\right] \tag{11}$$

which is identical to equation (7). This indicates that for high cooling rates (i.e., small values of ϵ) the cell behaves as though it did indeed contain only water. Of course, this implication is also clear from equation (8).

Higher-order terms can only be obtained explicitly by assuming $\psi \ll 1$, but then it can be shown that the small-ϵ solutions are actually contained in the result for Case 2, the small-ψ solutions.

Case 4: Solutions for $\epsilon \to \infty$. As cooling becomes infinitesimally slow (i.e., $\epsilon \to \infty$) the water remaining in a cell at a given temperature will be in equilibrium with the surrounding ice. In this case it is possible to obtain an exact solution to equation (1) without making any additional assumptions. The result, valid over the whole $0 \leq \theta \leq 1$ range, is

$$\psi = \frac{[e^{\gamma\theta/(1-\theta)} - 1]}{\left[e^{\gamma\theta/(1-\theta)} - \dfrac{1}{(1+\eta)}\right]} \tag{12}$$

Since equation (12) represents the equilibrium value of ψ at a given value of θ, we can expect that other solutions will tend toward equation (12) as ϵ increases for a fixed θ. In fact, it can be shown that equation (8) reduces to equation (12) in the limit as $\epsilon \to \infty$. Mazur's numerical solutions also exhibit this trend [6].

It is also important to recognize that if during freezing the cooling is instantaneously ceased, then ψ will increase at constant θ to a value given by equation (12), as shown in Fig. 3. Of course, in any real case an abrupt step in the cooling rate, B, is not possible, and the curves will exhibit some drift, as is indicated by the dashed lines in Fig. 3.

Cell Dehydration

Having some solutions to the fundamental differential equation, we are ready to consider the basic problem of predicting the effect of low temperature on the survival of living cells. We recall that there are two important phenomena associated with low-temperature exposure, both of which can have a profound effect on cell survival: the formation of intracellular ice crystals and cell dehydration.

It is clear from the solutions presented earlier that as θ increases ψ will increase. In other words, as the temperature is lowered, the cell will lose water. This water loss is due to the higher vapor pressure of the internal supercooled water relative to that of the external ice. If this dehydration proceeds beyond a certain limit (depending on the particular cell being considered) then the internal chemical alterations resulting from the increased concentration of solutes may become irreversible, and the dehydration may prove lethal to the cell. If we characterize this lethal level by saying that it is the level at which the ratio of the number of moles of solute to that of water has reached a critical value, then the value of ψ corresponding to this critical ratio

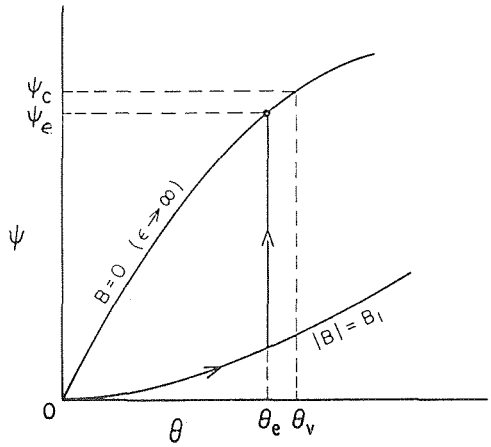

Fig. 4 Survival limit for cell dehydration

will be ψ_c where $(1 - \psi_c)$ is the ratio between the volume of water at which the concentration of solutes becomes critical and the initial volume of water within the cell. In general this critical volume of water will depend on temperature, but for $\theta \ll 1$ it will be essentially constant, and, therefore, ψ_c may be regarded as constant for a given cell. For some cells ψ_c may be as large as 0.9 or even 1.0, while for others it may be as small as 0.6.

Since the equilibrium value of ψ represents an upper bound, it is clear that the important value of θ is the value for which the equilibrium value of ψ, ψ_e, is equal to ψ_c. Calling this value of θ as θ_v, we see that cooling must cease at some $\theta_e < \theta_v$ to insure cell survival, as Fig. 4 shows.

Intracellular Freezing

Now we need to examine the conditions under which the phenomenon of intracellular freezing can occur. Since the freezing of supercooled water generally requires the presence of external ice, we conclude that the external ice must be the agent which nucleates the cell contents. However, it has been shown that even when external ice is present, the cytoplasm almost always remains supercooled at -5 deg C, and sometimes at even lower temperatures [4]. It appears, then, that the cell membrane is an effective barrier to nucleation at temperatures as low as -5 deg C, or lower. However, at still lower temperatures, the membrane apparently loses this ability to prevent nucleation and intracellular freezing occurs [4]. To resolve this problem it is necessary to take a closer look at the membrane.

Many physiologists believe that plasma membrane contains water-filled channels or pores [9–12]. Essentially, their conclusion is based on the discrepancies between the value of permeability constants for water derived from osmotic flow across cell membranes and those derived from the rate of diffusion of isotopic water under zero osmotic gradient. If we assume that such pores exist, that their diameters remain constant over the surface of a given membrane [9, 13] and that they are of cylindrical shape, then it is necessary to look at only a single pore to determine the conditions under which intracellular ice crystals will form.

Fig. 5 gives a schematic representation of the situation. The contact angle ϕ between the ice and the capillary wall is determined by the interfacial tensions between ice and water, between water and the capillary wall, and between ice and the capillary wall. Assuming these three forces to be in equilibrium we can obtain an expression for the freezing point of water in the capillary, or, in other words, the temperature at which ice and water in the capillary are in equilibrium, by carrying out an analysis similar to that of Jackson and Chalmers [14]. The present analysis, however, takes into account the decrease in T_c as dehydration lowers the freezing point of the water remaining in the cell (as a result of the increased concentration of the solutes). Writing the obtained expression in terms of the dimensionless variables θ and ψ yields

$$e^{\alpha\theta_c}\left(\frac{d\psi}{d\theta}\right)_{\theta_c} = -\frac{2Ak_g T_f \sigma \cos\phi}{aBV_i} e^{\alpha\theta_g} \tag{13}$$

where σ is the interfacial tension at the ice-water interface, a the pore radius, and θ_c and θ_g the values of θ at T_c, the freezing point of water in the capillary, and at T_g, the membrane permeability reference temperature, respectively. Once ψ is known as a function of θ, θ_c can be determined using equation (13).

In general the interfacial tension between the ice and the capillary wall is greater than that between the water and the capillary wall since there is usually some strain energy associated with a solid-substrate interface, whereas none is present at a liquid-substrate interface [14]. Thus, $\cos\phi > 0$, and, so, $\phi < \pi/2$. For $\phi < \pi/2$, T_c, the freezing point of the water in the capillary, is less than T_f, the freezing point of planar water, since the vapor pressure of the water is greater than that of the ice. If $\phi = \pi/2$, then freezing proceeds as though the membrane is not there, and $T_c = T_f$. For $\phi = 0$, the liquid wets perfectly the walls of the capillary preventing ice from nucleating at the substrate, and the freezing of the water follows the Kelvin equation. Experimental evidence suggests that ϕ is greater than zero but less than $\pi/2$ and also helps to explain how the membrane can act as a barrier against the formation of intracellular ice crystals for temperatures above -5 deg C to -10 deg C and cease to be a barrier at lower temperatures. The arguments leading to these conclusions are based on the low entropy of the water in membrane pores and its increase as water flows through the pores [15–17], since an increase in entropy ultimately results in a decrease in ϕ.

If for a given freezing situation θ exceeds the value of θ_c calculated from equation (13), then intracellular ice crystals will form almost instantaneously. Furthermore, since θ_c increases with increasing ϵ, it is only necessary to calculate θ_c corresponding to the particular freezing situation being studied since cessation of cooling at some $\theta_e < \theta_c$ will insure that intracellular ice crystals will not form, even as equilibrium is being approached.

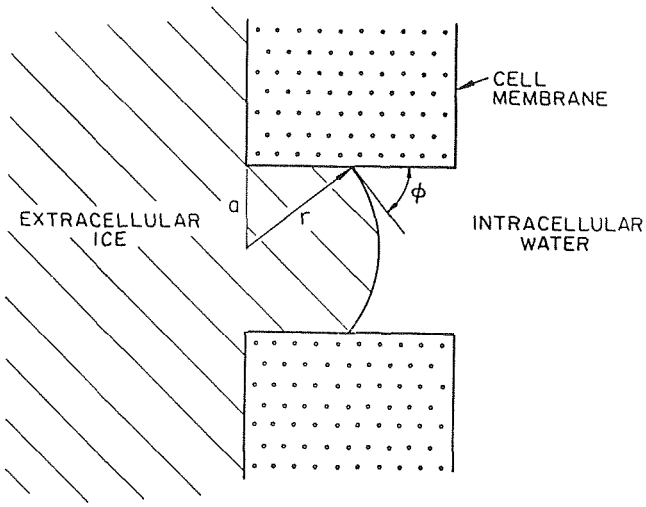

Fig. 5 Schematic of membrane pore during freezing

Interaction Between Cell Dehydration and Intracellular Freezing

Since all survival depends on avoiding both the formation of intracellular ice crystals and the level of lethal cell dehydration, it is obvious that cooling must cease at some θ_e less than the smaller of the two values θ_v and θ_c. Since equation (8) represents the physically most realistic and most widely applicable solution to equation (5), we use it to calculate θ_c. So, substituting equation (8) into (13) and solving for θ_c, we get

$$\theta_c = \frac{1}{(\beta - \alpha)} \ln\left[\frac{1}{1 - \frac{\delta}{\gamma}(\beta - \alpha)}\right] \tag{14}$$

where

$$\delta = \frac{2v\sigma \cos\phi}{aRT_f} \tag{15}$$

If care is taken in interpreting equation (14) as $(\beta - \alpha)$ approaches $\left(\frac{\delta}{\gamma}\right)^{-1}$ (i.e., as the cooling rate, B, decreases) then the result will continue to be physically meaningful, even when $(\beta - \alpha) > \left(\frac{\delta}{\gamma}\right)^{-1}$. Next, substituting $\psi = \psi_c$ and $\theta = \theta_v$ into equation (12) and solving for θ_v, we find

$$\frac{\left(\frac{1}{\gamma}\right)\ln\left[\frac{(1 - \psi_c) + \eta}{(1 + \eta)(1 - \psi_c)}\right]}{1 + \left(\frac{1}{\gamma}\right)\ln\left[\frac{(1 - \psi_c) + \eta}{(1 + \eta)(1 - \psi_c)}\right]} \tag{16}$$

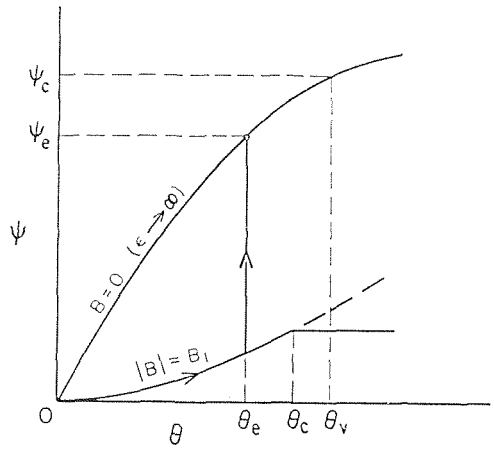

Fig. 6 Interaction between cell dehydration and intracellular freezing for the case $\theta_c < \theta_v$

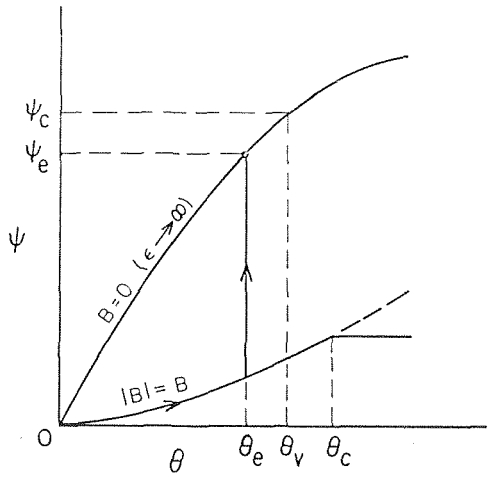

Fig. 7 Interaction between cell dehydration and intracellular freezing for the case $\theta_v < \theta_c$

In predicting the outcome of a given freezing experiment, two cases are of interest.

Case 1: $\theta_c < \theta_v$. As Fig. 6 shows, if cooling is ceased at $\theta_e < \theta_c$, then intracellular freezing will not occur, and, since $\theta_c < \theta_v$, ψ_e will be less than ψ_c, the lethal dehydration level.

Case 2: $\theta_v < \theta_c$. As Fig. 7 shows, if cooling is ceased at $\theta_e < \theta_v$, then ψ_e will be less than ψ_c, the lethal dehydration level, and, since $\theta_v < \theta_c$, intracellular freezing will not occur.

As was mentioned earlier, θ_c increases with increasing ϵ. This implies that for larger cells, lower cooling rates may be employed, while for smaller cells, higher cooling rates will be more desirable. In general, the goal is to freeze the cells to as low a temperature as possible without jeopardizing survival. In this case, it is desirable to choose ϵ such that $\theta_c \geq \theta_v$, since this results in the greatest possible amount of supercooling. The important conclusion here is that a single parameter, ϵ, which depends on the cooling rate, controls the fate of the cell when it is exposed to low temperature.

Comparison With Experimental Results

Using equations (14) and (16) for θ_c and θ_v, respectively, we can predict the effect of a given freezing experiment on the survival of a living cell to determine how well the theoretical analysis agrees with experimental results. The effects of low temperature on the survival of the yeast *Saccharomyces cerevisiae* have been studied thoroughly by Mazur [4], and so the results of his studies will be used as a basis for comparison with theoretical predictions based on equations (14) and (16).

Substituting the values of the cell parameters given by Mazur [6] for yeast cells along with the values of the various constants into equations (4), we get

$$\alpha = 8.85, \qquad \eta = 9.0 \times 10^{-3}, \qquad \gamma = 2.66,$$

$$\epsilon = -\frac{2.91 \times 10^4}{B}, \qquad B \text{ in deg K/min } (<0)$$

and

$$\beta - \alpha = 1 - \frac{2.62 \times 10^2}{B}$$

Mazur [4] notes that pore radii values calculated from permeability measurements usually range between 3Å and 8.5Å. He also indicates indirectly that 75 deg may be a reasonable value for the contact angle, ϕ. Fletcher [18] gives 20 ergs/cm² as a good estimate for σ near 0 deg C. Using these values, with $a = 6$Å, to calculate δ, we find

$$\delta = \frac{2v\sigma \cos \phi}{aRT_f} = 0.132$$

Thus, from equation (14),

$$\theta_c = \frac{1}{1 - \left(\frac{262}{B}\right)} \ln \left\{ \frac{1}{1 - 4.95 \times 10^{-2}[1 - (262/B)]} \right\}$$

Taking $(1 - \psi_c) = 0.2$, equation (16) gives

$$\theta_v = 1.32 \times 10^{-2}$$

Taking the limit as $B \to -\infty$ of θ_c, we find that the minimum value of θ_c is given by

$$(\theta_c)_{\min} = \lim_{B \to -\infty} \left[\frac{1}{1 - \left(\frac{262}{B}\right)} \times \ln \left\{ \frac{1}{1 - 4.95 \times 10^{-2}[1 - (262/B)]} \right\} \right] = 5 \times 10^{-2}$$

Since $\theta_v < (\theta_c)_{\min}$, θ_c will be greater than θ_v regardless of the cooling rate. This implies that if we cease cooling at some $\theta_e < \theta_v = 1.5 \times 10^{-2}$, then survival is assured, regardless of the cooling rate. Indeed, Mazur's results [4] show that survival was maximum (near 100 percent) for cells not cooled below about -5 deg C, which corresponds to $\theta_e = 1.47 \times 10^{-2}$. Thus, we see that the theoretical predictions are in excellent agreement with experimental results. Of course, it should be pointed out that the values of two important parameters, the pore radius, a, and the contact angle, ϕ, are not well known.

Further research is presently being carried out by us in an attempt to find ways by which θ_v and θ_c may be increased. Preliminary results indicate that slow cooling and the addition of protective additives will prove beneficial in this respect.

References

1 Luyet, B. J., and Gehenio, P. M., *Life and Death at Low Temperatures, Biodynamics*, Normandy, Mo., 1940.

2 Polge, C., Smith, A. U., and Parkes, A. S., "Revival of Spermatozoa After Vitrification and Dehydration at Low Temperatures," *Nature*, Vol. 164, p. 666.

3 Meryman, H. T., ed., *Cryobiology*, Academic Press, New York, 1966.

4 Mazur, P., "Physical and Chemical Basis of Injury in Single-Celled Microorganisms Subjected to Freezing and Thawing," *Cryobiology*, chap. 6, Academic Press, New York, 1966.

5 Meryman, H. T., "Review of Biological Freezing," *Cryobiology*, Chap. 1, Academic Press, New York, 1966.

6 Mazur, P., "Kinetics of Water Loss From Cells at Subzero Temperatures and the Likelihood of Intracellular Freezing," *Journal of General Physiology*, Vol. 47, 1963, pp. 347–369.

7 Rapatz, G. L., Menz, L. J., and Luyet, B. J., "Anatomy of the Freezing Process in Biological Materials," *Cryobiology*, chap. 3, Academic Press, New York, 1966.

8 Mazur, P., "The Effects of Subzero Temperatures on Microorganisms," *Recent Research in Freezing and Drying*, Charles C. Thomas, Springfield, Ill., 1960, p. 65.

9 Soloman, A. K., "Red Cell Membrane Structure and Ion Transport," *Journal of General Physiology*, Vol. 43 (suppl.), 1960, pp. 1–15.

10 Whittembury, G., "Action of Antidiuretic Hormone on the Equivalent Pore Radius at Both Surfaces of the Epithelium on the Isolated Toad Skin," *Journal of General Physiology*, Vol. 46, 1962, pp. 117–130.

11 Haus, R. M., and Leaf, A., "Studies on the Movement of Water Through the Isolated Toad Bladder With Its Modification by Vasopressin," *Journal of General Physiology*, Vol. 45, 1962, pp. 905–919.

12 Villegas, L., "Equivalent Pore Radius in Frog Gastric Mucosa," *Biochim. Biophys. Acta*, Vol. 75, 1963, pp. 131–134.

13 Mullins, L. J., "An Analysis of Pore Size in Excitable Membranes," *Journal of General Physiology*, Vol. 43 (suppl.), 1960, pp. 105–117.

14 Jackson, K. A., and Chalmers, B., "Freezing of Liquids in Porous Media With Special Reference to Frost Heave in Soils," *Journal of Applied Physics*, Vol. 29, 1958, pp. 1178–1181.

15 Hays, R. M., and Leaf, A., "The State of Water in the Isolated Toad Bladder in the Presence and Absence of Vasopressin," *Journal of General Physiology*, Vol. 45, 1962, pp. 933–948.

16 Hempling, H. G., "Permeability of the Ehrlich Ascites Tumor Cell to Water," *Journal of General Physiology*, Vol. 44, 1960, pp. 365–379.

17 Frank, H. S., and Evans, M. W., "Free Volume and Entropy in Condensed System (III)," *Journal of Chemical Physics*, Vol. 13, 1945, pp. 507–532.

18 Fletcher, N. H., *The Physics of Rain Clouds*, Cambridge University Press, Cambridge, England, 1962.

G. A. DOMOTO
Assistant Professor,
Department of Mechanical Engineering,
Columbia University,
New York, N. Y.

C. L. TIEN
Professor of Mechanical Engineering,
University of California,
Berkeley, Calif.

Thick Film Analysis of Radiative Transfer Between Parallel Metallic Surfaces[1]

The radiative transfer between two infinite parallel metallic surfaces separated by a nonconducting ideal dielectric is calculated on the basis of electromagnetic wave theory. The solution is restricted to the case of large spacing (thick film) wherein the effects of interference and radiation tunneling can be neglected. The optical properties of the metals are predicted via the anomalous skin effect theory, the Drude single electron theory and the Hagen-Rubens relation. A comparison of the predicted radiative fluxes indicates the large disparities which result from the three different specifications of the optical properties of metals. For practical applications at cryogenic temperatures, approximations are obtained for the thick film solution using the anomalous skin effect theory of the optical properties.

Introduction

This is the first of three papers considering radiative transfer between metallic surfaces at cryogenic temperatures. The subject is vitally important in the design and performance evaluation of high-performance cryogenic insulations. The fundamental and practical aspects of this subject have been extensively reviewed in two recent articles [1, 2].[2] The present paper analyzes the problem of radiative transfer between metallic surfaces when the surface spacing is large compared to the characteristic wavelength of radiation involved at the prescribed surface temperatures. In the second paper [3], the problem associated with small spacings is analyzed. The third paper [4] presents an experimental study of radiative transfer between metallic surfaces in the liquid-helium temperature range.

The analytical basis of the present paper consists of the electromagnetic wave theory of energy transmission and the theory of radiation (or optical) properties of metals. Many efforts have been made previously to incorporate the wavelength variation of the radiation properties of metallic surfaces in the prediction of radiative heat flux between metals. The primary basis for the specification of spectral radiation properties has been either the Drude single electron (DSE)[3] theory or the Hagen-Rubens (HR) relation for the optical properties of metals. For certain transi-

[1] This work constitutes part of the PhD thesis of G. A. Domoto, entitled, "Thermal Radiation of Metallic Surfaces at Liquid Helium Temperatures," Division of Mechanical Engineering, University of California, Berkeley, 1968. The authors wish to acknowledge the support of this work by NASA Grant NGR-05-003-285.

[2] Numbers in brackets designate References at end of paper.

Contributed by the Heat Transfer Division and presented at the Winter Annual Meeting, Los Angeles, Calif., November 16–20, 1969, of The American Society of Mechanical Engineers. Manuscript received at ASME Headquarters, July 29, 1969. Paper No. 69-WA/HT-6.

[3] For convenience the abbreviations DSE, HR, and ASE will be used throughout the text to denote Drude single electron, Hagen-Rubens, and anomalous skin effect, respectively.

Nomenclature

A = parameter defined in equation (23)
B = parameter defined in equation (25)
c = speed of light in vacuum
e = electronic charge or emissive power in vacuum
E = electric field amplitude
h = Planck's constant
I = radiation intensity in vacuum
k = Boltzmann's constant
m = effective electron mass
$\tilde{n}$ = complex refractive index of metal
n = refractive index
N = number density of free electrons
q = net radiative heat flux
r = complex amplitude reflection coefficient
Re = real part of a complex number
T = absolute temperature
T = transmission factor
TE = transverse electric
TM = transverse magnetic
v = $(3N/8\pi)^{1/3}(h/m)$ = velocity at surface of the Fermi distribution
$\bar{v}$ = v/c = dimensionless Fermi velocity
W = $1 + i\omega\tau$
z = depth into metal
Z = surface impedance
$\bar{Z}$ = $(c^2/4\pi\omega\tau\mu v)Z$ = dimensionless impedance
α = absorptivity
ϵ = emissivity
θ = angle from normal to surface

(Continued on next page)

tion metals, the Roberts two-electron theory has been also suggested. Parker and Abbott [5], and Rolling and Tien [6] have used the DSE theory to calculate the total radiation properties of metals. Holt, Grosh, and Geynet [7] have evaluated the radiative heat flux between metallic surfaces using the HR relation.

In connection with the thermal radiation properties of metals at cryogenic temperatures, there has been developed the anomalous skin effect (ASE) theory of the optical properties [8, 9, 10]. The basic difference between the ASE and DSE specifications is that the ASE theory takes into account the effect of spatial variation of the electric field on the electron as it moves along its finite path whereas the DSE theory does not. In addition to earlier experimental verifications, the validity of the ASE theory, especially for noble metals, has been greatly strengthened by the recent experimental work of Bennett and his co-workers [11]. The ASE theory has been used by Domoto, Boehm, and Tien [12] to predict total normal emissivity of metals. Their comparison of the predictions of total emissivity based on the ASE and DSE theories illustrates the large differences which result as a consequence of the different specifications of the optical properties.

The purpose of the present work is to calculate and compare the radiative flux between parallel specular metallic surfaces using the ASE, DSE, and HR theories. Since these models are based on the motion of free electrons, the photoelectric absorption is not taken into account and the results are restricted to wavelengths in the infrared or far infrared range, outside the photoelectric absorption bands for the metals. The results should be particularly applicable in the cryogenic temperature range where the radiation will be predominantly in the far infrared. Furthermore, the long wavelength radiation involved at cryogenic temperatures reduces surface roughness effects [13], and thus the specular surface assumption is a fairly good one.

Analysis

Consider the situation in which two optically smooth semi-infinite metals are separated by an ideal, nonconducting dielectric layer of uniform thickness. The geometry is shown schematically in Fig. 1, where 1, 2, and 3 designate properties and quantities associated with the upper metal, dielectric, and lower metal, respectively. When the metals, 1 and 3, are maintained at uniform but different temperatures, there will exist a net radiative heat flux between them. This radiative flux will depend on the reflectivities of the dielectric-metal interfaces as well as the temperatures of the metals and the thickness of the dielectric layer.

The influence of the separation between the two metals become important only when the separation is of the order of the characteristic wavelength of the thermal radiation as given by Wien's displacement formula [3, 14, 15]. Therefore, for dielectric thicknesses greater than the characteristic wavelength, one seeks a so-called thick film solution which neglects the small spacing effects of interference and radiation tunneling. This

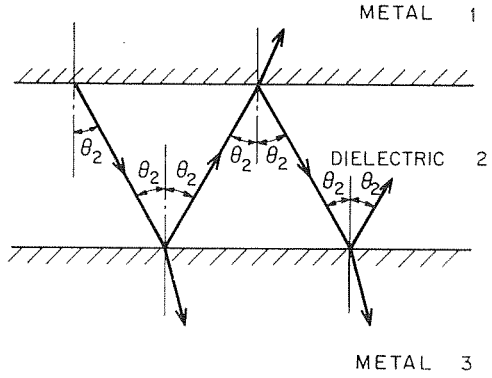

Fig. 1 Reflection and transmission of an electromagnetic wave in a dielectric layer between two metals

thick film solution is obtained by neglecting the effect of the phase of the waves and using the squares of the moduli of the amplitude reflection and transmission coefficients, i.e., the energy approach.

Thick Film Formulation. The starting point in the application of the energy approach is to consider the radiation emitted by the metal surfaces in an analysis similar to that used by Fragstein [16]. The approach taken avoids the problem of defining the equilibrium intensity of thermal radiation within the metal. Attention is focused on metal 1 at temperature T_1 whose emission is assumed to correspond to the equilibrium value, i.e., the resulting emission if both metals are at T_1. Under equilibrium conditions at temperature T_1, the radiation within the dielectric is unpolarized blackbody radiation whose intensity is given by Planck's law as

$$I_{b\nu}(T_1) = \frac{n_2^2 e_{b\nu}(T_1)}{\pi} = \frac{n_2^2 2h\nu^3}{c^2[\exp(h\nu/kT_1) - 1]} \tag{1}$$

The energy flux due to radiation contained within a differential solid angle $d\Omega$ about θ_2 incident upon and transmitted into the metal is given by

$$\tau_{21}(\theta_2, T_1, \nu)\frac{n_2^2 e_{b\nu}(T_1)}{\pi}\cos\theta_2 d\Omega \tag{2}$$

where τ_{21} is the transmissivity of the 2-1 interface.

Since at thermal equilibrium the radiation transmitted into the metal must be balanced by an equal amount emitted by the metal, equation (2) also represents the emission from metal 1 at angle θ_2. This specification of emission is assumed to hold even when metal 3 is at a temperature other than that of metal 1, i.e., for nonequilibrium conditions. The emission from metal 3 is obtained similarly as

$$\tau_{23}(\theta_2, T_3, \nu)\frac{n_2^2 e_{b\nu}(T_3)}{\pi}\cos\theta_2 d\Omega \tag{3}$$

Nomenclature

Ω = solid angle
τ = transmissivities of interfaces or free electron relaxation time
σ_0 = Stefan-Boltzmann constant
σ = d-c conductivity
$\bar{\sigma} = [\bar{\nu}(3\pi m\mu/Ne^2)^{1/2}]\sigma$ = dimensionless d-c conductivity
ν = frequency
$\bar{\nu} = [2(3\pi m/Ne^2\mu)^{1/2}/3\bar{\nu}]\nu$ = dimensionless frequency
ω = angular frequency
μ = magnetic permeability
$\xi = i\bar{\sigma}^3\bar{\nu}^3/(1 + i\bar{\sigma}\bar{\nu})^3$

Subscripts

1, 2, 3 = higher temperature metal, intervening dielectric layer, and lower temperature metal, respectively
b = blackbody value
h = hemispherical value
n = normal component
y = component parallel to interface
z = component perpendicular to interface
ν = spectral dependence

Superscripts

TE = transverse electric mode of polarization
TM = transverse magnetic mode of polarization
m = of or pertaining to metal
$'$ = denoting differentiation with respect to depth into the metal surface

With the two specifications of the angular and spectral distribution of the emitted radiation, the net flux is obtained by taking into account the multiple reflections and partial transmissions suffered by rays as they travel within the dielectric. The polarizing effect due to the difference in reflectivities or transmissivities for the two principle modes of polarization TM, transverse magnetic, and TE, transverse electric, is also taken into account by considering half of the blackbody intensities in equations (2) and (3) to be TE and half TM. The analysis is then carried out separately for TE and TM cases and added together to obtain the total net heat flux.

Fig. 1 shows the course of a typical ray as it is emitted by metal 1 at some angle θ_2 and undergoes the multiple reflections. If metal 1 is assumed to have the higher temperature, the net heat flux from 1 to 3 is the difference between the total energy emitted by 1 and that transmitted into 1. Considering either the TE or TM wave case, the total energy emitted by 1 is, according to equation (2)

$$\frac{1}{2}\int_0^\infty \int_\Omega \tau_{21}(\theta_2, T_1, \nu)\frac{n_2^2 e_{b\nu}(T_1)}{\pi}\cos\theta_2 d\Omega d\nu \tag{4}$$

The energy absorbed or transmitted into 1 originates from metal 1 or metal 3. That originating from 1 is

$$\frac{1}{2}\int_0^\infty \int_\Omega \tau_{21}(\theta_2, T_1, \nu)\frac{n_2^2 e_{b\nu}(T_1)}{\pi}\cos\theta_2 d\Omega d\nu[\rho_{23}(\theta_2, T_3, \nu) \times \tau_{21}(\theta_2, T_1, \nu) + \rho_{23}^2(\theta_2, T_3, \nu)\rho_{21}(\theta_2, T_1, \nu)\tau_{21}(\theta_2, T_1, \nu) + \ldots .$$

or

$$\frac{1}{2}\int_0^\infty \int_\Omega \frac{\rho_{23}(\theta_2, T_3, \nu)\tau_{21}^2(\theta_2, T_1, \nu)}{1 - \rho_{21}(\theta_2, T_1, \nu)\rho_{23}(\theta_2, T_3, \nu)} \times \frac{n_2^2 e_{b\nu}(T_1)}{\pi}\cos\theta_2 d\Omega d\nu \tag{5}$$

The energy flux transmitted into 1 originating from 3 is

$$\frac{1}{2}\int_0^\infty \int_\Omega \tau_{23}(\theta_2, T_3, \nu)\frac{n_2^2 e_{b\nu}(T_3)}{\pi}\cos\theta_2 d\Omega d\nu[\tau_{21}(\theta_2, T_1, \nu) + \rho_{21}(\theta_2, T_1, \nu)\rho_{23}(\theta_2, T_3, \nu)\tau_{21}(\theta_2, T_1, \nu) + \ldots .$$

or

$$\frac{1}{2}\int_0^\infty \int_\Omega \frac{\tau_{23}(\theta_2, T_3, \nu)\tau_{21}(\theta_2, T_1, \nu)}{1 - \rho_{21}(\theta_2, T_1, \nu)\rho_{23}(\theta_2, T_3, \nu)} \times \frac{n_2^2 e_{b\nu}(T_3)}{\pi}\cos\theta_2 d\Omega d\nu \tag{6}$$

so the portion of the heat flux corresponding to either TE or TM case is

$$q(\text{TE or TM}) = \frac{1}{2}\int_0^\infty \int_\Omega \left[\left(\tau_{21}(\theta_2, T_1, \nu) - \frac{\rho_{23}(\theta_2, T_3, \nu)\tau_{21}^2(\theta_2, T_1, \nu)}{1 - \rho_{21}(\theta_2, T_1, \nu)\rho_{23}(\theta_2, T_3, \nu)}\right) e_{b\nu}(T_1) - \left(\frac{\tau_{23}(\theta_2, T_3, \nu)\tau_{21}(\theta_2, T_1, \nu)}{1 - \rho_{21}(\theta_2, T_1, \nu)\rho_{23}(\theta_2, T_3, \nu)}\right) e_{b\nu}(T_3)\right]\frac{n_2^2}{\pi}\cos\theta_2 d\Omega d\nu$$

or

$$q(\text{TE or TM}) = \frac{1}{2}\int_0^\infty \int_\Omega \left[\frac{(1 - \rho_{21}(\theta_2, T_1, \nu))(1 - \rho_{23}(\theta_2, T_3, \nu))}{1 - \rho_{21}(\theta_2, T_1, \nu)\rho_{23}(\theta_2, T_3, \nu)}\right] \times \{e_{b\nu}(T_1) - e_{b\nu}(T_3)\}\frac{n_2^2}{\pi}\cos\theta_2 d\Omega d\nu \tag{7}$$

If a transmission factor is defined as

$$\mathsf{T} = \frac{(1 - \rho_{21}(\theta_2, T_1, \nu))(1 - \rho_{23}(\theta_2, T_3, \nu))}{1 - \rho_{21}(\theta_2, T_1, \nu)\rho_{23}(\theta_2, T_3, \nu)}$$

then adding together the TE and TM contributions, there obtains

$$q = \text{TE} + \text{TM} = \int_0^\infty \int_0^{\pi/2} (\mathsf{T}^{\text{TE}} + \mathsf{T}^{\text{TM}})\{e_{b\nu}(T_1) - e_{b\nu}(T_3)\} \times n_2^2 \cos\theta_2 \sin\theta_2 d\theta_2 d\nu \tag{8}$$

where the differential solid angle has been replaced by $2\pi \sin\theta_2 d\theta_2$.

Reflectivities. In order to obtain the net heat flux it is necessary to evaluate the integral in equation (8) so that a specification of the reflectivities is required. In the energy approach the reflectivities are obtained by squaring the modulus of the amplitude reflection coefficients as obtained from the boundary conditions at the interfaces. The most widely used formulation of the reflectivities is made through the Fresnel relations [17] and results in

$$\rho^{\text{TE}}(\theta_2, T, \nu) = |r^{\text{TE}}|^2 = \left|\frac{n_2\cos\theta_2 - (\tilde{n}^2 - n_2^2\sin^2\theta_2)^{1/2}}{n_2\cos\theta_2 + (\tilde{n}^2 - n_2^2\sin^2\theta_2)^{1/2}}\right|^2 \tag{9}$$

$$\rho^{\text{TM}}(\theta_2, T, \nu) = |r^{\text{TM}}|^2 = \left|\frac{\tilde{n}^2\cos\theta_2 - n_2(\tilde{n}^2 - n_2^2\sin^2\theta_2)^{1/2}}{\tilde{n}^2\cos\theta_2 + n_2(\tilde{n}^2 - n_2^2\sin^2\theta_2)^{1/2}}\right|^2 \tag{10}$$

The reflectivities given above in terms of the indices of refraction of the dielectric and metal are strictly applicable only when the current density within the metal is assumed to be proportional to the electric field at that point. With such an assumption, the Maxwell equations yield a solution for the electric field within the metal whose amplitude is damped exponentially with depth. Only for this form of electric field within the metal is a strict definition of a complex index of reflection possible.

In view of the above assumption made in defining the complex refractive index of the metal, a simplified free electron model, the Drude single electron theory [17], can be used to determine the frequency dependence of $\tilde{n}$ and of the reflectivities. In the long wavelength limit, the DSE theory approaches the Hagen-Rubens relation for the optical properties as would be expected. The use of the DSE or HR specification of the optical properties of metals in equations (9) and (10) and in the integration indicated by equation (8) constitutes the solution for the net radiant heat flux based on the DSE theory or HR relation.

A more general analysis has been performed by Reuter and Sondheimer [8], who did not make the classical assumption of current density proportional to electric field. Reuter and Sondhemier applied the Boltzmann transport equation to the free electrons to obtain the current density in terms of integrals involving the spatial variation of the electric field within the metal. This generalized current density, when used with the Maxwell equations, yields an integrodifferential equation which must be solved for the variation of the electric field amplitude. Once the form of the electric field within the metal is known, the so-called surface impedance can be calculated. This approach has been termed the anomalous skin effect theory.

Dingle [9] further investigated the anomalous skin effect and obtained series solutions for the normal surface impedance for cases of specular or diffuse electron reflection at the metal surface. In the infrared and far infrared portions of the spectrum to which the analysis has been restricted, the impedances for the TE and TM wave cases are nearly identical [10] and are given by Dingle [9]. For the case of diffuse electron reflection, which is the case most strongly indicated by experimental investigation, the nondimensional impedance obtained by Dingle is given as follows:

for $|\xi| \leq 0.8$

$$\frac{i}{W\bar{Z}} = 1.1547\xi^{1/2} - 0.2500\xi + 0.1540\xi^{3/2} - 0.1262\xi^{2} + 0.1188\xi^{5/2} - 0.1214\xi^{3} + 0.1307\xi^{7/2}[-0.148\xi^{4}] + 0.1685\xi^{9/2} + \ldots \quad (11)$$

for $|\xi| \geq 0.8$

$$\frac{i}{W\bar{Z}} = 1.1547(\pi\xi)^{1/3} - \{0.1351 \ln(\pi\xi) + 0.5330\} + 0.0416(\pi\xi)^{-1/3} - 0.0649(\pi\xi)^{-2/3} + (\pi\xi)^{-1}\{-0.0164 \ln(\pi\xi) + 0.0184\} + 0.0660(\pi\xi)^{-4/3} - 0.0307(\pi\xi)^{-5/3} + \ldots \quad (12)$$

where

$$\bar{Z} = (c^2/4\pi\omega\tau\mu v)Z$$
$$W = 1 + i\omega\tau$$
$$\xi = i\bar{\sigma}^2\bar{\nu}^3/(1 + i\bar{\sigma}\bar{\nu})^3$$
$$\bar{\sigma} = [v(3\pi m\mu/Ne^2)^{1/2}/c]\sigma$$
$$\bar{\nu} = [2c(3\pi m/Ne^2\mu)^{1/2}/3v]\nu$$

The desired reflectivities can be evaluated from the impedances yielded by the ASE theory by either of two methods. Since the complex refractive index no longer has the same significance (i.e., the field does not decay exponentially), equations (9) and (10) should be rewritten in terms of surface impedances. On the other hand, the complex refractive index can be redefined in terms of surface impedance and equations (9) and (10) can be used directly. The latter method will be employed here.

For the infrared and far infrared, the complex index of refraction can be redefined such that

$$\tilde{n}^2 = \left(\frac{4\pi}{cZ}\right)^2 + n_2^2 \sin^2\theta_2 \quad (13)$$

used in (9) and (10) will yield the correct reflectivities [8], [9], [10]. The net radiative heat flux based on the ASE theory is obtained from equation (8) by substituting the series (11) or (12) into (13) and then into (9) and (10) to obtain the reflectivities.

"Diffuse-Gray" Approximation. In addition to the energy approach, which yields the exact thick film solution, an approximation was sought in an effort to lessen the degree of complexity of the integration involved in the flux calculation. This approximation does not involve the assumption of diffuse or gray surfaces, rather, the manner in which angular and frequency dependences are taken into account results in a form for heat flux similar to that for the diffuse-gray case.

The transmission factors in equation (8) can be rewritten in terms of spectral angular emissivities as

$$\mathsf{T}(\theta_2, T_1, T_3, \nu) = [\epsilon_1^{-1}(\theta_2, T_1, \nu) + \epsilon_3^{-1}(\theta_2, T_3, \nu) - 1]^{-1} \quad (14)$$

for either TE or TM wave case. The approximation is made wherein the angular and frequency dependence of the transmission factor is approximated by using total hemispherical emissivities, i.e.,

$$\mathsf{T}(T_1, T_3) = [\epsilon_{1h}^{-1}(T_1) + \epsilon_{3h}^{-1}(T_3) - 1]^{-1} \quad (15)$$

where

$$\epsilon_h(T) = \frac{2}{\sigma_0 T^4}\int_0^{\infty}\int_0^{\pi/2}\left[1 - \frac{\rho^{\mathrm{TE}}(\theta, T, \nu) + \rho^{\mathrm{TM}}(\theta, T, \nu)}{2}\right] \times e_{b\nu}(T)\sin\theta_2\cos\theta_2 d\theta_2 d\nu \quad (16)$$

This approximation results in a net heat flux given by

$$q = \frac{n_2^2\sigma_0(T_1^4 - T_3^4)}{\epsilon_{1h}^{-1}(T_1) + \epsilon_{3h}^{-1}(T_3) - 1} \quad (17)$$

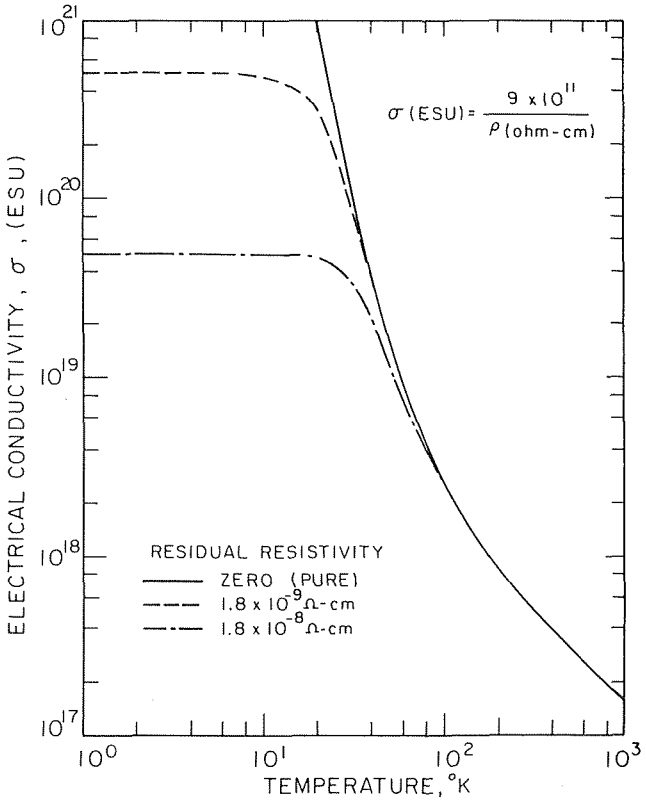

Fig. 2 Electrical conductivity of copper based on the Bloch-Gruneisen function and Matthiessen's rule

Results and Discussion

The exact thick film solution for the net radiative heat flux between parallel semi-infinite metals separated by a dielectric layer has been obtained by numerical integration of equation (8). The metals chosen for the calculations were both copper with a residual resistivity of 1.8×10^{-9} ohm-cm. The temperature dependence of the d-c electrical conductivity was obtained from the Bloch-Gruneisen function for ideal resistivity together with Matthiessen's rule to account for impurities or imperfections, as shown in Fig. 2. The actual electron mass and valence electron number density were used along with the Lorenz-Sommerfeld relation which relates the d-c electrical conductivity and free electron relaxation time.

A comparison of the heat flux predicted by the thick film solution based on ASE, DSE, and HR for the case of a vacuum gap, $n_2 = 1$, is shown in Fig. 3. Here the net radiative flux normalized by the total blackbody emissive power of the higher temperature surface, $q/\sigma_0 T_1^4$, is plotted as a function of the lower to higher temperature ratio, T_3/T_1, for various T_1. The fact that the anomalous skin effect results in higher values of spectral emissivity and absorptivity than those predicted by the DSE theory is illustrated in Fig. 3, where the flux based on ASE is always greater than that predicted by the DSE theory. When the level of temperatures is relatively high (T_1 high) and as T_3 approaches T_1, the DSE prediction approaches that of the ASE theory. For low temperature levels (T_1 low), the difference between ASE and DSE becomes pronounced as T_3/T_1 approaches zero and the anomalous skin effect becomes important.

Although the use of the HR relation in the prediction of the net heat flux is questionable, the calculations have been carried out and are presented in Fig. 3 for completeness. The fact that the HR relation is applicable only at very long wavelengths, i.e., only in predicting the absorptivity of the higher temperature metal for radiation from the much lower temperature metal, makes the prediction based on HR somewhat artificial but of possible utility as a basis for comparisons.

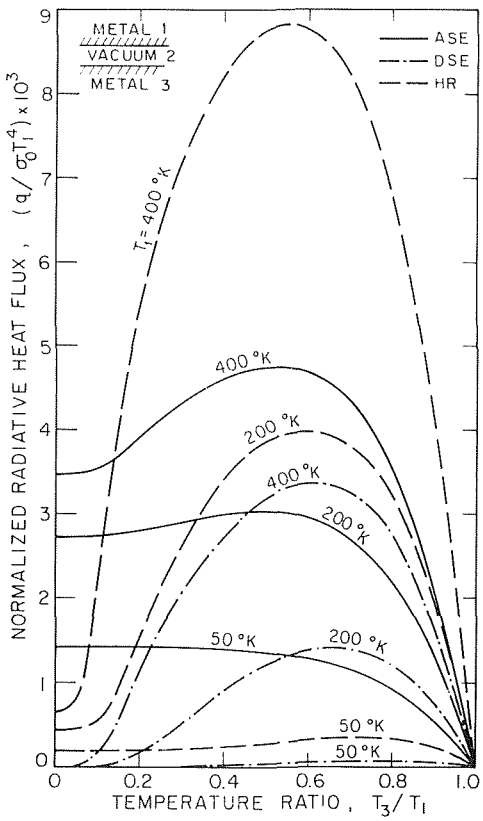

Fig. 3 Thick film solution for radiative heat transfer between two infinite parallel plates of copper with moderate impurity level (ρ_{0° K = 1.8 × 10^{-9} Ω cm)

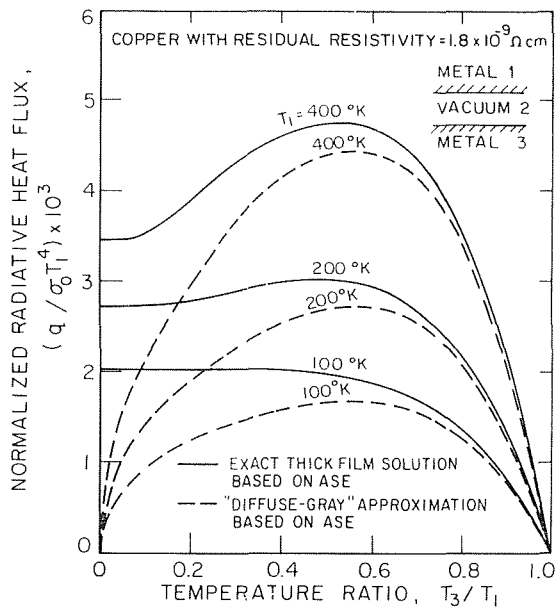

Fig. 4 Comparison of thick film solution and "diffuse-gray" approximation based on ASE

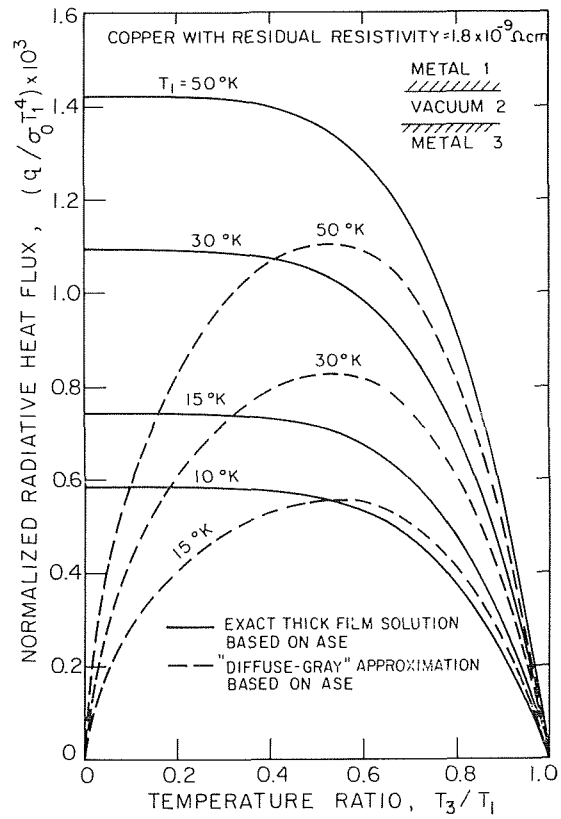

Fig. 5 Comparison of thick film solution and "diffuse-gray" approximation based on ASE

Figs. 4 and 5 represent a comparison of the exact thick film solution and the "diffuse-gray" approximation based on ASE for the case of an intervening vacuum. Quite clearly the approximation is quite accurate for temperature ratios greater than about 0.5. However, as the temperature ratio, T_3/T_1, approaches zero, the heat flux predicted by the "diffuse-gray" approximation approaches zero while the thick film solution approaches a finite value of heat flux.

It can be shown by using Dunkle's hemispherical emissivity factors [18] that the error introduced by using hemispherical emissivities to approximate the angular integration is negligible. Therefore, the error in the "diffuse-gray" approximation is due primarily to the use of total emissivities. The use of total emissivities fails to account for the situation in which T_3/T_1 is small so that the absorptivity, rather than the emissivity, of metal 3 plays the dominant role in determining the heat flux. Thus, whereas the total emissivity of 3 approaches zero as T_3 approaches zero and the "diffuse-gray" approximation predicts zero flux, the absorptivity of 3 remains finite and the thick film solution predicts a finite flux.

In order to obtain a better approximation to the thick film solution based on the ASE theory, a semiempirical approach was taken. The empirical formula was arrived at by noting that the net heat flux, when normalized by its value as T_3/T_1 approaches zero, can be well represented for $T_1 < 200$ K by

$$\frac{q(T_1, T_3)}{q\left(\frac{T_3}{T_1} \to 0\right)} = 1 - \left(\frac{T_3}{T_1}\right)^{4.5} \tag{18}$$

The limiting value of heat flux as $T_3/T_1 \to 0$ is obtained by using the total absorptivity of 3 in place of its total emissivity in the "diffuse-gray" approximation, i.e.,

$$q\left(\frac{T_3}{T_1} \to 0\right) \simeq \frac{n_2^2 \sigma_0 T_1^4}{[1.33\epsilon_{1n}^{-1}(T_1) + 1.33\alpha_{3n}^{-1}(T_1, T_3)]^{-1}} \tag{19}$$

where the normal absorptivity of 3 is given by

$$\alpha_{3n}(T_1, T_3) = \int_0^\infty [1 - \rho_{3n}(\nu, T_3)] \frac{e_{b\nu}(T_1)}{\sigma_0 T_1^4} \, d\nu \tag{20}$$

and unity has been neglected in the denominator of equation (19). Also, the hemispherical values have been replaced by 1.33 times the normal value of emissivity and absorptivity. Approximate expressions for the total radiation properties based on ASE can

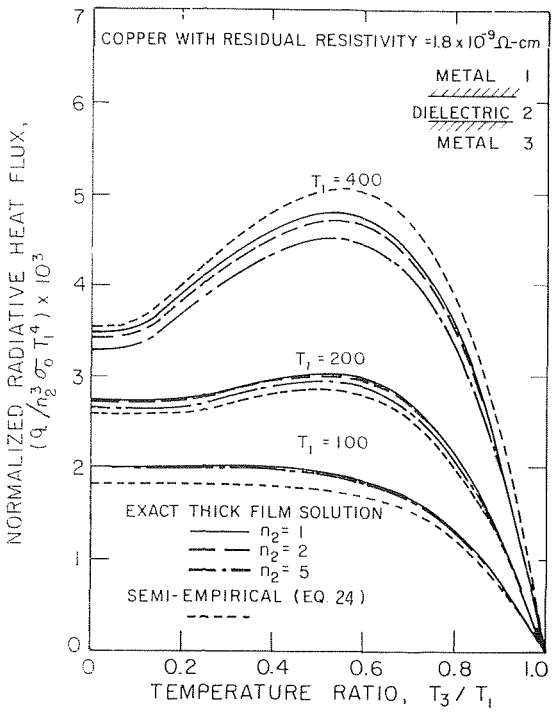

Fig. 6 Semiempirical curve and thick film solution based on ASE for various intervening dielectrics

be obtained for metals below room temperatures [12] as:

$$\epsilon_{1n}(T_1) = n_2(2.37)\bar{\nu}_1\left(\frac{3}{4} + \frac{\sqrt{3}}{\bar{\sigma}_1(T_1)}\right)\frac{A_1(T_1)}{1 + 1.70A_1(T_1)} \quad (21)$$

$$\alpha_{3n}(T_1, T_3) = n_2(2.37)\bar{\nu}_3\left(\frac{3}{4} + \frac{\sqrt{3}}{\bar{\sigma}_3(T_3)}\right)\frac{A_3(T_1)}{1 + 1.70A_3(T_1)} \quad (22)$$

where

$$A(T) = \frac{3}{2}\left[\frac{2}{3\bar{\nu}}\left(\frac{3\pi m}{Ne^2\mu}\right)^{1/2}\frac{kT}{h}\right]^{2/3} \quad (23)$$

and the multiplicative factor 1.70 has been added to the denominator to improve accuracy. If metals 1 and 3 are the same,

$$\frac{q}{n_2^3\sigma_0 T_1^4} \simeq \frac{(1.33)(2.37)\bar{\nu}B_1B_3A(T_1)}{(B_1 + B_3)(1 + 1.70A(T_1))}\left[1 - \left(\frac{T_3}{T_1}\right)^{4.5}\right] \quad (24)$$

where

$$B = \left(\frac{3}{4} + \frac{\sqrt{3}}{\bar{\sigma}(T)}\right) \quad (25)$$

This normalized heat flux is plotted in Fig. 6 together with the thick film solution for various values of the index of refraction of the dielectric layer. It is noted that the agreement is fairly good, so for practical calculation, equation (24) can be used in place of the integration of equation (8).

It is of interest to note that at low temperatures the net flux becomes proportional to the cube of the index of refraction of the intervening dielectric as seen from the thick film solution. This dependence is predicted by the semiempirical formula and is due to the impedance becoming very small at low temperature so that by expanding (9) for the TE case

$$\rho(\theta_2, T, \nu) = 1 - \epsilon(\theta_2, T, \nu) \simeq 1 - \frac{c\,\mathrm{Re}(Z)}{2\pi} n_2 \cos\theta_2 \quad (26)$$

With this approximation, the transmission factor given by equation (14) becomes

$$\mathsf{T}(\theta_2, T_1, T_3, \nu) \simeq \frac{cn_2\cos\theta_2}{2\pi}\left(\frac{1}{\mathrm{Re}(Z_1)} + \frac{1}{\mathrm{Re}(Z_3)}\right)^{-1} \quad (27)$$

The same n_2 dependence can be shown for the TM wave case. Using these transmission coefficients in equation (8) results in the cubic dependence at low temperatures.

References

1 Tien, C. L., and Cravalho, E. G., "Thermal Radiation of Solids at Cryogenic Temperatures," *Advances in Cryogenic Heat Transfer*, Chemical Engineering Progress Symposium Series, Vol. 64, No. 87, 1968, p. 56.

2 Caren, R. P., and Cunnington, G. R., "Heat Transfer in Multilayer Insulation Systems," *Advances in Cryogenic Heat Transfer*, Chemical Engineering Progress Symposium Series, Vol. 64, No. 87, 1968, p. 67.

3 Boehm, R. F. and Tien, C. L., "Small Spacing Analysis of Radiative Transfer Between Parallel Metallic Surfaces," JOURNAL OF HEAT TRANSFER, TRANS. ASME, Series C, Vol. 92, No. 3, Aug. 1970, pp. 405–411.

4 Domoto, G. A., Boehm, R. F. and Tien, C. L., "Experimental Investigation of Radiative Transfer Between Metallic Surfaces at Cryogenic Temperatures," JOURNAL OF HEAT TRANSFER, TRANS. ASME, Series C, Vol. 92, No. 3, Aug. 1970, pp. 412–417.

5 Parker, W. J., and Abbott, G. L., "Theoretical and Experimental Studies of the Total Emittance of Metals," *Symposium on Thermal Radiation of Solids*, NASA SP-55, 1965, p. 11.

6 Rolling, R. E., and Tien, C. L., "Radiant Heat Transfer for Nongray Metallic Surfaces at Low Temperatures," *Thermophysics of Spacecraft and Planetary Bodies*, Academic Press, New York, 1967, p. 677.

7 Holt, V. E., Grosh, R. J., and Geynet, R., "Evaluation of the Net Radiant Heat Transfer Between Specularly Reflecting Plates including Computed Emissivities," *International Journal of Heat and Transfer*, Vol. 6, 1963, p. 755.

8 Reuter, G. E. H., and Sondheimer, E. H., "The Theory of the Anomalous Skin Effect in Metals," *Proceedings of the Royal Society*, London, Series A, Vol. 195, 1948, p. 336.

9 Dingle, R. B., "The Anomalous Skin Effect and the Reflectivity of Metals. I," *Physica*, Vol. 19, 1953, p. 311.

10 Collins, J. G., "The Theory of the Anomalous Skin Effect in Metals for Obliquely Incident Radiation," *Applied Scientific Research*, Vol. 7B, 1958, p. 1.

11 Bennett, H. E., Bennett, J. M., Ashley, E. J., and Motyko, R. J., "Verification of the Anomalous-Skin-Effect Theory for Silver in the Infrared," *Physical Review*, Vol. 165, 1968, p. 755.

12 Domoto, G. A., Boehm, R. F., and Tien, C. L., "Predictions of the Total Emissivity of Metals at Cryogenic Temperatures," to be published in *Advances in Cryogenic Engineering*, Vol. 14, 1969.

13 Beckman, P., and Spizzichino, A., *The Scattering of Electromagnetic Waves From Rough Surfaces*, The Macmillan Company, New York, 1963, p. 10.

14 Cravalho, E. G., Tien, C. L., and Caren, R. P., "Effect of Small Spacing on Radiative Transfer Between Two Dielectrics," JOURNAL OF HEAT TRANSFER, TRANS. ASME, Series C, Vol. 89, 1967, p. 351.

15 Caren, R. P., "Theory of Electromagnetic Tunneling of Thermal Radiation between Highly Absorbing Media," *Proceedings of the Fourth Symposium on Thermophysical Properties*, ASME, 1968, p. 243.

16 Fragstein, "Energy Transfer at the Interface Between Two Absorbing Media with an Emphasis on the Heat Radiation in Absorbing Bodies," *Ann. Physik*, Vol. 7, 1950, p. 63.

17 Born, M. and Wolf, E., *Principles of Optics*, Pergamon Press, New York, 1965, p. 624.

18 Dunkle, R. V., "Emissivity and Inter-Reflection Relationships for Infinite Parallel Specular Surfaces," *Symposium on Thermal Radiation of Solids*, NASA SP-55, 1965, p. 39.

R. F. BOEHM
Assistant Professor of Mechanical Engineering, University of Utah, Salt Lake City, Utah

C. L. TIEN
Professor of Mechanical Engineering, University of California, Berkeley, Calif.

Small Spacing Analysis of Radiative Transfer Between Parallel Metallic Surfaces[1]

An attempt is made on the basis of electromagnetic theory to predict spacing effects on the radiative transfer between two closely-spaced, semi-infinite metals separated by a nonconducting dielectric. Electromagnetic energy transmission factors are derived for a general, three-medium system and their simplification for the metal-dielectric-metal system is shown. The net energy flux is calculated with these transmission factors and the estimated intensities in the metals. Numerical results are given which exhibit the effects of metal spacing, metal type, temperature level, and type of dielectric. Variations in the heat flux of several orders of magnitude are shown to exist in a system whereas the Stefan-Boltzmann relation indicates a constant flux, independent of spacing.

Introduction

This is the second of three papers considering radiative transfer between metallic surfaces at cryogenic temperatures. In the first paper [1],[2] theoretical results have been presented for the case when the surface spacing is large as compared to the characteristic wavelength of radiation involved. The present paper considers the problem associated with small spacings. An experimental study is presented in the third paper [2]. The practical importance of the small spacing effect on radiative transfer can be readily realized by considering the magnitudes of the spacing between two adjacent radiation shields and the characteristic wavelength of radiation involved in cryogenic insulation systems. In commonly used multilayer insulations for cryogenic applications [3], the spacing between two shields is often of the order of 10^{-3} cm or less while the characteristic wavelength of radiation according to Wien's displacement law ranges from 10^{-2} cm at liquid helium temperatures to 10^{-3} cm at liquid nitrogen temperatures.

The effect of small spacings on radiative transfer between two surfaces has its origin, on the basis of electromagnetic theory, in the optical phenomena of frustrated total internal reflection (i.e., radiation tunneling) and wave interference [4]. Emslie [5] first pointed out the applicability of these optical concepts to the calculation of radiative transfer between solids. A quantitative analysis was next performed by Cravalho, Tien, and Caren [6], who considered a system of two dielectrics separated by a vacuum gap. Caren [7] has recently made a valuable analysis of the radiation tunneling between two metals.

[1] This work constitutes part of the PhD thesis of R. F. Boehm, entitled, "Spacing Effects of Radiative Transfer Between Metals," Department of Mechanical Engineering, University of California, Berkeley, Calif., 1968. The authors wish to acknowledge the support of this work by NASA Grant NGR-05-003-285.

[2] Numbers in brackets designate references at end of paper.

Contributed by the Heat Transfer Division and presented at the Winter Annual Meeting, Los Angeles, Calif., November 16–20, 1969, of The American Society of Mechanical Engineers. Manuscript received by Heat Transfer Division, January 2, 1969; revised manuscript received July 1, 1969. Paper No. 69-WA/HT-8.

Nomenclature

c = speed of light in a vacuum
d = metal spacing distance
$\mathbf{E}$ = electric field vector
e = spectral emissive power
$\mathbf{H}$ = magnetic field vector
I = radiant intensity
i = imaginary operator = $\sqrt{-1}$
k = absorption coefficient
$\mathbf{k}$ = complex propagation vector
n = refractive index
$\tilde{n}$ = complex refractive index = $n + ik$
0 = order of magnitude
P, Q, R, S = groups of variables in transmission factor calculation
q = heat flux
$\mathbf{r}$ = position vector
$\mathbf{S}$ = Poynting vector
$\mathbf{T}$ = transmission factor
T = temperature
x, y, z = coordinate directions

(Continued on next page)

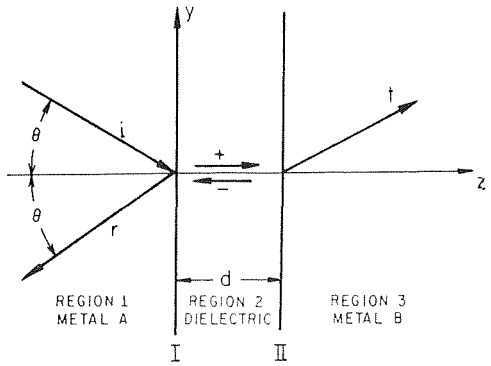

Fig. 1 The system under consideration

Formulation of the Problem

It is the purpose of this work to attempt an analytical prediction of the total radiation flux between two metals that are separated by a small distance, d. The physical system shown schematically in Fig. 1, is assumed to consist of two semi-infinite metals of uniform but different temperatures, T_1 and T_3. An ideal (nonconducting) dielectric is assumed to fill the space between the metals.

To calculate the net energy transfer, it is convenient first to evaluate the unidirectional heat flux (e.g., the flux that penetrates the second medium as a result of the intensity level of the first medium). From the usual definition of intensity [8] the unidirectional heat flux across the second boundary can be written

$$q_{13} = \int_0^\infty \int_\Omega I_{13} \cos\theta d\Omega d\nu \tag{1}$$

where the symbol Ω represents integration of the solid angle Ω over a half space. The usual definition of the electromagnetic energy transmission factor allows the transmitted intensity, I_{13}, to be expressed in terms of the incident intensity, I_1,

$$\mathsf{T}_{13} = I_{13}/I_1 \tag{2}$$

If the intensity is isotropic and unpolarized, as will be assumed here, the transmission factor can be taken to be the average of transverse magnetic (TM) and transverse electric (TE) polarization transmission factors [4]. In addition, the solid angle is conveniently expressed in terms of spherical coordinates θ and ϕ, allowing integration over ϕ to be readily carried out. Hence the flux in the second metal due to the intensity in the first can be written as

$$q_{13} = \pi \int_0^\infty \int_0^{\pi/2} I_1(\mathsf{T}_{13}^{\mathrm{TM}} + \mathsf{T}_{13}^{\mathrm{TE}}) \cos\theta \sin\theta d\theta d\nu \tag{3}$$

Utilization of the foregoing equation requires that the intensity within the metal be given. This can be accomplished by estimating the intensity in a metal necessary for equilibrium to exist across a metal-vacuum interface, assuming the vacuum be filled with blackbody radiation. Fragstein [9] corrected a result given by Laue [10] and found that an energy balance for normal incidence on a general interface yields:

$$I_1(n_1^2 + k_1^2)/n_1^4 = I_3(n_3^2 + k_3^2)/n_3^4 \tag{4}$$

where n and k are the refractive index and the absorption coefficient for the given medium, and I is the specific intensity. Although the normal incidence assumption is a simplification of the exact situation, it should be a good approximation on account of the isotropic nature of the radiation field. The intensity in a metal can now be expressed in terms of the blackbody emissive power based on the temperature of metal 1,

$$I_1 = \frac{1}{\pi} \frac{n_1^4}{n_1^2 + k_1^2} e_b(T_1) \tag{5}$$

The unidirectional flux thus becomes

$$q_{13} = \int_0^\infty \int_0^{\pi/2} (\mathsf{T}_{13}^{\mathrm{TM}} + \mathsf{T}_{13}^{\mathrm{TE}}) \frac{n_1^4}{n_1^2 + k_1^2} e_b(T_1) \times \cos\theta \sin\theta d\theta d\nu \tag{6}$$

where the transmission factors are to be specified in the next section. With the other unidirectional flux found in a similar manner, the net energy flux is given by

$$q = q_{13} - q_{31} \tag{7}$$

Transmission Factors Derivation

General Three Media Case. A very important aspect of the present work is the derivation of the transmission factors, which will now be considered. The method is one patterned after Caren [7]. In the present analysis it will be assumed that two parallel, semi-infinite media are separated by another medium. All three media are isotropic, nonmagnetic, contain no externally induced charges, and can be represented by a complex index of refraction. It is therefore expected [4] that, in general, the waves present will be plane and inhomogeneous in nature. As an ex-

Nomenclature

α = propagation vector for the interference case
β = propagation vector for the tunneling case
ϵ = electrical permittivity
Θ = square of electric field amplitude ratio
θ = angle of incidence measured from normal
λ = wavelength
μ = magnetic permeability
ν = frequency
Φ = square of magnetic field amplitude ratio
ϕ = angle of incidence or polar coordinate angle
χ = phase angle or angle between amplitude planes and phase planes
Ω = solid angle
ω = angular frequency $= 2\pi\nu$

Subscripts

b = blackbody
c = critical value
I = interference
i = incident
max = value at maximum point
0 = reference to base plane
r = reflected
T = tunneling
t = transmitted
x, y, z = coordinate directions
1, 3 = denotes particular metal
2 = denotes intervening dielectric

Superscripts

TE = transverse electric
TM = transverse magnetic
1 = real part of complex number
2 = imaginary part of complex number
+ = direction in intervening material from incident to transmitted
− = direction in intervening material from transmitted to incident
′ = denotes coordinate system beginning at second interface
* = complex conjugate

ample, then, the electric field can be represented as

$$\tilde{\mathbf{E}} = \tilde{\mathbf{E}}_0 \exp\{i[\tilde{\mathbf{k}}\cdot\mathbf{r} - \omega]t\} \tag{8}$$

A tilde represents a complex quantity, while an asterisk denotes a complex conjugate. Boldface type represents a vector quantity (hence $\tilde{\mathbf{k}}^*$ represents the complex conjugate propagation vector, $\tilde{\mathbf{k}}^* = \mathbf{k}^1 - i\mathbf{k}^2$).

Consider first the TE case. The x-components of the incident, reflected, "+," and "−" waves (note that in Fig. 1 the x-component is the only one present) are written similar to equation (8). The transmitted wave, however, is given as

$$\tilde{E}_{tx} = \tilde{E}_{t0x} \exp\{i[\tilde{\mathbf{k}}_t\cdot\mathbf{r}' - \omega t]\} \tag{9}$$

where $\mathbf{r}'$ applies to a coordinate system with datum at $z = d$ (see Fig. 1). Application of the continuity of field and propagation quantities at the first interface yields

$$\tilde{E}_{i0x} + \tilde{E}_{r0x} = \tilde{E}_{0x}{}^{+} + \tilde{E}_{0x}{}^{-} \tag{10}$$

$$\tilde{H}_{i0y} + \tilde{H}_{r0y} = \tilde{H}_{0y}{}^{+} + \tilde{H}_{0y}{}^{-} \tag{11}$$

and

$$\tilde{k}_{iy} = \tilde{k}_{ry} = \tilde{k}_y{}^{+} = \tilde{k}_y{}^{-} \tag{12}$$

where the latter relationship is required so that equations (10) and (11) hold anywhere on the boundary.

The Maxwell's equation [11] which involves the vector product of the electric field and the propagation vector is used to eliminate the magnetic field quantities of equation (10). Assuming that the permeability is essentially unity, and noting that

$$\tilde{k}_{iz} = -\tilde{k}_{rz} \tag{13}$$

and

$$\tilde{k}_z{}^{+} = -\tilde{k}_z{}^{-} \tag{14}$$

equation (11) becomes:

$$2\tilde{k}_{iz}\tilde{E}_{i0x} = \tilde{E}_{0x}{}^{+}(\tilde{k}_{tz} + \tilde{k}_z{}^{+}) + \tilde{E}_{0x}{}^{-}(\tilde{k}_{iz} - \tilde{k}_z{}^{+}) \tag{15}$$

where equation (10) has been used to eliminate the reflected electric field component.

A similar procedure is performed at the second interface. Thus, at $z = d(r_z' = 0, r_z = d)$

$$\tilde{E}_x{}^{+} + \tilde{E}_x{}^{-} = \tilde{E}_{tx} \tag{16}$$

$$\tilde{H}_y{}^{+} + \tilde{H}_y{}^{-} = \tilde{H}_{ty} \tag{17}$$

$$\tilde{k}_y{}^{+} = \tilde{k}_y{}^{-} = \tilde{k}_{ty} \tag{18}$$

Since the form of the wave in the intervening material is given similar to equation (8), equation (16) can be written as

$$\tilde{E}_{0x}{}^{+} \exp\{i\tilde{k}_z{}^{+}d\} + \tilde{E}_{0x}{}^{-} \exp\{-i\tilde{k}_z{}^{+}d\} = \tilde{E}_{t0x} \tag{19}$$

The abovementioned Maxwell equation is again invoked to express equation (17) in the following form:

$$\tilde{k}_z{}^{+}(E_{0x}{}^{+} \exp\{i\tilde{k}_z{}^{+}d\} - \tilde{E}_{0x}{}^{-} \exp\{-i\tilde{k}_z{}^{+}d\}) = \tilde{k}_{tz}\tilde{E}_{t0x} \tag{20}$$

Eliminating $\tilde{E}_{0x}{}^{+}$ and $\tilde{E}_{0x}{}^{-}$ between equations (19) and (20) and substituting the result into equation (15) there results after rearrangement,

$$\tilde{E}_{t0x} = \frac{4\tilde{k}_{iz}\tilde{k}_z{}^{+}\tilde{E}_{i0x}}{(\tilde{k}_{iz} + \tilde{k}_z{}^{+})(\tilde{k}_{tz} + \tilde{k}_z{}^{+}) \exp\{-i\tilde{k}_z{}^{+}d\} - (\tilde{k}_{iz} - \tilde{k}_z{}^{+})(\tilde{k}_{tz} - \tilde{k}_z{}^{+}) \exp\{i\tilde{k}_z{}^{+}d\}}. \tag{21}$$

Hence, the transmitted field has been found in terms of the incident field and the propagation vectors for the TE case.

The transmission factor through the intervening material is found from the ratio of the energy crossing interface II to that impinging upon interface I. Energy flow in a specific direction is readily found from consideration of the component of the Poynting vector in that direction [11]. For the transmitted energy it gives

$$\langle \mathbf{S}_{t0z} \rangle = \frac{1}{2} \operatorname{Re}\{\tilde{E}_t{}^{*} \times \tilde{H}_t\}_{z=d} \tag{22}$$

where the symbols $\langle\ \rangle$ represent the time averaged value. Eliminating H in the same manner as before, there results:

$$\langle \mathbf{S}_{t0z} \rangle = \frac{1}{2\omega} |\tilde{E}_{t0x}|^2 \operatorname{Re}\{\tilde{k}_{tz}\} = \frac{1}{2\omega} |\tilde{E}_{t0x}|^2 k_{tz}{}^{1} \tag{23}$$

Proceeding similarly for the incident energy gives

$$\langle \mathbf{S}_{i0z} \rangle = \frac{1}{2\omega} |\tilde{E}_{i0x}|^2 k_{iz}{}^{1} \tag{24}$$

The definition of the incident energy in this manner is open to question. Several authors (e.g., see the works of Fragstein [9], Knittl [12], and Salzberg [13]) have shown that waves incident on the interface between a general class of adjoining materials form a standing wave from the interaction of the incident wave and the reflected wave. In fact, in the close proximity to the interface there is an energy present in addition to the incident, reflected and transmitted energy. Equation (24) should hold, however, a short distance from the interface.

Now define the transverse electric transmission factor as

$$\mathbf{T}^{\mathrm{TE}} = \langle \mathbf{S}_{t0z} \rangle / \langle \mathbf{S}_{i0z} \rangle = \Theta k_{tz}{}^{1}/k_{iz}{}^{1} \tag{25}$$

where the definition

$$\Theta \equiv |\tilde{E}_{t0x}|^2 / |\tilde{E}_{i0x}|^2 \tag{26}$$

has been used. By use of equation (21), equation (26) can be expressed explicitly as

$$\Theta = \frac{16|\tilde{k}_{iz}|^2 |k_z{}^{+}|^2}{(P_i + 2R_i)(P_t + 2R_t) \exp\{2k_z{}^{2+}d\} - (Q_i - 2iS_i)(Q_t - 2iS_t) \exp\{2ik_z{}^{1+}d\} - (Q_i + 2iS_i)(Q_t + 2iS_t) \exp\{-2ik_z{}^{1+}d\} + (P_i - 2R_i)(P_t - 2R_t) \exp\{-2k_z{}^{2+}d\}}. \tag{27}$$

where, for example,

$$P_i \equiv |\tilde{k}_{iz}|^2 + |\tilde{k}_z{}^{+}|^2 \tag{28}$$

$$Q_i \equiv |\tilde{k}_{iz}|^2 - |\tilde{k}_z{}^{+}|^2 \tag{29}$$

$$R_i \equiv k_{iz}{}^{1}k_z{}^{1+} + k_{iz}{}^{2}k_z{}^{2+} \tag{30}$$

$$S_i \equiv k_{iz}{}^{1}k_z{}^{2+} - k_{iz}{}^{2}k_z{}^{1+} \tag{31}$$

Now consider the TM case. Following the basic derivation of Caren, the boundary conditions given in equations (10), (11), (16), and (17) are replaced by the following:

at boundary I

$$\tilde{H}_{i0x} + \tilde{H}_{r0x} = \tilde{H}_{0x}^{+} + \tilde{H}_{0x}^{-} \tag{32}$$

$$\tilde{E}_{i0y} + \tilde{E}_{r0y} = \tilde{E}_{0y}^{+} + \tilde{E}_{0y}^{-} \tag{33}$$

while at boundary II

$$\tilde{H}_{x}^{+} + \tilde{H}_{x}^{-} = \tilde{H}_{tx} \tag{34}$$

$$\tilde{E}_{y}^{+} + \tilde{E}_{y}^{-} = \tilde{E}_{ty} \tag{35}$$

In the TE case, the H component was eliminated in favor of the E component. Here, however, the procedure is the opposite. The Maxwell equation [11]

$$\tilde{E}_{y} = \omega\mu\tilde{k}_{z}\tilde{H}_{x}/\tilde{\mathbf{k}}\cdot\tilde{\mathbf{k}} \tag{36}$$

is used for this purpose. Note that additionally [11]

$$\tilde{\mathbf{k}}\cdot\tilde{\mathbf{k}} = \omega^2\tilde{\epsilon}\mu \tag{37}$$

Eliminating the electric component in equation (33) by use of the foregoing equations yields

$$\frac{\tilde{k}_{iz}}{\tilde{\epsilon}_i}\tilde{H}_{i0x} + \frac{\tilde{k}_{rz}}{\tilde{\epsilon}_r}\tilde{H}_{r0x} = \frac{\tilde{k}_{z}^{+}}{\tilde{\epsilon}}\tilde{H}_{0x}^{+} + \frac{\tilde{k}_{z}^{-}}{\tilde{\epsilon}}\tilde{H}_{0x}^{-} \tag{38}$$

where the $\tilde{\epsilon}$ without subscript refers to the intervening material. Equations (13) and (14) can be employed here in conjunction with the fact

$$\tilde{\epsilon}_i = \tilde{\epsilon}_r \tag{39}$$

and equation (32). The result is

$$\tilde{H}_{t0x} = \frac{4(\tilde{\epsilon}\tilde{k}_{iz})(\tilde{\epsilon}_i\tilde{k}_{z}^{+})\tilde{H}_{i0x}}{(\tilde{\epsilon}\tilde{k}_{iz} + \tilde{\epsilon}_i\tilde{k}_{z}^{+})(\tilde{\epsilon}\tilde{k}_{tz} + \tilde{\epsilon}_i\tilde{k}_{z}^{+})\exp\{-i\tilde{k}_{z}^{+}d\} - (\tilde{\epsilon}\tilde{k}_{iz} - \tilde{\epsilon}_i\tilde{k}_{z}^{+})(\tilde{\epsilon}\tilde{k}_{tz} - \tilde{\epsilon}_i\tilde{k}_{z}^{+})\exp\{ik_{z}^{+}d\}} \tag{40}$$

and some distinct similarities to equation (21) are noted.

With the definition of the transmitted and incident energy for the TM case, the transmission factor is found to be

$$\mathsf{T}^{\mathrm{TM}} = \langle \mathsf{S}_{t0z}\rangle/\langle \mathsf{S}_{i0z}\rangle = \Phi\frac{|\tilde{\epsilon}_i|^2(\epsilon_t{}^1k_{tz}{}^1 + \epsilon_t{}^2k_{tz}{}^2)}{|\tilde{\epsilon}_t|^2(\epsilon_i{}^1k_{iz}{}^1 + \epsilon_i{}^2k_{iz}{}^2)} \tag{41}$$

where

$$\Phi \equiv |\tilde{H}_{t0x}|^2/|\tilde{H}_{i0x}|^2 \tag{42}$$

Hence, with equation (40), there results

$$\Phi = \frac{16|\tilde{\epsilon}\tilde{k}_{iz}|^2|\tilde{\epsilon}_i\tilde{k}_{z}^{+}|^2}{(P_i + 2R_i)(P_t + 2R_t)\exp\{2k_{z}^{2+}d\} - (Q_i - 2iS_i)(Q_t - 2iS_t)\exp\{-2ik_{z}^{1+}d\} - (Q_i + 2iS_i)(Q_t + 2iS_t)\exp\{-2ik_{z}^{1+}d\} + (P_i - 2R_i)(P_t - 2R_t)\exp\{-2k_{z}^{2+}d\}} \tag{43}$$

where

$$P_i \equiv |\tilde{\epsilon}\tilde{k}_{iz}|^2 + |\tilde{\epsilon}_i\tilde{k}_{z}^{+}|^2 \tag{44}$$

$$Q_i \equiv |\tilde{\epsilon}\tilde{k}_{iz}|^2 - |\tilde{\epsilon}_i\tilde{k}_{z}^{+}|^2 \tag{45}$$

$$R_i \equiv (\epsilon^1k_{iz}{}^1 - \epsilon^2k_{iz}{}^2)(\epsilon_i{}^1k_{z}{}^{1+} - \epsilon_i{}^2k_{z}{}^{2+}) + (\epsilon^1k_{iz}{}^2 + \epsilon^2k_{iz}{}^1)(\epsilon_i{}^1k_{z}{}^{2+} + \epsilon_i{}^2k_{z}{}^{1+}) \tag{46}$$

$$S_i \equiv (\epsilon^1k_{iz}{}^1 - \epsilon^2k_{iz}{}^2)(\epsilon_i{}^1k_{z}{}^{2+} + \epsilon_i{}^2k_{z}{}^{1+}) - (\epsilon^1k_{iz}{}^2 + \epsilon^2k_{iz}{}^1)(\epsilon_i{}^1k_{z}{}^{1+} - \epsilon_i{}^2k_{z}{}^{2+}) \tag{47}$$

Transmission Factors for a Metal-Dielectric-Metal System. Since the transmission factors given in the previous section are quite general, they can be reduced significantly for a particular system of interest. By appropriate combination of Maxwell's equations for a homogeneous material containing no externally introduced charges or currents [11], it can be shown that

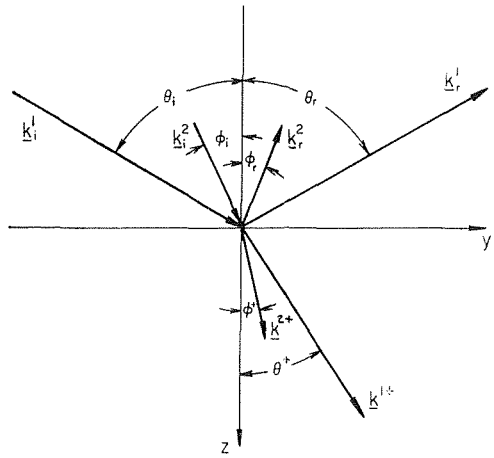

Fig. 2 Impingement of a nonhomogeneous wave on a boundary

$$\tilde{\mathbf{k}}\cdot\tilde{\mathbf{k}} = \tilde{\mu}\tilde{\epsilon}\omega^2 = (n + ik)^2\omega^2/c^2 = |\mathbf{k}^1|^2 - |\mathbf{k}^2|^2 + 2i\mathbf{k}^1\cdot\mathbf{k}^2 \tag{48}$$

In what follows, it will be assumed that

$$\tilde{\mu} = \mu^1 = 1 \tag{49}$$

which is essentially true for all materials at optical frequencies. Hence from equation (48) the relationship between the propagation vectors and the electrical permittivity can be determined. In particular, it can be shown that

$$|\mathbf{k}^1| = \frac{\omega}{c\sqrt{2}}[(n^2 - k^2) + \{(n^2 - k^2)^2 + 4n^2k^2/\cos^2\chi\}^{1/2}] \tag{50}$$

$$|\mathbf{k}^2| = \frac{\omega}{c\sqrt{2}}[-(n^2 - k^2) + \{(n^2 - k^2)^2 + 4n^2k^2/\cos^2\chi\}^{1/2}] \tag{51}$$

where χ is the angle between the planes of constant phase and the planes of constant amplitude.

With the magnitude of the propagation vector determined from the optical properties as outlined in the foregoing, the determination of its direction will complete the specification. For the sake of completeness, consider impingement of a nonhomogeneous wave on a metal-metal boundary as represented in Fig. 2 [11]. Planes perpendicular to the $\mathbf{k}^1$ vector represent planes of constant phase, while planes perpendicular to the $\mathbf{k}^2$ vector represent planes of constant amplitude. Identical space dependence of the electric and magnetic vector anywhere along the boundary requires that the component of the propagation vector parallel to the boundary must be continuous. A good example is the boundary condition given in equation (12) or (18), viz.

$$\tilde{k}_{iy} = \tilde{k}_{y}^{+} = \tilde{k}_{ty} \tag{52}$$

As can be seen from equations (48), (50), and (51), the complex propagation vector for planes of constant phase in the dielectric must be entirely real or entirely imaginary. It follows that the y-component must be either completely real or completely imaginary.

Snell's law, which is a result of equation (52), requires that: (see Fig. 2)

$$|\mathbf{k}_i^1| \sin \theta_i = |\mathbf{k}^{1+}| \sin \theta^+ \tag{53}$$

$$|\mathbf{k}_i^2| \sin \phi_i = |\mathbf{k}^{2+}| \sin \phi^+ \tag{54}$$

where the angles refer to the direction of particular vector makes with the normal. Hence, if the "+" region in Fig. 2 is taken to be a dielectric, equation (51) indicates that

$$|\mathbf{k}^{2+}| = 0 \tag{55}$$

and since $|\mathbf{k}_i^2| \neq 0$, then

$$\sin \phi_i = 0 \tag{56}$$

The important conclusion follows that the planes of constant amplitude in a parallel composite system containing at least one dielectric must be parallel to the interface planes.

Equation (52) reduces, in the case of a dielectric sandwiched between two metals, to

$$\tilde{k}_{iy} = k_{iy}^1 = k_y^{1+} = k_{ty}^1 \tag{57}$$

From geometrical considerations the vector is related to its y-component by

$$k_y^1 = |\mathbf{k}^1| \sin \theta \tag{58}$$

Also note that the dot product can be written as

$$\tilde{\mathbf{k}} \cdot \tilde{\mathbf{k}} = (\tilde{k}_y)^2 + (\tilde{k}_z)^2 \tag{59}$$

From the equations given above the vector transmitted perpendicular to the interface can be written

$$\tilde{k}_z^+ = \sqrt{(n_2^2\omega^2/c^2) - |\tilde{\mathbf{k}}_i|^2 \sin^2 \theta_i} \tag{60}$$

where propagation from a metal into a dielectric has been considered in this case.

When the quantity under the radical in equation (60) is positive the complex propagation vector in the dielectric is real, resulting in regular homogeneous plane waves (wave interference). On the other hand, a negative quantity under the radical due to the inequality

$$\sin^2 \theta_i \geq \frac{n_2^2\omega^2}{c^2|\tilde{\mathbf{k}}_i|^2} \tag{61}$$

is the situation for radiation tunneling.

It should be noted in passing that the angle for which the equality holds in equation (61) is called the critical angle, $\theta_{i,c}$. Rays impinging on the metal surface from the inside at angles greater than the critical angle are totally reflected back into the metal. The notation

$$\tilde{k}_z^+ \equiv \alpha \qquad \theta_i < \theta_{i,c} \tag{62}$$

$$\tilde{k}_z^+ \equiv i\beta \qquad \theta_i \geq \theta_{i,c} \tag{63}$$

will be adopted here for simplicity.

The form of the transmission factor, as given in equations (25) and (41), can now be simplified. Consider first the interference situation. After some rearrangement there results for the TE case

$$\Theta_I = \frac{8|\tilde{k}_{iz}|^2\alpha^2}{P_iP_t + 4R_iR_t - (Q_iQ_t - 4S_iS_t)\cos 2\alpha d - 2(S_iQ_t + S_tQ_i)\sin 2\alpha d}. \tag{64}$$

where the incident and transmitted P, Q, R, S quantities are defined similarly, e.g.,

$$P_i = |\tilde{k}_{iz}|^2 + \alpha^2 \tag{65}$$

$$Q_i = |\tilde{k}_{iz}|^2 - \alpha^2 \tag{66}$$

$$R_i = \alpha k_{iz}^1 \tag{67}$$

$$S_i = -\alpha k_{iz}^2 \tag{68}$$

and

$$\mathsf{T}_I^{\mathrm{TE}} = \Theta_I k_{tz}^1/k_{iz}^1 \tag{69}$$

In the TM case,

$$\Phi_I = \frac{8\alpha^2|\tilde{\epsilon}_t|^2|\tilde{k}_{tz}|^2(\epsilon)^2}{P_iP_t + 4R_iR_t - (Q_iQ_t - 4S_iS_t)\cos 2\alpha d - 2(S_iQ_t + S_tQ_i)\sin 2\alpha d}. \tag{70}$$

where

$$P_i = (\epsilon)^2|\tilde{k}_{iz}|^2 + \alpha^2|\tilde{\epsilon}_i|^2 \tag{71}$$

$$Q_i = (\epsilon)^2|\tilde{k}_{iz}|^2 - \alpha^2|\tilde{\epsilon}_i|^2 \tag{72}$$

$$R_i = \epsilon\alpha(\epsilon_i^1 k_{iz}^1 + \epsilon_i^2 k_{iz}^2) \tag{73}$$

$$S_i = \epsilon\alpha(\epsilon_i^2 k_{iz}^1 - \epsilon_i^1 k_{iz}^2) \tag{74}$$

and

$$\mathsf{T}_I^{\mathrm{TM}} = \Phi_I \frac{|\tilde{\epsilon}_i|^2(\epsilon_t^1 k_{tz}^1 + \epsilon_t^2 k_{tz}^2)}{|\tilde{\epsilon}_t|^2(\epsilon_i^1 k_{iz}^1 + \epsilon_i^2 k_{iz}^2)} \tag{75}$$

Now, for the tunneling situation, consider first the TE case. The results are

$$\Theta_T = \frac{16\beta^2|\tilde{k}_{iz}|^2}{(P_i + 2R_i)(P_t + 2R_t)\exp\{2\beta d\} + (P_i - 2R_i)(P_t - 2R_t)\exp\{-2\beta d\} - 2Q_iQ_t + 8S_iS_t} \tag{76}$$

where

$$P_i = |\tilde{k}_{iz}|^2 + \beta^2 \tag{77}$$

$$Q_i = |\tilde{k}_{iz}|^2 - \beta^2 \tag{78}$$

$$R_i = \beta k_{iz}^2 \tag{79}$$

$$S_i = \beta k_{iz}^1 \tag{80}$$

and

$$\mathsf{T}_T^{\mathrm{TE}} = \Theta_T k_{tz}^1/k_{iz}^1 \tag{81}$$

For the TM case, they are

$$\Phi_T = \frac{16\beta^2(\epsilon)^2|\tilde{k}_{iz}|^2|\tilde{\epsilon}_t|^2}{(P_i + 2R_i)(P_t + 2R_t)\exp\{2\beta d\} + (P_i - 2R_i)(P_t - 2R_t)\exp\{-2\beta d\} - 2Q_iQ_t + 8S_iS_t} \tag{82}$$

where

$$P_i = (\epsilon)^2|\tilde{k}_{iz}|^2 + \beta^2|\tilde{\epsilon}_i|^2 \tag{83}$$

$$Q_i = (\epsilon)^2|\tilde{k}_{iz}|^2 - \beta^2|\tilde{\epsilon}_i|^2 \tag{84}$$

$$R_i = \epsilon\beta(\epsilon_i^1 k_{iz}^2 - \epsilon_i^2 k_{iz}^1) \tag{85}$$

$$S_i = \epsilon\beta(\epsilon_i^1 k_{iz}^1 + \epsilon_i^2 k_{iz}^2) \tag{86}$$

and

$$\mathsf{T}_T^{\mathrm{TM}} = \Phi_T \frac{|\tilde{\epsilon}_i|^2(\epsilon_t^1 k_{tz}^1 + \epsilon_t^2 k_{tz}^2)}{|\tilde{\epsilon}_t|^2(\epsilon_i^1 k_{iz}^1 + \epsilon_i^2 k_{iz}^2)} \tag{87}$$

The behavior of the expressions represented by equations (69), (75), (81), and (87) can be investigated, in general, only through

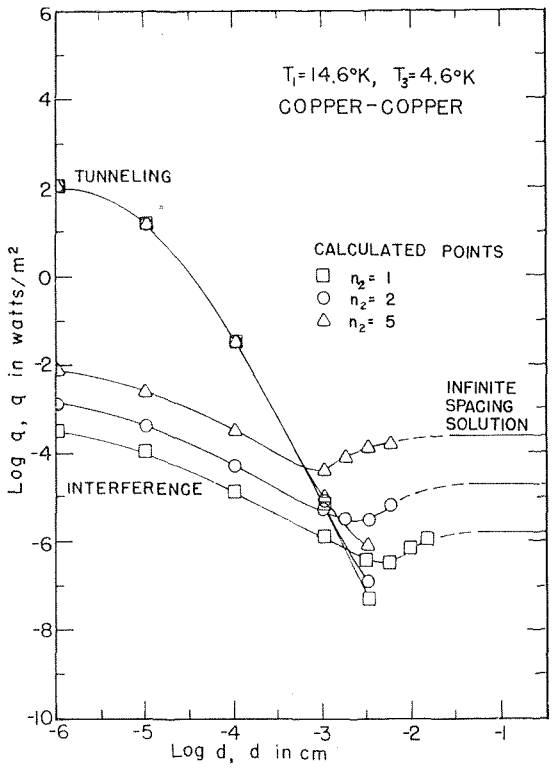

Fig. 3 The effects of intervening dielectric at low temperature

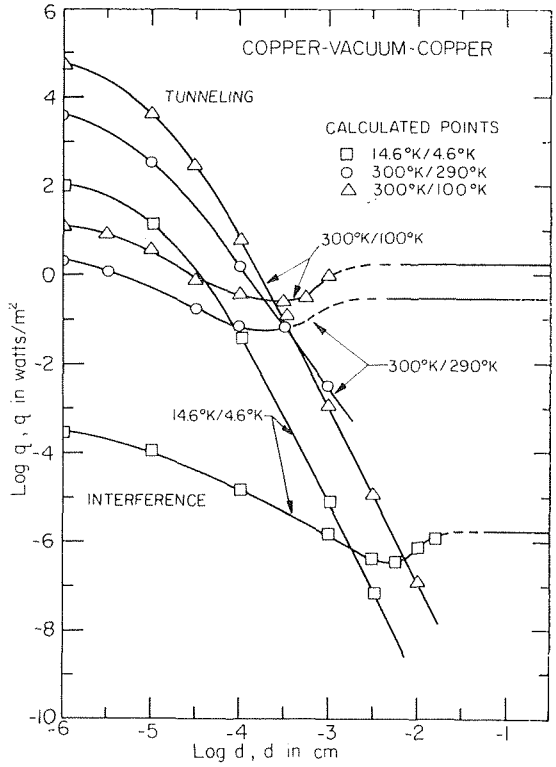

Fig. 4 The influence of temperature level on energy transfer

numerical means. However, some limiting values can be examined analytically. Specifically, all four equations reduce to a limit of unity at zero spacing for the special case of identical properties in both metals. Also, both tunneling factors, equations (81) and (87), yield zero values in the limit of infinite spacing for any property combinations.

Results and Discussion

Numerical results calculated from the present theory are shown in Figs. 3–5. In each case the fluxes corresponding to radiation tunneling and wave interference are shown. Infinite spacing results [1] of the present series of papers are also shown. A dashed line is used to indicate a possible behavior of the small spacing solution in approaching the infinite spacing solution. While this matching is open to question due to the two different calculation procedures, there appears to be a good correspondence between the results.

All calculations were performed using the anomalous skin effect theory for prediction of the optical properties. This theory accounts for both the time and space variation of the electric field in the metal. The Drude single electron theory, a theory that has often been used in calculations, accounts for the time variation only. When used in engineering calculations for radiation phenomena, the anomalous skin effect theory has been shown to be a better approximation to the actual situation than more classical methods, especially at cryogenic temperatures [14]. This theory is still under certain limitations, however, and this is probably the single greatest source of error in the present work. A more complete discussion of the anomalous skin effect theory and its application to engineering predictions can be found elsewhere [14]. Table 1 indicates the residual resistivity used in the present calculations [15].

Fig. 3 shows the effects of the intervening dielectric. A low temperature situation is given since this may have application to high-performance cryogenic insulations made of multilayered,

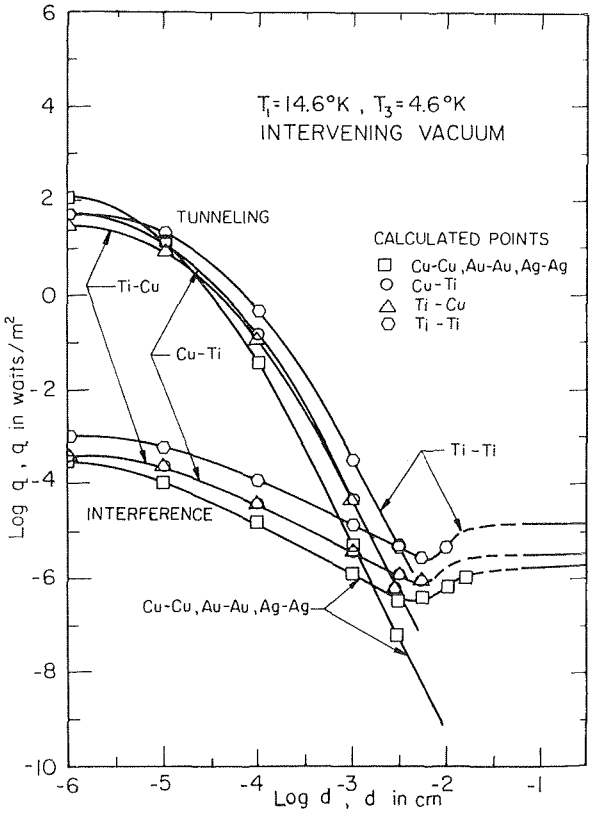

Fig. 5 Effects of metal type at low temperature

Table 1 Residual resistivity of metals under consideration

Metal	copper	silver	gold	titanium
Residual Resistivity (ohm-cm)	1.8×10^{-9}	9×10^{-9}	0	9×10^{-6}

metallic-coated-plastic sheets. From the figure it can be seen that at very small spacings where the tunneling contribution dominates, the dielectric's effect on heat transfer is negligible. However, in the large spacing asymptote, where tunneling effects are no longer important, the heat transfer increases markedly with an increasing dielectric index of refraction.

Effects of temperature level are illustrated in Fig. 4. Here an index of refraction in the dielectric is taken to be unity (vacuum). Along with the 14.6/4.6 deg K base curve, 300/100 deg K (which was chosen as it has approximately the same temperature ratio) and 300/290 deg K (which has the same temperature difference) curves are shown. In addition to the obvious fact of increased energy transfer with increased temperature level, the interference contribution reaches its minimum at much shorter distances, a manifestation of the shorter characteristic wavelengths in the higher temperature radiation spectrum. The 300/290 deg K curves indicate the effects on the heat flux when the lower temperature surface becomes important.

Fig. 5 indicates the effect of metal characteristics in the present theory. Generally, higher conductivity materials exhibit lower heat fluxes at all but very close spacings. This characteristic corresponds to the low values of emissivity that are expected for good electrical conductors. In mismatch cases, the interference calculation is symmetrical, e.g., copper/titanium yields the same results as titanium/copper. The tunneling situation does not appear to exhibit this characteristic. Also note that metals that are physically similar to copper, such as silver and gold, yield results essentially the same as those for copper.

The tunneling and interference contributions for a particular situation can be simply added to yield the total heat flux predicted by the present theory. It is of interest to compare this type of theoretical result qualitatively with those given for an all dielectric system by Cravalho, Tien and Caren [6]. While there seems to be a great similarity between the interference contributions calculated for the two different systems and also between the tunneling contributions, the total flux curves differ in one major characteristic. In the present theory the total flux exhibits a minimum value, whereas calculations for the dielectric system indicate a monatomically decreasing function which asymptotically approaches the infinite spacing result.

Some general trends in the present theory can be noted. The spacing variable will be nondimensionalized with the wavelength at which the maximum blackbody emission occurs. This wavelength is given by [8]

$$n_2 T \lambda_{max} = 0.2898 \text{ cm deg K} \tag{88}$$

The prime item of interest is the spacing above which the infinite spacing result should apply. It appears that this is given by

$$d/n_2\lambda_{max} > 0(1) \quad \text{(infinite-spacing solution valid)} \tag{89}$$

Note that Cravalho, Tien and Caren [6] found that for two dielectrics separated by a vacuum gap this limit is given by $d/\lambda_{max} = 3$. Radiation tunneling definitely becomes important for spacings which are smaller than this by an order of magnitude. So

$$d/n_2\lambda_{max} < 0(0.1) \quad \text{(all radiation tunneling)} \tag{90}$$

The limiting value of heat flux at zero spacing could apply to the prediction of radiant heat flux between relatively smooth surfaces almost in contact (i.e. in the determination of radiative contact resistance). A very rough approximation of this flux can be found from

$$q_{d=0} = [n_j^4/(n_j^2 + k_j^2)]q_{d=\infty} \qquad (j = 1, 3) \tag{91}$$

where n and k are values of the optical constants evaluated at some characteristic wavelength in the pertinent emissive power spectrum. Hence, the predicted ratio of the zero spacing flux to the infinite spacing flux can vary in copper from about 10^3 at room temperature up to about 10^8 at cryogenic temperatures.

Conclusions

1 Radiative heat flux at close spacings consists of two contributions. One is a radiative tunneling contribution which is found at zero spacing to be several orders of magnitude larger than the classical prediction but which decreases rapidly with distance. The other is a wave interference contribution, which decreases with increasing spacing and then increases to approach the large spacing results.

2 The spacing-independent solution holds for spacings given by $d/n_2\lambda_{max} > 0(1)$, while radiation tunneling is shown to be dominant for $d/n_2\lambda_{max} < 0(0.1)$.

3 The presence of a transparent material between two radiating metals has very little effect at very small spaces, but enhances heat exchange for larger spacings.

References

1 Domoto, G. A., and Tien, C. L., "Thick Film Analysis of Radiative Transfer Between Parallel Metallic Surfaces," JOURNAL OF HEAT TRANSFER, TRANS. ASME, Series C, Vol. 92, No. 3, Aug. 1970, pp. 399–404.

2 Domoto, G. A., Boehm, R. F., and Tien, C. L., "Experimental Investigation of Radiative Transfer Between Metallic Surfaces at Cryogenic Temperatures," JOURNAL OF HEAT TRANSFER, TRANS. ASME, Series C, Vol. 92, No. 3, Aug. 1970, pp. 412–417.

3 Caren, R. P., and Cunningham, G. R., "Heat Transfer in Multilayer Insulation Systems," *Advances in Cryogenic Heat Transfer*, Chem. Eng. Prog. Symp. Series, Vol. 64, No. 87, 1968, p. 67.

4 Born, M., and Wolf, E., *Principles of Optics*, Pergamon Press, New York, 1965, p. 47, p. 64.

5 Emslie, A. G., "Radiation Transfer by Closely Spaced Shields," *Aerodynamically Heated Structures*, (ed. by Glaser, P. E.), Prentice Hall, Englewood Cliffs, N. J., 1962.

6 Cravalho, E. G., Tien, C. L., and Caren, R. P., "Effect of Small Spacing on Radiative Transfer Between Two Dielectrics," JOURNAL OF HEAT TRANSFER, TRANS. ASME, Series C, Vol. 89, 1967, p. 351.

7 Caren, R. P., "The Theory of Electromagnetic Tunneling of Thermal Radiation Between Highly Absorbing Media," *Proceedings of the Fourth Symposium on Thermophysical Properties*, ASME, New York, 1968, p. 243.

8 Sparrow, E. M., and Cess, R. D., *Radiation Heat Transfer*, Brooks/Cole, Belmont, Calif., 1966.

9 Fragstein, C., "Energy Transfer at the Interface Between Two Absorbing Media with an Emphasis on the Heat Radiation in Absorbing Bodies," *Ann. Physik*, Vol. 7, 1950, p. 63.

10 Laue, M., "Heat Radiation in Absorbing Bodies," *Ann. Physik*, Vol. 32, 1910, p. 1085.

11 Stern, F., "Elementary Theory of the Optical Properties of Solids," *Advances in Solid State Physics* (ed. by Seitz, F., and Turnbull, D.), Academic Press, New York, Vol. 15, p. 299.

12 Knittl, Z., "On the Energy Balance in the Optics of Metals," *Czech. Journal of Physics*, Vol. 9, 1959, p. 133.

13 Salzberg, B., "A Note on the Significance of Power Reflection," *American Journal of Physics*, Vol. 16, 1948, p. 444.

14 Domoto, G. A., Boehm, R. F., and Tien, C. L., "Predictions of the Total Emissivity of Metals at Cryogenic Temperatures," *Advances in Cryogenic Engineering*, Vol. 14, 1969, p. 230.

15 Stewart, R., and Johnson, V. J. (eds.), "A Compendium of the Properties of Materials at Low Temperatures (Phase II)," WADD Technical Report 60-56, Chapter 6, 1961.

G. A. DOMOTO

Assistant Professor of Mechanical Engineering, Columbia University, New York, N. Y.

R. F. BOEHM

Assistant Professor of Mechanical Engineering, University of Utah, Salt Lake City, Utah

C. L. TIEN

Professor of Mechanical Engineering, University of California, Berkeley, Calif.

Experimental Investigation of Radiative Transfer Between Metallic Surfaces at Cryogenic Temperatures[1]

Experimental measurements of the radiative heat flux between two parallel copper disks in the liquid-helium temperature range are presented. The temperature levels investigated were primarily for the higher temperature disk (emitter) at 10.0 deg K and 15.1 deg K and the lower temperature disk (receiver) at approximately 4.5 deg K. For the 15.1 deg K emitter temperature, the spacing was varied from 0.201 cm to 0.001 cm. For the 10 deg K emitter case, the spacing was varied from 0.044 cm to 0.005 cm. Experimental data at small spacings show a definite spacing dependence of radiative transfer which agree qualitatively with the predicted result. Based on the measurements at large spacings, an estimate of the total hemispherical emissivity for the copper surfaces in the liquid-helium temperature range indicates a value of 0.015, which is approximately one order of magnitude higher than predicted. The possible causes for the discrepancies are discussed.

Introduction

This is the third of three papers considering radiative transfer between metallic surfaces at cryogenic temperatures. The present paper is concerned with the experimental investigation, while the first two papers [1, 2][2] present the theoretical analysis of the subject. The primary purpose of the present paper is to investigate experimentally the radiative transfer between two parallel metallic surfaces in a wide range of surface spacings so that both the small spacing effect and the thick film limiting value can be observed. The latter information can be used to estimate the total hemispherical emissivity of metallic surfaces under consideration. To achieve this aim requires experimental measurements in the liquid-helium temperature range under ultrahigh vacuum conditions.

Existing experimental investigations of the thermal radiation of solids at cryogenic temperatures have been largely concerned with measurements of radiation properties of metals in the temperature range from liquid-nitrogen temperatures to room temperature [3]. A limited amount of spectral radiation data do exist in the liquid-helium temperature range, but they are restricted to the near infrared and infrared spectrum. Due to the shift of the Planck function to long wavelengths at low temperatures, the spectral range of interest for thermal radiation transport calculations between metals at cryogenic temperatures is the far infrared. The difficulty in making the far infrared measurements arises from the difficulty of finding a suitable long wavelength source of sufficient intensity and also from the fact that the reflectivity of metals approaches very close to unity in the far infrared at cryogenic temperatures. Measurements of total radiation properties have been reported only in the liquid-nitrogen temperature range. A large portion of the data is for the total reflectance based on a room temperature source and thus provides little information concerning the emission characteristics or total emissivity used in engineering calculations.

In order to study experimentally the spacing effect on radiative transfer, direct measurements of radiative transfer between metallic surfaces at liquid-helium temperatures are particularly needed. This type of measurement has been totally lacking in the literature. Other than the preliminary data reported recently in conjunction with the description of the present apparatus and experimental techniques [4], no experimental study has ever been reported regarding the spacing effect on radiative transfer.

The present investigation reports measurements of the radiative transfer between two parallel copper disks with varying spacings at liquid-helium temperatures in a vacuum environment of about 10^{-12} torr. The experimental results indicate clearly the existence of a spacing effect at small spacings in qualitative agreement with the predicted trend. An estimate

---

[1] This work constitutes part of the PhD thesis of G. A. Domoto, entitled, "Thermal Radiation of Metallic Surfaces at Liquid Helium Temperatures," Department of Mechanical Engineering, University of California, Berkeley, Calif., 1968. The authors wish to acknowledge the support of this work by NASA Grant NGR-05-003-285.

[2] Numbers in brackets designate References at end of paper.

Contributed by the Heat Transfer Division and presented at the Winter Annual Meeting, Los Angeles, Calif., November 16–20, 1969, of THE AMERICAN SOCIETY OF MECHANICAL ENGINEERS. Manuscript received by the Heat Transfer Division, January 2, 1969. Paper No. 69-WA/HT-7.

of the total hemispherical emissivity has also been obtained for the copper surfaces in the temperature range of the experiment. The estimated value of 0.015, however, is approximately one order of magnitude higher than predicted. Discrepancies shown in the quantitative comparison between theory and experiment are discussed in detail in terms of possible areas of uncertainty in both the theoretical framework and experimental measurements.

Apparatus and Procedure

The apparatus and procedure used in the study have been described in detail by Cravalho, Domoto, and Tien [4]; therefore, only a brief summary will be given here. The apparatus consisted essentially of two 8.5 cm diameter copper disks termed the emitter and receiver. The emitter and receiver were mounted in a parallel coaxial configuration within a black-walled, ultrahigh vacuum chamber immersed in a liquid-helium bath. Both the emitter and receiver were connected to a base ring which in turn was attached to one end wall of the vacuum chamber. The thermal link between the receiver and the base ring was designed to offer a high resistance to heat flow. The temperature of the base ring acted as a base temperature for the measurements and attempts were made to control this base temperature at a constant value slightly above the liquid-helium bath temperature. The control device used was similar to that designed by Blake and Chase [5].

The instrumentation primarily consists of precalibrated germanium and carbon resistance thermometers mounted on the emitter, receiver, and base ring. Resistance measurements were made using four-lead techniques to an accuracy of at least 0.10 percent while dissipating less than 10^{-12} watts.

In order to eliminate the residual gas conduction between the emitter and receiver, an ultrahigh vacuum was provided by a molecular sorbent trapped diffusion pump and the cryopumping effect of the liquid-helium bath. The pressure levels attained with the vacuum chamber were believed to be below the 10^{-12} torr range, indicated by a Kreisman cold cathode gauge mounted at a room temperature location of the vacuum system.

The calorimetric technique employed in the heat flux measurements is similar to that developed by Caren [6]. The measurement technique consists of first calibrating the thermal link between the receiver and the base ring. The calibration is accomplished by allowing the emitter to cool to essentially the bath temperature, then dissipating known amounts of energy in resistors mounted on the receiver and measuring the temperature difference developed across the thermal link. Thus, the temperature difference across the thermal link becomes a quantitative measure of the net heat transferred into the receiver. If the base temperature is maintained at a constant value, the resistance of the receiver thermometer is indicative of the temperature difference and thus heat flux into the receiver. Once the thermal link has been calibrated, the rest of the measurements consist of heating the emitter to the desired temperature, setting the desired spacing, and recording the temperature difference developed across the thermal link (receiver resistance). From the calibration, the net heat flux for the various spacings and emitter and receiver temperatures is obtained.

It is noted that the temperature of the receiver changes very little throughout the experiment. Nevertheless, the change in resistance of the resistance thermometers is large enough and measured to sufficient accuracy so that the extremely small values of radiative flux can be measured. This calorimetric technique eliminates the problem of accounting for lead losses since the electrical leads are calibrated along with the thermal link.

Experimental Results

The radiative heat flux between parallel copper disks of 8.5 cm diameter has been obtained experimentally for emitter temperatures of approximately 15.1 K, 13.8 K, and 10.0 deg K with a receiver temperature of approximately 4.5 deg K in all cases. For the 15.1 deg K emitter case, the spacing between emitter and receiver ranged from 0.201 cm to 0.001 cm and for the 10.0 deg K emitter case, from 0.044 cm to 0.005 cm. The single point for the 13.8 deg K emitter temperature was taken at a spacing of 0.017 cm.

Table 1 represents the results of the calibration of receiver power input versus the resistance of the receiver temperature sensing element. With the emitter at low temperature so that the radiation interchange is negligible as compared to the elec-

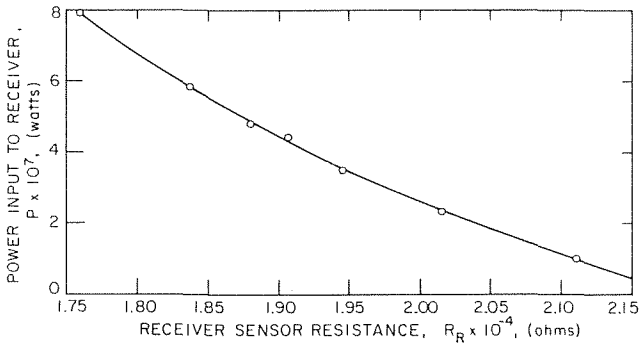

Fig. 1 Calibration for receiver of power input versus sensor resistance

Table 1 Calibration of receiver power input versus temperature sensor resistance

Receiver Sensor Resistance $R_R x 10^{-4}$ ohms	Receiver Temperature T_R °K	Base Sensor Resistance $R_B x 10^{-3}$ ohms	Base Temperature T_B °K	Corrected* Receiver Sensor Resistance $R_R x 10^{-4}$	Corrected* Receiver Temperature T_R^* °K	Receiver Power Input $Px10^7$ Watts
1.756	4.642	1.936	4.412	1.759	4.640	7.903
1.838	4.590	1.944	4.409	1.837	4.591	5.819
1.869	4.571	1.928	4.416	1.879	4.565	4.776
1.892	4.557	1.920	4.419	1.907	4.548	4.412
1.933	4.533	1.927	4.416	1.944	4.527	3.483
2.027	4.482	1.955	4.404	2.014	4.488	2.316
2.112	4.441	1.943	4.409	2.110	4.442	0.986

*Correction made to account for variation of measurements from base sensor resistance = 1942 ohms, base temperature = 4.410°K.

Table 2 Receiver response to various emitter temperatures and spacing

Spacing d cm	Emitter Sensor Resistance R_E ohms	Emitter Temperature T_E °K	Receiver Sensor Resistance $R_R \times 10^{-4}$ ohms	Receiver Temperature T_R °K	Base Sensor Resistance $R_B \times 10^{-3}$ ohms	Base Temperature T_B °K
0.201	40.65	15.58	2.061	4.465	1.956	4.406
0.0447	43.85	15.09	2.062	4.465	1.983	4.393
0.0155	45.93	14.80	2.054	4.464	1.999	4.386
0.0071	45.68	14.83	2.026	4.482	2.001	4.385
0.0036	43.03	15.21	1.971	4.511	1.942	4.410
0.0023	44.82	14.95	1.935	4.532	1.918	4.420
0.0010	42.25	15.33	1.837	4.591	1.930	4.415
0.0439	111.7	10.01	2.133	4.432	1.930	4.415
0.0152	112.9	9.97	2.130	4.433	1.944	4.409
0.0051	113.4	9.95	2.028	4.481	1.935	4.413
0.0046	110.4	10.06	1.994	4.498	1.934	4.413
0.0170	53.80	13.80	2.074	4.459	1.940	4.411

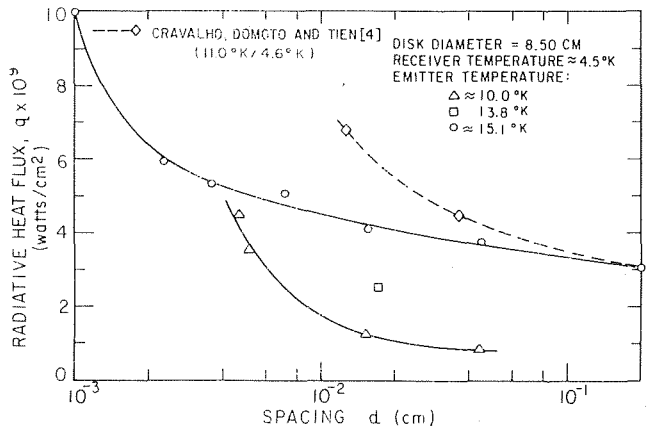

Fig. 2 Radiative heat flux versus spacing between parallel copper disks

Table 3 Corrected receiver response to various emitter temperatures and spacing

Spacing d cm	Emitter Temperature T_E °K	Corrected* Receiver Sensor Resistance $R_R^* \times 10^{-4}$ ohms	Corrected* Receiver Temperature T_R^* °K	Net Energy Transfer $q \times 10^7$ watts
0.201	15.58	2.054	4.469	1.73
0.0447	15.09	2.026	4.482	2.14
0.0155	14.80	2.014	4.488	2.32
0.0071	14.83	1.978	4.507	2.88
0.0036	15.21	1.971	4.511	3.01
0.0023	14.95	1.952	4.522	3.36
0.0010	15.33	1.845	4.586	5.65
0.0439	10.01	2.145	4.427	0.49
0.0152	9.97	2.129	4.434	0.71
0.0051	9.95	2.035	4.478	2.00
0.0046	10.06	2.000	4.495	2.52
0.0170	13.80	2.076	4.458	1.43

*Correction made to account for variation of measurements from base sensor resistance = 1942 ohms, base temperature = 4.410°K.

trical power input to the receiver, the thermal link was calibrated by recording the steady state values of receiver and base sensor resistances for the different power input levels shown. The temperature controller was used to hold the base-ring temperature as close to 4.410 deg K as possible.

In Column 4 of Table 1, it is indicated that the base temperature fluctuated slightly during the calibration despite the use of the temperature controller. In order that the receiver sensor readings give an accurate indication of heat input to the receiver, corrections were made to account for the differences in base temperature from 4.410 deg K. These corrections were made on the assumption that the thermal conductivity of the thermal link remained nearly constant for temperature changes of the order of the base temperature deviations. Thus, for a given power input level, the deviation in base temperature was accounted for by correcting both the base and receiver temperatures by the same amount, i.e., by keeping the same temperature difference across the thermal link. This correction procedure yielded the receiver sensor reading which would have existed for the given heat input level had the base temperature remained at 4.410 deg K. Fig. 1 is the calibration curve of electrical power input versus corrected receiver sensor resistance, i.e., the first portion of the experiment.

The second portion of the experiment, that of measuring the receiver sensor response as the emitter temperature and the spacing were varied, yielded the data tabulated in Table 2. Here again deviations in the base temperature were experienced and corrections were made as shown in Table 3. Using the corrected receiver sensor resistance values together with the calibration curve (Fig. 1) the net energy transfer was obtained as shown in Column 5 of Table 3. By dividing by the area of a disk, the net radiative flux was obtained for the various emitter temperatures. The resulting plot of radiative flux as a function of spacing for different emitter temperatures is shown in Fig. 2 together with the preliminary results of Cravalho, Domoto, and Tien [4]. It should be pointed out that maintaining the emitter temperature constant was found quite difficult in the 15.1 deg K emitter case, hence, the 15.1 deg value is an average value with deviations in emitter temperature of up to 3 percent as seen from Table 3.

Discussion

The experimental results confirm the relative significance of the spacing effect as indicated by the preliminary results. The present results indicate a lower value of heat flux than indicated by the preliminary results with the spacing effect becoming important at smaller spacings. The lower values of flux can be partly attributed to better control of the base temperature. In the preliminary work, the systematic error introduced due to the base temperature being slightly higher in the radiative flux measurements portion as compared to the calibration portion could have resulted in indication of higher values of flux than actually existed. In addition, differences in material and surface properties of the hand polished copper disks could partially account for the smaller values of heat flux.

The differences in spacing dependence can be attributed to slight deviations from parallelness of the emitter and receiver disks. This difficulty arises from the fact that there existed no means to assure uniform spacing over the whole area of the emitter and receiver as their temperature decreased from room temperature to the liquid-helium temperature. Whereas this limitation has little effect when the spacing is large, of the order of 10^{-1} cm, the nonparallelness becomes more and more critical as the spacing is further decreased. This nonparallelness affects both spacing measurements as well as the radiative flux between the two surfaces.

The spacing measurements will be affected by the nonparallelness due to the fact that the zero spacing reading is determined by the point at which first contact is made as the emitter is lowered toward the receiver. Thus the indicated spacing represents the minimum spacing between the two disks. For the smallest spacings measured (10^{-3} cm), the actual average spacing may be several times greater than that indicated due to the nonparallelness. Fortunately, the degree of nonparallelness should remain the same throughout a set of runs so that at least qualitative comparisons can be made within the present set.

Since at small spacings the radiative heat flux between the surfaces is highly dependent on the spacing, the nonparallelness of the surfaces can result in a high variation of flux over the surfaces. The heat fluxes measured under such circumstances are averages over the disks and thus do not represent an absolute quantitative measurement of heat flux as a function of spacing. The data do indicate qualitatively the magnitude of the spacing effect on heat flux as well as given an approximate value for the spacings at which this effect becomes important.

As the gap thickness increases and the small spacing effect becomes less important, the thick film limit is approached. Since the thick film solution involves infinite parallel surfaces, some assessment of the effect of the finite size of the disks on the heat flux must be made. Since the largest spacing of the present investigation is 0.2 cm, the maximum spacing-to-radius ratio is on the order of $(d/r) = 0.047$. Although the radiosity in this system is angularly dependent, some idea of the effect of finite size can be gained from the use of the angle factor which is strictly valid only for uniform radiosity situations. The view factor for the coaxial disk configuration is given by $[1 - (d/r)]$ for small (d/r). This would indicate that the experimental results at a spacing of 0.2 cm must be increased by 5 percent to be comparable to the true thick film situation. The corrections for the smaller spacings are proportionately smaller. The correction for finite size taking into account angular dependent emissivities and reflectivities will be larger than that obtained from the angle factor but the difference in the two corrections is expected to be small at these small (d/r) ratios. This expectation is based on the value of 1.33 obtained by Dunkle [7] for the ratio of hemispherical emissivity to normal emissivity for specular surfaces at large values of refractive index, i.e., the emissivity at the wide angles cannot be very much greater than the normal value. The experimental data, corrected for finite size at large spacing, can then be compared to the theoretically predicted heat flux.

Fig. 3 is a comparison of the total heat flux as measured and as predicted for the copper-vacuum-copper system [1, 2]. The predictions shown are based on the anomalous skin effect (ASE) theory of the optical properties of metals as applied to copper with an assumed residual resistivity level of 1.8×10^{-9} ohm-cm. The difference between theory and experiment is rather large, the measurements being one order of magnitude larger than the prediction. However, it is not obvious at this point that the theory should be discounted in favor of the experiment or vice versa. There are possible shortcomings in each.

As far as the theortical development is concerned there are several areas of uncertainty in the theoretical framework which require further attention. These have been indicated to some extent in Part 2 [2], but the primary source of uncertainty probably lies in the description of the optical properties. Although the anomalous skin effect theory is a vast improvement over the more classical approaches [8], the manner in which the damping of the electron motion is taken into account may be much too simplified. In addition to the temperature dependence of the damping coefficient, a frequency dependence should also be included. Holstein [9] and Schocken [10] have used a quantum mechanical treatment of the interaction between the free electrons and the lattice phonons and imperfections and the electromagnetic wave to take into account the frequency dependence of the damping phenomenon. This approach should be further developed and used in the calculation of radiative transfer involving metallic surfaces.

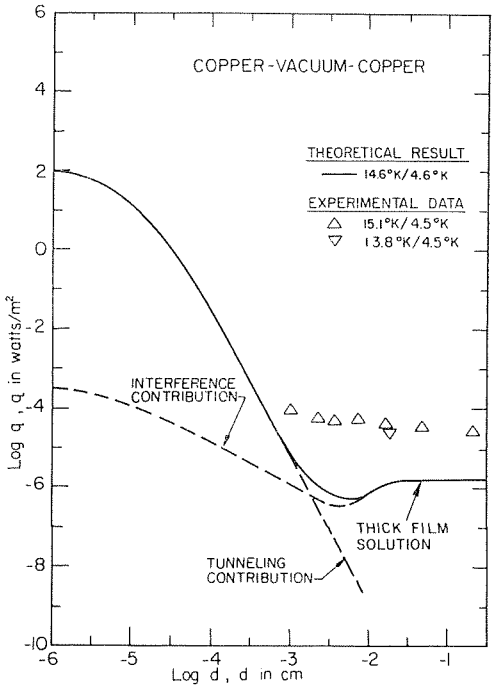

Fig. 3 Total heat flux versus spacing for low temperature copper

It is noted that the residual resistivity is a parameter to be specified in the predictions. In order to investigate the possibility of impurities and imperfections accounting for the high measured values, the residual resistivity used in the prediction was varied from 1.8×10^{-8} to 1.8×10^{-10} ohm-cm. The resulting predicted values of heat flux differed by only 10 percent from the predictions of Fig. 3. Thus the effect of high residual resistivity as predicted by the present form of the anomalous skin effect theory will not account for the discrepancy between theory and experiment.

Areas of uncertainty are found in the experimental measurements as well. The effect of the nonparallelness of the disks on the spacing measurements and on the heat flux have already been mentioned. In addition, the residual gas conduction may contribute significantly to the heat flux. However, estimates based on the Knudsen equation for free molecular flow of helium give in the worst case an estimate of residual gas conduction of less than 1 percent of the measured fluxes. Further, the real surface effects due to surface impurities and surface stresses could act to increase the heat flux to values greater than those predicted theoretically.

In addition to the comparison of the measured heat flux with that predicted, some indication of the total hemispherical emissivity of copper can also be obtained from the data. If the "diffuse-gray" approximation to the thick film solution is considered, and the emissivities are assumed to be identical and small, then there results

Table 4 Total hemispherical emissivity

Theoretical Prediction:

Basis of Prediction	Temperature (°K)	Total Hemispherical Emissivity ϵ_h
ASE*	15.0	1.48×10^{-3}
ASE*	10.0	1.17×10^{-3}
ASE*	4.5	7.17×10^{-4}

Experimental Determination: (assuming emissivities of both surfaces are identical)

Experimental Situation	Measured Net Heat Flux (watts/cm^2)	Ratio of Thick Film Solution to "Diffuse-Gray" Approximation	"Diffuse-Gray" Heat Flux (watts/cm^2)	Total Hemispherical Emissivity ϵ_h
T_E = 15.0°K, T_R = 4.5°K	3.2×10^{-9}	1.53	2.09×10^{-9}	1.46×10^{-2}
T_E = 10.0°K, T_R = 4.5°K	6×10^{-10}	1.34	4.47×15^{-10}	1.58×10^{-2}

*Electrical conductivities: 15.0°K, $\sigma = 4.42\times10^{20}$ esu; 10.0°K, $\sigma = 4.92\times10^{20}$ esu; 4.5°K, $\sigma = 5.00\times10^{20}$ esu.

$$q = \frac{\epsilon h}{2}\,\sigma_0(T_1^4 - T_3^4)$$

Also from the comparison of the thick film solution with the "diffuse-gray" approximation [1], the ratio of thick film heat flux to "diffuse-gray" can be obtained for the two cases: T_1 = 15.1 deg K, T_3 = 4.5 deg K, and T_1 = 10.0 deg K, T_3 = 4.5 deg K. Since the measured heat flux should correspond to the thick film solution, the "diffuse-gray" heat flux is obtained by dividing the measured heat flux by the above ratio as shown in Table 4. From the "diffuse-gray" heat flux, an approximate value of the total hemispherical emissivity is obtained. The order of magnitude of these values seems to be fairly consistent with the data reported by Betz [11] and Caren [6] in the liquid-nitrogen temperature range. Nevertheless, the anomalous skin effect prediction of total hemispherical emissivity falls approximately one order of magnitude lower than that experimentally obtained.

The foregoing considerations indicate that further refinements in both theory and experiment are required to bring the two into better agreement.

References

1 Domoto, G. A., and Tien, C. L., "Thin Film Analysis of Radiation Transfer Between Parallel Metallic Surfaces," JOURNAL OF HEAT TRANSFER, TRANS. ASME, Series C, Vol. 92, No. 3, Aug. 1970, pp. 399–404.

2 Boehm, R. F., and Tien, C. L., "Small Spacing Analysis of Radiation Transfer Between Parallel Metallic Surfaces," JOURNAL OF HEAT TRANSFER, TRANS. ASME, Series C, Vol. 92, No. 3, Aug. 1970, pp. 405–411.

3 Tien, C. L., and Cravalho, E. G., "Thermal Radiation of Solids at Cryogenic Temperatures," *Advances in Cryogenic Heat Transfer*, Chem. Eng. Prog. Symp., Vol. 64, No. 87, 1968, p. 56.

4 Cravalho, E. G., Domoto, G. A., and Tien, C. L., "Measurements of Thermal Radiation of Solids at Liquid-Helium Temperatures," *Progress in Aeronautics and Astronautics*, Vol. 22, (ed. Bevans, J. T.), Academic Press, New York, 1968, pp. 531–542.

5 Blake, C., and Chase, C. E., "Liquid Helium Temperature Regulator," *Review of the Scientific Institute*, Vol. 34, 1963, p. 984.

6 Caren, R. P., "Low-Temperature Emittance Determination," *Thermophysics and Temperature Control of Spacecraft and Entry Vehicles*, Academic Press, New York, 1966, pp. 61–73.

7 Dunkle, R. V., "Emissivity and Inter-Reflection Relationships for Infinite Parallel Specular Surfaces," *Symposium on Thermal Radiation of Solids*, NASA SP-55, 1965, p. 39.

8 Domoto, G. A., Boehm, R. F., and Tien, C. L., "Predictions of the Total Emissivity of Metals at Cryogenic Temperatures," *Advances in Cryogenic Engineering*, Vol. 14, 1969, pp. 230–239.

9 Holstein, T., "Optical and Infrared Reflectivity of Metals at Low Temperatures," *Physics Review*, Vol. 88, 1952, p. 1427.

10 Schocken, K., (ed.), "Optical Properties of Satellite Materials --- The Theory of Optical and Infrared Properties of Metals," NASA TN D-1523, 1963.

11 Betz, H. T., Olson, O. H., Schurin, B. D., and Morris, J. C., "Determination of Emissivity and Reflectivity Data on Aircraft Structure Materials, Part II," WADC TR 56–22, 1956 (ASTIA No. 202493).

Table 4 Total hemispherical emissivity

Theoretical Prediction:

Basis of Prediction	Temperature (°K)	Total Hemispherical Emissivity ϵ_h
ASE*	15.0	1.48×10^{-3}
ASE*	10.0	1.17×10^{-3}
ASE*	4.5	7.17×10^{-4}

Experimental Determination: (assuming emissivities of both surfaces are identical)

Experimental Situation	Measured Net Heat Flux (watts/cm^2)	Ratio of Thick Film Solution to "Diffuse-Gray" Approximation	"Diffuse-Gray" Heat Flux (watts/cm^2)	Total Hemispherical Emissivity ϵ_h
T_E = 15.0°K, T_R = 4.5°K	3.2×10^{-9}	1.53	2.09×10^{-9}	1.46×10^{-2}
T_E = 10.0°K, T_R = 4.5°K	6×10^{-10}	1.34	4.47×15^{-10}	1.58×10^{-2}

*Electrical conductivities: 15.0°K, $\sigma = 4.42\times10^{20}$ esu; 10.0°K, $\sigma = 4.92\times10^{20}$ esu; 4.5°K, $\sigma = 5.00\times10^{20}$ esu.

$$q = \frac{\epsilon h}{2}\,\sigma_0(T_1^4 - T_3^4)$$

Also from the comparison of the thick film solution with the "diffuse-gray" approximation [1], the ratio of thick film heat flux to "diffuse-gray" can be obtained for the two cases: T_1 = 15.1 deg K, T_3 = 4.5 deg K, and T_1 = 10.0 deg K, T_3 = 4.5 deg K. Since the measured heat flux should correspond to the thick film solution, the "diffuse-gray" heat flux is obtained by dividing the measured heat flux by the above ratio as shown in Table 4. From the "diffuse-gray" heat flux, an approximate value of the total hemispherical emissivity is obtained. The order of magnitude of these values seems to be fairly consistent with the data reported by Betz [11] and Caren [6] in the liquid-nitrogen temperature range. Nevertheless, the anomalous skin effect prediction of total hemispherical emissivity falls approximately one order of magnitude lower than that experimentally obtained.

The foregoing considerations indicate that further refinements in both theory and experiment are required to bring the two into better agreement.

References

1 Domoto, G. A., and Tien, C. L., "Thin Film Analysis of Radiation Transfer Between Parallel Metallic Surfaces," JOURNAL OF HEAT TRANSFER, TRANS. ASME, Series C, Vol. 92, No. 3, Aug. 1970, pp. 399–404.

2 Boehm, R. F., and Tien, C. L., "Small Spacing Analysis of Radiation Transfer Between Parallel Metallic Surfaces," JOURNAL OF HEAT TRANSFER, TRANS. ASME, Series C, Vol. 92, No. 3, Aug. 1970, pp. 405–411.

3 Tien, C. L., and Cravalho, E. G., "Thermal Radiation of Solids at Cryogenic Temperatures," *Advances in Cryogenic Heat Transfer*, Chem. Eng. Prog. Symp., Vol. 64, No. 87, 1968, p. 56.

4 Cravalho, E. G., Domoto, G. A., and Tien, C. L., "Measurements of Thermal Radiation of Solids at Liquid-Helium Temperatures," *Progress in Aeronautics and Astronautics*, Vol. 22, (ed. Bevans, J. T.), Academic Press, New York, 1968, pp. 531–542.

5 Blake, C., and Chase, C. E., "Liquid Helium Temperature Regulator," *Review of the Scientific Institute*, Vol. 34, 1963, p. 984.

6 Caren, R. P., "Low-Temperature Emittance Determination," *Thermophysics and Temperature Control of Spacecraft and Entry Vehicles*, Academic Press, New York, 1966, pp. 61–73.

7 Dunkle, R. V., "Emissivity and Inter-Reflection Relationships for Infinite Parallel Specular Surfaces," *Symposium on Thermal Radiation of Solids*, NASA SP-55, 1965, p. 39.

8 Domoto, G. A., Boehm, R. F., and Tien, C. L., "Predictions of the Total Emissivity of Metals at Cryogenic Temperatures," *Advances in Cryogenic Engineering*, Vol. 14, 1969, pp. 230–239.

9 Holstein, T., "Optical and Infrared Reflectivity of Metals at Low Temperatures," *Physics Review*, Vol. 88, 1952, p. 1427.

10 Schocken, K., (ed.), "Optical Properties of Satellite Materials --- The Theory of Optical and Infrared Properties of Metals," NASA TN D-1523, 1963.

11 Betz, H. T., Olson, O. H., Schurin, B. D., and Morris, J. C., "Determination of Emissivity and Reflectivity Data on Aircraft Structure Materials, Part II," WADC TR 56–22, 1956 (ASTIA No. 202493).

DISCUSSION

W. Wulff[3]

The authors are to be commended for further promoting our understanding of radiative transfer between closely spaced surfaces. The experimental study presented in this paper relates to the theoretial analyses reported in two preceding papers [1, 2] but I shall restrict my comments to the experiments.

Unfortunately, the authors refer repeatedly to as yet unpublished papers, particularly as regards the description of their apparatus. Consequently there remain several questions unanswered:

1 How was the distance between emitter and receiver measured and monitored during the experiment?

2 What was the clearance in the guidance system for the motion of the emitter, particularly at the cryogenic temperature of 10 deg K?

3 Were the results repeatable?

4 Inasmuch as the radiative transfer from metals is greatly affected by surface properties, I should like to know how the copper plates were treated prior to the test runs. Did the copper quality used resemble sufficiently well the optical properties on the basis of which the calculations were carried out?

Concerning the spacing problem I would like to have the authors comment on the possibility of monitoring the distance between the plates at three stategic points by capacitative or perhaps inductive sensors.

The description of the procedure to calibrate the thermal link between receiver and base ring is vague. The emitter is said to be allowed to cool "to essentially the bath temperature." It is my opinion, however, that the emitter should have been maintained at precisely the receiver temperature during calibration and thus should have served as a thermal guard. Should the difference between emitter and receiver temperatures during calibration reach an appreciable portion of that temperature difference attained during experimental runs, then it is clear that the measured radiative flux is less than the actual flux.

The authors claim to believe that their pressure is below 10^{-12} torr and base this statement on a pressure measurement with a Kreisman cold cathode gauge. It is known, however, that this gauge no longer functions at pressures below 10^{-10} torr and that one cannot distinguish, with that gauge, a pressure of 10^{-10} torr from a pressure of 10^{-12} torr.

I would like to point out that the thermal resistance of the thermal link appears rather low, as one can see from the temperature recordings in Table 2. Even though the temperatures are recorded with four significant digits, the resulting heat flux can be inferred from these temperatures to an accuracy of two significant digits at best, in some cases only of one significant digit. The graphical representation of the radiative flux shows remarkably little scatter.

Finally, I would like to ask the authors whether they would have the same confidence in their total hemispherical emissivity data as in the data obtained in a cryostat.

[3] Assistant Professor, School of Mechanical Engineering, Georgia Institute of Technology, Atlanta, Ga.

Authors' Closure

The authors wish to thank Professor Wulff for his comments. Answers to most of his questions can be found in reference [4] which was only available in pamphlet form (AIAA Paper No. 68-774) at that time but has since been published. In answer to some of the questions raised concerning the problem of maintaining uniform spacing over the area of the copper specimens, let me repeat the comments in the discussion of results. Due to the extreme environment of the experiment, parallelness of the disks could not be guaranteed to better than 10^{-3} cm across the surface of the specimens. The guidance system consisted of three linear ball bushings which guided three shafts attached to the back of the emitter disk. Since no lubricant was used in the ultrahigh vacuum environment, the tolerance in the ball bushings was made large enough to insure that no seizure of the shafts would occur.

The spacing for each experimental point was obtained by first reaching steady state, then measuring the displacement required to make first contact between emitter and receiver via the micrometer. Professor Wulff's suggestion of capacitative measurements of spacing is a good one and should prove very helpful.

Regarding the copper samples, the emitter disk was hand polished and chemically cleaned whereas the receiver, 1 mil copper film, was only chemically cleaned. The possible effect of impurities was investigated by using large residual resistivities in the theoretical models with only a 10 percent increase in the predicted flux. So the effect of reasonable amounts of impurities at these temperatures appears to be relatively small.

Due to the thermal characteristics of the system, the emitter temperature could not be lowered to the bath temperature during calibration, always staying several tenths of a degree above the receiver temperature. But since the radiant interchange is so low at these temperatures as compared to the electrical power input, this effect can be neglected. In additon, the thermal resistance of the thermal link does appear quite low, but this is due to calibrating the electrical leads along with the thermal link. Although the temperature of the receiver varies very little, the receiver resistance shows fairly large variation. This allows quite accurate measurement of heat flux.

The 10^{-12} torr pressure is an estimate of the pressure in the chamber at liquid helium temperature. Since the Kreisman gauge was located at a room temperature portion of the system, the cryopumping effect and the gettering should result in a chamber pressure several orders of magnitude lower than that indicated.

Lastly, since the calorimetric technique required long periods of time as well as large expenditures of liquid helium, the data points are all of those obtainable.

NENAD N. KONDIĆ
Associate Professor,
Department of Mechanical Engineering,
Indiana Institute of Technology,
Fort Wayne, Ind.

Lateral Motion of Individual Particles in Channel Flow—Effect of Diffusion and Interaction Forces

Consideration is given to dispersed systems in which the particle behavior is a function of systematic motion. The following phenomena governing the movement of the particles are analyzed from the channel entrance: convective effects, translation due to gravity, fluid drag, and circulation induced by the flow. External lateral forces and mutual particle interactions are not considered. Results are obtained for the magnitude and overall effects of the lateral force due to circulation around the particles. The analysis is closely related to the author's measurements of the deposition of micron-size water droplets in adiabatic vertical flow.

Introduction

PARTICLE-FLUID systems are of interest in fields of activity which sometimes have very little else in common, for example chemical engineering, biology, meteorology, and physics. This may be the reason that the problem is sometimes attacked thoroughly, but not with sufficient breadth. Some quite reliable results are contradictory when an attempt is made to explain them theoretically. Obviously, one cannot seek general solutions for real, complex systems.

The questions of interest in basic research as well as in engineering practice can be summarized in the following way:

1 How do the particles behave in the entrance region of channel flows and how is the particle entrance region defined?

2 In the developed flow of the carrier fluid, in which direction is the particle lateral motion: to the center (coring) or toward the walls (deposition)? On which variables does this direction depend? By deposition motion we mean the migration toward the walls, even when the boundary conditions do not allow for physical deposition.

3 How is the lateral particle motion affected by axial body forces (gravitation, magnetic field)? What is the relative contribution of these forces to diffusion in respect to the resulting particle behavior?

4 What is the magnitude and direction of surface forces arising in the fluid itself (interaction forces) and how do they interact with the axial body forces, thus causing the combined interaction [21][1] forces?

5 Under which circumstances must one take into account the

Contributed by the Heat Transfer Division and presented at the ASME-AIChE Heat Transfer Conference, Minneapolis, Minn., August 3–6, 1969. Manuscript received by the Heat Transfer Division, October 21, 1969. Paper No. 69-HT-32.

[1] Numbers in brackets designate References at end of paper.

Nomenclature

A = constant or area
B = constants or magnitudes, defined by subscripts
c = intensity of the vector ($\mathbf{c}$) of the resulting velocity ($\mathbf{c} = \mathbf{u} + \mathbf{v}$) of the fluid; c_p the same for the particle; subscript—concentration, or due to it
de = subscript—deposition, depositing
e = base of the natural logarithm
ex = subscript—exit
F = force
= frequency, probability, density function (distribution) and function generally; subscript—fluid (flow)
G = specific particle flux (per unit surface and unit time)
g = acceleration due to gravity, or general, and the corresponding subscript
h = subscript—hydraulic
I = intensity, defined in text or in figures
in = subscript—inlet, entrance
J = factor defined in text
j = subscript—joint (effect, etc.)
K = mass transfer coefficient
k = mass transport quotient, or deposition parameter, defined in text
L = F_y—lift force; L_l—lift force per unit length
l = length, distance; l_p—average, between two particles or up to the next obstacle; l_0—channel

(*Continued on next page*)

mutual influences of the diffusional (statistical) and the systematic (force-governed) behavior of particles?

6 In what way do walls, as limits of the system, affect the particle concentration field, especially in the region adjacent to the wall? This is of utmost importance for the two extreme cases: when particle deposition is the ultimate goal (filtration, separation, superheating), or when contact with the wall should be avoided (transport of material in suspended form, protection of red cells in artificial out-of-body blood circulation).

All these questions apply to various system parameters; besides the channel and particle geometry and their absolute dimensions, the most important among them are fluid characteristics and velocity, and the same for particles. Two absolute numerical values are of importance: the channel-flow Reynolds number (Re_f), showing as a good approximation the distinction between laminar and turbulent flow, and the particle concentration. When the particle concentration is moderately high, the apparent viscosity of the suspensions is altered and the fluid velocity field is deformed, i.e., there is significant momentum exchange. At still larger concentrations there is direct physical interaction among particles. Both situations reduce the probability of solutions not only in a finite analytical form, but also make difficult the formulation of differential (or differentio-integral) equations describing the phenomenon.

Having in mind the goal to obtain some useful and reliable results, we introduce the following limitations and simplifications:

(*a*) The system is incompressible, two-dimensional and adiabatic. Both phases are in equilibrium. In a time-averaged sense, the system is in steady state.

(*b*) The particles are rigid spheres. When dealing with a spectrum of particle size, they will be represented by appropriate mean values of the radius (linear, square, etc.).

(*c*) The particle radius is: (I) at least one order of magnitude smaller than the channel hydraulic radius; (II) of lower order of magnitude compared to the mean distance between particles; and (III) large compared to the molecular mean free path of the carrier fluid (or the dimensions and distances of the liquid molecules).

(*d*) No body forces act between particles, and no collisions occur. We note that (*c*) and (*d*) define the individual particles. In such cases, the system can also be a suspension of nonnegligible concentration, but the fluidized systems are excluded. From numerical values given in the paper, it can be shown that the heaviest natural fog fulfills the above conditions for individual behavior of particles.

(*e*) The fluid-velocity profile relative to the particle is replaced by its local tangent.

(*f*) When dealing with turbulent channel flow, the relative particle-to-fluid motion is assumed to be laminar. This is based on results of various authors [1, 2].

(*g*) Both phases have a uniform distribution of velocity and concentration at the channel entrance. Discontinuous entrance effects are not analyzed, although they are often present in the experiments (eddies due to a preceding flow section or due to entrance edges).

(*h*) No external lateral forces act upon the particles. The influence of such forces could be introduced through an additive term in the differential equation of motion. Also excluded are any energetic or attractive wall effects on moving particles. In this way, the particle deposition or inelastic recoil from the walls can be treated only as a system boundary condition.

Considerations of viscid and inviscid flow will be given later.

Literature Survey

Although it is recognized [2–4] that the phenomenon of particle radial migration usually occurs in the laminar sublayer or buffer region, there exist several papers dealing mainly with the turbulent flow of suspensions [1, 5] which generally neglect the existence (or at least the significant influence) of lateral forces.

According to Milne-Thomson [9], one can use the Kutta-Joukowsky expression for the lift force also in the case of viscid fluids [9–11], but the integration must stretch outside the geometrical shape of the particle [9, 35]. Soo [1] compared the drag and lift forces in a system, concluding on p. 28 that the latter is negligible for sufficiently small particles. His conclusion on p. 333 at least partly contradicts the one on p. 28. There, he derives the proportionality of the ratio (lift force/drag force) with particle radius. This should not be a criterion for neglecting the influence of the lift force for smaller particles: Even their small lateral displacements may cause measurable changes in the concentration field and eventually result in excessive wall damage. If one still accepts the full validity of Soo's arguments for the neglecting of the lateral force in turbulent flow, we note the following: The eddy-diffusivity tensor, which would remain as the only responsible factor for deposition, dies out in the neighborhood of the walls. Friedlander's approach [2], of combining the effects of eddies penetrating the laminar sublayer with the inertia of the particles extends the effect of the eddies up to the walls of the system. In this approach, the eddy-diffusivity field itself is modified by the relation which Lin, et al. [3] have established and experimentally proved, but only for particles about 100 or more times smaller than Friedlander's. It should be mentioned that his introduction of the Reynolds analogy to cover the whole radial region assumes only one extremum in the radial concentration distribution curve (a maximum in the flow axis). In the case of more extrema, the Reynolds analogy, if valid according to other criteria, must be separately applied to the regions on opposite sides of each of the extreme [31]. Soo's [7] measurements with ten times larger and Eichhorn's [26] with thirty times larger nondepositing particles show minima in the center of the channel, where the concentration field is not much affected by the wall-boundary condition. Both the electrostatic and convective effective contribute to the central concavity. Central concentration minima are observed by Kondić [19] and they also follow from a very detailed calculation by Fortier [32]. For sticky walls, as in [2], this would permit the existence of three extrema in the radial concentration field (a central minimum and two maxima closer to walls), and therefore demand a different interpretation of Reynold's analogy.

Nomenclature

length; l_f—mean free path; l_b—boundary layer thickness
- m = mass
- N = concentration (numerical)
- n = number; distance measured orthogonally in respect to the local velocity or local flux; subscript—volumetric average, nominal
- 0 = subscript for the characteristic lengths
- p = parameter, usually representing the ratio of two or more magnitudes; subscript— particle
- Re = Reynolds number, defined in text
- R_0 = half of the channel width (i.e., half of the hydraulic radius, $R_0 = 0.5\ R_h$)
- r_p = particle radius
- S = channel dimension (depth) orthogonal to the axes X and Y
- St = subscript—by, according to Stokes
- T = time
- t = T/T_{in}, relative time (dimensionless)
- u = (fluid) velocity in direction of X axis; subscript—normal, orthogonal to
- V = volume
- v = (fluid) velocity in direction of Y axis; subscript—nondepositing
- X = xR_0, axial coordinate measured from the inlet
- Y = yR_0, lateral coordinate measured from the wall
- α = angle
- μ = dynamic viscosity
- ν = kinematic viscosity
- ρ = density

Besides his book [1], Soo gives in his papers [23, 24] a detailed theoretical and experimental comparison of the eddy-diffusivity of the particles and of the carrier fluid. In this last results, Soo [1, 24] suggests that the particle diffusivity is smaller than that of the carrier fluid, which is in contradiction with Alexander [6], and Soo's previous work [23].

Beal [8] has correlated the data of several authors, including Friedlander's [2], but with the assumption that the particle flux is a *linear* (ramp) *function* of the distance from the wall. On the other hand, in [2] it is assumed that the particle flux is *constant* along the radius. It is striking that, nevertheless, interpretations of both authors show reasonable agreement between theory and experiment. The use of log-log presentation of data, although illustrative for larger ranges of the parameters, might have contributed to this controversy.

Since the creeping flow model is unable to yield a lift force, many authors appear to have assumed that this force is negligible. It should be emphasized, however, that there is no justification for a generalization of this assumption [36]. On the other hand, we are interested in the particle displacement, and not solely in the force contributing to this displacement.

A common observation is that for reduced particle numerical concentration, the lateral migration of particles is increased [4]. In the case of adhesive walls [2, 18] an increase in the mass transfer coefficient has resulted. This effect cannot be attributed to the role of eddies, and therefore requires a more complete model of the particle migration process. Concerning other possible mechanisms, Eichhorn and Small [33] have definitely proved the existence and have measured directly the magnitude of the lateral force in a laminar shear flow.

Parker and Grosh [29] have presented a very detailed monograph covering the field of droplets in gases. Altogether, the existence of lateral forces is proven at least in laminar flow [4, 33] where the driving potential, the slope of the velocity distribution curve near the wall, has a smaller value than in the turbulent flow. Therefore, there is no reason to state the nonexistent influence of this force in the wall regions of a turbulent flow.

One group of authors is concerned with the viscous effects of suspensions in capillary tubes and blood vessels [12–15]. The systems considered are nearly nongravitational. The work by Goldsmith [14] shows discrepancies between the behavior of spherical and nonspherical particles, especially in respect to a strongly increased coring effect for deformable, nonspherical particles. Their results prove the existence of a nongravitational, particle-to-fluid relative velocity, which is necessary to generate the Magnus force. This velocity is evaluated in two independent ways by Simha [17] and Starkey [12], the first result (which appears to be more reliable) equal to 2/3 of the second.

Fuchs [21] presents a comprehensive review of the forces acting on a particle in the very vicinity of the walls, while Schultz-Grunow [22] gives the theoretical solution and experimental proof for macromolecular suspensions in nonslip flow with a velocity gradient, accounting for inertial effects and neglecting the viscous ones (opposite to the Stokes approach). Particles on the walls [21], as well as microparticles close to the walls [22], are repelled from the walls.

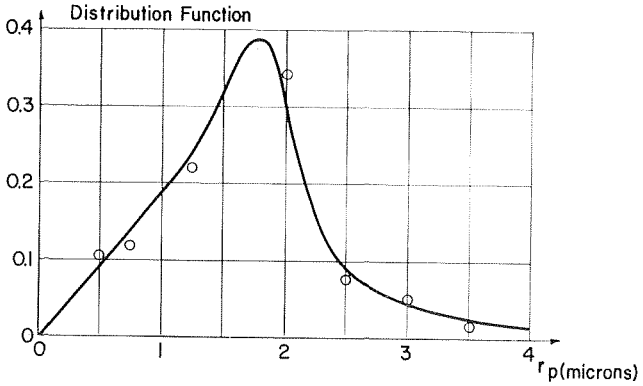

Fig. 1 Droplet spectrum

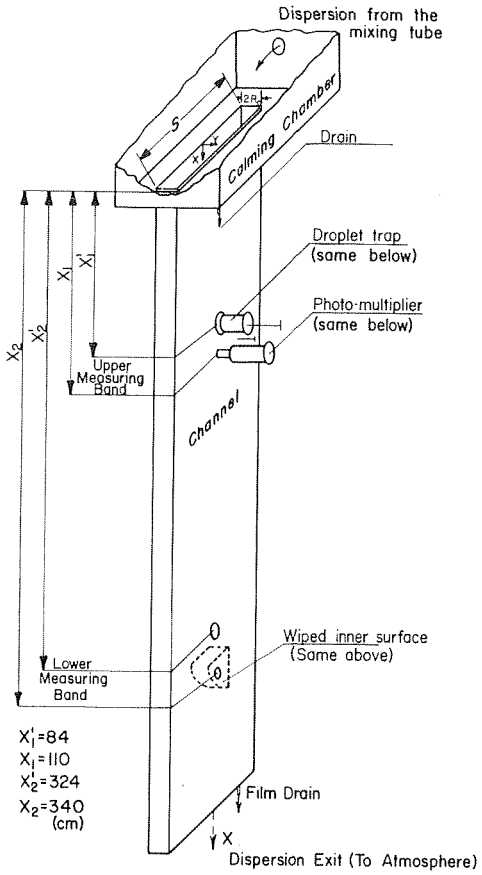

Fig. 2 Test section (not to scale)

Deposition of Water Droplets in Turbulent Downward Air Flow

The decision to work with fog flow was based on the need for additional information on droplet behavior in conventional and nuclear power plants. In addition, fog flow was convenient for the development of new measurement techniques which had been planned. A vertical two-dimensional channel with plane geometry was chosen. According to Laufer [30], a channel cross-section aspect ratio of 40/6 cm (inner dimension) enables one to neglect the effect of the smaller sides ($2R_0 = 6$ cm). The channel length of $l_0 = 400$ cm is nearly twice the velocity entrance length ($l_{in} = 20 \times 2 \times 6$ cm). The flow is in the lower region of turbulence (Re $\cong$ 10,000), a necessary range required by the droplet generation process and system stability.

The flowing water droplets were generated at atmospheric pressure by the volumetric expansion of slightly superheated (3–6 deg C) steam, mixed with the filtered atmospheric air. The micron-range particle spectrum was independent of flow velocity (Fig. 1, obtained by counting of 1500 droplets on microphotographs), and corresponds on the one hand to that occurring in steam turbines, and on the other to the liquid phase remaining after the last demister stage of a boiler.

As shown in Fig. 2, after the mixing chamber and mixing tube the fog enters the box-like calming chamber, then flows with uniform velocity and concentration over sharp edges into the test section. All flow passages were heavily insulated, in spite of the

small temperature differences between the fluid and room. The open-loop conditions were very strictly controlled. To illustrate, during one working day (18 hr), a maximum of one, or at most two, complete measurements were performed. No droplet coagulation occurred.

In addition to the measurement of the flow rate and state variables of both components, the following special measurements were made: On two marked measuring bands (Fig. 2) along the X axis, the droplet deposition rate was measured using light attenuation by the field of deposited droplets [18]. Nearby, samples of the mixture were trapped [19]. Immediate chemical bonding of the sedimented trapped droplets occurs on the sampling plates, allowing later measurement. This was done by scintillator-detector counting of the bound amount of radioactive tritium, previously added to the makeup tank (or boiler). These two papers describe the experimental procedure and also in more detail the loop as a whole. The two kinds of measurements provide the droplet deposition flux and their lateral concentration at the point of measurement, i.e., on two axial coordinates along the channel.

Although turbulent flow is not a system suitable for the theoretical treatment of particle behavior, which is insufficiently explained even in laminar flow, we shall try at least to obtain some kind of agreement between theoretical and experimental results.

Theory

We assume that the particle concentration field and wall deposition flux are mainly dependent on the forces acting upon the particles, and attempt to determine, therefore, the particle trajectory, which defines unambiguously the two fields. By this we do not state that the contribution of eddies is negligible but only that our present knowledge of the particle diffusivity field, especially in the velocity entrance region, is inadequate for mathematical analysis.

According to our assumption (c) in the Introduction, the existence and motion of particles does not contribute significantly to the fluid momentum balance, with the result that the fluid-velocity field will remain the same as that with zero particle concentration. In this way, the system momentum equation reduces to the balance of forces and moments acting on a representative particle. The continuity equation will be used only when discussing the particle concentration field. Concerning the energy balance, the droplets are assumed to be in thermal equilibrium with the surrounding saturated humid air, eliminating any heat and mass transfer. This has been proven by taking samples of droplets at two places along the flow, with no change in the average radii.

As particle rotation [1] does not influence the drag force, we shall omit it here. The influence of particle rotation on the lift force will be the subject of closer analysis in [36].

We shall first give a comprehensive list of all possible influences acting upon the particle in flow. The resulting inertial force on the particle is equal to the sum of the following forces:

1 Body forces resulting from existing fields. In our case this is the axially oriented gravity field, and this force contributes to particle behavior. The nonexistence of electrostatic forces has been separately checked, using special electrodes along the mist flow, which have been brought to 20,000 volts; magnetic forces are also excluded.

2 The Magnus force. It will also be included in the balance.

3 The intermolecular forces (van der Waals, etc. [34]). They are symmetrically distributed independently of particle positions. Therefore, except for the boundary conditions (adhesive walls) their influence on moving particles is neglected.

4 The forces induced in the very neighborhood of the walls, like the rolling effect and other hydrodynamical effects [21], as well as the velocity-gradient inertial force [22]. These forces are also neglected because in our case they become significant only at the distances close to the wall, where deposition is inevitable.

5 The static component of the drag force. It will be considered. It is a sufficiently good approximation for the whole drag effect in the region of particle Reynolds number for our case.

6 The kinetic part of the drag force, due to the acceleration of the apparent particle mass relative to fluid. This force will be neglected. Together with those listed under 7*a* and 8, the force 6 is negligible in the case when particle density is larger than the fluid density [1], which is our case.

7*a* The static pressure surface force.

7*b* Force caused by oscillating pressure.

8 The force due to the deviation of the flow pattern from the steady state (Basset effect).

9 Radiometric forces caused by the fluid temperature gradient (thermophoresis) and

10 The radiometric force caused by different illumination on opposite sides of the particles (photophoresis). Neither force exists in our dark adiabatic and isothermal system.

11 The resultant force due to molecular diffusion (diffusiophoresis); it might not be zero in parts of the field, but its effects are of the order of the Brownian motion, and shall be neglected in our analysis.

The force 7*b* is caused by the fluctuation of the time- and space-dependent pressure field. Such fluctuations might occur in turbulent flow or they might somehow be induced in pool or laminar systems. Any immersed particle of finite size will be acted upon by an oriented, net pressure force if the time average of any parameter of the pressure field changes with space coordinate(*s*). The resulting force may cause a systematic particle movement. The analysis of such a phenomenon would be very complicated. We shall restrict the study to spatially uniform pressure fluctuations, where fluctuations occur. Thus, the influence of the force caused by such a field will be neglected.

The balance of forces acting on the representative particle, with only 1, 2, and 5 remaining, reads in vectorial presentation

$$-m_p(d\mathbf{c}_p/dT) = (\mathbf{c}_p - \mathbf{c})B_p^{-1} - \mathbf{F}_g - \mathbf{F}_{\mathrm{Ma}} \tag{1}$$

where the symbols mean:

$$B_p^{-1} = \mathrm{Cu}^{-1}(6\pi r_p\mu) = F_g/c_{pf};\ \mathbf{c}_{pf} = \mathbf{c}_{\mathrm{St}} = \mathbf{c}_p - \mathbf{c} \tag{2}$$

and the Cunningham correction factor is

$$\mathrm{Cu} = 1 + (l_f/r_p)[1.23 + 0.4\exp(-0.88r_p/l_f)] \tag{3}$$

The gravitational force, or that due to any acceleration field is

$$\mathbf{F}_g = m_p\mathbf{g}(1 - p_\rho) \tag{4}$$

while p_ρ is given in equation (16) and the Magnus force by

$$\mathbf{F}_{\mathrm{Ma}} = B_{\mathrm{Ma}}r_p^3J_rJ_j\rho_f[(\mathrm{curl}\ \mathbf{c}) \times (\mathbf{c}_p - \mathbf{c})] \tag{5}$$

The constant B_{Ma} follows from the integration of the force per unit length (L_l), which is evaluated in [9, 35, 36] for the case of the infinite cylinder in a velocity gradient. Since Landau [37] states that this force is proportional to the thickness of the analyzed section of the body, we performed the integration taking special care of the curvature of the sphere. We are aware that, according to [22], the concept of irrotational flow does not hold strictly for the whole three-dimensional body. Therefore, we have compared our value of $B_{\mathrm{Ma}} = 8\pi/3 = 8.38$ with Prandtl's correction [38] for a wing of equal span/chord ratio. The difference found is less than 20 percent, and can be accounted for by the different shape of the wing and the sphere. Compared with Saffman's value [39], our B_{Ma} is equal to 70 percent of his value. Our result is also in accordance with [32].

The joint correction factor J_j is assumed to be a product of two factors, $J_j = J_{hd}J_{av}$ where J_{hd} is the correction factor due to the uncertainty in the hydromechanical evaluation of the magnitude B_{Ma}. J_{hd} is rather a function than a constant, but only for hydrodynamically similar systems one can neglect its variations. J_{hd} accounts for the nearly eight times larger value of B_{Ma} of

Saffman [39] relative to that of Rubinow-Keller [40]. Saffman reports M.D. Taylor's experiments showing even about ten times larger B_{Ma} than Saffman's! A survey of various B_{Ma} values is tabulated in [41]. The averaging factor J_{av} is different from unity only for trajectories where the change of values of variables in equation (5) cannot in an adequate way be taken into account during the force action.

Concerning J_r, we shall first reconsider the model of the particle submitted to a lateral force. As Tsien [35] in his nonviscid treatment states, his result holds when the field around the sphere is "integrated along a contour far away from the body." We shall next estimate how far this should be in our case. Soo [1] quotes Tsien's concept of "transport of a particle in a fluid element, although by time the fluid element may distort." In some regions, forces on the particle act to separate the particle from the fluid element in which it is traveling (for example, close to the wall). Swanson [11], although more concerned with rotation of larger bodies, states that the experimentally found value of circulation at the outer edge of the body boundary layer is in accordance with the calculated value for the ideal (Kutta-Joukowsky) model. On the other hand, Milne-Thomson [9] and Filon [10] extend the validity of the Kutta-Joukowsky equations for the Magnus force to viscid fluids by taking larger integration contours. Outside of this contour, i.e., Swanson's "boundary layer," the influence of the body on the fluid dies out. We shall assume that this contour, or the particle domain (which affects particle rotation), is defined with the radius R_p, given by the following expressions:

$$R_p = r_p + l_b \quad \text{if} \quad l_b < 0.5l_p - r_p \tag{6}$$

$$R_p = 0.5l_p \quad \text{if} \quad l_b \geq 0.5l_p - r_p \tag{7}$$

Equation (6) defines the viscous particle domain, which links the particles in a way also for $(r_p/l_b) \ll 1$, and equation (7) defines the concentration particle domain. The momentum boundary layer is [31]:

$$l_b = 1.5r_p(\mathrm{Re}_p)^{-0.5} \tag{8}$$

In real systems or parts thereof, R_p is position-dependent and it can be expressed as a combination or function of the two lengths, l_p and l_b, defined above, which in a way represent the extremes. The factor which thus takes care of the real particle domain could be defined by:

$$J_r = \left(\frac{R_p}{r_p}\right)^2 \tag{9}$$

Two scalar equations, corresponding to (1), with the time derivatives of X and Y representing the acceleration and velocity of the particle, read:

$$\ddot{X} + \dot{X}B_1 = u(X, Y)B_1 + g(1 - p_\rho) \tag{10}$$

$$\ddot{Y} + \dot{Y}B_1 = v(X, Y)B_1 + B_2 f_{\mathrm{Ma}}(X, Y) \tag{11}$$

where the function f_{Ma} and the constants are given by:

$$f_{\mathrm{Ma}}(X, Y) = (u - \dot{X})(\partial u/\partial Y - \partial v/\partial X)J \tag{12}$$

$$J = J_r J_j \tag{13}$$

$$B_1 = (B_p m_p)^{-1} = 4.5\nu p_\rho / r_p^2 \tag{14}$$

as dimensional, and B_2 as dimensionless constants

$$B_2 = 0.239B_{\mathrm{Ma}}p_\rho = 2p_\rho \tag{15}$$

$$p_\rho = \rho_f/\rho_p \tag{16}$$

The problem is now to solve the system of two simultaneous inhomogeneous partial differential equations of second order. We used the "PACE" analog computer, and in Fig. 3 is given the corresponding block diagram. For the particles the initial conditions are

$$t = 0: \quad X = 0 = x, \qquad Y = Y_{in}, \qquad \dot{X} = 0 = \dot{x}, \qquad \dot{Y} = 0 = \dot{y} \tag{17}$$

In addition, the walls are assumed to be adhesive, with no entrainment or recoil of droplets, as was proven in the experiments.

Concerning the fluid-velocity components, we shall introduce simplified expressions. They are a compromise between the following requirements:

(*a*) conditions at the extremes of the field,

(*b*) general trend of velocity development in accordance with experimental results, and

(*c*) a reasonable programing and computing time.

As our experiments have been performed within the region of Re_f numbers ($= u_n R_0^4/\nu$) where the "1/7 law" holds as a fairly good approximation, the axial velocity is expressed by the following equation, taking into account the conventional definition of the velocity entrance length:

$$u = 0.25u_n\left[5 - \exp\left(-\frac{x}{26.6}\right)\right] y^{\left[1-\exp\left(\frac{-x}{17.5}\right)\right]0.143} \tag{18}$$

The resulting curves are similar to those reported by Limberg [42]. The fluid lateral velocity component presented a much larger problem for computing. The lateral velocity was found with the use of the continuity equation and equation (18). Some simplifications were introduced, dictated mainly by the requirements of the computer. As the lateral velocity component dies out relatively fast, it has a slight effect on the particle trajectories. This was established a posteriori.

The preliminary calculation shows that the droplets will have been accelerated from rest at the entrance; first they will go through a period of retardation with respect to the fluid, then

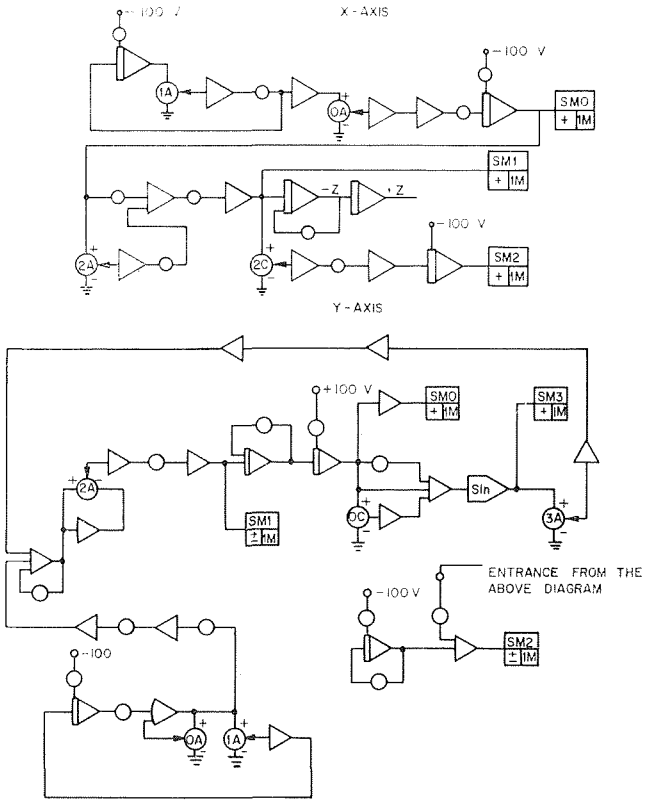

Fig. 3 "PACE" diagram

they will pass through zero relative velocity, and finally they will reach 99 percent of their final free-fall relative velocity. This all will occur within $X = 1$ cm. Runs performed on the computer in this "reversal region" have shown a small coring contribution added to that trajectory which results from the relative falling period only.

The trajectories are obtained by eliminating the time parameter (T) from PACE-recorded curves of $x(T)$ and $y(T)$. In Fig. 4 are shown several examples. Further comments and numerical data are given in the following Results section.

An approximate solution will be evaluated now, with two goals: first, to allow calculations and some analysis without the computer, and second, to show the order of magnitude of errors when treating the developing flow with equations valid for the developed regime. The following approximations are introduced:

1 Acceleration terms and the acceleration period are negligible. Consequently, the velocity difference in equation (12) is given by Stokes' law—equation (2)—and becomes:

$$\dot{X} - u = u_{pf} = (c_{pf})_x \tag{19}$$

2 The terms g/B_1 and v in equations (10) and (11) are negligible compared to the adjacent velocity terms.

3 $\partial v/\partial X$ is negligible compared with $\partial u/\partial Y$ in parentheses of equation (12).

4 The axial velocity is given by the following equation, in fact, the limit of equation (18) for $x = \infty$:

$$u/u_n = 1.25y^{1/7} \tag{20}$$

We note here that except for 4, all other assumptions listed above are numerically quite permissible for the system under consideration. Therefore, discrepancies will be due mostly to the steady (developed fluid-flow) velocity approximation.

Dividing equation (11) with (10), using (2) and (20) and integrating the result, one obtains:

$$y^2 = y_{in}^2 - JB_0x \tag{21}$$

where y_{in} is the dimensionless lateral coordinate where the particle enters the channel (at $x = 0$), and the dimensionless constant is given by:

$$B_0 = 0.0141g\left(\frac{1}{\rho_p} - 1\right) r^4/(R_0\nu^2) \tag{22}$$

Equation (21) is plotted for one value of y_{in} together with several trajectories obtained by PACE in Fig. 4.

We are now interested in finding the dependence between the coordinates y_{in} and x_{de}; the latter defines the place where the particle touches the wall, and deposits, as the wall is adhesive. Particles will be deposited when $Y = r_1 \equiv Y_{de}[r_1 = \bar{r}_p(\text{linear})]$. Then, equation (21) yields:

$$y_{in} = \sqrt{JB_0x_{de} + y_{de}^2} \tag{23}$$

From this relation we shall develop a new parameter.

Looking at two adjacent particle trajectories, the equality of the inlet and exit mass flow rates reads

$$G_{in}Sdy_{in} = G_{de}Sdx_{de} \tag{24}$$

The fraction of the deposition flux to the entrance flux we shall denote with k. This dimensionless deposition parameter, or mass transport quotient, follows from the above relations:

$$k = G_{de}/G_{in} = dy_{in}/dx_{de} = \frac{JB_0}{2y_{in}} = \frac{JB_0}{2\sqrt{JB_0x_{de} + y_{de}^2}} \tag{25}$$

On the other hand, the connection between this parameter and the "classical" mass transfer coefficient is very simple:

$$k = KN_{av}/(u_nN_{in}) \cong K/u_n \tag{26}$$

This holds in cases of negligible differences between the entrance

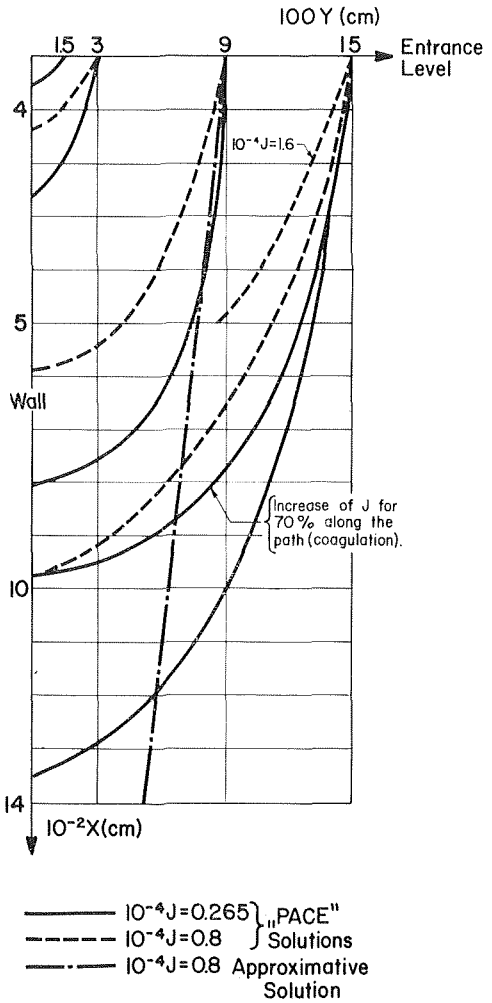

Fig. 4 Particle trajectories

(N_{in}) and average (N_{av}) particle concentration.

A similar procedure will be performed in the more exact solution using the computer results.

We wish to mention here that in the case of upward flow, the approximate solution is also given by equation (21), with a change of the sign in front of J. As a consequence, the trajectories tend toward the channel axis similar to [12, 16]. If the function $u(y)$ would be corrected to have a zero first derivative at $y = 1$, the trajectories would reach the channel axis asymptotically instead of parabolically.

Concerning the concentration field, the mass conservation condition, expressed in the form of a particle-continuity equation for steady state reads:

$$\nabla \cdot (N_p\mathbf{c}_p) = 0 \tag{27}$$

Applying this equation on the stream (or path) tube of width dn in the X-Y plane, and correlating the condition at the channel entrance with an arbitrary point at coordinate x, for $S = 1$ we obtain:

$$G_{in}dy_{in} = G_u dn = N_x c_{px} dn \tag{28}$$

where dn is normal to $c_{px} = c_p(x)$; we denote $N_x = N(x)$. It is assumed that the particles at the entrance have the average fluid velocity $u_n = c_n$.

With the following relation, used also in evaluating (24), and $u_{px} = u_p(x)$:

$$dy/dn = c_{px}/u_{px} = 1/\cos\alpha = \left[1 + \left(\frac{dy}{dx}\right)^2\right]^{0.5} \quad (29)$$

after omitting the subscript x, the local particle concentration is finally expressed by:

$$N_x = N = G_u/c_p = (G_{in}/c_p)(dy_{in}/dn)$$
$$= (G_{in}/u_p)(dy_{in}/dy) \quad (30)$$

Here, the derivative (dy_{in}/dy) is easily evaluated either from the previous equations (21) or the corresponding diagrams by PACE. As it connects the situation along the flow with that at the entrance, we recommend that only the more exact, programmed solution be used.

In the core, i.e., the central part of the flowing system, where the lateral particle velocity is negligible compared with the resultant one, or $c_p \cong u_p \cong u$, we have also

$$dy_{in}/dy = 1 \quad (31)$$

Finally, from (30), with $G_{in} = N_{in}u_n$, one obtains the concentration field as determined only by convection:

$$N_p = N = G_{in}/u_p \cong G_{in}/u = N_{in}(u_n/u) \quad (32)$$

Results

Numerical Values. From the diagram, Fig. 1, the following mean values of the droplet diameters have been calculated (in microns): linear $r_1 = 1.67$; square $r_2 = 1.74$; cubic (volumetric) $r_3 = 1.95$; optical [20] $r_{op} = 2.44$. Because of the selective deposition of larger droplets—according to equation (5)—when the corresponding correction is applied to the last result, we obtain $r_{op}' = 2.83\mu$. The optical radius is in agreement with the value obtained by application of Lambert-Beer's law: $r_{op}'' = 2.82\mu$, when the droplet mass concentration is calculated from the heat and mass balance. According to [34], water droplets of the above magnitude behave as rigid spheres. The thickness of the laminar sublayer was calculated to be 30–50 microns, and the buffer zone 400–700, for the range of fluid velocities in our experiments.

Other pertinent numerical values are listed in the table of results.

Deposition Flux. As an example, from [18] we reproduce Fig. 5, showing four curves from one stabilized series, where the abscissa is proportional to the intensity of light transmitted through the fog flow and the droplets deposited on promoter-treated glass (a coating which does not allow film deposition). At the peaks is shown the effect of mechanical wiping. The signal at the peaks where no droplets are present on the glass, compared with the signal for the empty channel, yielded the r_{op}''. As droplets deposit on the glass the signal decreases. The recording of 30 to 80 of such curves was required to obtain one representative value of the particle flux. The shape of each curve defines a light-attenuation parameter, which is obtained numerically by comparing the experimental curves with solutions evaluated for the system under consideration, and calculated by PACE. In this solution we took into account the surface coalescence [18]. With the determined attenuation parameter, the measured film flow, and

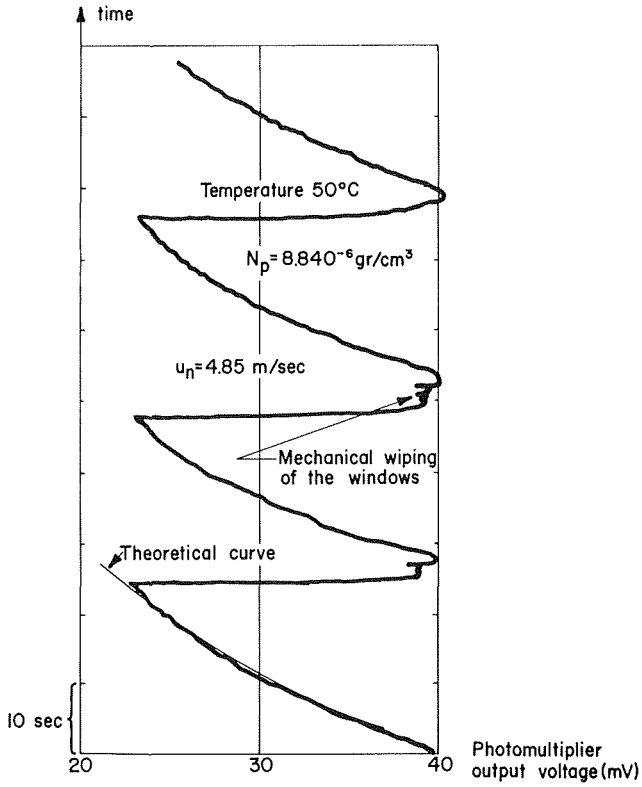

Fig. 5 Reproduction from the recorder: droplet deposition flux measurement by light attenuation

Table 1 Results of the experiments

Run no.	Gas temp. (deg C)	Average gas velocity (m/sec)	Channel Re number (Re_f)	Average inlet droplet mass concentration $\times 10^6$(gr/cm³)	Light attenuation parameter $\times 10^{-2}$(sec^{-1})
1	59.3	5.15	30,300	9	1.16
2	50.2	4.85	18,900	8.8	1.16
3	48.2	2.75	16,500	7.5	1
4	50.1	2.86	17,050	6.8	0.82
5	58.9	2.92	16,850	6.16	0.7
6	48.5	2.82	16,920	5.3	0.7
7	57.5	6.45	37,800	1	0.37
8	49.1	2.72	15,700	6.4	...
9	50.5	4.78	28,600	7.2	...
10	37.6	6.52	39,400	6.8	...
11	49.5	2.04	12,250	...	...
12	48.9	7.05	42,200	...	...
13	45	8.7	51,800	...	...
14	44	9.05	54,300	...	...

Additional information:

Runs 1 to 7: deposition measurements on both measuring bands.
Runs 8 to 10: droplets size measurements.
Runs 11 and 12: measurement of the length with no droplet deposition (X_v).
Runs 13 and 14: determination of the velocity needed to prevent droplet attachment.

Other runs, from 15 to 23 were used for the concentration field determination reported in [19] and in part in Fig. 8 here.

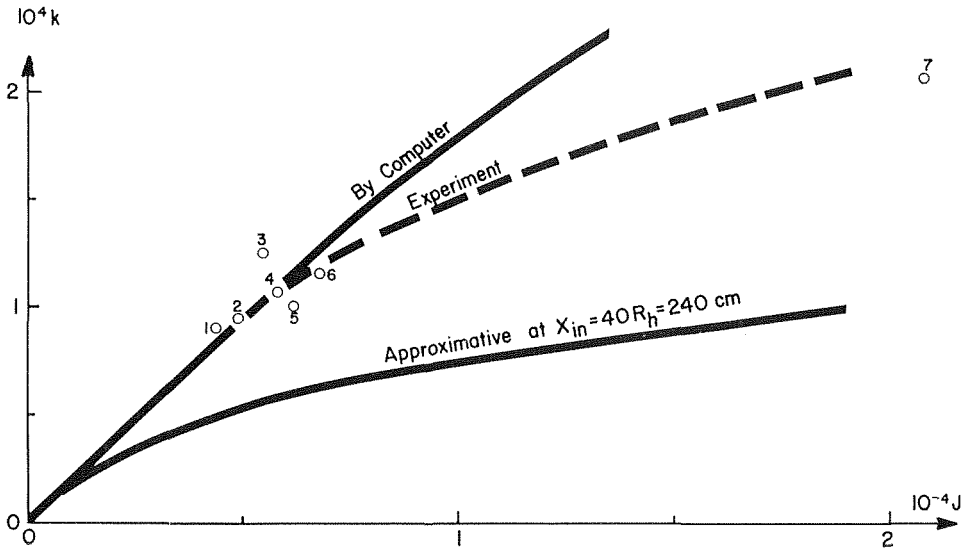

Fig. 6 Deposition parameter dependence on factor J

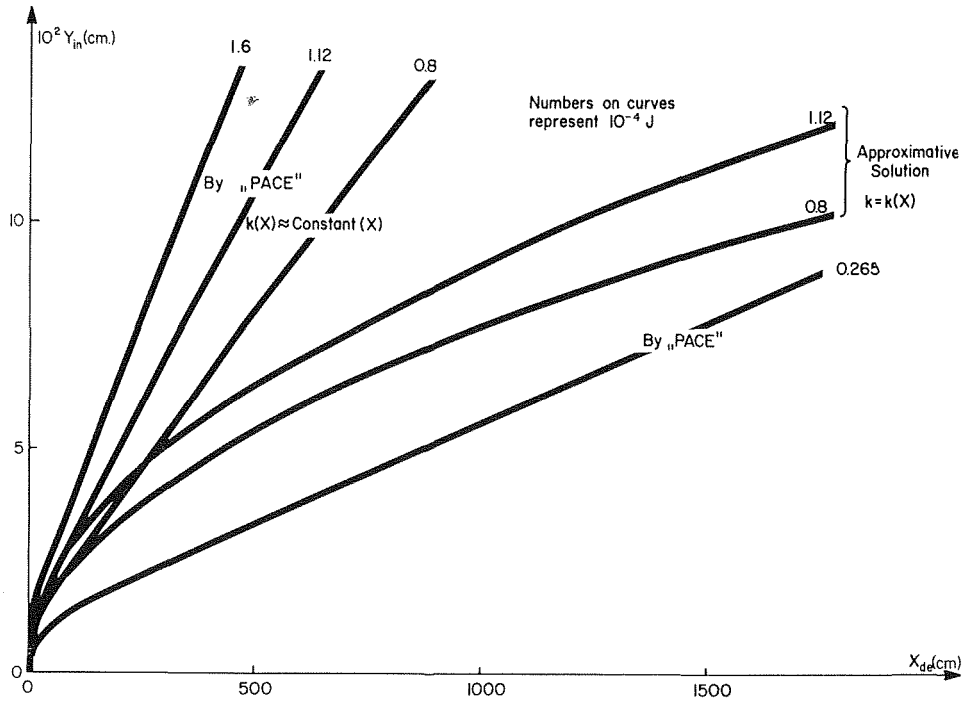

Fig. 7 Correlation between lateral entrance coordinate and axial depositing coordinate

knowing the average fluid velocity and properties, as well as the droplet concentration, the values for the quotient, k, were obtained and are plotted in Fig. 6. In our case, equation (7) defines R_p and in this way, through equation (9), J_r; the last is, thus, obtained from the concentrations. A more detailed description of the experimental procedure is given in [18], but we give here a condensed explanation.

Fig. 7 shows how the parameter k is obtained on the basis of PACE results, taken from Fig. 4. Looking at the computed curves in Fig. 7 we note that they bend not only in the vicinity of $X_{de} = 0 = Y_{in}$ but gradually also with increased X_{de} although this dependence is more pronounced for the curves of the approximate solution. Therefore, the values of k (upper curve in Fig. 6) are the analytical mean values for our apparatus.

The small inertia of the droplets causes a pronounced curvature of the function $Y = Y(J, X)$ only near the origin (Fig. 7). This enables the use of a constant mean $k(J)$ along the channel. In this way, entrance eddies, which have in our experiments—as in Friedlander's [2]—caused a "nondepositing length," did not affect the value of k, after the eddies have been damped. It is interesting to note that for two channel Reynolds numbers, 12,600 and 14,900, we have obtained nearly the same relative nondepositing lengths as in [2]: $1/4\, x_v = 10.8$ and 13. The small inertia of the particles also makes their trajectories independent of the average fluid velocity, in agreement with the exact and approximate solution. The results of Alexander [6] are also in agreement, showing proportionality of k to $u_n^{0.17} \approx 1$ for larger particles than in our case. This could be due to the contributive

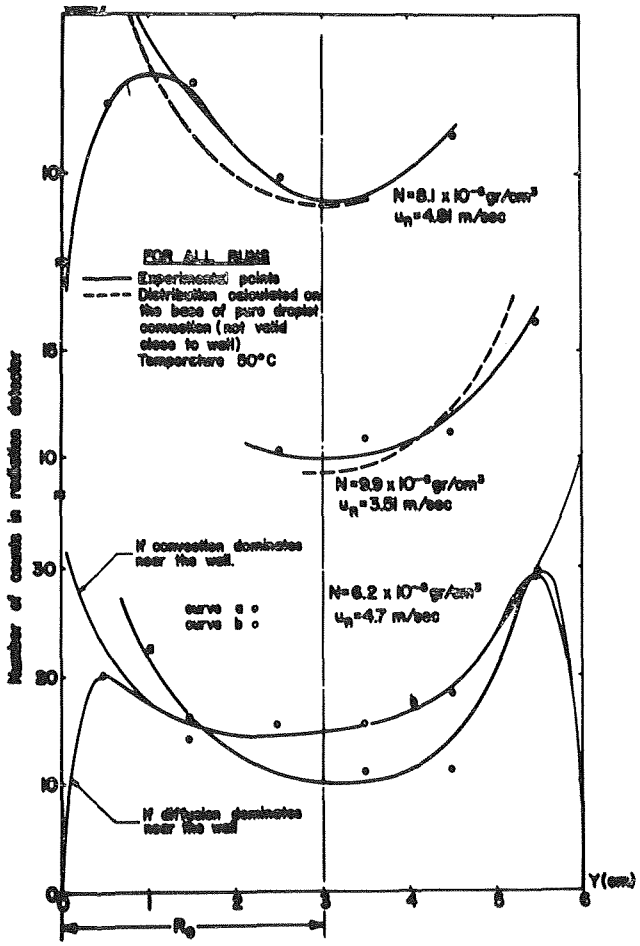

Fig. 8 Droplet mass concentration at lower band (X = 324 cm) by radioactive tracer

effect of eddy diffusion, or some specific wall effects.

Concerning the discrepancy between the computed and approximate solutions which is evident from Figs. 6 and 7 we stress here that except for very small values of J, even after the velocity profile has developed, neither the measured nor the PACE-computed values of k can coincide with the $k(J, X_{de})$ from the approximate solution. This is because the particle trajectories in the region $X > l_{in}$ are also affected by the developing velocity profile from the region $X < l_{in}$.

The J values of the abscissa of Fig. 6 are obtained for the experimental points with the calculated J_r and the joint factor $(J_{av}J_{hd}) = J_j = 3.2$, accounting for:

1 The selection of droplets of larger radii in the deposition process,

2 Coagulation in the region of deposition (only in lateral direction),

3 A possibly steeper velocity distribution than the approximate law $u(y)$ which was used,

4 The decrease of drag coefficient in the turbulent velocity field [25], resulting in a larger true B_p—equation (2)—i.e., larger relative velocity c_{pf}, and finally

5 The uncertainty of J_{hd} as already mentioned.

All these effects act to cause this product (J_j) to be greater than unity. For larger real values of B_{Ma}, (i.e., corrected by J_j), J_r could even be smaller than that given by equation (9), i.e., less sensitive on the particle domain, although in a similar way dependent.

Point No. 7 in Fig. 6, even with the tolerance interval of ±11.7 percent (for the algebraic summation of all errors) in k, shows a deviation from the computed prediction in the direction of the approximate solution. The explanation for this could be: The entrance region of 40 hydraulic radii (even 50 are suggested by Laufer [30]) is either too long, or the development of our turbulent velocity profile after equation (18) is mathematically not sufficiently in accordance with the real phenomenon.

Concentration Field. Focusing now on the influence of the eddy diffusivity in the central part of the flow (where the Magnus force is negligible), we refer to Fig. 8, reproduced from [19]. Several representative runs among numerous sample results are shown. All values are from the developed flow measurement place (lower band). The concave shape is in qualitative agreement with Eichhorn's [26] results for 50 times larger particles in horizontal flow, where the axial convection—equation (32) here—seems to have dominated. The results from the upper measuring band [19], being in the region of the entrance eddies, showed the particle-coring (deposition-preventing) effect due to the entrance eddies (this is not reproduced in Fig. 8). The dotted curve in Fig. 8 presents the interpretation of equation (32) with the help of equation (20). The developed-flow turbulent diffusion contributed evidently very little toward the uniformity of concentration. This cannot be attributed in these experiments to the distance needed for the development of the turbulence along the flow, for, according to Limberg [42], in our case this distance, as a function of the channel Reynolds number, is at most $l_0/4 = 100$ cm. Since the delay time—after turbulence is established—is for that kind of particle motion of the same order of magnitude as for systematic motion, both such explanations (i.e., based on distance and time) must be abandoned.

Concerning the wall region, no conclusion in respect to the slope of the concentration curve can be made from the samples because of the large interval between the measured points in the y direction. There is indicated a trend of lowering concentration, which can be (and probably is) caused by both effects (diffusion and forces). They result in particles approaching the wall with a finite velocity, affecting the registered deposition flux.

Conclusions

The analytical solution for the particle trajectories, taking into account the development of the fluid-velocity profile from the entrance into a rectangular channel, and the experiments performed, show the following:

1 The analytical solution is obtained without introducing artificial functions, but only factors shown to be of the expected order of magnitude. The concept of a particle domain (their radial region) dependent either on the particle boundary layer or the particle numerical concentration has been introduced into the analytical solution.

2 The numerical results of the predictions agree with the experimental data. The latter have been obtained employing a contactless light-attenuation method [18] and the use of radioactive tracers [19].

3 Particle deposition occurred along trajectories mainly developed in the laminar sublayer and the buffer region. The eddies due to entrance edges prevented deposition over the length x_v, with dependence $x_v(\mathrm{Re}_f)$ equal to that in [2].

4 Fluid-velocity profile development influences the particle behavior over a distance longer than the fluid entrance length. This is in accordance with Eichhorn, et al. [26].

5 For the particle sizes considered, the newly defined dimensionless deposition parameter, k, is independent of the axial coordinate and fluid velocity, after the length x_v. The independence on axial coordinate is in full agreement with [2] and on fluid velocity in reasonable agreement with Alexander [6].

6 In our results the parameter k has nearly the same values as in the case of Friedlander [2], although he used a different channel geometry. The values of concentration are different in his and our case, but the character of the $k(J)$ dependence is

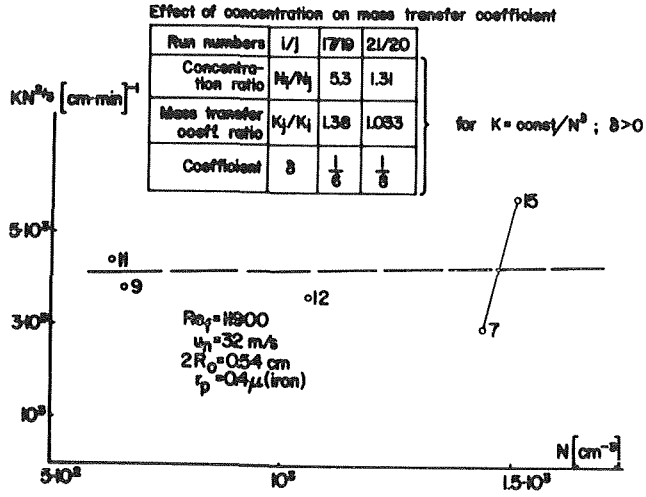

Fig. 9 Presentation of data from reference [2], Table III (given number of runs)

very similar. The relation between the mass transfer coefficient and the concentration which we have calculated from his results, and the tabulated values are presented in Fig. 9. Following from our equations—(7) and simplified (11)—the horizontal line and the quasi-inverse relations (K, N) could be explained through a contribution of the evaluated lateral force to the deposition. As in his case the flow is directed vertically upward; this effect is due either to a reversal in the direction of the force [11, 25, 27, 28] or is a consequence of the joint effect of diffusion and systematic motion. This idea is carefully analyzed in [36].

7 The concave shape of the droplet concentration curves (Fig. 8) indicates at least a nonprevailing role of the eddy diffusivity in our case. Due to the high concentration in the wall region, however, even the reduced diffusivity, acting upon the high concentration gradient, may contribute to particle lateral motion (deposition in this case).

The reasonable agreement achieved between the computed and measured results, especially in respect to the trend $k(J)$, is not considered as a definite proof of the dominant influence of systematic motion on the deposition phenomenon. Nevertheless, it indicates that this influence has the expected character.

The relative contributions of diffusivity and systematic particle motion to their overall lateral migration, and the dependence of this contribution on several variables, is one of the important problems in this field. Furthermore, three main branches of related problems await solution: diabatic and fluidized systems and those with particles other than rigid spheres, as well as combinations thereof.

Acknowledgments

The author wishes to express his gratitude to the head and personnel of the Reactor Heat Transfer Laboratory of the Boris Kidrič Institute of Nuclear Sciences, Beograd, Yugolsavia, who enabled him to perform the experiments. The Computer Center of the Institute also contributed a great deal to the achievement of the analytical solution and to the processing of the experimental data.

In addition, the author highly appreciates the fruitful and valuable discussions with Professor R. Eichhorn and the material support of the Mechanical Engineering Department of the University of Kentucky needed to complete this report.

References

1 Soo, S. L., *Fluid Dynamics of Multiphase Systems*, Blaidsell Publ. Co., Waltham, Mass., 1967.

2 Friedlander, S. K., and Johnstone, F. H., "Deposition of Suspended Particles from Turbulent Gas Streams," *Industrial and Engineering Chemistry*, Vol. 49, No. 7, 1957, p. 1151.

3 Lin, C. S., Moulton, R. W., and Putnam, G. L., "Mass Transfer Between Solid Wall and Fluid Streams," *Industrial and Engineering Chemistry*, Vol. 45, 1953, p. 636.

4 Young, D. F., "The Coring Phenomenon in the Flow of Suspensions in Vertical Tubes," ASME Paper No. 60-HYD-12, 1960.

5 Peskin, R. L., "Some Effects of Particle-Particle and Particle-Fluid Interaction in Two-Phase Flow Systems," PhD thesis, Princeton University, 1959.

6 Alexander, L. G., and Coldren, C. L., "Droplet Transfer from Suspending Air to Duct Walls," *Industrial and Engineering Chemistry*, Vol. 43, 1951, p. 1325.

7 Soo, S. L., et al., "Concentration and Mass Flow Distributions in a Gas-Solid Suspension," *Industrial and Engineering Chemistry, Fundamentals*, Vol. 3, No. 2, May 1964, p. 98.

8 Beal, S. K., "Transport of Particles in Turbulent Flow to Channel or Pipe Walls," *W-BAPL, Heat Transfer and Fluid Flow*—II, 1968, p. 347.

9 Milne-Thomson, L. M., *Theoretical Hydrodynamics*, fifth ed., Macmillan, New York, 1968.

10 Filon, L. N., "Forces on a Cylinder," *Proceedings Royal Society (A)*, Vol. 113, 1927, p. 7.

11 Swanson, W. M., "The Magnus Effect: A Summary of Investigations to Date," *Journal of Basic Engineering*, TRANS. ASME, Vol. 83, Series D, Sept. 1961, pp. 461–470.

12 Starkey, T. V., "The Laminar Flow of Streams of Suspended Particles," *British Journal of Applied Physics*, Vol. 7, Feb. 1956, p. 52.

13 Maude, A. D., "The Wall Effect and the Viscometry of Suspensions," *British Journal of Applied Physics*, Vol. 7, March 1956, p. 98.

14 Goldsmith, H. L., and Mason, S. G., "Axial Migration of Particles in Poiseuille Flow," *Nature*, Vol. 190, June 1961, p. 1095.

15 Vejlens, G., "The Distribution of Leucocytes in the Vascular System," *Acta Pathologica et Microbiologica Scandinavica, Supplementum* XXXIII, 1938, Uppsala, Sweden.

16 Gill, L. E., Hewitt, G. F., and Hitchon, J. W., "Sampling Probe Studies of the Gas Core in Annular Two-Phase Flow: Effect of Length on Phase and Velocity Distribution," *Chemical Engineering Science*, Vol. 18, 1963, p. 525.

17 Simha, R., "Untersuchungen über die Viskosität von Suspensionen und Lösungen," *Kolloid Zeitschrift*, Bd. 76, Heft 1, 1936.

18 Kondić, N., "Theory and Application of Light Attenuation for Mass Deposition Rate Measurement," *Proceedings of the Third All-Union Heat and Mass Transfer Conference*, Minsk, USSR, May 1968.

19 Kondić, N., and Kozomara, S., "Concentration Field Measurement of Flowing Condensed Droplets by Radioactive Tracer," *JSME Semi-International Symposium*, Tokyo, Japan, Sept. 1967.

20 van de Hulst, H. C., "Light Scattering by Small Particles," Wiley, New York, 1957.

21 Fuchs, N. A., "The Mechanics of Aerosols," Macmillan, New York, 1964.

22 Schultz-Grunow, F., "Entmischung Makromolekularer Lösungen in Scherströmungen," *Rheologica Acta*, Nol. 2/3, 1958, p. 289.

23 Soo, S. L., "Statistical Properties of Momentum Transfer in Two-Phase Flow," *Chemical Engineering Science*, Vol. 5, 1956, p. 57.

24 Soo, S. L., Ihrig, H. K., Jr., and El Kouh, A. F., "Experimental Determination of Statistical Properties of Two-Phase Turbulent Motion," ASME Paper No. 59-A-59, 1959–60.

25 Hoglund, R. F., *Journal of the American Rocket Society*, Vol. 32, 1962, p. 662.

26 Eichhorn, R., Shanny, R., and Navon, U., "Determination of the Solid Phase Velocity in a Turbulent Gas-Solids Pipe Flow," Project SQUID, Tech. Report PR-107-P, Dept. of Aerospace Engineering, University of Virginia, Charlottesville, Va., March 1964.

27 Makol, Sump., "Current Hydroaerodynamics of a Viscous Fluid," Part II, G. I. In. L. 1948, USSR, p. 183.

28 Garstand, T. E., "The Flow of Viscous Liquid Past Spinning Bodies," *Proceedings Royal Society*, 142 A, 1933.

29 Parker, R., and Grosh, J., "Heat Transfer to a Mist Flow," ANL-6291-Report, Argonne 1961.

30 Laufer, J., "Investigation of Turbulent Flow in a Two-Dimensional Channel," NACA Tech. Note 2123, 1962.

31 Rohsenow, W. M., and Choi, H. Y., *Heat, Mass and Momentum Transfer*, Prentice-Hall, Englewood Cliffs, N. J., 1961.

32 Fortier, A., *Mecanique des Suspensions*, Masson et Cie, Paris, 1967.

33 Eichhorn, R., and Small, S., "Experiments on the Lift and Drag of Spheres Suspended in a Poiseuille Flow," *Journal of Fluid Mechanics*, Vol. 20, part 3, 1964, p. 513.

34 Kruyt, H. R., *Colloid Science*, Vol. 1, II, Elsevier Publ. Co., Amsterdam, New York, 1952.

35 Tsien, H., "Symmetrical Joukowsky Airfoils in Shear Flow," *Quarterly Journal of Applied Mathematics*, Vol. 1, 1943, p. 130.

36 Kondić, N., "The Interaction Influence of Convection, Dif-

fusion and Forces on the Distribution of Particles Flowing in Channels of Finite Length," to be published, University of Kentucky, Mechanical Engineering Department, Lexington, Ky.

37 Landau, L. D., and Lifschitz, E. M., *Fluid Mechanics*, Addison Wesley Publ. Co., 1959.

38 Prandtl, L., "Applied Hydro and Aerodynamics," McGraw-Hill, London, New York, 1934.

39 Saffman, P. G., "On the Motion of Small Spheroidal Particles in a Viscous Fluid," *Journal of Fluid Mechanics*, Vol. 1, 1956, p. 540.

40 Rubinow, S. I., and Keller, J. B., "The Transverse Force on a Spinning Sphere in a Viscous Fluid," *Journal of Fluid Mechanics*, Vol. 11, 1961, p. 447.

41 Segré, G., and Silberberg, A., "Behavior of Macroscopic Rigid Spheres in Poiseuille Flow" (part 1 and 2), *Journal of Fluid Mechanics*, Vol. 14, 1962, pp. 115, 136.

42 Limberg, H., "Der Einlauf einer Turbulenten Kanalströmung," *Maschinenbautechnik*, Band 8, No. 12, 1959.

Vibration Effects on Convective Heat Transfer in Enclosures

R. E. FORBES
Assistant Professor. Assoc. Mem. ASME

C. T. CARLEY
Professor and Head. Mem. ASME

C. J. BELL
Associate Professor.

Department of Mechanical Engineering, Mississippi State University, State College, Miss.

The effect of mechanical vibrations on natural convective heat transfer in an enclosure of rectangular cross-section was investigated experimentally. The enclosure was comprised of two vertical and opposed surfaces which were maintained at different temperatures, surrounded by four other adiabatic surfaces. Vibration stresses were applied to this heat transfer cell by mounting it vertically on the armature of an electrodynamic vibrator. Frequencies from 0 to 4000 Hertz and accelerations from 0 to 110 g's were utilized in the investigation. The results show that vibration of a thermally active enclosure can have a significant effect on its heat transfer characteristics especially near the resonant natural frequency of the column of fluid contained within the enclosure. Increases in convective heat transfer coefficients of as much as 50 percent were obtained during this investigation. A correlation equation was developed by utilizing the dynamic response characteristics of the fluid column when considered as a seismic mass.

Introduction

Convective heat transfer within fluid-filled enclosures is an important mechanism in many physical systems. A modest amount of experimental data and no closed-form analytical solutions are currently available for predicting the heat flux and temperature and velocity distributions in such cases. A few numerical solutions exist for restricted ranges of the pertinent variables and then only for simple geometries.

The effect of mechanical vibrations, as well as sound waves, on heat transfer from bodies in an infinite atmosphere has been studied by many investigators. This paper, however, is apparently the first report on an investigation into the effect of enclosure vibration on heat transfer within a fluid-filled enclosure.

The data presented here are the result of an experimental research effort designed to determine the effect of vibration on heat transfer across a vertical gap. A rectangular enclosure was constructed so that the heat transfer would be essentially one-dimensional across the width of a narrow vertical cell. Data were recorded with four different widths of a water-filled cell utilizing temperature differences sufficient to produce a range of Rayleigh numbers from 10^5 to 10^8. The applied vibratory motion was parallel to the gravitational field and sinusoidal.

The data recorded from the experimental system are presented along with a proposed correlation equation. The effect of vibration on cell heat transfer characteristics is explained in terms of the dynamic characteristics of the enclosed fluid column. This explanation is supported by data from an experimental determination of the dynamic behavior of the liquid column. The investigation also included flow visualization studies utilizing neutrally bouyant particles, as well as measurement of horizontal temperature distributions within the fluid.

Contributed by the Heat Transfer Division and presented at the Winter Annual Meeting, Los Angeles, Calif., November 16–20, 1969, of The American Society of Mechanical Engineers. Manuscript received by the Heat Transfer Division, January 3, 1969; revised manuscript received July 25, 1969. Paper No. 69-WA/HT-13.

Nomenclature

a = maximum amplitude of vibration
A = area of hot plate
c_p = specific heat
f = frequency
f_n = natural frequency of fluid column
g = ratio of acceleration to acceleration of gravity
g_0 = acceleration of gravity
g_t = maximum shaker dimensionless acceleration
Gr = Grashof number
H = enclosure height
$\bar{h}$ = average convective heat transfer coefficient
k = thermal conductivity
Nu = Nusselt number $\bar{h}W/k$
Pr = Prandtl number $\mu c_p/k$
q = heat transfer rate
Ra = Rayleigh number (Gr Pr)
T_c = temperature of cold plate
T_h = temperature of hot plate
ΔT = temperature difference $(T_h - T_c)$
W = enclosure width
α = thermal diffusivity
β = volumetric coefficient of thermal expansion
μ = dynamic viscosity
ν = kinematic viscosity
ρ = density
ω = circular frequency

A review of the literature reveals that numerous investigators have determined, both analytically and experimentally, the effect of vibration on convective heat transfer in a variety of configurations. Geometries studied have included thin wires, cylinders, heat exchanger tubes, annuli, and flat plates. Both natural and forced convection have been investigated for such variables as body shape, size, and orientation, and direction and amplitude of vibration.

In some investigations the heated body was vibrated by some external mechanical means, while in others the fluid was vibrated using such devices as ultrasonic vibrators or acoustic fields.

Previous work in this area can be grouped into two general categories:

the effect of either body vibration or fluid vibration on natural convection from the exterior of a body to an infinite atmosphere; or

the effect of vibration on forced convection flow within heat exchanger tubes or annuli.

A complete review of the literature published in both these areas is given by Forbes [1].[1]

The literature apparently contains no report of any effort, either analytical or experimental, to determine the effects of vibration on natural convective heat transfer within a fluid-filled enclosure.

There have been numerous published reports concerning experimental investigations of the convective heat transfer mechanism within an enclosure without vibration. Significant experimental studies of natural convection within rectangular enclosures include those of Mull and Reiher [2], de Graff and van der Held [3], Eckert and Carlson [4], Dropkin and Somerscales [5], Emery and Chu [6], Landis and Yanowitz [7], Elder [8, 9], and most recently MacGregor and Emery [10]. The successful correlations and predictions of the effect of vibration on natural convective heat transfer from a body to its infinite atmosphere are usually based on a comparison of the vibration amplitude of the body and the thickness of the boundary layer of fluid flowing past the body. Such a comparison is not meaningful for vibration of an enclosed column of fluid. Rather, the fundamental physical phenomena to be studied are the dynamic characteristics of the fluid column and the enclosure and the effect that these characteristics have on the convective heat transfer. In order to carry out this study a guarded hot-plate test cell was constructed and mounted on an electrodynamic vibrator.

Experimental Systems and Procedures

The experimental system consisted of the natural convection heat transfer test cell, associated electrical and thermal instrumentation, and the electrodynamic vibration system.

A cross section of the guarded-plate test cell is shown in Fig. 1. The hot plate was machined from aluminum alloy, the surface in contact with the enclosed fluid measuring 16 in. in height and 7 in. in depth. Power was supplied to the eight strip heaters embedded in the heater plate by a direct current regulated power supply. A potentiometer in series with each heater permitted adjustment of the surface temperature of the plate to within 1 deg F of an isothermal condition. The hot plate surface temperature was indicated by sixteen 30 gauge copper-constantan thermocouples epoxied flush with the surface of the plate. The seven traversing thermocouples could be positioned horizontally at any point in the fluid including the hot and cold plate surfaces. These thermocouples were utilized to measure the temperature distribution in the enclosed fluid as well as to monitor the isothermal condition on the hot and cold plates under nonvibratory conditions.

The spacer plate was constructed of a low thermal conductivity phenolic material. Twenty eight thermocouples were located on the surfaces of the spacer plate so that the temperature differences across the plate and its edge could be monitored. The guard plate consisted of an aluminum alloy plate containing twelve strip heaters. The guard plate enclosed the phenolic spacer plate on all surfaces except the surface in contact with the heater plate. After the heater plate had been adjusted to an isothermal condition, the guard heaters were adjusted individually until a minimum temperature gradient existed through the phenolic spacer plate and its edges. At this condition, essentially all electrical energy dissipated in the heater plate was convected through the fluid. Electrical power input to the heater plate was individually measured for each of the eight heaters. Thermocouple e.m.f. for all thermocouples was indicated on a digital millivolt meter after the appropriate thermocouple had been selected by a rotary switch.

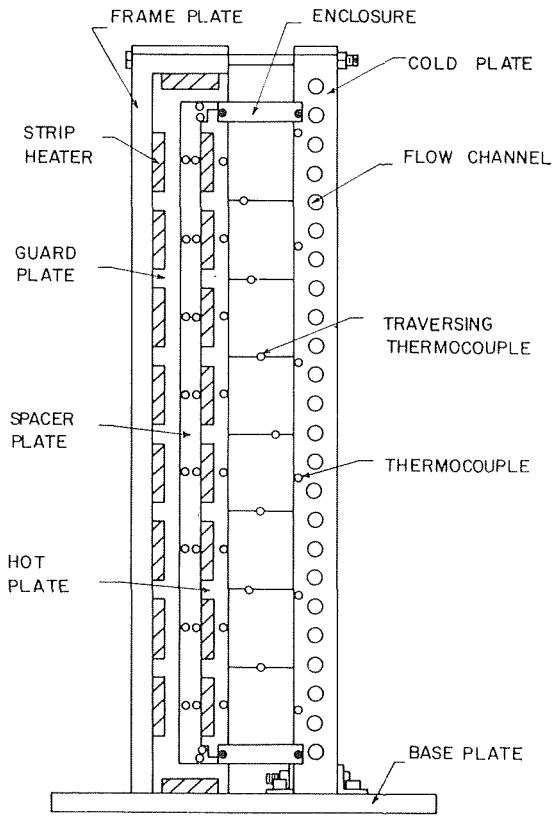

Fig. 1 Cross section of test cell

The water was contained between the hot plate and the cold plate by a four-walled plexiglas enclosure constructed of $^1/_2$ in. thick plexiglas which allowed observation of the test fluid during the recording of all data. The low thermal conductivity of the plexiglas produced an essentially adiabatic boundary at these four surfaces. The enclosure was filled with distilled water through a small opening in the top surface of the plexiglas, and allowance for expansion of the water was made using this same opening. A section of $^1/_8$ in. OD surgical tubing extended vertically upward from the fill plug in the top plexiglas wall. This allowed expansion of the water upon heating, as well as subjecting the enclosed fluid to atmospheric pressure at all times. After the enclosure was filled with water, numerous small bubbles developed on the hot plate surface when the heaters were energized. These bubbles were easily visible through the side plexiglas walls and were removed prior to any testing. Four plexiglas enclosures were constructed, giving widths between the hot and cold plates of 1.7, 1.0, 0.5, and 0.375 in. These gap thicknesses resulted in test cell height to width ratios (aspect ratios) of 9.4, 16.0, 32.0, and 42.7.

The cold plate was cooled by circulating chilled water through twenty-four $^3/_8$ in. dia holes drilled through the aluminum plate. The water flow rate could be varied for the individual channels, thus allowing the cold plate to be adjusted to within 1 deg F of an isothermal condition. The cold plate temperature was indicated by twelve thermocouples embedded in the surface of the plate.

[1] Numbers in brackets designate References at end of paper.

The test cell, weighing approximately eighty pounds, was mounted on the vibrator by bolting the test cell plate to the vibrator table. All vibration tests were conducted with the test cell in a vertical orientation and for vibration in a vertical direction.

The vibration system was an Unholtz-Dickie Vibration Testing System capable of producing a generated force at the shake table of 2000 pounds peak. The acceleration level which could be achieved with the heat transfer test cell depended on the selected frequency; however, acceleration levels, as indicated by the shaker table accelerometer, were varied from 0.55 g to 110 g by selecting appropriate frequencies.

With the test cell as constructed and integrated into the electrodynamic vibration facility, the following ranges of variables were available.

Aspect Ratio: 9.4 to 42.7
Temperature Difference Across the Cell: 18 F to 62 deg F.
Vibration Frequency: 0 to 4000 Hertz
Acceleration Level: 0 to 110 g

A qualitative analysis was performed in order to select a procedure for accumulating data. It was first necessary to decide whether to establish a thermal field and then impose a vibration field upon it or to establish these fields in the reverse order. In the light of the expected practical applications for the information to be produced, it was decided to first establish a thermal field in the test system and then to impose different vibrational stresses on the cell. Following this decision, it was necessary to establish a procedure for recording the data.

Out of an almost infinite number of combinations of vibration and thermal states, the following were selected. A chosen temperature difference was established across the test cell. This required adjusting the power inputs to the electrical heaters until isothermal conditions were established on the hot plate under nonvibratory conditions.

The shaker was then energized and brought to a preselected frequency. At this frequency the amplitude was adjusted to achieve a maximum acceleration level within the capability of the apparatus. The system parameters were then monitored until equilibrium had been achieved. No effort was made to readjust the temperature of the hot plate to its initial value, if a deviation from isothermal occurred, but the variations of temperature over the height of the hot plate and cold plate were recorded.

A study of the technical literature available in this area indicated that average surface velocity might provide the most satisfactory variable with which to correlate the heat transfer data in a vibrating system. On the basis of this, an enclosure velocity was selected which could be reached over the entire range of frequencies available. The enclosure velocity is defined as the product of the amplitude and frequency of vibration. The velocity selected was 1.70 ips.

This second series of tests was run with the same procedure as the first, except that at each frequency the amplitude was selected to produce an enclosure velocity of 1.70 ips rather than a maximum acceleration.

Observation of the boundary layers on the hot and cold plates under vibratory conditions indicated that a turbulent boundary layer existed over the entire surface of the plates in the vicinity of 200-400 Hertz. Under other vibratory conditions the boundary layer was either completely laminar or underwent transition from laminar to turbulent flow at some fixed distance up the plates.

Neutrally buoyant spherical particles were used to indicate the flow patterns in the enclosed fluid for both vibratory and nonvibratory conditions. A 1500 watt quartz iodide photoflood lamp was used to illuminate a $\frac{1}{8}$ in. wide vertical slit at the mid-depth of the enclosure. The flow patterns could be viewed or photographed from a horizontal position through the side plexiglas walls. Density gradients in the water could be visually observed in the vicinity of both the hot and cold plate surfaces.

The work of Schoenhals and Overcamp [11] indicated that the resonant frequency of a vibrating liquid column could be determined by mounting a pressure transducer in the container bottom. If the enclosure is vibrated at various frequencies while the acceleration level is maintained constant, the maximum output recorded with the pressure transducer will correspond to the resonant frequency of the fluid column.

In this manner, the resonant frequency of the $H/W = 9.4$ enclosure was determined to be approximately 270 Hertz. Testing at this frequency produced a turbulent boundary layer on the entire surface of both the hot and cold plates.

A digital computer program was written to convert the raw data into the dimensionless parameters Nusselt number and Rayleigh number.

Discussion of Results

Preliminary Investigation. The heat transfer results recorded during 274 runs with the water-filled test cell are shown in Figs. 2, 3, 4, 5, and 6. The hot and cold plate temperatures from which the temperature differences were calculated are averaged values obtained from the readings of 16 thermocouples on the hot plate and 12 thermocouples on the cold plate. All fluid properties in the

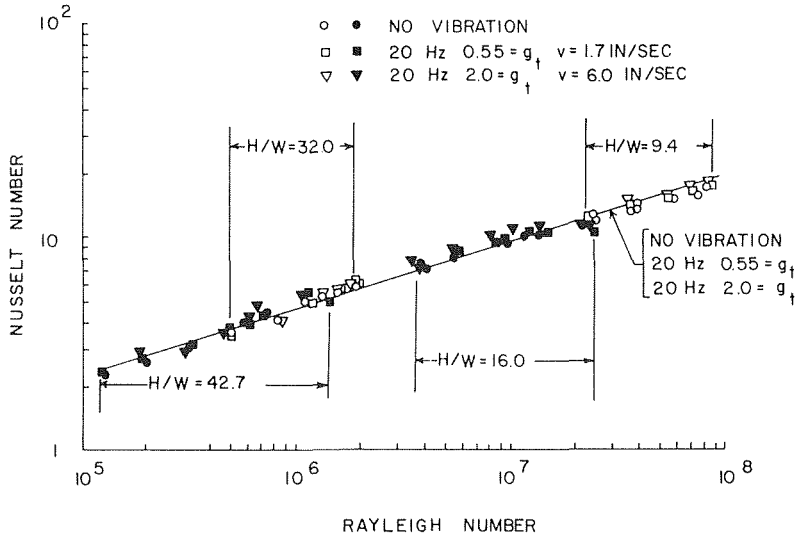

Fig. 2 Vibration effect on free convective heat transfer in a rectangular enclosure. Vibration frequency = 20 Hertz.

Grashof and Nusselt number have been evaluated at the mean fluid temperature, $(T_h + T_c)/2$. The average heat transfer coefficient, $\bar{h}$, was calculated from the relationship

$$\bar{h} = \frac{q}{A\Delta T} \tag{1}$$

On each figure, the Nusselt number has been plotted versus Rayleigh number for a given enclosure frequency with the dimensionless armature acceleration ratio $(a\ \omega^2)/g_0$ as a parameter. Acceleration ratios and the corresponding enclosure velocity $(a\ \omega)$ are also shown on each figure. The characteristic length in both the Nusselt number and Rayleigh number is the test cell gap width W. The heat transfer results recorded with no vibration of the enclosure are shown on each figure. Since data for both the vibratory and nonvibratory case are plotted on each figure, any change in the heat transfer produced by the vibration is readily apparent. The test cell aspect ratio for which data points were recorded has been indicated on each figure. Solid data points are for the 16.0 and 42.7 aspect ratios, while open points are for the 9.4 and 16.0 ratios. The selected temperature differences and aspect ratios produced overlapping data for the aspect ratios of 32.0 and 42.7, and 9.4 and 16.0, but no overlap between the 16.0 and 32.0 aspect ratio.

A curve which best represents the experimental heat transfer data has been drawn on each of Figs. 2 through 6. A discussion of the curve fitting procedures will be more meaningful if it is presented in light of the entire data; thus it will be delayed for the present.

Fig. 2 presents the heat transfer results for a shaker table frequency of 20 Hertz and accleration ratios of 0.55 and 2.0. In all following discussions the shaker table acceleration $a\ \omega^2/g_0$ will be indicated by the symbol g_t.

The $0.55 = g_t$ level corresponds to a shaker table velocity of 1.7 ips while the $2.0 = g_t$ level corresponds to a velocity of 6.0 ips. Fig. 2 reveals that the testing with twenty-five ΔT's and four aspect ratios produced data which is evenly distributed between Rayleigh numbers of 1.25 (10^5) to 8.3 (10^7). The corresponding Nusselt numbers varied from 2.3 to 17.4. The heat transfer was essentially unaltered by enclosure vibration at 20 Hertz for either of the acceleration ratios utilized. It is worthy of note that little effect was produced on the heat transfer by the 20

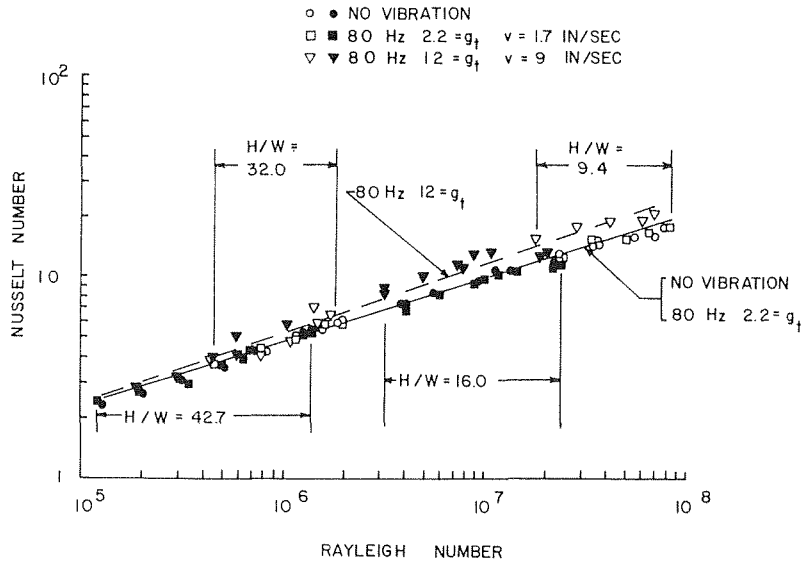

Fig. 3 Vibration effect on free convective heat transfer in a rectangular enclosure. Vibration frequency = 80 Hertz.

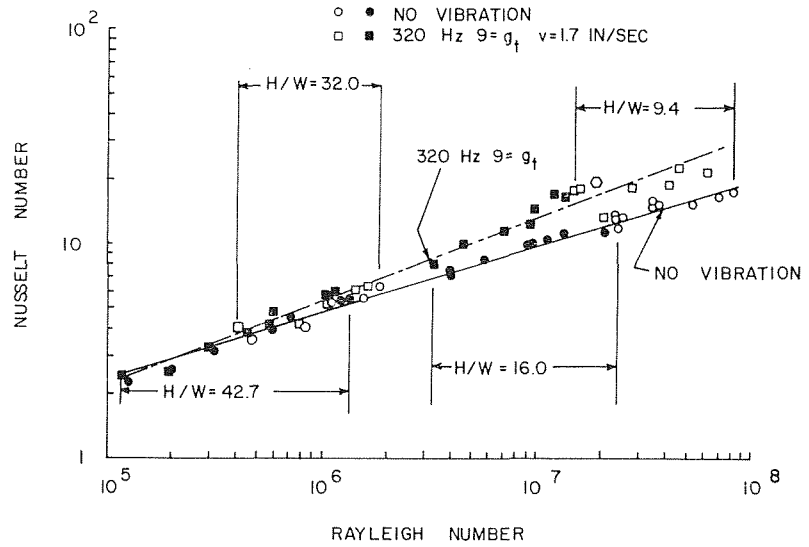

Fig. 4 Vibration effect on free convective heat transfer in a rectangular enclosure. Vibration frequency = 320 Hertz.

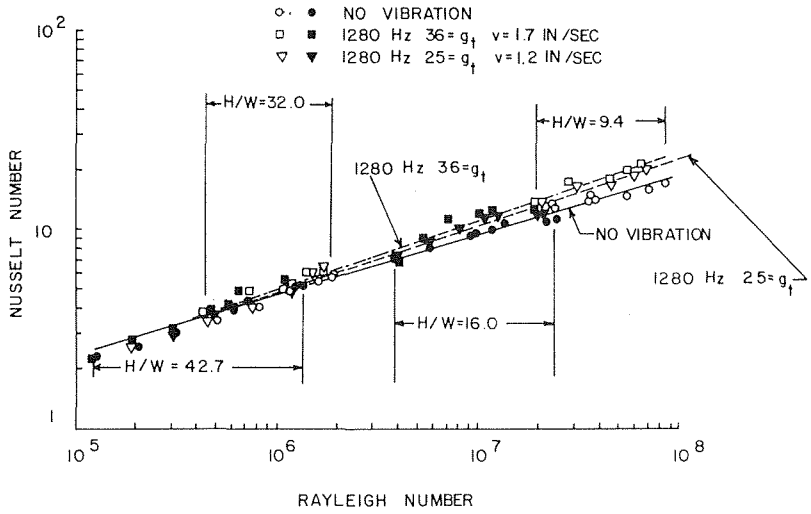

Fig. 5 Vibration effect on free convective heat transfer in a rectangular enclosure. Vibration frequency = 1280 Hertz.

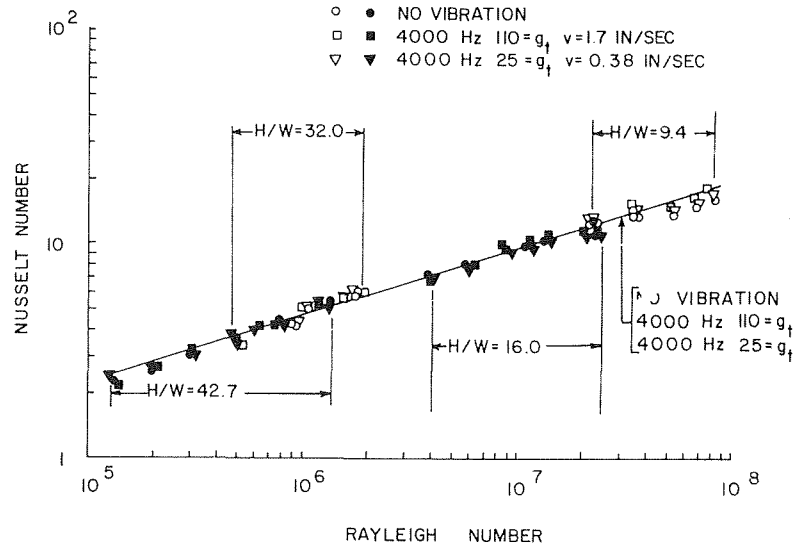

Fig. 6 Vibration effect on free convective heat transfer in a rectangular enclosure. Vibration frequency = 4000 Hertz.

Hertz vibration for flow conditions in which the boundary layers were in the transition flow regime prior to vibration. A boundary layer transition region was readily visible on both the heated and cooled plates at ΔT's above 50 deg. The onset of the 20 Hertz vibration had no effect on this region.

Fig. 3 presents data recorded for an enclosure frequency of 80 Hertz and acceleration ratios of 2.2 and 12.0 It is apparent that the 2.2 acceleration level produced little effect on the heat transfer, however, a noticeable increase in the Nusselt number was evident for the 12.0 acceleration level. The data points appear to be shifted upward and to the left of their corresponding nonvibratory reference point. Since $q = \bar{h}A\Delta T$, any increase in the average heat transfer coefficient, $\bar{h}$, must be accompanied by a corresponding decrease in ΔT; q/A being held constant for this work. The heat transfer rate, q, was determined from the summation of electrical power inputs to the eight strip heaters in the hot plate. For a given ΔT, the electrical power to the heaters was not changed as the vibration was applied. Thus an increase in the average Nusselt number produces a decrease in Rayleigh number. This upward and leftward shift of a data point from the corresponding nonvibratory point was characteristic of all data where a significant increase in the heat transfer coefficient was noted.

The average Nusselt number was increased by as much as 50 percent with the application of 320 Hertz at 9 g's as shown in Fig. 4. This vibration state produced larger changes in the heat transfer than any of the 20, 80, 1280, or 4000 Hertz vibrations.

A noticeable increase in the heat transfer coefficient resulted when vibration at 1280 Hertz and 25 and 36 g's was applied to the enclosure. This effect, which increases with increasing acceleration, is shown in Fig. 5.

Fig. 6 indicated that 4000 Hertz vibration had little or no effect on the heat transfer for acceleration levels as high as 110 g's.

Smith [12] has used standard least squares techniques to obtain a best curve which represents the data shown in the preceding figures. A curve of the form

$$\mathrm{Nu} = C_1(\mathrm{Ra})^{C_2} \tag{2}$$

was obtained for the no vibration case and for each of the vibratory states. This form was assumed since both the vibratory and nonvibratory data approximated straight lines when plotted on log-log coordinates. It should be noted that C_1 and C_2 are functions of the vibratory parameters since each curve represents a specific frequency and acceleration level.

The possibility that an aspect ratio dependency might improve

the data correlation was not overlooked. The least squares procedure was applied to the data for each individual aspect ratio and the aspect ratio pairs of 9.4 and 16.0, and 32.0 and 42.7. A slight decrease in the average deviation resulted due to the fact that a smaller number of points were available when considering the aspect ratios individually or in pairs. The slight increase in accuracy of the predictions was not considered sufficient to warrant the inclusion of an aspect ratio dependency in the overall correlations.

An examination of Figs. 3, 4, and 5 indicates that the curves fitted to the vibratory data converge to the no vibration line at the lower Rayleigh numbers. Using this fact, an attempt was made to force the curves to converge to a common point. In this procedure, the location of the common point of intersection was varied until the total sum of the squares of the deviations of all curves was a minimum. The common point was found to be at a Rayleigh number of 10^4. The resulting correlation equation is of the form

$$\mathrm{Nu} = 1.117\ (\mathrm{Ra}/10^4)^S \tag{3}$$

where the slope, S, is a function of the vibratory parameters. The correlation has thus been simplified since only S is a function of the vibratory variables, whereas for the form

$$\mathrm{Nu} = C_1\mathrm{Ra}^{C_2} \tag{2}$$

both C_1 and C_2 were dependent on the vibratory parameters.

It is perhaps significant to note the importance of the common intersection point at $\mathrm{Ra} = 10^4$. An examination of the previously cited literature shows that the Nusselt number should be approximately 1.0 for a Rayleigh number in the vicinity of 10^4. The Nusselt number of 1.0 is indicative of the conduction regime for rectangular enclosures. It is felt reasonable to assume that vibration should have little or no effect on heat transfer by conduction.

The most significant factor to be realized from the heat transfer results is that appreciable increases in the average heat transfer coefficient may be realized by vibrating the enclosure.

The no-vibration data is in good agreement with that of previous investigators and tends to lend support to those investigators who have found little or no dependency of the heat transfer on the aspect ratio. It is felt that the variance in aspect ratio was sufficient to give evidence of any dependency, if any existed. A comparison of this work and that of several other investigators is shown in Fig. 7 for the case of no vibration. The agreement is seen to be good.

An examination of Figs. 2 through 6 will show that numerous runs were made in order to check the reproducibility of both the vibratory and nonvibratory data. Agreement was good in all cases, especially for the no vibration case.

Both hot and cold plates could be adjusted to within 1 deg F of isothermal conditions for the no vibration runs. Upon application of vibration, it was noted that temperature variations of as much as 10 deg F might exist on the plates. The general variation from isothermality was indicated by a decrease in the temperature of the thermocouples near the top of the hot plate. To determine the effect of the variation from isothermality, several runs were made where the vibration was applied and the plates were adjusted back to isothermal conditions after the variation occurred. These points were in good agreement with the best fit of the data for the same vibratory state where no adjustment of the plates was made. One of these points is shown as a hexagon in Fig. 4. Subsequent to these tests, all data with vibration were recorded with no attempt to adjust the plates back to isothermal conditions when any deviation occurred.

Liquid Column Dynamics. Schoenhals [11] has studied the pressure distribution and bubble formation induced by longitudinal vibration of a flexible liquid-filled cylinder. Primary emphasis was placed on determining the pressure distribution in a column of methanol which partially filled a thin-walled plexiglas cylinder. The uniform shape of the plexiglas cylinder allowed Schoenhals

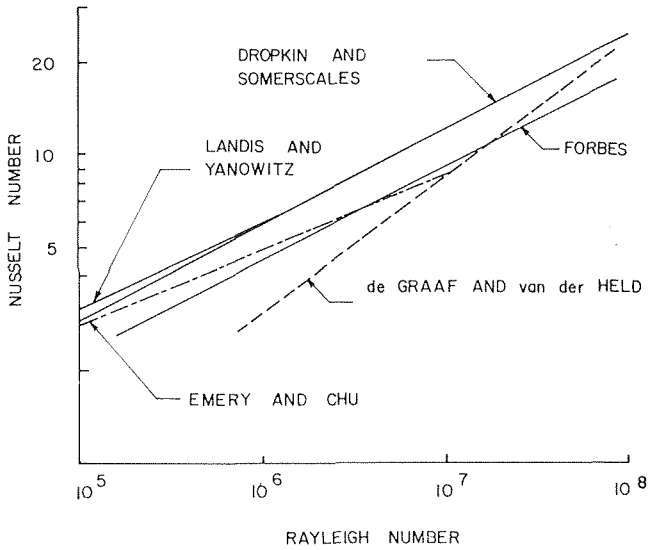

Fig. 7 Comparison of heat transfer data with that of other investigators. No vibration.

to include the effects of wall deformation into the acoustic wave equation which governs the pressure and velocity distribution in the fluid column. The resulting one-dimensional wave equation was solved to yield the pressure distribution in the column as a function of position and the input velocity at the base of the cylinder. Since the assumptions had included the neglecting of dissipation effects in the fluid, infinite pressures were predicted to occur in the fluid at the container bottom under certain modes of vibration. These infinite pressures at the container bottom were predicted for

$$\frac{\omega L}{c} = \frac{n\pi}{2}, \qquad n = 1, 3, 5, 7, \ldots . \tag{4}$$

where ω = circular frequency of vibration of column base
L = column length
c = longitudinal wave velocity in fluid.

The longitudinal wave velocity, c, was determined experimentally by varying the frequency until the first mode, $\omega L/c = \pi/2$, was obtained. This was evidenced by the existence of large pressures measured at the container bottom. The longitudinal wave velocity was found to be less than one third of the normally accepted speed of sound for the methanol. The flexing of the container walls materially reduced the wave propagation velocity through the fluid.

Such an analysis could probably be carried out for the rectangular container under discussion. However, the enclosure flexure would undoubtedly be a complex function, unlike the uniform cylinder considered by Schoenhals. In any event, there would be certain modes of vibration which would predict infinitely large pressure at the container bottom in the absence of dissipation in the fluid. The first natural mode could be determined experimentally in much the same manner as used by Schoenhals, namely, by vibrating a column of fixed length at different frequencies until a maximum pressure is detected at the container bottom. Interpretation of the pressure information is simplified if the container dimensionless acceleration $a\omega^2/g_0$ is maintained constant during the procedure, since the pressure would most likely be directly proportional to the container dimensionless accleration as in Schoenhals' prediction.

Since Schoenhals had indicated that the resonant modes of a vibrated fluid column might be easily determined, a piezoelectric pressure transducer was located near the bottom of the side wall on the 1.7 in. gap test cell. The output of this pressure transducer, where the root mean square value of oscillating pressure has been made dimensionless by dividing by the static pressure

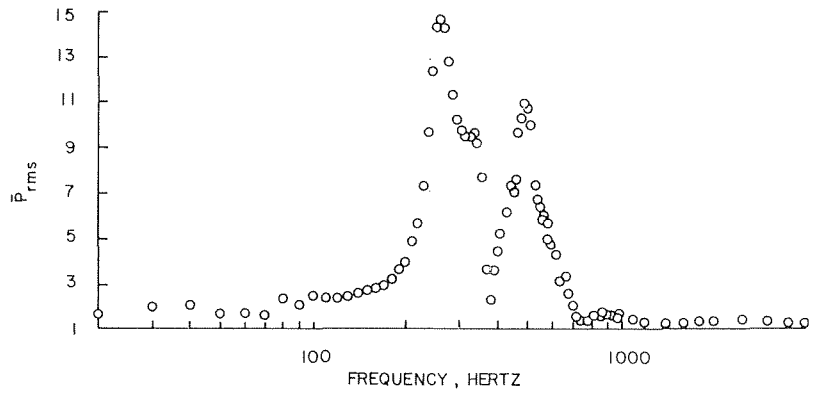

Fig. 8 Dimensionless oscillating pressure on enclosure side wall

$\rho g_0 H$, is shown in Fig. 8 for an enclosure acceleration level of 4 $= g_t$. The output of the pressure transducer was fed through a cathode follower into a vacuum tube voltmeter. This system gave an accurate measurement of the pressure, since the pressure wave forms exhibited nearly perfect sinusoidal shapes under all vibratory conditions when viewed on an oscilloscope.

Large values of the oscillating pressure were first evident in the vicinity of 270 Hertz, although the location of this maximum was a weak function of the enclosure acceleration level.

Visual observations of the boundary layers on the hot and cold plates revealed that the intensification of the turbulent portion of the boundary layer and the mixing and interacting of the boundary layers in the central portion of the test cell were the maximum which had been observed up to this point. Operation at 270 Hertz, 4 g's produced an intense entrainment of the boundary layers into the core with mixing occurring over the entire height of the cell. Operation at 270 Hertz, 6 g's for prolonged periods (greater than approximately 5 minutes) produced numerous small bubbles on the top plexiglas wall probably due to the existence of pressures in the liquid below the vapor pressure.

A peak in the oscillating pressure is also evident in the vicinity of 540 Hertz in Fig. 8.

Resonance Effects. The evidence of these apparent resonant conditions necessitated the recording of 77 additional heat transfer data points at these frequencies. Inasmuch as the previous data did not appear amenable to correlation for the constant velocity (1.7 ips) some of these additional data were obtained with a constant acceleration level $a\omega^2/g_0$. The following range of frequency and acceleration levels was chosen for the acquisition of this additional data:

80 Hertz	$4 = g_t$
270 Hertz (Fundamental Mode)	$2, 4, 6, = g_t$
320 Hertz	$2, 4, = g_t$
540 Hertz (First Harmonic)	$2, 4, = g_t$
1280 Hertz	$2, 4, = g_t$
2500 Hertz	$2, 4, = g_t$

The location of the two pressure peaks, as indicated by the transducer on the bottom wall, varied slightly with the acceleration level and ΔT across the gap. In order to assure operation at this peak pressure, the frequencies which produced maximum pressure were "sought out" for each run. This resulted in testing from 257 to 286 Hertz for the first peak and from 540 to 572 Hertz for the second peak.

The 80, 1280, and 2500 Hertz vibrations were found to have little or no effect on the average convective heat transfer coefficient at the 2 and 4 g level. A noticeable increase in the heat transfer coefficient was produced by testing at the first resonant frequency (approximately 270 Hertz). These results are shown in Fig. 9. Fig. 10 shows that the effect was approximately the same for the 320 Hertz and the 540–572 vibrations for equivalent accelerations.

The most significant factor to be pointed out is the increase in Nusselt number for the 270 Hertz vibration. Acceleration levels as low as 2 g's produced appreciable increases in the heat transfer coefficient at this frequency. For a given acceleration level, there is a greater change in the Nusselt number at the resonant frequency than for the 320 Hertz vibration which had previously produced the largest effects. The intense turbulence created throughout the cell at this frequency appears to be the major factor in increasing the heat transfer coefficient. The heat transfer rates recorded in the 540–572 Hertz range do not appear significantly different from those at 320 Hertz. There appears to be no uniqueness to this point insofar as the heat transfer is concerned. The resonant frequency of the entire test cell structure is apparently near 500–600 Hertz.

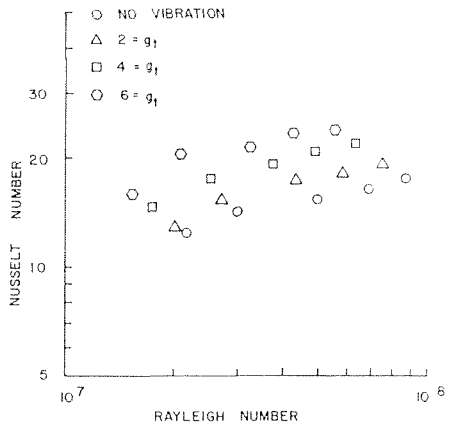

Fig. 9 Vibration effect on free convective heat transfer in a rectangular enclosure. Vibration frequency approximately 270 Hertz.

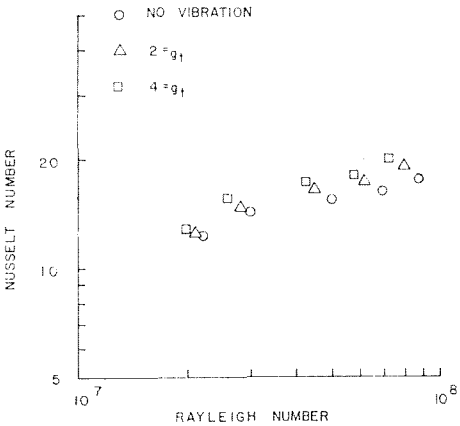

Fig. 10 Vibration effect on free convective heat transfer in a rectangular enclosure. Vibration frequency approximately 540 Hertz.

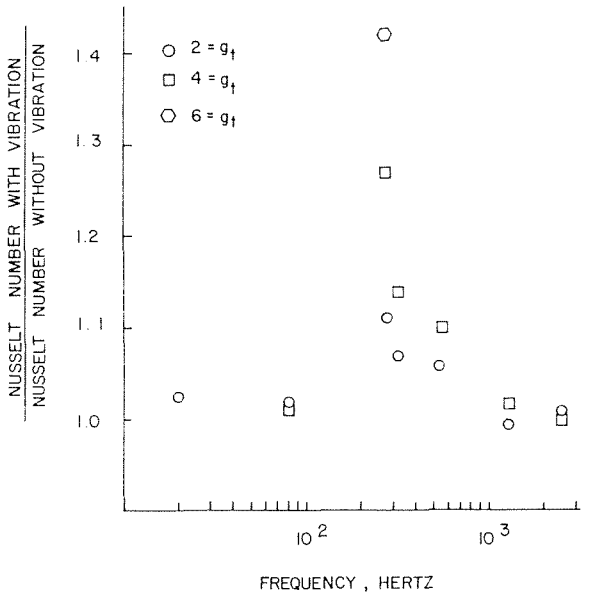

Fig. 11

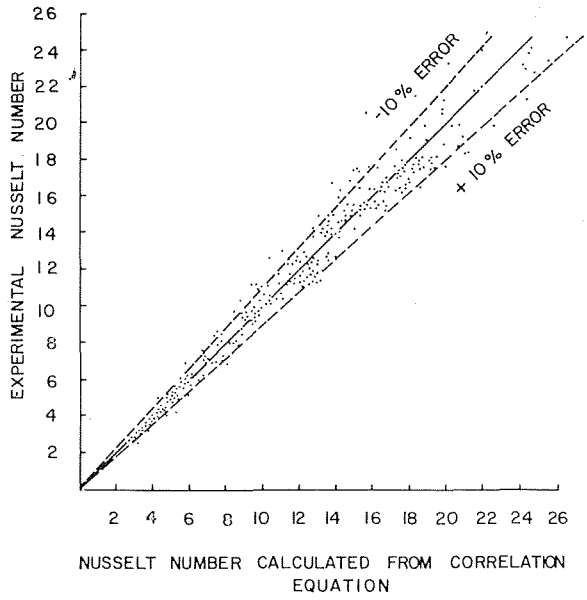

Fig. 12

In Fig. 11 the ratio of the Nusselt number with vibration to the Nusselt number with no vibration has been plotted versus frequency with the enclosure acceleration ratio as a parameter. This figure was based on data recorded with 1.7 in. gap width at a ΔT of 45 deg prior to application of vibration.

Correlation Equation. The data shown in Fig. 11 indicate the effects of both frequency and acceleration level for a Rayleigh number of approximately 6.9(10⁷) prior to application of vibration. If a curve is faired through the points in Fig. 11, it will be similar in shape to the response curve of a seismographic system (accelerometer) to a sinusoidal velocity input (see Ambrosius [13] p. 311).

After some trial and error, a prediction equation for the vibratory Nusselt number was found which could be fit to the data with acceptable accuracy.

The slope, S, in equation (3) was found to be

$$S = \frac{C_3 \dfrac{f}{fn}}{\sqrt{\left[1 - \left(\dfrac{f}{f_n}\right)^2\right]^2 + \left[2\lambda \dfrac{f}{f_n}\right]^2}} \ln (1 + g_t) + C_4 . \quad (5)$$

The first term takes the vibration frequency and acceleration level into account while the constant C_4 indicates the slope of the no vibration data. Letting

$$Z = \frac{\dfrac{f}{f_n}}{\sqrt{\left[1 - \left(\dfrac{f}{f_n}\right)^2\right]^2 + \left[2\lambda \dfrac{f}{f_n}\right]^2}} \quad (6)$$

equation (3) becomes

$$\mathrm{Nu} = 1.117 \left[\frac{\mathrm{Ra}}{10^4}\right]^{C_3 Z \ln (1 + g_t) + C_4} \quad (7)$$

Using all data and setting $f_n = 271.0$, the constants in equation (7) were determined to be

$$\lambda = 0.7327$$
$$C_3 = 0.03106$$

and

$$C_4 = 0.3042$$

giving

$$\mathrm{Nu} = 1.117 \left[\frac{\mathrm{Ra}}{10^4}\right]^{0.03106\, Z \ln (1 + g_t) + 0.3042} \quad (8)$$

where $f_n = 271.0$ and $\lambda = 0.7327$ are used in calculating the value of Z. The value of f_n was set equal to 271.0 which is the average value of frequencies tested near the first resonant mode.

The constant C_4 which indicates the slope of the nonvibratory data is seen to be in good agreement with the work of previous investigators. The value of λ and C_3 giving the best fit of the data were determined by an iterative least squares technique. The constant λ may be considered a damping factor in equation (8) since it prevents infinite response by the system when operating at the resonant mode. The particular values of λ and C_3 used in equation (8) were determined for the water-filled rectangular enclosure. Equation (8) is remarkably insensitive to variation in λ and C_3 and provides a good fit of the data for significant variation in these quantities. It is likely that both λ and C_3 are dependent on the properties of the contained fluid. Further testing, with various fluids, will be necessary before this dependency can be determined.

Fig. 12 presents a plot of the Nusselt number calculated from equation (8) versus the experimentally measured Nusselt number. Considering the nature of the phenomenon under investigation, the prediction equation is seen to give good results. The difference between the predicted and measured Nusselt number is less than 10 percent for approximately 90 percent of the data points. The average percent error for all data is 5.46 percent.

Conclusions

Natural convective heat transfer in a liquid-filled rectangular enclosure has been shown to be markedly increased at frequencies at or near the resonant natural frequency of the enclosed liquid column. Increases in the convective heat transfer coefficient of up to 50 percent were obtained for acceleration levels as low as 6 g's.

Experimental results indicate that the parameters which are significant for producing an effect on heat transfer are frequency and acceleration rather than amplitude and average velocity.

A correlation equation has been developed which allows prediction of the effect of vibration on heat transfer in rectangular enclosures. This equation, based on the dynamic response of the liquid column to a sinusoidal velocity input, predicts the 351 data points with an average percent error of 5.46. Further experimental investigations are recommended to determine the dependency of some terms in the equation of fluid properties.

Acknowledgments

This study was conducted under the sponsorship of the National Aeronautics and Space Administration through Contract NAS8-20284 administered by the Propulsion and Vehicle Engineering Laboratory of George C. Marshall Space Flight Center. The work represents a portion of the doctoral thesis of R. E. Forbes.

The Authors acknowledge with thanks the help of Mr. G. V. Smith in data collection and in the development of the correlation equation.

References

1 Forbes, R. E., "The Effect of Vibration on Natural Convective Heat Transfer in a Rectangular Enclosure," PhD dissertation, Mississippi State University, 1968.

2 Mull, W., and Reiher, H., "Der Warmeschutz von Luftschichten," *Gesund. Ing. Beihefte*, Reihe 1, No. 28 (1930). As reported in Jakob, M., *Heat Transfer*, Vol. I, Wiley, New York, 1949.

3 de Graff, J. G. A., and van der Held, E. F. M., "The Relation Between the Heat Transfer and the Convection Phenomena in Enclosed Plane Air Layers," *Applied Scientific Research*, Section A, Vol. 3, 1953, pp. 393–410.

4 Eckert, E. R. G., and Carlson, W. D., "Natural Convection in an Air Layer Enclosed Between Two Vertical Plates With Different Temperatures," *International Journal of Heat and Mass Transfer*, Vol. 2, 1961, pp. 106–120.

5 Dropkin, D., and Somerscales, E., "Heat Transfer by Natural Convection in Liquids Confined by Two Parallel Plates Which Are Inclined at Various Angles With Respect to the Horizontal," JOURNAL OF HEAT TRANSFER, TRANS. ASME, Series C, Vol. 87, No. 1, Feb. 1965, pp. 79–84.

6 Emery, A., and Chu, N. C., "Heat Transfer Across Vertical Layers," JOURNAL OF HEAT TRANSFER, TRANS. ASME, Series C, Vol. 87, No. 1, Feb. 1965, pp. 110–116.

7 Landis, F., and Yanowitz, H., "Transient Natural Convection in a Narrow Vertical Cell," Proceedings of the 3rd Int. Heat Transfer Conference, 2, 1966, pp. 139–151.

8 Elder, J. W., "Laminar Free Convection in a Vertical Slot," *Journal of Fluid Mechanics*, Vol. 23, Part 1, Sept. 1965, pp. 77–98.

9 Elder, J. W., "Turbulent Free Convection in a Vertical Slot," *Journal of Fluid Mechanics*, Vol. 23, Part 1, Sept. 1965, pp. 99–112.

10 MacGregor, R. K., and Emery, A. F., "Free Convection Through Vertical Plane Layers—Moderate and High Prandtl Number Fluids," ASME Paper No. 68—WA/HT-4.

11 Schoenhals, R. J., and Overcamp, T. J., "Pressure Distribution and Bubble Formation Induced by Longitudinal Vibration of a Flexible Liquid-Filled Cylinder," *Journal of Basic Engineering*, TRANS. ASME, Series D, Vol. 89, No. 4, Dec. 1967, pp. 737–747.

12 Smith, G. V., "The Effect of Vibration on Natural Convection in Rectangular Enclosures," Masters Thesis, Mississippi State University, August 1968.

13 Ambrosius, E. E., Fellows, R. D., and Brickman, A. D., *Mechanical Measurement and Instrumentation*, The Ronald Press Company, New York, 1966.

Acknowledgments

This study was conducted under the sponsorship of the National Aeronautics and Space Administration through Contract NAS8-20284 administered by the Propulsion and Vehicle Engineering Laboratory of George C. Marshall Space Flight Center. The work represents a portion of the doctoral thesis of R. E. Forbes.

The Authors acknowledge with thanks the help of Mr. G. V. Smith in data collection and in the development of the correlation equation.

References

1 Forbes, R. E., "The Effect of Vibration on Natural Convective Heat Transfer in a Rectangular Enclosure," PhD dissertation, Mississippi State University, 1968.

2 Mull, W., and Reiher, H., "Der Warmeschutz von Luftschichten," *Gesund. Ing. Beihefte*, Reihe 1, No. 28 (1930). As reported in Jakob, M., *Heat Transfer*, Vol. I, Wiley, New York, 1949.

3 de Graff, J. G. A., and van der Held, E. F. M., "The Relation Between the Heat Transfer and the Convection Phenomena in Enclosed Plane Air Layers," *Applied Scientific Research*, Section A, Vol. 3, 1953, pp. 393–410.

4 Eckert, E. R. G., and Carlson, W. D., "Natural Convection in an Air Layer Enclosed Between Two Vertical Plates With Different Temperatures," *International Journal of Heat and Mass Transfer*, Vol. 2, 1961, pp. 106–120.

5 Dropkin, D., and Somerscales, E., "Heat Transfer by Natural Convection in Liquids Confined by Two Parallel Plates Which Are Inclined at Various Angles With Respect to the Horizontal," JOURNAL OF HEAT TRANSFER, TRANS. ASME, Series C, Vol. 87, No. 1, Feb. 1965, pp. 79–84.

6 Emery, A., and Chu, N. C., "Heat Transfer Across Vertical Layers," JOURNAL OF HEAT TRANSFER, TRANS. ASME, Series C, Vol. 87, No. 1, Feb. 1965, pp. 110–116.

7 Landis, F., and Yanowitz, H., "Transient Natural Convection in a Narrow Vertical Cell," Proceedings of the 3rd Int. Heat Transfer Conference, 2, 1966, pp. 139–151.

8 Elder, J. W., "Laminar Free Convection in a Vertical Slot," *Journal of Fluid Mechanics*, Vol. 23, Part 1, Sept. 1965, pp. 77–98.

9 Elder, J. W., "Turbulent Free Convection in a Vertical Slot," *Journal of Fluid Mechanics*, Vol. 23, Part 1, Sept. 1965, pp. 99–112.

10 MacGregor, R. K., and Emery, A. F., "Free Convection Through Vertical Plane Layers—Moderate and High Prandtl Number Fluids," ASME Paper No. 68—WA/HT-4.

11 Schoenhals, R. J., and Overcamp, T. J., "Pressure Distribution and Bubble Formation Induced by Longitudinal Vibration of a Flexible Liquid-Filled Cylinder," *Journal of Basic Engineering*, TRANS. ASME, Series D, Vol. 89, No. 4, Dec. 1967, pp. 737–747.

12 Smith, G. V., "The Effect of Vibration on Natural Convection in Rectangular Enclosures," Masters Thesis, Mississippi State University, August 1968.

13 Ambrosius, E. E., Fellows, R. D., and Brickman, A. D., *Mechanical Measurement and Instrumentation*, The Ronald Press Company, New York, 1966.

DISCUSSION

R. J. Schoenhals[2]

The authors are to be commended for performing an investigation of considerable interest and involving complex interactions among system dynamics, fluid flow and heat transfer. The most significant features of this research appear to be the following.

1 Almost all previous experimental investigations of vibratory effects on free convection heat transfer have utilized either a vibrated surface in a large quiescent fluid, or a stationary surface suspended in a fluid subjected to pulsations or acoustic vibrations. The present study is distinctly different in that the fluid is enclosed within the heat transfer surfaces, so that vibration imposed on these surfaces was necessarily applied to the main body of fluid as well. Thus, the heat transfer surfaces and the fluid were simultaneously subjected to the imposed vibration.

2 Dynamic resonance has been established as the dominant feature associated with substantial increases in heat transfer for an enclosed liquid subjected to vibration.

3 Considering the complexity of the various phenomena involved, equation (8) correlates the data with fairly good accuracy.

4 There are a number of practical applications in which containers enclosing fluids are subjected to thermal and vibratory environments simultaneously. The cryogenic oxidizer tank of a liquid fuel rocket constitutes just one example. The reported results should be of considerable engineering value in dealing with systems such as this.

The discusser would like to raise a few questions in the hope that the authors will provide further clarification of the details of their study. These questions are grouped into three categories.

1 The authors indicate that both visual and photographic observations of the fluid were obtained. In the case of the visual observations, was a strobe-light used? It is the opinion of the discusser that detailed boundary layer observations would be difficult without the use of a strobe-light since attempts to focus on a particle or on a particular region would give rise to a blurring effect, particularly for the larger amplitudes.

2 It has been well established by various investigators that bubbles can be generated rapidly and easily in a vibrated liquid at near-resonant frequencies, even at low g-levels. The authors indicate the appearance of bubbles at the top of their system only after prolonged vibration at the first resonant frequency when the acceleration level was maintained at 6 g's. Were any bubbles sighted at the bottom or at other locations along the fluid column at frequencies in the vicinity of the two resonant frequencies of 270 and 540 Hertz? Also, what prevented the bubbles from forming immediately when vibration was imposed? Is it possible that bubble formation was partially prevented by the fact that the container was essentially sealed off, thus preventing the expansion required for bubble formation? Or, was the small opening in the top surface of the container left open during vibration to allow for this expansion? In considering these aspects, it is significant to note that nonsinusoidal pressure variations are usually observed in the presence of substantial bubble volumes even when the imposed vibration is sinusoidal. Were the observed pressure wave-forms essentially sinusoidal even under resonant conditions at 6 g's?

3 It is clear from Fig. 8 that there were resonant conditions at 270 and at 540 Hertz, and the resonance phenomenon appears to be the dominant effect in producing sizeable improvements in heat transfer at 270 Hertz. Can the authors conjecture as to why similar magnitudes of heat transfer improvement were not obtained at 540 Hertz? Could it be that the mixing action of the bubbles were dominant at 270 Hertz and that there were few or no bubbles present to cause such mixing at 540 Hertz?

[2] Professor of Mechanical Engineering, Purdue University, Lafayette, Ind.; Presently, Visiting Professor of Engineering, Arizona State University, Tempe, Ariz. Mem. ASME.

Authors' Closure

The authors appreciate Professor Schoenhals' comments and questions concerning our work.

A strobe light was used initially in performing both the photographic and visual observations. Preliminary indications, however, indicated that the desired results could be accomplished with very small amplitudes of vibration. The maximum double amplitude used was one tenth of an inch and most of the work was performed with the double amplitude much less than this value. The continued use of the strobe light was unnecessary in view of these small amplitudes.

As Professor Schoenhals has indicated bubble coalescence is difficult (if not impossible) to avoid in this type work.

Under some conditions the bubbles appeared immediately upon inception of vibration. The bubbles would normally form near the top of the completely filled test cell. When these conditions occurred, the testing was stopped and the bubbles removed before resuming testing. This procedure, often repeated several times, proved successful in preventing subsequent formation of the bubble areas with the exception of nine tests. For these nine tests the data were recorded with the bubbles present and the points were used in obtaining the best fit curves. The effect of the bubbles for these nine cases does not appear to be pronounced, probably due to the fact that the bubbles generally appeared singly and were never larger than $^1/_4$ in. in dia. The hydrostatic head imposed by the water-filled surgical tubing which extended upward from the test cell opening was also instrumental in preventing the formation of bubbles during the testing. The observed pressure wave-forms were not sinusoidal under conditions where bubble coalescence existed.

The relative peak in the pressure curve in the vicinity of 540 Hertz is attributed to the fact that the resonant frequency of the entire structure is near this point. Vibration amplification in the structure was sensed as pressure by the transducer due to its acceleration sensitivity. The 540 Hertz vibration produced an effect on the heat transfer, however it was not as pronounced as the effect produced at the resonant mode of the fluid column near 270 Hertz. Random vibration testing is presently being performed in an attempt to achieve a clearer understanding of the relationship between the effects at 270 and 540 Hertz.

Instantaneous Measurement of Heat Transfer From an Oscillating Wire in Free Convection[1]

B. H. THRASHER
Associate Principal Engineer,
Radiation Inc., Melbourne, Fla.

W. J. SCHAETZLE
Professor of Mechanical Engineering,
University of Alabama,
Tuscaloosa, Ala.

The instantaneous heat transfer properties are measured as a function of time for an oscillating wire (20 to 40 H_z) in still air. The wire is oscillated by thermal contractions and expansions which match the natural frequency based on wire mass and tension. The temperature variation results from the internal resistance heating of an alternating current. The wire temperature and velocity are measured as a function of time by photocells. This eliminates any instrumentation interference with the heat transfer. The results are plotted as a function of instantaneous and average Reynolds' number. The oscillatory heat transfer data are divided into two regimes of free and forced convection by the critical Reynolds number. Oscillatory heat transfer rates are smaller for forced convection and greater for free convection than those for steady state conditions recommended by McAdams [2][2] for the respective regimes. No significant difference is found in the heat transfer for oscillations in the vertical and horizontal planes. Due to the time variation of the variables an appreciable amount of emphasis is placed on the experimental apparatus and the recording of data. The recorded data is basically corrected by assuming first order linear systems.

Introduction

THE majority of the convective heat transfer analyses [2, 3, 4, 5, 6, 7, 8] hitherto were concerned with steady state conditions. Some data for oscillatory systems though available are limited primarily to average heat transfer, where only the time average temperature is described. There are no available data which describe the instantaneous heat transfer from an oscillating wire.

The purpose of this investigation is to gain some insight into the heat transfer phenomenon for an oscillating body by measuring the instantaneous heat transfer from an oscillating wire. The oscillation is induced by passing an alternating current through a wire fixed at both ends. The expansion and contraction of the wire due to temperature variation set up the vibration when the current frequency matches the natural frequency of the wire. The heat transfer is determined by measuring the heat generation, temperature and velocity as functions of time. Experimental data are taken over a frequency range of 20 to 40 Hz with a peak to peak amplitude range of zero to $1^1/_4$ in. and with wire diameters of 0.0031 and 0.008 in.

Survey of Work in Related Fields

McAdams [2] gives a compilation of work done by several investigators for forced convection heat transfer for flow normal to a cylinder under steady state conditions. In the range of Reynolds numbers between 0.1 and 1000 he gives the expression

$$\mathrm{Nu}_f = 0.32 + 0.43\ (\mathrm{Re})^{0.52} \tag{1}$$

Lemlich [3] measured the time average heat transfer coefficients for Nichrome wires of 0.0253, 0.0396, and 0.0810 in. dia, vibrating at frequencies from 39 to 122 Hz. Center point peak to peak amplitudes from 0.055 to 0.231 in. were used. He could find no significant difference in the average heat transfer for oscillations in the vertical and horizontal planes. The film coefficient was found to increase by as much as 400 percent over its value for no vibration. The wires used by Lemlich were of such large diameter as to be insensitive to the instantaneous variation of the heat transfer coefficient. Using a vibration Reynolds number given by:

$$\mathrm{Re}_v = 2AfD\ \rho/\mu \tag{2}$$

Lemlich correlated the ratio of average vibration heat transfer coefficient to the free convection coefficient as

$$\frac{h}{h'} = 0.75 + 0.0031\ \frac{(\mathrm{Re}_v)^{2.05}(\beta\Delta T)^{0.33}}{(\mathrm{Gr})^{0.41}} \tag{3}$$

[1] Portions of this paper are based on a PhD dissertation submitted to the University of Alabama by the primary author [1].

[2] Numbers in brackets designate References at end of paper.

Contributed by the Heat Transfer Division and presented at the Winter Annual Meeting, Los Angeles, Calif., November 16–20, 1969, of THE AMERICAN SOCIETY OF MECHANICAL ENGINEERS. Manuscript received by the Heat Transfer Division, March 4, 1968; revised manuscript received July 22, 1969. Paper No. 69-WA/HT-15.

where h' is the free convection coefficient at the same temperature difference and wire diameter as for h.

Anantanarayanan and Ramachandran [4] studied the time average effect of wire vibration on the forced convection heat transfer in parallel flow. They correlated their results by expressing the ratio of Nusselt number for vibration to the Nusselt number for a stationary wire in terms of the ratio of the vibration Reynolds number to the flow Reynolds number as

$$\frac{(\mathrm{Nu})_v}{(\mathrm{Nu})_s} - 1 = 4.25\left[\frac{(\mathrm{Re})_v}{(\mathrm{Re})_f}\right]^{0.977} \tag{4}$$

Deaver, Penney and Jefferson [5] oscillated a 0.007 in. dia platinum wire in water at frequencies from zero to 4.25 Hz and amplitudes up to 2.76 in. Temperature differences up to 140 F and Reynolds numbers up to 100 were used. They concluded that, in the range of their investigation, the time average heat transfer coefficient could be determined by considering the problem as one of flow normal to a cylinder by using a vibration Reynolds number.

General Analysis. Consider a wire stretched between two end supports and conducting an alternating current. The heat generation is given by:

$$Q = RI_m^2 \sin^2(\omega\theta) \tag{5}$$

The periodic heat generation causes periodic temperature fluctuations. These changes in temperature cause corresponding changes in wire length which, in turn, cause inverse changes in tension. The periodic fluctuations in tension under certain conditions induce instabilities in the wire. The position and velocity of a stretched wire are governed by the one dimensional wave equation which has as solution

$$y(x, \theta) = \sin\frac{\pi x}{L}\sin\left[\sqrt{\frac{Fg}{\rho A_x}}\,\frac{\pi\theta}{L}\right] \tag{6}$$

The fundamental frequency of the wire is given by

$$f = \frac{1}{2L}\sqrt{\frac{Fg}{\rho A_x}} \tag{7}$$

Resonance will be induced in the wire if the current frequency sychronizes with that given by equation (7).

Convective, radiative and conductive heat transfer work together to dissipate the generated heat, and to cause the wire to reach a steady oscillatory temperature. Considering the midpoint of the wire, calculations have shown the conduction is less than one percent of the heat transfered. These calculations assumed an extreme case of a linear temperature gradient from the midpoint to the supports at room temperature. The heat generated by friction has been investigated by Lemlick, [3] and shown to be negligible also. With these considerations the convective film coefficient can be expressed in the form

$$h = \frac{-m\,c_p\frac{dT}{d\theta} + RI^2 - \sigma Ae(T^4 - T_0^4)}{A(T - T_0)} \tag{8}$$

The right-hand side of equation (8) is determined experimentally by measuring the temperature, current, voltage and velocity of the wire over one complete cycle.

Wire temperature is the most sensitive measurement encountered in this experimental investigation. The large time temperature gradients require a fast time response of the temperature measuring system. The small diameter of the wire precludes any type of physical attachment to the wire such as a thermocouple. An optically sensitive silicon photoelectric cell is used to measure the wire temperature. This selection limits the minimum wire temperature to approximately 1200 F. Below this temperature the photocell output is not sufficiently above the noise level to give accurate results.

Wire resistance, specific heat and emissivity are all functions of temperature. They are calibrated separately from available published data [6] or by experimentation.

Experimental Equipment and Procedure

Wire Material Selection. Chromax[3] wire is used for the oscillating wire because of its mechanical properties at elevated tempera-

[3] Chromax is a registered trade name of the Driver-Harris Company, manufacturer of the wire.

Nomenclature

A = lateral area, ft²
A_x = cross-sectional area, ft²
C = 3.412 Btu/hr-watt
C_i = arbitrary constant, $i = 1, 2, 3, \ldots$
c_p = specific heat at constant pressure, Btu/lb$_m$-R
c_v = specific heat at constant volume, Btu/lb$_m$-R
D = wire diameter, ft
E = photocell output voltage, mv
E_f = photocell output voltage for steady state conditions, mv
E_{pc} = photocell output voltage, mv
e = emissivity, dimensionless
F = wire tension, lb$_f$
f = oscillation frequency, Hz
g = acceleration of gravity, 32.17 ft/sec²
Gr = Grashof number = $gD^3\beta\Delta T/\eta^2$
H = peak to peak amplitude of oscillation, ft
h = convective heat transfer coefficient, Btu/hr-ft²-F
$\bar{h}$ = time average convective heat transfer coefficient, Btu/hr-ft²-F
h' = free convective heat transfer coefficient evaluated at the same wire diameter and temperature as for h
Hz = symbol for cycles per sec
I = electrical current, amperes
I_m = maximum value of a sinusoidal current, amperes
K = calibration constant for temperature photocell
K_i = arbitrary constant, $i = 1, 2, 3, \ldots$
k = thermal conductivity, Btu/hr-ft-F
L = wire length, ft
m = mass, lb$_m$
Nu = Nusselt number, hD/k
Nu$_f$ = Nusselt number based on the film temperature T_f
n = slope of log plot for photocell output voltage versus wire temperature, dimensionless
Pr = Prandtl number, $\mu c_p/k$
Q = rate of heat flow, Btu/hr
Q_f = rate of heat generation due to friction, Btu/hr
Q_r = rate of radiative heat flow, Btu/hr
R = wire resistance, ohms
Re = Reynolds number based on instantaneous absolute wire velocity, $VD\rho/\mu$
Re$_v$ = vibration Reynolds number based on $V = 2Af$
T = temperature, deg F
T_c = time constant, hr
T_f = film temperature defined as average between surface temperature and surrounding air temperature, deg F
T_0 = temperature of surrounding air, deg F
μ = viscosity, lb/ft-hr
ν = kinematic viscosity, ft²/hr
V = velocity, ft/sec
x = position along wire, ft
y = transverse position of wire, ft
α = reciprocal of time constant, 1/hr
β = thermal coefficient of expansion, 1/F
γ = angle between plane of oscillation and vertical, deg
ΔT = temperature difference, deg F
θ = time, hr
λ = oscillation wave length, ft
π = 3.1415926
ρ = density, lb$_m$/ft³
σ = Stefan-Boltzmann constant, 0.1714×10^{-8} Btu/hr-ft²-R⁴
Φ = phase angle lag between wire temperature and current, rad
ω = angular velocity, rad/sec

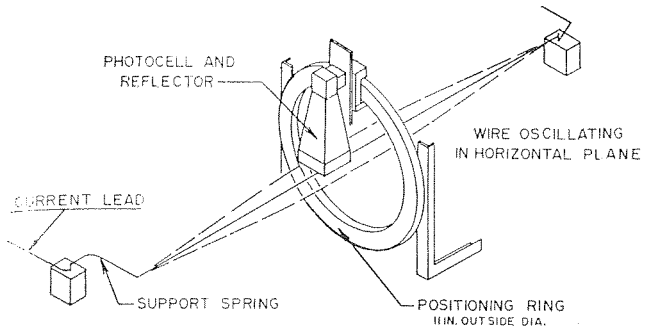

Fig. 1 Temperature measurement and oscillation apparatus

tures, relatively low cost, and large temperature coefficient of electrical resistance.

Oscillation Generation. The oscillating wire is supported as shown in Fig. 1. Electrical current is supplied by a 200 watt variable frequency power supply with a usable low distortion frequency range of 20 to 40k Hz.

The best sustained oscillations exist when one solid end support is replaced by a spring which allows two degrees of freedom. A number 20 gauge stranded, plastic insulated copper wire functions satisfactorily as support spring in the frequency range of 25 to 40 Hz when using a number 40 gauge oscillating wire. The support spring as shown in Fig. 1 serves as both an end support and a current conductor. When the spring is positioned perpendicular to the oscillating wire the oscillations then occur in the plane containing both the support spring and the oscillating wire.

Temperature Measurement. The wire temperature is measured with a calibrated silicon photoelectric cell. The cell is positioned to view the wire from a direction normal to the plane of oscillation as shown in Fig. 1. The positioning ring makes it possible to keep the distance from the photocell to the wire constant for any plane of oscillation.

The slope of the photocell output as a function of wire temperature is measured with the photocell viewing a large Chromax conductor, the temperature of which can be measured with a fine thermocouple. This makes the thermocouple mass and surface area small compared to wire properties and minimizes the effect of the thermocouple on wire temperature. Fig. 2 shows the curve of photocell output versus wire temperature for the large Chromax conductor. The slope n of this curve is assumed to be the same as that for the oscillation wires. The temperature is given by the equation

$$T = K(E_{pc})^{1/n} \tag{9}$$

The constant K is calibrated for each individual wire before and after each oscillation data run by measuring the photocell output and wire temperature with the wire heated by a d-c current. This technique was checked by using an optical pyrometer and was found to be correct to within the accuracy of the pyrometer.

Photocell Time Response. Silicon photocells have a fast response to changes in light intensity. This characteristic makes them suitable for measuring the rapidly changing wire temperature. Just as any other measuring system, the recorded photocell output, E, will lag behind the actual photocell output, E_f, by an amount $(E_f - E)$. It is assumed that the photocell-amplifier-galvanometer system is a first order system. This assumption is supported by the characteristics of the recorded data. The magnitude of the error is dependent (equation (10)) on the rate of change of the temperature and on the time constant of the photocell system.

The time constant of the system, T_c, is determined experimentally by exposing the photocell to a step change in light intensity of magnitude and duration time sufficient to produce a recorded steady state output of E_f. The duration time is then reduced while keeping the intensity constant.

With sufficient reduction in duration time the photocell output is significantly reduced by its inadequate response. Letting E be the photocell output at any time θ, the photocell system output can be described by

$$E_f - E = \theta_c \frac{dE}{d\theta} \tag{10}$$

where E_f is the height of the step change in the input and E is the output at time θ. Equation (10) has the solution

$$E = (E_i - E_f) \exp(-\theta/\theta_c) + E_f \tag{11}$$

where E_i is the initial value of the system output. Equation (11) can be solved for the time constant corresponding to $E_i = 0$,

$$\theta_c = \frac{-\theta}{\ln(1 - E/E_f)} \tag{12}$$

Experimentally imposing a step change in light intensity input of magnitude E_f and duration time θ, one obtains from equation (12) the time constant as a function of the output amplitude, E. Fig. 3 shows how a step change in light intensity is generated

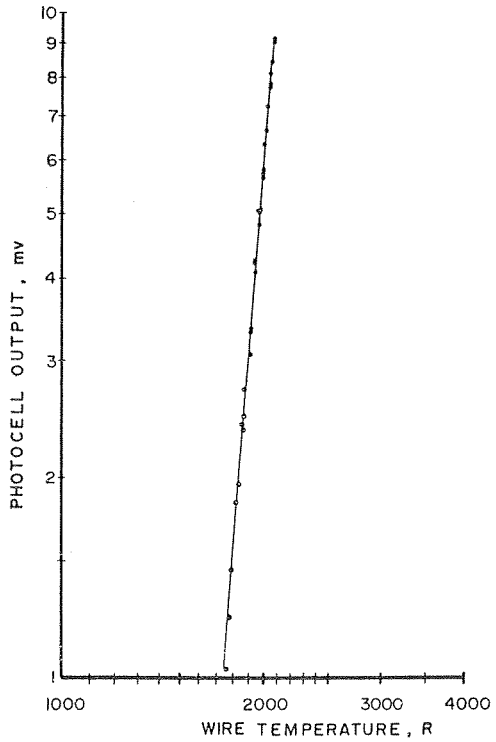

Fig. 2 Photocell output versus wire temperature

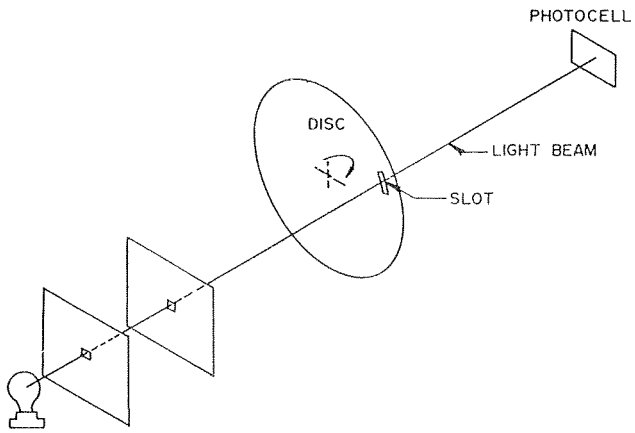

Fig. 3 Time response test arrangement

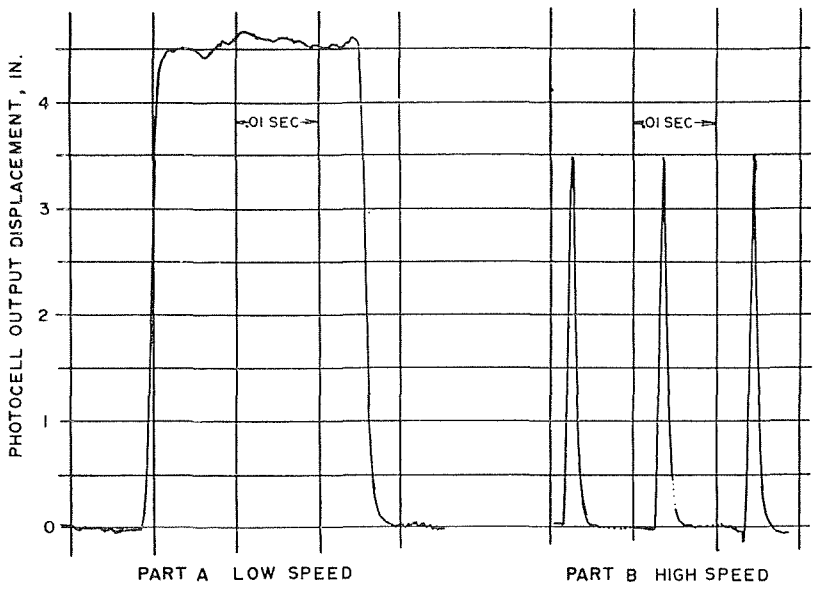

Fig. 4 Tracings of photocell output from time respone test

by passing a narrow light beam through a rotating disc located in front of the photocell. A narrow light beam and a relatively long slit are used to make the photocell rise time negligible compared to the on-time. Part A of Fig. 4 shows the form of the photocell output with the disc being rotated at low speeds. The ratio of on-time to the period of rotation is the same for the low speed and high speed, that is,

$$\theta_l f_l = \theta_h f_h \tag{13}$$

where

f_l = frequency of low speed rotation
f_h = frequency of high speed rotation
θ_l = on-time at low speed
θ_h = on-time at high speed

The term $\theta_l f_l$ is measured at low speed. The disk is then rotated at high speed and the photocell output recorded. Part B of Fig. 4 shows the form of this photocell output. The frequency, f_h, and magnitude of photocell output, E, are measured from the oscillograph recording.

The length of time that the photocell is exposed to the light beam at high speed is denoted θ, and is given by equation (13) as,

$$\theta_h = \theta_l \frac{f_l}{f_h} \tag{14}$$

Using the foregoing expression for θ, equation (12) gives

$$\theta_c = -\frac{f_l \theta_l}{f_h \ln (1 - E/E_f)} \tag{15}$$

Low speeds from 125 to 250 rpm and high speeds from 2400 to 6000 rpm have been used. The light intensity, E_f, is held in the same range as is the photocell output for temperature recordings.

A value of 0.572×10^{-3} sec has been measured for the time constant for the photocell system for a positive step change in light intensity. The possibility of a change in the time constant for a negative step change in light intensity has been investigated, with no significant difference being measured.

The recorded temperature data is then corrected to account for the photocell system lag. This is done by computing the rate of change of photocell output with respect to time and using it in equation (10), giving;

$$E_c = \theta_c \frac{dE}{d\theta} + E \tag{16}$$

where E is the recorded voltage and E_c its corrected value.

The data correction is made in the computer program used for data reduction. The derivative, $dE/d\theta$, is computed by using a second order curve to fit three consecutive data points.

Current Galvanometer Time Response. The recorded output, I, of the overly damped galvanometer used to record the sinusoidal wire current can be approximated by the first order differential equation

$$\theta_c \frac{dI}{d\theta} + I = K_1 \sin \omega\theta \tag{17}$$

where T_c is the effective galvanometer time constant.

This time constant is measured experimentally by comparing its recorded output to that of a high-frequency galvanometer (Honeywell M-3300) while they simultaneously record an a-c voltage at various frequencies. A value of 0.6452×10^{-3} sec results for the current galvanometer time constant.

Error Caused by a Change in Photocell Temperature. The effect of temperature on the photocell output at different light intensities has been measured. The output for nine light intensity levels was measured for cell temperatures ranging from 85 to 158 F. In the temperature range used for data recording the normalized data are well represented by the straight line

$$E(T)/E(70) = \left(1 - \frac{T - 70}{153 - 70}\right) \tag{18}$$

Photocell temperature is recorded during each data run. The cell output is corrected for photocell temperature by the above equation.

Velocity Measurement. Wire velocity is determined through the use of a silicon photocell with a response similar to that used for the temperature measurement by measuring the time required for the wire to travel between equally spaced openings.

Spacers are mounted in front of the photocell in such a manner that it views the wire intermittently. As the wire oscillates between extreme positions the photocell views it only during the time it is opposite an opening. The ratio of the distance between openings to the amplitude of wire displacement is approximately 0.066 to 1.0. Average velocity of the wire between two openings is determined by dividing the distance between two consecutive openings by the time required for the wire to travel between two such openings. The latter is determined by measuring the time between the two corresponding consecutive maxima on the oscillograph recording.

The velocity data are read to within ± 0.004 in. accuracy or approximately $\pm 5.2 \times 10^{-5}$ sec. This is less than four percent

of the shortest time between two peaks on the recorder printout. The random nature of reading error results in little net effect on the velocity curve.

The time marker of the recorder has been calibrated against the 600 Hz signal broadcast of the National Bureau of Standards over radio station WWV. The timer is accurate to within 0.5 percent. This corresponds to a possible 4 percent error in velocity.

The largest possible error exists in the range of the highest velocity where the error may be as large as 8 percent.

Electrical Resistance Verification. The electrical resistance of Chromax wire increases with increasing temperature. A verification of the resistance curve is made by measuring the wire resistance as a function of temperature. This is done by positioning three number 40 gauge Chromax wires inside an electrically heated furnace. Two number 20 gauge chromel-alumel thermocouples are placed at different positions near the Chromax wires to measure the furnace temperature, which is controlled by a variable transformer in the furnace input power line.

Heat Radiation. The radiation heat transfer is determined by measuring the heat dissipation from a d-c heated wire in a vacuum chamber where the low pressure renders the convective heat transfer negligible compared to the radiation. Pressures in the neighborhood of 3×10^{-5} mm hg and five number 32 gauge Chromax wires with approximate lengths of 1.4 ft are used in this test.

Wire temperature is computed from the wire resistance through the use of the relative resistance versus temperature curve. Room temperature resistance is measured by passing a small current through each wire and measuring the voltage drop across the wire.

Wire emissivity is computed from the equation

$$e = CEI/\sigma A(T^4 - T_0^4) \tag{19}$$

Heat conduction to the end supports has been investigated and found to be negligible compared to the radiation.

Specific Heat. The specific heat at constant volume, c_v, of most pure metals and compounds increases with temperature from zero at zero degrees Kelvin to approximately 6 cal/mole-K at higher temperatures. The specific heat at constant pressure, c_p, however, continues to increase with temperature [7].

Tabulated data for the specific heat at constant pressure for Chromax wire are not available. The specific heat for the solid solution can be approximated by using the sum of the products of the mole fractions of each constituent and its respective specific heat [8]. Chromax has a composition of 35 percent Ni, 20 percent Cr, and 45 percent Fe. Using the respective specific heats of nickel, chromium, and iron [6], the specific heat of Chromax wire based on mole fraction is;

$$c_p = 0.0852 + 4.289\ X\ 10^{-5}T \text{ Btu/lb-}R \tag{20}$$

$$\text{for } 536 \leq T \leq 1860\ R$$

and

$$c_p = 0.144 + 1.099 \times 10^{-5}T - 1.09 \times 10^{3}T^{-2} \text{ Btu/lb-}R \tag{21}$$

$$\text{for } 1860 \leq T \leq 2122\ R$$

The foregoing equations are used in their respective temperature ranges to calculate the specific heats for the experimental data.

Experimental Results

Five data runs of oscillatory heat transfer data were recorded including two runs for oscillations in the vertical plane and three for oscillations in the horizontal plane. The data are presented in graphical form and compared with the steady state standards. The steady state forced convection reference curves have been verified with the large temperature differences for the same size wire by Faircloth and Schaetzle [9].

The data for run three are plotted as a function of time in Fig. 5. Fig. 6 shows the data plotted as Nusselt number versus Reynolds number based on the absolute value of the instantaneous velocity. Data runs one, two, and three show a trend of departure from free to forced convection heat transfer at the critical Reynolds number. The data for runs four and five (for the larger, number 32 wire) lie below the critical Reynolds number and thus show little dependence on Reynolds number.

The critical Reynolds number for these data is approximately 1.3. The curve drawn through the data is given by,

$$\text{Nu} = 0.76 \text{ for Re} \leq 1.3 \tag{22}$$

$$\text{Nu} = 0.7(\text{Re})^{0.291} \text{ for Re} > 1.3 \tag{23}$$

This results in a standard deviation of 0.130.

The data for the vertical plane oscillations, (runs one and three) show higher Nusselt numbers for negative velocity data points than for the positive velocity data points at approximately the same Reynolds number (Fig. 5). This can be explained through an analysis of the free convective air currents surrounding the plane of oscillation.

The heat dissipated by the wire executing vertical oscillations tends to increase the temperature of a volume of air in the vicinity of the path of oscillation. This heated volume of air is forced upward by the buoyancy effect of the cooler surrounding air and thus superimposes a free convection velocity onto the sinusoidal wire velocity. The magnitude of the free convection velocity cannot be measured directly but can be approximated from the vertical oscillation data.

An approximation of the magnitude of the free convection velocity can be obtained by considering two points in the forced convection region (of runs one or three) which have velocities of opposite sign at approximately equal Nusselt numbers. The free convection velocity has a magnitude approximately equal to half the difference of the absolute values of the velocities of these two data points.

Fig. 7 shows a plot of the data of runs one through five with the vertical oscillation data of runs one and three adjusted for free convection. The critical Reynolds number for these data is approximately 1.4. The equations of the curves through these data points are

$$\text{Nu} = 0.74 \qquad \text{for Re} \leq 1.4 \tag{24}$$

$$\text{Nu} = 0.66\ (\text{Re})^{0.312} \text{ for Re} > 1.4 \tag{25}$$

The standard deviation from these curves is 0.122.

The free convective volume flow rate for the air heated by the wire is similar for vertical or horizontal oscillations for the same rate of heat dissipation. Therefore, the free convective velocity is inversely proportional to the horizontal flow area. The flow area is appreciably greater for horizontal oscillations than for vertical oscillations. This reduces the magnitude of the free convection velocity for horizontal oscillations well below the value for vertical oscillations. The total velocity for horizontal oscillations is also less affected by the free convection velocity because it is at right angles to the wire velocity. As a result of the above considerations no adjustment was made for the possible free convection air current for oscillations in the horizontal plane.

Conclusions

A procedure has been presented for an experimental investigation of oscillatory heat transfer. The following conclusions can be drawn from the experimental data obtained:

1 The existence of a critical Reynolds number is clearly evident which divides the heat transfer rates into free and forced convections.

2 Using the average of the oscillation heat transfer rates and Reynolds number from the data for runs one, two, and three, the average heat transfer rate with the wire oscillating is approximately 20 percent less than the rate recommended for steady state forced convection by McAdams [2].

3 There were no significant differences noted in the average

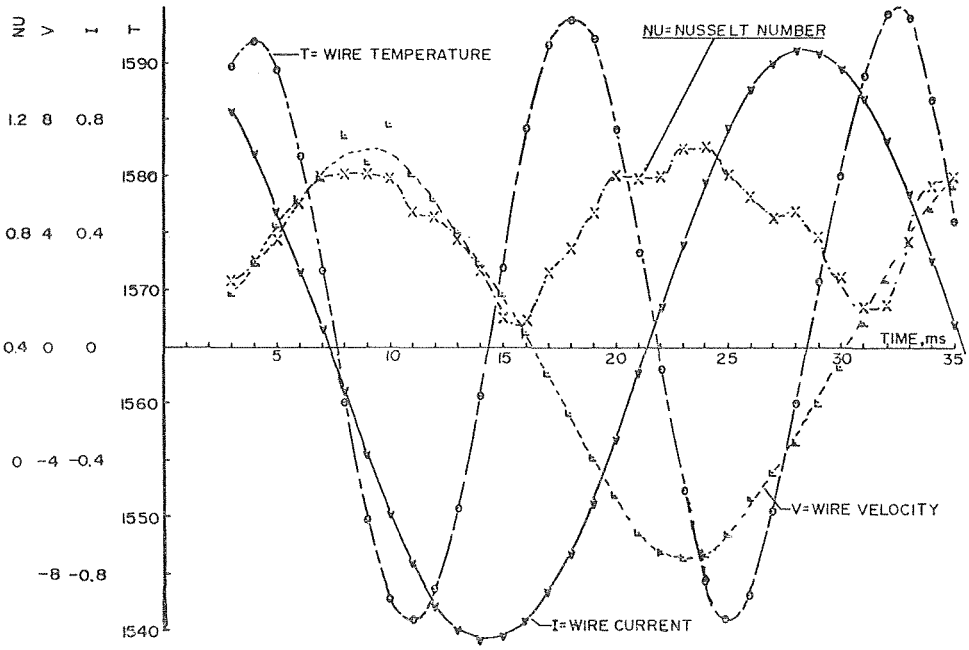

Fig. 5 Typical plot of wire temperature, current velocity, and Nusselt number versus time

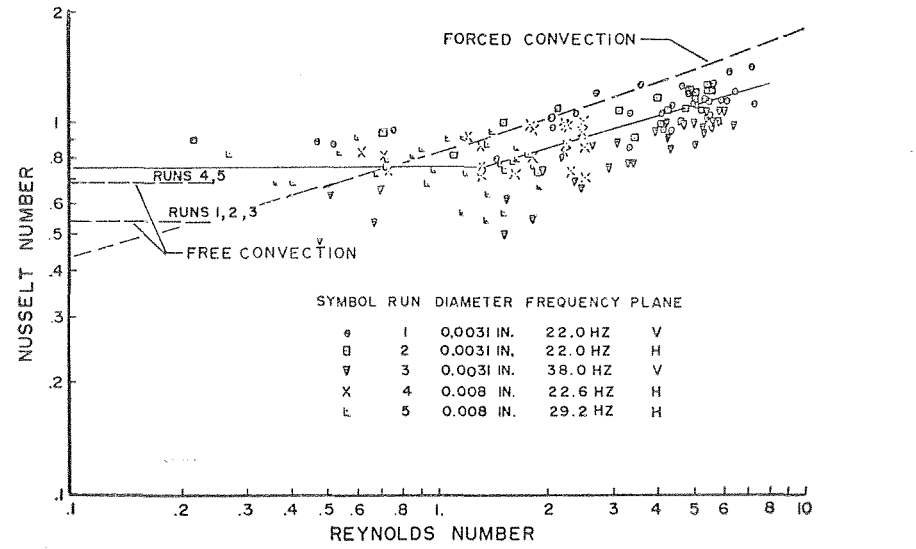

Fig. 6 Log plot of Nusselt number versus Reynolds number

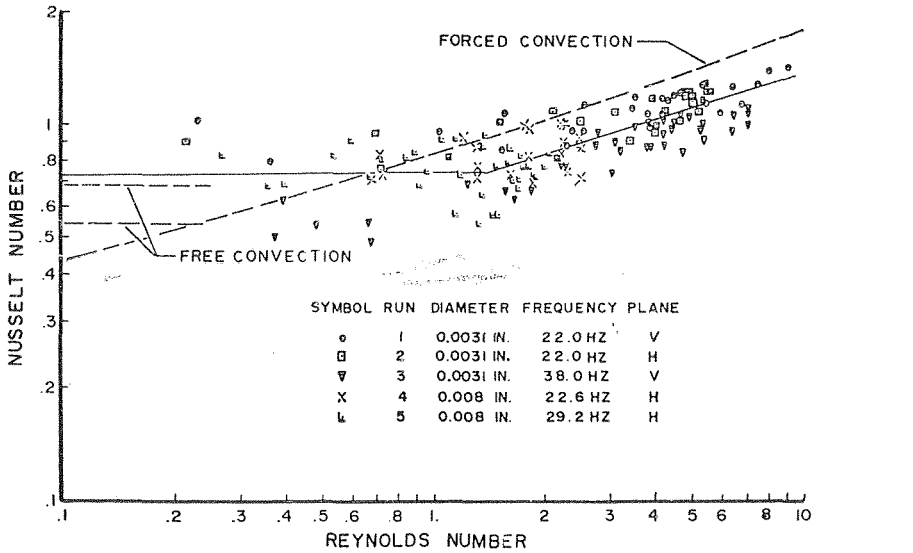

Fig. 7 Log plot of Nusselt number versus Reynolds number

heat transfer rates for oscillations in the vertical or horizontal planes.

4 Above the critical Reynolds number the instantaneous heat transfer data (when plotted as Nusselt number versus Reynolds number) have approximately the same slope as those for steady state forced convection.

5 Below the critical Reynolds number the data exhibit the dominance of free convection which is approximately $1^1/_2$ times the steady state free convection rates.

References

1 Thrasher, B. H., "Oscillatory Heat Transfer," PhD dissertation submitted to the University of Alabama, Tuscaloosa, Ala., 1967.

2 McAdams, William H., *Heat Transmission*, McGraw-Hill, New York, N. Y., 1954.

3 Lemlich, Robert, "Effect of Vibration on Natural Convection Heat Transfer," *Industrial and Engineering Chemistry*, Vol. 47, 1955, pp. 1175–1180.

4 Anantanarayanan, R., and Ramachandran, A., "Effect of Vibration of Heat Transfer From a Wire to Air in Parallel Flow," TRANS. ASME, Vol. 80, No. 4, Oct. 1958, pp. 1426–1432.

5 Deaver, F. K., Penney, W. R., and Jefferson, T. B., "Heat Transfer From an Oscillating Horizontal Wire to Water," JOURNAL OF HEAT TRANSFER, TRANS. ASME, Series C, Vol. 84, 1962, 2, pp. 251–256.

6 Wecks, C. E., and Block, F. E., "Thermodynamic Properties of 65 Elements—Their Oxides, Halides, Carbides, and Nitrides," Bureau of Mines, Bulletin 605.

7 Zemansky, Mark W., *Heat and Thermodynamics*, McGraw-Hill, New York, N. Y., 1957, pp. 260–275.

8 Hansen, J. P., Professor of Metallurgical Engineering, University of Alabama. Interview of January 5, 1967.

9 Faircloth, J. M., and Schaetzle, W. J., "Effect of Vibration on Heat Transfer for Flow Normal to a Cylinder," JOURNAL OF HEAT TRANSFER, TRANS. ASME, Series C, Vol. 91, No. 1, Feb. 1969.

heat transfer rates for oscillations in the vertical or horizontal planes.

4 Above the critical Reynolds number the instantaneous heat transfer data (when plotted as Nusselt number versus Reynolds number) have approximately the same slope as those for steady state forced convection.

5 Below the critical Reynolds number the data exhibit the dominance of free convection which is approximately $1^1/_2$ times the steady state free convection rates.

References

1 Thrasher, B. H., "Oscillatory Heat Transfer," PhD dissertation submitted to the University of Alabama, Tuscaloosa, Ala., 1967.

2 McAdams, William H., *Heat Transmission*, McGraw-Hill, New York, N. Y., 1954.

3 Lemlich, Robert, "Effect of Vibration on Natural Convection Heat Transfer," *Industrial and Engineering Chemistry*, Vol. 47, 1955, pp. 1175–1180.

4 Anantanarayanan, R., and Ramachandran, A., "Effect of Vibration of Heat Transfer From a Wire to Air in Parallel Flow," TRANS. ASME, Vol. 80, No. 4, Oct. 1958, pp. 1426–1432.

5 Deaver, F. K., Penney, W. R., and Jefferson, T. B., "Heat Transfer From an Oscillating Horizontal Wire to Water," JOURNAL OF HEAT TRANSFER, TRANS. ASME, Series C, Vol. 84, 1962, 2, pp. 251–256.

6 Wecks, C. E., and Block, F. E., "Thermodynamic Properties of 65 Elements—Their Oxides, Halides, Carbides, and Nitrides," Bureau of Mines, Bulletin 605.

7 Zemansky, Mark W., *Heat and Thermodynamics*, McGraw-Hill, New York, N. Y., 1957, pp. 260–275.

8 Hansen, J. P., Professor of Metallurgical Engineering, University of Alabama. Interview of January 5, 1967.

9 Faircloth, J. M., and Schaetzle, W. J., "Effect of Vibration on Heat Transfer for Flow Normal to a Cylinder," JOURNAL OF HEAT TRANSFER, TRANS. ASME, Series C, Vol. 91, No. 1, Feb. 1969.

DISCUSSION

C. T. Carley[4]

The authors should be congratulated upon using a novel experimental technique to attack an old problem. Two comments seem appropriate at this point.

The authors failed to site completely the literature available concerning the effect of vibration on heat transfer from cylinders. In particular, the work by Mabuchi and Tanaka.[5] This work describes a rather extensive investigation of the phenomena under discussion and lists four other references which are highly pertinent to the subject but which are not listed by the authors. The work by Mabuchi and Tanaka is evidently quite complete and includes the ranges of variables used by the authors.

It would have been instructive had the authors compared their data to those of other investigators. The Nusselt number predictions by the authors fall generally below those of other investigators. There is some question about the validity of equation (6). This equation apparently resulted from the solution of the one-dimensional wave equation under the assumption of constant tension in the wire. Since the wire in this study depended upon a variable tension in order to produce vibration, one wonders about the validity of equation (6).

There are so many editorial errors in the paper that a clear interpretation is prohibited. Some of these are listed in the following paragraphs.

The first sentence of the text indicates that references [2–8] inclusive are concerned with convective heat transfer analyses. This is obviously in error since references [6–8] have nothing to do with convective heat transfer.

Equation (2) is in error. The symbol A represents lateral area and should not appear in this equation. In its place should appear the symbol H which is the amplitude of oscillation. This same error appears in the definition of vibration Reynolds number in the nomenclature.

The symbol Re_f is not defined in the Nomenclature.

Equations (6) and (7) are both incorrect. The g appearing in both, as well as in the Nomenclature, should be g_c, the gravitational constant.

In equation (10), the symbol E_f is given three different definitions. In one case it is called "the actual photocell output." In another case it is called "a recorded steady state output" and finally in another case it is called "the height of the step change in the input." It seems clear that the symbol cannot represent all three parameters.

Above equation (10), the symbol T_c is used as defined in the nomenclature as the time constant in hours. Subsequently in equations (11), (12), (15), (16), and (17) the symbol θ_c is apparently used to represent the time constant and this symbol is not defined in the Nomenclature.

The symbol K_1 used in equation (17) is not defined either in the text or in the Nomenclature.

Immediately under equation (17) the symbol T_c is again incorrectly used to represent the time constant.

Equation (19) contains the symbol E which is evidently intended to represent the voltage drop across a wire. However, this symbol has already been defined in the nomenclature to represent the photocell output voltage.

The symbol T used in equations (20) and (21) apparently represents the absolute temperature in deg Rankine. However, this symbol was defined in the nomenclature as the temperature in degrees Fahrenheit. This same symbol is used for the radiative heat transfer term in equation (8) and again must be in absolute deg.

Equation (8) contains an assumption with respect to the radiative heat transfer from the wire. This assumption is implicit in the form of the term representing the radiative transfer and is as follows. The entire surroundings for the wire must be at the temperature T_0 which is given as the temperature of the surrounding air. If the wire may "see" any surface not at the temperature T_0 then the term given for the radiative transfer from the wire is incorrect. This factor is significant when experimentally determining the radiative loss as was done in this paper since the environment of the wire used to experimentally determine the radiative heat transfer is significantly different from the environment of the wire used during the tests.

R. Lemlich[6]

The authors are to be congratulated on their clever experimental approach to the problem of generating the vibrations and measuring their instantaneous effects. However, several questions come to mind.

Compared to say platinum or nickel, the resistance of Chromax wire does not vary much with temperature. Therefore, determination of its temperature from resistance measurements would seem to be imprecise. This lack of precision would then affect the evaluation of emissivity, which in turn would affect the accuracy of h. Similarly, any differences in surface characteristics (oxidation, etc.) between the wire heated in vacuum for the emissivity measurement, and the wire heated in air for the vibration runs proper, would also affect the emissivity and hence affect h. At the relatively high temperatures employed, the radiative contribution to heat dissipation from the vibrating wire is very considerable. In view of the subtractive form of the numerator

[4] Professor and Head, Mechanical Engineering Department, Mississippi State University, State College, Miss.

[5] Mabuchi, I., and Tanaka, T., "Experimental Study on Effect of Vibration on Natural Convective Heat Transfer From a Horizontal Fine Wire," *Bulletin of the Japan Society of Mechanical Engineers*, Vol. X, No. 41, 1967, pp. 808–816.

[6] Professor of Chemical Engineering, University of Cincinnati, Ohio.

in equation (8), the resulting error in h could be greatly magnified. Perhaps the authors would comment on the error propagation.

Doubtlessly, the authors conducted some control runs without any vibration. It would be informative if the authors could say how well such results compare with well-known correlations for free convection such as that of McAdams. In similar vein, it would be of interest to see the authors quantitatively compare their time-averaged results with vibration against those of previous investigators.

Finally, for vertical oscillation, the authors explain the difference in Nusselt numbers for positive versus negative velocity as being due to the superimposed free convective velocity. But this does not explain the difference in the Nusselt number *troughs* of Fig. 5, since such troughs correspond to nearly zero wire velocity. Therefore, it would seem that *location* (and temperature) also play a part, perhaps as follows: As the wire oscillates up, it moves "into" the heated volume of rising air. The local surrounding temperature is then higher than it is when the wire's downward motion tends to make the wire pass out through the bottom of the rising air into a locally cooler environment. This difference in local surrounding temperature affects the heat dissipation, making for an apparently higher Nusselt number when the vibrating wire is at its lowest position, and an apparently lower Nusselt number when the wire is at its highest position. At least this is the way the troughs compare in Fig. 5. Perhaps the authors would care to comment on this.

Authors' Closure

The authors wish to thank Dr. Carley and Dr. Lemlich for their comments. The additional reference presented by Dr. Carley is appreciated and may be helpful to persons interested in this area.

Equation (6), (which is correct except that it should have the quantity $(Fg/\rho A_x)$ raised to the $^1/_2$ power), is the solution of the one-dimensional wave equation under the assumption of constant tension. It is clear from the sinusoidal velocity curve of Fig. 5, that the assumption of constant tension is well founded for first order approximations. This is explained physically in that the tension consists of two components, the time average component and an oscillatory component. The average component is large compared to the oscillatory component. An order of magnitude approximation can be made of this by considering the average and oscillatory displacements of the wire support spring. The average displacment was approximately one inch while the oscillatory displacement was less than 0.05 in. which would indicate a ratio of 20:1 in the respective tension components.

An apology is expressed here to the reader for the nomenclature errors in the paper.

The implicit assumption in equation (8) with regard to the radiation environmental temperature being constant at T_0 is well founded. Because the wire was operating at a temperature in the range of 1500 deg F, the effect of any small variations in the ambient temperature, (even variations as large as 100 deg F), on the wire radiation are completely negligible.

The electrical resistance of Chromax wire increases approximately 22 percent in going from room temperature to 1600 deg F. The wire resistance was measured to an accuracy of 0.1 percent which yields the wire temperature and emissivity to within 5 deg F and 0.01, respectively. This variation of 0.01 in the emissivity causes an error on the order of less than one percent in the convective coefficient and is therefore negligible.

The authors conducted no control runs without vibration.

With regard to the difference in the Nusselt number troughs, there is nothing in the data which would indicate that the difference in the surrounding air temperature at the top and bottom displacement location would affect the heat dissipation in any way. The heat dissipation is dependent on the sinusoidal current and the wire resistance. The resistance is dependent on the wire temperature which, as shown in Fig. 5, has the same minimum value just prior to each of the Nusselt number troughs.

E. V. McASSEY, JR.
Department of Mechanical Engineering, Villanova University, Villanova, Pa.

HSUAN YEH
Director, Towne School of Civil and Mechanical Engineering, University of Pennsylvania, Philadelphia, Pa. Mem. ASME

Electron Heat Transfer in a Quiescent Nonequilibrium Plasma

An asymptotic solution has been obtained for the electron heat transfer to a spherical body immersed in a weakly ionized, quiescent plasma. Dimensional analysis of the governing equations shows that the problem can be divided into two regions: charge-separated and quasi-neutral. For the charge-separated region, the equations must be solved numerically, whereas the quasi-neutral solution can be expressed in closed form. From these studies it was found that the extent of the charge-separated region (i.e, sheath) is of the order of $\Lambda^{2/3}$. *Within the sheath the effects of ionization and recombination are of the order of* $\Lambda^{4/3}$. *The results include the variation of electron flux, electron heat transfer, and current as a function of body potential.*

The results are presented in a form to permit the easy determination of the electron heat transfer to a body immersed in a quiescent, weakly ionized plasma over a wide range of operating conditions. Furthermore, the electrical characteristics presented here can be used in conjunction with electron heating data to treat the body as a probe for diagnostic purposes.

Introduction

The present study examines the electron heat transfer to a spherical body immersed in a weakly ionized quiescent gas. Because of the relationship between electron and ion flux, data will also be supplied on the electrical characteristics of the body. The heat transfer to the body surface due to the motion of electrons consists of conduction due to electron temperature gradients at the surface and the flux of electrons, which after hitting the solid surface, recombine and thereby release their thermal as well as ionization energy. Thus the latter mode is of considerably greater influence. For this reason, this study will neglect the former and consider only heating due to electron flux. Chemical reactions in the form of ionization and recombination will also be included.

From a dimensional analysis of the governing equations four characteristic lengths appear. They are:

Debye length	R_D
Electron-neutral particle mean free path	λ
Body radius	r_p
Recombination length[1]	l_+

(The last quantity is defined as the distance that a charged particle travels by diffusion before it recombines.) Depending on the relative magnitudes of these four quantities, the problems can be quite distinct in their structure and require different meth-

Contributed by the Heat Transfer Division of The American Society of Mechanical Engineers for publication in the Journal of Heat Transfer. Manuscript received by the Heat Transfer Division, September 15, 1969.

[1] In previous works (references [4, 7, 8]) this quantity was referred to as the diffusion length.

Nomenclature

$D_\pm$ = ion, electron diffusion coefficient
e = charge of electron
E = electric field
F = nondimensional electric field
I = nondimensional current $= J_- - \beta J_+$
$J_\pm$ = normalized ion, electron flux, defined by equations (22), (23)
K_{ion} = ionization rate constant
K_{rec} = recombination rate constant
l_+ = recombination length $= (D_+/\nu)^{1/2}$
m = mass of particle
$N_\pm$ = ion, electron number density
$n_\pm$ = normalized number density
q_e = electron heat transfer rate
q_g = heat transfer due to neutral gas
Q_e = normalized electron heat transfer rate $= q_e/-D_{-\infty}N_{+\infty}/l_+$
r_p = probe radius
R_d = Debye length $= (\epsilon_0 kT_{-\infty}/e^2N_{-\infty})^{1/2}$
$T_\pm$ = ion, electron temperature
$S(\delta, \tau)$ = potential difference across sheath, equation (44)
V_p = potential at the surface
V_∞ = potential at infinity

ods of attack. For the present study, the following situation was considered:

$$\lambda << R_D << l_+ << r_p$$

Under the foregoing conditions, it is possible to divide the problem into two regions, the quasi-neutral region and the charge-separated region. Division of the total problem in this manner allows separate solutions for each region with the complete solution obtained by joining the individual ones. In the charge-separated region, the governing equations are non-linear and must be solved numerically. When the solutions are obtained in this manner, it becomes clear that the results are dependent on the following nondimensional parameters:

Ratio of Debye length to recombination length (Λ)
Ratio of probe radius to recombination length (r_p/l_+)
Ratio of ion to electron diffusion coefficient (β)
Ratio of electron temperature to ion temperature (τ)

Su and Lam [1][2] developed a continuum theory for a spherical electrostatic probe for the case where the ratio of the mean free path, λ, to the body radius, r_p, was much less than one. The theory considered a high density, weakly ionized, quiescent gas with no recombination or ionization. In the examination of a probe in a plasma, the boundary conditions at the probe surface greatly affect not only the numerical answers, but also the structure of the entire problem. Su and Lam assumed that the probe was at a negative potential, and also that at the probe surface the charged particle number density was zero. This latter condition is equivalent to taking the limit of the mean free path equal to zero.

Cohen [2] presented an asymptotic theory for a spherical probe under much the same situation as Su and Lam; however, he examines the case of moderate positive and negative probe potentials. An asymptotic solution is obtained by use of the natural ordering of the governing equations. The system of differential equations is reduced to a single equation. This equation is then transformed, using the technique of maximum balancing, so that the maximum number of terms is retained. The overall solution is accurate to a term of the order of $(R_D/r_p)^{2/3}$. The present authors make use of the tabulated results of Cohen [2] and [3] because within the sheath the same governing equations appear, using a slightly different parameter.

The most significant contribution of the work of Su, Lam, and Cohen is that by making use of controlling length parameters, these authors have shown the natural ordering of the probe problem. The technique of maximum balancing employed by Cohen results in a differential equation which describes a large class of sheath problems. Although the resulting equation is extremely difficult to integrate by solving in normalized form, the results have universal application. In this work, the governing parameters met the following conditions:

$$\lambda \ll R_D \ll r_p$$

and

$$\lambda/R_D \to 0 \qquad R_D/r_p \to 0$$

[2] Numbers in brackets designate References at end of paper.

Whitman and Yeh [4] have taken a somewhat different approach. These authors consider the problem of a probe in a weakly ionized, quiescent gas, but with the condition that a free fall region exists near the surface. While passing through this free fall region, the charged particles experience no collisions and are only under the influence of the probe potential. The boundary condition at the probe surface then consists of a balance of particle flux between the free fall region and the continuum region. In addition, the analysis considered recombination and ionization. A recombination length l_+, is defined which is equal to the distance a particle diffuses before recombining. The analysis is then conducted for the condition where l_+/r_p is less than one. This assumption allows the elimination of curvature considerations. Since in most cases of interest $R_D < l_+$, the governing equations can be expanded, using a perturbation analysis. The resulting perturbation solution [4] is uniformly valid if $R_D < \lambda$. In this way, a theory is obtained which is expressible in analytic form. This is the power of this approach because an analytic solution can be of great use in diagnostic work.

McKee and Mitchner [5] attack a similar problem, except they consider the case where $l_+/r_p \gg 1$. In this case, curvature must be considered. The resulting equations are solved by use of Green's functions and numerical integration. In reference [5], no region of charge separation is considered, which is valid as shown in [6], provided $R_D \ll \lambda$.

Analysis

Basic Equations. In a quiescent plasma, the electron heat transfer to a body immersed in a plasma is given by:

$$q_e = (\mathbf{\Gamma}_- c_1 T_- + \mathbf{\Gamma}_+ H)\cdot \mathbf{n} \tag{1}$$

where

$\mathbf{\Gamma}_-$ = electron flux
$\mathbf{\Gamma}_+$ = ion flux
$\mathbf{n}$ = unit normal to the surface
$c_1 T_-$ = total thermal energy per electron
H = ionization energy per electron

To determine the electron flux, the species conservation equation must be solved. Equation (2) presents the ion (subscript $+$) and electron (subscript $-$) conservation equation for a steady, slightly ionized plasma.

$$\nabla\cdot\mathbf{\Gamma}_\pm = -K_{\text{rec}} N_+ N_-^2 + K_{\text{ion}} N_- N_g \tag{2}$$

where

$$\mathbf{\Gamma}_\pm = -D_\pm N_g \mathbf{d}_\pm$$

$$\mathbf{d}_\pm = \nabla\left(\frac{N_\pm}{N_g}\right) \mp \frac{N_\pm e\mathbf{E}}{N_g k T_\pm}$$

In the foregoing equations, the subscript "g" refers to the total gas. The right-hand side of equation (2), representing the formation of charged particles due to collisions, is based on the assump-

Nomenclature

y = distance normal to wall
δ = $\{2(1+\beta\tau)/(1+\tau)\}^{1/2}$
β = D_+/D_-
δ = $\dfrac{-(J_- - J_+)}{(J_+ + \tau J_-)}$
$\Gamma_\pm$ = ion, electron particle flux
λ = electron-neutral particle mean free path
Λ = ratio of Debye length to recombination length
ϕ = normalized potential $\left(\nabla\phi = \dfrac{-e\mathbf{E}}{kT_{-\infty}}\right)$
α = $(1-\beta)/(1+\beta\tau)$
ν = $K_{\text{ion}} N_{g\infty}$
τ = T_-/T_+
ξ = y/l_+

Subscripts

$+$ = ion
$-$ = electron
g = neutral gas
∞ = equilibrium condition
p = probe condition

tion that the recombination process is predominantly controlled by three-body impact, i.e.,

$$A^+ + e + e \rightleftharpoons A + e$$

This is the case for a seeded noble gas at the temperatures of interest here.

In addition to equation (2), the charged particles are also governed by the Poisson's equation:

$$\nabla \cdot \mathbf{E} = \frac{e}{\epsilon_0}(N_+ - N_-) \tag{3}$$

Equations (2) and (3) plus suitable boundary conditions provide the complete description of the ionized particle distribution.

The assumption of slight ionization permits the decoupling of the neutral particles from the charged particle. In addition, the present study assumed constant values for the neutral gas density, the electron temperature, the diffusion coefficient and the rate constants for recombination and ionization. The assumption of constant electron temperature is perhaps the least defensible restriction; however, it was made to eliminate the necessity of introducing the electron energy equation. Although it is known that the recombination rate is very sensitive to the electron temperature, these assumptions are nevertheless made in order to simplify the problem to an acceptable level such that the impact of a number of significant parameters can be clearly delineated. For instance, we have calculated for values of Λ between 0.001 to 0.1, corresponding to a range of two orders of magnitude of the recombination rate, other things being equal.

To solve equations (2) and (3), the first step is to transform the equations to nondimensional form using the following variables:

$$n_\pm = \frac{N_\pm}{N_{\pm\infty}} \qquad \tau = \frac{T_-}{T_+} \qquad \bar{\nabla} = r_p \nabla$$

$$\nu = K_{\text{ion}} N_{g\infty} \qquad l_+ = (D_+/\nu)^{1/2}$$

In terms of these variables, the ion equation becomes:

$$\left(\frac{l_+}{r_p}\right)^2 \bar{\nabla} \cdot \{\bar{\nabla} n_+ + n_+ \tau \bar{\nabla}\phi\} = n_-(n_- n_+ - 1) \tag{4}$$

As mentioned earlier, the present study will consider the physical situation in which

$$\lambda \ll R_D \ll l_+ \ll r_p$$

Since $l_+/r_p \ll 1$, the effect of body curvature in the vicinity of the surface can be neglected (McAssey [7]) so that equation (4) can be written:

$$l_+ \frac{d}{dy}\left\{\frac{dn_+}{dy} + n_+ \tau \frac{d\phi}{dy}\right\} = n_-(n_- n_+ - 1) \tag{5}$$

where y is the distance normal to the surface measured from the surface such that $r = r_p + y$. This equation can be transformed by adopting the nondimensional distance $\xi = y/l_+$ yielding:

$$\frac{d}{d\xi}\left\{\frac{dn_+}{d\xi} + n_+ \tau \frac{d\phi}{d\xi}\right\} = n_-(n_- n_+ - 1) \tag{6}$$

In the same manner, the electron conservation equation and Poisson's equation become:

$$\frac{d}{d\xi}\left\{\frac{dn_-}{d\xi} - n_- \frac{d\phi}{d\xi}\right\} = \beta n_-(n_- n_+ - 1) \tag{7}$$

$$\Lambda^2 \frac{d^2\phi}{d\xi^2} = (n_- - n_+) \tag{8}$$

where

$$\Lambda = R_D/l_+$$

Far from the surface ($\xi \gg 1$) the ion and electron densities approach their equilibrium values and the equation for the potential is reduced to LaPlace's equation $\nabla^2\phi = 0$.

Boundary Conditions. To complete the formulation of the problem, appropriate boundary conditions must be determined. For the ionized species, two types of conditions are possible at the body surface:

1 free fall sheath
2 zero number density for each species (collision dominated).

Since the present problem considers the situation in which $\lambda \ll R_D$, the collision dominated condition will be used. This is equivalent to taking the limit in which λ goes to zero (references [7] and [8]). In addition to specifying the number density at the surface, the potential at the surface, ϕ_p, is also specified.

At infinity, the boundary conditions are:

1 the number density is equal to the equilibrium value,

$$N_+ = N_- = N_{-\infty}$$

2 the potential is equal to some specified free stream value,

$$\phi_\infty.$$

In summary, the boundary conditions for the present study are:

$$\begin{aligned} \xi = 0 \qquad & n_+ = n_- = 0 \\ & \phi = \phi_p \\ \xi = \infty \qquad & n_+ = n_- = 1 \\ & \phi = \phi_\infty \end{aligned} \tag{9}$$

Equations (5) through (9) therefore represent the complete statement of the problem under the present assumptions.

Quasi-Neutral Region. For the conditions considered in this paper $\Lambda \ll 1$, it is possible to carry out a perturbation expansion of equations (5), (6), and (7) using the following expansion:

$$\left.\begin{aligned} n_+ &= n_0 + \tau\Lambda^2 n_1 + \dots \\ n_- &= n_0 - \Lambda^2 n_1 + \dots \\ F &= F_0 + \Lambda^2 F_1 + \dots \end{aligned}\right\} \tag{10}$$

where

$$F = -d\phi/d\xi$$

Applying the foregoing expansion to equations (5) through (7) yields equations (11), (12), and (13), the zeroth order equations.

$$\frac{d^2 n_0}{d\xi^2} = \frac{\hat{\alpha}^2}{2} n_0(n_0^2 - 1) \tag{11}$$

$$\frac{d(n_0 F_0)}{d\xi} = -\gamma \frac{d^2 n_0}{d\xi^2} \tag{12}$$

$$\frac{dF_0}{d\xi} = (1 + \tau) n_1 \tag{13}$$

Whitman [6] has shown that the integrals of (11) and (12) are:

$$\frac{dn_0}{d\xi} = -\frac{\hat{\alpha}}{2}(n_0^2 - 1) \tag{14}$$

$$n_0 = \frac{A_1 e^{\hat{\alpha}\xi} - 1}{A_1 e^{\hat{\alpha}\xi} + 1} \tag{15}$$

$$F_0 = \frac{F_\infty}{n_0} - \frac{\gamma}{n_0}\frac{dn_0}{d\xi} \tag{16}$$

where

F_∞ = field at $\xi = \infty$
A_1 = constant of integration

The boundary conditions for the above equations are:
$\xi = \infty$

$$n_0 = 1$$
$$n_1 = 0$$
$$F_0 = F_\infty$$

$$\xi = 0$$
$$n_0 = 0$$

To satisfy the condition at $\xi = 0$

$$A_1 = 1$$

Equation (15) becomes

$$n_0 = \frac{e^{\hat{\alpha}\xi} - 1}{e^{\hat{\alpha}\xi} + 1} \tag{17}$$

Equations (14), (16), and (17) represent the quasi-neutral solution for the quiescent plasma. From equation (16), it is apparent that the present solution is singular at $\xi = 0$. This singularity is due to the elimination of the highest order derivative in equation (8) by the perturbation analysis. In addition, it can be shown that as $\xi \to 0$, n_0 varies as ξ and therefore equation (13) shows that n_1 will be proportional to $1/\xi^2$. This means that near the surface a region of significant charge separation is present and quasi-neutrality is no longer valid.

Charge-Separated Region. In the charge-separated or sheath region, the complete set of governing equations must be solved (i.e., equations (5), (6), and (7)).

These equations represent a set of coupled nonlinear ordinary differential equations. Numerical solution of these equations in the above form is extremely difficult because slight variation in starting conditions yields widely divergent results. However, the procedure can be significantly simplified by seeking an asymptotic solution as $(R_D/l_+) \to 0$ and making the following assumptions:

1 n_+, n_- are bounded above
2 the sheath is thin
3 the normalized flux to the wall is finite

Let us now transform the variables in the following manner:

$$s = \Lambda^a \xi$$
$$\bar{F} = \Lambda^b F$$
$$\bar{n}_+ = \Lambda^c n_+$$
$$\bar{n}_- = \Lambda^d n_-$$

The choice of the constants a, b, c, and d is made so that the maximum number of terms in the governing equations are retained consistent with assumptions (1), (2), and (3).

Transforming equations (5), (6), and (7), the following results:

$$\Lambda^{-c+2a}\frac{d^2\bar{n}_+}{ds^2} - \tau\Lambda^{-b-c+a}\frac{d}{ds}(\bar{F}\bar{n}_+) = \Lambda^{-c}\bar{n}_-(\bar{n}_+\bar{n}_-\Lambda^{-c-d} - 1) \tag{18}$$

$$\Lambda^{-d+2a}\frac{d^2\bar{n}_-}{ds^2} + \Lambda^{-b-d+a}\frac{d}{ds}(\bar{F}\bar{n}_-) = \beta\Lambda^{-c}\bar{n}_-(\bar{n}_+\bar{n}_-\Lambda^{-c-d} - 1) \tag{19}$$

$$\Lambda^{+2-b+a}\frac{d\bar{F}}{ds} = (\Lambda^{-c}\bar{n}_+ - \Lambda^{-d}\bar{n}_-) \tag{20}$$

Under the governing assumptions, the following observations can be made:

1 for a thin sheath $a < 0$
2 for n_+, n_- to be bounded $c \leq 0$, $d \leq 0$

Balancing equation (20), the following is obtained:

$$c = d$$
$$2 - b + a = c$$

Since $c = d$, balancing equation (18) will automatically balance equation (19). In order to balance the left-hand side of equation (18), the exponents of Λ must be equal.

$$-c + 2a = -b - c + a$$
$$a = -b$$

Therefore,

$$c = 2b - 2$$

Attempting to balance the first term on the right-hand side of equation (18) yields the result that $c = 2$. However, this violates the assumption that n_+, n_- are finite. If the second term is balanced with the left-hand side of equation (18), the result is $a = 0$; but this would mean that the sheath is not thin. Therefore, attempts to balance the right-hand side of equation (18) yield results which are contrary to the governing assumptions.

Using the results obtained thus far, equation (18) becomes:

$$\frac{d^2\bar{n}_+}{ds^2} - \tau\frac{d}{ds}(\bar{n}_+\bar{F}) = \Lambda^{2b}\bar{n}_-(\bar{n}_+\bar{n}_-\Lambda^{4-4b} - 1) \tag{21}$$

In addition, it can be shown that $0 \leq b \leq 1$.

This result means that the right-hand side of equation (21) is of higher order in Λ than the left-hand side. In the sheath, the effect of chemistry is not as important as diffusion. From equation (2), the particle flux to the surface can be written in the following nondimensional form:

$$\frac{\Gamma_+}{\dfrac{-D_{+\infty}N_{+\infty}}{l_+}} = J_+ = \frac{dn_+}{d\xi} - \tau n_+ F \tag{22}$$

$$\frac{\Gamma_-}{\dfrac{-D_{+\infty}N_{+\infty}}{l_+}} = J_- = \frac{dn_-}{d\xi} + n_- F \tag{23}$$

Transforming the ion flux to sheath variable, the following is obtained:

$$J_+ = \Lambda^{2-3b}\left\{\frac{d\bar{n}_+}{ds} - \tau\bar{n}_+\bar{F}\right\} \tag{24}$$

For the flux to be finite within the sheath, the exponent of Λ must equal zero. Therefore, b equals $^2/_3$ and from previous results $a = c = d = -^2/_3$. Equations (18), (19), and (20) become

$$\frac{d^2\bar{n}_+}{ds^2} - \tau\frac{d}{ds}(\bar{n}_+\bar{F}) = 0 + O(\Lambda^{4/3}) \tag{25}$$

$$\frac{d^2\bar{n}_-}{ds^2} + \frac{d}{ds}(\bar{n}_-\bar{F}) = 0 + O(\Lambda^{4/3}) \tag{26}$$

$$\frac{d\bar{F}}{ds} = (\bar{n}_+ - \bar{n}_-) \tag{27}$$

Considering only terms of order zero in Λ, the right-hand side of equations (25) and (26) can be neglected. This approximation will be satisfactory provided $\Lambda^{4/3} \ll 1$.

Equations (25) through (27) are similar to equations solved by Cohen [2] for which tabulated results are available. The procedure in the present study, therefore, has been to reduce these equations to a single equation for $\bar{F}$ (details in references [7] and [8]) and transform the resulting equation to the same form as Cohen so that the tabulated results can be used.

The required transformation is:

$$s = \frac{1}{(J_+ + \tau J_-)^{1/3}}\left\{\hat{s} + \frac{\tau}{2}\hat{F}_p^{\,2}\right\}$$
$$\bar{F} = \hat{F}(J_+ + \tau J_-)^{1/3}$$

Combining equations (25), (26), and (27) and applying the foregoing transformation yields equation (28).

$$(\tau - 1)\frac{d\hat{F}}{d\hat{s}} = \frac{1}{\hat{F}}\frac{d^2\hat{F}}{d\hat{s}^2} + \frac{(J_- - J_+)}{(J_+ + \tau J_-)}\frac{1}{\hat{F}} - \frac{\tau\hat{F}^2}{2} - \hat{s} \quad (28)$$

At the surface ($s = 0$)

$$\hat{s}_p = -\frac{\tau\hat{F}_p^2}{2}$$

$$\frac{d\hat{F}}{d\hat{s}} = 0$$

$$\frac{d^2\hat{F}}{d\hat{s}^2} = -\frac{(J_- - J_+)}{(J_+ + \tau J_-)} = \delta$$

The foregoing equation defines the quantity δ. It can be shown that as $s \to \infty$

$$\hat{F} = -\frac{\delta}{\hat{s}} + O\left(\frac{1}{\hat{s}^2}\right) \quad (29)$$

Therefore, the asymptotic solution to $\hat{F}$ as $\hat{s} \to \infty$ is $-\delta/\hat{s}$ plus higher order terms. This solution for $\hat{s} \to \infty$ determines the asymptotic form of the quasi-neutral solution as $\xi \to 0$ since the two solutions must match. Cohen's tabulated results are in terms of $\hat{s}_p$ and δ (reference [3]). This means that for a given probe field, $\hat{s}_p$, the current ratio, J_+/J_-, is determined independent of the quasi-neutral region. However, to obtain J_+ and J_-, the quasi-neutral solution must be obtained in asymptotic form and matched to the sheath.

Particle Fluxes and Matching. The particle flux normal to the surface is given by equations (22) and (23). Although in the sheath the flux of ions and electrons is constant (i.e., J_+, J_-), this is not true throughout the entire region because of the presence of chemistry. However, it can be shown that over the entire region the net flux is conserved. This condition will be used to establish a relationship between the field F_∞ and the fluxes at the wall.

From equations (22) and (23), the following is obtained:

$$(\Gamma_+ - \Gamma_-) = -\left(\frac{D_{+\infty}}{D_{-\infty}}J_+ - J_-\right)\frac{D_{-\infty}N_{-\infty}}{l_+} \quad (30)$$

Far from the surface as $\xi \to \infty$:

$$\frac{dn_+}{d\xi} = \frac{dn_-}{d\xi} \to 0$$

$$n_+ = n_- \to 1$$

$$(\Gamma_+ - \Gamma_-) = -(\beta\tau + 1)F_\infty\frac{D_{-\infty}N_{-\infty}}{l_+} \quad (31)$$

Combining equations (30) and (31) yields the result:

$$F_\infty = -\frac{(\beta J_+ - J_-)}{(\beta\tau + 1)} \quad (32)$$

To obtain the complete solution, the sheath and quasi-neutral results must be matched. In order to match the sheath solution, the asymptotic form of F_0 as $\xi \to 0$ must be determined. Combining (14) and (16), the following is obtained:

$$F_0 = \left(F_\infty - \frac{\hat{\alpha}\gamma}{2}\right)\frac{1}{n_0} + \frac{\gamma\hat{\alpha}}{2}n_0 \quad (33)$$

The asymptotic form of n_0 for small ξ can be obtained from equation (15) by expanding $e^{\hat{\alpha}\xi}$

$$n_0 = \frac{\hat{\alpha}\xi}{2} - \left(\frac{\hat{\alpha}\xi}{2}\right)^2 + O(\xi^3) \quad (34)$$

Therefore, as $\xi \to 0$

$$F_0 = \left(F_\infty - \frac{\hat{\alpha}\gamma}{2}\right)\frac{2}{\hat{\alpha}\xi} + O(\xi) \quad (35)$$

Substituting the results from equation (32), the following asymptotic form of F_0 as $\xi \to 0$ is obtained from the quasi-neutral solution:

$$F_0 = \left\{\frac{(\beta J_+ - J_-)}{(\beta\tau + 1)} + \frac{\hat{\alpha}\gamma}{2}\right\}\frac{-2}{\hat{\alpha}\xi} + O(\xi) \quad (36)$$

In order to match the quasi-neutral solution to the sheath solution, equation (36) must be first changed into sheath variables.

$$\hat{F}_0 = -\left\{\frac{2(\beta J_+ - J_-)}{\hat{\alpha}(\beta\tau + 1)} + \gamma\right\}\frac{1}{\hat{s}\left(1 + \frac{\tau F_p^2}{2\hat{s}}\right)} \quad (37)$$

As $\xi \to 0$, $\hat{s} \to \infty$, the quasi-neutral solution then yields,

$$\hat{F}_0 = -\left\{\frac{2(\beta J_+ - J_-)}{\hat{\alpha}(\beta\tau + 1)} + \gamma\right\}\frac{1}{\hat{s}} + 0\left(\frac{1}{\hat{s}^2}\right) \quad (38)$$

In order that $\hat{F}_0$ agrees with $\hat{F}$ from the sheath solution equation (29) to the order of $1/\hat{s}^2$, the following must be true:

$$\gamma + \frac{2(\beta J_+ - J_-)}{\hat{\alpha}(\beta\tau + 1)} = \delta \quad (39)$$

As discussed earlier, Cohen [2] has tabulated sheath solutions in terms of δ and $\hat{s}_p$. Using equation (39) and the definition of δ, the flux ratio and the flux of electrons is given by equations (40) and (41):

$$\frac{J_+}{J_-} = -\frac{(1 + \tau\delta)}{(\delta - 1)} \quad (40)$$

$$J_- = \frac{(\beta\tau + 1)\hat{\alpha}}{2\left(\beta\frac{J_+}{J_-} - 1\right)}\{\delta - \gamma\} \quad (41)$$

Equation (41) gives the electron flux to a term of the order of $\Lambda^{4/3}$. If the higher order terms had been included, the probe potential would appear explicitly in J_- (i.e., Cohen [2]).

Using equations (1) and (41), the normalized electron heat transfer can be written:

$$Q_e \equiv \frac{q_e}{-D_{-\infty}N_{+\infty}/l_+} = c_1T_{+\infty}\tau J_- + \beta J_+ H \quad (42)$$

$c_1T_{+\infty}\tau$ = thermal energy per electron
H = ionization energy

Potential Distribution. So far, the analysis has considered only the electric field; however, the basic boundary conditions are potential. The potential distribution, or more correctly, the potential difference for the quiescent plasma must be calculated. The potential difference between the surface and free stream is

$$\phi_p - \phi_\infty = (\phi_p - \phi_m) + (\phi_m - \phi_\infty) \quad (43)$$

The first term on the right-hand side of equation (43) represents the potential difference across the sheath and the second the difference across the quasi-neutral and equilibrium region. The first quantity is:

$$(\phi_p - \phi_m) = \int_0^{\xi_m} F d\xi = \int_{\hat{s}_p}^{\hat{s}_m} \hat{F} d\hat{s} = S(\delta, \tau) \quad (44)$$

where $S(\delta, \tau)$ has been tabulated by Cohen [2]. The second quantity can be calculated from equations (15) and (16).

$$\phi_m - \phi_\infty = \gamma \ln \frac{(e^{\hat{\alpha}\xi_m} - 1)}{(e^{\hat{\alpha}\xi_m} + 1)}$$

$$+ \frac{(\beta J_+ - J_-)}{(\beta\tau + 1)} \left\{ \hat{\alpha}\xi_m - 2 \ln \frac{e^{\hat{\alpha}\xi_m}}{e^{\hat{\alpha}\xi_m} - 1} - \frac{r_p}{l_+} \right\} \quad (45)$$

ξ_m is the point of matching of the sheath and quasi-neutral solution. In terms of the sheath variables, ξ_m becomes:

$$\xi_m = \frac{\Lambda^{2/3}}{(J_+ + \tau J_-)^{1/3}} \{\hat{s}_m - \hat{s}_p\} \quad (46)$$

Where $\hat{s}_m$ and $\hat{s}_p$ have been determined by Cohen [3] to agree with tabulated values of $S(\delta, \tau)$. The total potential difference is the sum of equations (44) and (45). The exact location of $\hat{s}_m$ will not influence the result on $\phi_p - \phi_\infty$, since the sheath and the quasineutral region overlap by a considerable distance along $\hat{s}$.

Results and Discussion

The analytical results have shown that the electron flux and, therefore, the electron heat transfer is dependent upon the following four parameters: Λ, r_p/l_+, β, τ. Rather than solving one specific problem for a particular set of these parameters, the approach of the numerical computations has been to examine a range of these parameters to establish the basic trends. Thus, the following cases have been investigated:

$$\Lambda = 0.1, 0.01, 0.001$$
$$r_p/l_+ = 10$$
$$\beta = 10^{-2}, 10^{-4}$$
$$\tau = 1, 2, 5$$

Before presenting the results, it is worthwhile considering the importance of each of these parameters.

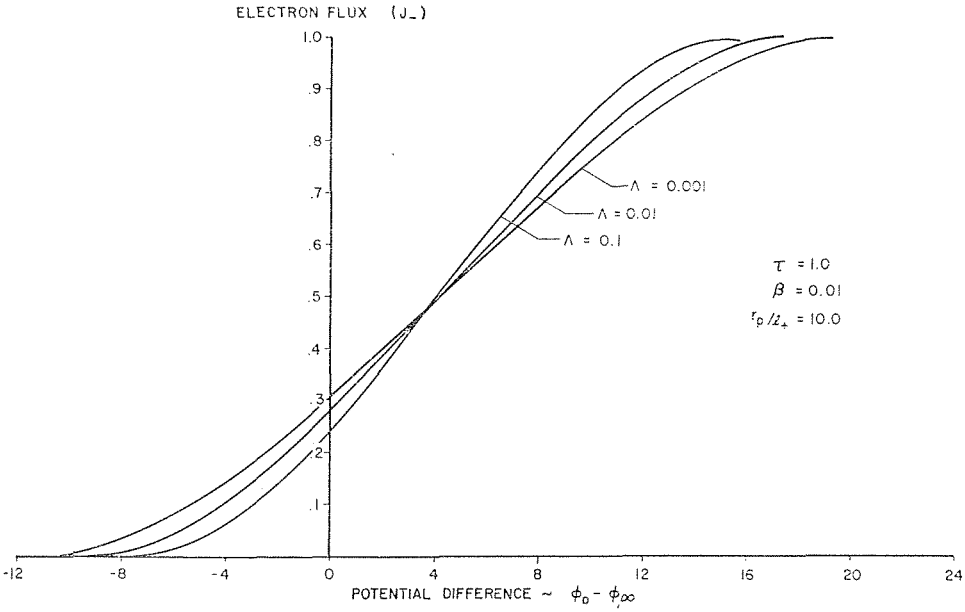

Fig. 1 Electron flux versus potential difference for $\tau = 1.0$

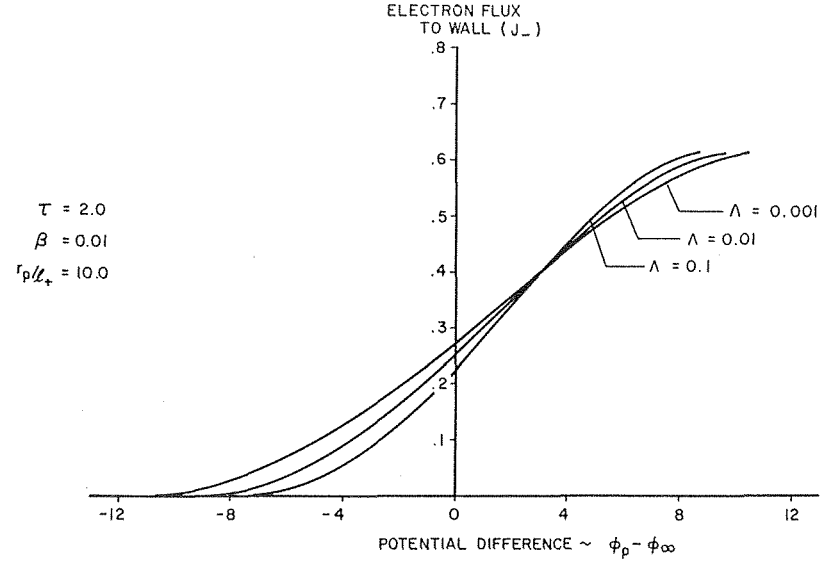

Fig. 2 Electron flux versus potential difference for $\tau = 2.0$

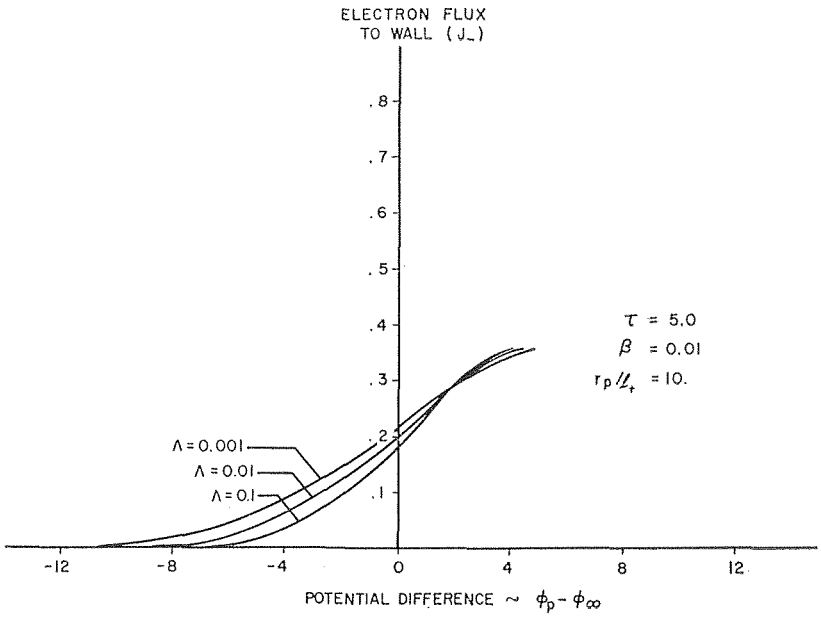

Fig. 3 Electron flux versus potential difference for $\tau = 5.0$

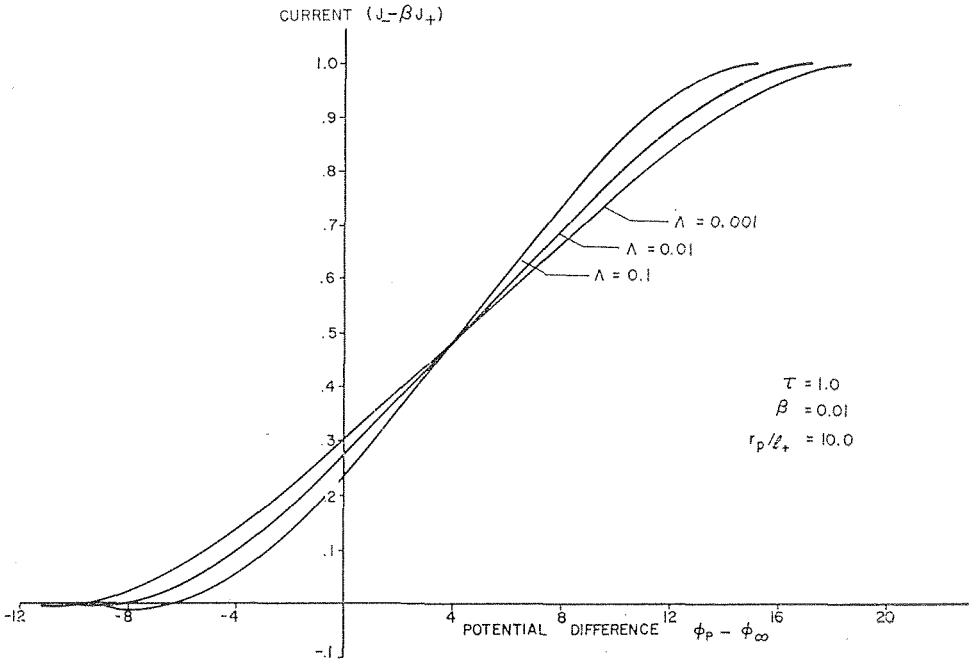

Fig. 4 Current versus potential difference for $\tau = 1.0$

The ratio of Debye length to recombination length appears explicitly only in equation (46) for the location of the matching point in the potential distribution integral. For this reason, the ion and electron flux and the electric field far from the surface are independent of this parameter. However, this ratio is the most critical parameter because we have obtained an asymptotic solution whose validity is dependent upon $\Lambda \ll 1$. For instance, from equations (25) and (26), it can be seen that the effect of chemistry which has been neglected within the sheath is 0 ($\Lambda^{4/3}$).

The parameter r_p/l_+ will only affect the magnitude of ($\phi_p - \phi_\infty$) and, therefore, a single value was chosen. The ratio of ion diffusion coefficient to electron diffusion coefficient is approximately equal to $(m_-/m_+)^{1/2}$. This parameter will determine the zero current potential of the body. The temperature ratio, τ, is, of course, arbitrary and depends upon the particular problem. However, τ does influence the electron heat transfer directly by affecting the flux and also the thermal energy per electron.

Figs. 1, 2, and 3 show the variations of electron flux with potential difference ($\phi_p - \phi_\infty$) for different values of Λ and τ. As discussed in the previous paragraph, Λ affects only the potential difference. Increasing Λ tends to reduce the potential difference required for electron saturation. The temperature ratio on the other hand has a strong influence on the flux. Comparing Figs. 1 and 3, it can be seen that increasing the ratio τ from 1.0 to 5.0 reduces the electron flux at saturation by 65 percent. Because of the importance of electrical characteristics Figs. 4, 5, and 6 present the net current for the same condition considered in Figs. 1 through 3. Because of the small value of β, the electron flux and

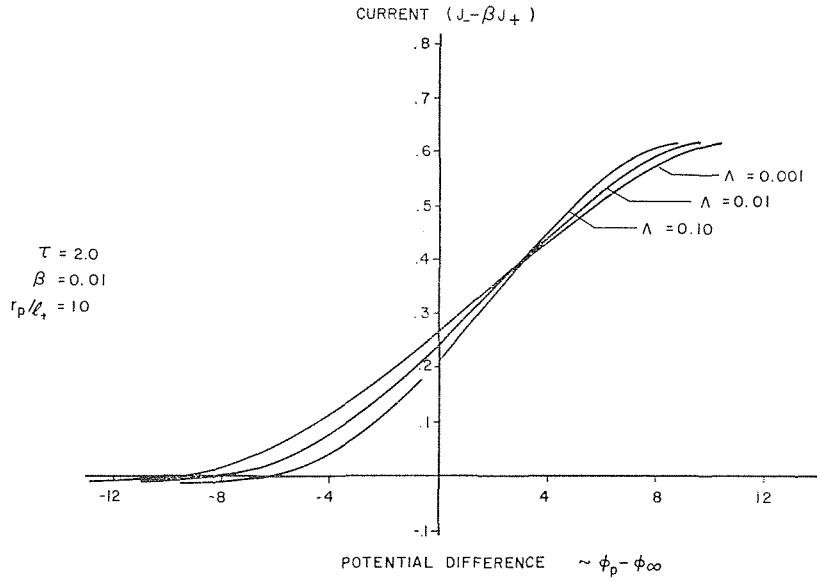

Fig. 5 Current versus potential difference for $\tau = 2.0$

net current are approximately equal above a potential difference of -4. For $\beta = 10^{-4}$, the zero net current condition occurs beyond the range of available sheath data. In comparing the results for different values of τ, it must be remembered that the nondimensional potential ϕ contains $T_{-\infty}$ so that the abscissa is a function of τ. This distortion is eliminated by defining a normalized potential in terms of $T_{+\infty}$. This approach is considered in the following paragraph when comparing the electron heat transfer.

Experimental Application. The electrical characteristics for the case where the body is a probe can be used in conjunction with heat transfer data for diagnostic purposes.

The procedure is as follows:

$$\frac{\text{Total heat transfer}}{\text{Total current}} = \frac{c_1 T_{+\infty}\tau J_- + \beta J_+ H}{e(J_- - \beta J_+)} + \frac{q_g}{\dfrac{D_{-\infty}N_{-\infty}}{l_+}\, e(J_- - \beta J_+)}$$

at ion saturation $J_- - 0$ this ratio, $-H/e + q_g/(\text{measured current})$, gives q_g. At electron saturation $J_+ = 0$ this ratio, $C_1 T_{+\infty}\tau/e + q_g/(\text{measured current})$, determines τ or $T_{-\infty}$. Knowing τ and the voltage at zero current, $(\phi_p - \phi_\infty)_{\text{floating}}$ can be established. This data and the Figs. 4, 5, and 6 determine Λ. Next the current $(J_- - \beta J_+)$ at the plasma potential can be determined. These results and the equation for current

$$I = -\frac{D_{-\infty}N_{-\infty}}{l_+}\, e(J_- - \beta J_+)$$

will establish $N_{-\infty}$. Thus the inclusion of heat transfer measurements offers an additional tool in plasma diagnostics.

To examine the variation of electron heat transfer, equation (42) for the normalized heat transfer Q_e must be considered. Fig. 7 shows the variation of heating due to thermal energy (i.e., τJ_-) as a function of potential difference and τ. To facilitate a comparison of the effect of τ, the normalized potential difference definition is modified to the following form:

$$\frac{e(V_p - V_\infty)}{kT_{+\infty}} = (\phi_p - \phi_\infty)\tau$$

The normalized heat transfer due to recombination at the surface is directly proportional, βJ_+, the ion flux to the surface. For positive probe potentials, this quantity is quite small. However, any comparisons of thermal heating and recombination heating will depend upon the ionization potential for a particular gas.

Conclusion

The problem of determining the electron heat transfer to a spherical body immersed in a weakly ionized quiescent plasma has been solved. The region of charge separation is of the order of $\Lambda^{2/3}$. The study has also shown that within the sheath the effects of ionization and recombination are of the order of $\Lambda^{4/3}$. An error of this order can be neglected; however, this assumption limits the allowable range of Λ. The heating due to electron thermal energy increases with electron temperature. This increase is due to the additional energy per electron which more than compensates the decrease in electron flux.

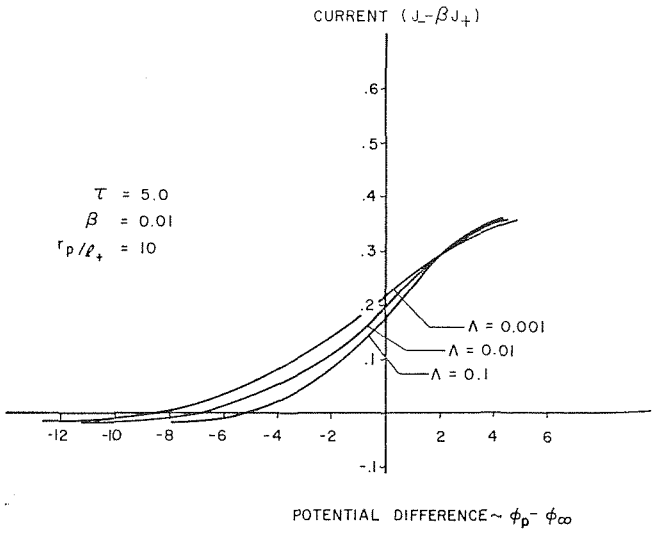

Fig. 6 Current versus potential difference for $\tau = 5.0$

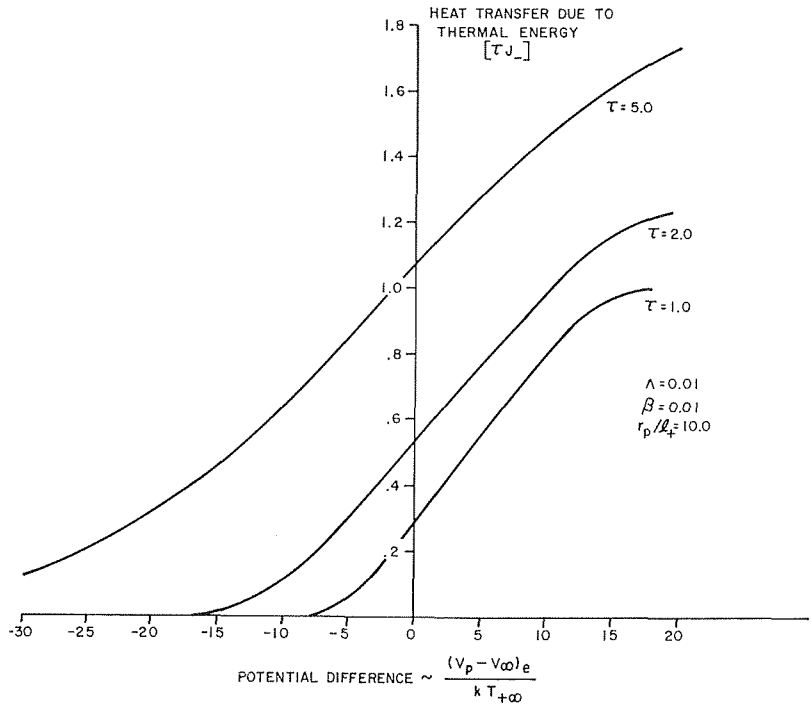

Fig. 7 Heat transfer due to thermal energy versus potential difference

References

1 Su, C. J., and Lam, S. H., "Continuum Theory of Spherical Electrostatic Probes," *The Physics of Fluids*, Vol. 6, 1969, p. 1479.

2 Cohen, I. M., "Asymptotic Theory of Spherical Electrostatic Probes in a Slightly Ionized, Collision-Dominated Gas," *The Physics of Fluids*, Vol. 6, 1963, p. 1492.

3 Cohen, I. M., "Asymptotic Theory of a Photo-Ionization Chamber," *The Physics of Fluids*, Vol. 8, 1965, p. 2097.

4 Whitman, A. M. and Yeh, H., "Characteristics of Plasma Probes in a MHD Working Fluid," *Electricity from MHD, I*, International Atomic Energy Agency, Vienna, 1966.

5 McKee, H. B., and Mitchner, M., "Electrostatic Probes for Diagnostics in a Collision-Dominated Weakly Ionized Plasma," Institute for Plasma Research Report SUIPR No. 77, Stanford University, Stanford, Calif., 1966.

6 Whitman, A. M., "Theory of the Electrostatic Probe in Magnetohydrodynamic Fluids," Doctoral Dissertation, University of Pennsylvania, Philadelphia, Pa., 1966.

7 McAssey, Jr., E. V., "Electron Heat Transfer in a Weakly Ionized Plasma," Doctoral Dissertation, University of Pennsylvania, Philadelphia, Pa., 1968.

8 McAssey, Jr., E. V., and Yeh, H., "Electron Heat Transfer and Probe Characteristics in a Moving Non-Equilibrium Plasma," AIAA Paper No. 69-699, 1969.

Acknowledgment

The authors wish to acknowledge the support of the National Science Foundation under Grant GK-2281.

N. R. DesRUISSEAUX
Assistant Professor.
R. D. ZERKLE
Associate Professor.
Department of Mechanical Engineering, University of Cincinnati, Cincinnati, Ohio

Temperature in Semi-Infinite and Cylindrical Bodies Subjected to Moving Heat Sources and Surface Cooling

The theory of moving heat sources is applied to two models to determine the effect of convective surface cooling on temperature distributions. The models chosen consist of a translating semi-infinite body and a rotating cylindrical body, each having a band heat source acting on a portion of the surface and convective cooling acting over the entire surface. The analytical results can be utilized to predict temperature distributions occurring in certain machining processes or other processes involving heat sources.

Introduction

THE classical work of Jaeger [1][1] has provided an analysis which has been used by numerous investigators to predict temperatures in machining processes [e.g. 2,3,4]. His analysis considers an adiabatic semi-infinite body with a band heat source moving on the surface. Jaeger [5] also investigated an adiabatic cylindrical body with a heat source rotating relative to the surface.

Because convective cooling is widely used in many processes to control dimensional accuracy and to reduce thermal damage, it is necessary that Jaeger's work be extended to include the effect of surface cooling.

The purpose of this paper is to present the results of theoretical analyses which consider the effect of surface cooling on temperature. Thermal models are chosen which approximate conditions which may occur in certain machining processes, such as grinding. The application of moving heat source theory to two models, the semi-infinite body and the cylindrical body, results in the derivation of temperature distributions and provides an indication of the effects of surface cooling on temperature. This paper is a partial summary of the work presented in reference [6].

[1] Numbers in brackets designate References at end of paper.

Contributed by the Heat Transfer Division for publication (without presentation) in the JOURNAL OF HEAT TRANSFER. Manuscript received by the Heat Transfer Division November 15, 1969; revised manuscript received February, 1970. Paper No. 70-HT-J.

Semi-Infinite Body

The model which is analyzed in this section is shown in Fig. 1. It consists of a stationary band heat source of width $2l$ on the sur-

Nomenclature

a = radius of cylinder, ft
bei_n = imaginary part of Bessel Function of order n with imaginary argument
ber_n = real part of Bessel Function of order n with imaginary argument
h = convective heat transfer coefficient, B/ft^2 hr deg F
H = dimensionless heat transfer coefficient, $2\alpha h/kV$
J_n = Bessel function of order n
K_0 = modified Bessel function of second kind, order zero
k = thermal conductivity, B/ft hr deg F
l = heat source half-width, ft
L = dimensionless heat source half-width, $Vl/2\alpha$
N_B = Biot number, ha/k, dimensionless
p = Laplace transform parameter, 1/hr
q_B = band heat source strength, B/ft^2 hr
q_c = convective heat flux, B/ft^2 hr
q_L = instantaneous line source strength, B/ft
$\dot{q}_L$ = line source strength, B/ft hr
q_p = instantaneous point source strength, B
r = radial coordinate, ft
r^* = dimensionless radial coordinate, r/a
t = time, hr
t^* = dimensionless time, $\alpha t/a^2$.
u, v = temperature rise above ambient temperature, deg F
u^* = dimensionless temperature, $\pi kVu/2\alpha\, q_B$
v^* = dimensionless temperature, $\pi kv/aq_B$
V = speed, ft/hr
x, y, z = Cartesian coordinates, ft
X, Z = dimensionless position variables, $Vx/2\alpha$, $Vz/2\alpha$
α = thermal diffusivity, ft^2/hr
θ = angular position variable, radians
ξ = Angular half-width of heat source, radians
ω = angular speed, rad/sec
ω_n = dimensionless angular speed, $a\sqrt{n\omega/\alpha}$

face of a moving semi-infinite body. The strength of the heat source is assumed constant in time and uniform over its width. The band heat source is infinite in length parallel to the y coordinate axis. It is further assumed that convective cooling occures over the entire surface with a constant and uniform heat transfer coefficient, h.

The desired steady-state temperature distribution is obtained by superimposing the solution due to an instantaneous point source which acts in a moving semi-infinite body. The point source solution satisfies the following set of equations

$$\nabla^2 u = \frac{1}{\alpha}\left[\frac{\partial u}{\partial t} - V\frac{\partial u}{\partial x}\right] \tag{1}$$

$$u(x, y, z, 0) = 0 \tag{2}$$

$$hu(x, y, 0, t) = k\frac{\partial u}{\partial z}(x, y, 0, t) \tag{3}$$

and is given by

$$u = \frac{\alpha q_P}{k}\exp\left\{-\frac{[(x - x') + V(t - t')]^2 + (y - y')^2}{4\alpha(t - t')}\right\} \times \left\{8[\pi\alpha(t - t')]^{-3/2}[e^{-(z-z')^2/4\alpha(t-t')} + e^{-(z+z')^2/4\alpha(t-t')}] - \frac{h/k}{4\pi\alpha(t - t')}\operatorname{erfc}\left[\frac{z + z'}{2\sqrt{\alpha(t - t')}} + \frac{h}{k}\sqrt{\alpha(t - t')}\right]\exp[(z + z')h/k + \alpha(t - t')(h/k)^2]\right\} \tag{4}$$

Equation (4) follows immediately from equation 14.9 (4) of reference [7], where x', y', z', t' specify the place and time at which the instantaneous point source acts.

Superposition of the point source solution (equation (4)) is carried out through the following steps:

1 Superposition in space to give temperature due to instantaneous line source

2 Superposition in time to give temperature due to continuously-acting line source, which acts on the surface, $z' = 0$

3 Superposition of line sources to give a continuously acting band source on the surface.

After these steps are carried out mathematically, the resulting two-dimensional, steady-state temperature distribution can be expressed in the following dimensionless form:

$$\frac{\pi k V}{2\alpha q_B}u(X, Z) = \int_{X-L}^{X+L} e^{-m}K_0([Z^2 + m^2]^{1/2})dm - \pi\mathrm{He}^{HZ}\int_0^\infty \tau e^{H^2\tau^2}\operatorname{erfc}\left(\frac{Z}{2\tau} + H\tau\right) \times \left[\operatorname{erf}\left(\frac{X + L}{2\tau} + \tau\right) - \operatorname{erf}\left(\frac{X - L}{2\tau} + \tau\right)\right]d\tau \tag{5}$$

The dimensionless quantity X respresents horizontal distance from the center of the heat source, Z the depth from the surface, L the half-width of the heat source, and H the dimensionless heat transfer coefficient.

The first term of equation (5) is identical to the result obtained by Jaeger [1] for the case of a semi-infinite body with no cooling ($h = 0$). A closed form expression for the integral is available for $Z = 0$ (see equation 10.7(11) in reference [7]), and the integral has been evaluated numerically for other values of Z. Tabulations are presented in reference [1].

An attempt by the authors to determine a closed form expression for the integral appearing in the second term of equation (5) was unsuccessful. Therefore this integral must also be evaluated numerically.

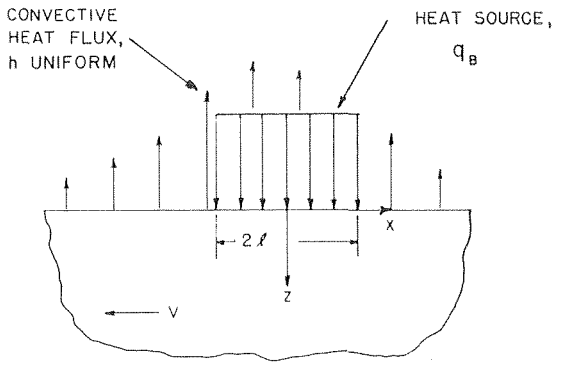

Fig. 1 Thermal model for semi-infinite body with convective cooling

Results for Semi-Infinite Body

Temperature distributions corresponding to specific values of the parameters L and H were determined from equation (5). The dimensionless temperature distribution on the surface is shown in Fig. 2 for values of $H = 0$, 0.1, and 1.0 for dimensionless half-width $L = 1.0$. It is seen that, if the heat transfer coefficient is sufficiently large, the temperature under the heat source can be greatly reduced.

The two-dimensional temperature distribution for $H = 1.0$ is shown in Fig. 3. It is seen that, under the heat source, the maximum temperature occurs at the surface. However, to the left of the heat source; that is, in the direction of motion of the body, the maximum temperature is seen to occur beneath the surface. This is more clearly illustrated in Fig. 4, which shows temperature versus depth for different values of x to the left of the center of the heat source.

Temperature distributions of the type discussed in this section are in steady-state with respect to a coordinate axis fixed at the center of the heat source. The thermal history of any particular element of material at a depth Z as it passes under the heat source (from $X > L$ to $X < -L$) is easily visualized. For example, the temperature distributions of Fig. 4 correspond to those in a very thin slab of material as it passes from $X = -0.5$ to $X = -1.0$, etc.

The effect of surface cooling over a range of dimensionless heat source width L is now examined. From the work of Jaeger [1] and from Fig. 2, it is known that the maximum temperature occurs on the surface and hear the trailing edge of the heat source Therefore, the dimensionless temperature at $Z = 0$ and $X = -L$ was determined as a function of L. This is shown in Fig. 5. With an increasing value of heat source half-width L, the temperature increases less when cooling is present than when the surface is adiabatic.

The results presented above correspond to convective cooling at all locations on the surface of the body. An expression relating the magnitude of the resultant convective heat flux to the strength of the band source and the dimensionless temperature distribution is

$$\frac{|q_c|}{q_B} = \frac{hu(x, 0)}{q_B} = \frac{Hu^*(X, 0)}{\pi} \tag{6}$$

The distribution of this ratio at the location of the band source is shown in Fig. 6 for $L = 1$, 5 and $H = 0.1$, 1.0. It is seen that for large values of L and H, convective cooling from the band source region removes a significant portion of the band source energy.

Therefore, it is concluded that for large values of L and H, convective cooling at the location of the band source has an extremely important effect on temperature reduction. But convective cooling at the location of the band heat source cannot be obtained in some physical situations. In that case the predicted surface temperatures, assuming $h = 0$ and h equal to a finite value over the entire surface, become bounding solutions.

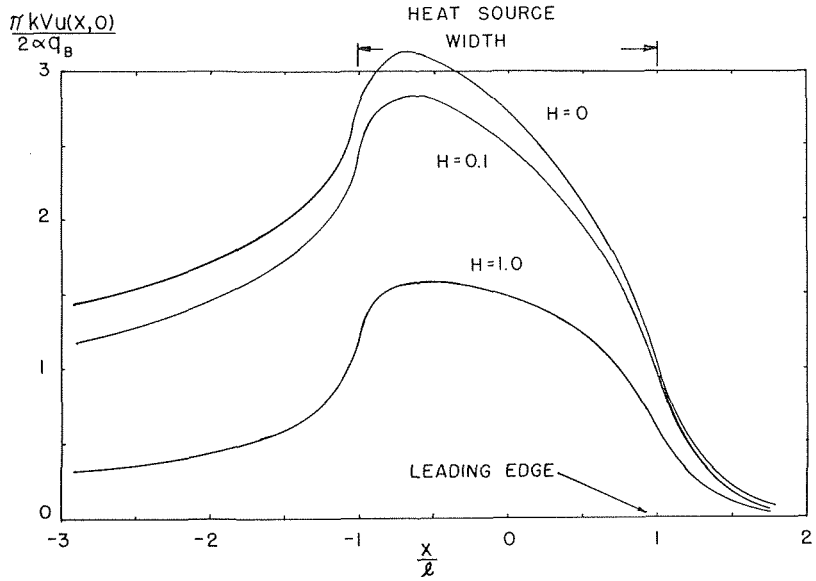

Fig. 2 Dimensionless surface temperature distribution for $L = 1$

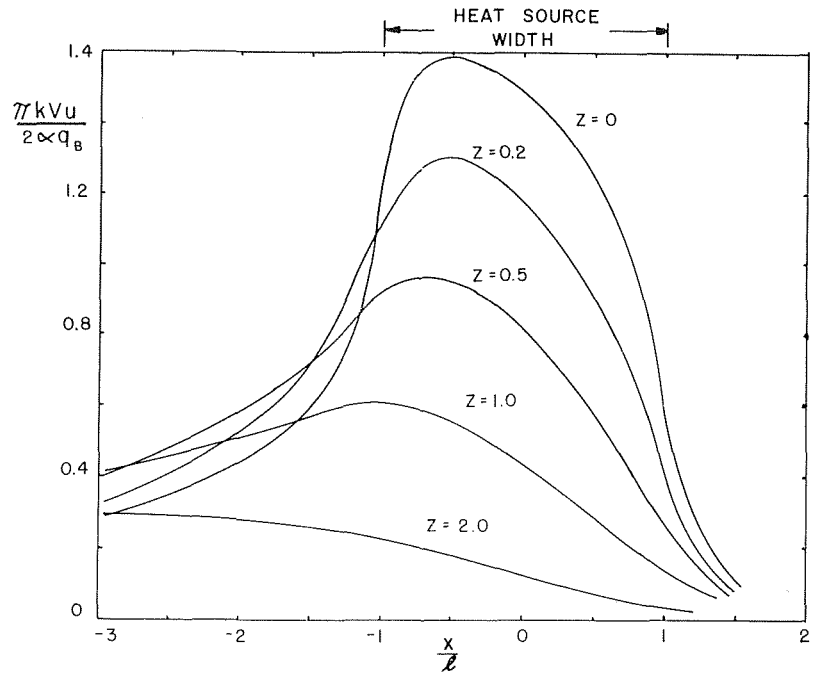

Fig. 3 Dimensionless temperature distribution for $H = 1$, $L = 1$

An *approximate* temperature distribution, corresponding to convective cooling outside of the band source region only, can be obtained from equation (5) by increasing the band source strength by an amount equal to the average convective flux which would have occurred in the band source region. An exact expression can be derived by superimposing line source solutions with the strength increased to compensate for local convective cooling in the band source region.

Cylindrical Body

The model which is analyzed in this section is shown in Fig. 7. It consists of a stationary band heat source of angular width 2ξ on the surface of a rotating cylindrical body of radius a. The strength of the heat source is assumed constant in time and uniform over its width. The heat source is infinite in a direction parallel to the cylinder axis. It is assumed that convective cooling occurs over the entire surface with a constant and uniform heat transfer coefficient, h.

The desired temperature distribution is obtained by superimposing the solution due to an instantaneous line source acting at an arbitrary location (r', θ') in the cylindrical body. Details are available in reference [6]. The instantaneous line source solution satisfies the following set of equations

$$\frac{\partial^2 v}{\partial r^2} + \frac{1}{r}\frac{\partial v}{\partial r} + \frac{1}{r^2}\frac{\partial^2 v}{\partial \theta^2} = \frac{1}{\alpha}\frac{\partial v}{\partial t} \tag{7}$$

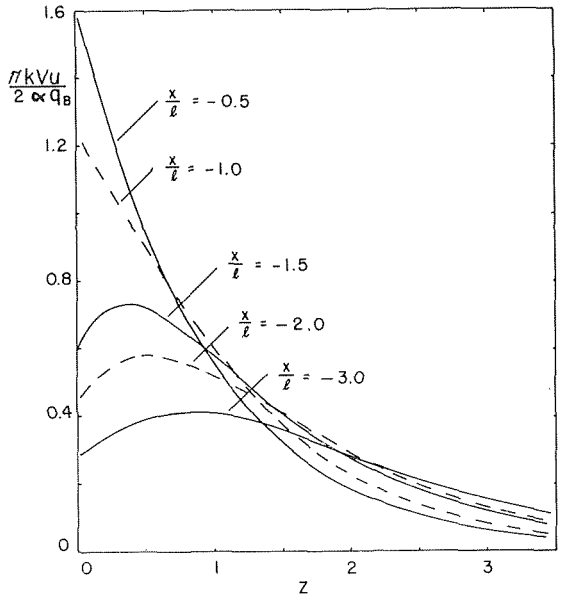

Fig. 4 Dimensionless temperature versus depth for $H = 1$, $L = 1$

$$-k\frac{\partial v}{\partial r}(a, \theta, t) = hv(a, \theta, t) \tag{8}$$

$$v(0, \theta, t) \text{ is finite} \tag{9}$$

$$v(r, \theta, t) = v(r, \theta + 2\pi, t) \text{ (Periodicity)} \tag{10}$$

$$\frac{\partial v}{\partial \theta}(r, \theta', t) = 0 \quad \text{(Symmetry)} \tag{11}$$

$$v(r, \theta, 0) = 0 \tag{12}$$

If an instantaneous line source of strength $q_L(B/\text{ft})$ acts on the surface; that is, $r' = a$, then the Laplace transform of the solution is

$$\bar{v}(r, \theta, p) = \frac{q_L}{2\pi k}\sum_{n=-\infty}^{\infty}\frac{\cos n(\theta - \theta')I_n(sr)}{a\left[sI_n'(sa) + \frac{h}{k}I_n(sa)\right]} \tag{13}$$

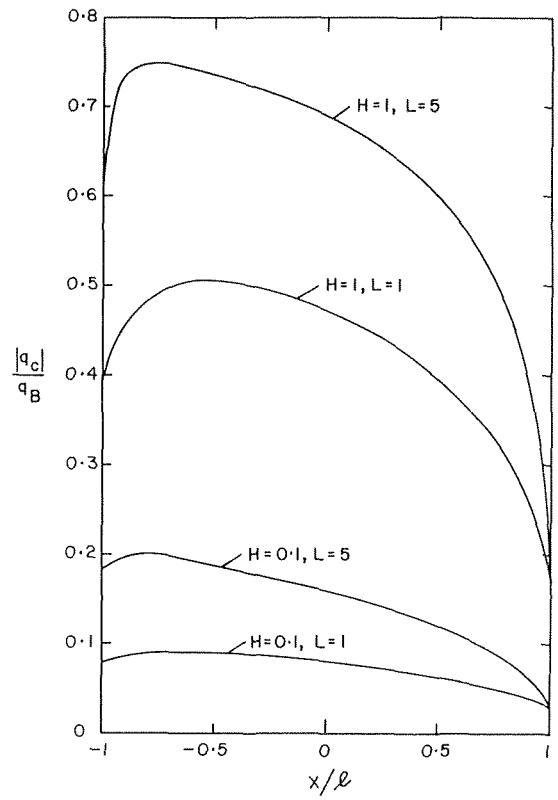

Fig. 6 Convective flux distribution in band source region

where

$$s = \sqrt{p/\alpha} \tag{14}$$

The solution for a continuously acting line source of strength $q_L(B/\text{ft hr})$, which rotates at an angular speed ω relative to the cylinder, can be determined in the manner of Jaeger [5]. The effect of rotation is introduced by defining

$$\theta' = \omega t' + \beta \tag{15}$$

where β is an arbitrary angular location. The resulting expression, which must be inverted to obtain the temperature distribu-

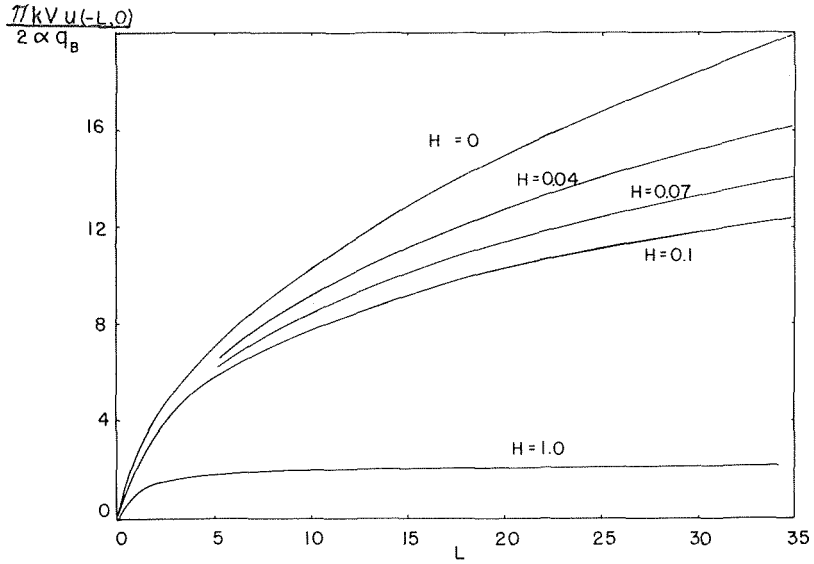

Fig. 5 Dimensionless surface temperature at trailedge of heat source versus dimensionless heat source half-width

tion due to a continuously acting line source on the surface of a rotating cylinder, is

$$\bar{v}(r, \theta, p) = \frac{\dot{q}_L}{\pi ak}\left\{\frac{I_0(sr)}{2p[sI_0'(sa) + (h/k)I_0(sa)]} + \sum_{n=1}^{\infty}\frac{I_n(sr)[p\cos n(\theta-\beta) + n\omega\sin n(\theta-\beta)]}{(p^2+n^2\omega^2)[sI_n'(sa)+(h/k)I_n(sa)]}\right\} \quad (16)$$

Equation (16) has been inverted and details are given in reference [6]. The resulting line source solution can then be superimposed to obtain the solution corresponding to a band source on the surface of a rotating cylinder. This is accomplished by expressing the strength of the line source in terms of an increment of the band source; that is,

$$\dot{q}_L = aq_B d\beta \quad (17)$$

and the line source solution is then integrated from $\beta = -\xi$ to $+\xi$.

After the previous steps are carried out, the transient two-dimensional temperature distribution for the model of Fig. 7 is obtained, and is given by the following dimensionless expressions:

$$v^* = v^*_{\text{periodic}} - 2\xi\sum_{j=1}^{\infty}\frac{J_0(\mu_{0,j}r^*)e^{-\mu_{0,j}^2 t^*}}{J_0(\mu_{0,j})[N_B^2+\mu_{0,j}^2]} + 4\sum_{n=1}^{\infty}\sum_{j=1}^{\infty}\times\left\{\frac{\mu_{n,j}^2[\mu_{n,j}^2\cos(n\theta)-\omega_n^2\sin(n\theta)]\sin(n\xi)J_n(\mu_{n,j}r^*)e^{-\mu_{n,j}^2 t^*}}{n[\mu_{n,j}^4+\omega_n^4][n^2-\mu_{n,j}^2-N_B^2]J_n(\mu_{n,j})}\right\} \quad (18)$$

where

$$v^*_{\text{periodic}} = \xi/N_B + 2\sum_{n=1}^{\infty}M_1\sin(n\xi) \times\left\{\frac{\omega_n M_2\cos[\omega_n^2 t^* - n\theta + \phi_1 - \phi_2] + N_B M_3\cos[\omega_n^2 t^* - n\theta + \phi_1 - \phi_3]}{n[(\omega_n M_2)^2 + (N_B M_3)^2 + 2N_B\omega_n M_2 M_3\cos(\phi_3-\phi_2)]}\right\} \quad (19)$$

where

$$M_1 = \sqrt{ber_n^2(\omega_n r^*) + bei_n^2(\omega_n r^*)}$$

$$M_2 = \sqrt{ber_n'^2(\omega_n) + bei_n'^2(\omega_n)}$$

$$M_3 = \sqrt{ber_n^2(\omega_n) + bei_n^2(\omega_n)}$$

$$\phi_1 = \tan^{-1}\left[\frac{bei_n(\omega_n r^*)}{ber_n(\omega_n r^*)}\right]$$

$$\phi_2 = \tan^{-1}\left[\frac{bei_n'(\omega_n)}{ber_n'(\omega_n)}\right]$$

$$\phi_3 = \tan^{-1}\left[\frac{bei_n(\omega_n)}{ber_n(\omega_n)}\right] \quad (20)$$

and $\mu_{n,j}$ are the roots of

$$\mu_{n,j}J_n'(\mu_{n,j}) + N_B J_n(\mu_{n,j}) = 0 \quad (21)$$

The first term of equation (18); that is, equation (19), can be evaluated with the following approximate expression (see reference [8]):

$$v^*_{\substack{\text{periodic}\\ \text{approx.}}} = \frac{\xi}{N_B} + \frac{2}{\sqrt{r^*}}\sum_{n=1}^{\infty}\sin(n\xi)\,e^{-\omega_n(1-r^*)/\sqrt{2}} \times\left\{\frac{\omega_n\cos\left[\omega_n^2 t^* - n\theta - \frac{\omega_n}{\sqrt{2}}(1-r^*) - \frac{\pi}{4}\right] + N_B\cos\left[\omega_n^2 t^* - n\theta - \frac{\omega_n}{\sqrt{2}}(1-r^*)\right]}{n[\omega_n^2 + N_B^2 + \sqrt{2}\,\omega_n N_B]}\right\} \quad (22)$$

Equation (19) approaches equation (22) as $r\sqrt{\omega/\alpha}$ and $a\sqrt{\omega/\alpha}$ approach infinity.

It should be noted that equation (18) does not reduce to the case of an adiabatic cylinder ($h = 0$). That solution is given in reference [6].

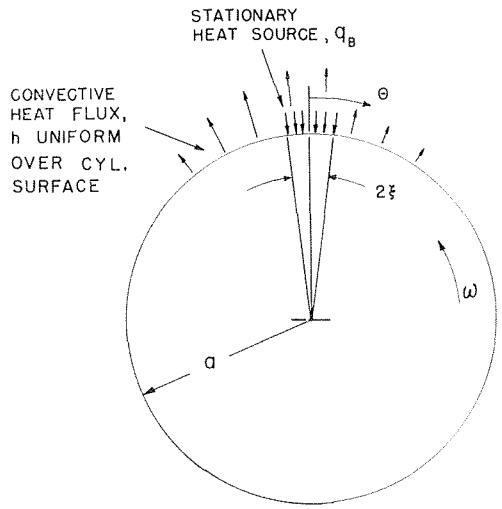

Fig. 7 Rotating cylindrical body with surface heat source and convective cooling

Results for the Cylindrical Body

Equations (18) and (22) were evaluated to give dimensionless temperatures as a function of $(a - r)$ and θ for different values of the heat transfer coefficient h. For computational purposes the following values were assumed:

$$k = 10\ \frac{B}{\text{ft hr deg F}},\ a = 0.5\text{ ft},\ \alpha = 0.172\ \frac{\text{ft}^2}{\text{hr}},\ \omega = 10\pi\ \frac{\text{radians}}{\text{sec}}$$

$$h = 20, 200, 1000, 2000, 10000, 20000\ \frac{B}{\text{ft}^2\text{ hr deg F}}$$

$$\xi = 0.001, 0.01 \text{ radians}$$

$$(a - r) = 0, 0.0001, 0.0002 \text{ ft}$$

Small values of ξ could correspond to heat source widths in machining processes.

Periodic Case. The transient terms (second and third terms) of equation (18) become insignificant after some interval of time. When this occurs the temperature distribution, referred to a nonrotating coordinate system, does not vary with time. With

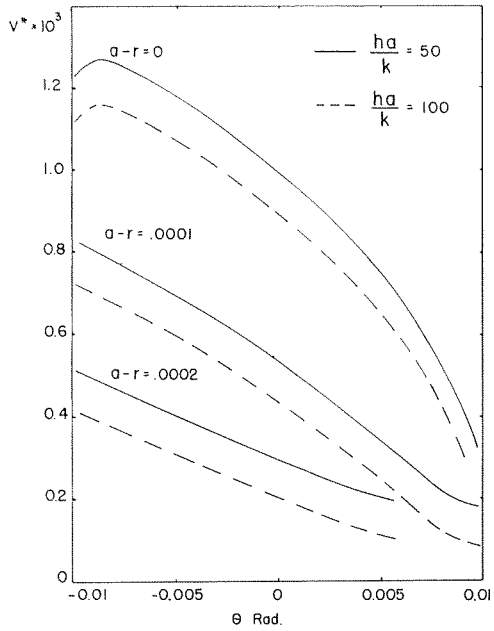

Fig. 8 Dimensionless temperature versus angular position for $\xi = 0.01$

respect to a point in the cylinder, the temperature is periodic with each revolution of the cylinder. This periodic condition is achieved when the rate of heat entering the cylinder equals the rate of heat convected away. The periodic condition is considered first with the evaluation of equation (22).

Fig. 8 shows typical dimensionless temperature distributions under the heat source for two different heat transfer coefficients. It is similar in form to those obtained in the first part of this paper for the semi-infinite body. It is seen that the maximum temperature occurs on the surface and near the trailing edge of the heat source (i.e., at $\theta = -0.01$ radians). The maximum temperature at some particular depth below the surface occurs in the direction of motion of the cylinder (right to left) away from the heat source.

It is seen that an increase in heat transfer coefficient results in a lower temperature at each depth. However, the reason for this is not because of significantly greater heat removal over the heat source, but rather because a point in the cylinder which approaches the heat source from the right is at a lower temperature. This result is apparent in Fig. 9. In this figure the dimensionless temperature of the surface is shown for the periodic condition for two different heat transfer coefficients. The temperature history of a point on the surface is determined by following the curve from the right, as the cylinder rotates toward the heat source. As the point passes under the heat source it goes through a peak temperature or "spike." Sometime after the point passes the heat source it has been cooled to a temperature which remains nearly constant for the rest of that revolution, for the case of small heat source width. Note that the magnitudes of the peaks above the temperature of an approaching point are the same in each case. Thus, if periodic conditions are established, the effect of improved cooling is to keep the bulk temperature at lower levels so that the peak or "spike" is superimposed on a lower bulk temperature of the cylinder. A similar effect is shown in Fig. 10, where very effective surface cooling results in lower surface temperatures. Again, the magnitudes of the spikes are approximately the same as those for the lower heat transfer coefficients shown in Fig. 9.

Fig. 11 shows the dimensionless temperature at the trailing edge of the heat source versus dimensionless heat transfer coefficient for the periodic condition. It is seen that, for the case investigated, the greatest reduction in temperature is obtained by raising h from 20 to 200 B/ft² hr deg F (ha/k from 1 to 10), which corresponds to a change from convective cooling by ambient air to effective liquid application.

Transient Center Temperature. By setting $r = 0$ in equation (18) the transient center temperature of the cylinder is determined as

$$v^*(r = 0, t) = \xi \left\{ \frac{k}{ah} - 2 \sum_{j=1}^{\infty} \frac{e^{-\mu_{0,j}^2 \alpha t/a^2}}{J_0(\mu_{0,j}) \left[\left(\frac{ha}{k} \right)^2 + \mu_{0,j}^2 \right]} \right\} \quad (23)$$

where $\mu_{0,j}$ are the roots of

$$\mu_{0,j} J_1(\mu_{0,j}) - \frac{ah}{k} J_0(\mu_{0,j}) = 0 \quad (24)$$

The dimensionless quantity $v^*(r = 0, t) \cdot (ha/k) \cdot 1/\xi$ is shown as a function of dimensionless time $\alpha t/a^2$ for different values of ha/k in Fig. 12. From this figure it is determined that transients die out faster with better cooling. Furthermore, it can be deter-

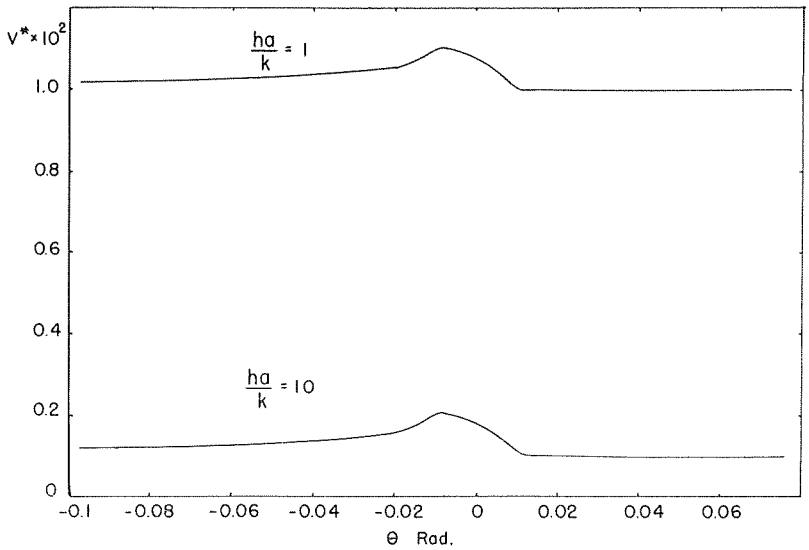

Fig. 9 Dimensionless surface temperature versus angular position for $\xi = 0.01$

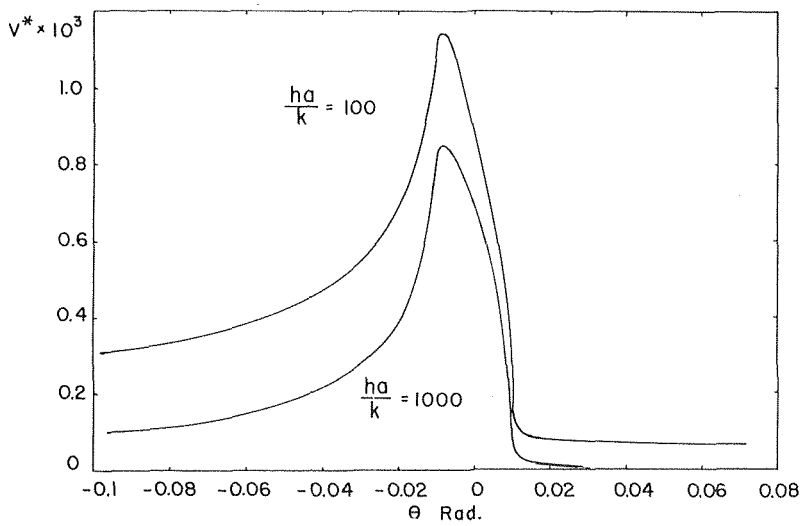

Fig. 10 Dimensionless surface temperature versus angular position for $\xi = 0.01$

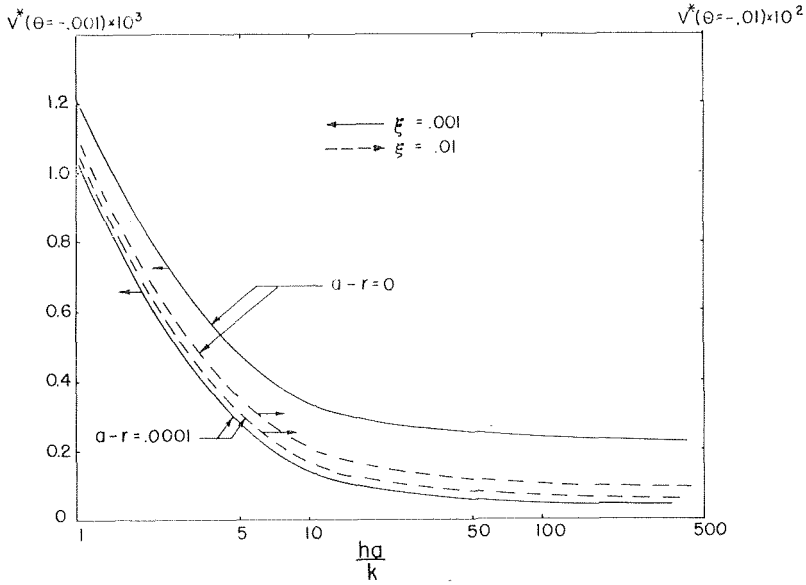

Fig. 11 Dimensionless surface temperature at rear edge of heat source versus Biot number

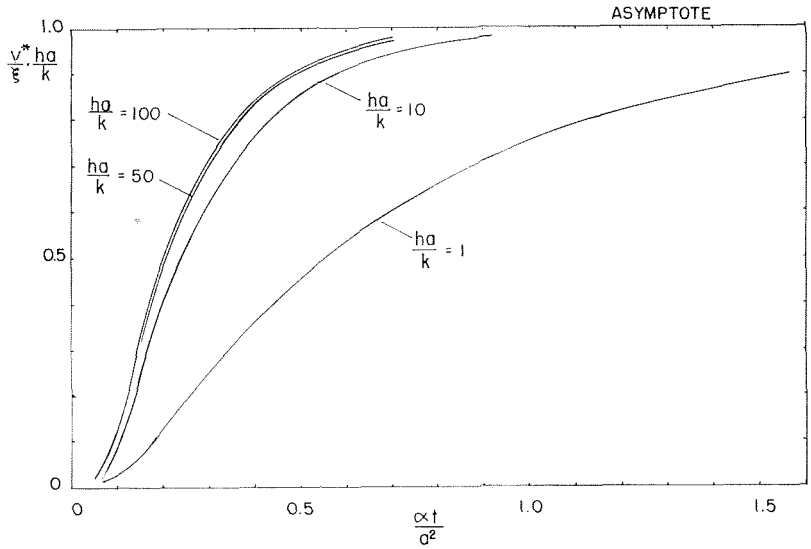

Fig. 12 Dimensionless center temperature versus dimensionless time

mined from Figs. 9, 10, and 12 that when periodic conditions are reached, the asymptotic center temperature is nearly the same as the surface temperature at locations away from the heat source; that is, the temperature throughout the cylinder is expected to be nearly uniform, except near the heat source.

Transient Surface Temperature. Equations (18) and (22) were evaluated for the case of $r = a$. Values of the dimensionless time, $\alpha t/a^2$, are chosen which correspond to many revolutions of the cylinder, such that the temperature is approaching that of the periodic case. The values of the third term of equation (18) are insignificant in this case. Thus, for a specific value of $\alpha t/a^2$, the temperature distribution is equal to the periodic temperature minus a constant given by the second term of equation (18) and the only dependence on θ is that which arises from the periodic temperature distribution.

The results are shown in Figs. 13, 14, and 15. Dimensionless surface temperature versus angular position is shown at different values of $\alpha t/a^2$. It is seen that the surface temperature, at values of θ greater than 0.04 radians to the right of the center of the heat source, reaches 90 percent of the periodic value at $\alpha t/a^2 =$ 1.3, 0.155, and 0.007 for $ha/k = 1$, 10, and 100, respectively. From Fig. 12 the corresponding times for the center temperature to reach 90 percent of the asymptotic value are $\alpha t/a^2 = 1.6$, 0.6, and 0.5. Therefore it is clear that periodic surface temperature distributions become established much more rapidly for large values of ha/k than for small values.

For the case of $a = 0.5$ ft and $\alpha = 0.172$ ft²/hr, the actual time for 90 percent of the asymptotic center temperature to be reached is 2.3, 0.87, and 0.73 hr for $ha/k = 1$, 10, and 100, respectively. For the case of $a = 0.1$ ft, these times are 0.093, 0.035, and 0.029 hrs.

Conclusion

Analytical solutions to two thermal problems involving heat sources have been obtained. The models consist of a moving semi-infinite body and a rotating cylinderical body, each with a band heat source assumed to act on a portion of the surface and convective cooling over the entire surface.

The steady-state two-dimensional temperature distribution is presented for the semi-infinite body, and the two-dimensional transient temperature distribution is obtained for the cylindrical body.

The results could be applied to determine temperatures which occur in such processes as grinding, turning, welding, or mechanical braking. The effect of surface cooling on temperatures occurring in such processes can be inferred from the results. In this regard it should be noted that the models considered in this in

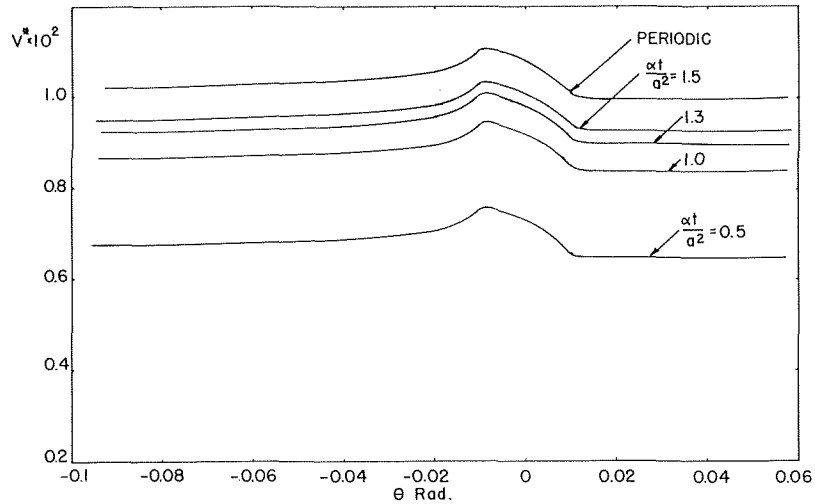

Fig. 13 Transient surface temperature for $\xi = 0.01$, $ha/k = 1$

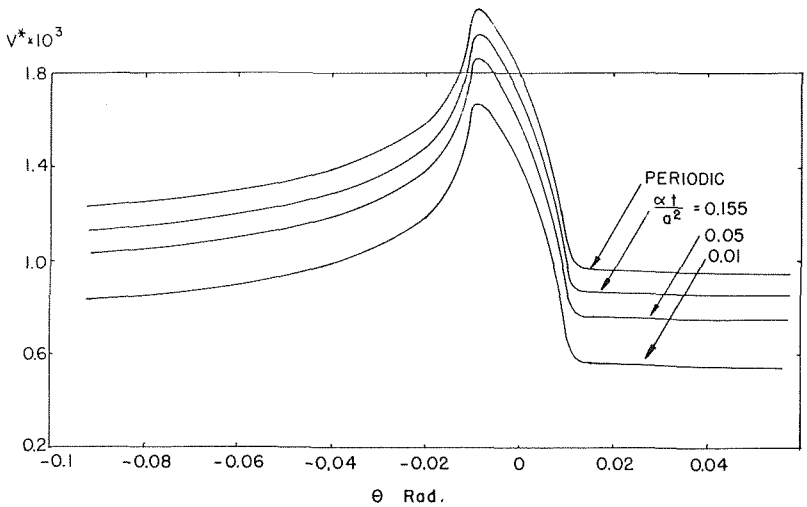

Fig. 14 Transient surface temperature for $\xi = 0.01$, $ha/k = 10$

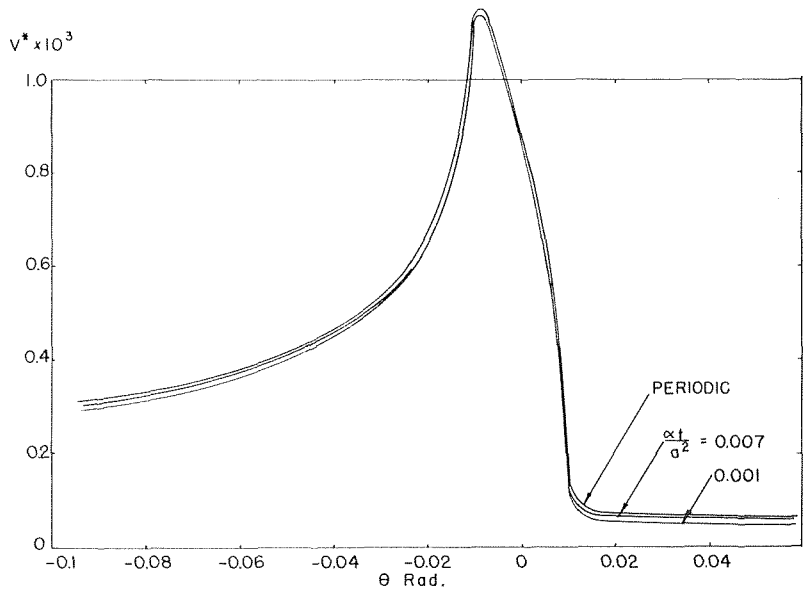

Fig. 15 Transient surface temperature for $\xi = 0.01$, $ha/k = 100$

vestigation do not include a receding boundary. This effect would, of course, become important for high speed machining processes utilizing large depths of cut. A discussion of geometrical effects associated with the grinding process, for example, is presented in reference [9].

Acknowledgment

This investigation was performed as part of Contract AF33-(615)-5412 for the Manufacturing Technology Division of the Air Force Materials Laboratory, WPAFB, Ohio.

References

1 Jaeger, J. C., "Moving Sources of Heat and the Temperature at Sliding Contacts," *Proceedings of the Royal Society of New South Wales*, Vol. 76, 1942, p. 203.

2 Outwater, J. O., and Shaw, M. C., "Surface Temperatures in Grinding," TRANS. ASME, Vol. 74, Jan. 1952, p. 73.

3 Chao, B. T., and Trigger, K. J., "Temperature Distribution at Tool-Chip and Tool-Work Interface in Metal Cutting," TRANS. ASME, Vol. 80, Feb. 1958, p. 311.

4 Loewen, E. G., and Shaw, M. C., "On the Analysis of Cutting-Tool Temperatures," TRANS. ASME, Vol. 76, Feb. 1954, p. 217.

5 Jaeger, J. C., "Some Problems Involving Line Sources in Conduction of Heat," *Philosophical Magazine*, Series 7, Vol. 35, 1944, p. 169.

6 DesRuisseaux, N. R., "Thermal Aspects of Grinding Processes," PhD thesis, University of Cincinnati, 1968.

7 Carslaw, H. S., and Jaeger, J. C., *Conduction of Heat in Solids*, Oxford University Press, London, 1947.

8 Whitehead, C. S., "On a Generalization of the Functions ber_x, bei_x, ker_x, kei_x," *Quarterly Journal of Mathematics*, Vol. 42, 1911, p. 316.

9 DesRuisseaux, N. R., and Zerkle, R. D., "Thermal Analysis of the Grinding Process," ASME Paper No. 69-WA/Prod-2, to be published in the TRANS. ASME, *Journal of Engineering for Industry*.

B. SHIRALKAR
Engineer, A.P.E.D.,
General Electric Co.,
San Jose, Calif. Assoc. Mem. ASME

P. GRIFFITH
Professor of Mechanical Engineering,
Massachusetts Institute of Technology,
Cambridge, Mass. Assoc. Mem. ASME

The Effect of Swirl, Inlet Conditions, Flow Direction, and Tube Diameter on the Heat Transfer to Fluids at Supercritical Pressure

An investigation has been made of the factors governing the heat transfer coefficient to supercritical pressure fluids, particularly at high heat fluxes. The deterioration in heat transfer to supercritical carbon dioxide has been experimentally studied with reference to the operating conditions of mass velocity and heat flux, tube diameter, orientation, tape induced swirl, inlet temperature, and pressure. A detailed comparison has been made with the apparently contradictory results of other investigators, and operating regions, in which the heat transfer coefficient behaves differently, have been defined. The terms used to describe these regions are the Reynolds number, a heat-flux parameter, and a free-convection parameter.

Introduction

A NUMBER of investigators in the past have observed that the heat transfer coefficient to supercritical fluids can vary greatly depending on the operating conditions; for example, the work of Styrikovich, et al. [1].[1] The heat transfer coefficient has been seen to increase by a large factor in the critical region [2] while under other conditions the heat transfer rate drops sharply [3]. In particular, in the region of high heat fluxes, where a deterioration takes place in the heat transfer coefficient, the amount and nature of the deterioration are greatly influenced by the operating conditions of mass velocity, heat flux, pressure, test section diameter, inlet enthalpy, and upstream flow disturbances. In reference [4], a theory was developed based on the radial integration of the differential equations governing the flow which predicted this deterioration behavior satisfactorily for conditions where the entrance effects and free-convection effects were not important. The basic cause of this de-

[1] Numbers in brackets designate References at end of paper.

Contributed by the Heat Transfer Division and presented at the Winter Annual Meeting, Los Angeles, Calif., November 16–20, 1969, of THE AMERICAN SOCIETY OF MECHANICAL ENGINEERS. Manuscript received at ASME Headquarters, June 6, 1969. Paper 69-WA/HT-1.

Nomenclature

C_p = local specific heat at constant pressure (Btu/lb deg F)
D = diameter of tube (ft)
g = acceleration due to gravity (ft/hr^2)
G = mass flow rate (lb/ft^2 hr)
Gr = Grashof number = $\frac{(\rho_b - \rho_w)}{\rho_b} \times \left(\frac{\rho_b}{\mu_w}\right)^2 gR^3$
h = heat transfer coefficient (Btu/ft^2 deg F hr)
k = local conductivity (Btu/ft hr deg F)
p = half pitch of twisted ribbon
Q_0/A = wall heat flux (Btu/ft^2 hr)
R = radius of tube (ft)
Re = Reynolds number = GD/μ_w
U = axial velocity (ft/hr)
y = distance from wall (ft)
Y = y/R
z = axial coordinate (ft)
μ = viscosity (lb/ft hr)
ρ = density (lb/ft^3)
τ = shear stress (lb/ft hr^2)

Subscripts

w = quantity at wall or wall temperature
b = bulk mean quantity
h = hydraulic (diameter, Re)

terioration is the rapid drop in viscosity and density near the heated wall without a compensating increase in core velocity. This occurs when the heat flux is sufficiently large as to produce a large temperature difference between the wall and the core of the flow in the fluid as it approaches the critical enthalpy region. What one then gets is a velocity level corresponding to core conditions with a density corresponding to wall conditions resulting in poor heat transfer in the buffer layer of the turbulent boundary layer. In this paper, the effects of the various operating conditions are examined.

Experimental Setup

The experiments reported in this paper were conducted with carbon dioxide as the working fluid, because of its convenient critical range (T_c = 88 deg F, P_c = 1071 psi). Carbon dioxide is also known to be stable in the critical region and its physical properties are fairly well known in this range. Several investigators have used carbon dioxide for supercritical pressure studies for the same reasons, e.g., Hall, Jackson, and Khan [5], Sabersky and Hauptmann [6], Koppel and Smith [7], etc. The properties of carbon dioxide used in this paper were obtained from reference [8].

The test loop (shown schematically in Fig. 1) consists of a closed circulation loop in which the system pressure was maintained with a hydraulic accumulator, using high-pressure nitrogen gas. A centrifugal pump was used to circulate the carbon dioxide, thus minimizing the pressure variations and oscillations in the system. Two heat exchangers were provided in the system. One was a once-through heat exchanger which used cold water flow counter current to the carbon dioxide flow. This was located in the main line. At a later stage, liquid nitrogen was blown through this in order to obtain greater inlet subcooling. Another heat exchanger was located in the pump bypass line consisting of a refrigeration loop with Freon 12 as the refrigerant. Three different test sections were employed in the carbon-dioxide tests. All were used in the vertical position. The first two sections were seamless stainless-steel tubes of $^1/_4$ in. ID and $^1/_8$ in. ID, respectively, and with a heated length of 60 in. Unheated lengths of 12 in. (L/D = 50 and 100) were provided at both ends of the heated length. The third section was a $^1/_4$-in-ID stainless-steel tube with the same heated length but with a twisted tape over the complete heated length to generate swirl in the fluid. A sheared strip of inconel 0.0135 in. thick was used to fabricate the twisted tape. Fourteen thermocouples (30 gage Cu-Cn) were located along the length of each test section. The inlet and outlet fluid temperatures were measured by inserting two thermocouples into the fluid at the entrance and exit of the test section. The unheated exit length and large fittings at the exit provide reasonably good mixing. The thermocouple output was recorded on a chart recorder type of potentiometer, which records the output of the 16 thermocouples in succession. The sections were heated electrically with d-c power supply consisting of a motor generator unit capable of about 12 kw. Apart from fiberglass insulation on the outside of the test section, no special precautions were taken to reduce heat loss, which was estimated to be less than 1000 Btu/hr ft². For the test section with the twisted tape it was estimated that less than 5 percent of the power was generated within the tape. The plumbing was arranged so that the flow could be either up or down in the test section.

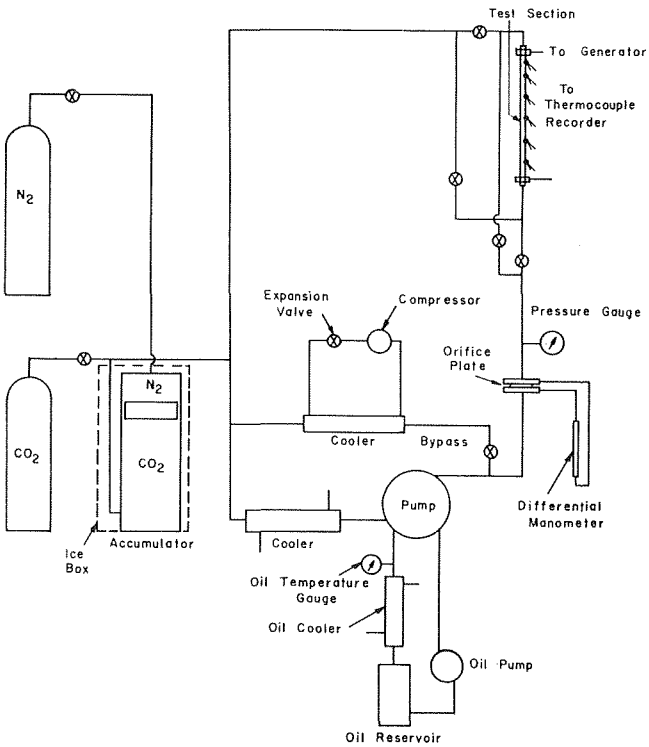

Fig. 1 Schematic drawing of experimental loop

The system pressure was monitored by means of a Heise-Bourdon gage, calibrated from 0–2000 psi in intervals of 2 psi. The flow was measured by means of a calibrated orifice plate with flange pressure taps. The pressure drop across the orifice was measured by a 5 ft differential manometer. A differential pressure gage was used for some of the smaller flows.

The carbon dioxide was obtained from Liquid Carbonic Division of General Dynamics and was 99.9 percent pure.

Tests were run in both upflow and downflow and at two pressures, 1100 and 1150 psi. The inlet temperature was varied from 0 deg F to supercritical. A wide range of Reynolds numbers (from 267,000 to 835,000) and heat fluxes (16,000 to 144,000 Btu/ft² hr) was investigated. The procedure consisted in fixing the heat flux and varying the inlet temperature and flow rate. Heat balance checks were satisfactory. It is estimated that all temperature readings were correct to within 2 deg F and the power input and flow rate within 5 percent. Uncertainty on the inner wall temperature was higher due to variation in the heat transfer coefficient and heat loss, but was estimated to be less than 5 deg F. Since the experiment was aimed at determining when large departure occurred from the smooth wall temperature profile at low heat fluxes and not at determining accurate values of heat transfer coefficient, this accuracy in temperature measurement was adequate. The pressure drop within the test section was not measured, but was calculated to be small (of the order of 1–2 psi for the $^1/_4$-in. tube, 3–4 psi for the $^1/_8$-in. tube and 5–10 psi for the swirl test section).

A detailed description of the loop and experimental procedures can be found in reference [9].

Experimental Results

Experimental results were obtained in the form of wall temperature profiles as a function of the length along the test section. Under the conditions of uniform heat flux, length along the test section can be interpreted as change in the bulk enthalpy. A computer program was written to reduce the data and obtain the inside wall temperature, the bulk temperature, and the heat transfer coefficient at the axial locations of the thermocouples. The inside wall temperature was calculated assuming no heat loss from the outer wall and negligible axial conduction in the tube wall. The bulk enthalpy and temperature were obtained from a heat balance along the test section.

As observed in a previous paper [4], at high enough heat flux, marked deterioration was found in the heat transfer to carbon dioxide which varied depending on the operating conditions.

1 Mass Velocity and Heat Flux. As the heat flux is increased for a particular flow rate, or the mass flow rate decreased for a

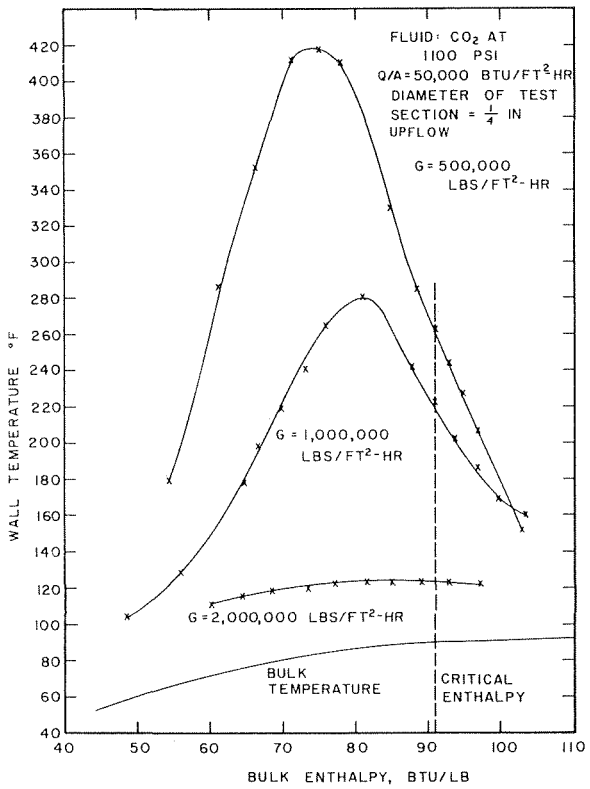

Fig. 2 Effect of mass velocity on wall temperature profiles

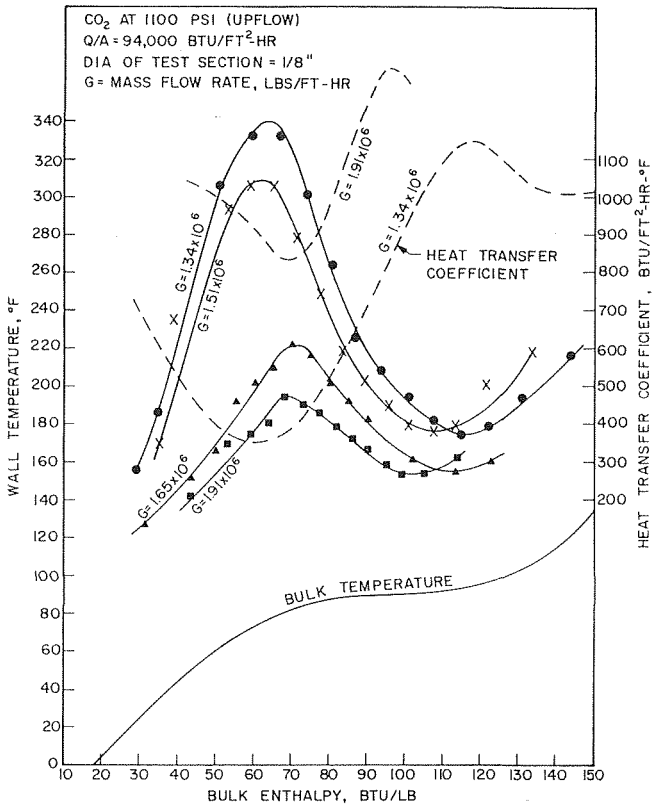

Fig. 3 Variation of the heat transfer coefficient and wall temperature profile for smaller diameter test section

fixed heat flux, the wall temperature profile exhibits a peak in the region where the bulk enthalpy is less than critical and the wall temperature is above critical. Fig. 2 shows some typical results for a heat flux of 50,000 Btu/ft² hr. A peak in wall temperature becomes noticeable at a mass flow rate of 10^6 lb/ft² hr and becomes higher as the mass velocity is reduced further. Further along the tube beyond the temperature peak, there is an improvement in heat transfer as seen from the fall in wall temperature in the region of the critical enthalpy. At large mass velocities, this improvement in heat transfer exists without any deterioration in the precritical enthalpy region, e.g., for G = 2,000,000 lb/ft² hr. The mass velocity and heat flux demarcate regions where either the deterioration or improvement in heat transfer predominate.

2 Diameter of Test Section. Fig. 3 shows results obtained with the 1/8-in. test section. Due to the larger L/D ratio in this case, with a corresponding higher bulk enthalpy range, the results show the characteristic S-shaped wall temperature profile which has been observed in other fluids in the supercritical region (e.g., Shitsman [3] for steam). The variation of the heat transfer coefficient is also shown in the figure. It was found that the wall temperature peaks were not as sharp or high as for the 1/4-in. test section. This was partly due to increased axial conduction in the relatively thicker tube wall. However, it was apparent that under equivalent conditions of mass flow rate and heat flux, the smaller test section diameter has the effect of reducing the degree of deterioration in heat transfer. This conclusion is also in agreement with the theory developed in reference [4]. The theory does not take natural convection into account, so that this conclusion may not be valid for very large diameter tubes, i.e., large Grashof numbers.

3 Upflow Versus Downflow. Under the conditions of mass velocities and test section diameters used, there was very little difference between upflow and downflow. Fig. 4 shows some

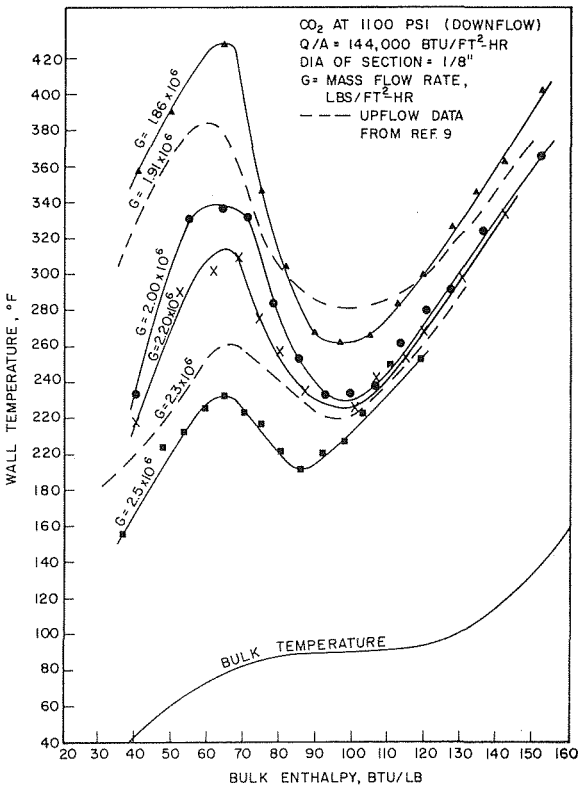

Fig. 4 Comparison between results for upflow and downflow

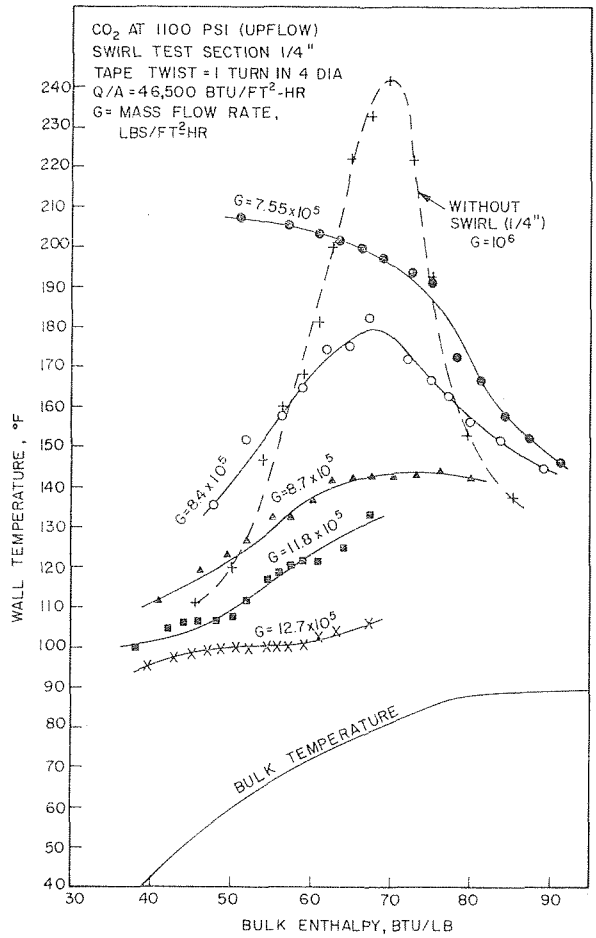

Fig. 5 Effect of swirl on the wall temperature profile

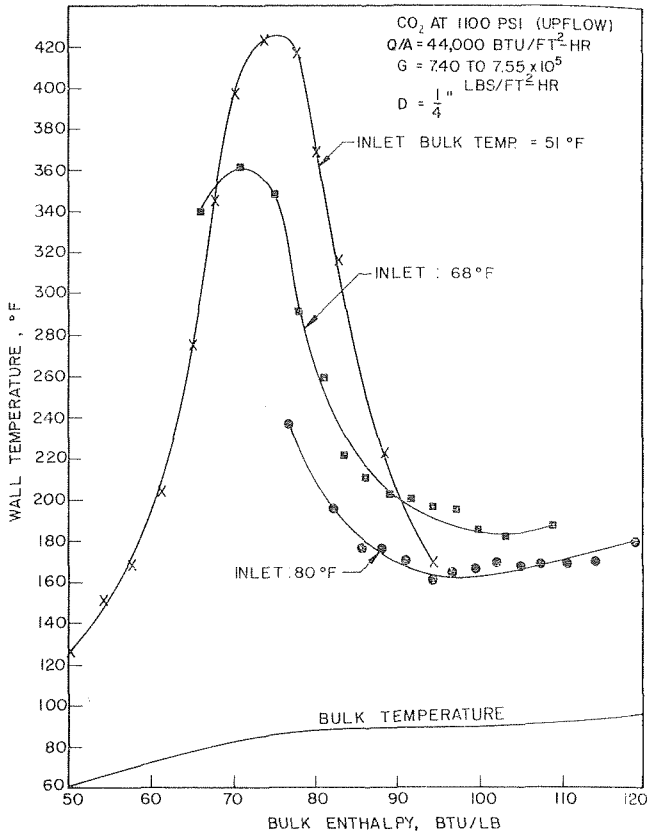

Fig. 6 Effect of inlet temperature

typical results for the 1/8-in. test section in downflow and results for upflow at comparable velocities are also shown. The upflow and downflow results are almost identical. Similar results were also obtained with the 1/4-in. test section even at the lowest mass velocity used, i.e., 640,000 lb/ft² hr. There has been conjecture in the literature [10] that free-convection effects in upflow are responsible for the peak in wall temperature. The results indicate that gravitational effects are not essential for the existence of the wall temperature peak.

4 Effect of Swirl. Tests were performed with a twisted ribbon inside a 1/4-in-ID tube. The ribbon used had a twist of one turn of 360 deg in four diameters ($p = 2$). The tape induces centrifugal forces in the fluid and helps to replace light fluid near the wall with the cooler and heavier fluid in the core of the flow. This was found to reduce the deterioration in heat transfer to a substantial extent, though peaks in wall temperature were not completely eliminated. Deterioration was found to occur in both up and downflow, though at higher fluxes than with the tube without the swirl tape. Fig. 5 shows some results with the swirl tape test section for a heat flux of 46,500 Btu/ft² hr. As the mass flow rate was decreased to 840,000 lb/ft² hr, deterioration in heat transfer was found to occur. For comparison, a wall temperature profile for a mass flow rate of 10^6 lb/ft² hr and the same heat flux is included for a 1/4-in.-ID tube without the swirl tape. This is shown by the dashed line in the figure. It is seen that for an equivalent mass velocity, the swirl completely eliminates the peak in wall temperature. It was generally found that the temperature peaks for the swirl section, when they did occur, were not as sharp as without tape and that the tape used increased the "allowable heat flux" (at which noticeable deterioration occurs) by a factor of about two.

An attempt was made to correlate the heat transfer coefficient using a method suggested by Lopina [11] which consists of a linear addition of a forced-convection heat transfer coefficient for axial flow to a "centrifugal" convection heat transfer coefficient. The latter is based on a free-convection coefficient, with the acceleration due to gravity replaced by centrifugal acceleration, i.e.,

$$\frac{hD_h}{k_w} = \frac{h_{fc}D_h}{k_w} + C\left[\left(\frac{\mathrm{Re}_h}{p}\right)^2\left(\frac{D_h}{D_e}\right)\frac{C_{p_{\mathrm{avg}}}}{k_w}\frac{\Delta\rho}{\rho_b}\right]^{1/2}$$

where

h_{fc} = heat transfer coefficient as predicted by the theory in reference [4]
D_h = hydraulic diameter
$\Delta\rho = \rho_b - \rho_w$
$C_{p_{\mathrm{avg}}}$ = average specific heat $= \dfrac{H_w - H_b}{T_w - T_b}$

The best value of C was found to be 0.115 to correlate the heat transfer coefficient at the inception of deterioration in heat transfer. Due to the large variation in properties and the nonlinear nature of the governing equations, a general value of C over a large range of heat transfer conditions could not be determined.

5 Inlet Enthalpy. The amount of deterioration is strongly influenced by the inlet enthalpy, and is reduced if the inlet enthalpy is not appreciably less than that at which deterioration occurs. The greatest deterioration occurs when the inlet enthalpy is sufficiently low. If the inlet temperature is lowered further, the deterioration is not affected. Fig. 6 shows the effect of inlet temperature on the wall temperature profile. As seen from the figure, the peak wall temperature is reduced substantially when the inlet bulk temperature is increased from 52 to 80 deg F. Above a certain inlet temperature (about 80 deg F), the deterioration in heat transfer is very small even though the inlet enthalpy

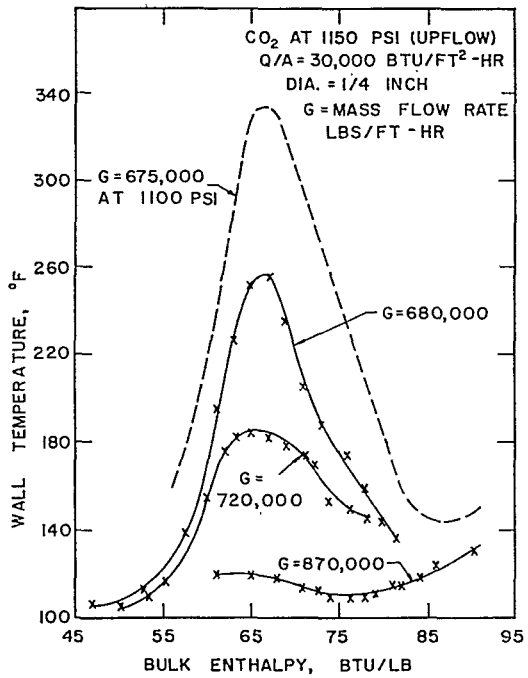

Fig. 7 Comparison between results at 1100 and 1150 psia

is less than critical. This is linked to the entrance effect which has considerable influence when the critical temperature is in the fluid film next to the wall in the entrance region. This is the reason why a majority of other investigators have not seen the deterioration phenomenon in carbon dioxide.

6 Pressure. The deterioration is the greatest near the critical pressure and is less at higher pressures. Fig. 7 shows that the wall temperature peaks are not as high or sharp at 1150 psi as at 1100 psi, under equivalent conditions of heat flux and mass velocity. This is to be expected because the change of properties is the largest and most rapid at the critical pressure.

Comparison With the Results of Other Investigators

It was mentioned earlier that most of the other investigators have not observed deterioration in heat transfer to supercritical pressure carbon dioxide in the form of temperature peaks. Moreover, one investigator (Hall, reference [12]) reports temperature peaks in upflow and none in downflow. A more detailed comparison between those results and the present work is made in this section with the objective of explaining the apparent contradictions. In Table 1, the results and operating conditions of Koppel and Smith [7], Tanaka [13], Hall [12], Krasnoschekov, et al. [14], and the present work (Shiralkar and Griffith) are compared. The parameter Gr/Re^2 was used to evaluate the importance of free convection. The reasons for using this are noted in the Appendix.

Koppel and Smith used a wide range of heat fluxes and mass velocities with inlet temperatures of 60 deg F and above. The test section used was horizontal and small in diameter (0.194 in.). Though no deterioration in heat transfer was reported as such, a number of anomalous results are shown. With some of the lower inlet temperatures used, there is often a sharp fall in the wall temperature with length. For example, for one run at a heat flux of 71,200 Btu/ft^2 hr, a sharp drop in wall temperature was observed from 180 to 140 deg F, which was attributed to entrance effects. In the light of the present investigation, this would appear to be the tail end of a temperature peak, modified by entrance effects. The use of the horizontal test section would also tend to reduce the amount of deterioration.

Tanaka, et al., have confined their experiments to very small heat fluxes and inlet temperatures above 80 deg F. Under these conditions it would not be possible to observe deterioration in heat transfer.

The results of Hall are especially interesting because they illustrate the effects of natural convection in large tubes (or large values of Gr/Re^2). A comparison with the results of Shiralkar shows that the Grashof number was much higher in these experiments and the mass flow rates smaller than those used by Shiralkar. Both these conditions serve to increase the dominance of buoyancy effects. A comparison of the nature of the peaks is also revealing. The peaks in Hall's results are much sharper; i.e., they occur over a much smaller enthalpy range, and they were not found in downflow. They also occur at a substantially smaller value of the bulk enthalpy. The results for supercritical water [9] also show a similar trend. The influence of natural convection thus tends to produce sharper peaks in upflow, which

Table 1 Comparison of results for carbon dioxide

No.	Source	Pressure psi.	Tube Dia. Inches	Comparison of Results for CO_2: G Lbs/Ft^2-Hr	Q/A Btu/Ft^2-Hr	Orientation of Flow	Min. Inlet Temp. °F	Enthalpy at Peak Btu/Lb	Nature of Peak	$Re = GD/\mu_w$	$\frac{\Delta\rho}{\rho_b}\left(\frac{\rho_b}{\mu_w}\right)^2 R^3_R$	$\frac{Gr}{Re^2}$ (Max.)
1	Shiralkar and Griffith	1100	0.25	640,000-2,000,000	16,000-117,000	Upflow	35°F	60-75	Sharp	267,000-835,000	2.3×10^8	3.2×10^{-3}
2	Shiralkar and Griffith	1100	0.25	640,000-2,000,000	28,000 110,000	Downflow	35°F	55-68	Sharp	267,000 835,000	2.3×10^8	3.2×10^{-3}
3	Shiralkar and Griffith	1100	0.125	1.2×10^6-2.6×10^6	50,000-144,000	Upflow	0°F	60-70	Not as Sharp as (1),(2)	250,000 540,000	0.28×10^8	4.5×10^{-4}
4	Shiralkar and Griffith	1100	0.125	1.3×10^6-3×10^6	50,000 144,000	Downflow	0°F	60-69	Similar to (3)	260,000-625,000	0.28×10^8	4.4×10^{-4}
5	Hall	?	0.75	468,000	16,000	Upflow	53°F	50	Sharp	586,000	61.4×10^8	1.73×10^{-2}
6	Hall	?	0.75	468,000	17,500	Upflow	53°F	49	Very Sharp	586,000	61.4×10^8	1.73×10^{-2}
7	Hall	?	0.75	468,000	17,500	Downflow	53°F	-	No Peak	586,000	61.4×10^8	1.73×10^{-2}
8	Koppel and Smith	1071-1100	0.194	93,000-930,000	20,000-200,000	Horizontal	70°F	-	No Peak Sharp Drop in Temp. at Inlet	30,000-300,000	-	-
9	Tanaka et al	1130	0.4	300,000-675,000	5,000-17,800	Upflow	83°F	-	No Peak	200,000-450,000	9.4×10^8	2.4×10^{-2}
10	Krasnoschekov et al	1130-1470	0.16	375,000-1,875,000	825,000 and below	Horizontal	70°F	-	No Peak Low Heat Trans. Coefficients	100,000-500,000	-	-
11	Calculations	1100	0.25 0.125	1,000,000	60,000	No Gravity Terms	-	77-79	Not as Sharp as Experiment in (1),(2)	415,000	-	-

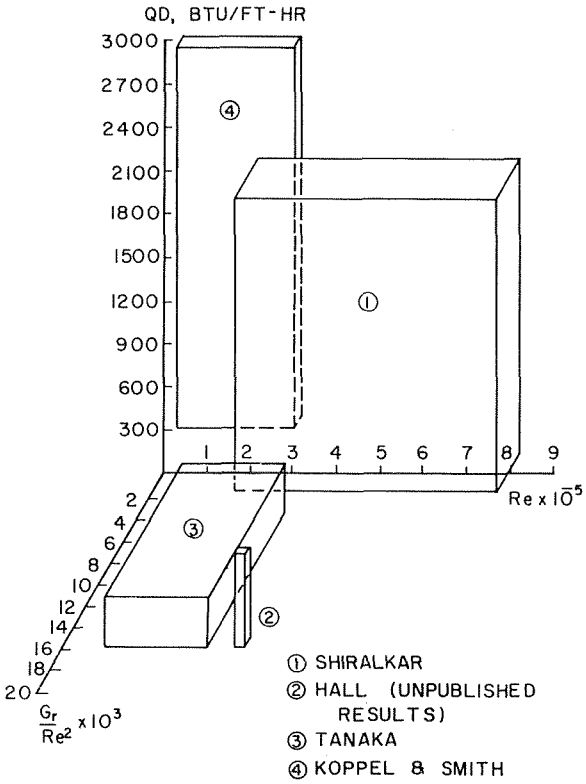

Fig. 8 Map showing regions of operation

occur at a smaller value of the bulk enthalpy. Here again, it can be seen that the inlet enthalpy can be important. Tanaka, et al., though working under nearly the same conditions of small Reynolds numbers and large Grashof numbers, did not report any comparable behavior in their results.

In a recent investigation by Krasnoschekov and Protopopov [14], the heat transfer to carbon dioxide at very high temperature drops was measured. Heat fluxes as high as 825,000 Btu/ft² hr were used at pressures of 1130 and 1420 psia. A horizontal test section 4.08 mm (0.16 in.) and with $L/D = 51$ was used for the purpose. The Reynolds number range used was 10^5 to 5×10^5. The lowest inlet temperature used was 70 deg F, and consequently, no sharp peaks were seen in the precritical enthalpy range. However, it was found that the heat transfer coefficient became increasingly small at high heat fluxes. Values as low as $^1/_{10}$th of the expected heat transfer coefficient, as calculated by correlations for supercritical pressure heat transfer at low heat fluxes, were encountered. They suggest a multiplication factor of $\left(\frac{\rho_w}{\rho_L}\right)^{0.4}\left(\frac{C_{p_{avg}}}{C_{pb}}\right)^n$ in order to adapt the low heat-flux correlation to their results, where n varies from 0.4–0.7 under different conditions.

These results lead one to the conclusion that the operating conditions governing the nature and extent of deterioration at a particular supercritical pressure are:

1 Heat-flux parameter.
2 Flow rate or Reynolds number.
3 A free-convection parameter, e.g., Gr/Re^2.
4 Inlet temperature.

It is seen from Table 1 that the parameter Gr/Re^2 is an order of magnitude higher in Hall's results than the highest value for the conditions of Shiralkar. A critical value of about 10^{-2} can be attached to Gr/Re^2 for carbon dioxide where the free-convection effects become important.

Fig. 8 shows a three-dimensional plot of the operating conditions of the investigators mentioned in this section and shows that these were quite different from each other. In particular, the region of investigation in the present work is seen to be in the portion where the heat fluxes were high and the importance of buoyancy effects very small. The influence of the inlet temperature is not shown in this map. A comparison in Table 1 shows, however, that Shiralkar and Griffith used the widest range of inlet temperatures and the lowest temperatures. Hall used a fairly low inlet temperature in the small sample of his results seen by this author (50 deg F). Koppel and Smith and Tanaka, et al., as well as Krasnoschekov, generally used inlet temperatures too high to allow observation of the temperature peaks.

Summary and Conclusions

1 The heat transfer coefficients for the heat transfer to a fluid at supercritical pressure differ sharply in different regions, the boundaries of which are governed by the mass velocity, a heat-flux parameter, and a parameter governing the relative importance of free convection to the forced convection. Depending on the region of operation, varying degrees of improved and deteriorated heat transfer rates are possible.

2 In the region where free-convection effects are not important (i.e., the region covered by the experiments in this investigation), deteriorated heat transfer can occur when the heat flux is sufficiently high and the bulk temperature is below the pseudocritical temperature. The deteriorated region is confined to a relatively small range of bulk enthalpies, depending on the fluid and the pressure.

3 The location and extent of the deterioration is sensitive to the details of the system geometry and the inlet subcooling.

4 Deterioration in heat transfer can occur in both upflow and downflow when the free-convection effects are not predominant.

5 The introduction of a swirl generating twisted tape within the test section substantially improves the heat transfer. However, if the heat flux is increased to a larger value, deterioration can occur again. This is not as sharp as the deterioration in the absence of twisted tape.

6 Deterioration in heat transfer to carbon dioxide was not observed by earlier investigators because the inlet temperatures were not low enough in their experiments. The different observations made by different investigators in other fluids can be explained in terms of influence of natural convection, orientation, and entrance effects.

References

1 Styrikovich, M. A., Margulova, T. Ch., and Miropolskiy, Z. L., "Problems in the Development of Designs of Supercritical Boilers," *Teploenergetika*, Vol. 14, (6), 1967, pp. 4–7.

2 Dickinson, N. L., and Welch, C. P., "Heat Transfer to Supercritical Water," TRANS. ASME, Vol. 80, 1958, pp. 746–752.

3 Shitsman, M. E., "Impairment of the Heat Transmission at Supercritical Pressures," *High Temperature*, Vol. 1, No. 2, 1963, pp. 237–244 (translated from *Teplofizika Vysokikh Temperatur*).

4 Shiralkar, B. S., and Griffith, P., "Deterioration in Heat Transfer to Fluids at Supercritical Pressure and High Heat Fluxes," JOURNAL OF HEAT TRANSFER, TRANS. ASME, Series C, Vol. 91, 1969, pp. 27–36.

5 Hall, W. B., Jackson, J. D., and Khan, S. A., "An Investigation of Forced Convection Heat Transfer to Supercritical Pressure Carbon Dioxide," 3rd Annual Conference in Heat Transfer, Institution of Mechanical Engineers Section, pp. 257–266.

6 Sabersky, R. H., and Hauptmann, E. G., "Forced Convection Heat Transfer to CO_2 Near the Critical Point," *International Journal of Heat and Mass Transfer*, Vol. 10, 1967, pp. 1499–1508.

7 Koppel, L. B., and Smith, J. M., "Turbulent Heat Transfer in the Critical Region," *International Developments in Heat Transfer*, Part 3, ASME, 1961, pp. 579–585.

8 Khan, S. A., "Forced Convection Heat Transfer to Fluids Near the Critical Point," PhD thesis, Victoria University of Manchester, 1965.

9 Shiralkar, B. S., and Griffith, P., "The Deterioration in Heat Transfer to Fluids at Supercritical Pressure and High Heat Fluxes," EPL Report No. DSR-70332-55, Department of Mechanical Engineering, M.I.T., June 1968.

10 Hall, W. B., "The Effects of Buoyancy Forces on Forced Convection Heat Transfer in a Vertical Pipe," Research Report, N.E.1, University of Manchester, Department of Nuclear Engineering, 1968.
11 Lopina, R. F., and Bergles, A. E., "Heat Transfer and Pressure Drop in Tape Generated Swirl Flow," EPL Report No. DSR-70281-47, Department of Mechanical Engineering, M.I.T., 1967.
12 Hall, W. B., Personal Communication.
13 Tanaka, H., Nishiwaki, N., and Hirata, M., "Turbulent Heat Transfer to Supercritical CO_2," Semi-International Symposium, JSME, Tokyo, Sept. 1967.
14 Krasnoschekov, E. A., and Protopopov, V. S., "An Experimental Study of Heat Exchange in CO_2 in the Supercritical Range at High Temperature Drops," *High Temperature*, Vol. 4, No. 3, 1966, pp. 375–382.

APPENDIX

Free-Convection Parameter

The relative importance of free convection to forced convection is determined by the Grashof and Reynolds numbers for the flow. The buoyancy effects will become dominant at large Grashof numbers and small Reynolds numbers. A free-convection parameter may be derived from the momentum equation for the flow as follows.

Neglecting momentum terms,

$$\frac{\partial \tau}{\partial y} - \frac{\tau}{R - y} - \left(\rho g + \frac{\Delta P}{\Delta z}\right) = 0 \tag{1}$$

where

y = distance from wall of tube
R = radius of tube
z = axial distance

which integrates to

$$\tau = \frac{R}{R - y}\tau_0 + \frac{1}{R - y}\int_0^y \left(\rho g + \frac{\Delta P}{\Delta z}\right)(R - y)dy \tag{2}$$

with the boundary condition

$$\tau = \tau_0 \text{ at } y = 0. \tag{3}$$

Using an overall force balance

$$\frac{2\tau_0}{R} + \rho_b g + \frac{\Delta P}{\Delta z} = 0 \tag{4}$$

where ρ_b = bulk density $= \dfrac{1}{\pi R^2}\displaystyle\int_0^R 2\pi\rho(R - y)dy$,

$\dfrac{\Delta P}{\Delta z}$ can be eliminated from equation (1) to give

$$\frac{\tau}{\tau_0} = (1 - Y) + \frac{Rg(\rho_b - \rho_w)}{\tau_0(1 - Y)}\int_0^Y \frac{(\rho - \rho_b)}{(\rho_b - \rho_w)}(1 - Y)dY \tag{5}$$

where $Y = y/R$.

When free-convection effects are neglected,

$$\frac{\tau}{\tau_0} = (1 - Y). \tag{6}$$

Thus the term $\dfrac{Rg(\rho_b - \rho_w)}{\tau_0}$ governs the magnitude of the distortion of the shear stress profile from the linear profile, due to buoyancy. This parameter can be used as a criterion for the relative importance of free convection to forced convection

$$\frac{Rg(\rho_b - \rho_w)}{\tau_0} = \left[\frac{R^3 g(\rho_b - \rho_w)}{\rho_b}\left(\frac{\rho_b^2}{\mu_w^2}\right)\right]\left[\frac{\mu_w^2}{R^2\rho_b\tau_0}\right]. \tag{7}$$

τ_0 can be expressed as $(f)\left(\dfrac{\rho_b U_b^2}{2}\right) = {}^1/_2\,\dfrac{fG^2}{\rho_b}$, where f is a friction factor, defined in the usual manner.

$$\therefore \frac{Rg(\rho_b - \rho_w)}{\tau_0} = 8\,\frac{\mathrm{Gr}}{f}\left(\frac{\mu_w}{DG}\right)^2. \tag{8}$$

If f is assumed to be almost constant in the region of high Reynolds numbers,

$$\frac{Rg(\rho_b - \rho_w)}{\tau_0} \sim \frac{\mathrm{Gr}}{\mathrm{Re}^2}. \tag{9}$$

10 Hall, W. B., "The Effects of Buoyancy Forces on Forced Convection Heat Transfer in a Vertical Pipe," Research Report, N.E.1, University of Manchester, Department of Nuclear Engineering, 1968.
11 Lopina, R. F., and Bergles, A. E., "Heat Transfer and Pressure Drop in Tape Generated Swirl Flow," EPL Report No. DSR-70281-47, Department of Mechanical Engineering, M.I.T., 1967.
12 Hall, W. B., Personal Communication.
13 Tanaka, H., Nishiwaki, N., and Hirata, M., "Turbulent Heat Transfer to Supercritical CO_2," Semi-International Symposium, JSME, Tokyo, Sept. 1967.
14 Krasnoschekov, E. A., and Protopopov, V. S., "An Experimental Study of Heat Exchange in CO_2 in the Supercritical Range at High Temperature Drops," *High Temperature*, Vol. 4, No. 3, 1966, pp. 375–382.

APPENDIX

Free-Convection Parameter

The relative importance of free convection to forced convection is determined by the Grashof and Reynolds numbers for the flow. The buoyancy effects will become dominant at large Grashof numbers and small Reynolds numbers. A free-convection parameter may be derived from the momentum equation for the flow as follows.

Neglecting momentum terms,

$$\frac{\partial \tau}{\partial y} - \frac{\tau}{R - y} - \left(\rho g + \frac{\Delta P}{\Delta z}\right) = 0 \tag{1}$$

where

y = distance from wall of tube
R = radius of tube
z = axial distance

which integrates to

$$\tau = \frac{R}{R - y}\tau_0 + \frac{1}{R - y}\int_0^y \left(\rho g + \frac{\Delta P}{\Delta z}\right)(R - y)dy \tag{2}$$

with the boundary condition

$$\tau = \tau_0 \text{ at } y = 0. \tag{3}$$

Using an overall force balance

$$\frac{2\tau_0}{R} + \rho_b g + \frac{\Delta P}{\Delta z} = 0 \tag{4}$$

where ρ_b = bulk density $= \dfrac{1}{\pi R^2}\displaystyle\int_0^R 2\pi\rho(R - y)dy$,

$\dfrac{\Delta P}{\Delta z}$ can be eliminated from equation (1) to give

$$\frac{\tau}{\tau_0} = (1 - Y) + \frac{Rg(\rho_b - \rho_w)}{\tau_0(1 - Y)}\int_0^Y \frac{(\rho - \rho_b)}{(\rho_b - \rho_w)}(1 - Y)dY \tag{5}$$

where $Y = y/R$.

When free-convection effects are neglected,

$$\frac{\tau}{\tau_0} = (1 - Y). \tag{6}$$

Thus the term $\dfrac{Rg(\rho_b - \rho_w)}{\tau_0}$ governs the magnitude of the distortion of the shear stress profile from the linear profile, due to buoyancy. This parameter can be used as a criterion for the relative importance of free convection to forced convection

$$\frac{Rg(\rho_b - \rho_w)}{\tau_0} = \left[\frac{R^3 g(\rho_b - \rho_w)}{\rho_b}\left(\frac{\rho_b^2}{\mu_w^2}\right)\right]\left[\frac{\mu_w^2}{R^2\rho_b\tau_0}\right]. \tag{7}$$

τ_0 can be expressed as $(f)\left(\dfrac{\rho_b U_b^2}{2}\right) = {}^1/_2\,\dfrac{fG^2}{\rho_b}$, where f is a friction factor, defined in the usual manner.

$$\therefore \frac{Rg(\rho_b - \rho_w)}{\tau_0} = 8\,\frac{\mathrm{Gr}}{f}\left(\frac{\mu_w}{DG}\right)^2. \tag{8}$$

If f is assumed to be almost constant in the region of high Reynolds numbers,

$$\frac{Rg(\rho_b - \rho_w)}{\tau_0} \sim \frac{\mathrm{Gr}}{\mathrm{Re}^2}. \tag{9}$$

DISCUSSION

W. B. Hall[2] and J. D. Jackson[2]

It is interesting to compare the authors' results for a ${}^1/_4$-in-dia pipe with our own results for a ${}^3/_4$-in-dia pipe,[3] and those of Bourke, et al.,[4] for a 0.9-in-dia pipe. In all three cases the pipe was vertical and uniformly heated, measurements were made with the flow in the upward and in the downward directions, and the fluid was CO_2 at a pressure of 1080 or 1100 lbf/in^2.

In the absence of buoyancy effects and dissipative effects a study of the basic equations in dimensionless form shows that the

[2] Simon Engineering Laboratories, University of Manchester, Manchester, England.
[3] Jackson, J. D., and Evans-Lutterodt, K., "Impairment of Turbulent Forced Convection Heat Transfer to Supercritical Pressure CO_2 Caused by Buoyancy Forces," Report NE2 Simon Engineering Laboratories, Manchester University, 1968.
[4] Bourke, P. J., Pulling, D. J., Gill, L. E., and Denton, W. H., "Forced Convective Heat Transfer to Turbulent CO_2 in the Supercritical Region;" U.K.A.E.A. Report A.E.R.E.-R-5952, 1969.

conditions for similarity between the three systems are that inlet temperature, wall temperature, $(Q_0/A).D$ and $G.D$ must be identical. Subject to these conditions the Reynolds numbers and temperature distributions will be the same and a unique relationship between wall temperature and bulk enthalpy will be obtained. The authors state that there was little difference between their results for upflow and downflow, which indicates that buoyancy effects were unimportant, but this was certainly not the case in our experiments and those of Bourke, et al.[4] Thus if the results for similar conditions are compared on a plot of wall temperature versus bulk enthalpy any differences must be attributable to buoyancy effects in the larger bore pipe experiments. The conditions for three approximately similar experiments are summarized below and the wall temperature distributions are shown in Fig. 9.

It will be seen from the foregoing table that the results selected are quite closely comparable on the basis of flow and thermal similarity. Fig. 9 shows, however, that the wall temperatures for the small pipe are very different from those for the two larger pipes. It will be seen that the wall temperatures for downflow in the two larger pipes are considerably less than those for the small pipe. (The slight differences between the downflow results for the two larger pipes are presumably accounted for by the slight differences between the values of $G.D$ and Q_0/AD.) Our own results for upward flow at the conditions chosen show that buoyancy peaks are developing (see Hall and Jackson[5] for a discussion

[5] Hall, W. B., and Jackson, J. D., "Laminarisation of a Turbulent Pipe Flow by Buoyancy Forces," ASME Paper 69-HT-55, presented at the ASME–AIChE Heat Transfer Conference, Minneapolis, Minn., Aug. 1969.

Reference	D(ft)	Q_0/A (Btu/ft²hr)	G (lb/ft²hr)	$G.D$	$(Q_0/A).D$	Pressure lbf/in²
Jackson and Evans-Lutterodt[3]	0.0625	16,500	415,000	25,900	10,300	1100
Bourke, et al.[4]	0.075	16,200	228,000	17,100	12,100	1080
Shiralkar and Griffith	0.0208	50,000	1,000,000	20,800	10,400	1100

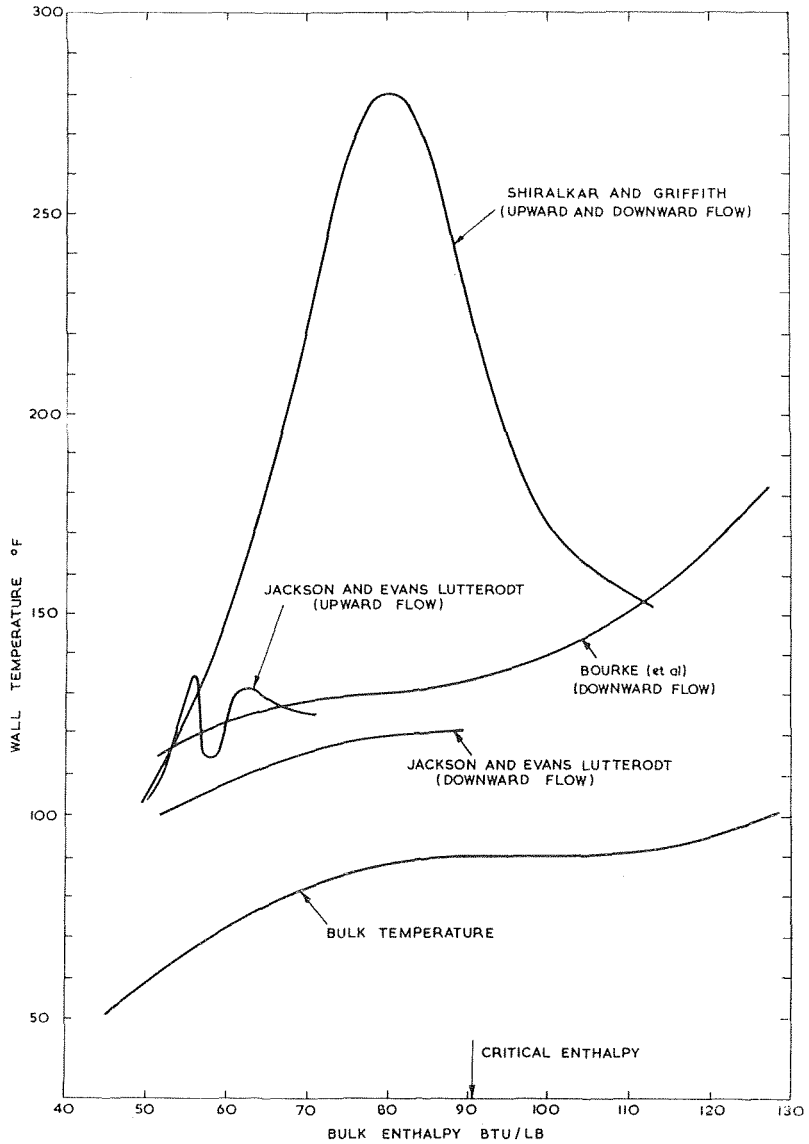

Fig. 9 Comparison of the authors' results with those of other recent investigations with larger bore tubes

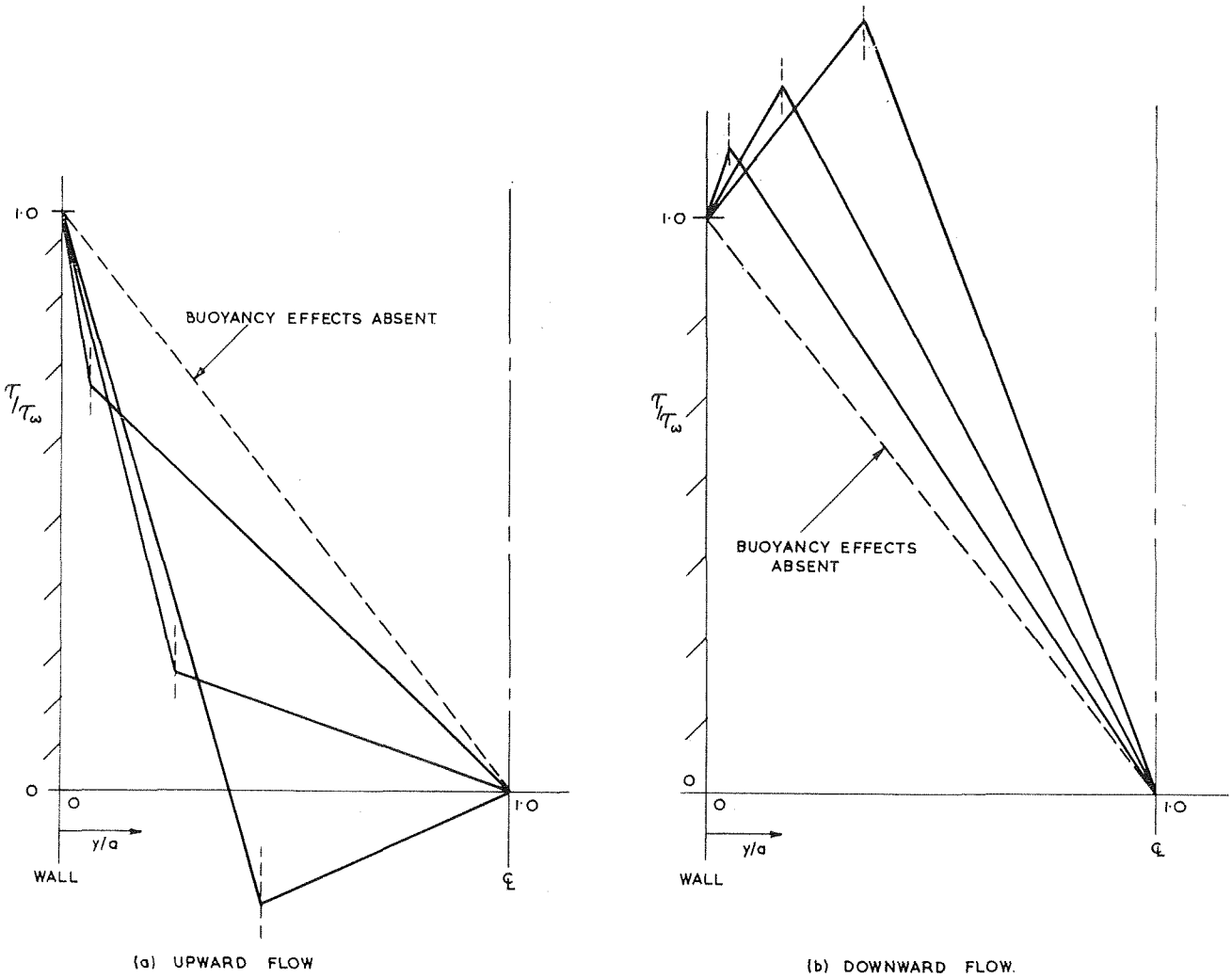

Fig. 10 Effect of buoyancy forces on shear stress for various conditions of low density layer thickness

of this phenomenon) but nevertheless the wall temperatures downstream of the initial peak are substantially lower than those obtained by the authors. It should be noted, however, that a 5 percent increase in wall heat flux causes the first buoyancy peak to reach 220 deg, without substantially affecting the wall temperatures downstream.

We have until recently tended to interpret our own results on the basis that the only anomalous effect was the peak observed in upward flow, and that the flat temperature distribution for downward flow was characteristic of the case when buoyancy forces, although present, were not greatly affecting heat transfer. This interpretation no longer seems tenable, and one is forced to the conclusion that in downward flow the buoyancy forces in the wall region, materially increase heat transfer. It also seems that in upward flow the heat transfer coefficient following a temperature peak caused by buoyancy forces reverts to a level which is higher than that for a flow in which buoyancy forces are negligible. A possible mechanism is illustrated diagrammatically in Fig. 10.

In the case of upward flow the shear stress is modified progressively as the low density layer adjacent to the wall thickens. A critical situation is reached at which the shear stress over the greater part of the cross-section is zero, and turbulence production in the region will then cease. If this is achieved with a sufficiently thin wall layer[5] a low heat transfer coefficient will result. Further thickening of the wall layer causes the shear stress to reverse in the central region, turbulence production will be restarted and heat transfer will improve. It now looks as though the final situation will result in a higher heat transfer coefficient than that obtained with no buoyancy forces.

With downward flow the shear stress is modified in such a manner that it increases everywhere resulting in a greater heat transfer coefficient than that obtained with a small buoyancy effect.

C. R. Kakarala[6]

The authors clearly explain the effects of the different variables and this was supported by the appropriate experimental data. Inlet enthalpy effect on the heat transfer deterioration was explained on the basis of considerable influence of entrance effect when the pseudocritical temperature is in the fluid film next to the wall. However, no mention was made nor any experimental data presented in the paper regarding a difference in heat transfer deterioration phenomenon in the inlet side of test section as compared to that on the outlet side.

The experimental data obtained at the Babcock & Wilcox Company with supercritical pressure water show there is a marked difference between "inlet temperature peaks" and those high temperatures occurring near the outlet of the test section.

[6] Senior Performance Engineer, Power Generation Division, Babcock & Wilcox Company, Barberton, Ohio.

This is clearly shown by the data in Figs. 7 and 8 of a technical paper to be presented at this conference.[7] In particular, the data in Fig. 8 of this reference for bulk temperatures much below pseudocritical temperature show there is a sharp temperature peak on the inlet side followed by sudden decrease in temperature prior to the more gradual but large increase near the outlet.

The large improvement in heat transfer in a short distance after the inlet temperature peak cannot be explained on the basis of bulk fluid properties, as the bulk temperature is far below the pseudo-critical temperature. In the authors' previous paper, the improvement in heat transfer following deterioration was attributed to the fact that the bulk temperature is very close to the pseudocritical temperature. On the basis of the above referenced results, it appears likely that the improvement in heat transfer after the first peak is associated with the effects near the wall rather than bulk fluid conditions. Some upstream entrance effect associated with the boundary layer development might be postulated for the behavior of heat transfer on the inlet side. The authors' opinions on what appears to be two regions of heat transfer deterioration would be of great value.

[7] Ackerman, J. W., "Pseudoboiling Heat Transfer to Supercritical Pressure Water in Smooth and Ribbed Tubes," Paper 69-WA/HT-2 Presented at the ASME Winter Annual Meeting, November, 1969, 8 pp.

Authors' Closure

The comments of Professors Hall and Jackson and Mr. Kakarala are appreciated.

Hall and Jackson have elaborated on a point made in the paper, viz., the importance of natural convection as a parameter in determining the heat transfer coefficient for supercritical pressure fluids, and have graphically demonstrated this by comparison with their data. We feel that the mechanism whereby the buoyancy effects influence the heat transfer is not completely understood at present and needs to be investigated further.

The "inlet temperature peaks" observed by the Babcock and Wilcox Company researchers, to which Kakarala refers, are probably also due to the influence of free convection, which is dominant for the low mass flux and large diameter tubes used in their tests. As mentioned in the paper, under these conditions, the temperature peaks are much sharper and do not occur in a well defined slightly subcritical enthalpy region.

B. MIKIC
Massachusetts Institute of Technology
Cambridge, Mass.
Mem. ASME

G. CARNASCIALI
Universidad de Los Andes,
Bogota, Colombia

The Effect of Thermal Conductivity of Plating Material on Thermal Contact Resistance

Plating of a base material of low thermal conductivity with materials of high thermal conductivity was considered. The solution for an elemental heat channel (single contact) is given. Experimental results for contact resistance of a plated single contact agreed well with the prediction. In general, results indicate that considerable reduction in thermal contact resistance can be achieved by plating; for example, stainless steel plated with copper of a thickness of the order of the contact size radius will reduce the resistance by more than an order of magnitude. A procedure is presented for extending the results for a plated elemental heat channel to the calculation of thermal contact resistance for nominally flat-plated surfaces in a vacuum.

Introduction

In the last twenty years, considerable work and publications have been devoted to the problems of thermal contact resistance. Initially, one contact point (an elemental heat channel) was considered. Some of the major theoretical contributions in this area are listed in references [1][1] to [8]. The solution for an elemental channel can be used for evaluation of contact resistance for multiple contacts for the contact between nominally flat, rough, surfaces (e. g. [2], [5], [7]) or directly applied for calculation of macroscopic constriction resistance for wavy, smooth surfaces (e. g. [4]). Combined roughness and waviness with cross effects on the respective contributions was also considered [9].

The result for thermal contact resistance through one half of an elemental heat channel in a vacuum can be expressed (see for example [7], [8]) as:

$$R \equiv \frac{\Delta T}{Q} = \frac{1}{4ka}\,\psi\left(\frac{a}{b}\right) \tag{1}$$

Q represents the heat flow rate through the channel. ΔT, a, and b are introduced in Fig. 1. $\psi\left(\frac{a}{b}\right)$ is a geometrical factor which can be approximately given ([7], [8]) as

$$\psi = C\left(1 - \frac{a}{b}\right)^{1.5} \tag{2}$$

Where $C = 1$ for a constant temperature condition over the actual contact area (πa^2) and $C = 32/3\pi^2$ for a constant heat flux condition over the contact area, k is thermal conductivity of the material where constriction of heat flow occurs.

It follows from relation (1) that thermal contact resistance is inversely proportional to thermal conductivity of the material in the disturbed region (where isothermal surfaces are not parallel with the interface). Thus any increase in thermal conductivity

[1] Numbers in brackets designate References at end of paper.

Contributed by the Heat Transfer Division and presented at the Winter Annual Meeting, Los Angeles, Calif., November 16–20, 1969, of The American Society of Mechanical Engineers. Manuscript received by Heat Transfer Division, June 6, 1969; revised manuscript received May 1, 1969. Paper No. 69-WA/HT-9.

Nomenclature

- a = radius of a contact
- b = radius of heat channel
- b_i = hypothetical intermediate radius
- H = hardness
- J_n = Bessel function of order n
- k = thermal conductivity
- n = number of contacts per unit area
- P = interface pressure
- Q = heat rate per channel
- R = contact resistance for one half of unplated channel
- R_δ = contact resistance for one half of plated channel
- $\overline{R}$ = contact resistance per unit area
- r = radial coordinate
- z = axial coordinate
- λ = eigenvalue
- β = eigenvalue
- δ = layer thickness
- ϕ, ϕ' = contact resistance factor
- ψ = contact resistance factor

- 1 = material of high conductivity
- 2 = material of low conductivity
- I, II = upper and lower halves of heat channel, respectively
- ar = average

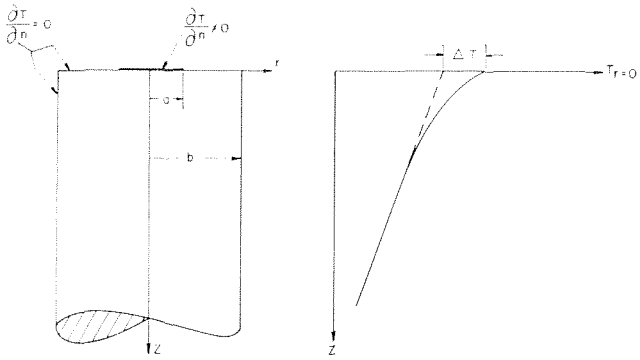

Fig. 1 Elemental heat channel

in the vicinity of contact points will reduce the value of thermal contact resistance *for a fixed geometry*. Consequently, the plating with materials of high conductivity should have significant effect on the reduction of the contact resistance. We should like to mention, however, that plating could be used also to *change geometry of a contact for the same interface load*. This effect is due to a generally different yield strength of plating material than the base (plated material), and was the motivation for some experimental work; e. g., Fried [10] measured contact resistance for stainless steel pair with one surface plated with magnesium and both surfaces plated with aluminum, respectively; Weills and Ryder [11] inserted at the interface a thin stainless steel disk plated on both sides with copper.

The last experiment is not related to the effects we are considering here. Also, the plating of only one contacting surface could have only a limited effect, since the whole constriction on the unplated side still has to take place in a low conductivity material. When both surfaces are plated, one gets combined effects of a change of thermal conductivity in the region of constriction and a change of the geometry of contact. Fried [10], as pointed out above, performed one experiment of this type. He obtained an order of magnitude reduction in the resistance and attributed the whole effect to the geometry changes (higher contact area).

The thermal conductivity effects in plating were never considered to be a factor in the resistance reduction. Moreover, from the available experimental results, it is not possible to separate and see the significance of the phenomena we are investigating in this work.

One can eliminate the effect of geometry change from thermal conductivity effects in actual experiments of nominally flat, low conductivity surfaces in contact, for example, by comparing the results when only one surface is plated and when both surfaces are plated, respectively. This type of experiment has never been done. These results, too, would be of limited value, since they cannot be generalized unless all the information concerning the number of contact points and their distribution, for a given pressure used in the experiments, are known.

It can be concluded, then, that the most useful results relevant to the goals of this work are the results for a plated elemental channel which can be then generalized and applied to multiple contact problems (in the same way as the result for an unplated channel is presently used for prediction of thermal contact resistance for two unplated surfaces in contact).

For the above reasons, the effect of thermal conductivity of plating material for a fixed geometry and fixed base material was studied first theoretically on an adapted model and then the validity of the solution was verified by the experimental results performed on a plated model of a contact point.

Analytical Solution

(a) Model. In Fig. 2, one half of a plated elemental heat channel is shown. The two conditions of constant temperature and constant heat flux over the contact area πa^2 will be investigated. The divergence of heat flow lines takes place partially in the plated region and partially in the base material. The problem is specified with the following relations:

$$\nabla^2 T = 0$$

$$\left.\begin{aligned} &\frac{\partial T}{\partial z} = 0 \qquad a < r < b \\ &T = \text{const or } -k_1 \frac{\partial T}{\partial z} = \frac{Q}{\pi a^2} \qquad 0 < r < a \end{aligned}\right\} z = 0$$

$$\frac{\partial T}{\partial r} = 0 \qquad r = b$$

and

$$-k_2 \frac{\partial T}{\partial z} = \frac{Q}{\pi b^2} \qquad z \to \infty$$

where Q is the heat flow rate through the channel and k_1 thermal conductivity of the plating material ($0 < z < \delta$).

In order to get the true temperature distribution in the composite cylinder, one has to consider separately the two regions, equating the temperature and the heat flux at all points over $0 < r < b$, $z = \delta$. However, since we are looking here only for the value of thermal contact resistance, rather than the exact temperature distribution, an attempt will be made to estimate the total resistance by considering only the resistances in the two separate regions as follows.

It will be assumed that the contribution to the total constriction resistance due to the constriction occurring in the plated region (R_1) could be represented by an equivalent constriction through the disk of plating material ($0 < z < \delta$), see Fig. 2(b), from πa^2 area at $z = 0$ to πb_1^2 area at $z = \delta$, with constant heat flux conditions there. Physically, πb_1^2 represents the area at $z = \delta$ which is effectively used to transfer the heat from the plated layer to the base (see Fig. 2). How much of the plated layer is used effectively depends, of course, on all geometric parameters (δ/a, a/b) as well as the conductivity ratio between the two regions. Initially, the value for b_1 is unknown. The analytical solution for this part of the problem is given in the Appendix. When constant heat flux is imposed over the contact area πa^2 at $z = 0$, the thermal contact resistance for the plate can be expressed as

$$R_1 = \frac{4}{\pi k_1 a} \phi' \left(\frac{\delta}{a}, \frac{a}{b_1} \right) \tag{3}$$

An analytical expression for ϕ' is presented in the Appendix and also given graphically as a function of a/b_1 in Fig. 3 for different values of parameter δ/a.

For conditions of constant temperature over contact area (πa^2), ϕ' in the expression (3) should be replaced with ϕ. The expression for ϕ is given in the Appendix and also presented in Fig. 4.

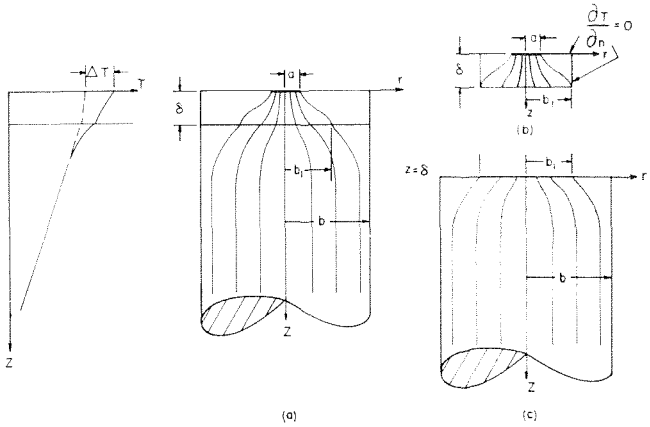

Fig. 2 Model of elemental heat channel for plated contact

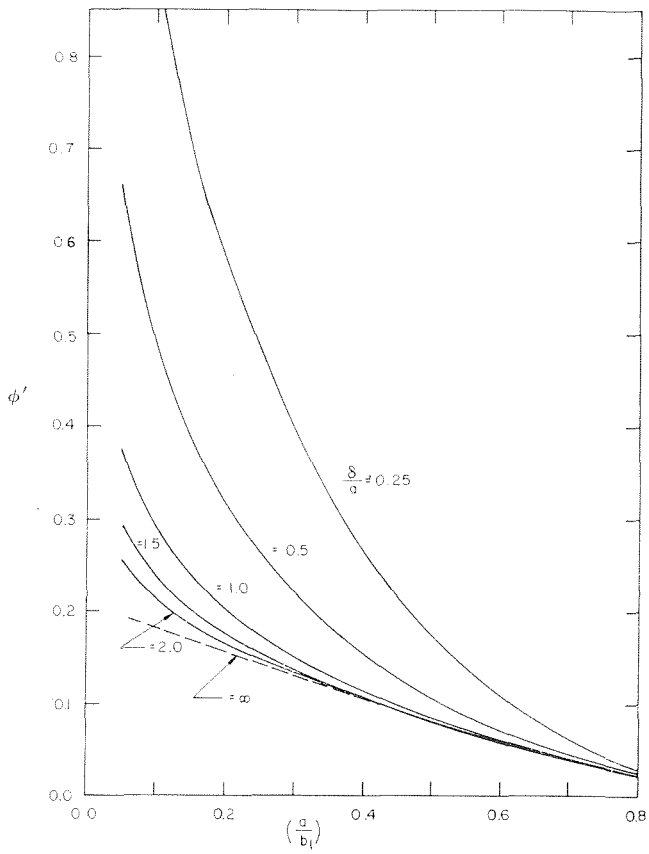

Fig. 3 Contact resistance factor for plate. Uniform heat flux at source spot.

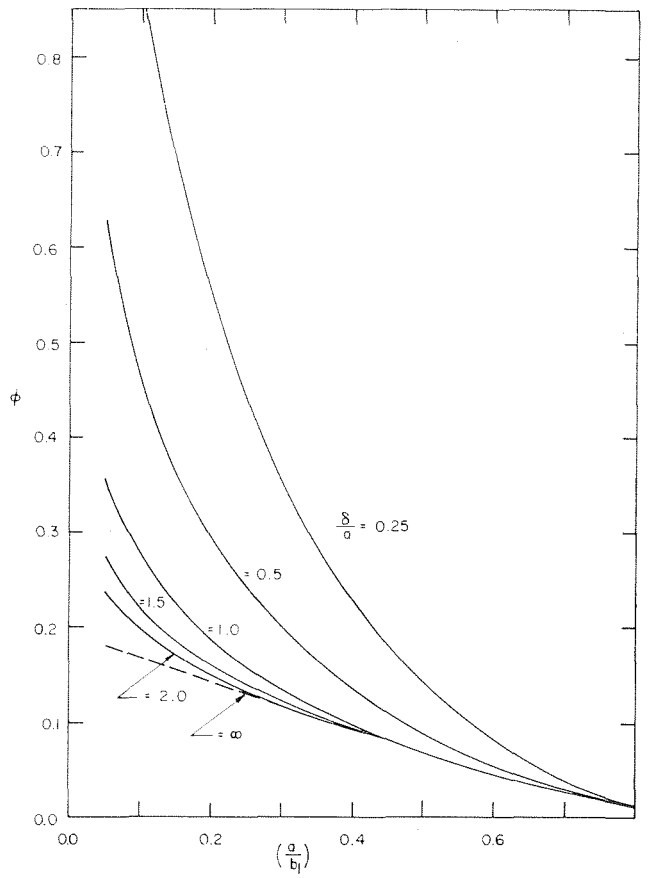

Fig. 4 Contact resistance factor for plate. Constant temperature at source spot.

The constriction resistance in the base material (R_2) will be represented by the resistance caused by the constriction of heat flow from πb_1^2 area at $z = \delta$, where the uniform heat flux condition exists, to πb^2 area far away from $z = \delta$, where the isothermal surfaces are parallel with the interface. This resistance, then, can be written, using equation (1), as

$$R_2 = \frac{1}{4k_2 b_1} \psi\left(\frac{b_1}{b}\right) \tag{4}$$

where k_2 is thermal conductivity of the base material. The exact expression for ψ is presented in reference [8] and can be approximated with relation (2) ($C = 32/3\pi^2$) where a in equation (2) should be replaced with b_1.

The combined resistance for the disk and base material, as considered in the model, is given, then, by the following expression:

$$R' = R_1 + R_2 = \frac{1}{4k_2 a}\left[\frac{16}{\pi}\frac{k_2}{k_1}\phi\left(\frac{\delta}{a}, \frac{a}{b_1}\right) + \frac{a}{b_1}\psi\left(\frac{b_1}{b}\right)\right] \tag{5}$$

If constant heat flux is prescribed over the contact area, ϕ in equation (5) should be replaced with ϕ'.

It should be noted that equation (5) does not represent the exact solution to the problem at hand, since the condition of equality of the temperatures of the plating and base material was not satisfied for every point across their junction plane ($z = \delta$). Rather, the space-averaged temperature (in the region $0 < r < b_1$) of the two materials was kept equal.

(b) Evaluation of the Overall Thermal Contact Resistance. Expression (5) still does not represent the total resistance of the plated elemental channel (Fig. 2(a)); the value for b_1 is not known. For fixed a, k_1, k_2, and b, relation (5) will yield different values for R' for different b_1. It can be seen from Fig. 4 that the first term on the right-hand side of equation (5) increases with increasing b_1. The second term will decrease with increasing b_1 (see equation (2)). To determine the value of b_1 which one should use in expression (5) to approximate the total resistance of the plated channel, we recall that of all possible resistances which can be obtained by an artificial choice of flow line distributions, the actual resistance (without changing the boundary conditions) would be the one which gives the minimum resistance. Hence, for a fixed geometry and given thermal conductivities, the choice for $b_1 (a \leq b_1 \leq b)$ for which R' has a minimum will approximate the actual constriction resistance of the channel. It is expected that $R'_{\min}$ (denoted further with R_1) will approximate the constriction resistance for the channel, giving an upper bound for the resistance, since the model used (Fig. 2(b)) imposed more restriction of flow path distribution than the actual channel (Fig. 2(a)).

The relative reduction of the thermal contact resistance, accomplished by plating, may be approximated then (from (5) and (1)) as:

$$\frac{R_\delta}{R} = \frac{\left[\frac{16}{\pi}\frac{k_2}{k_1}\phi\left(\frac{\delta}{a}, \frac{a}{b_1}\right) + \frac{a}{b_1}\psi\left(\frac{b_1}{b}\right)\right]_{\min}}{\psi\left(\frac{a}{b}\right)} \equiv F\left(\frac{a}{b}, \frac{\delta}{a}, \frac{k_1}{k_2}\right) \tag{6}$$

For constant heat flux over the contact area, ϕ in (6) should be replaced with ϕ'.

For each particular geometry $\left(\frac{a}{b} \text{ and } \frac{\delta}{a}\right)$ and the conductivity ratio $\left(\frac{k_1}{k_2}\right)$ the minimization of the term in the brackets in equation (6) were carried out on an IBM computer 1130. The re-

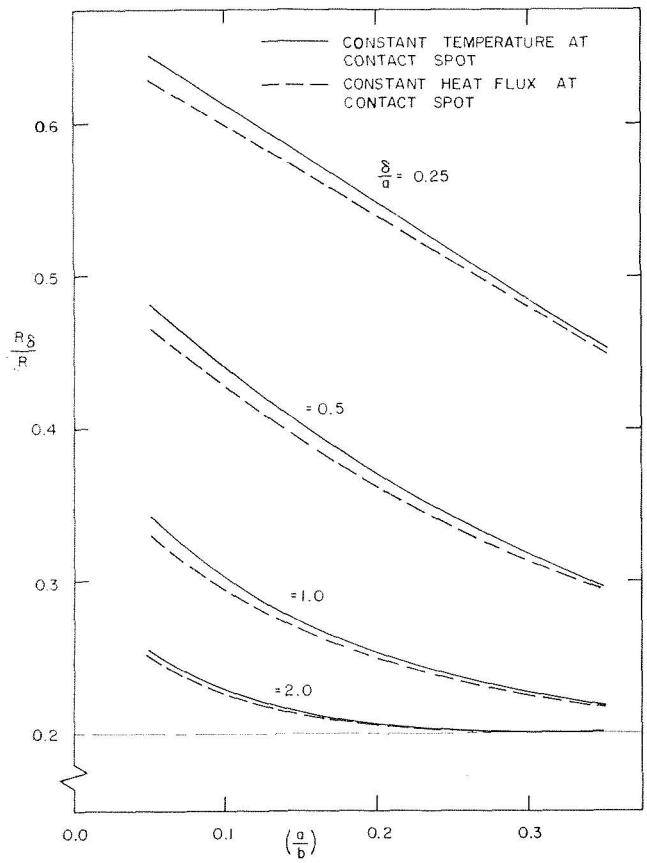

Fig. 5 $\frac{R_\delta}{R}$ versus $\left(\frac{a}{b}\right)$ with $\frac{K_1}{K_2} = 5.0$

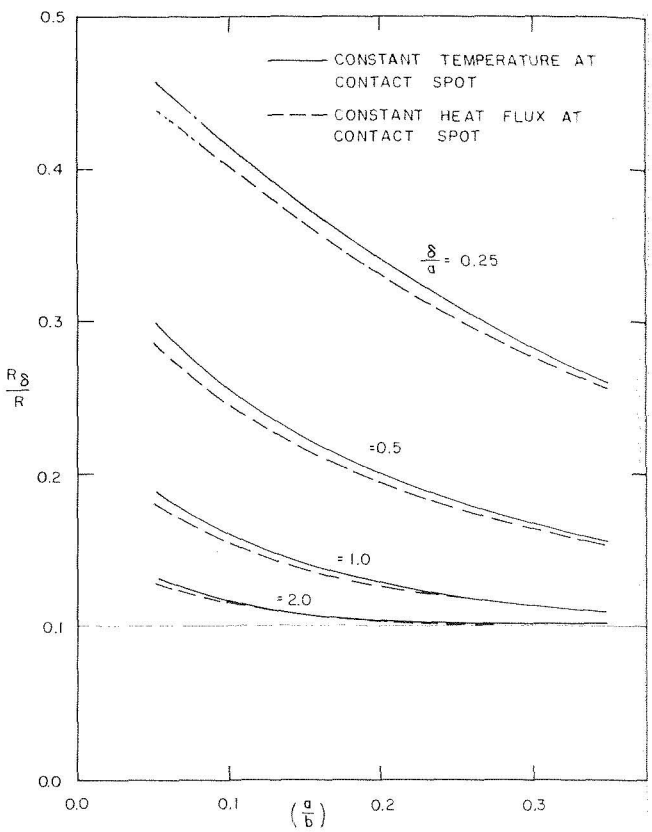

Fig. 6 $\frac{R_\delta}{R}$ versus $\left(\frac{a}{b}\right)$ with $\frac{K_1}{K_2} = 10.0$

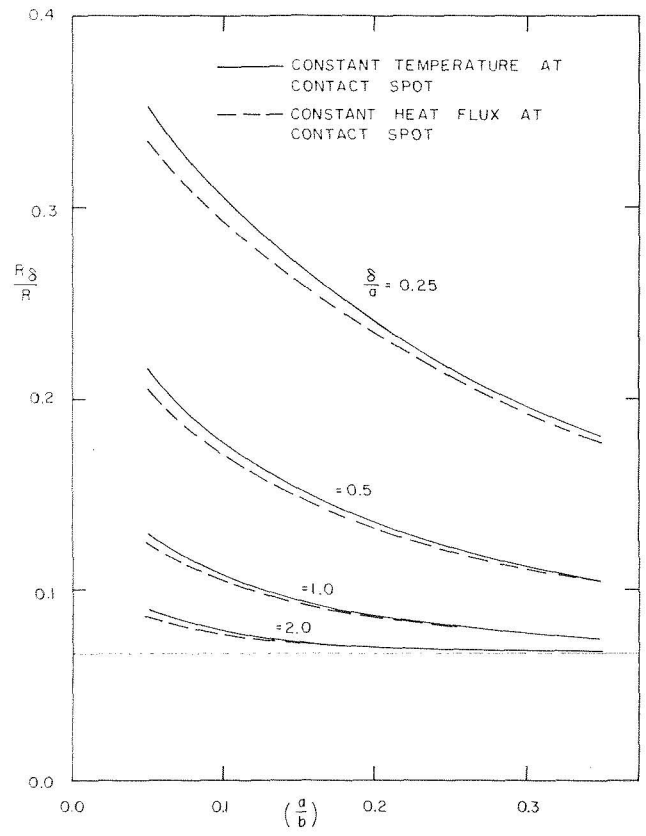

Fig. 7 $\frac{R_\delta}{R}$ versus $\left(\frac{a}{b}\right)$ with $\frac{K_1}{K_2} = 15.0$

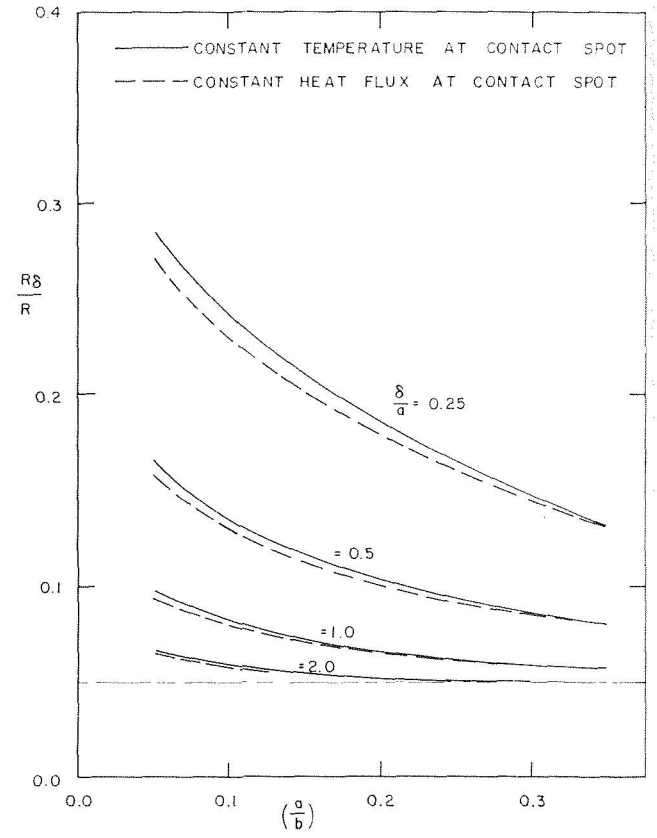

Fig. 8 $\frac{R_\delta}{R}$ versus $\left(\frac{a}{b}\right)$ with $\frac{K_1}{K_2} = 20.0$

sulting values for R_δ/R as a function of $\left(\frac{a}{b}\right)$ with $\frac{\delta}{a}$ as a parameter, are presented in Figs. 5 to 8 for four different values of $\frac{k_1}{k_2}$ (from 5 to 20 in increments of 5). Both types of boundary conditions over the contact area are presented. As it can be seen, results for the two different conditions considered are about identical.

The effect of plating (reduction in the contact resistance) increases with increasing δ/a, a/b, and k_1/k_2. The limiting value for R_δ/R is k_2/k_1 (occurring for sufficiently thick plating). According to the results presented in the figures, considerable reduction can be accomplished with relatively thin plating.

The results, we should like to emphasize again, are not based on exact solutions but rather on the model which introduces some equivalent area of engagement, πb_1^2 (see Fig. 2). To check the validity of our model, a series of experiments were carried out on specimens which represented one half of a plated elemental channel.

Experimental Results and Their Comparison With Prediction

Specimens which represent one half of a plated channel are made in the following way: A 3-in. dia by 3-in. long stainless steel cylinder (SS 303 type) was soldered to a 3-in. dia by 2.5-in. long copper cylinder (B 133 type) over one of their bases which had previously been made optically flat (in order to minimize the effect of soldering). The thermal resistance across the soldered interface was then investigated in an experiment where temperature gradients, in one dimensional heat flow, were measured in both copper and stainless steel cylinders. No measurable resistance across the soldered interface was detected. Following the soldering resistance test, the copper part of the composed cylinder was machined to produce a specimen of the type presented in Fig. 9(*a*). In this way the plating material and smaller cylinder (of radius a) are made of the same piece and thus the only constriction resistance in the system was the constriction resistance occurring partially in the plated region of the larger cylinder (of radius b) and partially in the base material. One half of a plated channel then is represented by the large composite cylinder. The role of the small cylinder is to supply heat over πa^2 area. It is known that the value for constriction resistance is not very sensitive to a choice of the mode of heat supply over the contact area (see for example [8], or compare constant C's in equation (2)). Consequently, one should not expect that the way heat was supplied in our model (through the copper cylinder of radius a) would effect applicability of the experimental results. The above was experimentally verified by measuring the thermal contact resistance for a specimen which was made of one material

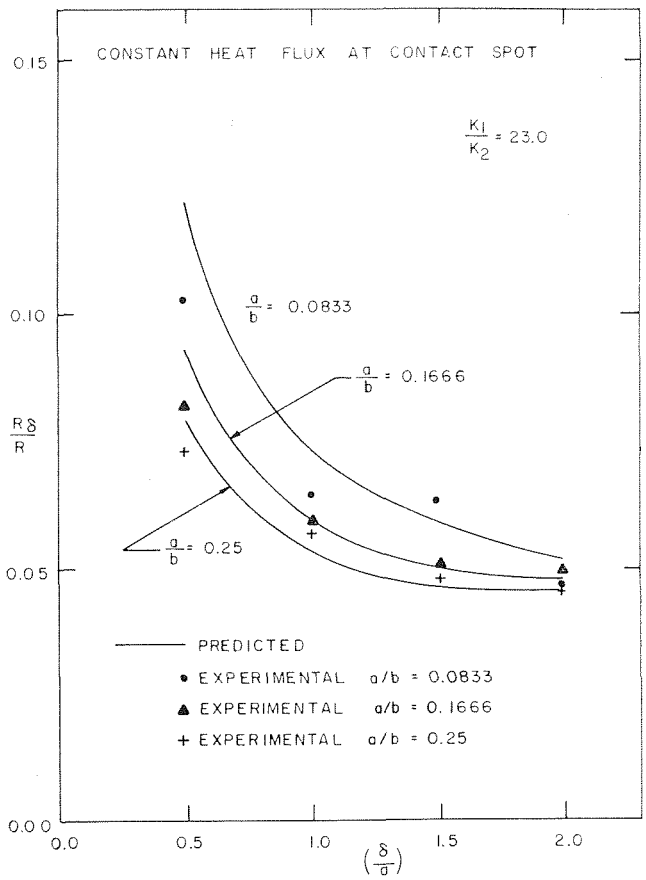

Fig. 10 Results for $\frac{R_\delta}{R}\left(\frac{\delta}{a}, \frac{a}{b}\right)$

(stainlesss steel) and had the same geometry as the plated specimens (Fig. 9(*a*)). The recorded value agreed very well with the prediction obtained from equations (1) and (2) with choice for C corresponding to constant heat flux conditions over πa^2 area.

The experiments on a plated contact were carried out for three different values of parameter a/b (0.0833; 0.1666; 0.25) and four values of δ/a (0.5; 0.1; 1.5; 2.0) for each value of a/b. The conductivity ratio (k_1/k_2) was 23.

The locations of 28 gauge chromel-alumel thermocouples (used in the tests) are indicated in Fig. 9. The thermocouple beads were placed at the center line of the specimens (through holes of 0.062-in. dia) with the exception of the specimen with the smallest dia of copper cylinder (0.25 in.) where holes in the copper

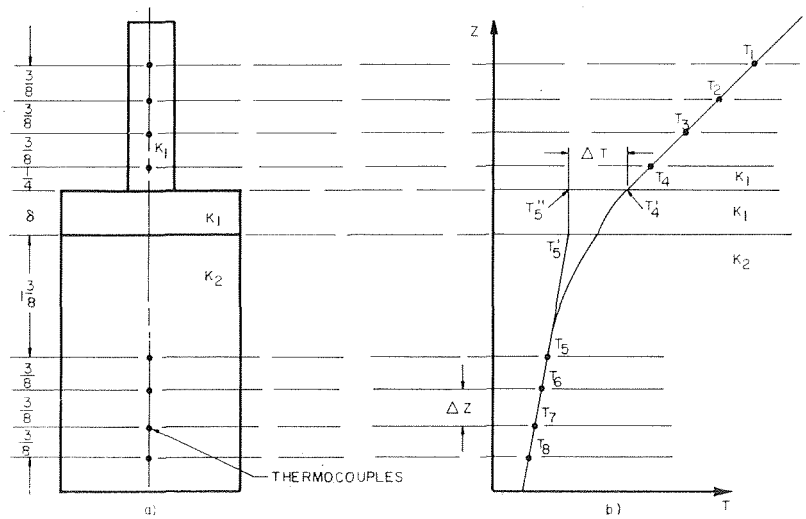

Fig. 9 Temperature distribution in plated contact model

part of the specimen were $^1/_{32}$ in. in depth (in order to avoid significant disturbance of heat flow, which would be produced by drilling the holes to the centerline).

The test specimens were employed as heat meters. From the measured temperature distribution, Q was calculated for both cylinders (stainless steel and copper). The agreement between the two values was within 1 percent.

In Fig. 9(b) it is shown how the temperature drop (ΔT) due to the constriction was calculated. T_5' was obtained by the extrapolation from readings of thermocouples five to eight. T_4' was found similarly from thermocouples one to four. In the process of extrapolation, temperature dependence of the respective thermal conductivities was considered (using information from reference [12]).

Temperature T_5'' was obtained from known thermal conductivity k_1, heat flow rate Q, and temperature T_5'.

In all the tests performed, the direction of the heat flow was from copper (smaller cylinder) to stainless steel. The average ΔT encountered in the experiments was around 20 deg F (minimum 6 deg F, recorded only once, and maximum 42 deg F). The average mean interface temperature was around 170 deg F (minimum 94 deg F, maximum 278 deg F). A detailed description of experimental procedure and tables with measured quantities for each run can be found in reference [13].

A comparison between experimental results and the prediction calculated from equation (5), using constant heat flux conditions over the contact area, is presented in Fig. 10. As can be seen from the figure, the agreement is good. The maximum discrepancy was about 20 percent, occurring at low values of δ/a. In this range, the experiments show even higher reduction in the constriction resistance than predicted. This trend was expected since, as it was pointed out earlier, the actual resistance should be smaller than or equal to the resistance caused by any artificial choice of heat flow path.

Application

Based on the good agreement between the theoretical prediction and experimental results demonstrated in the previous section, the acceptance of the model and the conclusions achieved seems to be warranted. From this position, we will briefly describe applicability (and limitations) of the presented results:

We consider the effect of plating on one half of an elemental heat channel. Consequently, when real contact is to be considered, contact resistance for both halves should be taken into account separately.

Thus, for a whole channel: $R = R_{\mathrm{I}} + R_{\mathrm{II}}$ where R_{I} and R_{II} are the respective resistances for the two halves. Generally, they would be different.

For good results one has, for the same base material of low conductivity, to plate both sides of the interface. The procedure for evaluating the thermal contact resistance for nominally flat, plated surfaces in contact is as follows:

From assumption of plastic deformation of surface irregularities one can determine the geometric factor (a/b) as:

$$\left(\frac{a}{b}\right) = \left(\frac{P}{H_1}\right)^{1/2} \tag{7}$$

where P is the interface pressure and H_1, microhardness of the softer material at the interface.

Estimate the number of contacts per unit area. The procedure, based on the assumption of normal distribution of surface irregularity, is outlined in reference [7].

Assuming that all contacts are of equal size, one gets the contact resistance per unit area:

$$\bar{R} = \frac{R_{\mathrm{I}}}{n} + \frac{R_{\mathrm{II}}}{n} \tag{8}$$

Since $n = \dfrac{1}{\pi b^2}$ (by definition), then from (7):

$$a = \left(\frac{P}{n\pi H_1}\right)^{1/2} \tag{9}$$

Finally, from (6) and (7):

$$\bar{R} = \frac{\psi}{4an}\left[\frac{1}{(k_2)_{\mathrm{I}}}F_{\mathrm{I}} + \frac{1}{(k_2)_{\mathrm{II}}}F_{\mathrm{II}}\right] \tag{10}$$

where $\left(\dfrac{a}{b}\right)$ follows from (8) and ψ, for known $\left(\dfrac{a}{b}\right)$ from Fig. 2.

From calculated a (equation (10)) and known δ_{I} and δ_{II}, as well as $(k_1/k_2)_{\mathrm{I}}$ and $(k_1/k_2)_{\mathrm{II}}$, one can evaluate F_{I} and F_{II} from Figs. 6 to 9, for conditions of constant temperature over the contact area, using extrapolation if necessary.

The foregoing procedure applies only for flat surfaces in contact, where contact size (a) is sufficiently small so that reasonable plating $\left(\text{with } \dfrac{\delta}{a} \text{ of order } 0.25\right)$ would have significant effect on the contact resistance. In the case of wavy surfaces in contact, the radius of the contour area (which contains microscopic contacts) is much too large to be affected by a plating. Thus, we may conclude that a favorable effect of plating could be achieved only for contacts where the microscopic part of the interface resistance is predominant.

Conclusions

Plating of conducting metallic surfaces in contact, in addition to changing the deformation parameters, provides a layer where part of the heat flow line constriction will take place. The latter effect, for the case of a layer of higher thermal conductivity than the plated material, was considered in this work.

Based on the adapted model, in which the contact resistance is divided into contributions from the plated and base region separately, a theoretical prediction for a plated contact is developed. The result, for different values of pertinent parameters, is presented graphically. The experimental measurements on a model of a plated contact agreed very well with the predictions.

For nominally flat surfaces, or more generally, when microscopic constriction is the predominant resistance in the system, the effect of plating of contacting surfaces on reduction of the thermal contact resistance could be very significant—in some cases producing an order of magnitude reduction in the resistance.

References

1 Weber, H., "Ueber Bessel'sche Functionen und ihre Anwendung auf die Theorie der elektrischen Ströme," *Crelle*, Bd. 74, 1873, p. 75.

2 Holm, R., *Electrical Contacts Handbook*, 3rd Ed., Springer Verlag, Berlin, 1958.

3 Cetinkale, T. N., and Fishenden, M., "Thermal Conductance of Metal Surfaces in Contact," International Conference of Heat Transfer, Institute of Mechanical Engineers, London, 1951.

4 Fenech, H., and Rohsenow, W. M., "Prediction of Thermal Conductance of Metallic Surfaces in Contact," JOURNAL OF HEAT TRANSFER, TRANS. ASME, Series C, Vol. 85, No. 1, Feb. 1963, p. 15.

5 Laming, L. C., "Thermal Conductance of Machined Metal Contacts," ASME International Heat Transfer Conference, Boulder, Colorado, Paper No. 8, 1961.

6 Clausing, A. M., and Chao, B. T., "Thermal Contact Resistance in a Vacuum Environment," University of Illinois, Report ME-TN-242-1, Aug. 1963.

7 Cooper, M. G., Mikic, B. B., and Yovanovich, M. M., "Thermal Contact Conductance," to appear in *International Journal Heat Mass Transfer*, 1969.

8 Mikic, B. B., and Rohsenow, W. M., "Thermal Contact Resistance," M.I.T. Report No. 4542-41, Sept. 1966.

9 Greenwood, J. A., "Constriction Resistance and the Real Area of Contact," *British Journal of Applied Physics*, Vol. 17, 1966.

10 Fried, E., "Study of Interface Thermal Contact Conduc-

tance," General Electric, Summary Report No. 65SD4394, March 1965.
11 Weills, N. D., and Ryder, E. A., "Thermal Resistance Measurements of Joints Formed Between Stationary Metal Surfaces," TRANS. ASME, Vol. 71, No. 3, 1949.
12 Taylor, L., ed., *Metals Handbook*, Vol. I, p. 422, American Society for Metals, Ohio, 1961.
13 Carnasciali, G., "Effect of Plating Upon the Thermal Contact Resistance," MS thesis, M.I.T., Mechanical Engineering Dept., Jan. 1968.

APPENDIX

Contact Resistance in Plated Region

The model for a plated region is given in Fig. 2(*b*). It consists of a disk of radius b_1 and thickness δ. At the top of the disk ($z = 0$), over the area πa^2, heat is supplied. At $z = \delta$, heat flux is uniformly distributed over the area πb_1^2.

For the case when *heat is uniformly supplied* over the πa^2 area the following relations determine the problem.

$$\nabla^2 T = 0 \tag{A1}$$

$$-k\frac{\partial T}{\partial z} = \frac{Q}{\pi a^2} \qquad 0 \leqslant r < a \qquad \text{at } z = 0 \tag{A2}$$

$$-k\frac{\partial T}{\partial z} = 0 \qquad a < r \leqslant b_1$$

$$-k\frac{\partial T}{\partial z} = \frac{Q}{\pi b_1^2} \qquad \text{at } z = \delta \tag{A3}$$

$$-k\frac{\partial T}{\partial r} = 0 \qquad \text{at } r = b_1 \tag{A4}$$

$$-k\frac{\partial T}{\partial r} = 0 \qquad \text{at } r = 0 \tag{A5}$$

The solution of (A1) which satisfies (A3) and (A5) can be written as:

$$T = C_0 + \frac{Q}{\pi k b_1^2}(\delta - z) + \sum_{n=1}^{\infty} C_n \cosh\{\beta_n(\delta - z)\} J_0(\beta_n r) \tag{A6}$$

where eigenvalues, as a consequence of (A4), are the roots of:

$$J_1(\beta_n b_1) = 0 \tag{A7}$$

The boundary condition at $z = 0$ (A2) can be expressed in the form of Fourier Bessel series as:

$$-k\left(\frac{\partial T}{\partial z}\right)_{z=0} = +\frac{Q}{\pi b_1^2} + \frac{2Q}{\pi a}\sum_{n=1}^{\infty}\frac{J_1(\beta_n a)J_0(\beta_n r)}{(\beta_n b_1)b_1 J_0^2(\beta_n b_1)} \tag{A8}$$

From (A8) and (A6)

$$C_n = \frac{2Q}{\pi k a}\frac{J_1(\beta_n a)}{(\beta_n b_1)^2 J_0^2(\beta_n b_1)\sinh(\beta_n \delta)} \tag{A9}$$

With (A9), (A6) changes into

$$T = C_0 + \frac{Q}{\pi k b_1^2}(\delta - z) + \frac{2Q}{\pi k a}\sum_{1}^{\infty}\frac{\cosh\beta_n(\delta - z)J_1(\beta_n a)J_0(\beta_n r)}{\sinh(\beta_n\delta)(\beta_n b_1)^2 J_0^2(\beta_n b_1)} \tag{A10}$$

C_0, of course, cannot be found with the type of boundary conditions specified here. However, it readily follows from (A10) and (A7) that C_0 is the average temperature at $z = \delta$.

The thermal contact resistance is specified with

$$R = \frac{T_{\mathrm{I}} - T_{\mathrm{II}}}{Q} - \frac{\delta}{\pi k b_1^2} \tag{A11}$$

where

$$T_{\mathrm{I}} \equiv \frac{2\pi}{\pi a^2}\int_0^a T_{z=0}\, r dr$$

and

$$T_{\mathrm{II}} \equiv \frac{2\pi}{\pi b_1^2}\int_0^{b_1} T_{z=\delta}\, r dr$$

T_{I} and T_{II} are the average temperatures over πa^2 area at $z = \delta$, respectively.

From the foregoing one easily calculates the contact resistance in the form:

$$R = \frac{4}{\pi k a}\left(\frac{b_1}{a}\right)\sum_{n=1}^{\infty}\frac{J_1^2(\beta_n a)}{\tanh(\beta_n\delta)(\beta_n b_1)^3 J_0^2(\beta_n b_1)} \equiv \frac{4}{\pi k a}\phi'\left\{\frac{a}{b_1}, \frac{\delta}{a}\right\} \tag{A12}$$

$\phi'\left\{\frac{b_1}{a}, \frac{\delta}{a}\right\}$ is plotted in Fig. 3 for different values of parameters $\frac{a}{b}$ and $\frac{\delta}{a}$.

In the case when over the πa^2 area *constant temperature* is specified, boundary condition (A2) should be replaced with

$$T = T_0 \qquad 0 \leqslant r < a$$

$$-k\frac{\partial T}{\partial z} = 0 \qquad a < r \leqslant b_1$$

For small values of $\frac{a}{b_1}$ one can approximate the above conditions [1] with:

$$-k\frac{\partial T}{\partial z} = \frac{Q}{2\pi a(a^2 - r^2)^{1/2}} \qquad 0 \leqslant r < a \qquad z = 0 \tag{A12a}$$

$$-k\frac{\partial T}{\partial z} = 0 \qquad a < r \leqslant b_1$$

Then from (A1), (A2*a*), (A3), (A4), (A5), and (A11) one can calculate the thermal contact resistance for this case as

$$R = \frac{4}{\pi k a}\frac{1}{2}\left(\frac{b_1}{a}\right)\sum_{n=0}^{\infty}\frac{\sin(\beta_n a)J_1(\beta_n a)}{\tanh(\beta_n\delta)(\beta_n b_1)^3 J_0^2(\beta_n b_1)} \equiv \frac{4}{\pi k a}\cdot\phi\left\{\frac{a}{b_1}, \frac{\delta}{a}\right\} \tag{A13}$$

ϕ is plotted in Fig. 4.

tance," General Electric, Summary Report No. 65SD4394, March 1965.
11 Weills, N. D., and Ryder, E. A., "Thermal Resistance Measurements of Joints Formed Between Stationary Metal Surfaces," TRANS. ASME, Vol. 71, No. 3, 1949.
12 Taylor, L., ed., *Metals Handbook*, Vol. I, p. 422, American Society for Metals, Ohio, 1961.
13 Carnasciali, G., "Effect of Plating Upon the Thermal Contact Resistance," MS thesis, M.I.T., Mechanical Engineering Dept., Jan. 1968.

APPENDIX

Contact Resistance in Plated Region

The model for a plated region is given in Fig. 2(*b*). It consists of a disk of radius b_1 and thickness δ. At the top of the disk ($z = 0$), over the area πa^2, heat is supplied. At $z = \delta$, heat flux is uniformly distributed over the area πb_1^2.

For the case when *heat is uniformly supplied* over the πa^2 area the following relations determine the problem.

$$\nabla^2 T = 0 \tag{A1}$$

$$-k\frac{\partial T}{\partial z} = \frac{Q}{\pi a^2} \qquad 0 \leqslant r < a \qquad \text{at } z = 0 \tag{A2}$$

$$-k\frac{\partial T}{\partial z} = 0 \qquad a < r \leqslant b_1 \qquad \text{at } z = 0 \tag{A2}$$

$$-k\frac{\partial T}{\partial z} = \frac{Q}{\pi b_1^2} \qquad \text{at } z = \delta \tag{A3}$$

$$-k\frac{\partial T}{\partial r} = 0 \qquad \text{at } r = b_1 \tag{A4}$$

$$-k\frac{\partial T}{\partial r} = 0 \qquad \text{at } r = 0 \tag{A5}$$

The solution of (A1) which satisfies (A3) and (A5) can be written as:

$$T = C_0 + \frac{Q}{\pi k b_1^2}(\delta - z) + \sum_{n=1}^{\infty} C_n \cosh\{\beta_n(\delta - z)\} J_0(\beta_n r) \tag{A6}$$

where eigenvalues, as a consequence of (A4), are the roots of:

$$J_1(\beta_n b_1) = 0 \tag{A7}$$

The boundary condition at $z = 0$ (A2) can be expressed in the form of Fourier Bessel series as:

$$-k\left(\frac{\partial T}{\partial z}\right)_{z=0} = +\frac{Q}{\pi b_1^2} + \frac{2Q}{\pi a}\sum_{n=1}^{\infty}\frac{J_1(\beta_n a)J_0(\beta_n r)}{(\beta_n b_1)b_1 J_0^2(\beta_n b_1)} \tag{A8}$$

From (A8) and (A6)

$$C_n = \frac{2Q}{\pi k a}\frac{J_1(\beta_n a)}{(\beta_n b_1)^2 J_0^2(\beta_n b_1)\sinh(\beta_n \delta)} \tag{A9}$$

With (A9), (A6) changes into

$$T = C_0 + \frac{Q}{\pi k b_1^2}(\delta - z) + \frac{2Q}{\pi k a}\sum_{1}^{\infty}\frac{\cosh\beta_n(\delta - z)J_1(\beta_n a)J_0(\beta_n r)}{\sinh(\beta_n\delta)(\beta_n b_1)^2 J_0^2(\beta_n b_1)} \tag{A10}$$

C_0, of course, cannot be found with the type of boundary conditions specified here. However, it readily follows from (A10) and (A7) that C_0 is the average temperature at $z = \delta$.

The thermal contact resistance is specified with

$$R = \frac{T_I - T_{II}}{Q} - \frac{\delta}{\pi k b_1^2} \tag{A11}$$

where

$$T_I \equiv \frac{2\pi}{\pi a^2}\int_0^a T_{z=0}\, rdr$$

and

$$T_{II} \equiv \frac{2\pi}{\pi b_1^2}\int_0^{b_1} T_{z=\delta}\, rdr$$

T_I and T_{II} are the average temperatures over πa^2 area at $z = \delta$, respectively.

From the foregoing one easily calculates the contact resistance in the form:

$$R = \frac{4}{\pi k a}\left(\frac{b_1}{a}\right)\sum_{n=1}^{\infty}\frac{J_1^2(\beta_n a)}{\tanh(\beta_n\delta)(\beta_n b_1)^3 J_0^2(\beta_n b_1)} \equiv \frac{4}{\pi k a}\phi'\left\{\frac{a}{b_1}, \frac{\delta}{a}\right\} \tag{A12}$$

$\phi'\left\{\frac{b_1}{a}, \frac{\delta}{a}\right\}$ is plotted in Fig. 3 for different values of parameters $\frac{a}{b}$ and $\frac{\delta}{a}$.

In the case when over the πa^2 area *constant temperature* is specified, boundary condition (A2) should be replaced with

$$T = T_0 \qquad 0 \leqslant r < a$$

$$-k\frac{\partial T}{\partial z} = 0 \qquad a < r \leqslant b_1$$

For small values of $\frac{a}{b_1}$ one can approximate the above conditions [1] with:

$$-k\frac{\partial T}{\partial z} = \frac{Q}{2\pi a(a^2 - r^2)^{1/2}} \qquad 0 \leqslant r < a \qquad z = 0 \tag{A12a}$$

$$-k\frac{\partial T}{\partial z} = 0 \qquad a < r \leqslant b_1 \qquad z = 0 \tag{A12a}$$

Then from (A1), (A2*a*), (A3), (A4), (A5), and (A11) one can calculate the thermal contact resistance for this case as

$$R = \frac{4}{\pi k a}\frac{1}{2}\left(\frac{b_1}{a}\right)\sum_{n=0}^{\infty}\frac{\sin(\beta_n a)J_1(\beta_n a)}{\tanh(\beta_n\delta)(\beta_n b_1)^3 J_0^2(\beta_n b_1)} \equiv \frac{4}{\pi k a}\cdot\phi\left\{\frac{a}{b_1}, \frac{\delta}{a}\right\} \tag{A13}$$

ϕ is plotted in Fig. 4.

DISCUSSION

C. J. Moore, Jr.[2]

The authors have presented results which provide a means of making approximate calculations on the effect of plating on thermal contact resistance. The basic idea being that the addition of a layer of a good thermal conductor on the contact surface should spread the flux more rapidly and thereby help alleviate the constriction resistance. The development of the analytical expressions is straightforward and requires no further comment. However, a fundamental question of procedure appears to be in order.

[2] Associate Professor of Mechanical and Aerospace Engineering, North Carolina State University, Raleigh, N. C.

It seems neither necessary nor prudent to run the experiments described in the paper in order to obtain data with which to compare the approximate analytical results. The problem analyzed is one of pure thermal diffusion. In the experimental model care was taken to make it also a pure diffusion model. Thus the experimental results amount to a test of diffusion theory. In this type of experimental work where one has to calculate slopes, extrapolate measured temperature profiles, etc., inaccuracies of the order of 10–20 percent are common. In view of this it seems not only unnecessary to use experimental results but, indeed, unfair to the analytical work to compare it so.

Since the problem under study is one of pure diffusion it would seem more appropriate to compare the approximate analytical results with results obtained from an accurate numerical solution. Well-conditioned finite-difference computer codes for diffusion problems of this type can be used to obtain results to any practical degree of accuracy desired. In this way the usefulness of the approximations could be better judged.

Authors' Closure

Professor Moore's suggestion concerning the use of a finite-difference method for a verification of the approximate analytical results was a very good alternative. However, a possible inaccuracy of the experimental method (used in the work) of the order of 10–20 percent is still an order of magnitude lower than the effects we were looking for. For this reason, it was thought that the results from the method are sufficiently accurate for our purpose.

A finite-difference approach which would give better accuracy and cover the same range of variables as was accomplished by the experiments was considered to be less economical under the present circumstances.

P. S. SCHMIDT
Assistant Professor of Mechanical Engineering, University of Texas at Austin, Austin, Texas

G. LEPPERT
Professor, Mechanical Engineering Department, Clarkson College of Technology, Potsdam, N. Y. Mem. ASME

Heat Transfer From Plasma in Tube Flow

Heat transfer data are reported for partially ionized argon flowing in a water-cooled circular tube, $^1/_2$ in. in dia. Experiments were run with initial mixed-mean temperatures up to 21,000 deg R at Reynolds numbers from 140–527 based on equilibrium properties evaluated at the entrance mixed-mean temperature. Measured plasma flow Nusselt numbers computed on an enthalpy basis correlate well with low temperature, constant property results after the first 5–10 diameters of the tube entrance region; closer to the entrance, Nusselt numbers were about 30 percent higher than constant property entrance region predictions. The tendency of the data to approach the constant property solution rapidly was predicted by a laminar finite-difference analysis for plasma flow published earlier [1].[1] The analysis was modified for the present study to improve its accuracy. The finite-difference theory under predicts the heat transfer in the first few tube diameters; two possible reasons for this discrepancy are the poor resolution in the inlet enthalpy profiles near the tube wall and nonequilibrium between electrons and heavy particles in this region.

Introduction

THE design of devices requiring containment of a plasma, such as nuclear rockets, gaseous-fueled reactors, and magnetogasdynamic generators, demands accurate information for prediction of heat transfer between working fluid and the solid structure surrounding it. This information becomes particularly critical when desirable operating temperatures for these devices may considerably exceed the melting temperature of even the exotic metals.

The flow of a partially ionized gas in a channel is characterized by the predominance of several effects which are of lesser importance at temperatures below the ionization level. Variations in thermodynamic and transport properties between tube centerline and wall may reach order of magnitude proportions; radial convection, usually neglected in heat transfer at relatively lower temperatures, may be appreciable due to large radial density gradients; and radiant energy fluxes comparable in magnitude to the convective heat flux may exist because of ion-electron recombination and high energy electronic excitation.

Measurements of variable property heat transfer in tubes by Davenport and Leppert [2] and by Kays and Nicoll [3] indicate no significant departure from constant property results for laminar flows below 2,300 deg F. The same is true for turbulent flow experiments of Humble, et al. [4] and Kays [5] for wall-to-bulk temperature ratios from 1.0–0.38. Massier, Back, and Roschke [6] have measured heat transfer in argon at temperatures up to 13,900 deg R and found that, although temperature and velocity profiles in the boundary layer differ markedly from the constant properties case, gross heat transfer behavior is essentially unchanged.

Heat transfer measurements for helium, nitrogen, and argon flowing in water-cooled, circular tubes have been reported by Johnson, Choksi, and Eubank [7] and by Skrivan and von Jaskowsky [8]. In these investigations, maximum entering temperatures for the argon tests were less than 7,000 deg K, which is well below the temperature at which ionization effects become significant. Also, in the study of Johnson, et al., the flow under-

[1] Numbers in brackets designate References at end of paper.

Contributed by the Heat Transfer Division and presented at the Winter Annual Meeting, Los Angeles, Calif., November 16–20, 1970, of THE AMERICAN SOCIETY OF MECHANICAL ENGINEERS. Manuscript received by the Heat Transfer Division, September 11, 1969; revised manuscript received March 9, 1970. Paper No. 69-WA/HT-54.

Nomenclature

c_p = specific heat
D = tube diameter
G = mass flow per unit cross-sectional area
h = enthalpy
k = thermal conductivity
N_{Nu} = Nusselt number, $\dot{q}''D/(k/c_p)_m(h_m - h_w)$
N_{Pr} = Prandtl number, $\mu_m c_{p,m}/k_m$
N_{Re} = Reynolds number, GD/μ_m
N_{St} = Stanton number, $\dot{q}''/(h_m - h_w)G$
q'' = heat flux per unit area
r = radius
r_0 = tube radius
v = velocity
x = axial distance from tube entrance
x^+ = nondimensional axial distance from tube entrance, $x/r_0 N_{Re} N_{Pr}$
μ = viscosity
ϵ = error in energy balance

Subscripts

m = property evaluated at mixed mean temperature
L = local condition
0 = condition at tube entrance
w = property evaluated at wall temperature
x = condition based on axial distance from tube entrance
h = quantity calculated on enthalpy basis

went a sharp expansion upon entering the constant-diameter test section, and the flow pattern must therefore have been quite different from that in a constant-diameter duct.

The case of laminar plasma flow in a circular tube, including the effects of variable properties, radial convection, and radiation, has been studied analytically by Incropera and Leppert [1]. To facilitate comparison of these analytical predictions with experimental data, certain modifications to the finite-difference procedure were made in the present study [10]. Enthalpy and velocity profiles at the tube entrance were measured for three representative laminar flow conditions using a calorimetric probe. These starting profiles were then used as initial conditions in the finite-difference analysis, and predicted heat transfer results were compared with the tube measurements for the three test cases. Heat transfer data were also obtained for several cases in the flow regime considered to be transitional or turbulent.

Description of the Experiment

A plasma generator of the Gerdien arc-jet type was used in this investigation to produce a stream of partially ionized argon with bulk enthalpies up to 4,450 Btu/lb (i.e., mixed mean temperatures to 21,000 deg R). Initial enthalpy of the plasma was determined by an energy balance on the arc generator. A copper anode with a $^1/_2$-in-dia straight nozzle section was used so that no area change was encountered when the gas stream entered the $^1/_2$-in-dia test section upon leaving the plasma generator.

The test section, shown schematically in Fig. 1, consisted of a series of individually cooled segments, each containing a $^3/_4$ in. length of the $^1/_2$-in-dia copper tube. These segments were mounted atop the plasma generator to form a channel 24.75 in. long.

Heat flux through each tubular segment was obtained by measuring the temperature rise of that segment's cooling water. Flow rate was determined by a weight-bucket technique, and temperature rise was measured using copper-constantan thermocouples installed in the inlet and outlet water lines. Individual heat flux measurements were taken only in the first six segments; the remaining segments were connected in series, and a single average heat flux was determined for the group. The water flow rate through the segments in series was adjusted to give a temperature rise comparable to that in the single segments, i.e., about 30–50 deg R, except in Run 101 when the temperature rise in the last group was 84 deg F. Because the argon properties are nearly constant with temperature variations of this magnitude, the wall temperature can be treated as constant. Temperature of the gas leaving the test section was measured with a chromel-alumel thermocouple.

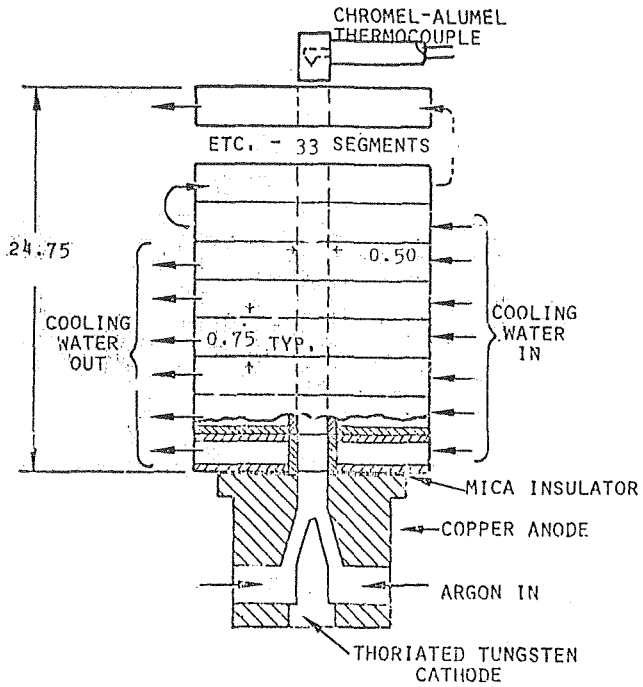

Fig. 1 Diagram of test section (dim. in in.)

To determine tube entry profiles for the laminar cases, a Greyrad Model G-1-7 calorimetric probe was used. The probe consists basically of a water-cooled sampling tube, $^1/_{16}$ in. outside diameter, instrumented to provide an energy balance on the cooling water and the gas sample, which is drawn through a 0.022-in-dia hole in the probe tip. The local enthalpy of the plasma stream is determined by taking the difference between the energy transferred to the probe when acting as an impact tube and the energy transferred when a gas sample is being drawn [11].

For the three laminar test conditions, a single tube segment was mounted on the plasma generator and the probe was traversed across the stream diameter with the tip at the entrance to this segment. The single segment thus provided a solid boundary for the stream and excluded the diffusion of air into the argon plasma. A Beckman oxygen analyzer installed in the probe gas-sample line indicated a negligible concentration of oxygen in the argon sample.

It must be acknowledged that the use of a single tube segment to guide and contain the flow beyond the section where the probe tip was located was determined by practical limitations imposed by the probe shape. In principle, of course, it would have been desirable to probe the incoming flow with a sensor of negligible size with the full test section in place. However, use of the probe at the entrance with even two segments in place was impractical. Since the blockage ratio for the probe in a half-inch tube is small, as is the Mach number, the authors felt that the most likely source of error from the use of a single segment would be back-diffusion of air from the atmosphere. The apparent absence of this, as evidenced by the oxygen measurement, was accepted as adequate assurance of the validity of the entrance condition measurements.

Table 1 summarizes test conditions for the six run series, three in the laminar regime, and three in the transitional or turbulent regime. All tests were conducted at atmospheric pressure, and each series represents three individual data runs between which segment flow rates were varied to bring out any possible systematic errors in the tests. A fourth laminar run series (Series 300) was discarded because of instability of the arc jet at that particular operating condition.

The data reduction procedure included an uncertainty analysis which estimated probable errors based on 20:1 odds in all calculated parameters [12]. Uncertainties in individual measurands were recorded as data during the tests, and these values were added to the known instrument precision errors in determining

Table 1 Summary of heat transfer tests

($h_{m,o}$ in Btu/lb, $T_{m,o}$ in thousands of deg R, $\dot{m}$ in. lb/min)

Run	100	200	400	500	600	700
$N_{Re,o}$	150	205	186	256	295	527
$h_{m,o}$	3850	2200	4450	3575	4150	2150
$T_{m,o}$	20.3	16.45	21.0	19.88	20.6	19.15
$\dot{m}$	0.052	0.074	0.061	0.091	0.100	0.193
$N_{Pr,o}$	0.795	0.585	0.808	0.780	0.805	0.748
ϵ, %	3.5	1.9	4.7	2.2	4.0	9.0
Flow	Lam	Lam	Lam	Trans	Turb	Turb

the contribution of each measured variable to the uncertainty of the final result.

The Nusselt number for each segment was computed on the basis of mixed mean enthalpy according to the definition:

$$N_{\mathrm{Nu},h} = \frac{\dot{q}''D}{(k/c_p)_m(h_m - h_w)}$$

Mixed mean enthalpy at the entrance of each segment was computed by subtracting the energy removed from the gas in all preceding segments from the enthalpy at the tube entrance. Exit enthalpy was, then, the segment-entrance enthalpy less the energy removed in that segment. The average enthalpy, h_m, was taken as the arithmetic average of entrance and exit values.

Preliminary calculations of the heat transfer resistances to be expected between the plasma and the cooling water showed that the controlling resistance would, in all cases, be on the plasma side. Wall temperature measurements were made with copper-constantan thermocouples welded to the water side of the tube walls in preliminary tests to confirm this fact and to permit the accurate calculation of the inside (plasma side) wall enthalpy from the average cooling water temperature and flow rate in each segment. This preliminary calibration made it unnecessary to use these thermocouples in subsequent tests, thereby making assembly and disassembly of the test sections easier.

Thermodynamic property values were taken from the calculated results of Drellishak, Knopp, and Cambel [13], and transport properties were obtained from the results of DeVoto [14].

Results

The experimental results consist of the entrance enthalpy and velocity profiles obtained with the calorimetric probe and of the heat transfer rate measurements along the test section, all obtained as a function of the characteristic operating conditions of the jet. Analytical results consist of the theoretical curves obtained by a finite-difference solution of the laminar flow equations (1).

Laminar Starting Profiles. Enthalpy and velocity profiles at the tube entrance for Run Series 100 are shown in Fig. 2, and data for Run Series 100, 200, and 400 are given in Table 2. The three operating conditions were chosen to give a representative spread of laminar Reynolds numbers within the enthalpy range obtainable with the arc-jet. The upper limit of Reynolds number (based on properties evaluated at the mixed mean temperature) for laminar flow was taken to be approximately 200 from the free-jet transition data of Incropera and Leppert [9]. Experimental uncertainties in the calorimetric probe measurements were within ±5 percent over most of the tube radius, becoming somewhat higher in the low temperature region near the wall.

Mass fluxes calculated from integrated probe measurements agreed with measured arc-jet mass fluxes within 10 percent, and integrated enthalpy fluxes agreed within 17 percent. These mass and energy balance closures were within the errors predicted on the basis of component uncertainties [10].

All enthalpy profiles exhibit a tendency to "peak" at the center; these peaks rise to approximately twice the mixed mean enthalpy, resulting in typical temperatures of 24,000 deg R at the center line, roughly thirty times the absolute gas temperature at the tube wall, 1/4 in. away. The velocity profiles are similarly peaked toward the center; while center-line velocities are quite high, Mach numbers are well below 0.1 for all cases because of the high sonic velocity of plasma temperatures.

Laminar Heat Transfer. Local heat fluxes, plotted as functions of normalized tube length, are shown in Figs. 3(*a*), (*b*), and (*c*) for the three laminar run series. Overall energy balances, obtained by subtracting the energy absorbed in the test section segments from the entering plasma enthalpy and comparing the difference

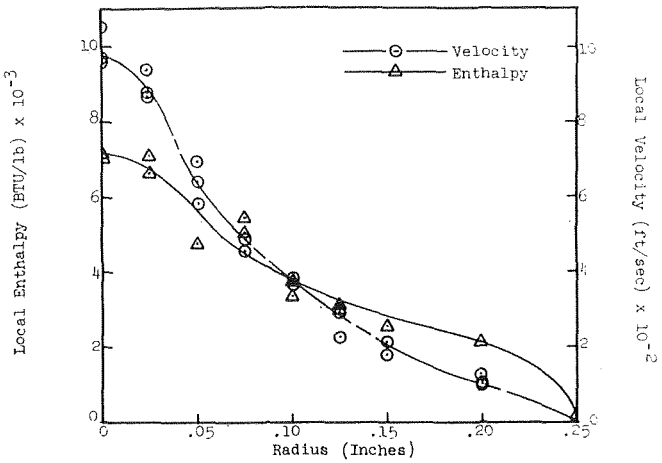

Fig. 2 Measured inlet enthalpy and velocity profiles for Run Series 100. Data for all laminar runs are given in Table 2.

Table 2 Measured inlet profiles for laminar flow runs

(Radius is in inches; enthalpy is in thousands of Btu/lb; velocity is in hundreds of ft/sec)

	Series 100		Series 200		Series 400	
r	h	v	h	v	h	v
0	7.1	10.6	7.2	7.8	9.3	9.7
0	7.0	9.7	6.2	7.6	8.1	9.4
0	-	9.6	5.2	7.2	7.2	9.1
0.025	7.0	9.5	6.7	7.4	8.6	9.4
0.025	6.6	8.8	6.2	7.3	8.4	9.2
0.025	-	8.[illegible]	6.1	7.2	8.1	9.0
0.050	4.7	7.0	6.1	6.6	7.9	7.4
0.050	-	6.4	6.0	6.5	6.4	7.3
0.050	-	5.9	-	-	-	7.0
0.075	5.0	4.8	5.8	5.6	6.0	5.5
0.075	5.5	4.5	5.7	5.4	5.7	5.3
0.075	-	-	5.3	-	-	-
.100	3.8	3.7	4.0	4.5	5.0	4.2
.100	3.4	3.5	4.1	4.4	4.4	4.0
.100	-	-	4.3	-	-	-
.125	3.0	2.9	4.0	3.7	4.1	3.3
.125	2.9	2.1	-	3.6	3.8	3.3
.125	-	-	-	3.5	-	3.1
.150	2.6	2.0	3.3	3.1	3.0	2.8
.150	-	1.7	3.5	3.0	-	2.5
.150	-	-	-	-	-	-
.200	2.4	1.1	1.0	1.8	1.9	1.3
.200	-	1.0	1.1	1.5	1.7	1.1
.200	-	1.0	1.4	-	1.6	-
.250	0.09	0	0.09	0	0.09	0

with the measured gas temperature at the tube exit, closed within ±5 percent for all cases.

On each plot are shown two theoretical curves calculated with the finite-difference analysis [1], using the measured starting profiles as initial conditions. The upper curve in each case represents the sum of radiative and convective transfer, assuming that all radiation is radially directed (i.e., radiation to the tube walls upstream and downstream is not included); the gas is optically thin; and the tube walls are black. The lower curve includes only the convective portion of the total heat flux. For all three cases, a consistent trend is noted of large initial discrepancy be-

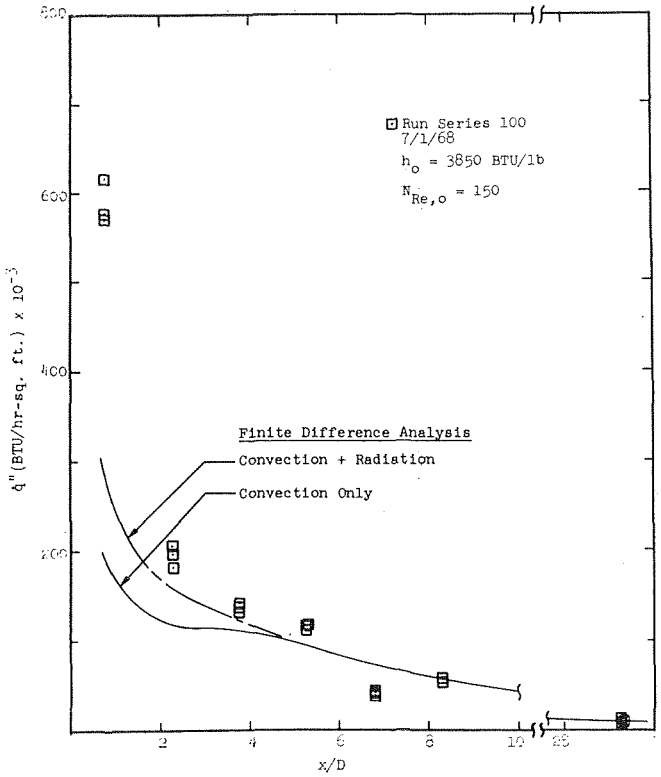

Fig. 3(*a*) Comparison of predicted and measured heat fluxes for laminar tests: Run Series 100

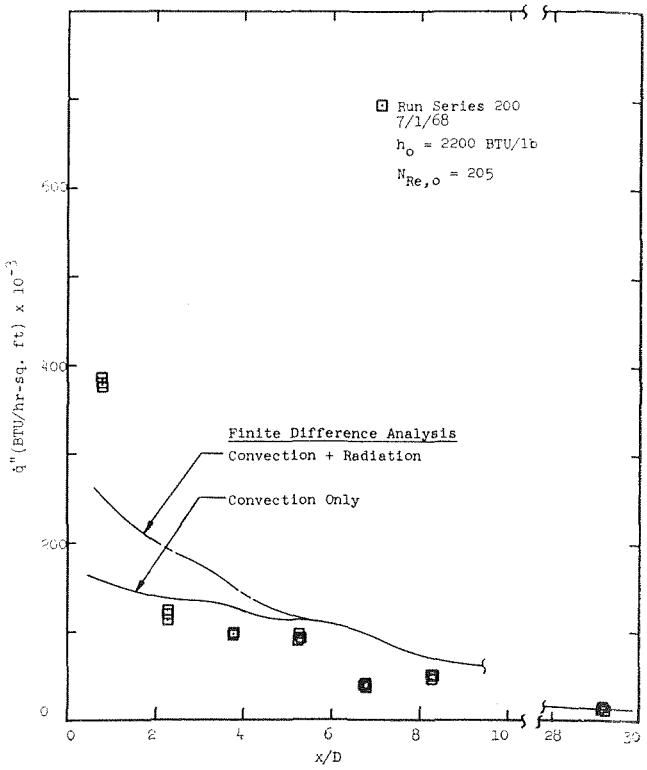

Fig. 3(*b*) Comparison of predicted and measured heat fluxes for laminar tests: Run Series 200

tween theory and experiment at the tube entrance, followed by fairly good agreement beyond four to five diameters downstream. Neither radiation from the arc-jet cathode nor gas radiation can account for the large error in the theory in the early entrance region; even when the most conservative of available argon radiation data were used in the calculations, the radiation heat transfer component was increased by, at most, 50 percent.

One possible explanation is poor resolution near the tube wall in the determination of inlet enthalpy profiles, which results from the high uncertainty of the calorimetric probe data in the low-temperature region [11]. Since the slope of the profile at the wall is not accurately defined, a large error might be introduced in the initial heat flux computations. After several axial steps, however, the analysis tends to become less sensitive to the wall slope at the entrance and the method becomes increasingly more accurate.

Another possible explanation for the discrepancy is the occurrence of nonequilibrium between ion and electron temperatures near the wall in the highly ionized tube entrance region. Measurements of Bahadari and Soo [15] taken in two-dimensional flow of an argon plasma at temperatures below 19,000 deg R (<3 percent ionization) indicate that electron temperatures adjacent to a cooled wall are typically four times the heavy particle temperatures, giving rise to thermal conductivities as much as ten times the equilibrium wall temperature values. In the present experiments, the gas entering the tube is up to 20 percent ionized, and the nonequilibrium effect might reasonably be expected to be even stronger.

Mixed mean temperatures for the low Reynolds number tests are plotted as a function of axial location in Figs. 4(*a*), (*b*), and (*c*). Above 16,000 deg R, where ionization causes a large increase in the specific heat, even the large errors in heat flux do not produce large temperature errors. Below 16,000 deg R, the low value of the specific heat results in a high sensitivity of the temperature to enthalpy errors. This behavior suggests that nondimensionalization of heat transfer results might best be carried out on the basis of an enthalpy conductance rather than a temperature conductance.

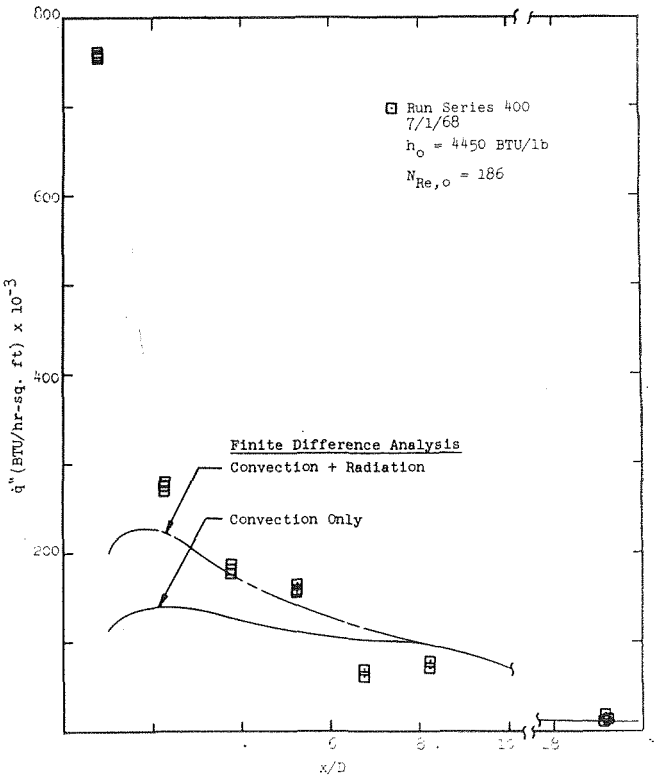

Fig. 3(*c*) Comparison of predicted and measured heat fluxes for laminar tests: Run Series 400. Test conditions are given in Table 1, measured data in Table 3.

High Reynolds Number Heat Transfer. Heat flux and mixed mean temperature data for three run series in the Reynolds number range above 200 are presented in Table 3; representative data (Run Series 500) are plotted in Figs. 5 and 6. The dotted lines in these figures are intended only as a visual aid and do not indicate comparison with theory.

Table 3 Measured heat flux and calculated mixed mean temperature

($\dot{q}$" is in Btu/hr-sq ft; T_m is in deg R x 10^{-3})

	Series 100		Series 200		Series 400		Series 500		Series 600		Series 700	
x/D	$\dot{q}$"	T_m	$\dot{q}$"	T_m	$\dot{q}$"	T_m	$\dot{q}$"	T_m	$\dot{q}$"	T_m	$\dot{q}$"	T_m
0	-	20.3	-	16.5	-	21.0	-	19.9	-	20.5	-	19.2
0	-	20.3	-	16.5	-	20.9	-	19.9	-	20.7	-	19.2
0	-	20.2	-	16.5	-	21.0	-	19.8	-	20.6	-	19.1
0.75	617	19.0	387	14.7	758	19.9	792	18.9	983	19.6	1042	18.4
0.75	577	19.1	381	14.5	759	19.9	791	18.8	973	19.9	1047	18.4
0.75	570	19.0	380	14.7	762	20.0	782	18.8	998	19.7	1029	18.4
2.25	181	15.7	124	11.1	279	17.4	321	16.4	412	17.4	496	16.6
2.25	205	16.0	115	11.1	275	17.3	314	16.2	399	18.0	468	16.7
2.25	196	15.7	121	11.2	271	17.6	317	16.2	415	17.6	473	16.7
3.75	133	13.0	97	9.5	177	15.1	217	14.2	261	15.5	409	15.0
3.75	138	13.2	100	9.5	185	14.9	232	13.8	267	16.4	428	15.1
3.75	142	12.9	99	9.6	182	15.4	231	13.7	270	15.8	416	15.1
5.25	113	10.4	97	8.1	152	12.5	183	11.9	207	13.4	292	13.4
5.25	116	10.6	94	8.1	157	12.1	189	11.4	216	14.6	309	13.4
5.25	117	10.1	93	8.2	163	12.8	179	11.4	211	13.7	312	13.3
6.75	39	8.8	38	7.1	62	10.6	91	10.3	127	11.6	193	12.0
6.75	44	8.9	41	7.1	67	10.2	90	9.7	127	12.9	201	12.0
6.75	43	8.5	41	7.2	183	9.7	110	9.6	124	12.0	189	12.0
8.25	54	7.8	49	6.4	71	9.4	96	9.2	67	10.5	93	11.2
8.25	56	7.9	50	6.4	78	8.9	99	8.6	63	11.9	110	11.1
8.25	55	7.4	50	6.5	142	6.8	86	8.4	65	10.9	117	11.1
29.25	9.1	4.7	12	3.6	13	5.7	21	5.2	30	5.8	50	7.1
29.25	9.5	4.6	12	3.6	18	3.7	21	4.6	30	7.2	51	6.9
29.25	9.3	4.2	12	3.6	13	2.4	21	4.5	30	6.2	50	7.0

As might be expected from low-temperature studies, heat flux tends to increase with increasing Reynolds number; as in the laminar cases, a steep gradient in the heat transfer occurs in the first one or two tube diameters, the gradient becoming less marked as the flow develops downstream.

Discussion

Nusselt numbers for all runs computed on the basis of mixed mean enthalpy, as defined above, are summarized in Fig. 7. The abscissa is the dimensionless distance from the tube entrance, with Reynolds and Prandtl numbers computed on the basis of local mixed mean temperature properties:

$$N_{\mathrm{Re},L} = \frac{GD}{\mu_{m,L}}$$

$$N_{\mathrm{Pr},L} = \left(\frac{\mu_m c_{p,m}}{k_m}\right) L$$

$$x_L^+ = \frac{x}{r_0} \frac{1}{N_{\mathrm{Re},L} N_{\mathrm{Pr},L}}$$

Several other correlating parameters, such as Nusselt and Stanton numbers based on mixed mean temperature, wall temperature, and intermediate reference temperature, were investigated, and the coordinates chosen were found to give the most consistent correlation.

For comparison, the constant property combined entry length solution of Kays [16] is shown. Two features of particular interest are noted.

First, there is no sharply defined difference in the nondimensional heat transfer rate between the laminar runs and those for which the flow was transitional or turbulent. During the tests, it was evident from the sound emitted by the gas flow in the test section that a flow transition did indeed occur above entering Reynolds numbers of about 200, as expected [9]. The data suggest, however, that even at Reynolds numbers well above 200, the heat transfer retains a laminar character. This might be explained by the high thermal conductivities existent in the partially ionized gas, resulting in a situation somewhat analogous to that encountered in liquid metals, where molecular thermal diffusivities are of comparable magnitude to eddy diffusivities. Alternatively, a laminarization may be brought about by the rapid cooling of the plasma entering the tube. In argon, the viscosity reaches a maximum at a temperature of about 20,000 deg R, beyond which it drops off sharply. Thus in a turbulent gas being rapidly cooled from a temperature above 20,000 deg R, a sharp rise in viscosity occurs which might be sufficient to effect laminarization. It should be noted that, while the mixed mean temperature in these experiments fell below 20,000 deg R within the first few tube diameters, the temperature in the core flow remained above this level for a considerable distance downstream.

The second point, and perhaps the more important from the engineering standpoint, is the remarkable agreement between the plasma tube flow data and the simpler laminar constant-properties prediction. For $x^+ < 0.07$, the data fall about 30 percent higher than the constant properties solution, due, at least in part, to the radiative heat flux from the plasma. This trend is in agreement with measurements for the heating of nitrogen and helium in the 2,300 deg F range [2]. The tendency of the Nusselt number to rapidly approach the constant property value was also predicted by an earlier analysis [1].

For design purposes, it appears that a Nusselt number of 3.66 based on enthalpy is applicable for x/D greater than about 10. For the early entrance region, the data shown in Fig. 7 may be used with the reservation that inlet profiles much different from those encountered in the present tests may cause significant error.

Since radiation in this region may account for a substantial portion of the total energy flux, appropriate radiation corrections should be applied when extending the present results to gases other than argon and pressures other than one atmosphere.

However, the present status of available radiation data even for argon plasma is, at best, uncertain. Published results [17–21] show order of magnitude discrepancies in the temperature range of interest, and, for this reason, no attempt was made in this study to separate the relative magnitudes of the radiative and convective heat transfer components. Work is presently under way at Stanford University to measure the magnitude of the radiation contribution.

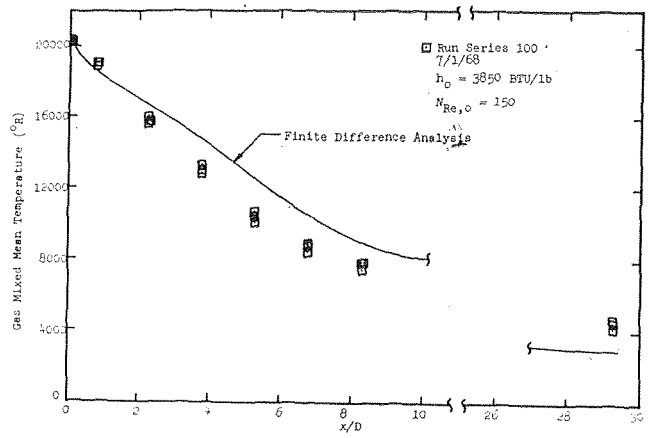

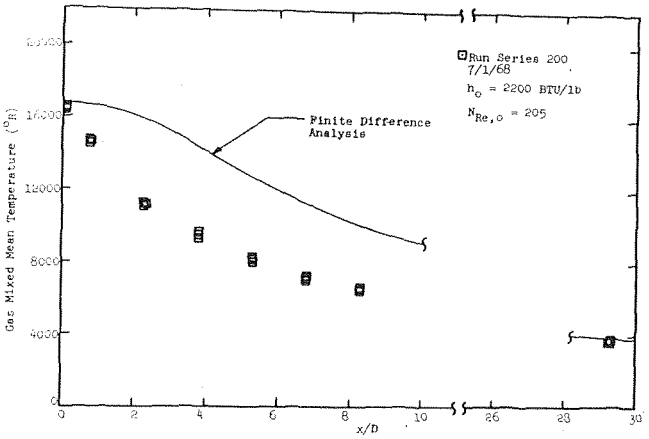

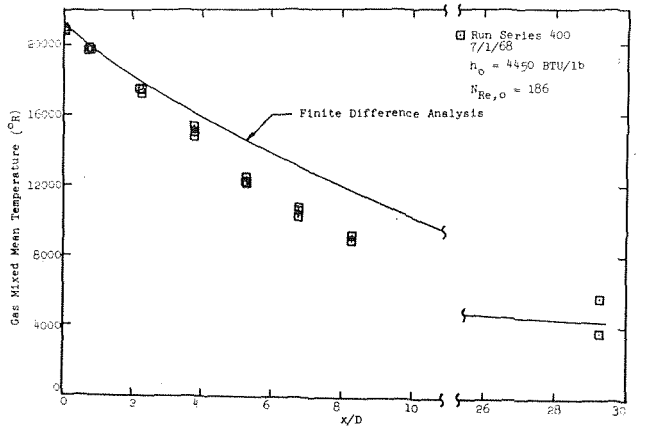

Fig. 4 Comparison of predicted and measured mixed mean temperatures for laminar tests. Tests conditions are given in Table 1, measured data in Table 3.

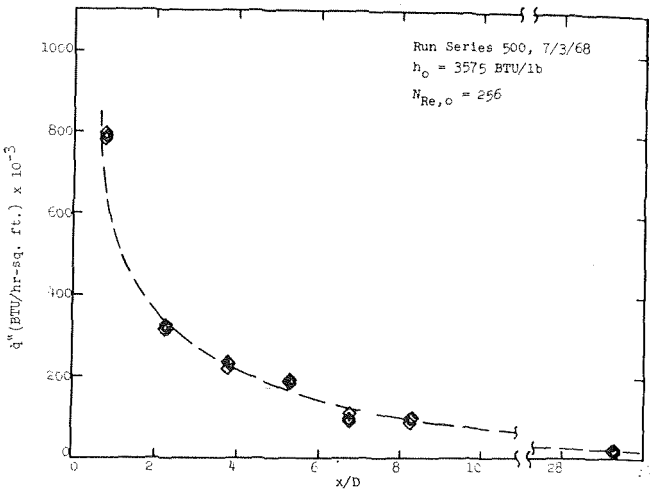

Fig. 5 Heat flux versus axial position for Run Series 500. Measured data for all runs appear in Table 3.

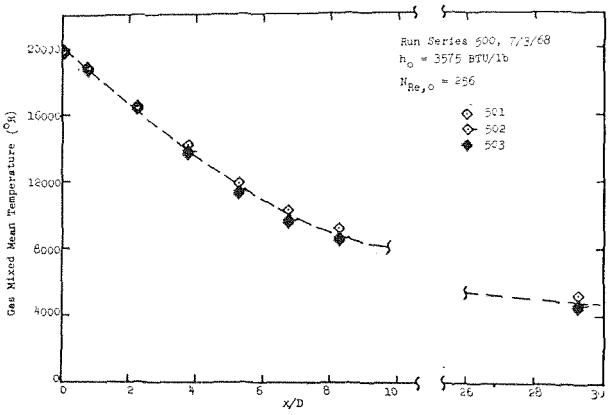

Fig. 6 Mixed mean temperature of gas versus axial location for Run Series 500. Data for all runs appear in Table 3.

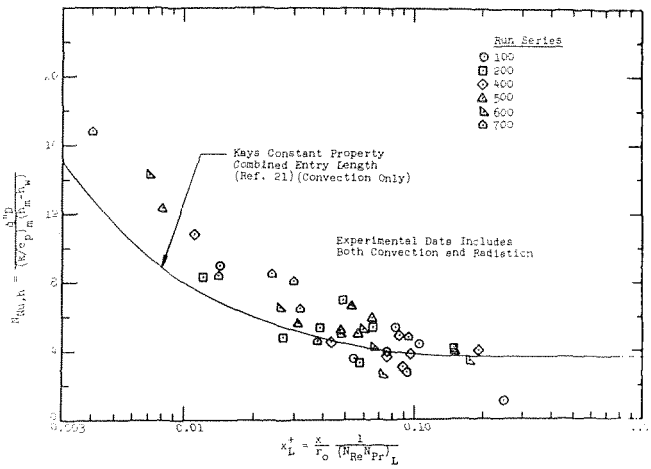

Fig. 7 Experimental Nusselt numbers compared with constant property, combined entry length solution [16]

In Fig. 8, heat transfer results from the present tests are compared with the data of Massier, Back, and Roschke [6]. For purposes of comparison, Nusselt numbers were calculated from the heat flux vs. tube length curves shown in reference [6], using their probe-measured enthalpy as a starting point. The present data fall somewhat higher than their lower temperature results, but the curve slopes are in agreement.

Conclusions

The data obtained in these experiments correlate within the experimental uncertainty for entrance Reynolds number from 140–530 when Nusselt number computed on the basis of mixed mean enthalpy, according to definition

$$N_{\mathrm{Nu},h} = \frac{\dot{q}''D}{(k/c_p)_m(h_m - h_w)}$$

is plotted against nondimensional x-distance based on local mean temperature properties. The laminar finite-difference analysis [1] accurately predicts heat transfer from the gas after five to ten diameters downstream of the tube entrance. In the

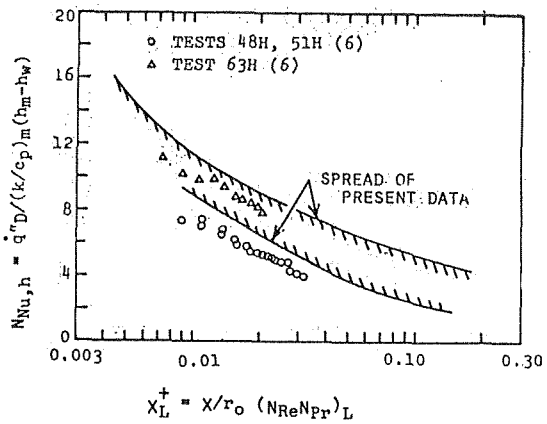

Fig. 8 Comparison of experimental results compared with data of Massier, et al. [6]

early entrance region of the tube, particularly in the first one or two diameters, the accuracy of the analysis appears to be highly sensitive to the shape of the assumed initial enthalpy and velocity profiles near the wall.

The constant property combined entry-length solution predicts heat transfer rates within the experimental uncertainty in the region $x^+ > 0.07$ when Nusselt numbers are computed as defined previously. In the region $x^+ < 0.07$, measured Nusselt numbers for the particular inlet conditions tested were about 30 percent higher than predicted by the constant property theory.

Acknowledgments

This paper is based on work carried out by the authors at Stanford University and on a dissertation submitted by P. S. Schmidt in partial fulfillment of the requirements for the degree of Doctor of Philosophy. Professors R. J. Moffat and W. M. Kays made valuable contributions to the planning and execution of this project. The assistance of Messrs. Bruce Hunn, Patrick Hee, and Charles Smith in many phases of the development of the experiment and acquisition of data is also gratefully acknowledged. This research was sponsored by the U. S Atomic Energy Commission, Division of Reactor Development, under contract number AT(04-3)-247.

References

1 Incropera, F. P., and Leppert, G., "Laminar Flow Heat Transfer from an Argon Plasma in a Circular Tube," *International Journal of Heat and Mass Transfer*, Vol. 10, 1967, pp. 1861–1873.

2 Davenport, M. E., and Leppert, G., "The Effect of Transverse Temperature Gradients on the Heat Transfer and Friction for Laminar Flow of Gases," JOURNAL OF HEAT TRANSFER, TRANS. ASME, Series C, Vol. 87, 1965, pp. 191–196.

3 Kays, W. M., and Nicoll, W. B., "Laminar Flow Heat Transfer to a Gas with Large Temperature Difference," JOURNAL OF HEAT TRANSFER, TRANS. ASME, Series C, Vol. 85, 1963, pp. 329–338.

4 Humble, L. V., Lowdermilk, W. H., and Desmon, L. G., "Measurements of Average Heat Transfer and Friction Coefficients for Sub-Sonic Flow of Air in Smooth Tubes at High Surface and Fluid Temperatures," NACA Rept. 1020, 1951.

5 Nicoll, W. B., and Kays, W. M., "The Influence of Temperature Dependent Properties on Gas Flow Heat Transfer in Circular Tubes," Tech. Report No. 43, Stanford University, Dept. of Mech. Eng., 1959.

6 Massier, P. F., Back, L. H., and Roschke, E. J., "Heat Transfer and Laminar Boundary-Layer Distributions in an Internal Subsonic Gas Stream at Temperatures up to 13,900 deg R," JOURNAL OF HEAT TRANSFER, Trans. ASME, Series C, Vol. 91, No. 1, Feb. 1969, pp. 83–90.

7 Johnson, J. R., Choksi, N. M., and Eubank, P. T., "Entrance Heat Transfer from a Plasma Stream in a Circular Tube," *Industrial and Engineering Chemistry Process Design and Development*, Vol. 7, No. 1, Jan. 1968, pp. 34–41.

8 Skrivan, J. F., and von Jaskowsky, W., "Heat Transfer From Plasma to Water-Cooled Tubes," *Industrial and Engineering Chemistry Process Design and Development*, Vol. 4, No. 4, Oct. 1965, pp. 371–379.

9 Incropera, F. P., and Leppert, G., "Flow Transition Phenomena in a Subsonic Plasmajet," *AIAA Journal*, Vol. 4, No. 6, 1966, pp. 1087–1088.

10 Schmidt, P. S., "Heat Transfer From a Plasma in Tube Flow," Tech. Rept. No. SU247-14 and Doctoral Dissertation, Department of Mechanical Engineering, Stanford University, 1968.

11 Incropera, F. P., and Leppert, G., "Investigation of Arc-Jet Temperature Measurement Techniques," *ISA Transactions*, Vol. 6, No. 1, 1967, pp. 35–41.

12 Kline, S. J., and McClintock, F. A., "Describing Uncertainties in Single-Sample Experiments," *Mechanical Engineers*, Vol. 75, No. 1, 1953, pp. 3–8.

13 Drellishak, K. S., Knopp, C. F., and Cambel, A. B., "Partition Functions and Thermodynamic Properties of Argon Plasma," AEDC-TR-63-146, Aug. 1963.

14 DeVoto, R. S., "Transport Properties of Partially Ionized Argon," *Physics of Fluids*, Vol. 10, No. 2, 1967, pp. 354–364.

15 Bahadari, M. N., and Soo, S. L., "Non-equilibrium Transport Phenomena of Partially Ionized Argon," *International Journal of Heat and Mass Transfer*, Vol. 9, No. 1, 1966, pp. 17–34.

16 Kays, W. M., "Numerical Solutions for Laminar Flow Heat Transfer in Circular Tubes," Vol. 77, No. 8, 1955, pp. 1265–1274.

17 Tankin, R. S., and Berry, J. M., "An Experimental Study of the Radiant Energy Transfer From a Plasma," AEDC-TDR-64-233, 1964.

18 Evans, D. L., and Tankin, R. S., "Measurement of Emission and Absorption of Radiation from an Argon Plasma," *Physics of Fluids*, Vol. 10, No. 6, June 1967.

19 Barzelay, M. E., "Continuum Radiation From Partially Ionized Argon," *AIAA Journal*, Vol. 4, No. 5, May 1966.

20 Tankin, R. S., and Berry, J. M., "Experimental Investigation of Radiation from an Argon Plasma," *Physics of Fluids*, Vol. 7, No. 10, Oct. 1964.

21 Emmons, H. W., "Arc Measurement of High Temperature Gas Transport Properties," *Physics of Fluids*, Vol. 10 No 6, June 1967.

J. W. ACKERMAN
Research Engineer,
Research & Development Division,
The Babcock & Wilcox Company,
Alliance, Ohio

Pseudoboiling Heat Transfer to Supercritical Pressure Water in Smooth and Ribbed Tubes

Investigations of heat transfer to supercritical pressure fluids have been going on for some time, and correlations have been developed for both free and forced-convection conditions. In these investigations, unpredictable heat transfer performance has sometimes been observed when the pseudocritical temperature of the fluid is between the temperature of the bulk fluid and that of the heated surface. The unusual performance has been attributed to many causes, but one for which more evidence is being collected is that of a pseudofilm-boiling process similar to film boiling which occurs at subcritical pressures. This paper, which is an extension of work reported earlier on forced-convection heat transfer to supercritical pressure water, presents experimental evidence which suggests that a pseudofilm-boiling phenomenon can occur in smooth-bore tubes. During the period from 1963–1966, tubes with ID's from 0.37 to 0.96 in. were tested at pressures from 3300–6000 psia and at heat fluxes and mass velocities in the range of interest in steam-generator design. The effects of heat flux, mass velocity, tube diameter, pressure, and bulk fluid temperature on both the occurrence and characteristics of pseudofilm boiling are discussed. Results of a second series of tests conducted in 1967, which show that ribbed tubes suppress pseudofilm boiling at supercritical pressure much like they do film boiling at subcritical pressures, are also discussed.

Introduction

In recent years the area of heat transfer to fluids near their critical pressure has been investigated because of interest in developing supercritical pressure steam generators and nuclear reactors, and in cooling rocket motors and gas turbine blades. Based on these investigations, correlations have been developed for both free and forced-convection conditions. In particular, the increasing demand for supercritical pressure steam generators has required continued accurate predictions of water and steam heat transfer coefficients over a wide range of operating conditions.

In the process of conducting experiments to study supercritical pressure heat transfer, many investigators have reported unusual performance in the pseudocritical temperature region. (The pseudocritical temperature is that temperature at which the density gradient and specific heat attain maximum values.) This unusual performance has been observed in experiments while heating water under forced convection [1–6][1] and other fluids under both forced and free convection [7–12].

The unusual performance has for the most part been observed when the pseudocritical temperature of the fluid occurs in the thermal boundary layer between the lower-temperature bulk fluid and the higher-temperature heating surface. Further, it has taken one of two different forms:

1 A sudden *increase* in the heat transfer coefficient over that associated with normal forced convection, which has been attributed to a boilinglike process similar to that observed under subcooled nucleate boiling at subcritical pressure.

2 A sudden *decrease* in the heat transfer coefficient below that associated with normal forced convection, which has been attributed to a pseudofilm-boiling process similar to film boiling at subcritical pressure. This second form has usually been observed to occur at higher heat fluxes than that in the first.

Contributed by the Heat Transfer Division and presented at the Winter Annual Meeting, Los Angeles, Calif., November 16–20, 1969, of The American Society of Mechanical Engineers. Manuscript received by the Heat Transfer Division, May 22, 1968. Paper No. 69-WA/HT-2.

[1] Numbers in brackets designate References at end of paper.

Nomenclature

G = mass velocity based on tube ID, lb/hr-ft²
H = enthalpy of fluid, Btu/lb
ID = tube inside diameter, or major inside tube diameter for ribbed tube, in.
P = pressure, psia
T_b = local bulk fluid temperature, deg F
T_i = inside tube surface temperature based on calculation using ID, deg F
X = steam quality by weight, percent
ϕ = heat flux, Btu/hr-ft²

SOURCE: GOLDMANN (REFERENCE 2)

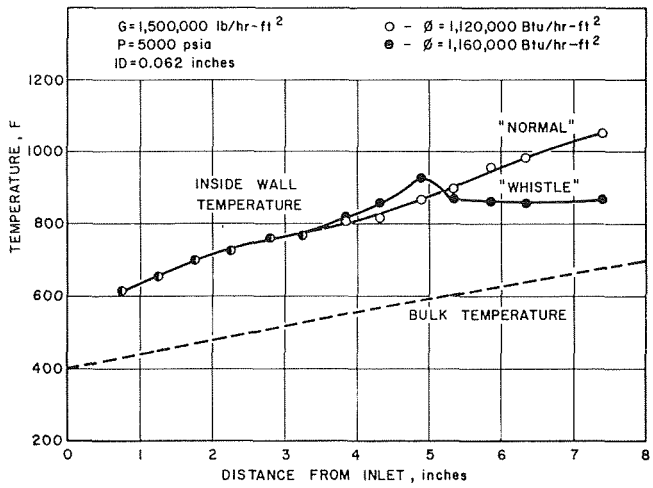

Fig. 1 Wall temperatures with "normal" heat transfer and with "whistle"

SOURCE: SHITSMAN (REFERENCE 3)

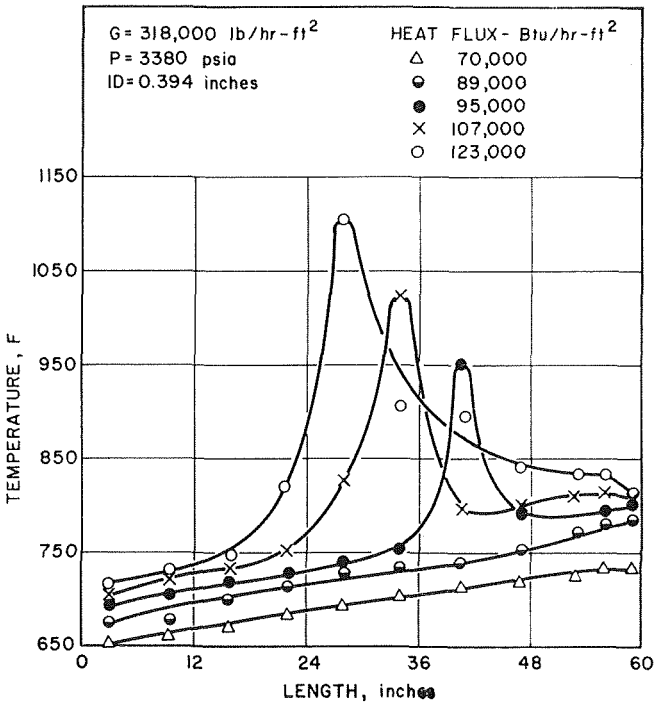

Fig. 2 Distribution of wall temperatures along tube length

For example, Goldmann [2] observed an unusual mode of heat transfer which he believed could be explained by a boilinglike phenomenon resembling nucleate boiling. In tests with supercritical pressure water flowing through a 0.062-in-ID tube at high mass flow rates, two different tube temperature profiles were observed as shown in Fig. 1. He explained that the open circles show "normal" forced convection, whereas the closed circles show conditions of increased heat transfer coefficient with subcooled boiling at subcritical pressures. He also detected "boiling noise" when this phenomenon occurred, which has also been heard during subcritical boiling.

Shitsman [3] observed the second unusual mode of heat transfer which he attributed to a crisislike process analogous to the process by which film boiling occurs at subcritical pressures. In tests with supercritical water flowing through a tube at high mass flow and under high heat-flux conditions, a sudden decrease in the heat transfer coefficient and resulting increase in tube temperature was observed as shown in Fig. 2. When the heat flux was increased above a certain value, a sudden decrease in the coefficient (increased tube temperature) occurred in the outlet portion of the 5-ft-long tube. Further increase in heat flux caused higher tube temperatures, with the peak temperature moving toward the inlet of the tube. The author attributed this to blanketing of the heat transfer surface by a lighter phase fluid, like steam blanketing at subcritical pressure.

One of the more recent studies in this area has been by Nishikawa and Miyabe [11] in which they present photographs of what they consider to be normal boiling and film boiling of supercritical pressure carbon dioxide under free convection. Based on their work, the authors report that they are convinced both of a boilinglike phenomenon, and the occurrence of a film-boiling phenomenon at supercritical pressure which they feel explains the sudden deterioration of heat transfer coefficient.

The significance to the steam generator or reactor designer of the possible occurrence of a pseudofilm-boiling phenomenon at supercritical pressure is that, for the same operating conditions, the heat transfer coefficient under film boiling is much lower than predicted by available forced-convection correlations. If pseudofilm boiling does occur when the heat flux is sufficiently high, the heat transfer surface may become overheated.

The Babcock & Wilcox Company has been investigating supercritical pressure heat transfer for over 10 years, with the results of some of our earlier work presented in 1964 [5]. Since that time, we have continued our investigation and have collected considerable experimental evidence of what is considered pseudofilm boiling at supercritical pressure. One objective of this paper is to discuss our observations from a first series of tests conducted from 1963–1966 with smooth-bore tubes and describe the effects of various parameters on both the occurrence and characteristics of pseudofilm boiling with supercritical pressure water.

Another objective is to describe the results of a second series of tests conducted in 1966 and 1967 which show that ribbed tubes suppress pseudofilm boiling at supercritical pressure and permit safe operation at conditions where smooth tubes are unsatisfactory.

Range of Variables. The operating conditions covered for the tests described are, in general, those encountered in modern, central station, supercritical pressure steam generators.

The range of variables investigated were:

Pressure:	3300, 3600, 4000, 4500, 6000 psia
ID heat flux:	40,000 to 550,000 Btu/hr-ft²
Mass velocity:	100,000 to 1,600,000 lb/hr-ft²
ID:	0.37, 0.47, 0.73, 0.96-in. smooth-bore tubes, 0.71-in. ribbed tube
Bulk fluid temperature:	170–900 F

Although all combinations of the foregoing variables were not covered, there was sufficient overlap to establish the various trends of the data as described in this paper.

Experimental Apparatus

A schematic diagram of the apparatus used is shown in Fig. 3. The equipment consists of two separate systems.

1 The system used for controlling the fluid conditions at the test section inlet.

2 The system composed of the test section and power supply.

This apparatus has been described in detail previously [5, 13] and, therefore, descriptions of only the major components will be repeated here.

System for Controlling Fluid Conditions. Referring to Fig. 3, feedwater is first deionized to maintain a specific conductance of the water between 0.05 and 0.20 mhos/cm. A chemical feed pump

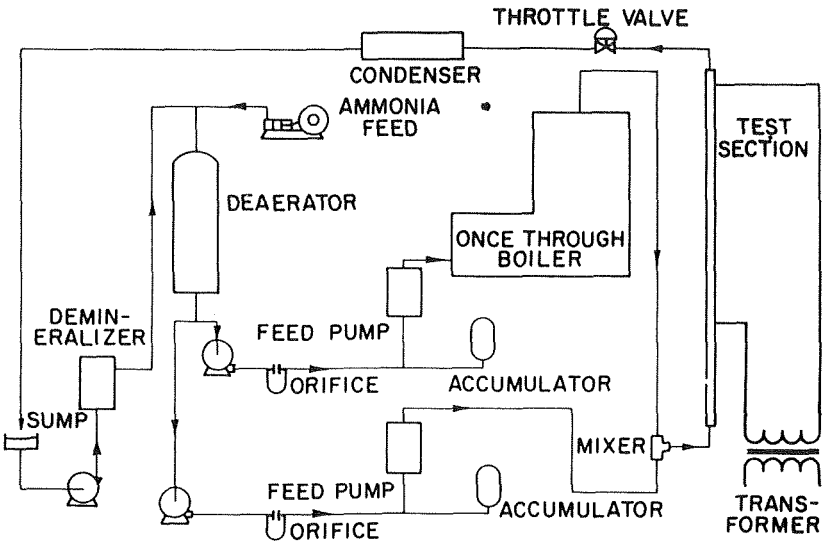

Fig. 3 Schematic diagram of system

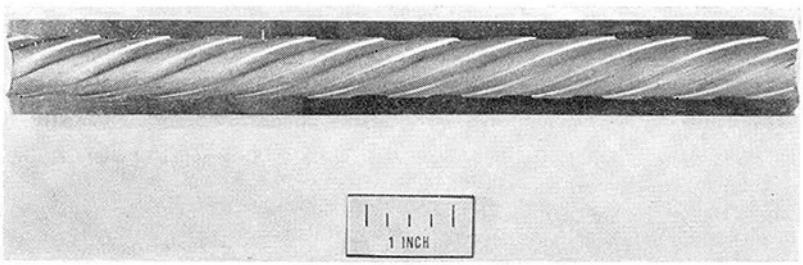

Fig. 4 Photograph of 6-rib multilead ribbed tube

adds ammonium hydroxide to maintain a pH of 9.5 at 77 F, and the deaerator reduces the oxygen to less than 5 ppb.

The desired fluid temperatures and mass velocities covered in these tests were established by means of two independently operated flow circuits. The fluid in one circuit was heated by a once-through monotube boiler, whereas the fluid in the other circuit was unheated. Each circuit contained its own centrifugal booster pump, flow measuring orifice, accumulator, and high-pressure positive-displacement feed pump. When both circuits were being used, the two fluids were combined in a mixer with the total flow at the desired conditions progressing on to the test section. A valve was located in the unheated circuit ahead of the mixer to prevent flow instabilities.

Flow rates were measured by utilizing manometers connected across orifice plates located in the low-pressure part of each circuit. All orifice plates were calibrated in place by weighing the water flow through the orifice over a measured period of time.

Fluid temperatures were measured with thermocouples installed in wells located ahead of the mixer in both flow circuits and at the test section inlet and outlet. The thermocouples were calibrated in place against saturation temperatures for known pressures.

System pressure was controlled by an air-operated throttle valve located between the test section and the condenser, while pressure was measured with Bourdon-tube gages ahead of the mixer in both circuits and at the test section inlet and outlet.

Test Sections and Power Supply. Data were obtained on four smooth-bore test sections and one ribbed tube test section.

The smooth-bore test sections were AISI type 304 stainless-steel tubes having inside diameters of 0.37, 0.47, 0.73, and 0.96 in. Each test section had unheated approach and discharge sections. All had 6-ft heated lengths except the 0.73-in-ID tube which had a 9-ft heated length. Each test section was heated electrically as a resistance element in the secondary circuit of a 137-kva transformer, the output of which was controlled by a saturable reactor to maintain a constant heat flux on the tube for each test run.

The ribbed tube test section was an internally ribbed, stainless-steel tube having a 0.71-in. major ID (rib valley to rib valley). Six ribs were in the form of a helix, and the pitch was 0.86 in. A longitudinal section of the tube is shown in Fig. 4. The heated length of this tube was also 6 ft.

Chromel-alumel thermocouples were resistance-welded to the tube surface on diametrically opposite sides of each test section to measure test section OD metal temperatures along the length of the tube. The thermocouple outputs were passed through a selector switch and measured with a Leeds and Northrup precision potentiometer, using an ice-bath junction.

Voltage taps were welded to the surface of the various tubes at 6-in. intervals to measure the incremental voltage drop along the tube. These voltages were then used to calculate local heat fluxes along the heated length of the test section.

Procedure

The procedure used for this work has also been described in detail earlier [5]. Briefly, the specific steps of the test procedure were:

1 Data were taken at several heat-input rates for constant mass velocity, inlet fluid temperature, and pressure.

2 The inlet fluid temperature was then changed and step 1 repeated.

3 The mass velocity was changed and steps 1 and 2 repeated.

4 The same procedure as in steps 1, 2, and 3 were followed for different pressures.

Results With Smooth-Bore Tubes

In the process of studying heat transfer to supercritical pressure water, tubes of several different diameters were investigated.

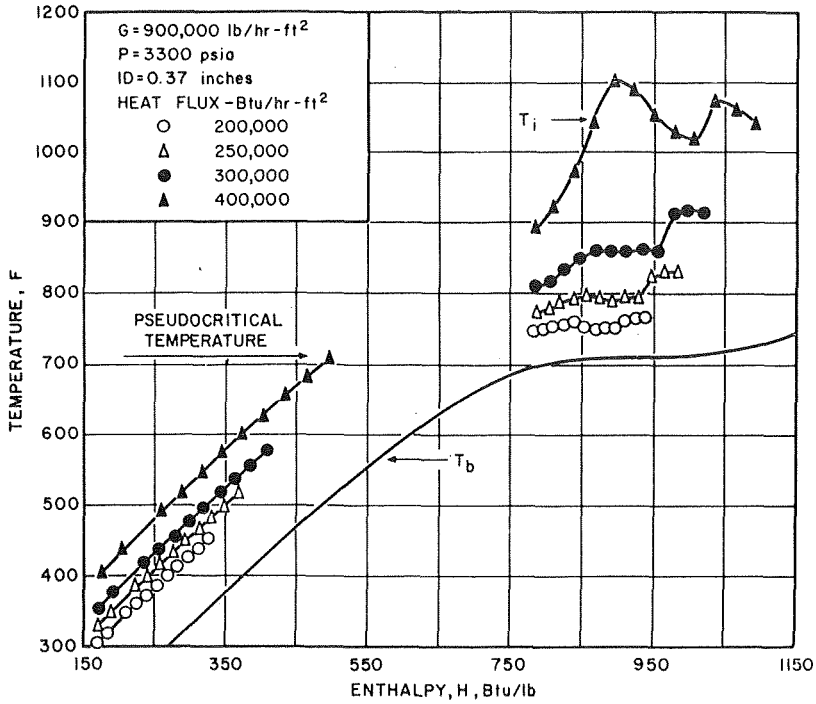

Fig. 5 Temperature profile for 0.37-in-ID smooth tube

Examples of the experimental data that have been obtained and observations that have been made are presented in the following paragraphs.

Extensive tests were conducted on a 0.371-in-ID smooth-bore tube for a range of mass velocities, heat fluxes, and pressures. Data which are considered to be normal forced-convection data as well as data exhibiting the characteristics of film boiling noted previously were collected. For example, Fig. 5 shows test section temperature profiles at 3300 psia, a mass velocity of 900,000 lb/hr-ft², and various nominal heat fluxes of 200,000, 250,000, 300,000, and 400,000 Btu/hr-ft².

The first significant item shown in the figure is that all data in the lower fluid temperature range exhibit normal trends which are readily predictable by available forced-convection correlations.

However, the second group of data at higher inlet fluid temperature but still below the pseudocritical temperature exhibit tube temperature profiles that might be considered in the region of both pseudoboiling and filmboiling. As the heat flux was increased, temperature peaking became more severe. Additional data obtained at bulk fluid temperatures above the pseudocritical temperature exhibited readily predictable trends very similar to the low-temperature data.

Tests over a range of mass velocities on this same size tube indicate that, with all other variables held constant (i.e., pressure, heat flux, inlet fluid temperature, tube ID), pseudofilm boiling is the most severe at low mass velocities. Increases in mass velocity tend to eliminate the occurrence of the phenomenon. For example, Fig. 6 shows test section temperature profiles at 4500 psia, a heat flux of 150,000 Btu/hr-ft², and mass velocities of 400,000, 500,000, and 900,000 lb/hr-ft². Pseudofilm boiling was not observed at the two higher mass velocities, but at 400,000 lb/hr-ft² temperature peaking was readily observed.

Tests at other pressures up to 6000 psia show that, with all other variables held constant, temperature peaking is the most severe at pressures near the critical pressure. As pressure is increased above 3300 psia, temperature peaking becomes less severe.

Additional tests were conducted on a 0.731-in-ID smooth tube, but over a less extensive range of conditions than covered on the smaller tube. An example of data from these tests is given in

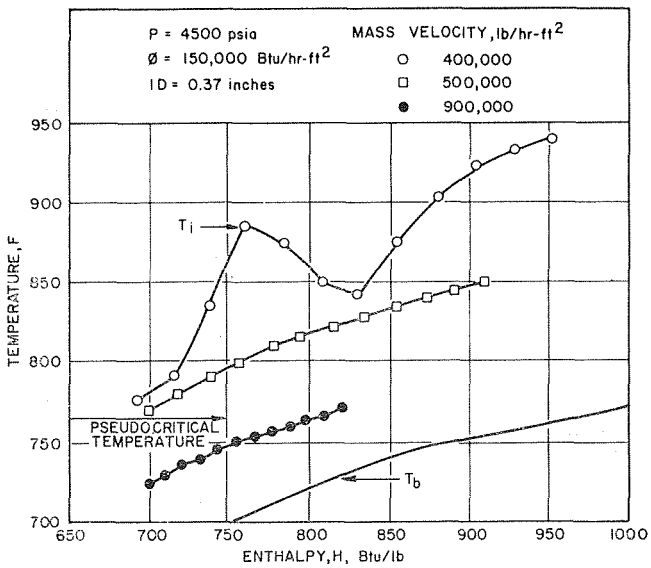

Fig. 6 Effect of mass velocity on pseudofilm boiling

Fig. 7, which is for 3600 psia, a mass velocity of 300,000 lb/hr-ft², and various nominal heat fluxes.

It is apparent from the data at higher fluid temperatures also that when the pseudocritical temperature occurs in the boundary layer between the heated surface and the bulk fluid, temperature profiles can occur that are unpredictable with present correlations. It is of interest to note at this point that, for this size tube, two different locations on the tube show somewhat different evidence of pseudofilm boiling. That is, the temperature peaking on the outlet portion of the tube, Fig. 7, occurs initially as heat flux is increased and takes the form of rises which cover a considerable length of the tube and which are moderately heat-flux sensitive. At still higher heat fluxes, temperature peaking begins on the inlet portion of the tube. These peaks are extremely heat-flux sensitive and take the form of localized temperature rises. The tube temperatures between the "inlet" and "outlet" peaks are

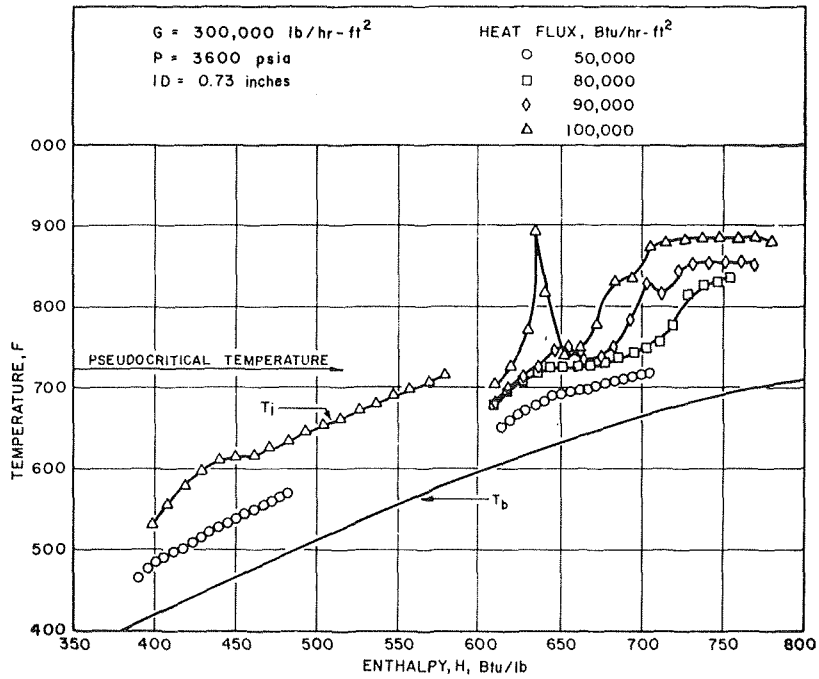

Fig. 7 Temperature profile for 0.73-in-ID smooth tube

significantly reduced and approach values which would be predicted by present correlations. It is very likely that this different peaking along the length of the tube is a result of nonequilibrium fluid conditions which occur both radially and along the tube length in this transient heat transfer phenomenon.

The effect of heat flux on the severity of the temperature peaking is also shown. As the flux is progressively increased from 80,000–100,000 Btu/hr-ft², temperature peaking on the inlet portion of the tube becomes the most severe. Further increases in the flux would have led to physical destruction of the tube.

Tests at other mass flow rates and pressures showed the same trends as observed with the smaller diameter tube.

A final example of what is considered to be film boiling in smooth tubes is shown in Fig. 8 for a 0.96-in-ID tube. The data are for 3600 psia, a mass velocity of 300,000 lb/hr-ft², and various nominal heat fluxes.

Both groups of data are in the pseudocritical fluid-temperature range, and the unpredictable temperature profiles are evident for both. The lower fluid-temperature data show that only minor temperature peaking occured at a heat flux of 90,000 Btu/hr-ft², but an increase to 100,000 Btu/hr-ft² caused a severe peak in the inlet portion of the tube. Peaking in the outlet portion of the tube also occurred, but the peaks were not as severe as those at the inlet.

The second group of data show that at higher inlet fluid temperatures, temperature peaking at the inlet portion of the tube was severe at a heat flux of only 70,000 Btu/hr-ft². This same trend was seen for all of the various conditions covered; that is, as the fluid temperature approached the pseudocritical temperature, lower heat fluxes were required to initiate temperature peaking, and the peaking was more sensitive to heat-flux increases.

Tests at other mass flow rates and pressures showed the same trends with the large-diameter tube as were described previously for smaller tubes.

With the tests which have been conducted and the evidence of temperature peaking that has been obtained, we believe that a pseudofilm boiling phenomenon at supercritical pressure can occur. The similarity of trends of the peaking data at supercritical pressure with film boiling data at subcritical pressure further suggests that an analogous mechanism is occurring.

Based on an examination of all the data obtained, the following general trends may be identified.

1 For a given pressure, mass velocity, heat flux, and tube diameter, pseudofilm boiling can occur when the fluid temperature is below the pseudocritical temperature and the pseudocritical temperature occurs in the boundary layer. Increases in test section inlet fluid temperature cause increasing severity of the tube temperature peaking up to a certain point. This point is usually just below the pseudocritical temperature. Further increases in inlet fluid temperature cause decreasing differences between tube and fluid temperatures until temperature peaking completely disappears at fluid temperatures above the pseudocritical temperature.

2 For a given pressure and tube diameter, the relation between the minimum heat flux which will cause pseudofilm boiling (whatever the fluid temperature required) and mass velocity is shown in Fig. 9. This sketch of a "limit" curve shows that operation in the region below and to the right of the line for a given diameter will cause pseudofilm boiling to occur. Operation above and to the left will result in normal forced-convection heat transfer that is readily predictable. It can also be seen that as mass flow increases, higher heat fluxes can be sustained without the danger of causing pseudofilm boiling to occur at any fluid temperature.

3 For given pressure and mass velocity, the use of smaller diameter tubes allows higher heat fluxes before initiation of psuedofilm boiling. This is also shown in Fig. 9. In the area of our interests, a 40 percent increase in the allowable heat flux occurs when going from a 0.96-in. tube down to a 0.37-in-dia tube.

4 For a given mass velocity, an increase in pressure above the critical pressure allows operation at higher heat fluxes without causing pseudofilm boiling to occur. That is, the limit curve in Fig. 9, in general, shifts to the right as pressure is increased.

As the foregoing results were being accumulated, it became obvious that presently available correlations for supercritical pressure heat transfer did not adequately describe the complete heat transfer process. In fact, use of these correlations to design heat transfer equipment without recognizing that pseudofilm boiling can occur, and without knowing the conditions under which it will occur, could lead to inadequate designs. Therefore, use of these correlations is limited to some minimum mass

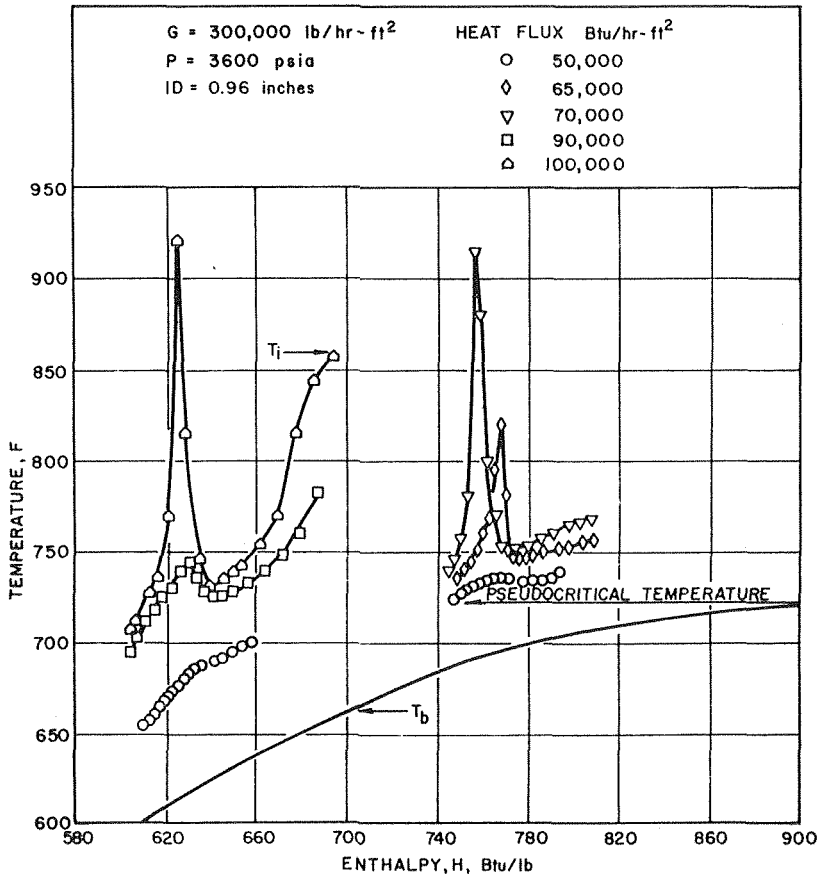

Fig. 8 Temperature profile for 0.96-in-ID smooth tube

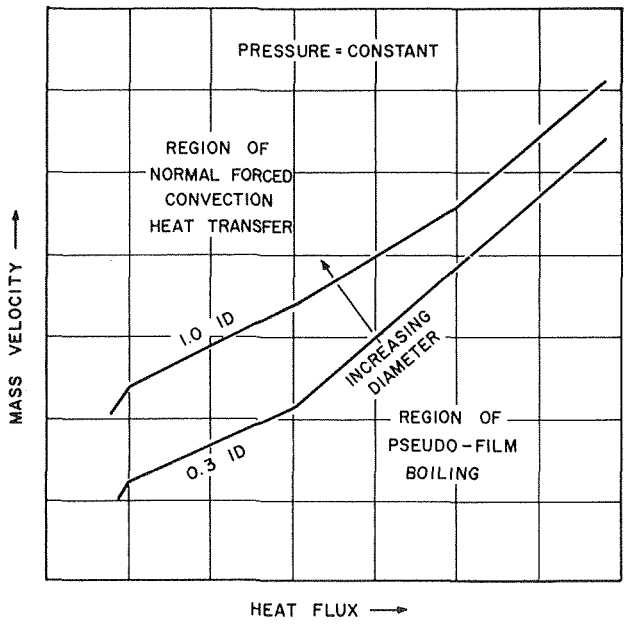

Fig. 9 Pseudofilm boiling limit curve

SOURCE: SWENSON (REFERENCE 13)

CURVE	TUBE	PRESSURE PSIA	MASS VELOCITY LB/HR-FT^2	HEAT FLUX BTU/HR-FT^2	DIAMETER IN.
A	SMOOTH	3000	700,000	157,000(I.D.)	0.408
B	RIBBED	3000	700,000	157,000(I.D.)	0.411(MIN.)

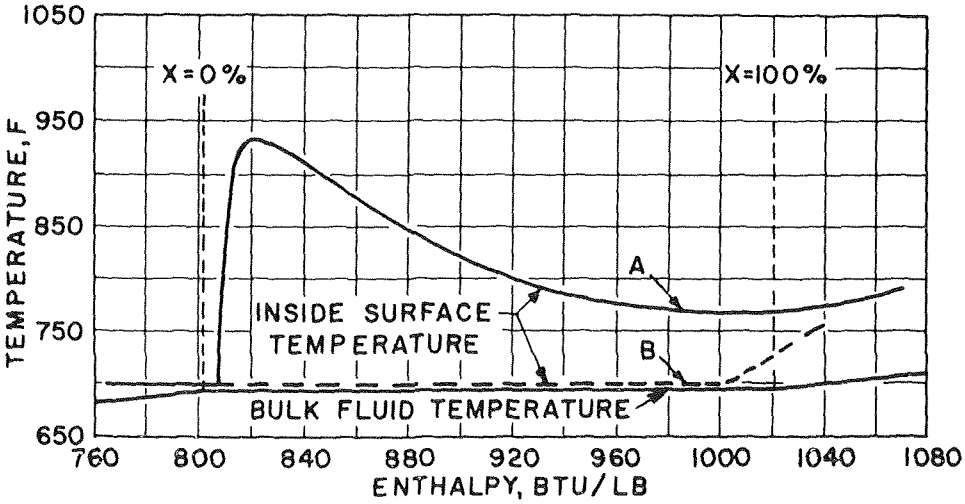

Fig. 10 Comparison of heat transfer performance with smooth and ribbed tube

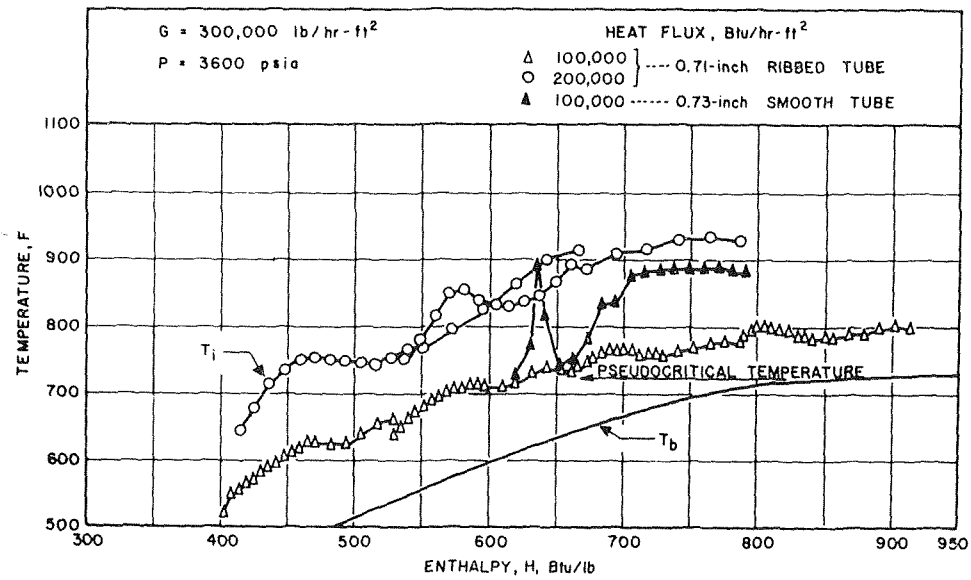

Fig. 11 Temperature profile for 0.71-in-ID ribbed tube

velocity or some maximum heat flux for any particular set of operating conditions.

Results With Ribbed Tube

Earlier experience with ribbed tubes at subcritical pressure showed that these tubes inhibit the occurrence of film boiling [13]. That is, it was shown that at subcritical pressure certain configurations of internally ribbed surfaces in steam-generating tubes will prevent film boiling from occurring at lower mass velocities and higher heat fluxes than those at which film boiling would occur in smooth tubes. For example, Fig. 10 shows the improvement attained with a ribbed tube as described in reference [13]. With a smooth tube, film boiling was initiated at about 3 percent steam quality, whereas a ribbed tube operating at the same conditions prevented film boiling from occurring until about 90 percent steam quality.

This performance suggested that a similar improvement could be attained with ribbed tubes at supercritical pressure since the film-boiling phenomenon appeared to be so similar. Therefore, a second series of supercritical pressure tests were conducted on a ribbed tube, Fig. 4, to determine if it did prevent pseudofilm boiling.

One example of the results of these tests is shown in Fig. 11. Tube temperature profiles for the ribbed tube are shown for 3600 psia, a mass velocity of 300,000 lb/hr-ft^2, and heat fluxes of 100,000 and 200,000 Btu/hr-ft^2. Data at 100,000 Btu/hr-ft^2 for a smooth tube of about the same diameter are also shown for comparison.

From these data it can be seen that at a heat flux of 100,000 Btu/hr-ft^2, the ribbed tube does suppress film boiling and provides superior heat transfer performance over the smooth tube. In fact, at a heat flux of 200,000 Btu/hr-ft^2, the ribbed tube con-

times to suppress film boiling, whereas tube temperatures for the same heat flux in a smooth tube would clearly be excessive. It should be noted that the temperature profiles for the ribbed tube do show slight temperature peaking at the inlet of the tube, particularly at the highest flux shown. However, this peaking is seen to be much less severe and considerably less sensitive to heat-flux changes than the temperature peaks observed for smooth tubes and, as a result, is not a significant consideration in the range of operating conditions covered.

Results for the same ribbed tube at other pressures, mass velocities, and heat fluxes show the same significant improvement in performance over smooth tubes.

There was also interest in the ribbed tube's pressure-drop performance since this, too, is an important consideration in design work. Accordingly, isothermal pressure-drop tests were conducted, and it was found that the friction factors for the ribbed tube are approximately 25 percent higher than friction factors for a smooth tube.

Summary

1 Based on experimental data obtained on smooth tubes over a wide range of operating conditions, it is believed that a pseudofilm boiling phenomenon can occur at supercritical pressures.

2 The occurrence of pseudofilm boiling and its characteristics are affected by pressure, bulk fluid temperature, mass velocity, heat flux, and tube diameter, and the effect of each variable has been described.

3 An internally ribbed tube will suppress pseudofilm boiling and permit operation at higher heat fluxes than would have been possible with smooth tubes.

Acknowledgment

The author wishes to acknowledge the contributions of A. R. Brunsvold, S. C. Garg, and J. S. Slotnik, who assisted in obtaining and analyzing the data presented.

References

1 Dickinson, N. L., and Welch, C. P., "Heat Transfer to Supercritical Water," TRANS. ASME, Vol. 80, 1958, pp. 746–752.

2 Goldmann, K., "Heat Transfer to Supercritical Water at 5000 psi Flowing at High Mass Flow Rates Through Round Tubes," *International Developments in Heat Transfer*, Part III, ASME, 1961, pp. 561–568.

3 Shitsman, M. E., "Impairment of the Heat Transmission at Supercritical Pressure," *Teplofizika Vysokikh Temperatur*, Vol. 1, No. 2, Sept.-Oct. 1963, pp. 267–275.

4 Vikhrev, Yu. V., and Lokshin, V. A., "Experimental Investigation of Temperature Regime of Horizontal Steam Generating Tubes at Supercritical Pressures," *Teploenergetika*, Vol. 11, No. 12, 1964, pp. 79–82.

5 Swenson, H. S., Carver, J. R., and Kakarala, C. R., "Heat Transfer to Supercritical Water in Smooth-Bore Tubes," JOURNAL OF HEAT TRANSFER, TRANS. ASME, Series C, Vol. 87, 1965, pp. 477–484.

6 Bishop, A. A., Sandberg, R. O., and Tong, L. S., "Forced-Convection Heat Transfer to Water to Near-Critical Temperatures and Supercritical Pressures," WCAP-2056, Part IV, Feb. 1965.

7 Powell, W. B., "Heat Transfer to Fluids in a Region of a Critical Temperature," *Jet Propulsion*, Vol. 27, July 1957, pp. 776–783.

8 Griffith, J. D., and Sabersky, R. H., "Convection in a Fluid at Supercritical Pressures," *ARS Journal*, Vol. 30, Mar. 1960, pp. 289–291.

9 Koppel, L. B., and Smith, J. M., "Turbulent Heat Transfer in the Critical Region," *International Developments in Heat Transfer*, Part III, ASME, 1961, pp. 585–590.

10 Bonilla, C. F., and Sigel, L. A., "High Intensity Natural-Convection Heat Transfer Near the Critical Point," *Chemical Engineering Progress, Symposium Series*, Vol. 87, 1961, pp. 87–95.

11 Nishikawa, K., and Miyabe, K., "On the Boiling-Like Phenomena at Supercritical Pressures," *Memoirs of Faculty of Engineering*, Kyushu University, Vol. 25, No. 1, Dec. 1965, pp. 1–25.

12 Kafengauz, N. L., "Characteristics of the Heat Transfer to a Turbulent Flow at Supercritical Pressure," *Soviet Physics—Doklady*, Vol. 12, No. 3, Sept. 1967, pp. 278–280.

13 Swenson, H. S., Carver, J. R., and Szoeke, G., "The Effects of Nucleate Boiling Versus Film Boiling on Heat Transfer in Power Boiler Tubes," *Journal of Engineering for Power*, TRANS. ASME, Series A, Vol. 84, 1962, pp. 365–371.

tinues to suppress film boiling, whereas tube temperatures for the same heat flux in a smooth tube would clearly be excessive. It should be noted that the temperature profiles for the ribbed tube do show slight temperature peaking at the inlet of the tube, particularly at the highest flux shown. However, this peaking is seen to be much less severe and considerably less sensitive to heat-flux changes than the temperature peaks observed for smooth tubes and, as a result, is not a significant consideration in the range of operating conditions covered.

Results for the same ribbed tube at other pressures, mass velocities, and heat fluxes show the same significant improvement in performance over smooth tubes.

There was also interest in the ribbed tube's pressure-drop performance since this, too, is an important consideration in design work. Accordingly, isothermal pressure-drop tests were conducted, and it was found that the friction factors for the ribbed tube are approximately 25 percent higher than friction factors for a smooth tube.

Summary

1 Based on experimental data obtained on smooth tubes over a wide range of operating conditions, it is believed that a pseudofilm boiling phenomenon can occur at supercritical pressures.

2 The occurrence of pseudofilm boiling and its characteristics are affected by pressure, bulk fluid temperature, mass velocity, heat flux, and tube diameter, and the effect of each variable has been described.

3 An internally ribbed tube will suppress pseudofilm boiling and permit operation at higher heat fluxes than would have been possible with smooth tubes.

Acknowledgment

The author wishes to acknowledge the contributions of A. R. Brunsvold, S. C. Garg, and J. S. Slotnik, who assisted in obtaining and analyzing the data presented.

References

1 Dickinson, N. L., and Welch, C. P., "Heat Transfer to Supercritical Water," TRANS. ASME, Vol. 80, 1958, pp. 746–752.

2 Goldmann, K., "Heat Transfer to Supercritical Water at 5000 psi Flowing at High Mass Flow Rates Through Round Tubes," *International Developments in Heat Transfer*, Part III, ASME, 1961, pp. 561–568.

3 Shitsman, M. E., "Impairment of the Heat Transmission at Supercritical Pressure," *Teplofizika Vysokikh Temperatur*, Vol. 1, No. 2, Sept.-Oct. 1963, pp. 267–275.

4 Vikhrev, Yu. V., and Lokshin, V. A., "Experimental Investigation of Temperature Regime of Horizontal Steam Generating Tubes at Supercritical Pressures," *Teploenergetika*, Vol. 11, No. 12, 1964, pp. 79–82.

5 Swenson, H. S., Carver, J. R., and Kakarala, C. R., "Heat Transfer to Supercritical Water in Smooth-Bore Tubes," JOURNAL OF HEAT TRANSFER, TRANS. ASME, Series C, Vol. 87, 1965, pp. 477–484.

6 Bishop, A. A., Sandberg, R. O., and Tong, L. S., "Forced-Convection Heat Transfer to Water to Near-Critical Temperatures and Supercritical Pressures," WCAP-2056, Part IV, Feb. 1965.

7 Powell, W. B., "Heat Transfer to Fluids in a Region of a Critical Temperature," *Jet Propulsion*, Vol. 27, July 1957, pp. 776–783.

8 Griffith, J. D., and Sabersky, R. H., "Convection in a Fluid at Supercritical Pressures," *ARS Journal*, Vol. 30, Mar. 1960, pp. 289–291.

9 Koppel, L. B., and Smith, J. M., "Turbulent Heat Transfer in the Critical Region," *International Developments in Heat Transfer*, Part III, ASME, 1961, pp. 585–590.

10 Bonilla, C. F., and Sigel, L. A., "High Intensity Natural-Convection Heat Transfer Near the Critical Point," *Chemical Engineering Progress, Symposium Series*, Vol. 87, 1961, pp. 87–95.

11 Nishikawa, K., and Miyabe, K., "On the Boiling-Like Phenomena at Supercritical Pressures," *Memoirs of Faculty of Engineering*, Kyushu University, Vol. 25, No. 1, Dec. 1965, pp. 1–25.

12 Kafengauz, N. L., "Characteristics of the Heat Transfer to a Turbulent Flow at Supercritical Pressure," *Soviet Physics—Doklady*, Vol. 12, No. 3, Sept. 1967, pp. 278–280.

13 Swenson, H. S., Carver, J. R., and Szoeke, G., "The Effects of Nucleate Boiling Versus Film Boiling on Heat Transfer in Power Boiler Tubes," *Journal of Engineering for Power*, TRANS. ASME, Series A, Vol. 84, 1962, pp. 365–371.

DISCUSSION

B. S. Shiralkar[6]

The author is to be complimented on a comprehensive experimental study of heat transfer to supercritical pressure water. It was gratifying for us to find many of the trends in this data qualitatively similar to those for carbon dioxide described in our paper 69-WA/HT-1.[7]

We feel that the author has not stressed the differences between the results for small and large dia tubes, which we believe to be due to free convection. An examination of data for water and carbon dioxide[8] has shown that the nature of the temperature peak changes considerably when free convection is dominant. In this case, the temperature peaks are much sharper and not as well behaved, i.e., do not occur in a well defined subcritical bulk enthalpy range. The same phenomenon can be seen by comparing Fig. 5 for the 0.37-in-dia tube versus Fig. 7 and 8 for larger tubes in the paper. Based on previous data for water, we had suggested[8] that this transition occurs when a free convection parameter Gr/Re^2 is of the order of magnitude of 2×10^{-3}, where the Reynolds number and Grashof number are based on viscosity at the wall temperature.

For the data shown in Figs. 5, 7, and 8 we have calculated approximately, the value of Gr/Re^2 as shown in the following:

Fig.	Gr/Re^2	Nature of Temperature Peak
5	0.55×10^{-3}	Not Sharp - free convection not important
7	9.25×10^{-3}	Sharp - free convection dominant
8	12.70×10^{-3}	Sharp - free convection dominant

These values appear to support our value of 2×10^{-3} for Gr/Re^2 as a transition value. We would be interested to know whether sharp unpredictable peaks were obtained in the wall temperature profile, with the 0.37-in. tube and if so, the mass velocities at which they occurred.

There are also indications[9] that in large diameter tubes, temperature peaks do not occur in downflow. Did the author perform any tests in downflow?

---

[6] Engineer, Core Development, A.P.E.D., General Electric Co., San Jose, Calif. Assoc. Mem. ASME.

[7] Shiralkar, B., Griffith, P., "The Effect of Swirl, Inlet Conditions, Flow Direction and Tube Diameter on the Heat Transfer to Fluids at Supercritical Pressure," Paper No. 69-WA/HT-1, presented at the Winter Annual Meeting of the ASME, Nov. 1969.

[8] Shiralkar, B. S., and Griffith, Peter, "The Deterioration in Heat Transfer to Fluids at Supercritical Pressure and High Heat Fluxes," Report No. DSR-70332-55, Department of Mechanical Engineering, Massachusetts Institute of Technology, June 1968.

[9] Jackson, J. D., and Evans-Lutterodt, K., "Impairment of Turbulent Forced Convection Heat Transfer to Supercritical Pressure CO_2 Caused by Buoyancy Forces," Report NE2, Simon Engineering Laboratories, Manchester University, 1968.

Author's Closure

The general philosophy of The Babcock & Wilcox Company, in regard to pseudoboiling heat transfer at supercritical pressure, is to avoid temperature peaking rather than design for it. Because the nature of peaking is sensitive to operating conditions, we feel the best approach is to define the conditions that cause peaking not predicted by our correlations, and then design our steam generators to avoid these conditions entirely.

Accordingly, we have not stressed differences in the *nature* of temperature peaks observed on small and large diameter tubes. These differences are of only minor importance to us. We are more interested in the conditions that cause *initiation* of temperature peaking.

Because of our concentration on initiation of peaks, we are unable to agree or disagree with Mr. Shiralkar's analysis of the nature of peaks. However, we can say that all data on small diameter tubes are like that presented in the paper.

For anyone who is interested in analyzing data from the 0.37-india tube, the data are available from the Library of Congress. (Request document 8110 from Chief, Photo Duplication Service, Library of Congress, Washington, D. C.)

No tests were run with downflow, although tests are continuing on both smooth and internally ribbed tubes at various inclinations.

W. M. KAYS
Professor of Mechanical Engineering.

R. J. MOFFAT
Associate Professor of Mechanical Engineering.

Stanford University, Stanford, Calif.

W. H. THIELBAHR
Graduate Student in Mechanical Engineering, Stanford University; Presently, Naval Weapons Center, China Lake, Calif.

Heat Transfer to the Highly Accelerated Turbulent Boundary Layer With and Without Mass Addition

Experimental heat transfer data are presented for a series of asymptotic accelerated turbulent boundary layers for the case of an impermeable wall, and several cases of blowing, and suction. The data are presented as Stanton number versus enthalpy thickness Reynolds number.

As noted by previous investigators, acceleration causes a depression in Stanton number when the wall is impermeable. Suction increases this effect, while blowing suppresses it. The combination of mild acceleration and strong blowing results in Stanton numbers which lie above the correlation for the same blowing but no acceleration.

Velocity and temperature profiles are presented, from which it is possible to deduce explanations for the observed behavior of the Stanton number. A prediction scheme is proposed which is demonstrated to quite adequately reproduce the Stanton number results, using correlations derived from the profiles.

Introduction

In 1965, Moretti and Kays [1][1] presented the results of an experimental investigation of heat transfer to a highly accelerated turbulent boundary layer. Of particular interest was the fact that for very strong accelerations Stanton number was observed to decrease abruptly and to approach what one would predict for a purely laminar boundary layer. These results have been frequently cited as evidence that a strong favorable pressure gradient tends to cause a retransition of a turbulent boundary layer to a laminar boundary layer. The phenomenon of retransition has been the subject of numerous recent studies, Launder [2], Launder and Stinchcombe [3], and Patel and Head [4], among others. The term "laminarization," suggested by Launder, has been frequently used instead of retransition.

It seems now to be generally agreed that a turbulent boundary layer will "laminarize," or undergo a retransition to a laminar boundary layer, in the presence of a sufficiently strong favorable pressure gradient. However, there is a very important region of technical applications in the range of moderately strong favorable pressure gradients where the boundary layer is definitely not laminar but where laminar-like behavior is observed and, in particular, Stanton number is observed to fall substantially below what would be predicted by earlier theories. The present paper is concerned with the heat transfer behavior in this region, including the effects of transpiration (blowing and suction).

[1] *Numbers in brackets designate References at end of paper.*

Contributed by the Heat Transfer Division of The American Society of Mechanical Engineers and presented at the AIChE-ASME Heat Transfer Conference, Minneapolis, Minn., August 3–6, 1969. Manuscript received by the Heat Transfer Division, March 3, 1969. Paper No. 69-HT-53.

Nomenclature

A^+ = constant in the Van Driest damping factor
C_f = friction coefficient ($= \tau_0/(\rho u_\infty^2/2)$)
c_p = specific heat
D_v = Van Driest mixing-length damping factor
F = blowing fraction ($= v_w/u_\infty$)
H = boundary layer shape factor ($= \delta_1/\delta_2$)
h = convective heat transfer coefficient
K = acceleration parameter ($= (\nu/u_\infty^2)(du_\infty/dx)$)
k = mixing-length constant
l = mixing-length
$\dot{q}$ = heat transfer rate
t = temperature
t_w = wall, or surface, temperature
t_∞ = free-stream temperature
u = velocity in x-direction
u_∞ = free-stream velocity
u_τ = friction velocity ($= u/(u_\infty\sqrt{C_f/2})$)
v_w = velocity in y-direction at the wall (transpiration velocity), positive v_w for blowing, negative for suction
x = distance along surface
y = distance normal to surface

(Continued on next page)

Both Moretti and Kays, and Launder, proposed that a significant acceleration parameter, K, can be defined as follows

$$K = \frac{\nu}{u_\infty^2}\frac{du_\infty}{dx} \tag{1}$$

Various combinations of K and the friction coefficient have also been proposed. For example, in the analysis of a Couette flow, the effect of a pressure gradient occurs in the form of a nondimensional P^+, which is related to K as follows

$$P^+ = -K/(C_f/2)^{3/2} \tag{2}$$

The parameter K, however, has the virtue of being entirely dependent upon externally imposed conditions and is, therefore, a convenient descriptor of the boundary conditions imposed upon the flow. Launder suggested that laminarization will occur when K is greater than 2×10^{-6}; Moretti and Kays suggested 3.5×10^{-6}. The present paper is concerned with values of K in the range 0.0 to 2.5×10^{-6}, and thus is concerned with a region of what is believed to be stable turbulent boundary layers.

Further insight into the significance of the parameter K can be gained by examination of the momentum integral equation of the boundary layer, and the energy integral equation of the boundary layer. For constant property flow along a flat plate, it is possible to express the *momentum* integral equation of the boundary layer in the following form

$$\frac{d\mathrm{Re}_M}{dR_x} = \frac{C_f}{2} - K(1 + H)\mathrm{Re}_M + F \tag{3}$$

where

$$dR_x = u_\infty \rho dx/\mu$$

$$F = v_w/u_\infty$$

For constant free-stream temperature and constant surface temperature, the corresponding form of the *energy* integral equation of the boundary layer is

$$\frac{d\mathrm{Re}_H}{dR_x} = \mathrm{St} + F \tag{4}$$

Note that K appears explicitly only in the momentum equation, and of particular interest is the fact that a sufficiently large *positive* value of K can cause a decrease in Re_M. In fact, it appears that if K is maintained as a positive constant over a sufficient length of surface, and if F is zero or a positive constant, then the rate of change of Re_M will tend towards zero. This yields a boundary layer of constant momentum thickness Reynolds number, Re_M, which will be termed an "asymptotic" accelerating boundary layer. Exact solutions for asymptotic laminar boundary layers have been obtained (5), and Launder and Stinchcombe have demonstrated that such asymptotic boundary layers can be obtained for turbulent flows. Under such conditions, not only is Re_M constant, but also $C_f/2$ and the shape factor H. It also follows that under asymptotic conditions the velocity profiles at various stations along the surface will possess both inner and outer region similarity.

On the other hand, examination of equation (4) reveals that so long as F is zero or a positive constant, the energy thickness Reynolds number, Re_H, will always continue to grow. (The same conclusions apply for small negative values of F. However, strong suction leads to an asymptotic *suction* layer, regardless of K, with no growth in either Re_M or Re_H.) One can conclude that for prolonged accelerations at any constant value of K and positive F, Re_M will approach a constant value, whereas Re_H will increase indefinitely.

This behavior suggests one reason why, even at moderate values of K, Stanton number will tend to decrease in an accelerated flow. Re_H can only increase indefinitely if the thermal boundary layer grows outside of the momentum boundary layer into a region of zero eddy conductivity and higher heat transfer resistance. This phenomena is discussed by Launder and Lockwood [13]. It will be seen later that this is not the only reason for decreasing Stanton numbers in accelerated flows, but it is certainly a contributing factor.

An acceleration at constant K is particularly easy to establish experimentally with an incompressible fluid, since it can be shown from continuity that flow between two convergent flat surfaces yields a nearly constant K when the blowing fraction, F, is uniform. *Asymptotic* constant K boundary layers are even more convenient for experimental study because once the asymptotic condition has been closely approached, it is relatively easy to accurately deduce the friction coefficient using equation (3). Furthermore, it is a simple matter to obtain a nearly asymptotic boundary layer by arranging a starting length with constant free-stream velocity (before acceleration) such that Re_M at the beginning of acceleration is close to the anticipated asymptotic value, thereby avoiding a lengthy transition region. For most of the experimental results presented by Moretti and Kays, Re_M was considerably greater than the asymptotic value at the beginning of acceleration even though K was nearly constant, and thus the reported heat transfer results were primarily in a region of rapidly decreasing Re_M. Such accelerated boundary layers will be referred to as "overshot"; obviously boundary layers can also be "undershot" if the value of Re_M before acceleration is less than the asymptotic value.

Nomenclature

γ = thermal conductivity
γ_t = turbulent thermal conductivity, or eddy conductivity
γ_{eff} = $(\gamma + \gamma_t)$
δ = 99 percent thickness of momentum layer
δ_1 = displacement thickness $= \int_0^\infty \left(1 - \frac{u}{u_\infty}\right) dy$
δ_2 = momentum thickness $= \int_0^\infty \left(1 - \frac{u}{u_\infty}\right)\left(\frac{u}{u_\infty}\right) dy$
Δ_2 = enthalpy thickness $= \int_0^\infty \left(\frac{u}{u_\infty}\right)\left(\frac{t - t_\infty}{t_w - t_\infty}\right) dy$
λ = a turbulence length scale
μ = viscosity coefficient
μ_t = turbulent viscosity, or eddy viscosity
μ_{eff} = $(\mu + \mu_t)$
ν = kinematic viscosity (μ/ρ)
ρ = density
τ = shear stress
τ_w = shear stress at wall
P^+ = a pressure gradient parameter $(= -K/(C_f/2)^{3/2})$
Pr = Prandtl number $(\mu c_p/\gamma)$
Pr_t = turbulent Prandtl number $(\mu_t c_p/\gamma_t)$
Re_M = momentum thickness Reynolds number $(= u_\infty \delta_2/\nu)$
Re_H = enthalpy thickness Reynolds number $(= u_\infty \Delta_2/\nu)$
R_x = an integrated x-distance Reynolds number $\left(= \int_0^x \frac{u_\infty}{\nu} dx\right)$
St = Stanton number $(= h/(u_\infty \rho c_p))$
t^+ = nondimensional temperature $= \frac{(t - t_w)}{(t_\infty - t_w)} \frac{1}{u_\infty^+ \mathrm{St}}$
u^+ = nondimensional velocity $(= u/u_\tau)$
v_w^+ = nondimensional blowing parameter $(= v_w/(u_\infty \sqrt{C_f/2}))$
y^+ = nondimensional distance from wall $(= yu_\tau/\nu)$
x^+ = nondimensional distance along the wall $(= xu_\tau/\nu)$

The Stanford Heat and Mass Transfer Apparatus was designed for accurate measurement of local heat transfer coefficients along a flat surface through which transpiration (either blowing or suction) can take place in any prescribed manner, and over which free-stream velocity can be varied in any arbitrary manner. Extensive experimental results obtained from this apparatus for the case of constant free-stream velocity and the entire spectrum of blowing and suction have been presented in Moffat and Kays [6], and Simpson, Moffat, and Kays [7]. The apparatus is also ideally suited for a study of the behavior of asymptotic accelerated turbulent boundary layers with blowing or suction. This paper is a brief summary of a few of the results of such an investigation. As such, it is a continuation of the work of Moretti and Kays, but differing in two major respects:

(*a*) An attempt is made to obtain close to asymptotic boundary layers, and thus to carry out a more controlled experiment;
(*b*) The additional effects of blowing and suction on acceleration are studied, with emphasis on certain unexpected results of the coupling of blowing and acceleration.

More complete and extensive data resulting from this investigation will be presented in a later paper.

Objectives of This Paper

The specific objectives of this paper are to:

(*a*) Present the results of a systematic series of heat transfer experiments on asymptotic accelerated turbulent boundary layers for a series of values of the acceleration parameter K up to 2.5×10^{-6}, and blowing fraction, F, from -0.002 to $+0.006$;
(*b*) Present representative velocity and temperature profiles, and on the basis of these profiles to attempt to explain the physical phenomena observed;
(*c*) Present some results of an analytic prediction scheme, based on a finite difference solution of the boundary layer equations, to demonstrate a mathematical model of the phenomena observed.

Apparatus and Data Reduction

The Stanford Heat and Mass Transfer Apparatus contains a 24-segment porous plate eight ft long and 18 in. wide, which forms the bottom surface of a rectangular flow duct. The main stream flow and the transpiration flow are both air. Each of the 24 segments is provided with separately controllable transpiration flow and electric power. Fig. 1 shows a cross section of one segment. The balsa wood insulation on the walls of the plenum, the preplate, and the honeycomb flow straighteners serve to ensure uniform air temperature entering the working plate. Five thermocouples are imbedded in the plate, in the center six-in. span. The working plate is 0.25 in. thick, made of sintered bronze with an average particle diameter of 0.005 in. Heater wires are imbedded in grooves in the bottom of the plate, close enough together so that the top surface of the plate is uniform in temperature to within 0.04 deg F at maximum power and blowing. Pressure drop through the working plate is approximately 12 in. of water at maximum blowing, so that the maximum streamwise pressure gradient (approximately 0.5 in. of water per segment width) has only a small effect on the distribution of the transpiration flow.

Two different top covers, shown in Fig. 2, were used for the test duct. One with a single hinge line across it, and one with two hinge lines, permitted constant K flows to be established by setting the desired slope of the top surface. Static pressures were measured with side-wall taps spaced 2 in. apart in the flow direction. Static pressure traverses of the main stream and boundary layer showed no more than 0.002 in. H_2O variation across a plane in the accelerating region.

Temperature and velocity traverses were made with manually operated micrometer driven traverse gear. Flat mouthed total pressure probes were used with tips 0.012 in. high and 0.040 wide. Temperature traverses were made using iron-constantan thermocouples with junctions flattened to 0.009 in.

Stanton numbers reported here are based on the heat transfer from the plate to the boundary layer as deduced by an energy balance on each plate.

$$\dot{q} = \text{Net Power} - \text{ECONV-}\Sigma\text{QRAD-}\Sigma\text{QCOND}$$

ECONV measures the energy transport associated with the transpiration flow. Radiation from the top and bottom of the plate is calculated, based on measured emissivities of the plate. Heat is also lost by conduction from the center span of the plate to the ends of the plate and to the casting. All corrections were evaluated as functions of plate temperature and transpiration rate and appropriately entered into the data program.

A somewhat more detailed description is presented by Moffat and Kays [6].

Qualification of the Experimental System

Validity of the data reduction program as a mathematical model of the apparatus was established by a series of energy balance tests conducted with no main stream flow. The energy balances closed within 2 percent for most blowing cases and 4

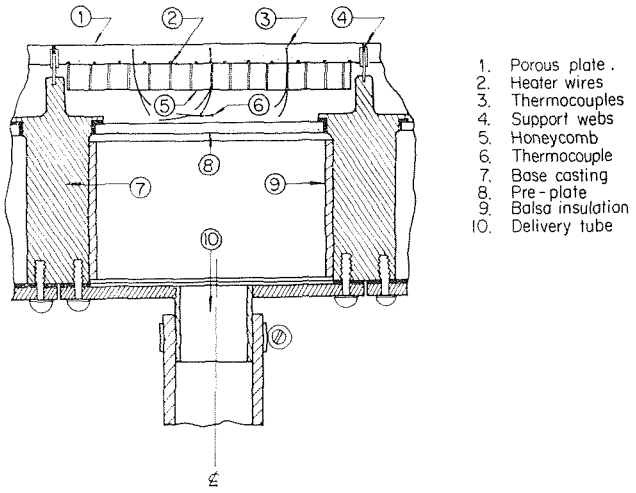

Fig. 1 A segment of the porous test plate showing transpiration system and plate heating system

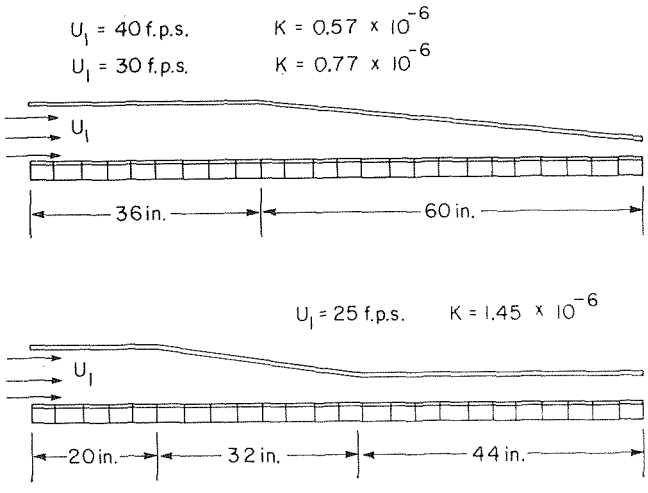

Fig. 2 Arrangement of top covers of test duct to obtain constant K acceleration

percent for most suction cases. The Stanton numbers reported here are believed to be reliable to within 0.0001 units, for the blown cases, and 0.0002 units for suction.

Free-stream turbulence intensities ($\sqrt{\overline{u'^2}}/u_\infty$) were found to be between 0.8 and 1.2 percent although velocity profiles taken in the uniform velocity section satisfy Coles' criterion for "normal" boundary layers [8].

Two side effects must be investigated before the observed change in Stanton number behavior can be attributed solely to the effects of acceleration. It must be shown that the data are not influenced by surface roughness and that data for various uniform velocities will display a universal relationship when plotted against enthalpy thickness Reynolds number.

Surface roughness and velocity effects were investigated by a series of tests at 40, 86, and 126 fps. Stanton number data shows the same relationship to enthalpy thickness Reynolds number for all three velocities, although the velocity profiles show a slight drop in u^+ for the data at 126 fps. Plate roughness elements, considered as half the particle diameter, are calculated to remain inside the viscous region of the boundary layer as best as this can be determined.

Two-dimensionality of a flow can only be established by elaborate probing of the boundary layers. This was not done. Secondary evidence, however, can be had by comparing enthalpy thickness derived from plate heat transfer measurements with values determined from temperature and velocity profiles. Such checks show agreement within 8 percent for all blowing runs. This is within the uncertainty calculated for the enthalpy thickness integrals using the method of Kline and McClintock [9].

Results

Stanton number data are shown in Figs. 3 through 6, plotted against enthalpy thickness Reynolds number, Re_H. Each figure shows the effect of varying K while holding F constant. Surface temperatures were held constant, for all tests, at approximately 100 deg F, while free-stream stagnation temperature was 60–70 deg F. The Stanton numbers were corrected to approximately constant property conditions by the factor $(T_w/T_\infty)^{0.4}$.

Fig. 3 shows the data for $F = 0.0$ using solid symbols to represent data in the accelerating region and hollow symbols for the constant velocity approach. Note that acceleration immediately depresses the Stanton number below the constant velocity results, with the magnitude of the depression increasing as K increases.

The data for $K = 2.5 \times 10^{-6}$ behaves almost as would be expected from a laminar boundary layer, based on the rate of change of Stanton number as enthalpy thickness increases. Shape fac-

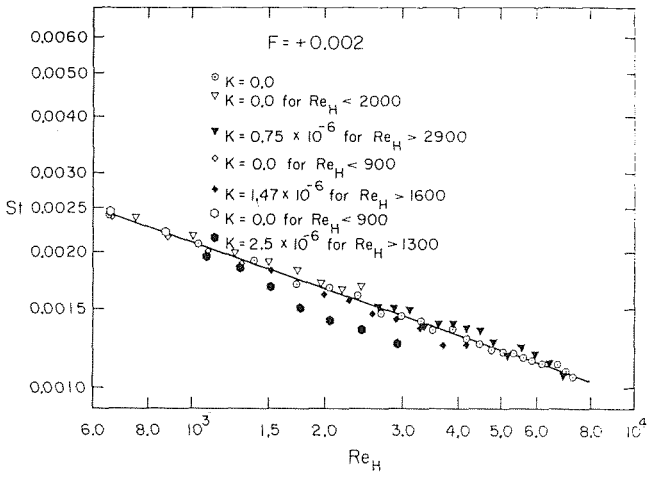

Fig. 4 Heat transfer results for four values of the acceleration parameter, K, for moderately strong blowing, $F = +0.002$

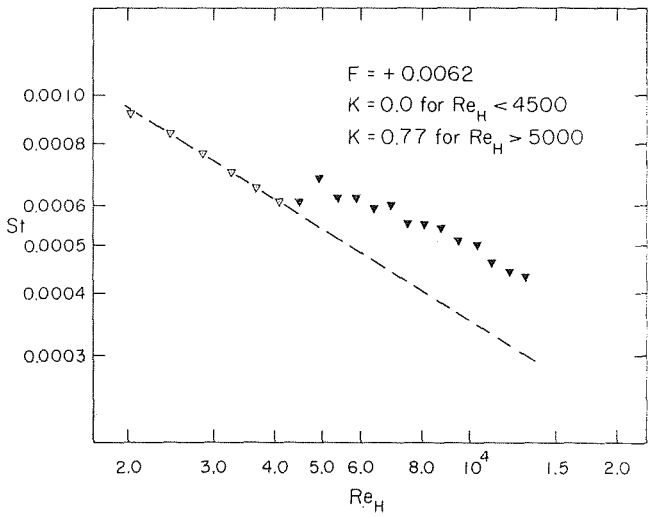

Fig. 5 Heat transfer results for a case of strong blowing, and moderate acceleration

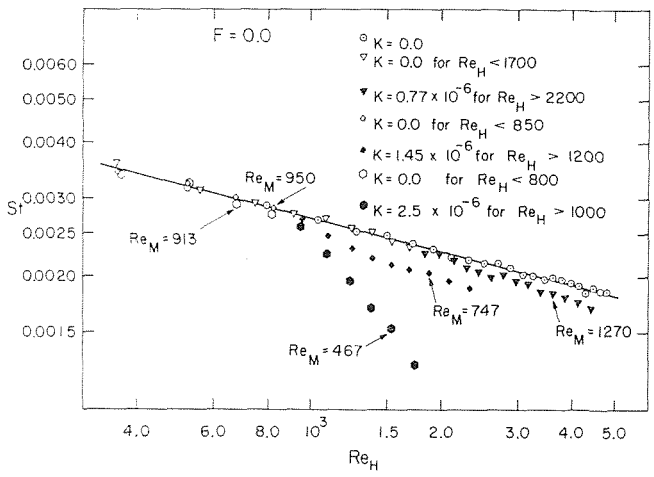

Fig. 3 Heat transfer results for four values of the acceleration parameter, K, for no transpiration, $F = 0.0$

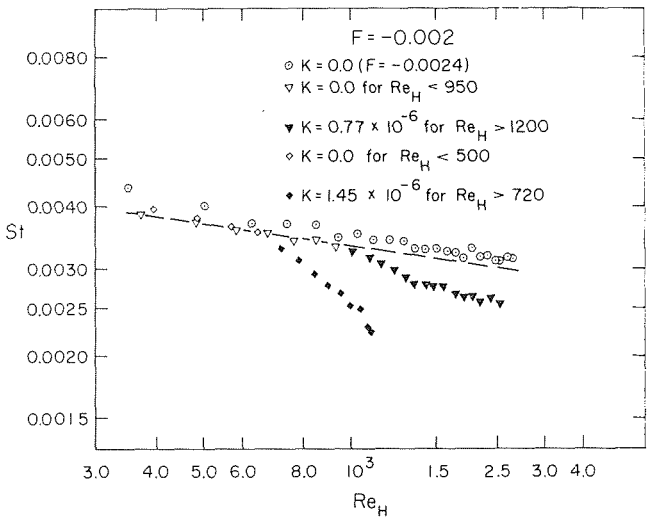

Fig. 6 Heat transfer results for three values of the acceleration parameter, K, for moderately strong suction, $F = -0.002$

tors, determined from the velocity profiles are approximately 1.4 to 1.5 for this acceleration, suggesting that the boundary layer is still turbulent (the shape factor for the asymptotic laminar layer is 2.0). No effort was made to measure turbulence intensities inside the layer.

It can be seen from Fig. 3 *that the boundary layers were slightly* "overshot," in that the momentum thickness Reynolds numbers *decrease* in the flow direction. The boundary layers are believed to be close to the asymptotic condition at the points where Re_M is marked in the accelerating region.

Fig. 4 presents Stanton number data for the same values of K as does Fig. 3, but with blowing: $F = +0.002$. All of the data for the different values of K lie much closer to the baseline data, taken from Moffat and Kays [6]. The spread in the data is reduced, and the entire pattern is shifted upward. Acceleration at $K = 0.75 \times 10^{-6}$ now results in a slight rise in Stanton number above the uniform velocity case, rather than a drop, and even the strongest acceleration ($K = 2.5 \times 10^{-6}$) produces only a relatively minor depression.

The upward shift indicated by Fig. 4 is seen much more clearly *in the results at higher blowing* (Fig. 5: $F = +0.0062$), and the opposite trend is observed for suction (Fig. 6: $F = -0.002$). In the presence of strong blowing, even a moderate acceleration ($K = 0.77 \times 10^{-6}$) causes a dramatic upward shift from the uniform velocity values for the same blowing. Moderate suction, $F = -0.002$, increases the spread between the data for various K values and causes a general downward shift relative to the uniform velocity results.

The combination of blowing and acceleration can thus result in either an increase or a decrease in Stanton number (at fixed Re_H) in spite of the fact that either condition, applied alone, results in a decrease. Stanton number is thus not simply related to Re_H, K, and F even for the restricted case studied here of asymptotic boundary layers. It is not unreasonable to suppose that highly "overshot" or "undershot" layers will display somewhat *different characteristics, raising the number of variables* from 3 to 5. Experimental studies of these effects are planned for the near future, as well as investigations into the behavior of the boundary layer under conditions of variable K, and in the recovery region downstream of an acceleration.

Velocity profiles with $K = 1.45 \times 10^{-6}$ and $F = 0$ are shown on Fig. 7 with solid symbols, while one profile in the non-accelerating region of this run is shown with hollow symbols. This figure shows some of the important characteristics of accelerated turbulent boundary layers, and asymptotic boundary layers in particular. Note that the three profiles in the accelerated region are close to similar in both the inner and outer regions, and the boundary layer is not significantly growing at successive stations

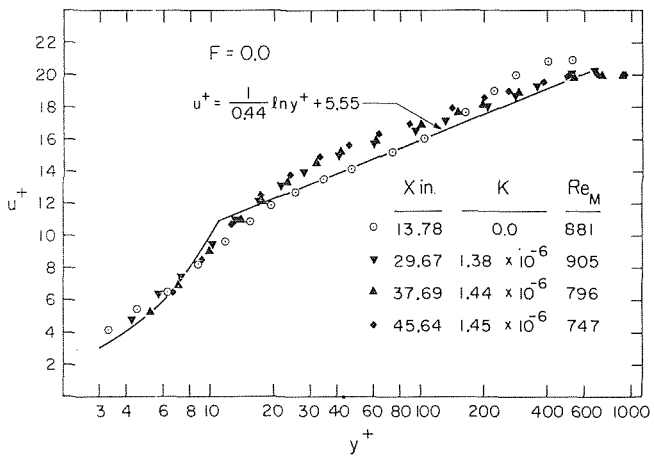

Fig. 7 Velocity profiles for a nearly asymptotic boundary layer at approximately $K = 1.45 \times 10^{-6}$, $F = 0.0$

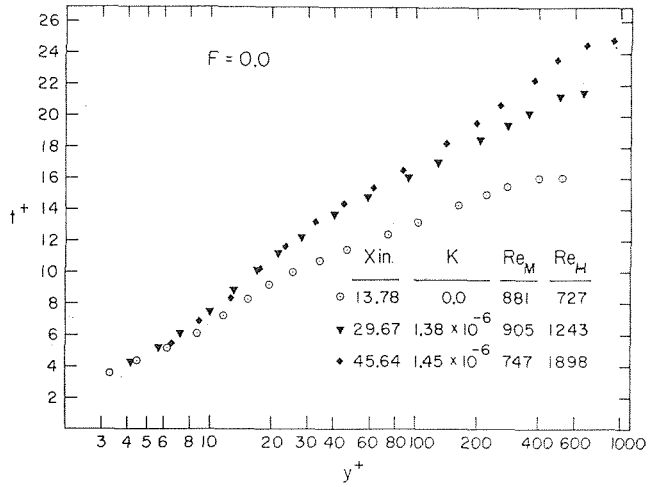

Fig. 8 Temperature profiles for the same case shown in Fig. 7

along the surface. The usual rise in u^+ in the "wake" region has disappeared, and the viscous inner region has significantly grown so that u^+ lies above the nonaccelerated curve in the middle region.

On the basis of examination of these velocity profiles, as well as other asymptotic profiles at different values of K, it is concluded that increasing K causes an increase in the thickness of the viscous region and a decrease in the values of u^+ and y^+ at the outer edge of the boundary layer. Such a trend with increasing K must ultimately lead to a disappearance of the turbulent region entirely, i.e., a laminar boundary layer.

A succession of temperature profiles taken under the same flow conditions are shown on Fig. 8. Two trends are apparent. In the inner region the curves in the accelerated region come together, but with a greater slope than in the non-accelerated region, evidently a direct result of the thickening of the viscous region near the wall. In the outer region the important observation is that the thermal boundary layer continues to grow at successive stations along the surface, unlike the momentum boundary layer, and is seen to penetrate into a region where the velocity gradient is small, or zero. Stanton number varies inversely as the maximum value of t^+, and thus the observed decrease in Stanton number in Fig. 3 is seen also in Fig. 8.

In summary, it appears that the depression in Stanton number observed in accelerating flows results from a combination of an increase in the viscous region thickness, and the growth of the thermal boundary layer beyond the momentum boundary layer.

Prediction Method

The heat transfer data presented here are only of limited value unless they can be used as the basis of some kind of prediction method that can be employed in design. However, any attempt at satisfactory overall empirical correlation of the data shown on Figs. 3 to 6 would appear to be a virtually hopeless task because of *the great variety of possible conditions and resulting behavior.* For constant free-stream velocity, the data of Moffat and Kays [6], and subsequent work on the same project not yet published, show that Stanton number can be expressed as a simple function of Re_H, and a blowing parameter, and is only weakly dependent upon any other parameters. Thus a reasonably satisfactory prediction scheme can be developed using the integral energy equation. The data for acceleration, but no blowing (i.e., Fig. 3), *show a certain orderliness,* but even a superficial examination of these results suggests that Stanton number is a function of at least Re_H, K, and the value of Re_H (or Re_M) where acceleration starts, and these data only represent the behavior under essentially constant K conditions. When blowing or suction are

superimposed, the number of variables even for uniform F and K is obviously out of hand, and behavior such as seen in Fig. 5 discourages any attempt at simple correlation.

The obvious next step is to attempt to correlate the experimental data at a more fundamental level by devising empirical correlations which can be used in mathematical models of the momentum and energy exchange processes. Not only can perhaps the desired generality be obtained, but a better understanding of the physics as well.

The scheme to be described here is based on a finite-difference solution of the momentum and thermal energy differential equations of the boundary layer, using the Spalding/Patankar [10] program as the basic mathematical tool. Any desired physical model of the momentum and energy exchange processes can be inserted into the program, subject only to the restriction that the equations are in parabolic form, so that one must be willing to use the concept of eddy viscosity and eddy conductivity. However, one is free to evaluate these quantities in any way desired, and the possibilities range from direct empirical correlations, to deductions based on solution of the turbulence energy equation, which can be solved simultaneously by the same program, if desired.

For present purposes a direct empirical mixing-length correlation is used, based on a modification of the Van Driest mixing-length hypothesis. The equations used are as follows

$$\mu_{\text{eff}} = \mu + \mu_t \qquad \text{effective viscosity}$$

$$\mu_t = \rho l^2 \left(\frac{du}{dy}\right) \qquad \text{turbulent viscosity}$$

$$l = kyD_v \quad \text{for} \quad y < (\lambda\delta/k)$$
$$l = \lambda\delta D_v \quad \text{for} \quad y > (\lambda\delta/k) \qquad \text{mixing-length}$$

where δ is the 99 percent momentum boundary layer thickness

$k = 0.44$ mixing-length constant

$\lambda = 0.25\ \text{Re}_M^{-1/8}[1 - 67.5(v_w/u_\infty)]$ turbulence length scale

if $\lambda < 0.085$, $\lambda = 0.085$

$$D_v = 1 - \exp\left(-y\rho\sqrt{\tau/\rho}/A^+\mu\right)$$

Van Driest damping factor
(note that τ is *local*, not wall, shear stress)

$$A^+ = 4.42/(v_w^+ + 0.17) + f(P_e^+) + f(P_e^+, v_w^+)$$

where

$$f(P_e^+) = -1133P_e^+ \quad \text{for} \quad -P_e^+ < 0.012$$
$$= -2133P_e^+ + 12.0 \quad \text{for} \quad -P_e^+ > 0.012$$

$$f(P_e^+, v_w^+) = -1990(-P_e^+ v_w^{+0.25})^{1.10} \quad \text{for} \quad v_w^+ > 0.0$$
$$= 6.78(-P_e^+)^{0.7}(-v_w^+)^{1.40} \quad \text{for} \quad v_w^+ < 0.0$$

P_e^+ is an "effective" value of P^+, described in the following.

$$\gamma_{\text{eff}} = \gamma + \gamma_t \qquad \text{effective conductivity}$$

$$\gamma_t = \mu_t c_p/\text{Pr}_t \qquad \text{turbulent conductivity}$$

$$\text{Pr}_t = (1/\text{Pr})[1 - 0.1(26/A^+)^{0.4}\sqrt{\mu_t/\mu}](1 + 20P^+)$$
if $\text{Pr}_t < 0.86$, $\text{Pr}_t = 0.86$ turbulent Prandtl number

Although the quantity of empirical input appears formidable, it should be pointed out that correlating λ with Re_M and v_w/u_∞ has only a minor influence, and that is at low Reynolds numbers only. A constant value, $\lambda = 0.085$, will also yield results close to those to be shown. Similarly, constant turbulent Prandtl number, $\text{Pr}_t = 0.90$, will yield Stanton numbers in close agreement with those to be shown. The rather complex expression used is based on direct measurements of Pr_t [11] which indicate a variation through the boundary layer starting high near the wall. In the prediction scheme it was found that such a variation in Pr_t is needed to obtain accurate temperature profiles. $\text{Pr}_t = 0.90$ is simply an effective average.

The real core of the correlation scheme is in the expression for A^+. Note that for $v_w^+ = 0$ and $K = 0$, $A^+ = 26$, a frequently used value. This correlation is presented as only tentative and illustrative of what can be done. Essentially A^+ is related to the thickness of the viscous sublayer (in y^+ coordinates), and the correlation reflects the thickening of this region in a *favorable* pressure gradient as observed in Fig. 7. It also includes a decrease in thickness observed for blowing, as determined from the data of Simpson, et al. [7], and a cross-coupling effect. Note that the *local* value of shear stress is employed in the Van Driest damping factor. If A^+ is held constant at 26, as some analysts have proposed, a thickening of the sublayer will be obtained for a favorable pressure gradient because τ decreases with y, but the present experimental data indicate that a substantia ly greater thickening is needed. The same thing is observed for wall suction, and the opposite for blowing.

The correlation for A^+ is based on velocity profiles for equilibrium boundary layers, i.e., the asymptotic cases such as shown in Fig. 7. The viscous sublayer of the real boundary layer apparently does not instantaneously assume its new equilibrium configuration when a new pressure gradient is imposed; there is a lag, and detailed examination of the experimental data shows this lag very clearly. Launder and Jones [12] propose a reasonable and simple scheme for introducing such a lag into the calculations, and it is used here with slight modification. An effective value of P^+ is defined (P_e^+) such that it approaches but lags behind the local value of P^+ as one moves in the x-direction. The following differential equation is then solved for P_e^+

$$\frac{dP_e^+}{dx^+} = C(P_e^+ - P^+)$$

C is established from the experimental data, and is tentatively given the value 0.0002.

Some sample results of predictions based on the above described model are shown in Figs. 9, 10, and 11. The imposed boundary conditions correspond closely in each case to the test results in Figs. 3 to 6.

The results in Fig. 9 are quite good, although it appears that in the case of $K = 2.5 \times 10^{-6}$ a slightly higher value of A^+ might be used.[2] The results on Fig. 10 are equally satisfactory. For the case of $F = -0.002$ and $K = 0.57 \times 10^{-6}$ the descrepancy is due to the fact that the prediction was run at somewhat different

[2] For this case A^+, as calculated in the prediction scheme, reaches a maximum value of 56.8.

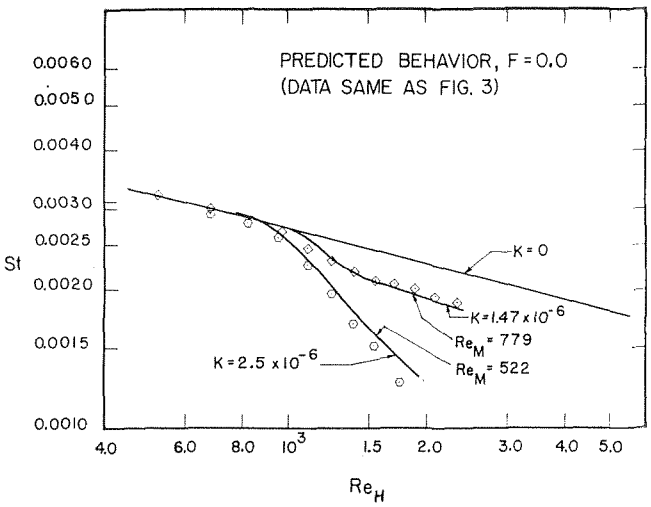

Fig. 9 Predicted heat transfer performance for three values of K, for no transpiration, $F = 0.0$

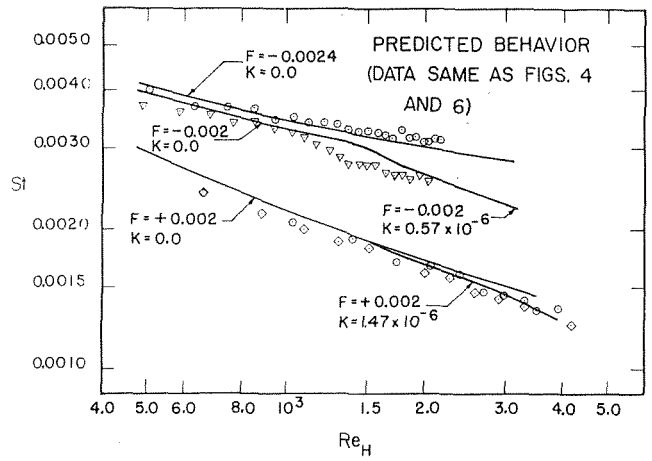

Fig. 10 Predicted heat transfer performance showing some effects of blowing, suction, and combinations of transpiration and acceleration

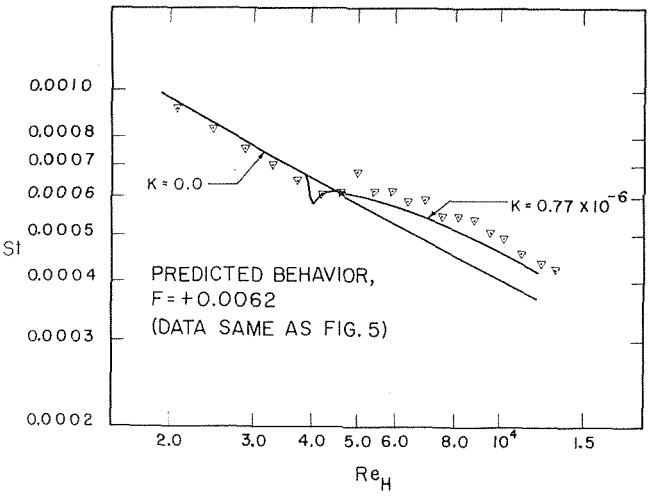

Fig. 11 Predicted heat transfer performance for a case of strong blowing, and moderate acceleration, corresponding approximately to the conditions of Fig. 5

conditions than the experiments, and in particular acceleration started at a higher value of Re_H.

The most spectacular success of the prediction is shown on Fig. 11. Here the unexpected *increase* in Stanton number with a mild acceleration, seen experimentally on Fig. 5, comes through very clearly. Note that the values of Stanton number are a decade lower than on Figs. 9 and 10, and experimental uncertainty is significantly greater.

The main conclusion which can be drawn from the results of the analysis is that the primary effects of acceleration, transpiration, and a combination of both, can be introduced into the analysis merely through the constant in the Van Driest damping term, A^+. If A^+ is evaluated properly, everything else follows. The fact that Stanton number sometimes increases and sometimes decreases with acceleration is merely attributable to the response of the boundary layer equations to the imposed conditions.

Summary and Conclusions

In this paper experimental data on heat transfer to close to asymptotic accelerated turbulent boundary layers, with and without transpiration, have been presented. It is shown that acceleration causes a depression in Stanton number for the case of no transpiration, and for suction. For an accelerated boundary layer with blowing it is shown that acceleration can cause an increase in Stanton number under certain conditions.

Examination of velocity and temperature profiles suggests that acceleration causes an increase in the thickness of the viscous sublayer. It has been shown earlier that blowing causes a decrease in sublayer thickness, while suction increases thickness. Acceleration can cause the momentum thickness Reynolds number to decrease, and an acceleration at a constant value of the parameter K will lead to a constant value of momentum thickness Reynolds number. The enthalpy thickness Reynolds number will always increase, however (except for strong suction, and excepting the case of varying surface temperature), with the result that prolonged acceleration will lead to penetration of the thermal boundary layer beyond the momentum boundary layer. The decrease in Stanton number observed for accelerated boundary layers is believed to result from a combination of the effects of a thicker sublayer and a thermal boundary layer penetrating beyond the momentum boundary layer.

Finally, a mathematical model based on the Van Driest mixing-length hypothesis, and incorporating the observed effects of acceleration and transpiration on the sublayer thickness, is shown to be capable of quite satisfactorily reproducing the experimental data for accelerations up to $K = 2.5 \times 10^{-6}$, and a wide range of blowing or suction.

The empirical correlations used will undoubtedly be modified and refined as more experimental data become available. The authors are presently engaged in obtaining additional data, including highly overshot boundary layers, varying K, the region of recovery to $K = 0.0$, turbulence measurements, and are investigating use of the turbulent kinetic equation in place of the mixing-length model. The latter appears more promising for non-equilibrium boundary layers.

References

1 Moretti, P. M., and Kays, W. M., "Heat Transfer to a Turbulent Boundary Layer With Varying Free-Stream Velocity and Varying Surface Temperature—An Experimental Study," *International Journal of Heat and Mass Transfer*, Vol. 8, p. 1187.

2 Launder, B. E., "Laminarization of the Turbulent Boundary Layer in a Severe Acceleration," *Journal of Applied Mechanics*, Vol. 31, TRANS. ASME, Vol. 86, No. 4, Dec. 1964, p. 787.

3 Launder, B. E., and Stinchcombe, H. W., "Non-Normal Similar Turbulent Boundary Layers," Imperial College, Mechanical Engineering Department, TEF/TN/21, 1967.

4 Patel, V. C., and Head, M. R., "Revision of Turbulent to Laminar Flow," *Journal of Fluid Mechanics*, Vol. 34, Part 2, 1938, p. 371.

5 Pohlhausen, K., Z. angew, "Zur naherungsweisen Integration der Differentialgleichung der Grenzschicht," *Mathematical Mechanics*, Vol. 1, 1921, p. 252.

6 Moffat, R. J., and Kays, W. M., "The Turbulent Boundary Layer on a Porous Plate: Experimental Heat Transfer With Uniform Blowing and Suction."

7 Simpson, R. L., Moffat, R. J., and Kays, W. M., "The Turbulent Boundary Layer on a Porous Plate: Experimental Skin Friction With Variable Injection and Suction" (to be published in the *International Journal of Heat and Mass Transfer*).

8 Coles, D. E., "The Turbulent Boundary Layer in a Compressible Fluid," RAND Report R-403-PR, 1962.

9 Kline, S. J., and McClintock, F. A., "Describing Uncertainties in Single Sample Experiments," *Mechanical Engineering*, Jan. 1953, p. 3.

10 Patankar, S. V., and Spalding, D. B., *Heat and Mass Transfer in Boundary Layers*, Morgan-Grampian Press, Ltd., London, 1967.

11 Simpson, R. L., Whitten, D. G., and Moffat, R. J., "Experimental Determination of the Turbulent Prandtl Number of Air" (to be published in the *International Journal of Heat and Mass Transfer*).

12 Launder, B. E., and Jones, W. P., "On the Prediction of Laminarization," presented at a meeting of the ARC Heat and Mass Transfer Sub-Committee, April 5, 1968.

13 Launder, B. E., and Lockwood, F. C., "An Aspect of Heat Transfer in Accelerating Turbulent Boundary Layers," ASME Paper No. 68-WA/HT-13.

Acknowledgments

This work was made possible by a research grant from the National Aeronautics and Space Administration, NgR 05 020 134. The interest and encouragement of Mr. Robert W. Graham of the Lewis Research Center, Cleveland, Ohio, is greatly appreciated.

C. W. COON
Assistant Professor, Thermal and Fluid Sciences Center, Southern Methodist University, Dallas, Texas; Formerly, Research Assistant, The University of Arizona, Tucson, Ariz

H. C. PERKINS
Professor, Energy, Mass and Momentum Transfer Laboratory, Aerospace and Mechanical Engineering Department, The University of Arizona, Tucson, Ariz.

Transition From the Turbulent to the Laminar Regime for Internal Convective Flow With Large Property Variations

The results of a primarily experimental study of the transition from turbulent flow to laminar flow as a consequence of high heating rates are presented. Results are reported for hydrodynamically fully developed, low Mach number flows of air and helium through a vertical, circular tube. The electrically heated section was 100 diameters in length; entering Reynolds numbers ranged from 1700–40,000, and maximum wall-to-bulk temperature ratios reached 4.4. As a means of predicting the occurrence of a transition from turbulent flow to laminar flow, the experimental results are compared to the acceleration parameter suggested by Moretti and Kays and to a modified form of the parameter that is appropriate to a circular tube. It is suggested that the variable property turbulent flow correlations do not provide acceptable predictions of the Nusselt number and the friction factor if the value

$$\frac{4\mu q''}{G^2 D T c_p} \simeq 1.5 \times 10^{-6}$$

based on bulk properties, is exceeded for an initially turbulent flow situation. It is further suggested that Nusselt numbers and friction factors at locations down-stream from the point

$$\left(\frac{x}{D}\right)_{\text{laminar}} \simeq (2 \times 10^{-8})(T_{\text{inlet}})(Re_{\text{b, inlet}})^2 \left(\frac{T_w}{T_b}\right)^{-1}_{\text{max}}$$

for bulk temperatures in degrees Rankine may be obtained from the laminar correlation equations even though the flow is initially turbulent.

Introduction

The problem of reverse transition, defined in this study as a transition from a turbulent flow to a laminar flow, is of interest both for practical reasons, i.e., in the design of nuclear rocket engines, and for fundamental reasons, i.e., as a possible contribution to the nature of the transition process. This study is concerned with a primarily experimental investigation of the reverse transition process in a circular tube. The reverse transition is caused by the action of large heating rates which in turn cause significant transport property variations, especially in the viscosity. The viscosity increases such that the Reynolds number based on tube diameter decreases sufficiently for the flow to undergo a transition from turbulent to laminar.

The phenomenon of an internal flow transition from a turbulent flow to a laminar flow due to variation in gas properties has achieved interest by virtue of the proposed use of gas-cooled nuclear reactors as space propulsion systems. The shut-down period of reactor operation is characterized by low propellant flow rates; an unexpected transition from turbulent to laminar flow in the cooling tubes would cause a sharp decrease in the energy transfer to the gas and a subsequent rise in the wall temperature causing possible failure of the tubes.

Previous Investigations

Several authors have discussed various aspects of the turbulent to laminar transition process. The adiabatic studies of Sibulkin [1][1] for circular tubes and of Badrinarayanan [2] for two-dimen-

Contributed by the Heat Transfer Division of The American Society of Mechanical Engineers and presented at the ASME-AIChE Heat Transfer Conference, Minneapolis, Minn., August 3–6, 1969. Manuscript received by the Heat Transfer Division, June 9, 1969. Paper No. 69-HT-9.

[1] Numbers in brackets designate References at end of paper.

sional channels have described the response of initially turbulent flows to changes in area. Sergienko and Gretsov [3], Sternberg [4], Wisniewski and Jack [5], and Richards and Stollery [6] have observed the occurrence of transition in high-speed flow situations. The occurrence of simultaneous turbulent and laminar flow has been observed by Senoo [7, 8] in a turbine nozzle cascade and by Eckert and Irvine [9] and Cremers and Eckert [10] in a triangular duct. Cannon [11] has reported a reduction in the heat transfer to a fluid flowing in a rotating tube; the flow was characterized by a nonrotating, turbulent inner core and a rotating outer ring with a laminar structure.

The transition from turbulent to laminar flow in external boundary layers has been investigated by several authors. Launder [12] has examined adiabatic flow over a flat plate with a strong favorable pressure gradient and examined the experimental data in the context of the Schlichting-Ulrich stability curve. The heat transfer to external flows has been studied by Back and his associates [13, 14, 15] and by Moretti and Kays [16]. The salient feature of these latter investigations was the departure from fully turbulent flow that was indicated by the heat transfer measurements; Moretti and Kays observed that the heat transfer had a tendency, in strongly accelerated flows, to approach laminar values after a delay of about 200 times the momentum thickness. The quantity chosen by Moretti and Kays [16] for prediction of reverse transition was the "acceleration parameter'

$$K = \frac{\nu}{u_\infty^2}\frac{du_\infty}{dx} \tag{1}$$

which is similar to the parameters employed by Back, Massier' and Gier [13] and by Launder [12]. The authors argue that the relevance of the Reynolds number (based on momentum thickness) to the acceleration parameter is probably small, and the stated critical value of K for the occurrence of reverse transition is $K_c = 3 \times 10^{-6}$, independent of the Reynolds number. This value was obtained from analysis of the experimental data, but it can be justified by examination of the momentum integral equation as explained by Kays [17]. Laminar analysis is suggested for situations where K_c is exceeded for large distances, and it was found that the quantity K/St provided an acceptable correlation for heat transfer results. It is interesting to note that the critical value of K was confirmed by Schraub and Kline [18] in connection with visual studies using water.

Results for reverse transition in internal flow are less complete. McEligot [19], during an investigation that was primarily devoted to heat transfer with turbulent flow in tubes, obtained some data in the transition region and presented a correlation equation for the transition results. The first published investigation mentioning turbulent-to-laminar transition for *tube flow* was that due to Perkins and Worsoe-Schmidt [20]. The authors examined the local heat transfer and friction factors for gas flow in a tube with wall-to-bulk temperature ratios as high as seven; it was noticed that the effects of variable properties were in some cases sufficient to cause an apparent transition to laminar flow. This tendency was observed even though the bulk Reynolds number did not come near the critical value; it was suggested that the conditions at the wall might be appropriate for correlation purposes. It was found that the friction factors, based on bulk properties, could be advantageously normalized by an isothermal friction factor correlation evaluated at the same wall Reynolds number; the wall Reynolds number, designated as the "modified wall Reynolds number," was defined as

$$\mathrm{Re}_w = \frac{4\dot{m}}{\pi D\mu_w}\left(\frac{T_b}{T_w}\right) \tag{2}$$

The heat transfer data were well correlated on both bulk and wall properties, but an attempt at correlation with film properties met with little success. The authors suggested that the transition to laminar-like flow was evidenced by the departure of the friction and heat transfer results from the turbulent correlations. A technique for categorizing the experimental results as laminar, transitional, or turbulent according to the departure from turbulent correlations was presented by McEligot, Ormand, and Perkins [21], and the results thus classified were displayed on a plot of the wall-to-bulk temperature ratio versus the wall Reynolds number.

During the study of the parallel channel stability problem associated with gas-cooled nuclear reactor cores, Bankston, Sibbitt, and Skoglund [22] encountered the phenomenon of transition from turbulent flow to laminar flow. An experiment was conducted using a tube with almost simultaneous hydrodynamic and thermal entry lengths; therefore, the effect of heating on the usual laminar-to-turbulent transition could be investigated. It was found that the transition point was quite sensitive to heating rate and axial location; the general effect of heating was to increase the bulk Reynolds number at which transition occurred. The authors employed hot wire anemometer probes to obtain evidence of turbulent to laminar transition, and it was found that the turbulent intensities were greatly reduced from their turbulent flow values during certain test runs with heating. The classification scheme presented by McEligot, Ormand, and Perkins [21], using the modified wall Reynolds number, was used to obtain boundaries for the laminar, transition, and turbulent regimes; it was found that the divisions could also be represented by the parameter

$$Y = \mathrm{Re}_b\left(\frac{T_b}{T_w}\right)^2 \tag{3}$$

The relationship between these two parameters can be seen by noting that

$$\mathrm{Re}_b = \frac{VD\rho_b}{\mu_b} = \frac{4\dot{m}}{\pi D\mu_b}$$

The Reynolds number can be converted to a wall condition by evaluating the density and viscosity at the wall temperature so that, for a perfect gas,

$$\mathrm{Re}_w = \frac{VD\rho_w}{\mu_w}\frac{\rho_b}{\rho_b}\frac{\mu_b}{\mu_b} = \frac{VD\rho_b}{\mu_b}\frac{\rho_w}{\rho_b}\frac{\mu_b}{\mu_w} = \mathrm{Re}_b\frac{T_b}{T_w}\frac{\mu_b}{\mu_w} \tag{4}$$

Since the viscosity varies with the temperature to a power close

Nomenclature

c_p = specific heat at constant pressure
D = tube diameter
f = friction factor = $\tau_w/[\rho V^2/2g_c]$
g_c = dimensional constant = 32.174 lbm-ft/lbf-sec^2
G = mass velocity = ρV
h = heat transfer coefficient = $q_w''/[T_w - T_b]$
k = thermal conductivity
K = reverse transition parameter
$\dot{m}$ = mass flow rate
q'' = heat flux
T = temperature
u = external flow velocity
V = tube flow bulk velocity
x = length
Y = parameter defined by equation (3)
μ = absolute viscosity
ν = kinematic viscosity
ρ = density
τ = shear stress
Nu = Nusselt number = hD/k
Pr = Prandtl number = $\mu c_p/k$
Re = Reynolds number = $VD\rho/\mu = 4\dot{m}/\pi D\mu$
St = Stanton number = Nu/Re Pr

Subscripts

b = bulk (evaluated at bulk properties)
c = critical
w = wall (evaluated at wall properties)
ϕ = circular tube
∞ = free stream (external flow)

to unity, the quantity defined by equation (3) is essentially the same as that defined by equation (2).

Experimental Apparatus

The experimental apparatus constructed for this study was basically a tube in which the flow conditions typical of gas cooled nuclear rocket engines could be approximated. A detailed discussion and schematic diagrams are given in reference [23]. The test assembly was composed of a test section that was resistively heated with alternating current in order to provide an approximate constant wall heat flux boundary condition, a vacuum system that was used to minimize both the heat loss from the test section and the oxidation of the test section at high temperature, and a liquid nitrogen system that was used to precool the gas prior to heating in order that high wall-to-bulk temperature ratios could be achieved with conventional test section materials. Auxiliary systems allowed the control and measurement of the test section heating power, the control and measurement of the mass flow rate of gas, the measurement of appropriate temperatures, and the measurement of axial pressure drops in the test section. The test section was constructed from drawn, seamless Inconel 600 tubing with a nominal outside diameter of 0.250 in. and a nominal wall thickness of 0.010 in.; and nine pressure taps, made of 0.0625 in. outside diameter Inconel tubing, were brazed onto the tube at various axial locations. The test section was fabricated from a four foot length of tubing with electrodes brazed to the center and to one end. A 100 diameter hydrodynamic entry length was thus provided without a connection between tubes near the point where heating began.

The possible buckling of the test section at high temperature was prevented through the use of a spring which supplied a constant tensile force in the axial direction along the test section.

Twenty-three Chromel-Alumel thermocouples made of 0.005-in-dia premium grade wire were attached to the test section. Each of the two wire ends for every thermocouple was separately spot welded directly to the tube in order to provide an assurance that the temperature measuring junction was not separated from the wall by the thickness of a wire. A copper box was installed inside the vacuum system to serve as an isothermal region for thermocouple wire connections. In order to compensate for the fact that the reference junction in the circuit described above was not at ice temperature, a Chromel-Alumel junction was formed and immersed in an ice bath. The Chromel and Alumel wires from this junction were conducted into the vacuum system and connected to copper wires inside the copper isothermal box. These copper wires were then returned to the outside of the vacuum system and the circuit to the measuring instrument was completed. An identical scheme was used for thermocouples that were located outside the vacuum system. During some of the heat loss calibration runs, a thermocouple probe was inserted into the test section and placed at the axial locations of the various wall thermocouples as a means of determining the depression of the test section wall temperature due to the presence of the thermocouple wires.

The test gas was supplied to the test section through a series of three pressure regulators connected to a four-cylinder high-pressure manifold. The flow rate of the gas through the system was measured upstream from the test section by one of two Brooks Rotameters that had been individually calibrated by the factory to an accuracy of one percent with air flow. For helium flow the flowmeters were calibrated on site to an accuracy of three percent. When possible, the flow rate was measured downstream from the test section by a wet test meter. The pressure drops between the test section pressure taps were measured by a selection of manometers having different ranges and sensitivities. Because the technique used to calculate the friction factors employed two adjacent pressure drops, i.e., three pressure taps, an attempt was made to pair the manometers and measure adjacent pressure drops simultaneously. The manometers consisted of a pair of 60 in. vertical water manometers and a pair of 60 in. inclined water manometers with ten in. range. In addition, a Meriam Model 34FB2 micromanometer was available for the measurement of very small pressure drops.

The precooling of the test gas with liquid nitrogen was achieved by passing the gas through a copper coil that was inside a cylindrical Dewar flask which was open to the atmosphere; the gas passed directly from the coil into the entry mixer and then into the hydrodynamic entry length of the test section. A liquid nitrogen-cooled shield was provided for the hydrodynamic entry length of the test section in order to decrease the energy gain of the test gas prior to the start of heating.

The acquisition of data from the test assembly required the use of a wide variety of measuring instruments. A concerted effort was made to obtain the best equipment that was available and to assure that the various instruments were performing at their optimum level during the duration of the experiment.

After the installation of the test section and prior to the beginning of the heated flow runs, a series of adiabatic flow runs was conducted to serve as a calibration of the pressure taps attached to the test section. Before the beginning of the runs that employed helium as the test gas, the flow system was purged with a small mechanical vacuum pump in order to insure the presence on only one gas in the apparatus.

The energy balance from which the energy transfer from the heated wall to the flow stream was determined required the specification of the energy loss by radiation from the test section at each thermocouple location. In order to determine the radiation heat loss, several series of calibration runs were performed during which the test section was heated without gas flow. The technique involved the measurement of the temperature of the test section wall, the temperature of the surroundings, and the energy generation rate.

Particular attention was devoted to various features of the experimental apparatus, such as the temperature difference between the outside and the inside of the test section wall, which could cause erroneous results. The computer programs used for data reduction contained sections which took into account the following:

1 the increase in momentum of the flow due to heating,

2 the thermal expansion of the test section in both the radial and the axial direction,

3 the conduction heat transfer through the test section wall in an axial direction, and

4 the energy transfer to the precooled gas due to conduction through the electrodes.

In addition, local gas properties were employed in the calculation of local Nusselt numbers and local friction factors.

Results

The experimental apparatus described above was used for the demonstration and quantitative evaluation of the process of transition from turbulent to laminar flow in a circular tube. The conditions were such that initially turbulent flows could be subjected to high heating rates; local Nusselt numbers and friction factors were obtained and compared with accepted correlations. The experimental results provided by the test facility encompassed a range of conditions broader than that which was specifically applicable to the study of the phenomenon of turbulent-to-laminar transition; some data were obtained in domains reported by other investigators in order to establish a level of confidence for the test section and the data reduction techniques. For example, the adiabatic runs with turbulent flow provided local friction factors which were compared with the Blasius friction factor that would prevail at the bulk entry Reynolds number for each run; agreement between the two was within ten percent.

Friction factors in the laminar regime were obtained during two runs with bulk entry Reynolds number less than 2100, rela-

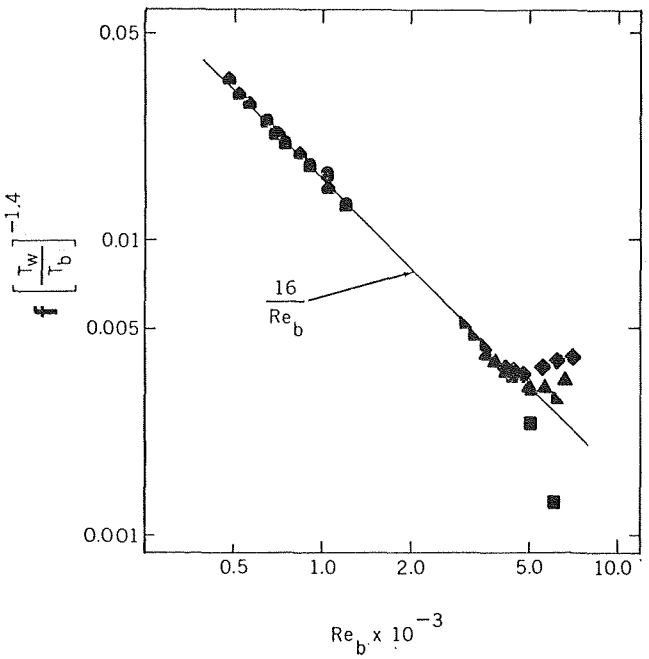

Fig. 1 Friction factor data compared to a laminar variable properties correlation

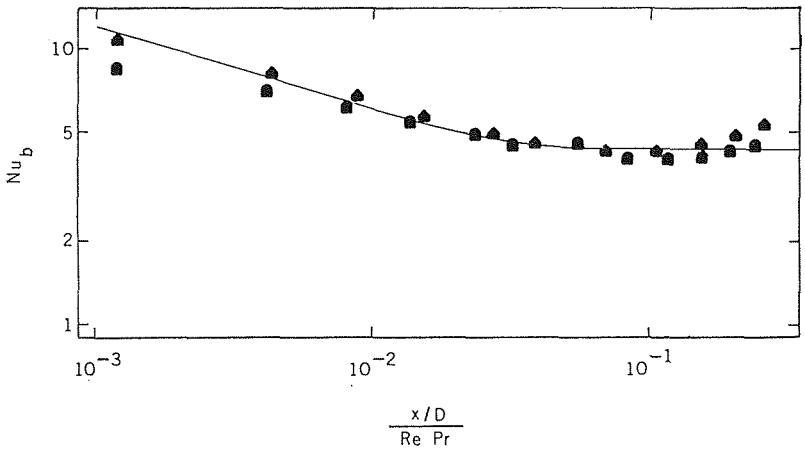

Fig. 2 Bulk Nusselt number data compared to Graetz solution length parameter—laminar flow

tively high heating rates, and precooling. The results are shown in Fig. 1, which employs the correlation relationship

$$f = \frac{16}{\mathrm{Re}_b}\left(\frac{T_w}{T_b}\right)^{1.4} \tag{5}$$

to account for the variable properties effects; the maximum deviation from the laminar line is about ten percent. These results are in good agreement with those of other investigators [22, 25].

The heat transfer results for these laminar flow runs are shown in Fig. 2; the coordinates are the bulk Nusselt number and the bulk Graetz solution length parameter $(x/D)/\mathrm{RePr}$. The solid line represents the analytical thermal entry length solution for laminar flow with constant fluid properties and constant wall heat flux in a circular tube [24]. Examination of Fig. 2 reveals good agreement between the analytical prediction and the experimental results; except for data points which were obtained near the ends of the test section, the deviation of the experimental results from the prediction is no greater than ten percent. As with the friction results, these results indicate good agreement with the work of other investigators [25, 26] who have previously noted that the constant properties correlation applied for laminar flow with strong heating.

Several experimental runs involving heated flow without precooling were conducted in order to provide low heat flux results $(T_w/T_b < 1.5)$ for comparison with the findings of other investigators. Both air and helium were employed, and the range of Reynolds numbers was large enough to include the region of primary interest. The conventional heat transfer parameters applicable to the downstream region of the tube $(x/D > 40)$ were found to agree within five percent with the following correlation equation chosen to represent the data points:

$$\mathrm{Nu}_b = 0.022\mathrm{Re}_b^{0.8}\mathrm{Pr}_b^{0.4}\left(\frac{T_w}{T_b}\right)^{-0.5} \tag{6}$$

This equation is of the same form as that used by other authors [12, 20]. The friction factor information provided by the runs for which the gas was heated but not precooled was found to be within ten percent agreement with the Blasius correlation. Other investigators have also found that, at low heating rates, the friction factors are correlated by constant property expressions.

On the basis of the agreement of the foregoing results with ac-

cepted correlations, it was felt that the experimental apparatus was well qualified for a study of reverse transition. A graphical representation with the coordinates of Fig. 2 provides the most lucid description of the process of transition from turbulent to laminar flow. Fig. 3 depicts several of the runs in which transition was present along with a completely laminar run and a completely turbulent run for comparison; numerical information concerning the runs is listed in Table 1. The Nusselt numbers for the downstream region of the tube for the transition runs have values characteristic of laminar flow, but the Reynolds numbers based on bulk properties at corresponding locations are considerably in excess of 2000. Thus the heat transfer for these situations is best represented by the laminar flow relationship despite the fact that the value of the Reynolds number suggests the presence of turbulent flow.

A comparison of the experimental data with the turbulent flow, variable properties correlation, equation (6), provides further evidence of transition. In a typical case, the data and the correlation show good agreement at 40 diameters, but the data are more than 50 percent below the correlation at 100 diameters.

The friction factor data provided another source of information concerning the transition from turbulent to laminar flow. An attempt was made to correlate the data for transition runs using the variable properties relationship for purely turbulent flow suggested by Perkins and Worsoe-Schmidt; agreement between the correlation and the data was poor, indicating that the flow was not turbulent. Good results were obtained, however, with the laminar flow correlation described by equation (5); results for the reverse transition runs are shown in Fig. 1.

For purposes of comparison and discussion, each of the heated flow runs was classified according to the type of flow that was found to be present. The primary basis of the classification scheme was the graphical representation of Fig. 3. Downstream data points for runs classified as laminar, transitional, i.e., showing evidence of reverse transition, or turbulent were displayed on a graph of wall-to-bulk temperature ratio versus modified wall Reynolds number as suggested by McEligot, Ormand, and Perkins [21]; good agreement with the suggested borderlines was obtained. The classification of the experimental runs in the present study was also in good agreement with the classification scheme used by Bankston, Sibbitt, and Skoglund in which the parameter defined by equation (3) was used in place of the modified wall Reynolds number.

Another parameter used in the description of the turbulent to laminar transition process was the quantity described by equation (1) which was defined by Moretti and Kays [16] for external boundary-layer flows subjected to strong accelerations. It is of interest to investigate the utility of this parameter for an internal flow situation. Moretti and Kays found that the onset of transition was marked by large increases in the value of K, and it was suggested that laminar results would be obtained if the value of K exceeded 3.0×10^{-6}. For the experimental runs associated with the present work, local values of the parameter K were obtained by using the bulk velocity and the bulk kinematic viscosity. Average values of the quantity K are listed in Table 1; it is interesting to note that the internal flow reverse transitional runs exhibit good agreement with the critical numerical value suggested by Moretti and Kays while the completely laminar and completely turbulent runs differ by about an order of magnitude from the critical value. For tube flow the value of K exhibits little change with axial distance along the tube; no sudden increase is apparent. The disparity between this fact and the results of Moretti and Kays can be explained in terms of the velocity required by the definition of K; the mass velocity, G

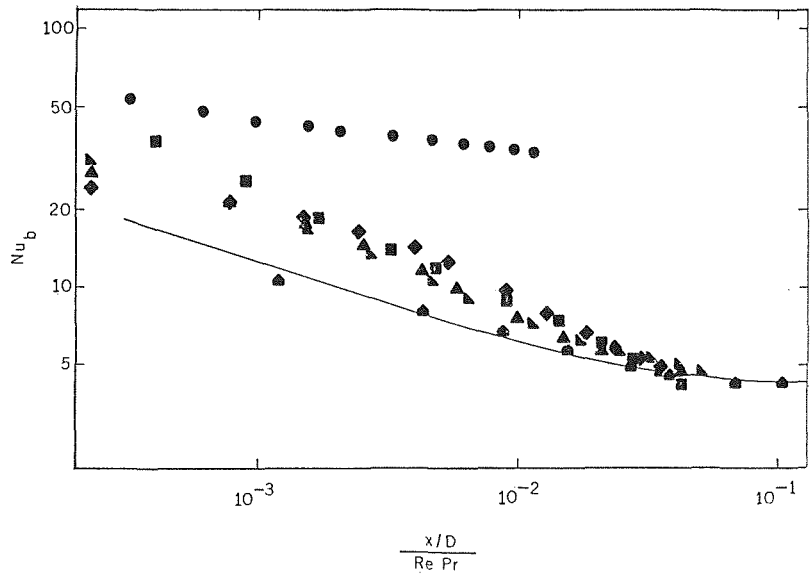

Fig. 3 Bulk Nusselt number data compared to Graetz Solution length parameter—laminar flow, turbulent flow, and flow with reverse transition

Table 1

Symbol	Gas	Regime	$T_{w,max}$	$(T_w/T_b)_{max}$	Bulk Reynolds Inlet	Bulk Reynolds Exit	K	K_ϕ
●	Air	Turbulent	999°R	1.35	17728	12940	2.85×10^{-7}	2.86×10^{-7}
■	Air	Transition	1699	4.43	16944	3458	3.08×10^{-6}	3.05×10^{-6}
◆	Helium	Transition	874	2.12	8720	4160	1.80×10^{-6}	1.87×10^{-6}
▲	Helium	Transition	1124	2.68	8795	3527	2.50×10^{-6}	2.59×10^{-6}
◣	Helium	Transition	1392	3.30	9052	2968	3.44×10^{-6}	3.57×10^{-6}
●	Helium	Laminar	1057	2.04	1711	612	1.09×10^{-5}	1.12×10^{-5}
◆	Helium	Laminar	1506	2.39	1724	459	1.77×10^{-5}	1.82×10^{-5}

for tube flow is not subject to arbitrary change, but the free stream velocity in the external flow experiment was deliberately increased by a variation of the duct geometry. It should also be noted that Back and Seban [15] found that a value of K equal to 2×10^{-6} for the external flow form of the parameter was in better agreement with their data than was the value suggested by Moretti and Kays.

The external flow acceleration parameter, K, can be translated into terms more pertinent to tube flow through the use of the continuity equation, the equation of state for a perfect gas, and an energy balance on an element of the tube; the result is

$$K_\phi = \frac{4}{G^2 D} \frac{\mu}{T} \frac{q''}{c_p} \tag{7}$$

Average values of K_ϕ for the experimental runs are shown in Table 1, and, as expected, these are in agreement with the values of K. The general features and the trends are the same as those described for the external flow parameter, but K_ϕ is composed of quantities that are more readily available from the specification of a design problem for a tube flow situation than are the quantities that comprise K, Re_w, or T_w/T_b. Thus a classification of experimental runs on the basis of K_ϕ should prove more helpful to the designer than would a classification based on any of the previously mentioned parameters.

It can be observed that the runs involving turbulent flow with mild heating exhibit values of K_ϕ in the neighborhood of 10^{-7}, while the completely laminar runs have values in the vicinity of 10^{-5}. It is also interesting to note that a number of points are grouped together near the value

$$K_\phi = 1.5 \times 10^{-6}$$

and that these are precisely the runs for which a significant departure from the turbulent prediction can be observed in the graphs involving the Graetz solution length parameter, Fig. 3. It is therefore suggested that the variable properties turbulent flow correlations do not provide acceptable predictions if the above value of K_ϕ is exceeded for an initially turbulent flow situation.

The axial distance required for a *complete* transition from turbulent flow to laminar flow was also examined on the basis of the experimental data presented in the preceding material. It was regarded as a foregone conclusion that, for a sufficiently long tube and continuous heating, the flow would eventually become laminar because of the increase in viscosity regardless of the value of K_ϕ; the effects of high heating rates are to reduce the distance required for the transition process to occur and to increase the value of K_ϕ. It was assumed that a relationship that would predict the onset of laminar flow could be formulated in terms of the bulk inlet Reynolds number and the wall-to-bulk temperature ratio. The resulting expression, determined from cross plots of the data, is:

$$\left(\frac{x}{D}\right)_{\text{laminar}} \simeq (2 \times 10^{-8})(T_{\text{inlet}})(\mathrm{Re}_{b,\,\text{inlet}})^2 \left(\frac{T_w}{T_b}\right)^{-1}_{\max} \tag{8}$$

for T_{inlet} in degrees Rankine. This expression was found to yield reasonable, i.e., ± 20 percent, estimates of the axial location at which the experimentally measured Nusselt numbers attained the values predicted by the constant properties laminar flow solution for runs both with and without precooling. This relationship encompasses both the present data, taken on a 100 diameter heated section, and that of reference [20] taken on a 160 diameter heated section. The presence of the bulk inlet temperature in equation (8) allows the expression to be used for various inlet temperatures. A form of equation (8) without the inlet temperature was found to yield good agreement with experimental data for precooled runs, but agreement was poor for runs with ambient inlet temperatures. It is postulated that this discrepancy may be traced to the difference in the rate of change of viscosity with temperature above and below 200 deg R for the test gases used.

It should be mentioned that the foregoing relationship for predicting the axial location of the existence of laminar flow was obtained from the experimentally determined heat transfer parameters, and the possibility exists that the friction factors have a greater degree of sensitivity to heating rate than do the Nusselt numbers.

Conclusions

The following conclusions, pertinent to the flow of a gas through a circular tube with a constant heat flux boundary condition, may be drawn from the results of this investigation:

1 High heating rates may cause laminar values of heat transfer coefficients and friction factors even though the bulk Reynolds number lies well above 2200.

2 If the value of

$$K_\phi = \frac{4\mu q''}{G^2 D T c_p} \simeq 1.5 \times 10^{-6}$$

based on bulk properties, is exceeded for an initially turbulent flow situation, then the turbulent flow correlations no longer provide acceptable predictions of the Nusselt number and the friction factor.

3 The Nusselt numbers and friction factors at locations downstream from the point

$$\left(\frac{x}{D}\right)_{\text{laminar}} \simeq (2 \times 10^{-8})(T_{\text{inlet}})(\mathrm{Re}_{b,\,\text{inlet}})^2 \left(\frac{T_w}{T_b}\right)^{-1}_{\max}$$

for bulk inlet temperatures in degrees Rankine, may be obtained from the laminar correlation equations even though the flow is initially turbulent.

Acknowledgments

This paper is based on a dissertation submitted by C. W. Coon to the University of Arizona in partial fulfillment of the requirements for the degree Doctor of Philosophy. Financial assistance during the course of the project was provided by the National Aeronautics and Space Administration through institutional funds provided to the University, by the National Science Foundation through an Initiation Grant awarded to Professor Perkins, and by the U. S. Army Research Office (Durham). Professor D. M. McEligot provided assistance throughout all phases of the project. Lt. Col. Joseph Spitler, U. S. Army, was responsible for a considerable portion of the computer program used for data reduction, and Mr. R. W. Shumway provided the flowmeter calibrations for helium.

References

1 Sibulkin, M., "Transition From Turbulent to Laminar Pipe Flow," *The Physics of Fluids*, Vol. 5, 1962, p. 280.

2 Badrinarayanan, M. A., "An Experimental Study of Reverse Transition in Two-Dimensional Channel Flow," *Journal of Fluid Mechanics*, Vol. 31, 1968, p. 609.

3 Sergienko, A. H., and Gretsov, V. K., "Transition From a Turbulent Into a Laminar Boundary Layer," *S. S. Doklady*, Vol. 4, 1959, p. 275.

4 Sternberg, J., "Transition From a Turbulent to a Laminar Boundary Layer," Ballistics Research Laboratory Report No. 906, 1954.

5 Wisniewski, R. J., and Jack, J. R., "Recent Studies on the Effect of Cooling on Boundary-Layer Transition at Mach 4," *Journal of the Aerospace Sciences*, Mar. 1961, p. 250.

6 Richards, B. E., and Stollery, J. L., "Further Experiments on Transition Reversal at Hypersonic Speeds," *American Institute of Aeronautics and Astronautics Journal*, Vol. 4, 1966, p. 2224.

7 Senoo, Y., "The Boundary Layer on the End Wall of a Turbine Nozzle Cascade," TRANS. ASME, Vol. 80, Nov. 1958, p. 1711.

8 Senoo, Y., "Three-Dimensional Laminar Boundary Layer in Curved Channel With Acceleration," TRANS. ASME, Vol. 80, Nov. 1958, p. 1721.

9 Eckert, E. R. G., and Irvine, T. F., Jr., "Pressure Drop and

Heat Transfer in a Duct With Triangular Cross Section," JOURNAL OF HEAT TRANSFER, TRANS. ASME, Series C, Vol. 82, No. 2, May 1960, p. 125.

10 Cremers, C. J., and Eckert, E. R. G., "Hot-Wire Measurements of Turbulence Correlations in a Triangular Duct," *Journal of Applied Mechanics*, Vol. 19, TRANS ASME, Vol. 84, No. 4, Dec. 1962, p. 609.

11 Cannon, J. C., "Heat Transfer From a Fluid Flowing Inside a Rotating Cylinder," PhD dissertation, Mechanical Engineering Department, Stanford University, 1965.

12 Launder, B. E., *Laminarization of the Turbulent Boundary Layer by Acceleration*, Massachusetts Institute of Technology Gas Turbine Laboratory, Report No. 77, 1964.

13 Back, L. H., Massier, P. F., and Gier, H. L., "Convective Heat-Transfer in a Convergent-Divergent Nozzle," *International Journal of Heat and Mass Transfer*, Vol. 7, 1964, p. 549.

14 Back, L. H., Massier, P. F., and Cuffel, R. F., "Some Observation on Reduction of Turbulent Boundary-Layer Heat Transfer in Nozzles," *American Institute of Aeronautics and Astronautics Journal*, Vol. 4, 1966, p. 2226.

15 Back, L. H., and Seban, R. A., "Flow and Heat Transfer in a Turbulent Boundary Layer with Large Acceleration Parameter," *Heat Transfer and Fluid Mechanics Institute*, Stanford University Press, 1967.

16 Moretti, P. M., and Kays, W. M., "Heat Transfer to a Turbulent Boundary Layer with Varying Free-Stream Velocity and Varying Surface Temperature—An Experimental Study," *International Journal of Heat and Mass Transfer*, Vol. 8, 1965, p. 1187.

17 Kays, W. M., *Convective Heat and Mass Transfer*, McGraw-Hill, New York, 1966.

18 Schraub, F. A., and Kline, S. J., "A Study of the Structure of the Turbulent Boundary Layer With and Without Longitudinal Pressure Gradients," Thermosciences Division, Mechanical Engineering Department, Stanford University, Report MD-12, 1965.

19 McEligot, D. M., "The Effect of Large Temperature Gradients on Turbulent Flow of Gases in the Downstream Regions of Tubes," PhD dissertation, Stanford University (TID-19446), 1963.

20 Perkins, H. C., and Worsoe-Schmidt, P. M., "Turbulent Heat and Momentum Transfer for Gases in a Circular Tube at Wall-to-Bulk Temperature Ratios of Seven," *International Journal of Heat and Mass Transfer*, Vol. 8, 1965, p. 1011.

21 McEligot, D. M., Ormand, L. W., and Perkins, H. C., Jr., "Internal Low Reynolds Number Turbulent and Transitional Gas Flow With Heat Transfer," JOURNAL OF HEAT TRANSFER, TRANS ASME, Vol. 88, No. 2, May 1966, p. 239.

22 Bankston, C. A., Sibbitt, W. L., and Skoglund, V. J., "Stability of Gas Flow Distribution Among Parallel Heated Channels," AIAA 2nd Propulsion Joint Specialist Conference, AIAA Paper 66–589, 1966.

23 Coon, C. W., "Transition from the Turbulent to the Laminar Regime for Internal Convective Flow with Large Property Variations," PhD dissertation, The University of Arizona, 1968.

24 Siegel, R., Sparrow, E. M., and Hallman, T. M., "Steady Laminar Heat Transfer in a Circular Tube With Prescribed Wall Heat Flux," *Applied Science Research*, Series A, Vol. 7, 1958, p. 386.

25 Davenport, M. E., and Leppert, G., "The Effect of Transverse Temperature Gradients on the Heat-Transfer and Friction for Laminar Flow of Gases," JOURNAL OF HEAT TRANSFER, TRANS ASME, Series C, Vol. 87, May 1965, p. 191.

26 Worsoe-Schmidt, P. M., and Leppert, G., "Heat Transfer and Friction for Laminar Flow of Gases in a Circular Tube at High Heating Rates," *International Journal of Heat and Mass Transfer*, Vol. 8, 1965, p. 1281.

The Heat Transfer and Pressure-Drop Characteristics of Gas Flow Inside Spirally Corrugated Tubes[1]

G. J. KIDD, JR.[2]
Oak Ridge National Laboratory,
Oak Ridge, Tenn. Mem. ASME

Heat transfer and pressure-drop experiments have been performed for gas flow inside nine, 1/2-in-OD, 0.035-in. wall thickness, A-nickel, spirally corrugated tubes. The corrugations, which varied from 0.003–0.028 in. deep, were formed by pulling the tubes through a rotating head containing four embossing tools; corrugation-spacing-to-corrugation-depth ratios (P/e) ran from 16–41. The data, for heat transfer to nitrogen, at approximately 200 psig, were correlated by an expression of the form $N_{Nu,B}(N_{Pr,B})^{-0.4} \times (T_W/T_B)^{0.5} = A(N_{Re,B})^m$, *where all the physical properties were evaluated at bulk gas conditions. The exponent, m, on the Reynolds number was observed to be consistently greater (0.854–0.900) than the value of 0.8 found for smooth tubes; the constant, A, varied from 0.0095–0.0195 with no apparent correlation with P/e. Friction factors, measured with adiabatic airflow, were found to be up to 1.7 times that for smooth tubes. Tubes of this geometry were found to be very effective in enhancing heat transfer. On an equal pumping power basis, for example, a tube with P/e = 22 had a heat transfer coefficient 22 percent greater than a smooth tube.*

Introduction

An experimental study has been made of the heat transfer and pressure-drop characteristics of gas flow inside spirally corrugated tubes. This type of tube was first studied at the Oak Ridge National Laboratory by Lawson, et al. [1],[3] whose results showed that spirally corrugated tubes were very effective in enhancing the heat transfer to water. Because of a continuing interest at ORNL in advanced gas-cooled reactor technology, the decision was made to see if tubes of this type would also be effective in transferring heat to gases.

Nine tubes were examined in the present study. Four tubes, typical of those tested, are shown in Fig. 1, and the significant geometric parameters of the nine tubes are listed in Table 1. The first number of the tube designation gives the approximate corrugation pitch in hundredths of an inch and the second number gives the corrugation depth in thousandths of an inch. The test sections were made of 1/2-in-OD by 0.035-in. wall A-nickel tubing 13 in. long. The tubes were corrugated by pulling them (on a draw bench) through a rotating head that contained four spherically tipped embossing tools. The pitch of the spiral was varied by adjusting the relative speed of the draw bench and the rotating head, and the depth of the groove was changed by moving the embossing tools in or out. The pitch was defined as the distance between adjacent grooves or, since this was an essentially quadruple thread, 1/4 of the lead. The corrugating was done in the

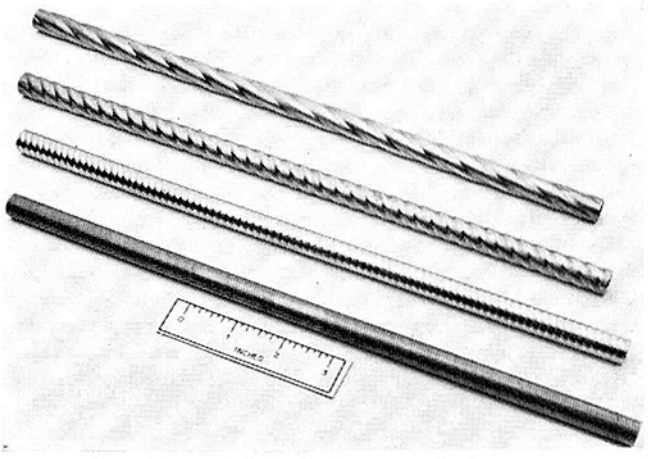

Fig. 1 Typical spirally corrugated tubes

[1] Research sponsored by the U. S. Atomic Energy Commission under contract with Union Carbide Corporation.
[2] Presently, Oak Ridge Gaseous Diffusion Plant, Oak Ridge, Tenn.
[3] Numbers in brackets designate References at end of paper.
Contributed by the Heat Transfer Division and presented at the Winter Annual Meeting, Los Angeles, Calif., November 16–20, 1969, of The American Society of Mechanical Engineers. Manuscript received by the Heat Transfer Division, June 12, 1969. Paper No. 69-WA/HT-3.

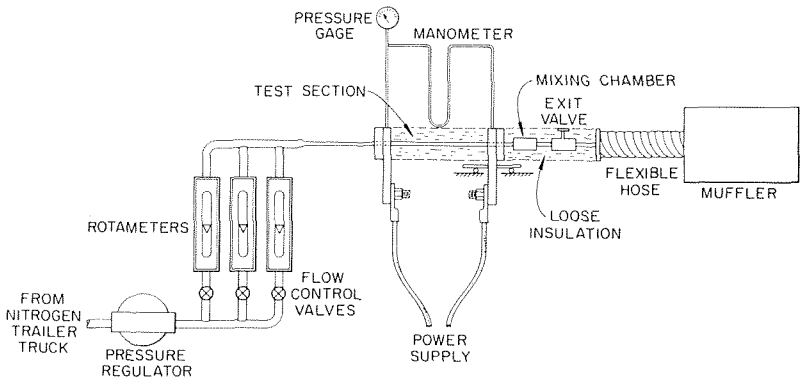

Fig. 2 Apparatus used to determine heat transfer characteristics of spirally corrugated tubes

Table 1 Physical characteristics of spirally corrugated tubes

Tube designation	Groove pitch P (in.)	Groove depth e (in.)	P/e	Maximum inside diameter of tube (in.)
8-3	0.078	0.003	26	0.421
14-6	0.14	0.006	23	0.428
22-11	0.22	0.011	20	0.427
35-16	0.35	0.016	22	0.435
44-28	0.44	0.028	16	0.440
51-16	0.51	0.016	31	0.438
65-18	0.63	0.018	36	0.442
85-24	0.85	0.024	35	0.442
102-25	1.02	0.025	41	0.446

research shops of the ORNL Metals and Ceramics Division.

In this study, the maximum inside diameter, D, was chosen as the characteristic dimension since it gives the most conservative values for the friction factor and heat flux. The physical properties used in the Nusselt, Reynolds, and Prandtl numbers were evaluated at the mean gas temperature. For these experiments, the maximum Mach number was 0.1, the maximum heat flux was 10^5 Btu/hr-ft^2, and the maximum wall-to-bulk temperature ratio was 2.0.

Heat Transfer Measurements

The heat transfer characteristics of the tubes were measured using the system shown in Fig. 2. In this system, nitrogen was conveyed to the test section from a storage trailer, through a pressure regulator, which controlled the inlet pressure at 200 psig and a set of three rotameters. Direct Joule heating was used for the experiments; the power was supplied from a 440 volt, 60 cps line, stepped down to approximately 3 volts through a saturable reactor and multitap transformer. System temperatures were measured with chromel-alumel thermocouples; the readout was a 12-point Brown recorder. The average inside wall temperature, T_W, was calculated from the arithmetic average of nine thermocouples spot-welded to the outside of the tubes. A correction was made for the temperature drop across the wall; this drop ranged from a few degrees at high flows and low heat fluxes up to 50 deg for the reverse conditions. In general, it represented less

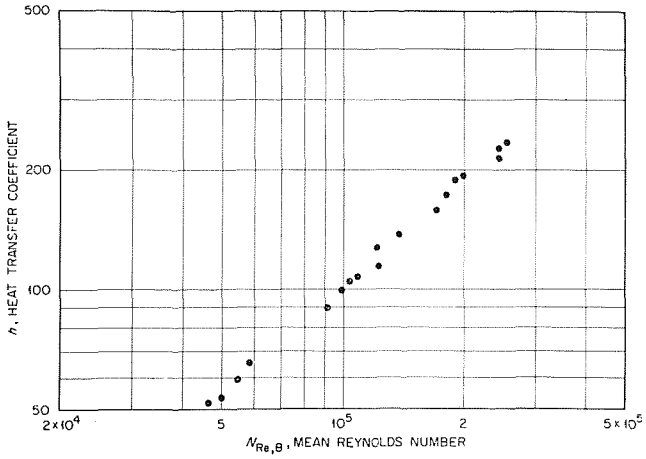

Fig. 3 Heat transfer coefficient as a function of Reynolds number for tube 35-16

than 5 percent of the wall-to-gas temperature difference. The bulk gas temperature, T_B, was taken as the average of the inlet and outlet gas thermocouple readings. Test section inlet pressure was measured with a Heise gauge and the overall pressure drop, from a point upstream of the test section to one downstream, was monitored on a "U" tube manometer. The test sections were silver-soldered into $^1/_2$-in-thick copper electrodes, which also served as flanges, at each end, thus giving an effective heated length of 12 in. In order to keep heat losses to a minimum, the test sections and mixing chamber were insulated with approximately 2 in. of loose fiberglass insulation. Heat loss through the insulation, and conduction losses to the electrodes, each represented only a few percent of the total heat generated in the system.

A typical set of heat transfer results is shown in Fig. 3 which depicts the heat transfer coefficient as a function of the bulk Reynolds number for tube 35-16. The scatter in the data is due to the variation in wall-to-bulk temperature ratio. When the results are cast in terms of a modified Dittus-Boelter correlation, which includes this temperature ratio, the scatter is reduced as

Nomenclature

A = constant
D = maximum inside diameter of tube
e = depth of corrugation
E = effectiveness of heat transfer surface
f = Blasius friction factor
g_c = gravitational constant
h = heat transfer coefficient
L = length of tube between pressure taps
m = exponent on Reynolds number
n = exponent on temperature ratio
N_{Nu} = Nusselt number
N_{Pr} = Prandtl number
N_{Re} = Reynolds number
p = pressure
P = spacing of corrugations
T = absolute temperature
V = velocity
ρ = density

Subscripts

B = bulk
W = wall

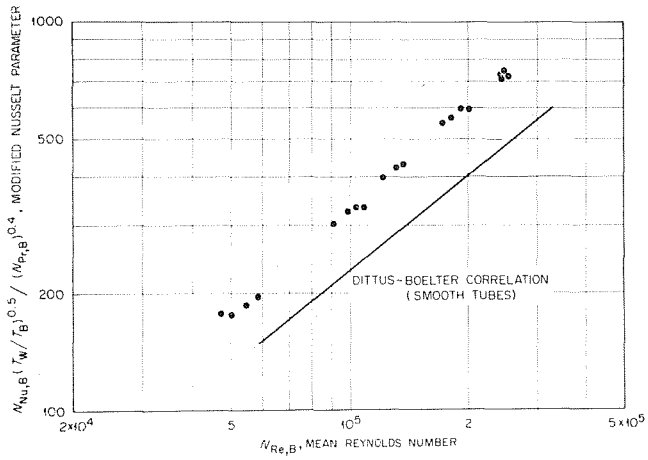

Fig. 4 Heat transfer characteristics for tube 35-16 in terms of a modified Nusselt parameter

Table 2 Values of constants for heat transfer correlation

$N_{Nu,B}(N_{Pr,B})^{-0.4}(T_W/T_B)^{0.5} = A(N_{Re,B})^m$ for spirally corrugated tubes

Tube designation	Constant A	Exponent m
8-3	0.0095	0.899
14-6	0.0131	0.876
22-11	0.0195	0.862
35-16	0.0153	0.866
44-28	0.0104	0.900
51-16	0.0143	0.864
65-18	0.0160	0.854
85-24	0.0116	0.883
102-25	0.0147	0.861

can be seen in Fig. 4. The form of the temperature ratio correction factor $(T_W/T_B)^n$ was based on the work of Taylor [3] who studied a variety of gases at temperature ratios up to 23. In general, it was found that an exponent, n, of 0.5 gave the best fit to most of the data. For a few tubes, a value of 0.6 or 0.7 gave a slightly lower standard error but the difference in the standard error was too small to be of any statistical significance. Thus, for spirally corrugated tubes, a wall-to-bulk temperature correction with an exponent of 0.5 is recommended.

Heat transfer characteristics from all of the tubes are presented in Table 2. These are the "best-fit" values of A and m for a linear least-squares analysis of the data using the expression

$$\log [N_{Nu,B}(N_{Pr,B})^{-0.4}(T_W/T_B)^{0.5}] = \log A + m \log N_{Re,B}.$$

For the runs used in the analysis, the heat balances (electrical input minus conduction losses through the insulation and to the electrodes divided by the sensible heat rise of the gas) were all better than ±10 percent and were usually within ±5 percent. As mentioned previously, the heat losses through the insulation and to the electrodes amounted to about 5 percent of the power input.

An interesting feature of these tubes is the fact that the exponent on the Reynolds number is consistently greater than the value of 0.8 obtained for smooth tubes [4] while for other common heat-transfer enhancement devices, such as wire coils or twisted tapes, the exponent is usually near 0.8. This means that corrugated tubes become "better" enhancement devices as the flow increases. In applications where it occasionally becomes necessary to remove amounts of heat greater than the design value, this characteristic of corrugated tubes allows them to do the job with a relatively low increase in flow. As can be seen from Table 2, the "rougher" tubes, that is, those with the deepest corrugations and the smallest pitch-to-depth, P/e, ratios, generally had the steeper slopes. More tests are needed to define the relationship between roughness and the values of A and m, but it is interesting to note that tube 44-28, which had the smallest value of P/e, had the greatest slope. The test sections were of the order of 25–30 equivalent diameters in length; they were preceded by a straightening section 50-dia long, the first 15 dia of which contained aluminum honeycomb. Work by Boelter, et al. [5], has shown that for this type of geometry the results are representatives of fully developed flow to within 2 percent, so additional corrections for length-to-diameter effects were not required.

Friction-Factor Measurements

The pressure-drop characteristics of these tubes were measured on the apparatus shown schematically in Fig. 5. Although it was originally planned to make the pressure measurements concurrently with the heat transfer measurements in the heat transfer system, it was found that the location of the pressure taps was extremely critical and reliable data could not be obtained with the restrictions imposed by the heat transfer experiments; in the heat transfer system, pressure taps could be located only in the electrodes at the ends of the tubes. Instead, it was necessary to put 10 pressure taps along the tubes (5 on corrugation peaks and 5 in corrugation valleys) and use these to develop the pressure profile along the tube from which the friction factor could be calculated. These tests were made with the same tubes used in the heat transfer experiments so that a direct comparison between the heat transfer and pressure-drop measurements could be made. As a check on the reliability of the data, pressure taps were placed in long sections of smooth tube both upstream and down of the corrugated tubes, and the smooth-tube friction factors were calculated for each run. In this system, 80 psi instrument air was the working fluid instead of nitrogen. The flow rates were measured with rotameters and the pressure drops were measured on water filled "U" tube manometers. Blasius friction factors were calculated from the expression

$$\Delta p = f \frac{L}{D} \frac{\rho V^2}{2g_c}.$$

By operating the system at 80 psi, it was possible to keep the Mach number below 0.1 so that compressibility effects were negligible.

The results of a typical run are given in Fig. 6. The friction factor for the corrugated tube and that for the smooth tube are shown. As can be seen the smooth tube data are in reasonable agreement with the Karman-Nikuradse line indicating that the system was functioning properly. This behavior was typical of all the friction-factor measurements.

Fig. 7 is a composite of all the friction-factor measurements for the corrugated tubes.[4] Even with multiple taps on the tubes, considerable scatter was frequently found in the data and the shaded areas indicated that scatter.

There did not, however, appear to be any significant variation in friction factor with axial position, indicating that the flow in the corrugated tubes developed in a very short distance. This is not surprising since the flow was already well developed in the smooth section upstream of the test section.

Effectiveness of Spirally Corrugated Tubes

One method of evaluating the effectiveness (E) of an "enhanced" tube is to compare the heat transfer coefficient for the tube at some pumping-power level with the heat transfer coefficient for a smooth tube at the same pumping power. Stated mathematically, the effectiveness E is

$$E = \left[\frac{h_{\text{enhanced}}}{h_{\text{smooth}}}\right]_{\text{equal pumping power}}$$

[4] Tube 22-11 was destroyed while removing it from the electrodes used in the heat transfer portion of the experiment; thus friction-factor values were not obtained for it.

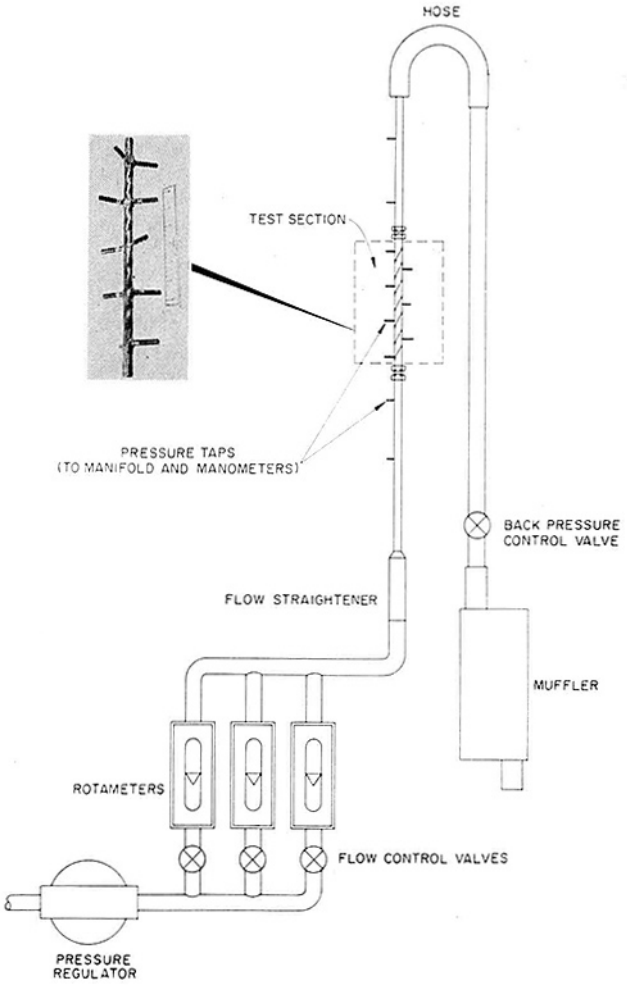

Fig. 5 Schematic diagram of apparatus used in pressure-drop measurements

Naturally, if E is greater than 1, the enhanced tube looks very attractive; however, even when the ratio is less than 1 there are other factors such as material cost, space limitation, etc., that make some enhanced tubes have merit in certain applications.

To illustrate the effectiveness of the spirally corrugated tubes let us examine the results for tube 35-16. Assuming the smooth and enhanced tubes will operate at the same conditions, the ratio of heat transfer coefficients becomes

$$\frac{h_{\text{enhanced}}}{h_{\text{smooth}}} = \frac{[N_{\text{Nu},B}(N_{\text{Pr},B})^{-0.4}(T_W/T_B)^{0.5}]_{\text{enhanced}}}{[N_{\text{Nu},B}(N_{\text{Pr},B})^{-0.4}(T_W/T_B)^{0.5}]_{\text{smooth}}}$$

Bergles and Morton [6] show that at the same pumping power the relationship between the Reynolds numbers in smooth and enhanced tubes is given by

$$(N_{\text{Re}})_{\text{smooth}} = (N_{\text{Re}^3\,\text{enhanced}} f_{\text{enhanced}}{}^{5.37})^{0.358}.$$

At a Reynolds number of 10^5, tube 35-16 has a friction factor of 0.0295; for a corresponding smooth tube, $N_{\text{Re smooth}} = 1.21 \times 10^5$. At this Reynolds number, the Nusselt parameter for the smooth tube would be 267; however, this parameter for the corrugated tube is 325. The effectiveness therefore is

$$E = \frac{325}{267} = 1.22$$

and this tube at these conditions thus has better heat transfer properties than a smooth tube for the same pumping power. This result corroborates the earlier conclusions of Lawson, et al. [1], based on studies with water flowing inside spirally corrugated tubes, that this type of tube effects significant increases in heat transfer over that observed for smooth tubes at the same conditions.

Summary and Conclusions

Heat transfer and pressure-drop characteristics have been determined for gas flow inside 9 spirally corrugated tubes. Data, for heat transfer to nitrogen, at heat fluxes up to 10^5 Btu/hr-ft^2 and wall-to-bulk temperature ratios to 2.0, were correlated by the expression:

$$N_{\text{Nu},B}(N_{\text{Pr},B})^{-0.4}(T_W/T_B)^{0.5} = AN_{\text{Re},B}{}^m$$

where the values of A and m are as listed in Table 2. Values for

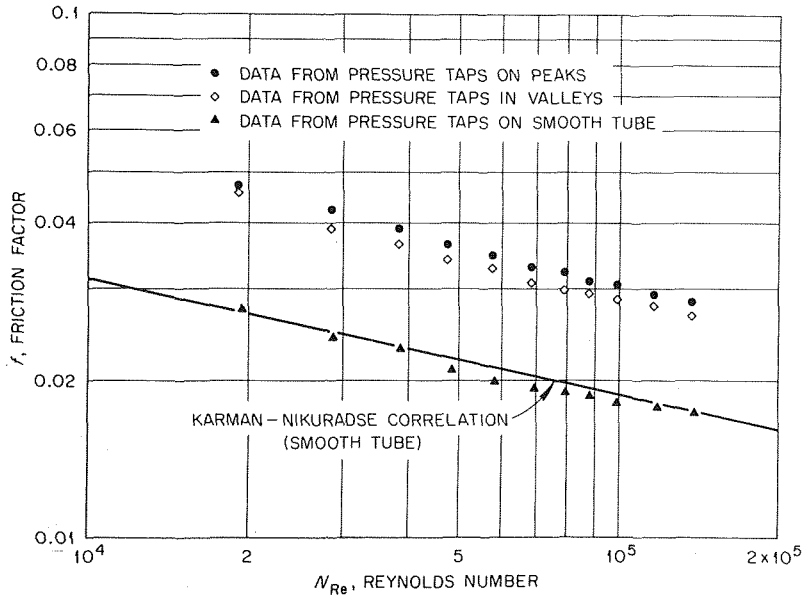

Fig. 6 Typical pressure-drop results for tube 35-16

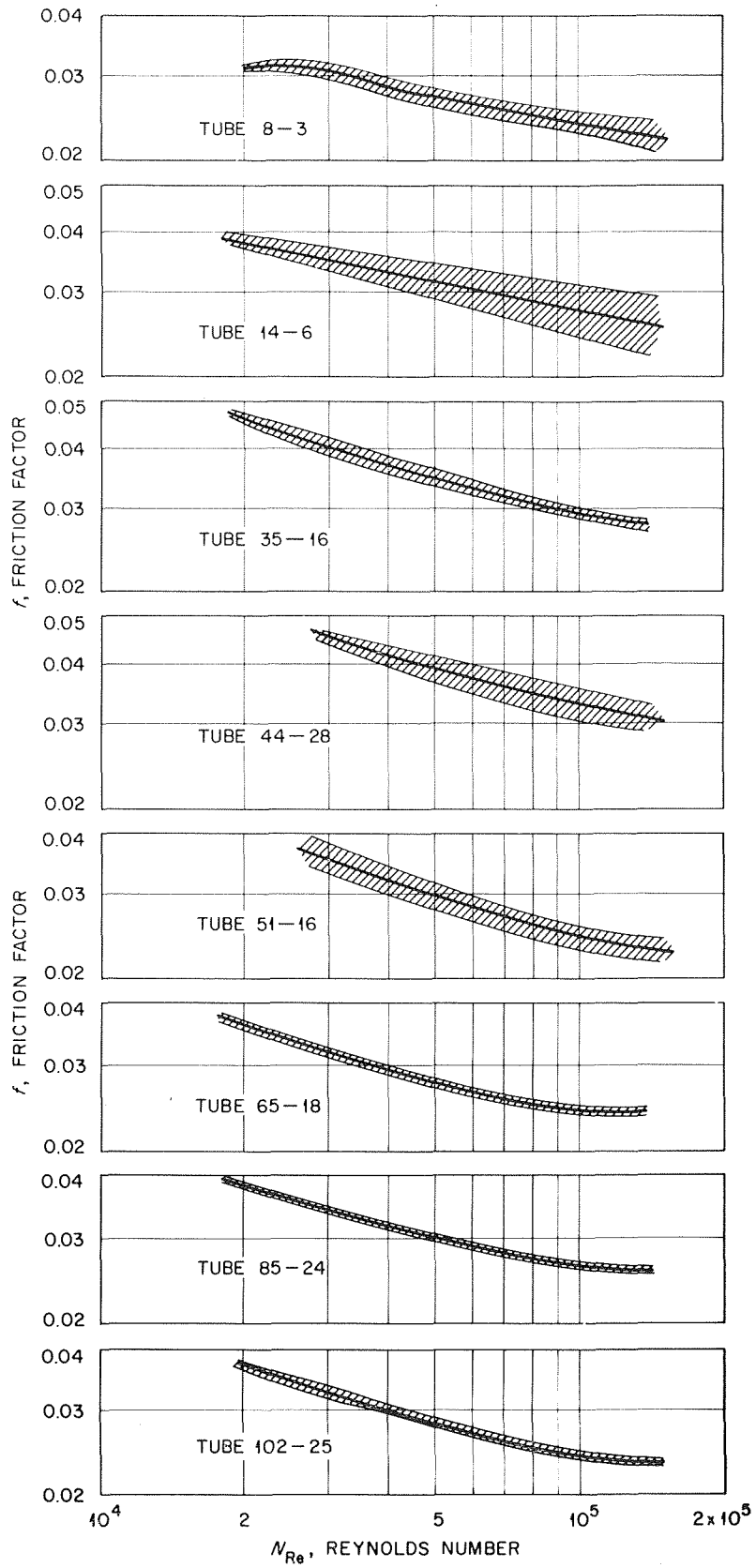

Fig. 7 Friction-factor characteristics of spirally corrugated tubes

m were consistently greater than 0.8 and generally depended on the roughness of the corrugations; there was no apparent correlation of the values for A with roughness. Isothermal friction factors were measured using air and were found to be up to 70 percent greater than smooth-tube friction factors. Spirally corrugated tubes were found to be effective devices for enhancing heat transfer to gases. A tube, which had a P/e ratio of 22, had a heat transfer coefficient 22 percent higher than a smooth tube requiring the same pumping power. Because of their effectiveness in enhancing heat transfer to both liquids and gases, spirally corrugated tubes merit further investigation. Results so far cover a limited range of parameters and further studies are needed to define such things as the effects of length-to-diameter ratio on heat transfer and pressure drop, optimized corrugation dimensions, the effect of heat transfer on pressure drop, and the effectiveness of corrugated tubes for a wide variety of fluids in single and two-phase flows.

References

1 Lawson, C. G., Kedl, R. J., and McDonald, R. E., "Enhanced Heat-Transfer Tubes for Horizontal Condensers With Possible Applications in Nuclear Power Plant Design," *Transactions of the ANS*, Vol. 9, No. 2, Oct.–Nov. 1966, pp. 565–566.

2 Dittus, F. W., and Boelter, L. M. K., "Heat Transfer in Automobile Radiators of the Tubular Type," *University of California Publications in Engineering*, Vol. 2, No. 13, Oct. 1930, pp. 443–461.

3 Taylor, M. F., "Correlation of Local Heat-Transfer Coefficients for Single-Phase Turbulent Flow of Hydrogen in Tubes With Temperature Radios to 23," Lewis Research Center, National Aeronautics and Space Administration, Jan. 1968, NASA TN D-4332.

4 McAdams, W. H., *Heat Transmission*, McGraw-Hill, 3rd ed., 1954, p. 219.

5 Boelter, L. M. K., Young, G., and Iversen, H. W., "An Investigation of Aircraft Heaters, XXVII—Distribution of Heat-Transfer Rate in the Entrance Section of a Circular Tube," National Advisory Committee for Aeronautics, July 1948, NACA TN No. 1451.

6 Bergles, A. E., and Morton, H. L., "Survey and Evaluation of Techniques to Augment Convective Heat Transfer," Report 5382-34, Massachusetts Institute of Technology, Feb. 1965.

m were consistently greater than 0.8 and generally depended on the roughness of the corrugations; there was no apparent correlation of the values for A with roughness. Isothermal friction factors were measured using air and were found to be up to 70 percent greater than smooth-tube friction factors. Spirally corrugated tubes were found to be effective devices for enhancing heat transfer to gases. A tube, which had a P/e ratio of 22, had a heat transfer coefficient 22 percent higher than a smooth tube requiring the same pumping power. Because of their effectiveness in enhancing heat transfer to both liquids and gases, spirally corrugated tubes merit further investigation. Results so far cover a limited range of parameters and further studies are needed to define such things as the effects of length-to-diameter ratio on heat transfer and pressure drop, optimized corrugation dimensions, the effect of heat transfer on pressure drop, and the effectiveness of corrugated tubes for a wide variety of fluids in single and two-phase flows.

References

1 Lawson, C. G., Kedl, R. J., and McDonald, R. E., "Enhanced Heat-Transfer Tubes for Horizontal Condensers With Possible Applications in Nuclear Power Plant Design," *Transactions of the ANS*, Vol. 9, No. 2, Oct.–Nov. 1966, pp. 565–566.

2 Dittus, F. W., and Boelter, L. M. K., "Heat Transfer in Automobile Radiators of the Tubular Type," *University of California Publications in Engineering*, Vol. 2, No. 13, Oct. 1930, pp. 443–461.

3 Taylor, M. F., "Correlation of Local Heat-Transfer Coefficients for Single-Phase Turbulent Flow of Hydrogen in Tubes With Temperature Radios to 23," Lewis Research Center, National Aeronautics and Space Administration, Jan. 1968, NASA TN D-4332.

4 McAdams, W. H., *Heat Transmission*, McGraw-Hill, 3rd ed., 1954, p. 219.

5 Boelter, L. M. K., Young, G., and Iversen, H. W., "An Investigation of Aircraft Heaters, XXVII—Distribution of Heat-Transfer Rate in the Entrance Section of a Circular Tube," National Advisory Committee for Aeronautics, July 1948, NACA TN No. 1451.

6 Bergles, A. E., and Morton, H. L., "Survey and Evaluation of Techniques to Augment Convective Heat Transfer," Report 5382-34, Massachusetts Institute of Technology, Feb. 1965.

DISCUSSION

E. V. Seymour[5]

In his discussion of friction-factor measurements the author states there appeared to be no significant variation in friction factor with axial position, indicating that the flow in the corrugated tubes developed within a very short distance. I would like to present one relevant result I obtained in a study of the frictional characteristics of twisted tape swirl inducers[6] (helically twisted metal strips with a width equal to the internal dia of the tube).

Fig. 8 shows the variation of friction factor (defined as in the author's article) with distance from the front end of the tape for different twist ratios, λ, defined as the number of 360 deg twists per dia. The conditions here are somewhat different from those used in the author's experiments in that the flow is forced to follow the helical path immediately and the flow upstream from the end of the tape had a flat velocity profile having just left a settling chamber via a contraction. However, one would expect, from my experiments, to find in the case of the spirally corrugated tubes an initial high friction factor over the short length where the flow pattern is established. This initial variation in friction factor may not have been detected by the author's pressure measurement system. Moreover, it may be important to include this "inlet loss" in determining the overall pressure drop for a length of spirally corrugated tube.

J. H. Van Sant[7]

Heat exchanger designers are always searching for methods to improve convection heat transfer coefficients without increasing pumping power. If the effectiveness of spirally corrugated tubes is indeed greater than unity as indicated by the author then this can be accomplished. Several other methods such as rough surfaces, grooves, twisted tapes, etc., have also been tried in tubes with about equal success as described by Bergles and Morton [6]. Spirally corrugated tubes having a small pitch are expected to effect the flow much like a rough surface and a large pitched corrugated tube should cause the flow to swirl much like in a tube with a twisted tape. A spiral motion is probably the better condition as it gives an increased velocity at the tube wall and also induces a secondary convective flow. The corrugated tube may be a better way to generate vortex flow as it has less fluid-solid interface but more heat transfer surface than a tube with a twisted tape inside.

If one assumes the flow in the 35-16 tube described in Table 1 does indeed spiral with the corrugations, then a mean velocity near the tube wall can be estimated from the lead and depth of the groove and the maximum diameter of the tube by

$$V_B^* = \sqrt{\frac{[\pi(D - e)]^2 + 16P^2}{4P}}\, V_B = CV_B$$

A Reynolds number that includes this velocity can be determined by $N_{\mathrm{Re},B}^* = CN_{\mathrm{Re},B}$ and a new friction factor from $f^* = f/C^2$. Data given in Figs. 4 and 6 have been replotted in Fig. 9 in terms of Stanton numbers ($N_{\mathrm{St},B}^* = N_{\mathrm{Nu},B}/N_{\mathrm{Re},B}^* N_{\mathrm{Pr},B}$), f^* and $N_{\mathrm{Re},B}^*$. Note that the data agree much better with correlations for heat transfer and pressure loss in smooth tubes. If friction

[5] Shell Pipe Line Corp., Houston, Texas.

[6] E. V. Seymour, "Fluid Flow Through Tubes Containing Twisted Tapes," *The Engineer*, October 28, 1966, Vol. 222, pp. 634–642.

[7] Mechanical Engineer, Lawrence Radiation Laboratory, Livermore, Calif.

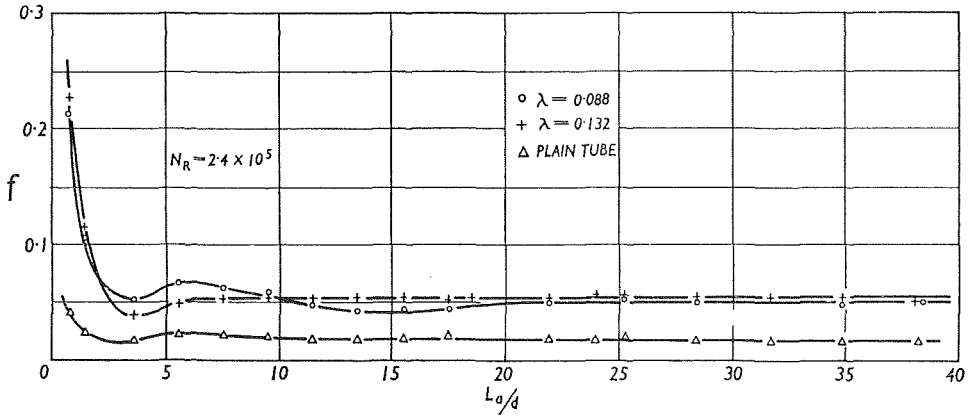

Fig. 8 Variation of local axial friction factor with tape length

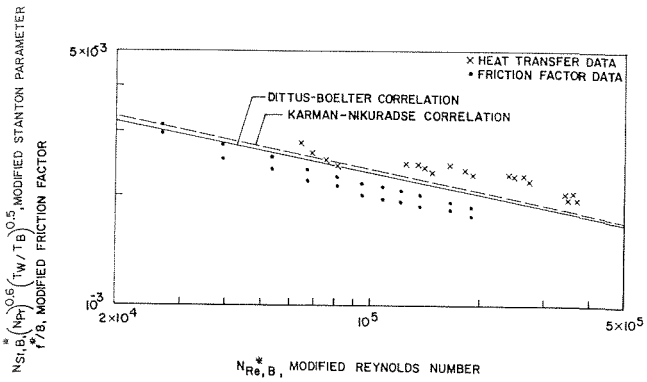

Fig. 9 A replot of data given in Figs. 4 and 6 using estimated swirl velocities

factors had been measured in heat transfer conditions they would be even closer to the Karman-Nikuradse correlation. This implies that the fluid boundary layers in the corrugated tube behaves much the same as in smooth tubes and the Colburn correlation[8] $N_{St,B}{}^*(N_{Pr,B})^{0.6}(T'_w/T_B)^{0.5} = f^*/8$ gives a reasonable prediction of heat transfer and pressure loss. Consequently, the effectiveness should differ little from unity.

The wall thickness of the corrugated tubes were probably not constant around the tube periphery which should have resulted in a circumferential variation of heat flux during testing. Shouldn't one expect then, the measured heat transfer coefficients to be different from those for a tube with constant heat flux?

Whenever possible one should make a statement about the accuracy of the results of experimental measurements by giving an estimate of the combined effect of all probable measurement errors. For example, what is the uncertainty interval of the 1.2 effectiveness value given for the 35-16 tube?

Author's Closure

The efforts of the discussers in reviewing the paper and extending its content are sincerely appreciated.

As Dr. Seymour indicates, one would expect to find some entrance effect on the friction factor for this type of tube. However, the scatter in the data and the rather wide spacing of the pressure taps apparently obscured any effect that was present. It is suspected that the magnitude of the entrance loss should have been quite small since the test section was preceeded by a smooth straight tube approximately 50 diameters long, so that the flow was well developed prior to entering the corrugated section. If, however, the flow does become rotating in nature, as Dr. Van Sant's success in correlating the data using a swirling velocity implies, then there should be an angular acceleration which would manifest itself as an entrance loss. Rather than speculate further on this point without adequate information, it would appear that a series of three dimensional velocity profile and flow visualization studies should be performed to resolve these questions on the entrance region and the nature of the flow. It would then be possible to include the "inlet loss," whatever its value, in the overall pressure drop of a corrugated tube as Dr. Seymour points out.

Although the use of a rotating velocity has proved useful in correlating this and other data, it is felt that the linear velocity has the advantage of giving the designer a parameter that is more directly comparable from geometry to geometry. There was, to be sure, some variation in wall thickness between the peaks and valleys of the corrugation, giving rise to both circumferential and axial variations in heat flux. It would seem that the effect of these variations was relatively small compared to that created by the corrugations on the flow field. This conclusion is implied from both the pressure drop portion of this study, in which there was no heat being transfered, and from the study of Lawson, et al. [1], in which condensing steam was the heat source. Nevertheless this point should be checked; perhaps an experiment using a heavy walled tube with the corrugations machined on the inside and resistance heaters wrapped around the outside would provide some additional insight into the matter.

In response to Dr. Van Sant's question about measurement errors, it is felt that the precision of the measurements is within ±5 percent. The experiments were performed using standard instrumentation for this type of work, 0.5 percent meters for the electrical measurements, calibrated flowmeters, recorders, thermocouples etc. The accuracy of the measurements is best reflected in the scatter of the data. As was mentioned, the heat balances were generally within ±5 percent while the friction factor data ranged from ±5 percent to more than ±20 percent. For the 35-16 tube the scatter in the friction factor results was relatively small so that the uncertainty in the effectiveness was of the order of 15 percent or

$$E = 1.2 \pm 0.18$$

[8] Holman, J. P., *Heat Transfer*, 2nd ed., McGraw-Hill Book Co. (1968), p. 163.

DAVID HANSEN
Professor,
Chemical Engineering Department,
Rensselaer Polytechnic Institute,
Troy, N. Y.

WALTER H. BREYER
Celanese Corporation,
Charlotte, N. C.

WALTER J. RIBACK
Scott Paper Corporation,
Philadelphia, Pa.

Steady State Heat Transfer in Partially Liquid Filled Porous Media

Introduction

THE FLOW of fluids and of heat through capillary porous media have been subjects of research for at least fifty years. Early research on this subject included the studies of moisture migration in soils by Boyoucos [1],[1] Winterkorn [2], Taylor and Cavazza [3], and Rollins, Spangler, and Kirkham [4]. Other workers, such as Krischer and Esdorn [5], studying heat transfer and drying did experiments at higher temperatures and over a broad range of moisture contents. They established that the vapor and liquid movement can act in concert when coupled with local evaporation or condensation. Liquid can evaporate, diffuse as a vapor, and recondense. Simultaneously, there can be flow of liquid either concurrent with or counter to the vapor diffusion. The driving force for liquid flow is presumed to be a gradient in capillary pressure due to a gradient of liquid concentration and/or the effects of the temperature gradient on surface tension.

Quantitative analysis of the transport phenomena in porous media has been tackled from both the microscopic (capillary) process level and from the phenomenological, macroscopic view. It is possible to consider separately each of the transport mechanisms for each phase which would include conduction in solid, liquid, and gas, diffusion in gas, and capillary flow in liquid. These transports are, of course, governed by Fourier's law, Fick's law, and D'Arcy's law, respectively (thermal effects on diffusion and capillary flow must also be considered). Further, these transports are coupled by a phase transition (evaporation—condensation). The difficulty of proceeding with an essentially microscopic analysis is that the geometry of the structure is not amenable to quantitative description and the individual transport processes relate to local (microscopic) values of temperature, pressure, and concentrations which are not measurable. Probably the most extensive and thorough analysis of this sort has been given by Philip and de Vries [6] and de Vries [7]. While their results illuminate the character of the interdependence of the microscopic processes, their quantitative validity or range of applicability has been tested against only very limited experimental data.

More recently, several investigators have applied the formalisms of nonequilibrium thermodynamics to analyze the simultaneous transfer of mass and energy. One of the best known is the treatment presented by Lykov and Mikhaylov [8] although, as has been pointed out by Valchar [9], their analysis does not rigorously follow the tenets of nonequilibrium thermodynamics. Other analyses have been published by Ash and Barrer [10], Cary

[1] Numbers in brackets designate References at end of paper.

Contributed by the Heat Transfer Division for publication (without presentation) in the JOURNAL OF HEAT TRANSFER. Manuscript received by the Heat Transfer Division, October 10, 1968; revised manuscript received, May 6, 1970. Paper No. 70-HT-N.

Nomenclature

G = Gibbs free energy
H = enthalpy
J = flux with respect to motion of the center of mass
k = thermal conductivity
L = coefficient in flux-force equations
M = molecular weight
P = pressure
P_l = liquid pressure
P_g = gas phase pressure
P_c = suction potential = $P_g - P_l$
R = gas constant
S = entropy
T = temperature
V = volume
X = driving force in flux-force equations
Y_i = mole fraction of component i in gas phase
λ = latent heat of vaporization
μ_i = chemical potential
ρ = density
ρ_i = density of pure component i
ψ = liquid saturation, fraction of pore space occupied by liquid

Subscripts

g = gas
0 = solid
1 = liquid
2 = vapor of liquid
3 = noncondensable gas

[11], Taylor and Cary [12], Evans, Watson, and Mason [13], Vink [14], and Mokadam [15, 16]. The phenomenological approach via nonequilibrium thermodynamics bypasses the need for a description of the microscopic geometry and can yield a complete, rigorous analysis subject only to questions about the basic validity of this approach. The results, however, are in terms of complex transport coefficients and thermodynamic driving forces which do not relate simply and directly to the usual measured quantities.

In this study we have undertaken the limited objectives of one, testing the validity of a linear flux-force equation in a closed system at steady state and two, experimentally probing for the mechanisms which will limit attainable heat transfer at steady state. The study was further limited to closed systems where the macroscopic mass flux of liquid and vapor must add to zero.

Phenomenological Analysis

If a macroscopic view is taken of the porous medium and the entire system is sufficiently larger than the pore dimensions, then the system may be considered locally homogeneous. From this view the entire system is a single "phase" composed of the following components: solid, liquid, vapor of the liquid, and noncondensable gases. These components are designated by the subscripts 0, 1, 2, and 3, respectively. The determination of the flux-force relationships is directly as given by many authors including de Groot [17] or Fitts [18]. Various forms are possible. The one given directly below is based on the form used by de Groot [17] where the flux-force products are the components of entropy production rate multiplied by temperature.

$$\begin{aligned} J_q &= L_{qq}X_q + L_{q0}X_0 + L_{q1}X_1 + L_{q2}X_2 + L_{q3}X_3 \\ J_0 &= L_{0q}X_q + L_{00}X_0 + L_{01}X_1 + L_{02}X_2 + L_{03}X_3 \\ J_1 &= L_{1q}X_q + L_{10}X_0 + L_{11}X_1 + L_{12}X_2 + L_{13}X_3 \\ J_2 &= L_{2q}X_q + L_{20}X_0 + L_{21}X_1 + L_{22}X_2 + L_{23}X_3 \\ J_3 &= L_{3q}X_q + L_{30}X_0 + L_{31}X_1 + L_{32}X_2 + L_{33}X_3 \\ J_r &= L_{rr}X_r \end{aligned} \tag{1}$$

where J_q refers to the heat flux; J_0, J_1, J_2, and J_3 refer to the fluxes of solid, liquid, vapor, and noncondensable gas, respectively. J_r is the local evaporation rate. All mass fluxes are relative to the motion of the local center of gravity. The L_{ij} are the phenomenological coefficients which are presumably related by the Onsager reciprocal relations. The driving forces are defined as follows:

$$X_q = -\nabla \ln T; \quad X_i = -T\nabla \frac{\mu_i}{T}; \quad X_r = \mu_1 - \mu_2 \tag{2}$$

where T is absolute temperature and μ_i is the chemical potential of component i. To apply these equations to the analysis of a specific problem requires that the chemical potentials be related to more directly measurable quantities.

The set of equations (1) is not an independent set since by definition:

$$J_0 + J_1 + J_2 + J_3 = 0 \tag{3}$$

Further, for the closed system at steady state:

$$\begin{aligned} J_0 &= 0 \\ J_1 + J_2 &= 0 \\ J_3 &= 0 \end{aligned} \tag{4}$$

These restrictions may be used to reduce the original six equations to three. If an assumption is made of local equilibrium between liquid and vapor, two further simplifications occur. One, the expression for J_r can be discarded as J_r must simply take the value necessary to maintain equilibrium. Secondly, vapor-liquid equilibrium implies $\mu_1 = \mu_2$ or, therefore, that $X_1 = X_2$. Together the conditions of steady state and vapor-liquid equilibrium serve to reduce the original equations to:[2]

$$J_q = L_{qq}X_q \tag{5}$$

This is, of course, simply Fourier's law as we should expect. However, it does not refer to heat transferred only by molecular conduction in the usual sense but rather to the heat transfer process in the porous medium including energy transferred via a balanced combination of liquid flow and vapor diffusion. It should apply only under the specified restrictions: a closed system at steady state with vapor-liquid equilibrium. Detailed discussion of special forms and cases of the transport equations for porous media is given in a thesis by Breyer [19].

Experiments to Measure Conductivity

To test the validity of equation (5) and to observe the magnitude of L_{qq} and its dependence on temperature and composition, experiments were performed on the apparatus described in Fig. 1. Fluids from constant-temperature baths maintained upper and lower surfaces at constant temperatures. The porous medium sample was sandwiched in series with glass plates between the constant-temperature surfaces. Thermocouples in small holes drilled to the center of brass plates recorded temperatures on either side of the glass plates. Other thermocouples recorded temperatures within the porous medium. Sample dimensions were 6 in. square by 2 in. thick. Temperatures were recorded from thermocouples ($^1/_{16}$-in. dia) located at $^1/_4$-in. intervals through the thickness. The thermocouple readings yielded a description of the temperature profile and the temperature difference across the glass plates (of known thermal conductivity) permitted a calculation of the heat flux. The composition, or liquid distribution, in the sample was measured by an x-ray intensity scan using apparatus and techniques described by Adams [20]. The apparatus was immersed in several inches of silica aerogel insulation to minimize lateral heat flow.

[2] See Appendix for more details on derivation of equation (5).

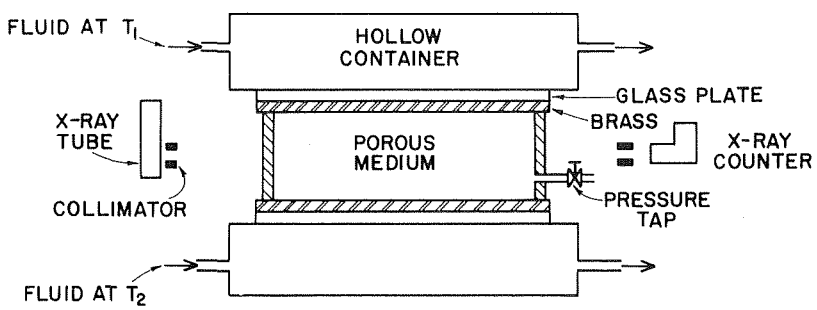

Fig. 1 Schematic diagram of apparatus

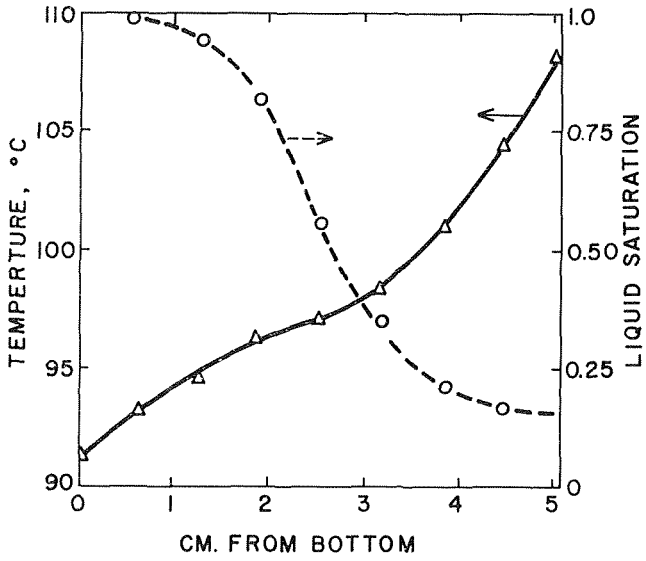

Fig. 2 Example of temperature and liquid saturation profiles from an experiment on glass beads at 61 percent average liquid saturation and 54.4 in. mercury total gas pressure

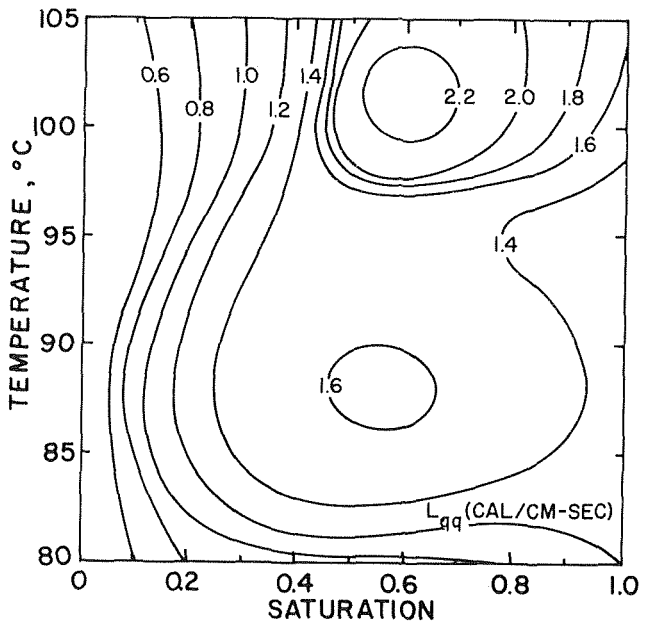

Fig. 3 L_{qq} as a function of temperature and saturation for glass beads-water-air; gas phase pressure controlled at 54.4 in. mercury absolute

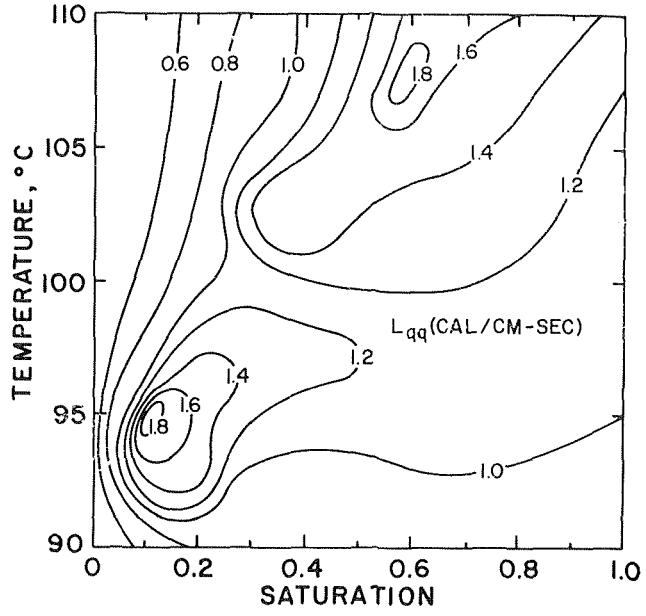

Fig. 4 L_{qq} as a function of temperature and saturation for rayon felts-water-air; gas phase pressure controlled at 45 in. mercury absolute

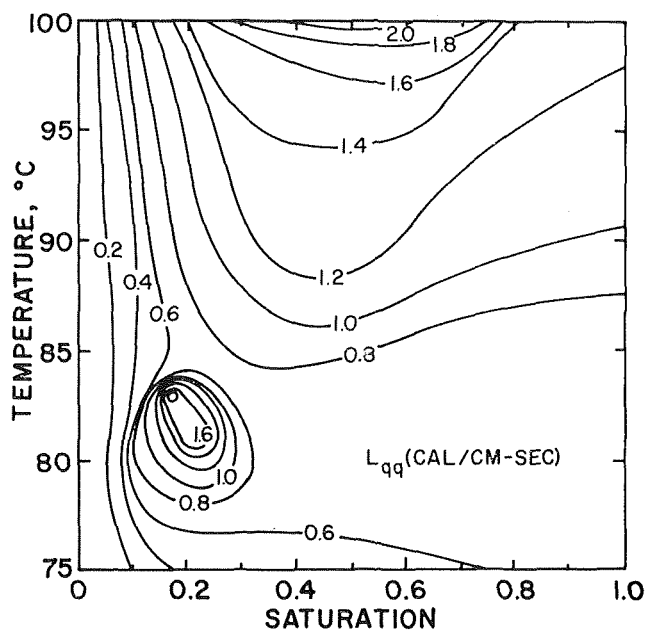

Fig. 5 L_{qq} as a function of temperature and saturation for rayon felts with holes-water-air; gas phase pressure controlled at 45 in. mercury absolute

Measurements were made using glass beads[3] about 300 microns in diameter and also on beds of rayon felts.[4] The felts were of nominal $^1/_4$-in. thickness but were compressed 8 to the inch in these experiments. The glass bead specimens had a void fraction of 32 percent and the felt layers 80 percent. More detailed description of the apparatus and experiments is given by Breyer [19].

A typical experimental result is shown in Fig. 2 for an experiment done on the glass beads at an overall average liquid saturation of 61 percent and a gas phase pressure of 54.4 in. of mercury absolute. Numerous such experiments were done covering a range of temperatures, temperature differences, and average liquid saturations while keeping the gas phase pressure constant through a series of experiments. From each experiment a series of values of L_{qq} was obtained by calculating $X_q = (-\nabla \ln T)$ from linear interpolation of successive thermocouple readings and dividing this value of driving force into the heat flux. Thus a given experiment yielded eight values of L_{qq} each at a different temperature and liquid saturation. The results from two series of such experiments on the glass beads and air, respectively, are summarized in Figs. 3 and 4 as contour plots of L_{qq} as a function of temperature and liquid saturation. Curiously, each of these plots shows two maxima.

Two additional sets were also run with felt samples. For the first, vertical holes $^1/_4$-in. dia were drilled at 1-in. centers in the felt samples. For the second, using the felts with holes, air was excluded by evacuating the system before charging with water. The results from these sets are summarized in Figs. 5 and 6.

[3] Minnesota Mining and Manufacturing "Super-Brite" type 090-5005.

[4] American Felts type 72RV32.

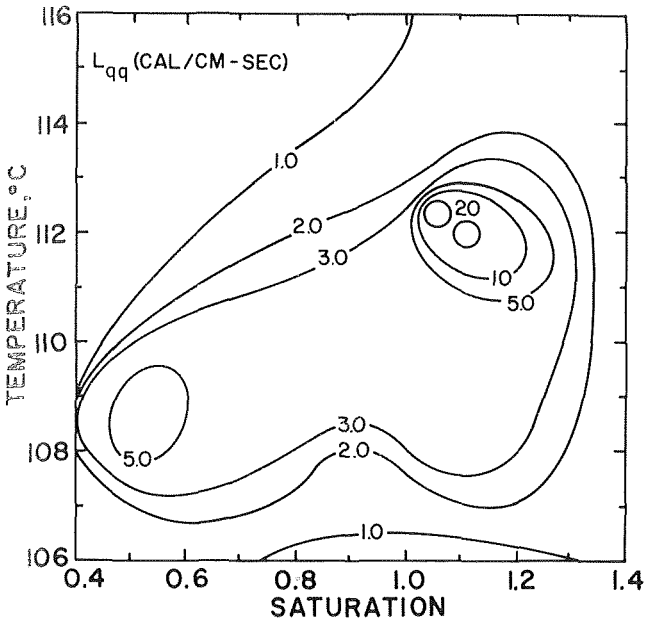

Fig. 6 L_{qq} as a function of temperature and saturation for rayon felts with holes-water, no air present

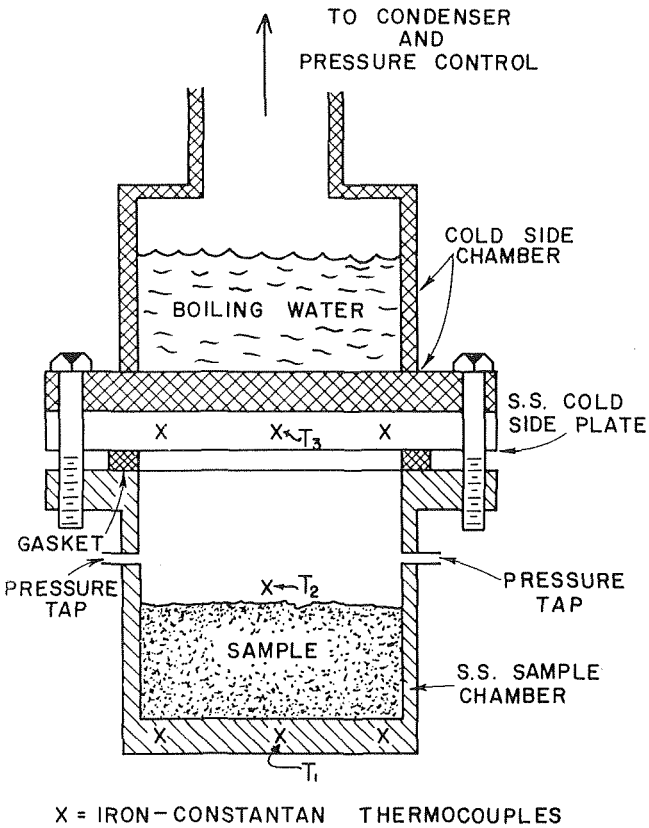

Fig. 7 Schematic diagram of apparatus

Since the contour plots were prepared by cross plots and interpolations from the raw data, no experimental points are shown on the contours. One contour plot derives from 15 experiments yielding 120 data points. The largest error source comes from uncertainty in the heat flux arising from edge losses and errors in temperature measurements. The estimated precision of the L_{qq} values is ± 10 percent based on the precision of temperature measurements used in the calculations and the potential error in estimating ∇T by linear interpolation.

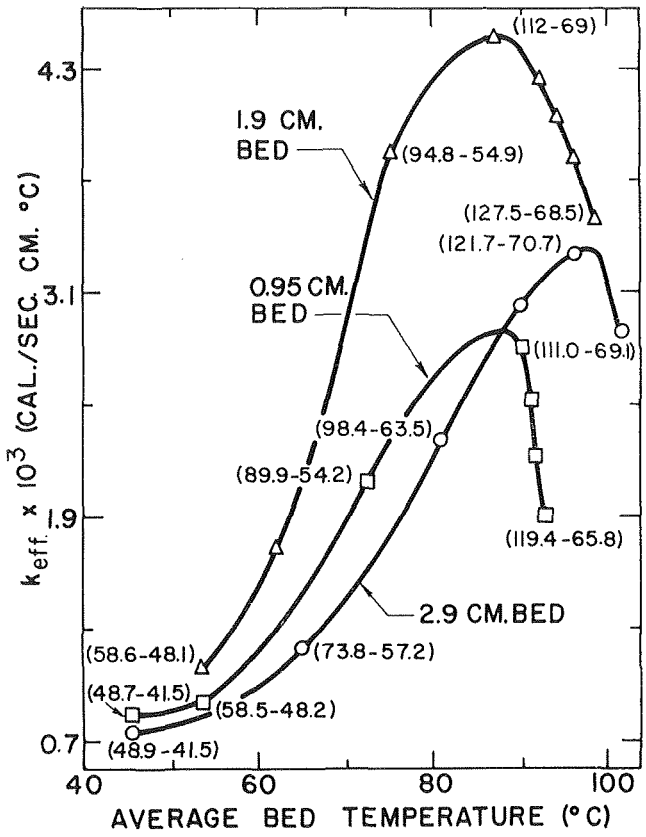

Fig. 8 Summary of results on glass bead beds; data points labeled with bed temperature range in deg C

Experiments at High Fluxes

The system for conductivity measurements was limited to operations at relatively modest heat fluxes. To observe behavior on forcing larger heat fluxes a second apparatus was constructed. This equipment, shown schematically in Fig. 7, held a sample in a stainless steel chamber with the bottom surface heated by quartz-tube infrared lamps. The temperature of the upper surface was maintained by a liquid above it boiling at constant pressure. This liquid was condensed and returned from a condenser in which a monitor on cooling-water flow rate and temperature permitted calculation of the heat flux through the system. Insulation minimized lateral heat flow. Temperatures were monitored by thermocouples in the upper and lower sample-container surfaces and one mounted inside the sample container. Further details on this apparatus and experiments are given by Riback [21].

For the tests the sample chamber was partially filled with the porous material, either glass beads or copper shot. Water was added sufficient to fill approximately 50 percent of the pore volume. The temperature of the upper surface was set by adjusting the pressure on the condenser and heat flux was regulated by setting the input to the quartz-tube lamp. By working with a partially filled chamber and measuring temperature at the two porous bed surfaces, the condensation part of the evaporation-diffusion-condensation cycle was effectively put external to the system under observation.

The glass beads used were the same as described earlier.[5] The copper beads[6] were somewhat ellipsoidal with a major axis about 0.0419 cm and a minor axis about 0.0297 cm. Tests with the glass beads were run with the sample chamber containing 0.95 cm, 1.9 cm, and 2.9 cm of beads. With the copper shot, bed

[5] Minnesota Mining and Manufacturing "Super-Brite" type 090-5005.

[6] Purchased from Belmont Smelting and Refining Works.

thicknesses of 2.9 cm and 7.6 cm were used.

Fig. 8 summarizes the data obtained with the glass bead beds. An "effective thermal conductivity" (heat flux times sample thickness divided by temperature difference between sample surfaces) has been plotted versus average bed temperature (mean of sample surface temperatures, $^1/_2(T_1 + T_2)$ per Fig. 7). While this is a convenient way of summarizing the data, the plot cannot be regarded as a functional relationship. "Effective thermal conductivity" is a convenient normalized parameter but lacks precise definition when calculated from the ∇T over the entire sample. Likewise "average bed temperature" calculated as the mean between the hot and cold sample surfaces is arbitrarily defined. (To complete specification of the experiments each data point has been labeled with two temperatures corresponding to the top and bottom surfaces of the sample, respectively.) However, though the parameters may lack precise definition, they are adequate to bring out some obvious features. There is in each case a definite maximum in the effective conductivity or ability of the system to transport heat. There is also an apparent optimum with respect to the sample thickness. The 1.9-cm bed yielded higher effective conductivities than either the 0.95-cm bed or the 2.9-cm bed. At low temperatures, the 0.95-cm bed was more effective than the 2.9-cm bed but the reverse applied at higher temperatures.

Tests with the copper beads yielded similar results as may be seen from Fig. 9. The largest recorded steady state values of the effective conductivities were 0.133 cal/cm·sec·deg C for the 2.9-cm bed. Attempts to achieve larger conductivities (or fluxes) by increasing temperature led to much smaller values and generally to unstable operation which prevented location of specific maxima in Fig. 9. A second set of experiments with copper beads but with air excluded yielded the results summarized in Fig. 10.

Discussion

The data from experiments to determine L_{qq} support the validity of equation (5). In the preparation of the contour plots there was extensive overlap of data which were consistent. That is, for the same temperature and liquid content in different experiments the same values of L_{qq} obtained *even though temperature gradients were different.* Further, some experiments were run with the higher temperature on top and some with it on the bottom. In the former situation the capillary liquid flow must counter gravity while in the latter it is aided by gravity. When the shift of orientation in the gravitational field is made holding other boundary parameters and conditions constant, a higher heat flux obtains with gravity aiding the capillary flow. However, this is also reflected in the temperature and liquid distribution profiles and the L_{qq} values, as they should be, are apparently independent of orientation in the gravitational field.

Comparing L_{qq} values between glass beads and felt shows them to be of the same magnitude. The maximum in L_{qq} at the lower temperature for the felts (which have a much larger void fraction) does occur at lower fractional saturation. Comparing Figs. 5 and 6 we see modestly larger L_{qq} values for the felt with holes but find the low-temperature maximum shifted from about 95 deg C to about 82 deg C. The holes would be expected to have their primary effect in lowering the resistance for vapor diffusion. Removing air from the system takes the vapor transfer from a diffusion process to a capillary flow process and, as the comparison

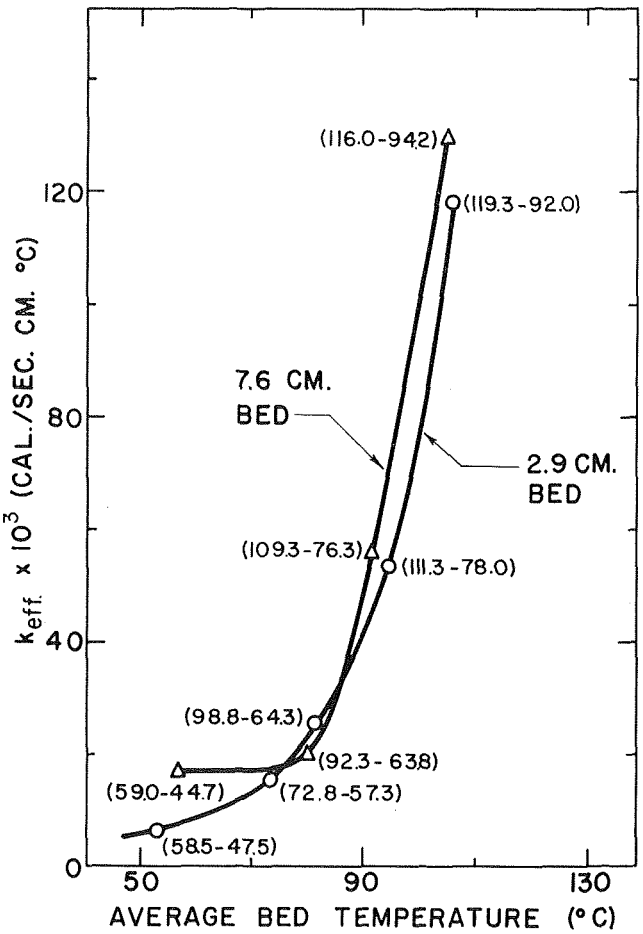

Fig. 9 Summary of results on copper bead beds; data points labeled with bed temperature range in deg C

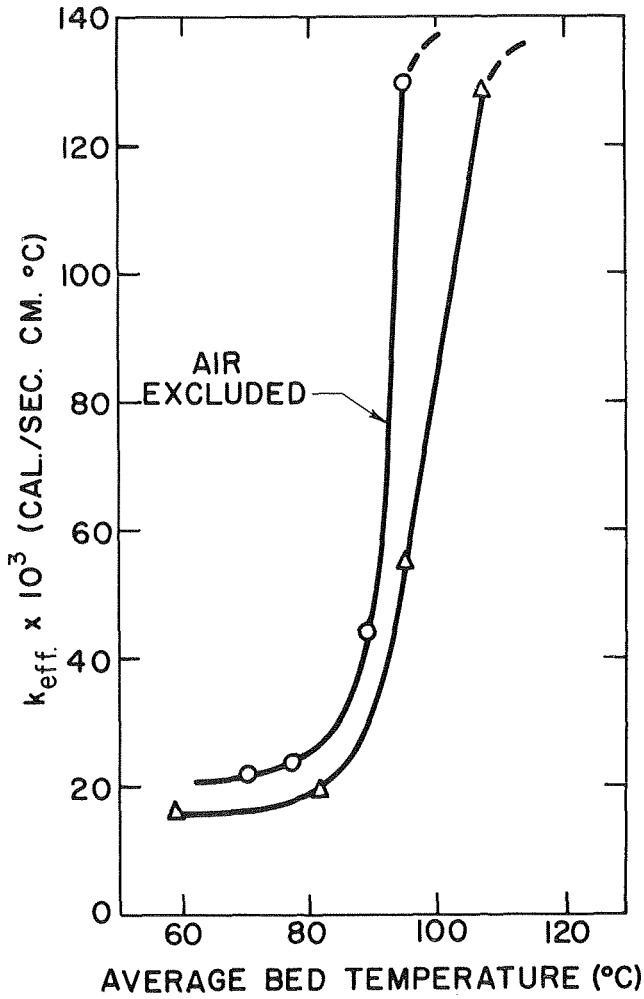

Fig. 10 Comparison of results with and without air present in 2.9-cm copper bead bed

of Fig. 5 and 6 shows, yields an order-of-magnitude increase in L_{qq} over a limited range of temperature and liquid content. (For the experiments without air the system was evacuated and charged with deaerated water. However, no steps were taken to remove or insure further the absence of noncondensables.) The saturations in Fig. 6 were based on porosity of the structure without holes. Values greater than 1.0 indicate the presence of liquid in the holes.

The double maxima in the L_{qq} contours may be related to the nature of the suction potential curves. Generally suction potential curves, as a function of liquid saturation, are *S*-shaped. There is a mid-range in saturation where the slope is small, and hence driving forces for capillary flow are small unless the saturation gradients are large.

While running these experiments, efforts were made to operate under conditions where large fluxes would obtain. However, it becomes apparent that this could not be done. In the hotter portions of the bed there's a net evaporation. The energy for this evaporation must be delivered to the liquid interfaces by a process of (molecular) conduction. With a low-conductivity solid matrix and a relatively low-conductivity liquid, this process is limiting and leads to the establishment of conditions corresponding to small values of L_{qq} in these regions. In the cooler regions there is net condensation which is also limited by the necessity of carrying the latent heat away by (molecular) conduction. Only in an intermediate region where there is negligible net evaporation or condensation can conditions for larger values of L_{qq} obtain. In this region it is apparent from the experimental results that vapor diffusion may be limiting, as decreasing the diffusion resistance by removing noncondensables markedly increased L_{qq}. Large effective thermal conductivities can be maintained throughout a porous medium only if liquid and vapor are both generated and condensed externally or if solid and/or liquid have large (molecular) thermal conductivities, i.e., if one or both are metals.

The second group of experiments was designed to probe this limiting feature. The general character of the results showing an initial rapid increase in effective conductivity with temperature and/or temperature gradient is expected from the effect of temperature on vapor pressure. The appearance of a maximum followed by sharp decline (or unstable operation with the copper beads) indicates a breakdown in the evaporation-diffusion-condensation-capillary flow cycle. If these items are not kept in balance, then one part of the system will dry out and become a region of large resistance or small effective conductivity, thus limiting the flux that can be transferred through the system. This drying condition is related to a failure of the capillary flow to maintain an adequate flow and distribution. Under the conditions of these experiments the capillary flow would result from the action of two driving forces, gravity and any suction potential gradients established in the system. When the heat flux exceeds the capacity for capillary flow, drying at the hot surface ensues.

It is, however, not so obvious why the copper bead systems were able to sustain fluxes 35 times as great as the glass bead system as is seen by comparison in Fig. 11. While the copper beads have a much higher thermal conductivity than glass, direct molecular conduction can account for only a small fraction of the heat flow in the experiments at high flux. However, in all cases, glass or copper, drying-out occurs in the temperature range near the normal boiling point of water. With these experiments in a sealed container at modest temperature, the pressure was near 1 atm. and the gas phase was primarily air. However, as the temperatures approached 100 deg C, the pressure increased dramatically and the gas phase became as much or more water vapor than air. While this may yield pressure gradients favorable to the vapor flow, it can simultaneously act to retard the capillary flow. The effectiveness of suction potential gradients related to liquid-air-solid interfaces may be destroyed and gravity effects overcome. Hence, drying appears as a temperature- and pressure-sensitive phenomenon rather than a direct response to large heat flux.

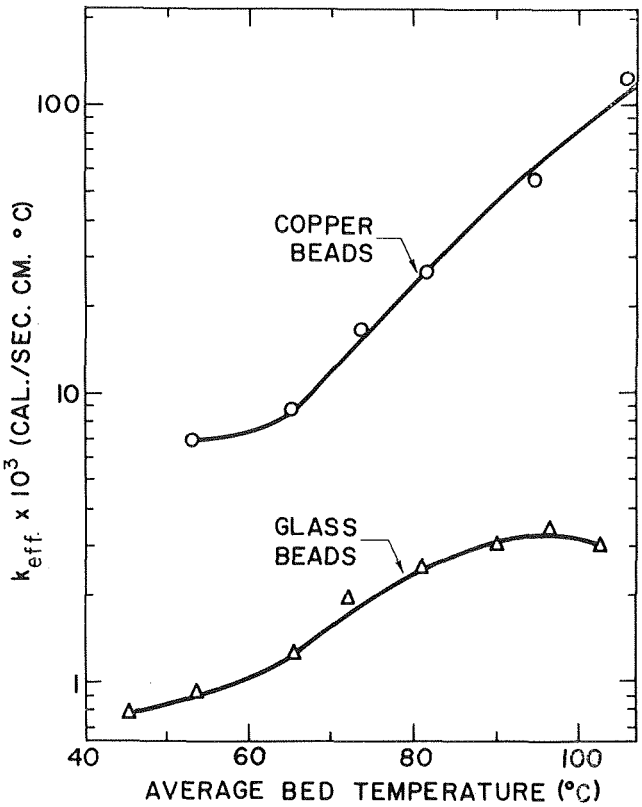

Fig. 11 Comparison of results with glass and copper beads in 2.9-cm bed

As a check on this interpretation of drying-out, another series of experiments was run with the 2.9-cm copper bead bed. In this series the sample chamber was evacuated after adding the copper beads and water. This removed most of the air. The results of this series are compared to the comparable series with air present in Fig. 10. The series without air yielded higher effective conductivities—presumably because of the decreased resistance to diffusion. However, the maximum effective conductivity achieved before drying-out was no higher and occurred at a lower temperature than with air present. This is consistent with the interpretation of drying-out previously given.

In Fig. 11 the effective conductivities achieved with copper are compared with the glass bead values. As noted above, the effective conductivities achieved with the copper bead beds was about 35 times that achieved with the glass bead beds. Except at the lower temperatures the major fraction of heat is carried by the mass transfer mechanism, and the higher basic thermal conductivity of the copper does not directly account for the much higher "effective conductivities." However, the mass transfer mechanism requires first the evaporation of liquid. At steady state in the sealed system it is expected that the evaporation would take place at or near the hot surface. The data indicate, however, that the evaporation zone extends well into the bed. With the glass beads the 1.9-cm bed was most effective, presumably because it provided more evaporation surface than the 0.95-cm bed. The 2.9-cm bed was less effective than the 1.9-cm bed, presumably because no more evaporation surface could be utilized and the increased thickness also increased resistance to diffusion and capillary flow. With the copper beads, the 7.6-cm bed was more effective than the 2.9-cm bed.

The energy for evaporation must be conducted (through liquid and/or solid) to the evaporation surface, and the higher copper conductivity is effective in two ways. First, for equal temperature gradient, it can deliver more energy to the evaporation sites

Second, it can deliver sufficient energy to permit more of the bed to be utilized in the evaporation process.

Commentary

The results of this study indicate that, for at least some porous systems, heat transfer at steady state in a closed system may be described by Fourier's law. However, while Fourier's law may be valid for these systems, it is not, in general, sufficient to analyze a heat transfer problem because the point-by-point composition is not known. Consider the simple problem represented by the experiments reported in this paper. A closed system was subjected to a temperature difference in one dimension. A fixed quantity of liquid was added to the system corresponding to a specific average saturation. Before the heat flux can be calculated, both the temperature field and the liquid distribution at steady state must be predicted. Fourier's law and a knowledge of k or L_{qq} as a function of temperature and liquid saturation are not sufficient to do this. However, the assumption of liquid-vapor equilibrium adds another restriction, namely that $\mu_1 = \mu_2$ or $X_1 = X_2$. To proceed it is necessary to have values of the thermodynamic properties of the porous medium. In some situations it is possible to estimate these from the properties of the components. For example, if the gas phase (air and vapor) may be considered an ideal gas mixture, if the structure is nonswelling, and if the heat of wetting the porous structure can be neglected, then the following expressions for the chemical potentials can be derived [19, 22]:

$$\mu_1 = \bar{G}_1^\circ - P_c/\rho_1$$
$$\mu_2 = \bar{G}_2^\circ + \frac{RT}{M_2} (\ln y_2) \tag{6}$$

$\bar{G}_1^\circ$ refers to the pure component standard state partial free energy.

With the assumption of vapor-liquid equilibrium $\mu_1 = \mu_2$, and equations (6) yield

$$\lambda - \frac{P_c}{\rho_1} \nabla \ln T - \frac{RT}{M_2} \nabla (\ln y_2) = \frac{1}{\rho_1} \nabla P_c \tag{7}$$

Further, if suction potential is a unique function of temperature and relative liquid saturation, then (7) may be written:[7]

$$\lambda - \frac{P_c}{\rho_1} - \frac{T}{\rho_1} \frac{\partial P_c}{\partial T} \nabla (\ln T) - \frac{RT}{M_2} \nabla (\ln y_2) = \frac{1}{\rho} \frac{\partial P_c}{\partial \psi} \tag{8}$$

An iterative procedure can then be used to solve the heat transfer problem by estimating temperature profile, calculating a liquid saturation profile from equation (8), evaluating L_{qq} or k from these profiles, calculating the heat fluxes at each point, and iterating by adjusting the temperature profile until fluxes are equal. To use equation (8), however, independent information on the suction potential as a function of temperature and pressure is required. Also, if noncondensable gas is present, it is necessary to estimate the gas phase composition y_2. This can be done only if a reasonable assumption can be made about the gas phase pressure, P_g. Calculations of this sort were made corresponding to the conditions of several experimental runs. For the runs with air it was assumed that P_g was constant. These calculations yielded the observed heat fluxes within 5 percent and temperatures within a few degrees. Calculated saturation profiles showed larger discrepancies, which is not surprising in view of the uncertainties in the suction potential values as discussed in the following:

If an assumption about P_g is not permitted, or for the more general situation of a multicomponent system, then even the steady state, closed system, heat transfer problems can be solved only as a limit of a transient problem. For this purpose knowledge of L_{qq} alone is not sufficient. A knowledge of six transport coefficients is required (three coefficients if no noncondensable gas is present). The suction potential relationship can be used to decrease this to five coefficients (or two with no noncondensable gas present). To determine these coefficients, open system experiments with measurements of $(J_1 + J_2)$ and J_3 would be required. Of course, if one begins by assuming cross coefficients to be small, then L_{qq} can be determined from closed system heat transfer experiments, and the mass transfer coefficients $(L_{11} + 2L_{12} + L_{22})$ and L_{33} can be measured in isothermal capillary flow experiments. These are then the only coefficients required. Note, however, that assuming the cross coefficients to be small is not saying that mass transfer is independent of heat transfer. As has been demonstrated, the mass transfer may be the primary mode of heat "conduction."

For the calculations already discussed, it was necessary to measure the suction potential curve. This was done by a U-tube technique which indicated significant hysteresis and did not yield entirely consistent results. Adams [20] has demonstrated that large liquid saturation gradients can develop and persist even in the shallow beds used for U-tube measurements, making the evaluation of such measurements difficult. For the foregoing calculations, suction potential values based on imbibition measurements in the U-tube were used.

In the second set of experiments reported here, the sample chamber was only partly filled so that the condensation part of the mass transfer cycle was external to the system. In a completely filled system a condensation section would operate much as the converse of the evaporating section. Again the latent heat would need to be removed by molecular conduction, and adequate condensing surface would be required. The converse to drying would be flooding of the condensation section.

With a system that included both an evaporation and a condensation band, it is also conceivable that one could establish conditions whereby the evaporation and condensation bands would meet and limit the attainable flux. That is, the optimum thickness effect observed for the evaporation should also apply to condensation.

Carrying large energy fluxes by transporting a vapor and then condensing it is like a boiler operation. In a porous medium system two other dependent factors are part of the system: diffusion and capillary flow. While the diffusion resistance is significant, the diffusion driving force can become large. The capillary flow driving force, however, is limited and can be disrupted by the temperature–temperature-gradient effects. "Heat pipes" have been operated at very large fluxes. The liquid metals used in these devices are effective not only because of their high thermal conductivity but also because of their low viscosity, large latent heat, and large diffusivity. The geometry of the "heat pipe" is also significant. First, relatively large regions for evaporation and condensation are provided. Secondly, the direction of conduction of energy in for evaporation (and out for condensation) is normal to the direction of the primary heat flux in the "heat pipe." This second factor is important because under these conditions the capillary flow is not as directly susceptible to disruption by the temperature gradients which must be maintained for the conduction processes.

Finally, it should be pointed out that the limits reported here were from steady state experiments. Under transient conditions, higher fluxes could obtain while a net redistribution of liquid was in progress.

Acknowledgment

This research was supported by a grant from the National Science Foundation. The experimental work was performed at Rensselaer's Materials Research Center sponsored by the National Aeronautics and Space Administration.

[7] For more detail on these relationships and the thermodynamics of porous media see the thesis by Breyer [19].

References

1 Boyoucos, G. J., "The Effect of Temperature on the Movement of Water Vapor and Capillary Moisture in Soils," *Journal of Agricultural Research*, Vol. 5, 1915, pp. 141–172.

2 Winterkorn, H. F., "Fundamental Similarities Between Electro-Osmotic and Thermo-Osmotic Phenomena," *Highway Research Board Proceedings*, Vol. 27, 1947, pp. 443–455.

3 Taylor, S. A., and Cavazza, L., "The Movement of Soil Moisture in Response to Temperature Gradients," *Soil Science Society of America Proceedings*, Vol. 18, No. 4, 1954, pp. 351–365.

4 Rollins, R. L., Spangler, M. G., and Kirkham, D., "Moisture Migration in Soils," *Highway Research Board Proceedings*, Vol. 33, 1954, pp. 492–508.

5 Krischer, O., and Esdorn, H., "Simultaneous Transfer of Heat and Mass Transfer in Porous Media," *Forsch. Ing-Wis.*, Vol. 1, 1956, pp. 1–14.

6 Philip, J. R., and de Vries, D. A., "Moisture Movement in Porous Materials Under Temperature Gradients," *Transactions American Geophysical Union*, Vol. 38, No. 2, 1957, pp. 222–232.

7 de Vries, D. A., "Simultaneous Transfer of Heat and Moisture in Porous Media," *Transactions American Geophysical Union*, Vol. 39, No. 5, 1958, pp. 909–916.

8 Lykov, A. V., and Mikhaylov, Y. A., *Theory of Energy and Mass Transfer*, translated by W. Begell, Prentice-Hall, Englewood Cliffs, N. J., 1961.

9 Valchar, J., "Heat Moisture Transfer in Capillary Porous Materials From the Point of View of the Thermodynamics of Irreversible Processes," *Proceedings of the Third International Heat Transfer Conference*, Chicago, Ill., August 1966, Vol. 1, pp. 409–418.

10 Ash, R., and Barrer, R. M., "Three-Phase Flow in a Temperature Gradient," *Transactions of the Faraday Society*, Vol. 59, 1963, pp. 2260–2267.

11 Cary, J. W., "An Evaporation Experiment and Its Irreversible Thermodynamics," *International Journal of Heat and Mass Transfer*, Vol. 7, 1964, pp. 531–538.

12 Taylor, S. A., and Cary, J. W., "Moisture Transfer in Soils," *Soil Science Society of America Proceedings*, Vol. 20, 1964, pp. 111–118.

13 Evans, R. B. III, Watson, G. M., and Mason, E. A., "Gaseous Diffusion in Porous Media at Uniform Pressure," *Journal of Chemical Physics*, Vol. 35, No. 6, 1961, pp. 2076–2083; "Gaseous Diffusion in Porous Media. II. Effect of Pressure Gradients," Vol. 36, No. 7, 1962, pp. 1894–1904.

14 Vink, H., "Diffusion in Porous Media," *Arkiv for Kemi*, Vol. 17, 1962, pp. 311–317.

15 Mokadam, R. G., "Thermodynamic Analysis of the Darcy Law," TRANS. ASME, Series E, *Journal of Applied Mechanics*, Vol. 83, No. 3, June 1961, pp. 208–212; Vol. 84, No. 3, June 1962, pp. 425–428.

16 Mokadam, R. G., "Application of the Thermodynamics of Irreversible Process to the Flow of a Multicomponent Liquid Through Porous Media," *International Chemical Engineering*, Vol. 3, 1963, pp. 571–576.

17 de Groot, S. R., *Thermodynamics of Irreversible Process*, North Holland Publishing Co., Amsterdam, 1961.

18 Fitts, D. D., *Nonequilibrium Thermodynamics*, McGraw-Hill, New York, 1962.

19 Breyer, W. H., "Heat Transfer in Porous Media," D. Eng. thesis, Rensselaer Polytechnic Institute, Troy, N. Y., June 1968.

20 Adams, E. F., "The Mechanism of Drying," PhD dissertation, Rensselaer Polytechnic Institute, Troy, N. Y., November 1962.

21 Riback, W. J., "Heat Transfer in Porous Media," PhD dissertation, Rensselaer Polytechnic Institute, Troy, N. Y., June 1968.

22 Edelfsen, N. E., and Anderson, A. B. C., *Hilgardia*, Vol. 15, 1943, pp. 31–287.

APPENDIX

Derivation of Equation (5)

By definition $J_0 + J_1 + J_2 + J_3 = 0$. Adding the equations for these four fluxes and setting the result equal to zero requires then that:

$$L_{0q} + L_{1q} + L_{2q} + L_{3q} = 0$$
$$L_{00} + L_{10} + L_{20} + L_{30} = 0$$
$$L_{01} + L_{11} + L_{21} + L_{31} = 0$$
$$L_{02} + L_{12} + L_{22} + L_{32} = 0$$
$$L_{03} + L_{13} + L_{23} + L_{33} = 0$$

Using these relations and the Onsager relation permits rewriting equations (1) as:

$$J_q = L_{qq}X_q + L_{q1}(X_1 - X_0) + L_{q2}(X_2 - X_0) + L_{q3}(X_3 - X_0)$$
$$J_1 = L_{q1}X_q + L_{11}(X_1 - X_0) + L_{12}(X_2 - X_0) + L_{13}(X_3 - X_0)$$
$$J_2 = L_{q2}X_q + L_{12}(X_1 - X_0) + L_{22}(X_2 - X_0) + L_{23}(X_3 - X_0)$$
$$J_3 = L_{q3}X_q + L_{13}(X_1 - X_0) + L_{23}(X_2 - X_0) + L_{33}(X_3 - X_0)$$
$$J_r = L_{rr}X_r$$

Assuming equilibrium between liquid and vapor eliminates the equation for J_r as $X_r = 0$. Also with $X_1 = X_2$ there is no effective distinction between liquid and vapor fluxes except in combination, so a reduced set of flux-forced equations is then:

$$J_q = L_{qq}X_q + (L_{q1} + L_{q2})(X_2 - X_0) + L_{q3}(X_3 - X_0)$$
$$J_1 + J_2 = (L_{q1} + L_{q2})X_q + (L_{11} + L_{22} + 2L_{12})(X_2 - X_0) + (L_{13} + L_{23})(X_3 - X_0)$$
$$J_3 = L_{q3}X_q + (L_{13} + L_{23})(X_2 - X_0) + L_{33}(X_{33} - X_0)$$

In a closed system at steady state it is further required that $J_3 = 0$, and thus $L_{q3} = 0$, $(L_{13} + L_{23}) = 0$, $L_{33} = 0$. Also, the closed, steady state system requires that $J_1 + J_2 = 0$, and thus $(L_{q1} + L_{q2}) = 0$ and $(L_{11} + L_{22} + 2L_{12}) = 0$. The flux-force equations thus reduce to

$$J_q = L_{aq}X_q$$

A. E. ZINNES
Member of the Technical Staff,
Bell Telephone Laboratories,
Allentown, Pa.

The Coupling of Conduction With Laminar Natural Convection From a Vertical Flat Plate With Arbitrary Surface Heating

A method has been developed for coupling conduction in a solid with natural convection in a surrounding fluid. The problem investigated is that of steady, constant-property, two-dimensional, laminar natural convection from a vertical, heat-conducting flat plate of finite thickness with an arbitrary heating distribution in its surface. Using this method it is possible to predict the variation of temperature in the plate and the velocity and temperature profiles in the boundary layer as a function of the heating distribution and the thermal properties of the plate and fluid. The equations for conduction in the plate and convection in the boundary layer are written in finite difference form, coupled through the common heat flux at the plate-fluid interface, and solved numerically by an iterative technique. Experimental corroboration of the numerical results is provided by measuring temperatures, both with thermocouples and a laser holographic interferometer, along ceramic and glass plates heated by thin film resistance heating elements vacuum deposited on their surface. The results indicate that the degree of coupling between conduction in the plate and natural convection in the fluid is greatly influenced by the plate-fluid conductivity ratio.

Introduction

Many practical thermal problems involve natural convection heat transfer from nonuniformly heated surfaces. Sparrow and Gregg [1][1] were the first to consider vertical plates with restricted distributions of heat flux or temperature, finding similarity solutions for plate thermal conditions varying as x^n and e^{mx}. Yang [2] later showed that these are the only thermal conditions for which similarity solutions are possible in steady natural convection from vertical plates. An integral solution was given by Sparrow [3] in which he considered wall flux or temperature variations of the form $1 \pm \epsilon(x/x_a)^r$, $r > 0$. Sparrow's integral analysis was extended to more general plate heat flux variations by Tribus [4]. Hill [5] confirmed the results of these integral studies experimentally. Another integral analysis is that of Scherberg [6], who considered the effect of the leading edge on natural convection and included longitudinal conduction through the fluid. Kuiken [7] gave a series solution for natural convection from a nonisothermal flat plate with a general class of nonlinear wall temperature distributions. Two series solutions, valid for small and large values of x, were joined graphically.

Schetz and Eichorn [8] employed a Mach-Zehnder interferometer to investigate experimentally natural convection from a plate with a step change in surface temperature, finding good agreement with the similarity solution up to the step. Hayday, et al. [9], studied the same problem analytically using a numerical technique in which the streamwise derivatives were approximated by finite differences. An ordinary differential equation in

[1] Numbers in brackets designate References at end of paper.

Contributed by the Heat Transfer Division and presented at the Sixth National Congress of Applied Mechanics, Harvard University, June 15–19, 1970. Manuscript received at ASME Headquarters, March 9, 1970. Paper No. 70-HT-I.

Nomenclature

- a = plate height
- b = plate thickness
- g = acceleration of gravity
- G = nondimensional heat flux ($qG\beta a^4/K_f\nu^2$)
- h = heat transfer coefficient
- j_a = number of nodes in the x-direction
- k_a = number of nodes in the y-direction
- k_w = number of plate nodes in the y-direction
- K = thermal conductivity
- Nu = nondimensional heat transfer coefficient (ha/K_f)
- Pr = Prandtl number (ν/α)
- q = heat flux
- T = temperature
- u = longitudinal velocity
- U = nondimensional longitudinal velocity (ua/ν)
- v = transverse velocity
- V = nondimensional transverse velocity (va/ν)
- x = longitudinal length coordinate
- X = nondimensional length coordinate (x/a)
- y = transverse length coordinate
- Y = nondimensional length coordinate (y/a)

(Continued on next page)

terms of the coordinate normal to the plate was then solved numerically at each location along the plate. Hellums and Churchill [10] applied a set of explicit finite-difference equations to the classical problem of the infinite vertical isothermal plate and to the region inside an infinite horizontal cylinder with the vertical halves of the wall maintained at different uniform temperatures, determining the steady solution as the limit of a transient solution. Bodoia and Osterle [11] used a finite-difference procedure to study the development of natural convection in vertical ducts with uniform temperature walls.

The effect of coupling thermal conduction in the plate has so far received scant attention in the natural convection literature. Lock and Gunn [12] coupled the similarity solution for a power law temperature distribution with the solution for one-dimensional conduction in a fin using the corresponding convection coefficient. Kelleher and Yang [13] studied the coupled convection-conduction problem by using a series solution of the boundary layer equations with nonuniform surface temperature distribution, and Fourier transforms to solve for the conduction in the heat-generating plate. The temperature and heat flux were matched at the interface to complete the solution.

There is little hope at this time for an exact solution to problems involving coupled conduction and steady, two-dimensional laminar natural convection from a vertical flat plate with an arbitrary heating distribution on its surface. It is the purpose of this paper to present a numerical procedure for the solution of such complex problems based on finite-difference techniques. Using this procedure it is possible to determine the temperature variation in the plate and the temperature and velocity profiles in the boundary layer for a wide class of problems as a function of the plate-heating distribution as well as the thermal properties of the plate and fluid.

The numerical procedure has been applied to a series of cases which simulate glass and ceramic plates with localized strip heat sources on their surface. Experimental corroboration is provided by measuring plate and boundary layer temperatures with thermocouples and with a laser holographic interferometer. Thermal radiation could not be ignored in these experiments but its inclusion in the numerical procedure presents no added difficulties.

Differential Formulation

Consider the situation pictured in Fig. 1(*a*) which shows a vertical flat plate of height a, thickness b, and depth of infinite extent. The plate is heated by some arrangement of surface strip heaters, each having a uniform heat flux q_s. Any heating distribution, localized or continuous, may be represented by dividing the surface into a finite number of strip heat sources with some uniform flux over each strip. Heat generated in each source is transferred directly from the source and indirectly after traveling along the plate by natural convection to a fluid and radiation to nonreflecting, black surroundings, both at temperature T_∞. The rear face and top and bottom edges are insulated, although the theoretical approach is not limited to these boundary conditions.

The boundary layer equations, expressing conservation of mass, momentum, and energy, for steady laminar free convection from a vertical plate are as follows:

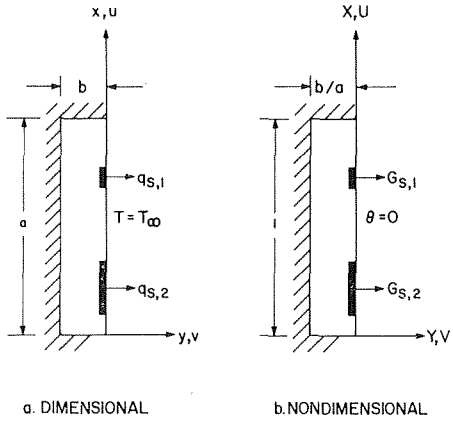

Fig. 1 Geometrical configuration

$$\frac{\partial u}{\partial x} + \frac{\partial v}{\partial y} = 0 \tag{1}$$

$$u\frac{\partial u}{\partial x} + v\frac{\partial u}{\partial y} = g\beta(T - T_\infty) + \nu\frac{\partial^2 u}{\partial y^2} \tag{2}$$

$$u\frac{\partial T}{\partial x} + v\frac{\partial T}{\partial y} = \alpha\left(\frac{\partial^2 T}{\partial x^2} + \frac{\partial^2 T}{\partial y^2}\right) \tag{3}$$

Standard boundary layer assumptions have been employed, except that longitudinal conduction in the fluid is included in order to accommodate possible large temperature gradients in localized regions near the plate. Although this is somewhat inconsistent with the usual assumptions leading to the boundary layer equations, these temperature gradients should be so localized that they have little effect on the velocity field. All properties are assumed constant with the exception of the density variation in the buoyancy term of the momentum equation. Viscous dissipation and work against the gravity field have been neglected.

If thermal conductivity is constant, the energy equation for steady conduction in the plate reduces to the Laplace equation:

$$\frac{\partial^2 T}{\partial x^2} + \frac{\partial^2 T}{\partial y^2} = 0 \tag{4}$$

The system of equations (1)–(4) is subject to the following boundary conditions:

$$\begin{aligned}
&0 \le x \le a \quad \text{and} \quad y = \infty: \quad u = 0, \quad T = T_\infty \\
&0 < y \le \infty \quad \text{and} \quad x = 0: \quad u = 0, \quad T = T_\infty \\
&-b \le y \le 0 \quad \text{and} \quad x = 0, a: \quad \partial T/\partial x = 0 \\
&0 \le x \le a \quad \text{and} \quad y = -b: \quad \partial T/\partial y = 0 \\
&0 < y \le \infty \quad \text{and} \quad x = a: \quad \partial^2 T/\partial x^2 = 0
\end{aligned} \tag{5}$$

The last boundary condition eliminates longitudinal conduction at the top of the fluid region and provides a convenient bound on the fluid region for the numerical solution employed in this study.

The equation expressing the continuity of heat flux at the plate-fluid interface is not, strictly speaking, a boundary condition, but is a coupling condition between the plate and fluid problems, since

Nomenclature

Greek

α = therma' diffusivity
β = fluid expansion coefficient
δ = constant defined after equation (22)
ϵ = emittance
θ = nondimensional temperature $(g\beta a^3(T - T_\infty)/\nu^2)$
ν = kinematic viscosity
ρ = fluid density
σ = radiation constant, $0.00366 \times 10^{-8} w/\text{in}^2K^4$

Subscripts

c = convection
f = fluid
j = node index in the x-direction
k = node index in the y-direction
r = radiation
s = heat source
w = plate
∞ = ambient conditions

the temperatures and temperature gradients are not known a priori. For $y = 0, 0 \leq x \leq a$:

$$K_w \frac{\partial T}{\partial y}(0^-) = K_f \frac{\partial T}{\partial y}(0^+) + q_s(x) - q_r(x) \tag{6}$$

where $q_s(x)$ is the heat flux attributed to the heat sources and $q_r(x)$ is the radiant heat flux.

Equations (1)–(6) may be put into a more convenient form by introducing the following dimensionless variables:

$$X = \frac{x}{a} \qquad Y = \frac{y}{a}$$

$$U = \frac{ua}{\nu} \qquad V = \frac{va}{\nu} \tag{7}$$

$$\theta = \frac{g\beta a^3(T - T_\infty)}{\nu^2} \qquad G = \frac{g\beta a^4 q}{K_f \nu^2}$$

Fig. 1(*b*) shows the resulting geometrical configuration.

Nondimensionalizing of equations (1)–(6) results in the following system:

Fluid $\qquad 0 < Y \leq \infty, \qquad 0 \leq X \leq 1$

$$\frac{\partial U}{\partial X} + \frac{\partial V}{\partial Y} = 0 \tag{8}$$

$$U\frac{\partial U}{\partial X} + V\frac{\partial U}{\partial Y} = \theta + \frac{\partial^2 U}{\partial Y^2} \tag{9}$$

$$U\frac{\partial \theta}{\partial X} + V\frac{\partial \theta}{\partial Y} = \frac{1}{\mathrm{Pr}}\left(\frac{\partial^2 \theta}{\partial Y^2} + \frac{\partial^2 \theta}{\partial X^2}\right) \tag{10}$$

with boundary conditions

$$\begin{aligned} &0 \leq X \leq 1 \quad \text{and} \quad Y = \infty: \quad U = \theta = 0 \\ &0 \leq X \leq 1 \quad \text{and} \quad Y = 0: \quad U = V = 0 \\ &0 < Y \leq \infty \quad \text{and} \quad X = 0: \quad U = \theta = 0 \\ &0 < Y \leq \infty \quad \text{and} \quad X = 1: \quad \partial^2\theta/\partial X^2 = 0 \end{aligned} \tag{11}$$

Plate $\qquad -b/a \leq Y \leq 0, \qquad 0 \leq X \leq 1$

$$\frac{\partial^2 \theta}{\partial X^2} + \frac{\partial^2 \theta}{\partial Y^2} = 0 \tag{12}$$

with boundary conditions

$$\begin{aligned} &-b/a \leq Y \leq 0 \quad \text{and} \quad X = 0, 1: \quad \partial\theta/\partial X = 0 \\ &0 \leq X \leq 1 \quad \text{and} \quad Y = -b/a: \quad \partial\theta/\partial Y = 0 \end{aligned} \tag{13}$$

Interface Coupling Condition

$$0 \leq X \leq 1, \qquad Y = 0$$

$$\frac{K_w}{K_f}\frac{\partial \theta}{\partial Y}(0^-) = \frac{\partial \theta}{\partial Y}(0^+) + G_s - G_r \tag{14}$$

Note that the nondimensional temperature θ has the same form as a conventional local Grashof number, while the heat flux parameter G is equivalent to the modified Grashof number introduced by Sparrow and Gregg [14] in their work on the plate with uniform constant heat flux. The nondimensional velocities U and V are local Reynolds numbers.

A nondimensional convective heat transfer coefficient, or local Nusselt number, may be defined through the nondimensional convective heat flux G_c:

$$G_c = -\frac{\partial \theta}{\partial Y} = \left(\frac{ha}{K_f}\right)\theta = \mathrm{Nu}_c\theta \tag{15}$$

Similarly, for the radiant flux:

$$G_r = \left[\frac{\sigma\epsilon}{\theta}\left(\frac{g\beta a^4}{K_f\nu^2}\right)(T^4 - T_\infty^4)\right]\theta = \mathrm{Nu}_r\theta \tag{16}$$

where T and T_∞ in (16) are absolute temperatures.

From the preceding discussion it is evident that the complete solution to this problem must have the following functional dependence:

$$\left.\begin{matrix}\theta \\ U \\ V\end{matrix}\right\} = f\left(X, Y, \frac{b}{a}, \frac{K_w}{K_f}, \mathrm{Pr}, G_s(X), \epsilon, T_\infty\right) \tag{17}$$

The last two parameters may be dropped if radiation is ignored.

Finite-Difference Formulation

Consider a rectangular mesh over both the plate and fluid regions as shown in Fig. 2. The plate height is divided into nonuniformly-spaced horizontal strips of width ΔX_j, while in the Y-direction the node spacings are ΔY_w and ΔY_f in the plate and fluid, respectively. Writing heat balances around nodes inside the plate ($k < k_w$) and on the interface ($k = k_w$) gives the following finite-difference energy equations, which may be further specialized to account for the boundary conditions (13):

$k < k_w$

$$\frac{\Delta\bar{X}_j}{\Delta Y_w}(\theta_{j,k-1} - \theta_{j,k}) + \frac{\Delta\bar{X}_j}{\Delta Y_w}(\theta_{j,k+1} - \theta_{j,k}) + \frac{\Delta Y_w}{\Delta X_{j+1}}(\theta_{j+1,k} - \theta_{j,k}) + \frac{\Delta Y_w}{\Delta X_j}(\theta_{j-1,k} - \theta_{j,k}) = 0 \tag{18a}$$

$k = k_w$

$$\frac{\Delta Y_w}{2\Delta X_{j+1}}(\theta_{j+1,k} - \theta_{j,k}) + \frac{\Delta Y_w}{2\Delta X_j}(\theta_{j-1,k} - \theta_{j,k}) + \frac{\Delta\bar{X}_j}{\Delta Y_w}(\theta_{j,k-1} - \theta_{j,k}) + \frac{\Delta\bar{X}_j}{\Delta Y_f}\frac{(\theta_{j,k+1} - \theta_{j,k})}{K_w/K_f} - \frac{\mathrm{Nu}_{r,j}\Delta\bar{X}_j}{K_w/K_f}\theta_{j,k} = -\frac{G_{s,j}\Delta X_j + G_{s,j+1}\Delta X_{j+1}}{2K_w/K_f} \tag{18b}$$

where $\Delta\bar{X}_j$, the average area per node for transverse heat transfer, is defined as

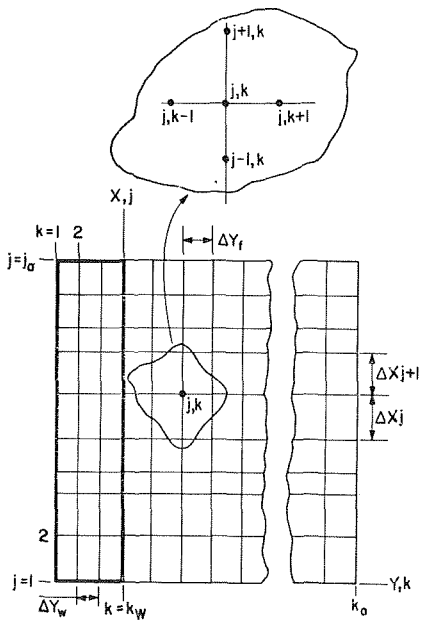

Fig. 2 Finite-difference mesh

$$\Delta\bar{X}_j = \frac{1}{2}(\Delta X_j + \Delta X_{j+1}) \tag{19}$$

In the fluid, two forms of both the momentum and energy equations, depending on the sign of V, are required for an adequate simulation of equations (9) and (10). For $V < 0$, forward differences are used to approximate $\partial U/\partial Y$ and $\partial\theta/\partial Y$, while backward differences are used when $V > 0$. After rearrangement and solution for the dependent variables at any point (j, k) in the fluid in terms of the variables at neighboring points, the finite-difference equations for the fluid take the form:

$$V_{j,k} = V_{j,k-1} - \frac{\Delta Y_f}{\Delta X_j}(U_{j,k} - U_{j-1,k}) \tag{20}$$

$$U_{j,k} = \frac{\theta_{j,k}(\Delta X_j) + U_{j-1,k}U_{j,k} + (U_{j,k+1} + U_{j,k-1})\dfrac{\Delta X_j}{\Delta Y_f{}^2}}{U_{j,k} + \dfrac{2\Delta X_j}{\Delta Y_f{}^2} + |V_{j,k}|\dfrac{\Delta X_j}{\Delta Y_f}} + \frac{|V_{j,k}|\dfrac{\Delta X_j}{\Delta Y_f}\begin{cases} U_{j,k+1} & \text{if } V < 0 \\ U_{j,k-1} & \text{if } V > 0 \end{cases}}{U_{j,k} + \dfrac{2\Delta X_j}{\Delta Y_f{}^2} + |V_{j,k}|\dfrac{\Delta X_j}{\Delta Y_f}} \tag{21}$$

$$\theta_{j,k} = \frac{\theta_{j+1,k}\left(\dfrac{\delta}{\Pr(\Delta X_{j+1})}\right) + \theta_{j-1,k}\left(U_{j,k} + \dfrac{\delta}{\Pr(\Delta X_{j+1})}\right)}{U_{j,k} + \dfrac{2}{\Pr}\left(\dfrac{\delta}{\Delta X_{j+1}} + \dfrac{\Delta X_j}{\Delta Y_f{}^2}\right) + |V_{j,k}|\dfrac{\Delta X_j}{\Delta Y_f}} + \frac{(\theta_{j,k+1} + \theta_{j,k-1})\dfrac{\Delta X_j}{\Pr\Delta Y_f{}^2} + |V_{j,k}|\dfrac{\Delta X_j}{\Delta Y_f}\begin{cases} \theta_{j,k+1} & \text{if } V < 0 \\ \theta_{j,k-1} & \text{if } V > 0 \end{cases}}{U_{j,k} + \dfrac{2}{\Pr}\left(\dfrac{\delta}{\Delta X_{j+1}} + \dfrac{\Delta X_j}{\Delta Y_f{}^2}\right) + |V_{j,k}|\dfrac{\Delta X_j}{\Delta Y_f}} \tag{22}$$

where

$$\delta = \begin{cases} 0 \text{ for } j = j_a (X = 1) \\ 1 \text{ otherwise} \end{cases}$$

Using two forms of the momentum and energy equations renders the systems of equations (20)–(22) diagonally row dominant. In addition these systems are irreducible. It may be proved [16, 17] that a solution of a diagonally dominant and irreducible system by the method of successive displacements must converge. Solving the classical problem in the unsteady case, Hellums [15] used a stability argument to arrive at a similar conclusion regarding the difference forms required for the first derivatives. These criteria for convergence strictly apply to linear, uncoupled systems of equations, but it seems reasonable to expect the nonlinear, coupled systems (20)–(22) to converge with an iterative solution as long as they remain diagonally dominant at every stage of computation.

Method of Solution

An outline of the method of solution of the finite-difference equations is given in this section. Further details may be found in reference [18]. The first step is to establish some initial estimate of the velocity and temperature distributions. In [18] is described a procedure whereby one-dimensional plate conduction is coupled iteratively with the Sparrow-Tribus integral convection solution [4]. Alternatively, uniform velocity and temperature values throughout the flow field may be chosen.

The finite-difference calculation then proceeds as follows:

1 Beginning at the second row ($j = 2$) one node from the plate ($k = k_w + 1$) compute $V_{j,k}$ from equation (20), noting that $V_{j,k_w} = 0$. Using this value, compute $U_{j,k}$ from equation (21) and then $\theta_{j,k}$ from equation (22), always using the most recently computed values for V, U, and θ. Consider the plate-fluid interface temperatures found previously to be a boundary condition for the fluid solution.

2 Continue along the row, repeating step 2 at each point until $k = k_a - 1$.

3 Repeat steps 2 and 3 for each row until $j = j_a$.

4 Repeat steps 1–4 a fixed number of times. Ten iterations have given good results.

5 Considering equation (18) to represent a system of simultaneous linear algebraic equations for temperatures in the plate, compute the matrix coefficients, noting that the convection term for the interface points is calculated from the gradient found in the last fluid iteration. Solve the system by a Gauss-Jordan matrix reduction, yielding temperatures at each node in the plate.

6 Repeat steps 1–5 until some convergence tolerance is satisfied.

The iterative procedure is not used for the plate region because of slow convergence when the conductivity ratio is high. In such cases the diagonal dominance of the system (18) is slight, a condition often leading to poor convergence in iterative processes.

The computational procedure outlined above has been tested by applying it to the uniform flux problem solved by Sparrow and Gregg [14]. Agreement between the finite-difference and similarity solutions is very good, being within about 5 percent for both velocity and temperature for $X > 0.1$. Extensive numerical experiments have demonstrated the importance of a fine longitudinal node spacing, ΔX_j, near the leading edge for satisfactory agreement between the two solutions.

In comparing analytical and experimental results some consideration should be given to the temperature at which the properties are evaluated. Since there is no a priori reference temperature for the nonuniform flux problem, all properties, with the exception of plate conductivity, have been chosen at T_∞; plate conductivity is taken at 100 deg C. The results should be most sensitive to changes in kinematic viscosity with temperature, but no attempt has been made to account for the effect of this or any other property variation. However, work done by Sparrow and Gregg [19] on natural convection from isothermal vertical plates to gases with variable fluid properties indicates that property variations resulting from temperature differences of the magnitude occurring in this study should not affect the final results by more than about 3 percent.

Experimental Program

In order to corroborate the above numerical procedure when applied to a nonuniformly heated plate, thermocouples and a laser holographic interferometer were used to measure plate and boundary layer temperatures along glass (Corning 7059) and ceramic (AlSiMag 772, 99.5 percent Al_2O_3) microelectronic substrates on which were deposited three 4000Å tantalum nitride thin film strip resistance heating elements. Fig. 3 shows the front and back faces of a typical plate. The thermocouple locations correspond to $X = 0.10, 0.25, 0.50, 0.75$, while the heaters, which simulate localized surface heat sources, are centered at $X = 0.25, 0.50, 0.75$. Thin gold wires bonded around the edge of the plate and from the top of the plate provide electrical connection between the heating elements and an external power source.

Symmetry is maintained by assembling the complete test specimen from two deposited substrates with a blank substrate spacer between them for electrical isolation. The test specimen is then held at the upper corners with an insulating clamp made of transite and mounted so as to minimize the effect of room air movement on the boundary layer near the plate.

For a given substrate the three strip heaters allow seven combinations of heating arrangements. In all tests the power to each heater was 2 watts, corresponding to a nondimensional heat flux $G_s = 1.669 \times 10^9$. The remaining test variables were:

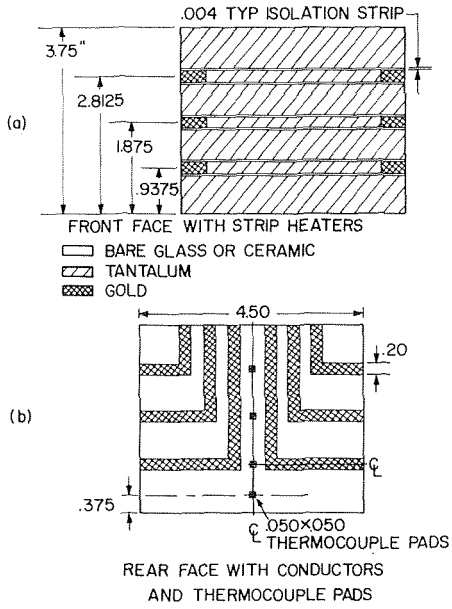

Fig. 3 Test specimen configuration

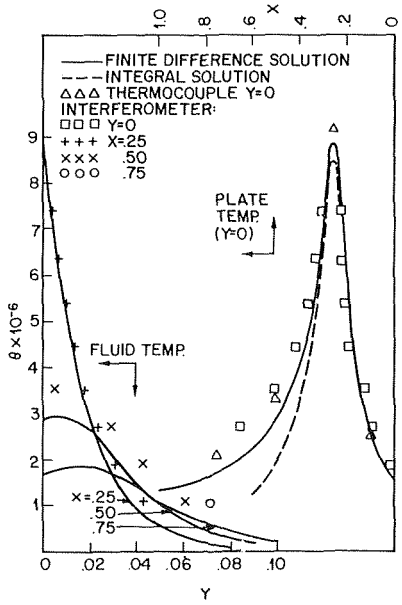

Fig. 5 Plate and fluid temperatures—glass plate with lower heater active

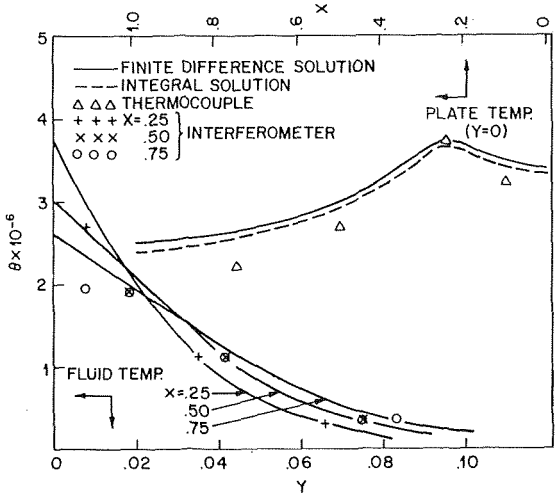

Fig. 4 Plate and fluid temperatures—ceramic plate with lower heater active

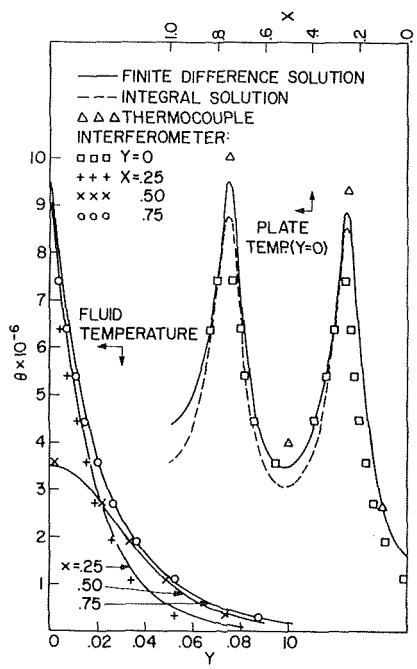

Fig. 6 Plate and fluid temperatures—glass plate with upper and lower heaters active

$$
\begin{aligned}
b/a &= 0.012 \\
\mathrm{Pr} &= 0.72 \\
K_w/K_f &= 1100 \text{ for ceramic} \\
&= 40 \text{ for glass} \\
\epsilon &= 0.366 \text{ for tantalum nitride on ceramic} \\
&= 0.387 \text{ for tantalum nitride on glass}
\end{aligned}
$$

These latter emittance values were measured using a Barnes RM-2B radiometric microscope.

Thermocouple temperature measurements were made for both the ceramic and glass plates using 0.003 in. Chromel-Alumel thermocouples which had previously been calibrated to within 1 deg C at both the ice and boiling points of water. Double exposure laser holographic interferometry was the technique used to observe visually the natural convection boundary layer. Further discussion of the holographic process and its application to interferometry may be found in references [18, 20, 21]. Though produced in a different manner, the interferogram fringes are related to temperature just as is done in conventional interferometry [22].

Results

The numerical procedure has been applied to a series of cases simulating the glass and ceramic plates described in the previous section. Results of these numerical computations are given by the solid lines in Fig. 4 for the ceramic plate with the lower heater active and in Figs. 5 and 6 for the glass plate with the lower heater and both the upper and lower heaters active.

These figures all display the expected plate temperature peaks at the heat sources and the corresponding trends in the fluid temperature profiles. The temperature peaks and gradients are particularly pronounced for the low-conductivity glass plate, indicating that for these cases the coupled plate conduction is not

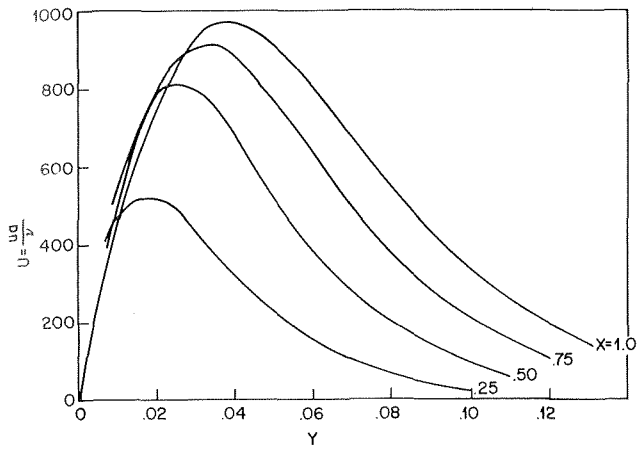

Fig. 7 Typical velocity profiles—glass plate with lower heater active

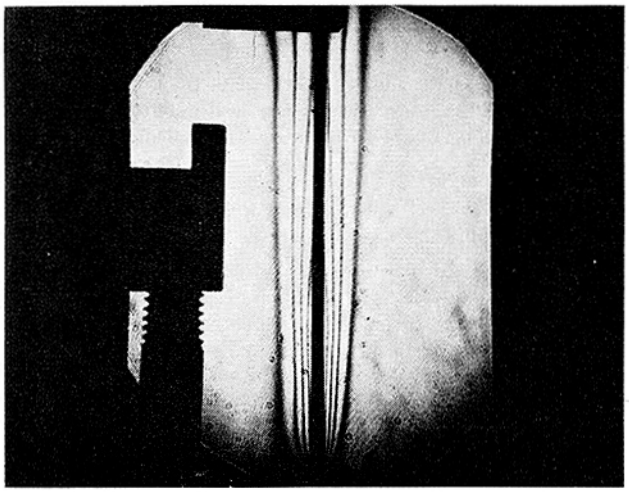

Fig. 8 Interferogram for the ceramic plate with the lower heater active

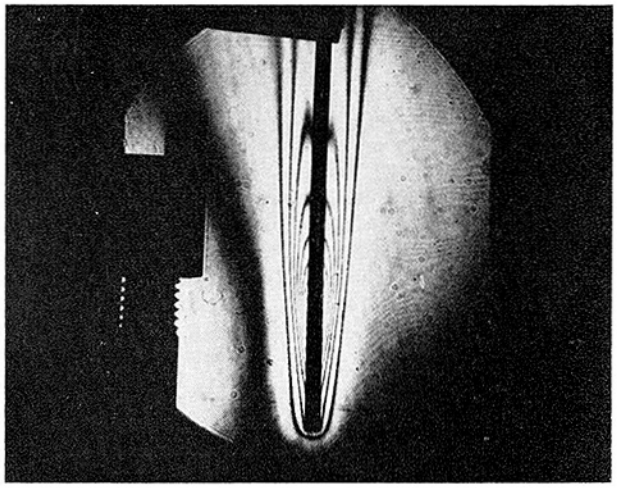

Fig. 9 Interferogram for the glass plate with the lower heater active

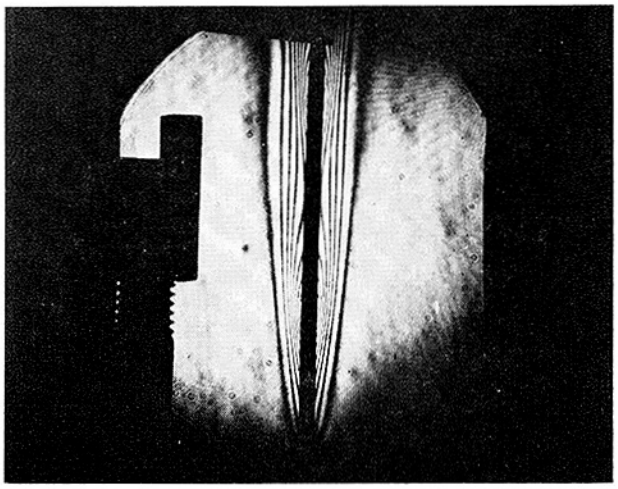

Fig. 10 Interferogram for the glass plate with the upper and lower heaters active

very effective in carrying the generated heat away from the sources along the plate. As a matter of fact, in some cases the fluid convection so dominates the plate conduction that a temperature inversion occurs and heat is transferred from the fluid to the plate. This is evidenced by the positive temperature gradients near the plate at $X = 0.50$ and 0.75 in Fig. 5. In such cases it is possible for the longitudinal velocity gradient $\partial U/\partial X$ to become negative in localized regions near the plate. Then, by the continuity equation (8) the transverse velocity V can become positive (fluid flow away from the wall). The change in sign of $\partial U/\partial X$ is indicated by the crossing of the velocity profile curves in Fig. 7. Heat transfer back to the plate has been experimentally observed by Hill [5] for the case of arbitrary heat flux on the lower half of the plate and no heating on the upper half.

Computations for several cases were repeated after perturbing the initial integral solution by 20 percent. In all cases the final solution converged to the same result as found previously, indicating that the computational procedure was both reliable and stable. When longitudinal fluid conduction was ignored, the results were not significantly different from those with conduction, another indication of the validity of the conventional boundary layer assumptions even in the presence of steep temperature gradients. Radiation, accounting for almost 40 percent of the heat transfer in some of the cases considered, could not be ignored. Its inclusion presented no difficulties in the calculations, however.

On the basis of numerical experiments and the uniform heat flux test case, all the computations portrayed in Figs. 4–6 assumed fluid mesh spacings of $\Delta Y_f = 0.010$ and ΔX_f varying between 0.005 and 0.05. All the ceramic cases required about 20 columns of fluid nodes, while 30 were used for the glass cases. These values were adequate since increasing them to extend the calculations further into the surrounding fluid had no significant effect on the results near the plate. All cases converged within 200 iterations to a tolerance of $\theta = 50$, corresponding to a temperature change of about 0.0004 deg C. Such calculations typically took about 5–10 min to complete on an IBM 360-50 digital computer.

Interferograms corresponding to the cases shown in Figs. 4–6 are given in Figs. 8–10. Fluid temperature profiles found from the interferograms are plotted at $X = 0.25$, 0.50, 0.75 in Figs. 4–6. In all cases the predicted trends and magnitudes are confirmed. Fig. 9 clearly shows the positive fluid temperature gradients near the plate as predicted by the theory. The large temperature gradients near the glass plate produce sharp, easily distinguished fringes, the intersections of which with the plate surface give another indication of the plate temperature distribution. These experimental points follow the expected trends in each case; the maximum discrepancy in position of the fringes is within 5 percent of the plate height. A reliable estimate of plate temperatures

could not be found from the interferograms for the ceramic specimens because of the uncertainty in locating the positions of the fringes.

Thermocouple data points are also plotted in Figs. 4–6. The data exhibit the expected trends, with agreement best near the temperature peaks and worst at the thermocouple nearest the leading edge ($X = 0.1$) where plate conduction down through the leading edge may be important, an effect also reported by Scherberg [6]. All the data, including that at $X = 0.1$, fall within 20 percent of the theoretical results; in dimensional terms the largest discrepancy in $T - T_\infty$ is about 9.5 deg C out of 97 deg C (glass plate with three heaters active).

Conclusions

Based on both the physical and numerical experiments it appears that the computational procedure described in this paper gives a reliable, stable, convergent, and economic solution to a wide class of problems involving coupled conduction and natural convection with arbitrary surface heating. It may be extended with confidence to other situations, such as to different plate boundary conditions and to other fluid Prandtl numbers. In the latter case, varying fluid node spacing ΔY_f should be used to allow for the greatly differing velocity and temperature boundary layer thicknesses.

For the specific configuration considered here, that of glass and ceramic plates with localized surface heat sources, it has been found that a large degree of coupling can occur between the plate and fluid. Fig. 11 shows a plot of plate surface temperature, ignoring radiation, for different values of the plate-fluid conductivity ratio when the upper and lower heaters are active. For large conductivity ratios the plate conduction dominates and thermal interaction occurs mostly through the plate; the problem approaches that of an isothermal wall. For $K_w/K_f = 2500$ the temperature variation is about 5 deg C in 65 deg C, while for $K_w/K_f = 5000$ the variation is only about 2 deg C. At the other extreme, low-conductivity ratios of about $K_w/K_f = 1$ correspond to the case in which there is little or no conduction in the plate, so that thermal interaction occurs almost solely through the boundary layer and most of the heat must leave in the vicinity of the sources. It thus appears that for any given configuration, the conductivity ratio is the factor to be considered in deciding whether to use the numerical procedure presented in this paper or some other simplified analysis. For the configuration considered here, the numerical procedure is most useful for $K_w/K_f < 5000$.

The local heat transfer coefficient as computed from equation (15) is shown in Fig. 12 for the ceramic and glass plates with the lower heaters active. Negative value indicate heat transfer back to the plate. It is obvious that the assumption of a uniform heat transfer coefficient, as is often done in simplified thermal design,

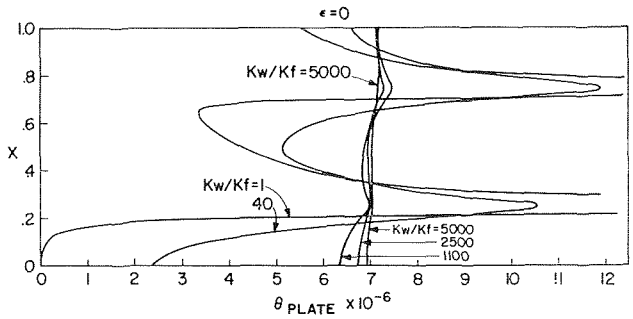

Fig. 11 Effect of conductivity ratio on natural convection from a vertical plate

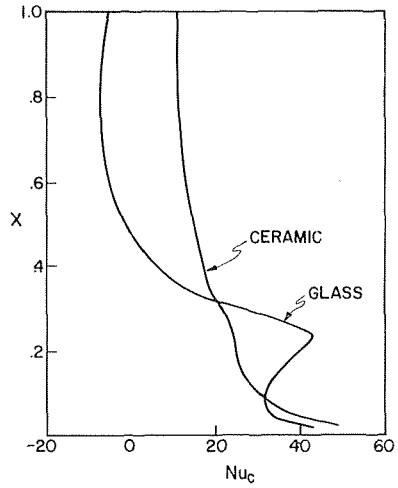

Fig. 12 Local Nusselt number—ceramic and glass plates with the lower heater active

is not warranted, particularly in the case of the low-conductivity plate. In addition, since there is no well defined temperature difference, the concept of average heat transfer coefficient has little significance.

Acknowledgments

The author would like to express his appreciation to the Bell Telephone Laboratories for its support of this investigation toward his doctoral dissertation at Lehigh University. He is especially grateful for the cooperation and encouragement of F. L. Howland and J. W. Elek, and to his thesis advisor B. E. Nevis. R. O'Regan was particularly cooperative in making available the interferometer system and aiding in making the holograms.

References

1 Sparrow, E. M., and Gregg, J. L., "Similar Solutions for Free Convection From a Nonisothermal Vertical Plate," TRANS. ASME. Vol. 80, Feb. 1958, pp. 379–386.

2 Yang, K. T., "Possible Similarity Solutions for Laminar Free Convection on Vertical Plates and Cylinders," *Journal of Applied Mechanics*, Vol. 27, TRANS. ASME, Series E, Vol. 82, No. 2, June 1960, pp. 230–236.

3 Sparrow, E. M., "Laminar Free Convection on a Vertical Plate with Prescribed Non-Uniform Wall Heat Flux or Prescribed Non-Uniform Wall Temperature," NACA TN 3508, July 1955.

4 Tribus, M., "Discussion on Similar Solutions for Free Convection From a Nonisothermal Vertical Plate," TRANS. ASME, Vol. 80, July 1958, pp. 1180–1181.

5 Hill, R. C., "An Experimental Investigation of Free Convection Heat Transfer From a Nonisothermal Vertical Flat Plate," Master's thesis, University of California, Los Angeles, 1961.

6 Scherberg, M. G., "Natural Convection Near and Above Thermal Leading Edges on Vertical Walls," *International Journal of Heat and Mass Transfer*, Vol. 5, 1962, pp. 1001–1010.

7 Kuiken, H. K., "General Series Solution for Free Convection Past a Non-Isothermal Flat Plate," *Applied Scientific Research*, Vol. 20, 1969, pp. 205–215.

8 Schetz, J. A., and Eichorn, R., "Natural Convection with Discontinuous Wall Temperature Variations," *Journal of Fluid Mechanics*, Vol. 18, No. 2, 1964, pp. 167–176.

9 Hayday, A. A., Bowlus, D. A., and McGraw, R. A., "Free Convection From a Vertical Flat Plate with Step Discontinuities in Surface Temperature," JOURNAL OF HEAT TRANSFER, TRANS. ASME. Series C, Vol. 89, No. 3, Aug. 1967, pp. 244–250.

10 Hellums, J. D., and Churchill, S. W., "Computation of Natural Convection by Finite Difference Methods," *International Developments in Heat Transfer*, Proc. of the 1961–62 International Heat Transfer Conference, American Society of Mechanical Engineers, pp. 985–993, 1963.

11 Bodoia, J. R., and Osterle, J. F., "The Development of Free Convection Between Heated Vertical Plates," JOURNAL OF HEAT

TRANSFER, TRANS. ASME, Series C, Vol. 84, No. 1, Feb. 1962, pp. 40–44.

12 Lock, G. S. H., and Gunn, J. C., "Laminar Free Convection From a Downward Projecting Fin," JOURNAL OF HEAT TRANSFER, TRANS. ASME, Series C, Vol. 90, No. 1, Feb. 1968, pp. 63–70.

13 Kelleher, M. D., and Yang, K. T., "A Steady Conjugate Heat Transfer Problem with Conduction and Free Convection," *Applied Scientific Research*, Vol. 17, 1967, pp. 249–269.

14 Sparrow, E. M., and Gregg, J. L., "Laminar Free Convection From a Vertical Plate with Uniform Surface Heat Flux," TRANS. ASME, Vol. 78, Feb. 1956, pp. 435–440.

15 Hellums, J. D., "Finite Difference Computation of Natural Convection Heat Transfer," PhD Dissertation, University of Michigan, Ann Arbor, Mich., 1961.

16 Forsythe, G. E., and Wasow, W. R., *Finite-Difference Methods for Partial Differential Equations*, Wiley, 1960.

17 Varga, R. S., *Matrix Iterative Analysis*, Prentice-Hall, 1962.

18 Zinnes, A. E., "An Investigation of Steady, Two-Dimensional Laminar Natural Convection From a Vertical Flat of Finite Thickness With Plane Localized Heat Sources on Its Surface," PhD dissertation, Lehigh University, 1969.

19 Sparrow, E. M., and Gregg, J. L., "The Variable Fluid-Property Problem in Free Convection," TRANS. ASME, Vol. 80, May 1958, pp. 879–886.

20 Heflinger, L. O., Wuerker, R. F., and Brooks, R. E., "Holographic Interferometry," *Journal of Applied Physics*, Vol. 37, No. 2, Feb. 1966, pp. 642–649.

21 Brooks, R. E., "New Dimension for Interferometry," *Electronics*, Vol. 40, No. 10, May 15, 1967, pp. 88–93.

22 Eckert, E. R. G., and Soehngen, E. E., "Studies on Heat Transfer in Laminar Free Convection with the Zehnder-Mach Interferometer," Air Force Technical Report 5747, USAF Air Materiel Command, Wright-Patterson AFB, Dayton, Ohio, Dec. 1948.

K. T. FELDMAN

Associate Professor of Mechanical Engineering, The University of New Mexico, Albuquerque, N. M.; Formerly, NDEA Fellow, University of Missouri, Columbia, Mo. Mem. ASME

R. L. CARTER

Professor of Electrical and Nuclear Engineering, The University of Missouri, Columbia, Mo.

A Study of Heat Driven Pressure Oscillations in a Gas

Large amplitude acoustical pressure oscillations can be generated in a gas by a steady heat addition. The thermoacoustical oscillation known as the Sondhauss oscillation occurs in a pipe having only one closed end. Experiments were performed to determine thermoacoustic oscillator characteristics for different system geometries and for different operating conditions. Based on these experimental studies, a physical explanation of the mechanism causing Sondhauss thermoacoustical oscillations is presented. The driving mechanism consists of two separate components, that of driving by simple thermal expansion, and that of expansion by the mixing of hot and cold gas in the pipe. The initiation of the oscillations is discussed. Thermoacoustic oscillation phenomena are shown to be analogous to the interaction occurring in a regenerative heat engine, where a steady heat input causes an oscillating mechanical energy output. A comparison of experiment and generalized theory is presented.

I Introduction

The phenomena of acoustical pressure oscillations generated in a gas by a steady heat source may be separated into two distinct types—Rijke oscillations and Sondhauss oscillations. The Rijke oscillation occurs when heat is added to an internal grid located in the lower half of a vertical pipe having both ends open and having a flow of gas upward through the pipe [1].[1] The Sondhauss oscillation occurs when heat is added internally or externally to the closed end of a gas filled pipe having at least one closed end and having no net flow of gas through the pipe [2]. A considerable amount of research has been done on the Rijke oscillation, but the more simple Sondhauss oscillation has received very little attention. References on both the Rijke and Sondhauss oscillations are reviewed in previous publications [3, 4].

The thermoacoustic oscillations described in this paper are related to the heat generated gas oscillations that occur in rocket combustion chambers. Similar thermoacoustic oscillations have been observed in gas furnaces and certain cryogenic experiments where a gas column had a large temperature gradient imposed along its length [5, 6, 7]. More recently, a useful application of the Sondhauss phenomenon as a possible plasma oscillator for an alternating-current magnetohydrodynamic power generator has been proposed [8]. Another application is in environmental testing where very high intensity sounds need to be generated [9]. However, the utilization and control of thermoacoustic oscillations has been limited because the basic phenomenon causing the oscillations has not been completely understood.

The purpose of this paper is to briefly describe some experiments and to offer a physical explanation for the heat exchange mechanism causing the Sondhauss thermoacoustic oscillation.

II Experiments

A series of preliminary experiments were conducted in order to learn more about the quantitative performance of simple Sondhauss pipes. It was discovered that a pyrex glass Sondhauss pipe, like that shown in Fig. 1, had to be heated almost to its melting temperature to produce an audible sound output. Such externally heated Sondhauss pipes could not generate sound pressure levels greater than approximately 80 db (refer to 0.0002 dynes/cm^2). An interesting effect of large intensity sound pulses was observed when small amounts of water vapor were introduced into the heated end of the tube.[2] Rayleigh mentions that alcohol vapor and ether vapor also tend to encourage the oscillations in a tube [10].

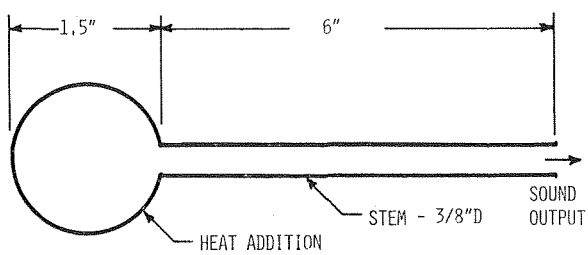

Fig. 1 Simple bulb-end Sondhauss pipe with external flame heating studied by Sondhauss, 1850, and by Rayleigh, 1878

[1] Numbers in brackets designate References at end of paper.

Contributed by the Heat Transfer Division and presented at the Winter Annual Meeting, Los Angeles, Calif., November 16–20, 1969, of THE AMERICAN SOCIETY OF MECHANICAL ENGINEERS. Manuscript received by the Heat Transfer Division, September 23, 1968; revised manuscript received June 10, 1969. Paper No. 69-WA/HT-11.

[2] This effect was observed by R. Wren of The University of Missouri Glass Shop.

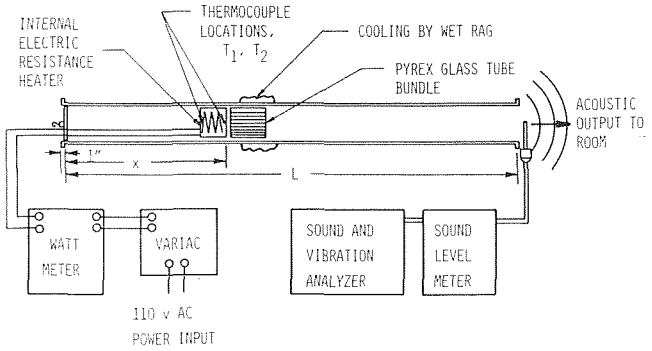

Fig. 2 Open-end glass Sondhauss pipe and experimental equipment

The most effective geometry for a thermoacoustic pipe utilized an internal electric heater and internal glass tube bundle, as is shown in Figs. 2 and 3. The addition of thermal insulation over the heated end and an external water bath heat sink increased the acoustic output for a constant heat input. It was found that for maximum thermoacoustic efficiency the heater and tube bundle should be touching one another. The large-amplitude air displacement at the tube mouth was observed to be greater than 1 in. peak to peak for a 60-cps oscillation of 130-db sound pressure level. At the tube mouth the interaction of the oscillating air column with the still, surrounding air and produced a toroidal air flow; that is, an inward flow occurred around the periphery of the pipe and an outward flow resulted along the axis of the pipe. The toroidal flow extended only about 1 or 2 in. into the pipe interior.

When chalk powder was sprinkled on the inside of the pipe small piles were formed about $^3/_4$ in. apart. It was concluded that the distance between chalk piles was a measure of the wavelength of the longitudnal vibration of the pipe itself.

Tube bundles made of copper tubes of the proper diameter and length did not permit oscillations to occur. This was apparently due to the fact that the copper tube bundle greatly decreased the temperature gradient between the hot and cool regions of the pipe.

Experiments in the Open-End Thermoacoustic Pipe. Measurements of sound pressure level at the mouth of a 4-in. ID pyrex thermoacoustic pipe were made for variations in pipe length, heater-tube bundle position along the pipe, heater power, and tube bundle diameter and length. A diagram of the experimental apparatus is shown in Fig. 2. Experimental sound pressure levels taken at the open tube mouth and heater temperatures were measured for heater powers of 400, 500, and 600 watts, for nine different tube bundles and for a variety of heater-tube bundle positions. As would be expected, higher sound pressure levels were generated at higher heater powers and higher heater temperatures. It was found that an optimum position for the heater-tube bundle in the open-end thermoacoustic pipe was at x/L 0.35 to 0.40. The tube bundles having length to ID ratios, l/d, of 10 to 15 were the most efficient.

In Fig. 4 the acoustic oscillation frequency f, Hz, is plotted versus pipe length, L, inches. The heater-tube bundle was held fixed at $x = 24$ in. from the closed end; the heater power was 500 watts, and the 8 mm ID × 10 cm tube bundle was used. Frequency varies with pipe length according to the hyperbola, $f = a_0/4L$. Thus the oscillation is a quarter wavelength standing wave.

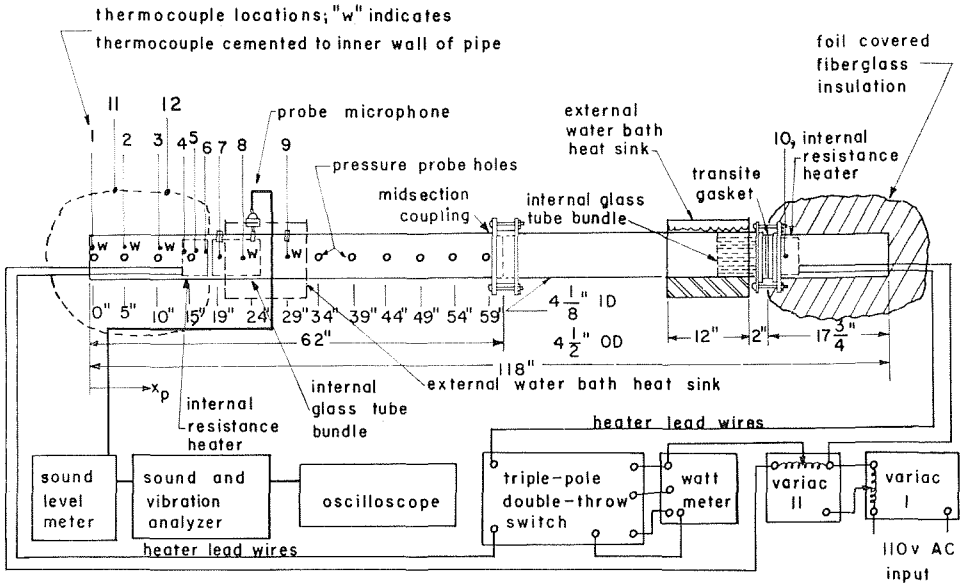

Fig. 3 Closed, double-end Sondhauss pipe showing heaters, tube bundles, heat sinks, pressure probe holes, thermocouples and experimental measuring equipment

Nomenclature

a_o = speed of sound at steady state averaged along the pipe, (ft/sec)
A = inside cross-sectional area of pipe, (ft²)
c_p = specific heat at constant pressure, (Btu/lbm deg R)
C = molar specific heat at constant pressure, (Btu/mole deg R)
d = inside diameter of a tube in a bundle tube, (mm)
D = inside diameter of thermoacoustic pipe, (in.)
f = frequency, (cps or Hertz)
k = ratio of specific heats, (c_p/c_v)
l = tube-bundle tube length, (cm)
L = thermoacoustic pipe length overall, (in.)
p = acoustic over pressure, (psf)
p_o = atmospheric pressure, (psf)
$\dot{Q}$ = heat release rate from heater, (Btu/sec)
Q = heat transfer from hot gas to cold gas during mixing, (Btu)
q = heat release rate per unit mass, (Btu/lbm-sec)
SPL = rms sound pressure level, (decibles, db) (reference 2×10^{-4} dynes/cm²)
T_o = average temperature, (deg R)
w = heat release rate per unit area from heater, (Btu/ft²-sec) where the cross-sectional area of the pipe (at the heater) is used
x = distance from closed end of the thermoacoustic pipe, (in.)
x_p = distance from closed end of pipe to microphone probe, (in.)
η_{ta} = thermoacoustic efficiency, $(A\rho^2/2\rho_o a_o \dot{Q})$
ρ_o = average density, (lbm/ft³)

Experiments in the Closed Double-End Thermoacoustic Pipe. Measurements of sound pressure level, temperature, and frequency distribution along the closed pipe were made for variations in the heater power, tube-bundle tube diameter and length, and for air and argon as the operating gases. The experimental apparatus is shown in Figs. 3 and 5.

Sound pressure levels (db) at locations along the pipe, temperatures (deg F) at points along the pipe (see Fig. 3 for thermocouple locations), and heat sink cooling rate (Btu/hr), were measured for heater powers of 300, 400, and 500 watts and for 6-mm ID tube bundles of 5, 10, and 15 cm lengths in the air-filled double-end pipe. In Fig. 6 a typical plot from the data is shown. Obviously, the highest sound pressure levels correspond to the highest heater powers and occur near the cool side of the tube bundle. The double-end thermoacoustic generator oscillates in a "push-pull" manner, where a pressure maximum occurs at one end while a minimum occurs at the other. The frequency distribution of the sound was measured at specific locations along the pipe. The highest sound pressure levels occurred at 60 cps, which was the fundamental frequency of the oscillation. The fundamental mode predominated all along the pipe except at the midsection where the fundamental passes through a node and the second harmonic becomes a maximum.

The same measurements described previously for air were made with argon as the working gas. The corresponding sound pressure levels achieved were several decibels less than for air and the fundamental resonance frequency was 56 cps instead of 60 cps which occurred with air.

In order to generalize the experimental data, dimensionless groups were chosen: x/L ($L=62$ in.) the heater-tube bundle position ratio; l/d, the tube bundle length to ID ratio; and the thermoacoustic efficiency, $\eta_{ta}=Ap^2/2\rho_0 a_0 \dot{Q}$. The thermoacoustic efficiency is simply the output acoustic intensity divided by the power input. In Fig. 7, thermoacoustic efficiency is plotted versus pressure-probe location ratio for three tube-bundle length to diameter ratios. The curves in Fig. 7 indicate that the tube bundle having $l/d=8.33$ was the most efficient, with the highest efficiency occurring at $x/L=0.40$ near the tube bundle.

Three additional experiments were made to check specific

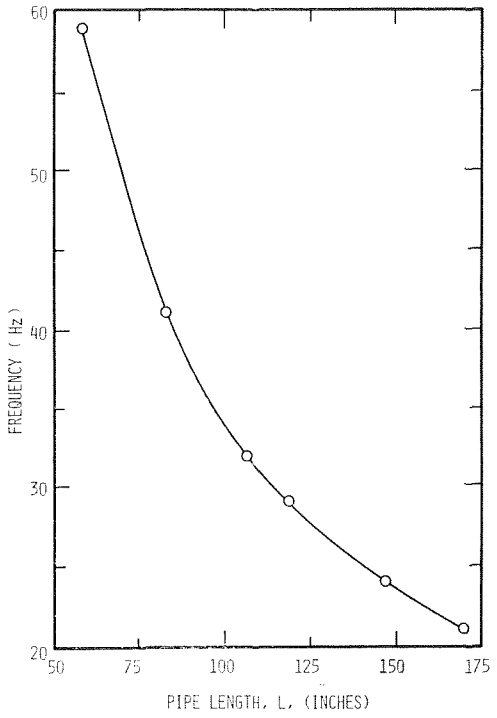

Fig. 4 Frequency versus pipe length in the 4-in. ID Sondhauss pipe or heater-tube-bundle position fixed at $x=24$ in. for 500 watts input power, and 8-mm ID x 10-cm tube bundle

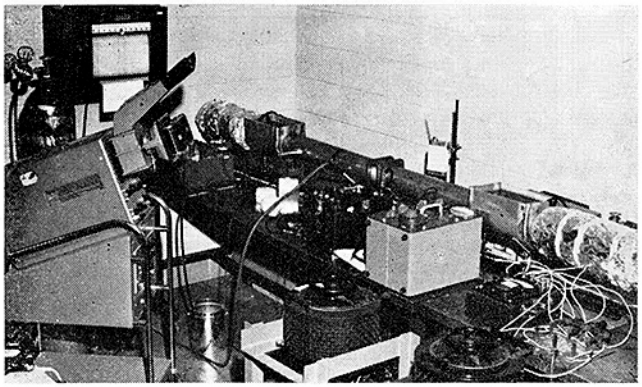

Fig. 5 Closed, double-end Sondhauss pipe system and experimental equipment

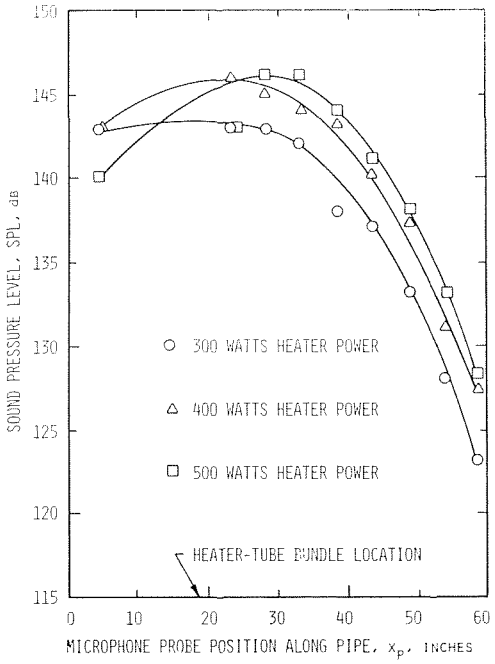

Fig. 6 Sound pressure level versus microphone probe position along pipe for air in the closed, double-end Sondhauss pipe for heater powers of 300, 400, and 500 watts and for 6-mm ID x 10-cm tube bundle

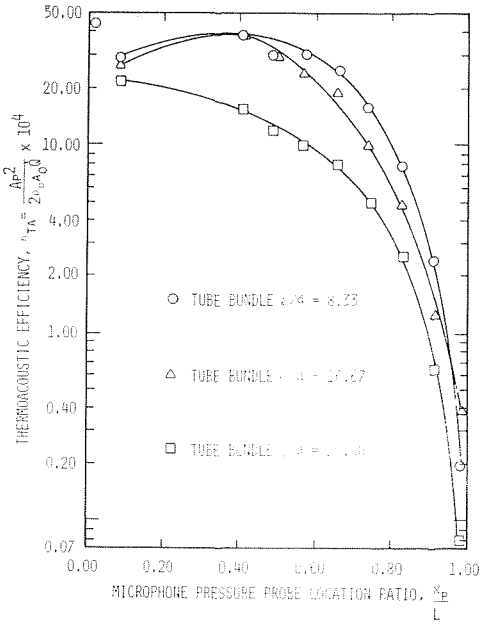

Fig. 7 Thermoacoustic efficiency versus ratio of microphone pressure probe location to one-half pipe length for air in the 4-in. ID x 118-in. closed, double-end Sondhauss pipe with 6-mm x 5, 10, and 15 cm tube bundles having l/d = 8.33, 16.67 and 25.00, and for 400 watts heater power

operating characteristics. First, the "push-pull" mode of oscillation in the double-end thermoacoustic pipe was verified by placing a microphone in each end and noting that the pressure is high in one end when it is low in the other; that is, the pressure waves were 180 deg out of phase. A second experiment indicated that the double-end thermoacoustic pipe would not oscillate with a heat source in only one end. Third, the profile of the pressure wave was measured with a transverse sliding probe and was found to be very nearly a perfect plane wave. Additional details of the experiments may be found in reference [11].

III Thermoacoustic Driving Mechanism

Based on the experiments briefly discussed in section II, a physical explanation for the heat exchange mechanism causing Sondhauss-type thermoacoustical oscillations can be formulated.

Lord Rayleigh stated that in order to encourage oscillations when heat is added in a gaseous system, the heat must be added at the moment of greatest compression or be removed at the moment of greatest expansion [10]. In such a case the basic driving mechanism is simple thermal expansion. All that is required to start and maintain a thermoacoustic oscillation in a system like that shown in Figs. 1, 2, or 4 is a steady-state heat addition to the cavity. It has been experimentally determined that a fluctuating heat source is not required. But there are many instances of heat addition into a cavity where thermoacoustic oscillations do not occur. Therefore, it is important to examine the particular physical conditions which encourage the initiation of these thermoacoustical oscillations.

Obviously, the first requirement to initiate and maintain a thermoacoustical oscillation is to have a minimum rate of heat addition, $\dot{Q}_{\min}$, into a cavity which is of sufficiently high thermal power density and temperature to drive the oscillation and to supply the inherent system losses. Based on previous experiments, a heater power density of approximately 30 watts/in.^{3} is required.

The second requirement necessary to encourage a thermoacoustical oscillation is to have the heated cavity shaped so that a resonant gas oscillation can occur. Based on experimental work, the cavity should be a hollow tube or pipe having a length to diameter ratio (L/D) of approximately 8 to 50, with $L/D=12$ giving the best results.

The third requirement is to locate the heat source at a point in the pipe where both the acoustic gas velocity and pressure are appreciable [12]. This is necessary because the heat transfer driving the oscillations is proportional to the acoustic velocity and gives rise to pressure oscillations. Normally this condition will be met when the acoustic pressure and velocity are both moving in the same direction and are of similar amplitude, as, for example, in the region about one-third of the pipe length from the closed end of a Sondhauss pipe. In a standing wave-type oscillation the pressure and velocity are $^1/_4$ cycle out of phase. When heating occurs the heat transport lags the velocity somewhat [13]. Thus some of the heat input can be in phase with the pressure and drive the oscillation. Therefore, it has been found that the heater must be located approximately at one-third of the overall pipe length from the closed end.

A fourth condition must be provided to start the oscillation, since the system is not entirely self starting even though it may be unstable. This fourth condition can be either of two distinct mechanisms. For low rates of heat addition, the preheated slightly unstable system must be set into oscillation by some random external disturbance. Such disturbances as random thermal convection, random room noises, or blowing or slapping across the open mouth of the thermoacoustic pipe have been observed to start the oscillation. For much higher rates of heat addition of the order of $qL/c_p a_o T_o > 1$, thermal expansion pressure waves are a major starting mechanism. High rates of release include thermal explosions as an upper limiting case.

The final requirement for the initiation of a thermoacoustic oscillation is that the response of the heat source to the initial disturbance be such that the disturbance is amplified. That is, there must be a net increase of the total energy of the system after each cycle of oscillation. Steady heating by a ribbon or wire electric-heating element or an external flame heat source has been found to produce a growing oscillation in the Sondhauss oscillator.

Engine Analogy. The similarity between thermoacoustical oscillations in a pipe and the oscillatory motion of a piston in the cylinder of an engine is known as the engine analogy [14]. In the Sondhauss thermoacoustic oscillator, as in regenerative heat engines (Stirling engines) a steady heat input and heat rejection cause a time-varying output by driving an acoustic pressure wave. Thus the work done by a thermoacoustic "engine" may be described by a specific thermodynamic cycle and plotted on a pressure-volume diagram [15].

Function of the Tube Bundle. In the more efficient Sondhauss oscillators an internal bundle of glass tubes is required. The bundle of glass tubes performs three essential functions. First, it makes a small contribution as a regenerator; that is, it absorbs heat during the expansion and cooling strokes, and gives up heat during the return compression and heating strokes, like the Stirling engine.

Secondly, the tube bundle acts as a porous low-friction insulator; that is, it thermally insulates the heated region from the cooled region while allowing the oscillating gas to pass freely from one region to the other. The heat source and tube bundle must be placed as close together as possible so that a gas particle can encounter the largest possible temperature differences during each cycle of oscillation. Consequently, the tube bundle should be as short as possible to bring the heat source and heat sink close together, but it must be long enough to maintain the thermal insulation between the source and sink.

The third essential function of the tube bundle is to act as an acoustic impedance. That is, it causes a phase shift between the pressure and specific volume which may be plotted as a p-v diagram to describe the thermodynamic cycle and work done.

Driving Oscillations by Mixing Expansions. The preceding discussion of the Sondhauss thermoacoustical oscillation was based on simple thermal expansion described by the equation of state of an ideal gas with constant specific heats. However, at high temperatures the specific heats of real gases are not constant. Consequently, when very high rates of heat release occur in a thermoacoustical system, high temperatures result and the variation of specific heats with temperature must be considered.

Feingold has shown that, for conditions where specific heat varies with temperature, the mixing of two quantities of the same gas at the same original pressure but different original temperatures will cause a rise in pressure of the mixture [16]. This fact was expressed by a simple equation derived from basic thermodynamic relationships,

$$\frac{P_m}{p} = 1 + \frac{QR}{PV_m}\left(\frac{1}{C_a} - \frac{1}{C_b}\right) \tag{1}$$

Equation [1] indicates that p_m equals p only when C_a equals C_b. When the gas in some region B is warmer than in a nearby region A, then $T_b > T_a$ and $C_b > C_a$. Then there will be a pressure rise due to mixing, and conversely, for $C_a > C_b$ ($T_a > T_b$) the pressure will decrease.

Thus, for large temperature gradients between the hot and cold regions in the thermoacoustic oscillator, the variation of specific heats with temperature cause small pressure changes which encourage oscillations. For the case of air oscillating between a region at 1000 deg F and one at 100 deg F, equation (1) predicts that the ratio of pressures would be $p_m/p = 1.0072$. Consequently, driving by mixing expansions contributes only a small amount to the maintenance of the oscillations.

The phenomenon of mixing expansions explains, at least partially, why the addition of water into the heated end of a Sondhauss pipe encourages the thermoacoustic oscillation. The change of molar specific heat for water between the liquid and vapor

phases is large enough to give a substantial pressure increase as predicted by equation (1).

IV Comparison of Experiment and Theory

The general phenomenon of heat-generated pressure oscillations in a gas has been theoretically analyzed by Chu and others [3]. The pressure field generated by a moderate rate of heat release is described by a modified wave equation which had the following solution for heat addition in a plane [17]:

$$p = \frac{k-1}{a_0} \dot{w} \tag{2}$$

The moderate rate of heat release was defined by $qL/c_pT_oa_o << 1$. For higher rates of heat release the generated pressure is described by

$$\frac{p}{p_o} = 0.325 \left(\frac{\dot{w}}{a_o p_o} \right)^{2/3} \tag{3}$$

The comparison between these general theoretical equations and the experimental data indicated that equation (2) may be used to predict sound pressures generated at the mouth of the open-end thermoacoustic pipe (Fig. 2), with less than 1 percent deviation in the range tested. Equation (3) was found to predict sound pressures generated in the higher power closed-end thermoacoustic pipe (Fig. 3), with less than 4 percent deviation in the range tested. As one would expect, the fundamental frequency of the thermoacoustic oscillations was almost exactly described by the equation

$$f = a_o/4L \tag{4}$$

where $a_o = 1160$ fps, which was the mean value of the speed of sound in the air-filled thermoacoustic systems.

V Conclusions

The Sondhauss-type thermoacoustical oscillation is the most simple of all thermoacoustical oscillations; therefore, a clear understanding of the Sondhauss oscillation will help explain the origin of other related thermoacoustical phenomena, such as the Rijke oscillation and combustion oscillations.

Based on the thermoacoustics research reviewed, the mechanism causing Sondhauss oscillations consists of two components, that of driving by simple thermal expansions and compressions occurring periodically, and that of periodic expansions and compressions due to the mixing of cold and hot gas in the system. The driving process is analogous to that occurring in a regenerative heat engine. The Sondhauss oscillator operates on a definite thermodynamic cycle and requires a steady high-power density heat source at high temperature and a heat sink at low temperature. A tube bundle or other restriction of low thermal conductivity is required to separate the heat source and sink, to provide a small regenerative effect, and to provide a phase shift between the acoustic pressure and velocity waves. The oscillations may be initiated by thermal convection, by random acoustic perturbation, or for high heat addition rates by an initial thermal expansion wave. The addition of a vaporizable liquid into the heater region temporarily causes large increases in the generated sound pressure level. This effect is due to the sudden vapor expansions that occur and partly to mixing expansions.

The sound pressure level and frequency of the acoustic output can be accurately predicted. Sound pressures generated at the mouth of the open-end thermoacoustic pipe may be accurately predicted by equation (2) and those generated inside the closed thermoacoustic pipe may be predicted by equation (3). Frequency is predicted almost exactly by equation (4). With these equations and the available experimental data a Sondhauss-type thermoacoustic oscillator can be designed to produce a desired sound pressure level and frequency [18].

References

1 Rijke, P. L., "Notiz uber eine neue Art, die in einer an beiden Enden offenen Rohre enthaltene luft in Schwingungen zu verstezen," *Poggendorff Annalen der Physik and Chemie*, Vol. 107, May 1859, pp. 339–345.

2 Sondhauss, C., "Uber die Schallschwingungen der Luft in erbitizten Glasrohren und in gedeckten Pfeifen von ungleicher Weite," *Poggendorff Annalen der Physik und Chemie*, Vol. 79, Feb. 1850, pp. 1–34.

3 Feldman, K. Thomas, Jr., "Review of the Literature on the Sondhauss Thermoacoustic Phenomena," *Journal of Sound and Vibration*, Jan. 1968, pp. 71–82.

4 Feldman, K. Thomas, Jr., "Review of the Literature on the Rijke Thermoacoustic Phenomena," *Journal of Sound and Vibration*, Jan. 1968, pp. 83–89.

5 Putnam, A. A., and Dennis, W. R., "A Study of Burner Oscillations of the Organ-Pipe Type," TRANS. ASME, Vol. 75, No. 1, Jan. 1953, pp. 15–28.

6 Clement, J. R., and Gaffney, J., "Thermal Oscillations in Low-Temperature Apparatus," *Advances in Cryogenic Engineering*, Proceedings of 1954 Cryogenic Engineering Conference, Boulder, Colo., Paper No. 7, Vol. 1, 1954, p. 302.

7 Thurston, R. S., "Thermal-acoustic Oscillations Induced by Forced Convection Heating of Dense Hydrogen," PhD dissertation, Mechanical Engineering, University of New Mexico, Albuquerque, 1966.

8 Carter, R. L., Feldman, K. T., Jr., and McKinnon, C. N., Jr., "Applicability of Thermoacoustic Phenomena to MHD Conversion Systems," University of Missouri Engineering Experiment Station, Columbia, Mo., Reprint Number 64, July 1964. Reprinted from Proceedings of the Fifth Symposium on Engineering Aspects of Magnetohydrodynamics, Massachusetts Institute of Technology, Cambridge, Mass., April 1–2, 1964, p. 67.

9 Henderson, R. L. (Environmental Test Group, Sandia Laboratory, Albuquerque, N. M.), Private Communication, June 1965.

10 Rayleigh, Lord, *Theory of Sound*, New York: Dover Publications, 1945, Vol. II, pp. 224–234.

11 Feldman, K. T., Jr., "A Study of Heat Generated Pressure Oscillations in a Closed End Pipe," PhD dissertation, Mechanical Engineering, University of Missouri, Columbia, Mo. Feb. 1966; also available as Bureau of Engineering Research Report ME-18, University of New Mexico, Albuquerque, New Mexico; and as Research Report SC-DC-66-1293, Sandia Corporation, Albuquerque, N. M., 198 pp.

12 Friedlander, M. M., and Smith, T. J. B., "Experiments on the Rijke Tube Phenomenon," Paper B6 presented at the New York meeting of the Acoustical Society of America (May 1964), and *Journal of Acoustical Society of America*, Vol. 36,1009(A), 1737(L), 1964.

13 Carrier, G. G., "The Mechanics of the Rijke Tube," *Quarterly of Applied Mathematics*, Vol. 12, pp. 383–395.

14 Chu, B. T., "Stability of Systems Containing a Heat Source—The Rayleigh Criterion," *National Advisory Committee for Aeronautics*, Research Memorandum 56D27, June 1956.

15 Feldman, K. T., Jr., and Hirsch, H., "The Mechanism Causing Heat Driven Pressure Oscillations in a Gas," Bureau of Engineering Research Report ME-22, University of New Mexico, Albuquerque, N. M., June 1966.

16 Feingold, "Mixing of Gases at the Same Original Pressure but Different Original Temperatures," Paper presented at the Missouri Academy of Sciences, University of Missouri, Columbia, Mo., Apr. 1964.

17 Chu, B. T., "Pressure Waves Generated by Addition of Heat in a Gaseous Medium," *National Advisory Committee for Aeronautics*, Technical Note 3411, June 1955.

18 Feldman, K. T., "The Mechanism Causing Heat Driven Pressure Oscillations in a Gas-Thermoacoustic Generator Design," Bureau of Engineering Research Report ME-29, University of New Mexico, Albuquerque, N. M., Sept. 1967.

DISCUSSION

A. A. Putnam[3]

The study of heat driven pressure oscillations in other than thrust producing devices (such as rockets) is receiving rapidly increasing attention. Increased emphasis on silencing sources of industrial noise has resulted in interest in both combustion driven oscillations and combustion roar. The possibilities of profitable usage of combustion driven oscillations are being examined at several laboratories. This paper outlines a thermal driving mechanism that must be considered when diagnosing problems related to heat driven oscillations.

Some questions arise from the results reported and comments made in this paper. For instance, the 300-watt curve of Fig. 6 resembles the sine wave curve that one would expect for a standing wave. However, the two higher heat input curves have pressure maxima not at the ends of the chamber but in the region of heat input. Is this a result of damped traveling wave components, a temperature gradient effect, or some other cause? As another point, a comment is made that the $^3/_4$-in. spacing of piles of chalk powder is related to the wavelength of the longitudinal vibration. Since this wavelength is many times larger (wavelength for 60 Hz in air at room temperature is about 230 in.), a more complete discussion of this point would be appreciated.

Heat pipes are receiving considerable attention at present. These devices have the same elements as the authors' experimental equipment, but in a different proportion. Do the authors have any opinion as to the possibility of Sondhauss oscillations being set up in such devices. If they would occur, or could be made to occur, would they be helpful or harmful? By the same token, could Stirling cycle engines be made to work better if timed to their Sondhauss frequency?

P. Thullen[4]

It is interesting to note that heat sustained pressure oscillations are also of great importance in the design of helium temperature cryogenic equipment. It is frequently necessary to include in the design of such equipment a length of small dia piping which is in thermal communication with both the ambient environment and with the helium temperature environment. This piping will have a relatively steep axial temperature gradient in its wall, and is frequently terminated with a valve or gage of finite dead volume. This leads to a configuration similar to that shown in Fig. 1 of the paper. As a consequence of this, severe pressure oscillations can be set up, and the heat leak to the low temperature region can be increased by orders of magnitude.

Our interest in this phenomenon at the Cryogenic Engineering Laboratory of MIT caused us to initiate a study of these oscillations with the goal of predicting their behavior as well as discovering ways to prevent them. In our study of the literature we uncovered some useful references [19, 20, 22][5] which the authors have not cited. Among these was a reference to a cyclic heat engine known as Griffiiths' Engine [20] which does indeed operate on thermally sustained pressure oscillations. We were able to formulate a piecewise linear lumped parameter mathematical model which described this heat engine in a relatively simple fashion. We then built and instrumented a Griffith's Engine and were able to obtain good agreement between the theoretical predictions and the behavior of the physical system. These results were reported in the recent cryogenic literature [19].

Further analysis of these oscillations has been undertaken by a student in our laboratory, using a distributed heat transfer model [21]. His results appear encouraging and lend further insight into the heat transfer mechanism active in cryogenic systems.

When considering the analogy between these oscillating systems and cyclic heat engines it is interesting to note that while the use of a perfect regenerator in a Stirling cycle will make the engine more efficient, the use of a perfect regenerator in a Sondhauss Oscillator will cause it to cease oscillating. This is because a perfect regenerator will remove the phase shift between the pressure variation and volume variation which is necessary for the production of net work in a cycle.

This paper should be of value in furthering the understanding of heat driven pressure oscillations in a gas.

Additional References

19 Thullen, P., Smith, J. L., Jr., "Model for Thermally Sustained Pressure Oscillations Associated With Liquid Helium," *Advances in Cryogenic Engineering*, Vol. 13, Plenum Press, New York, 1968, p. 215.

20 Griffiths, E. H., *Thermal Measurement of Energy*, Cambridge, University Press, 1901, p. 50.

21 Howsen, R. J., "Thermally Sustained Pressure Oscillations in Liquid Helium Apparatus," MS thesis, Mechanical Engineering Department, Massachusetts Institute of Technology, Cambridge, Mass., May, 1968.

22 Kropschot, R. H., Birmingham, B. W., and Mann, D. B., Editors, *Technology of Liquid Helium, National Bureau of Standards Monograph III*, U. S. Government Printing Office, Washington, D. C., 1968, p. 192.

Authors' Closure

In reply to Dr. Putnam's question about Fig. 6, the decreasing pressure amplitude in the closed end of the pipe is due to a decreasing temperature of several hundred deg F and possibly also to some damping effects. The comment on the chalk powder piles spaced $^3/_4$ in. apart not being due to the 60 Hz air oscillation is correct. At this time a satisfactory explanation of this observation is not available.

The question about incorporation of the Sondhauss oscillation into a heat pipe is certainly of interest since the increased turbulence of the oscillation would cause increased heat transfer rates. This idea occurred to the author sometime ago because of his experiments with heat pipes. A "wick fed" Sondhauss oscillator-heat pipe was built and tested but results were unsuccessful, because the Sondhauss oscillator requires a large temperature gradient while the heat pipe inherently has a small temperature gradient. Thus it appeared that the two systems were incompatible.

In reply to Dr. Thullen's comments about the Griffith's engine, Dr. Carter participated in some similar engine experiments with Dr. Theodore Finkelstine at Atomics International in 1961. The conclusion was that the thermoacoustic engine was inefficient and difficult to harness.

During the same period as the Griffith's reference [20], a Douglas Knipp, reportedly of Illinois Institute of Technology (1890), studied the thermoacoustic phenomenon. Efforts to locate the original references have been unsuccessful, but a Sondhauss type thermoacoustic oscillator is available commercially in the Cenco catalog as No. 85180 Cenco-Knipp singing Tube.

---

[3] Mechanical Engineering Department, Columbus Laboratories, Battelle Memorial Institute, Columbus, Ohio.

[4] Assistant Professor, Department of Mechanical Engineering, Massachusetts Institute of Technology, Cambridge, Mass.

[5] Numbers in brackets designate Additional References at end of discussion.

journal of heat transfer

technical briefs

This section consists of contributions of 1500 words or less (about 2 1/2 double-spaced typewritten pages, including figures). Technical Briefs will be reviewed and approved by the specific division's reviewing committee prior to publication. After approval such contributions will be published as soon as possible, normally in the next issue of the Journal.

Frequency Distribution of Boiling-Generated Sound

T. AOKI[1] **and J. R. WELTY**[2]

Introduction

THE generation of sound accompanying boiling heat transfer has been studied by several investigators. The studies of Westwater, Lowery, and Pramuk [1][3] indicated that boiling sound was a function of the heat transfer rate as well as the temperature difference between the boiling surface and the bulk liquid. Sound pressure level was found to increase very rapidly with temperature difference in the nucleate region and moderately in the region of transition boiling. Schwartz and Siler [2] obtained a sound pressure level versus temperature difference curve which was similar in shape to the usual heat flux versus temperature difference plot; the sound pressure level decreased as the temperature difference increased during transition boiling. More recent studies by Ponter and Haigh [3] have been concerned with sound generation in the nucleate region in a subcooled boiling system. They found that the intensity of boiling sound was co-dependent on the heat flux and water temperature so that measurement of the sound level together with only one of the other parameters did not completely specify the boiling situation.

The purpose of the present communication is to present the results of an experimental investigation in which unique sound generation was observed during transition boiling [4].

Description of Experiment

Stable transition pool boiling was produced with a horizontal copper disk as the boiling surface and saturated normal pentane, having a vapor pressure of 1 atm at 97 deg F, as the boiling medium. The schematic diagram of the boiling apparatus is shown in Fig. 1.

The thin copper fins (a) transmitted heat uniformly to the boiling surface (b) from the condensing water vapor. Saturation pressure in the pressure vessel (c) was controlled to achieve a desired boiling surface temperature. Controlling the boiling surface temperature rather than heat flux made it possible to attain stable transition boiling. The boiling surface was a copper disk, 2 *in.* in diameter and 0.094 *in.* thick. Heat flux values were determined from the rate of n-pentane condensate accumulation corrected with appropriate heat loss allowance obtained from separate experiments.

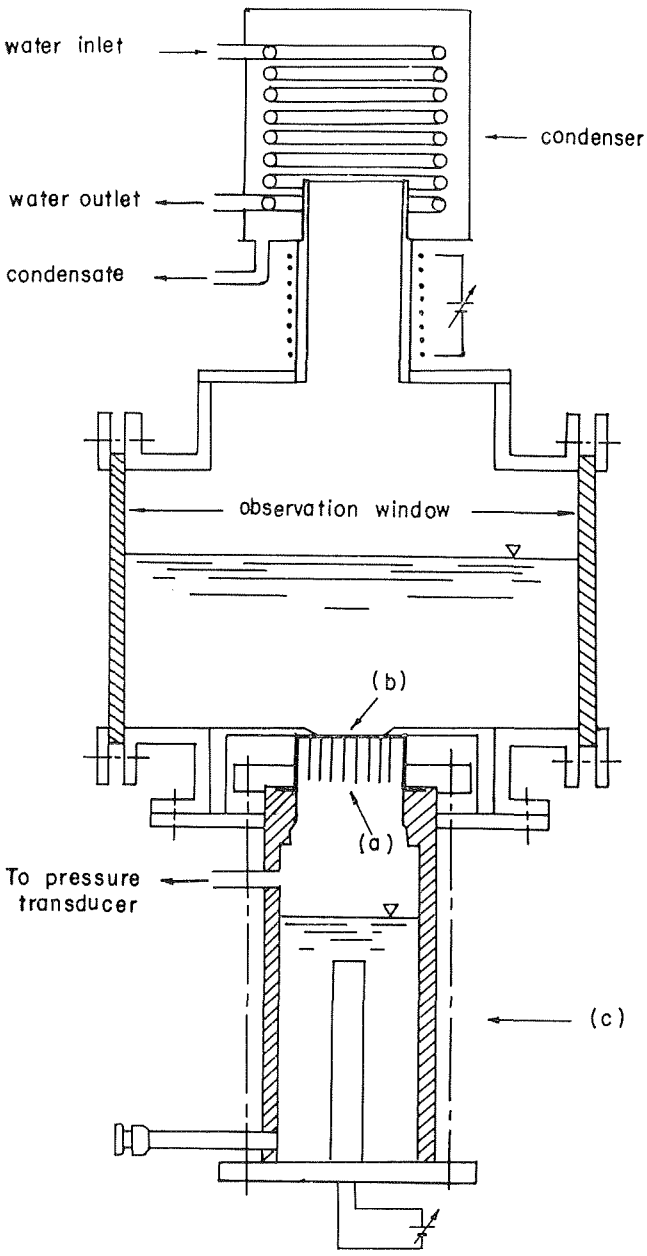

Fig. 1 Schematic of experimental apparatus

[1] Department of Mechanical Engineering, Oregon State University, Corvallis, Ore.; Heat Transfer Research Inc., Alhambra, Calif.

[2] Professor of Mechanical Engineering, Oregon State University, Corvallis, Ore. Mem. ASME.

[3] Numbers in brackets designate References at end of Technical Brief.

Contributed by the Heat Transfer Division of THE AMERICAN SOCIETY OF MECHANICAL ENGINEERS. Manuscript received by the Heat Transfer Division, September 4, 1969; revised manuscript received January 16, 1970.

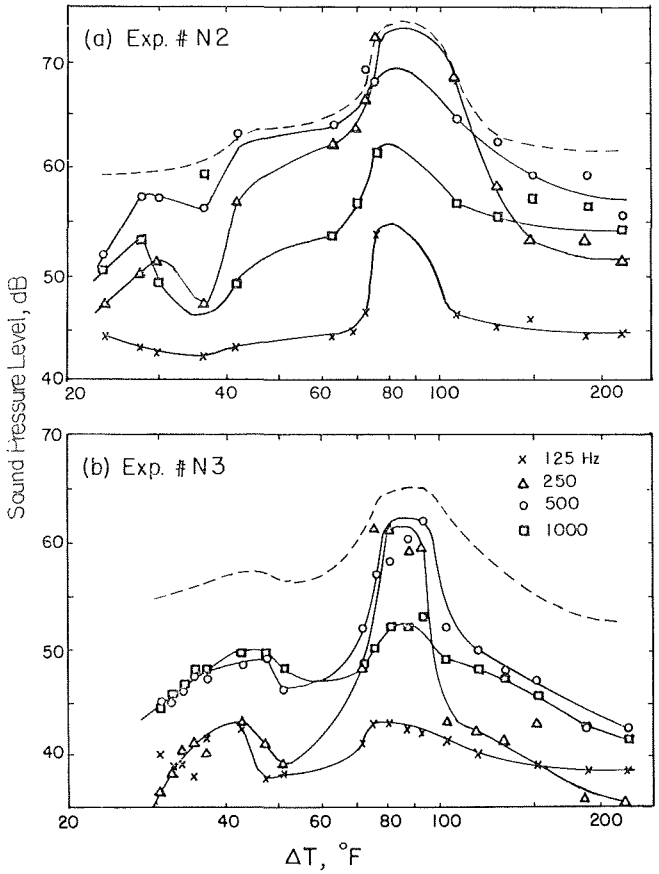

Fig. 2 Characteristic boiling sound curve

Sound detection was accomplished using a condenser microphone immersed in the *n*-pentane. Two microphone locations were used. For experiment N2 the microphone was positioned directly adjacent to the 0.75-in. effective radius boiling surface; in experiment N3 the microphone was located laterally 1.375 in. from the center of the boiling surface and 1.75 in. above it. The boiling sound was recorded on a magnetic tape at different boiling surface temperatures from which subsequent frequency analyses were made. For each experiment all-pass-band and octave-band sound pressure levels were recorded on charts from the magnetic tape by means of a graphic level recorder and an octave-band analyzer. The reference sound pressure level (SPL) is 20 micronewtons/m² and SPL is defined as

$$SPL = 20 \log_{10} \frac{P}{0.00002}\ db \qquad \text{re} \qquad 20\ \mu\text{N/m}^2 \tag{1}$$

where P = root-mean-square sound pressure in N/m² for the sound in question.

Discussion of Results

Sound pressure level data plotted as decibels versus ΔT_s, the temperature difference between the boiling surface and saturated *n*-pentane, are presented in Fig. 2. The dashed line and solid lines represent overall sound pressure level and frequency components of sound pressure level, respectively. Overall sound pressure level data in Fig. 2(*a*) differ by an average of 7.2 db from those in 2(*b*) due to the location of the microphone as discussed in the previous section. Since the sound pressure varies inversely as the distance from the source and the ratio of the distances for experiment N3 and for N2 is about 2.47 to 1, the difference of SPL may be calculated assuming that the sound originates at a point source located at the center of the boiling surface; thus,

$$(SPL)_{N2} - (SPL)_{N3} = 20 \log_{10} \frac{2.41}{1} = 7.85\ \text{db} \tag{2}$$

which is in agreement with experimental results. A distinctive peak in sound pressure level appears in the transition region at a surface temperature difference (ΔT_s) near 80 deg F. The predominant frequency components at the peak are 250 and 500 Hz.

The characteristic boiling sound curve obtained in this experiment differs from the results obtained by Westwater, Lowery, and Pramuk [1] and Schwartz and Siler [2]; the present experiment shows the highest sound pressure level to be in the transition boiling region. The sound of boiling was found to be an increasing function of heat flux during nucleate boiling, but it leveled off (experiment N2) or dropped (experiment N3) at the region of maximum heat flux. This is due to the large vapor region, formed by the bubble coalescence above the boiling surface, attenuating the sound generated at the surface. This vapor region should not be confused with the thin vapor film which is formed directly above the boiling surface and is the chief feature of film

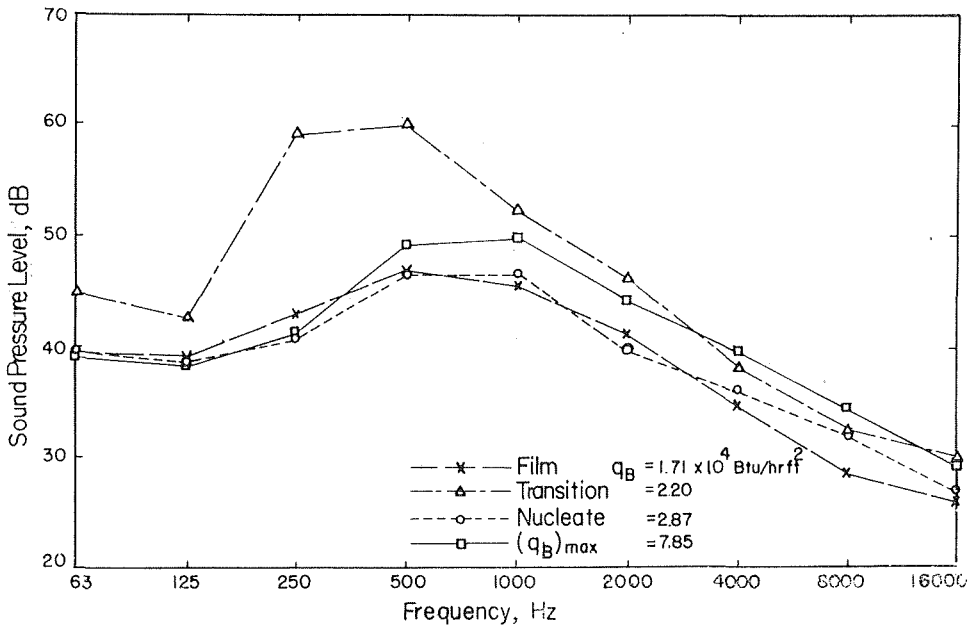

Fig. 3 Octave-band analysis of boiling sound

boiling. When the maximum heat flux is passed and the large vapor region disappears, the sound pressure level rises again.

Typical frequency spectra for sound generated in nucleate, transition, and film boiling as well as at the maximum heat flux (burnout) point are shown in Fig. 3. The sound pressure level for the transition region was again observed to be large between 125 and 1000 Hz with major components in the 250 to 500 Hz range. Investigation by the authors [5] has indicated that, during transition pool boiling, the "quenching" of a hot surface due to direct contact by the saturated liquid is followed by the existence of the liquid in a spheroidal state before the thin vapor film reforms between the solid and liquid. In the transition boiling regime, "quenching" occurring on a small region of the heated surface, where direct contact with the liquid occurred, resulted in a sudden temperature drop of about 40 deg F at lower heat flux levels and 20 deg F at higher levels in a period of about 2-millisec. A droplet evaporating on a heated surface has the shortest lifetime at the maximum boiling rate which corresponds to the "burnout-point" [6]. At this point the droplet is in violent motion due to rapid evaporation which occurs at the expense of large energy, thus resulting in a high sound pressure level. For liquid pentane at 1 atm the boiling surface at a temperature difference, ΔT_s, near 80 deg F momentarily provides favorable conditions for the maximum boiling rate when the liquid contacts it and produces a sudden temperature drop of about 30 deg F. Thus the large sound pressure level observed near 80 deg F during transition boiling is attributed to the rapid evaporation rate of liquid droplets coming into direct contact with the boiling surface and also to the high frequency of such contact (quenching). As ΔT_s increases, quenching frequency decreases, resulting in a decrease in overall sound pressure level.

References

1 Westwater, J. W., Lowery, A. J., and Pramuk, F. S., "Sound of Boiling," *Science*, Vol. 121, 1955, pp. 332–333.

2 Schwartz, F. L., and Siler, L. G., "Correlation of Sound Generation and Heat Transfer in Boiling," JOURNAL OF HEAT TRANSFER, TRANS. ASME, Series C, Vol. 87, Nov. 1965, pp. 436–438.

3 Ponter, A. B., and Haigh, C. P., "Sound Emission and Heat Transfer in Low Pressure Pool Boiling," *International Journal of Heat and Mass Transfer*, Vol. 12, 1969, pp. 413–428.

4 Aoki, T , "An Experimental Investigation of Transition Pool Boiling," PhD thesis, Oregon State University, Dept. of Mechanical Engineering, Corvallis, Ore., 1970.

5 Aoki, T., and Welty, J. R., "Energy Transfer Mechanisms in Transition Pool Boiling," *International Journal of Heat and Mass Transfer* (to be published).

6 Satcunanthan, S., "Evaporation of Rates of Liquid Droplets Evaporating in the 'Spheroidal' State on a Hot Surface," *Journal of Mechanical Engineering Science*, Vol. 10, No. 5, 1968, pp. 438–441.

Inertial Component Thermal Drift Due to Damping Fluid Convection Currents—Approximate Transient Analysis

R. W. ALLEN[1] and D. W. SEATON[2]

Nomenclature

u, v = velocity components in x and y directions
g_0 = acceleration of gravity
β = coefficient of expansion
T = temperature
T_r = ambient reference temperature
$\theta_{\max}$ = $T_{\max} - T_r$
δ = fluid gap thickness
ρ = fluid density
ρ_r = ambient reference density
μ = coefficient of viscosity
ν = kinematic viscosity = μ/ρ
u_{ref} = $\dfrac{g_0\beta\theta_{\max}\delta^2}{\nu}$
U = u/u_{ref}
V = v/u_{ref}
X = x/δ
Y = y/δ
R = inner radius of annulus
R' = R/δ
t = time
t_{ref} = δ/u_{ref}
t' = t/t_{ref}
p = pressure
P_{ref} = $\rho_r u_{\text{ref}}^2$
p' = p/p_{ref}
θ' = $\dfrac{T - T_r}{T_{\max} - T_r}$
α = thermal diffusivity
Fo = $\dfrac{\alpha t_{\text{ref}}}{\delta^2}$
Gr = $\dfrac{g_0\beta\theta_{\max}\delta^3}{\nu^2}$
Pr = ν/α

[1] Professor of Mechanical Engineering, University of Maryland, College Park, Md.

[2] Section Leader—Mechanical Analysis, Vitro Laboratories, Silver Spring, Md.

Contributed by the Heat Transfer Division of THE AMERICAN SOCIETY OF MECHANICAL ENGINEERS. Manuscript received by the Heat Transfer Division, April 28, 1970.

Introduction

THE analysis of reference [1][3] provides solutions for the steady state thermal drift, resulting from damping-fluid viscous drag, of a floated inertial reference device with an unsymmetrical temperature distribution about the vertical.

It is the purpose of this note to provide an approximate method of determining the transient behavior for a perfectly centered gimbal subjected to a temperature gradient unsymmetrical about the vertical axis. The method provides a means of computing the natural convection of the damping fluid and the resultant viscous drag, and hence thermal drift, at any instant after the stepwise application of a unit, circumferentially linear temperature distribution between points (1) and (2) along the outer wall of the fluid annulus (Fig. 1). We consider a floated gimbal with coordinates as shown in Fig. 1.

The following conditions prevail:

(a) The annular thickness is much less than the float radius.

(b) Temperature differences are sufficiently small so that fluid motion can be characterized as quasisteady, creeping laminar flow in the x direction.

(c) Damping fluid properties are constant except for the variation of density with temperature.

(d) The Prandtl number of the damping fluid is much greater than unity.

An order of magnitude analysis of the basic equations given in reference [2] yields the following governing equations of fluid motion:

$$\frac{\partial^2 U}{\partial Y^2} = Gr\,\frac{\partial p'}{\partial X} - \theta'\cos\psi \qquad (1)$$

[3] Numbers in brackets designate References at end of Technical Brief.

boiling. When the maximum heat flux is passed and the large vapor region disappears, the sound pressure level rises again.

Typical frequency spectra for sound generated in nucleate, transition, and film boiling as well as at the maximum heat flux (burnout) point are shown in Fig. 3. The sound pressure level for the transition region was again observed to be large between 125 and 1000 Hz with major components in the 250 to 500 Hz range. Investigation by the authors [5] has indicated that, during transition pool boiling, the "quenching" of a hot surface due to direct contact by the saturated liquid is followed by the existence of the liquid in a spheroidal state before the thin vapor film reforms between the solid and liquid. In the transition boiling regime, "quenching" occurring on a small region of the heated surface, where direct contact with the liquid occurred, resulted in a sudden temperature drop of about 40 deg F at lower heat flux levels and 20 deg F at higher levels in a period of about 2-millisec. A droplet evaporating on a heated surface has the shortest lifetime at the maximum boiling rate which corresponds to the "burnout-point" [6]. At this point the droplet is in violent motion due to rapid evaporation which occurs at the expense of large energy, thus resulting in a high sound pressure level. For liquid pentane at 1 atm the boiling surface at a temperature difference, ΔT_s, near 80 deg F momentarily provides favorable conditions for the maximum boiling rate when the liquid contacts it and produces a sudden temperature drop of about 30 deg F. Thus the large sound pressure level observed near 80 deg F during transition boiling is attributed to the rapid evaporation rate of liquid droplets coming into direct contact with the boiling surface and also to the high frequency of such contact (quenching). As ΔT_s increases, quenching frequency decreases, resulting in a decrease in overall sound pressure level.

References

1 Westwater, J. W., Lowery, A. J., and Pramuk, F. S., "Sound of Boiling," *Science*, Vol. 121, 1955, pp. 332–333.

2 Schwartz, F. L., and Siler, L. G., "Correlation of Sound Generation and Heat Transfer in Boiling," JOURNAL OF HEAT TRANSFER, TRANS. ASME, Series C, Vol. 87, Nov. 1965, pp. 436–438.

3 Ponter, A. B., and Haigh, C. P., "Sound Emission and Heat Transfer in Low Pressure Pool Boiling," *International Journal of Heat and Mass Transfer*, Vol. 12, 1969, pp. 413–428.

4 Aoki, T , "An Experimental Investigation of Transition Pool Boiling," PhD thesis, Oregon State University, Dept. of Mechanical Engineering, Corvallis, Ore., 1970.

5 Aoki, T., and Welty, J. R., "Energy Transfer Mechanisms in Transition Pool Boiling," *International Journal of Heat and Mass Transfer* (to be published).

6 Satcunanthan, S., "Evaporation of Rates of Liquid Droplets Evaporating in the 'Spheroidal' State on a Hot Surface," *Journal of Mechanical Engineering Science*, Vol. 10, No. 5, 1968, pp. 438–441.

Inertial Component Thermal Drift Due to Damping Fluid Convection Currents—Approximate Transient Analysis

R. W. ALLEN[1] and D. W. SEATON[2]

Nomenclature

u, v = velocity components in x and y directions
g_0 = acceleration of gravity
β = coefficient of expansion
T = temperature
T_r = ambient reference temperature
$\theta_{\max}$ = $T_{\max} - T_r$
δ = fluid gap thickness
ρ = fluid density
ρ_r = ambient reference density
μ = coefficient of viscosity
ν = kinematic viscosity = μ/ρ
u_{ref} = $\dfrac{g_0\beta\theta_{\max}\delta^2}{\nu}$
U = u/u_{ref}
V = v/u_{ref}
X = x/δ
Y = y/δ
R = inner radius of annulus
R' = R/δ
t = time
t_{ref} = δ/u_{ref}
t' = t/t_{ref}
p = pressure
P_{ref} = $\rho_r u_{\text{ref}}^2$
p' = p/p_{ref}
θ' = $\dfrac{T - T_r}{T_{\max} - T_r}$
α = thermal diffusivity
Fo = $\dfrac{\alpha t_{\text{ref}}}{\delta^2}$
Gr = $\dfrac{g_0\beta\theta_{\max}\delta^3}{\nu^2}$
Pr = ν/α

[1] Professor of Mechanical Engineering, University of Maryland, College Park, Md.

[2] Section Leader—Mechanical Analysis, Vitro Laboratories, Silver Spring, Md.

Contributed by the Heat Transfer Division of THE AMERICAN SOCIETY OF MECHANICAL ENGINEERS. Manuscript received by the Heat Transfer Division, April 28, 1970.

Introduction

THE analysis of reference [1][3] provides solutions for the steady state thermal drift, resulting from damping-fluid viscous drag, of a floated inertial reference device with an unsymmetrical temperature distribution about the vertical.

It is the purpose of this note to provide an approximate method of determining the transient behavior for a perfectly centered gimbal subjected to a temperature gradient unsymmetrical about the vertical axis. The method provides a means of computing the natural convection of the damping fluid and the resultant viscous drag, and hence thermal drift, at any instant after the stepwise application of a unit, circumferentially linear temperature distribution between points (1) and (2) along the outer wall of the fluid annulus (Fig. 1). We consider a floated gimbal with coordinates as shown in Fig. 1.

The following conditions prevail:

(a) The annular thickness is much less than the float radius.

(b) Temperature differences are sufficiently small so that fluid motion can be characterized as quasisteady, creeping laminar flow in the x direction.

(c) Damping fluid properties are constant except for the variation of density with temperature.

(d) The Prandtl number of the damping fluid is much greater than unity.

An order of magnitude analysis of the basic equations given in reference [2] yields the following governing equations of fluid motion:

$$\frac{\partial^2 U}{\partial Y^2} = Gr\,\frac{\partial p'}{\partial X} - \theta'\cos\psi \qquad (1)$$

[3] Numbers in brackets designate References at end of Technical Brief.

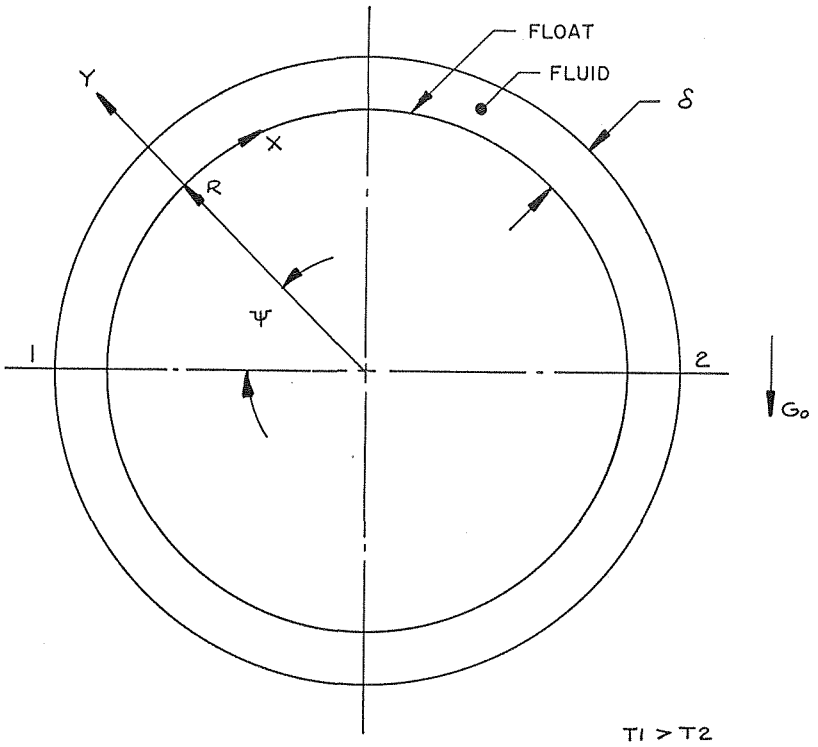

Fig. 1 Floated gimbal coordinates and schematic diagram

$$\frac{\partial p'}{\partial Y} = 0 \tag{2}$$

$$Fo\,\frac{\partial^2 \theta'}{\partial Y^2} = \frac{\partial \theta'}{\partial t'} \tag{3}$$

$$\frac{\partial U}{\partial X} = 0 \tag{4}$$

The unsteady terms in equation (1) as well as the viscous and body force terms in equation (2) are omitted because of conditions (a) and (b).

For a typical inertial reference device, the thermal response (i.e., the solution) can be considered to consist of two phases. The first involves diffusion through the fluid and attainment of a radially linear fluid temperature profile. In the second phase the float acts as a heat sink, and the radial and circumferential fluid temperature gradients are variable in time but remain spatially linear.

Application of references [3] and [4] shows that a quasisteady boundary layer analysis can be used for a typical system. The natural convection boundary layer will, during the first phase, propagate radially inward through the damping fluid approximately 3.5 times faster than the time required to attain a linear temperature profile. Also, for the small fluid thickness under consideration, the time to attain a radially linear temperature profile (phase I) is much shorter than the heat sink response of the float (phase II). This implies that equation (3) reduces to a gradient $\frac{d\theta'}{dY}$ which is a function $C(X, t)$ of circumferential position X and time t. This gradient is entered into the momentum equation to find the corresponding quasisteady velocity distribution at the same instant of time.

As a consequence of the prescribed linear circumferential boundary condition and the linear radial temperature distribution in phase II, the temperature at any point in the fluid is a linear function of both X and Y and can be represented by the following dimensionless relationship:

$$\theta' = 1 - \frac{X}{\pi R'} + C(X, t)[Y - 1] \tag{5}$$

When θ' is substituted into equation (1) the equation takes the form

$$\frac{\partial^2 U}{\partial Y^2} = Gr\,\frac{\partial p'}{\partial X} - \left[1 - \frac{X}{\pi R'} + C(X)Y - C(X)\right]\cos\frac{X}{R'}$$

or

$$\frac{\partial^2 U}{\partial Y^2} = [f(X) + g(X)] - g(X)Y \tag{6}$$

where

$$f(X) \equiv f = Gr\,\frac{\partial p'}{\partial X} + \left[\frac{X}{\pi R'} - 1\right]\cos\frac{X}{R'}$$

$$g(X) \equiv g = C(X)\cos\frac{X}{R'}$$

Integrating equation (6) twice with respect to radial direction Y gives the following equation

$$U = \frac{f + g}{2}\,Y^2 - \tfrac{1}{6}gY^3 + [-\tfrac{1}{3}g - \tfrac{1}{2}f]Y \tag{7}$$

where the boundary conditions $U = 0$ at $Y = 0, 1$ have been used.

The inner wall shear stress is given, by definition

$$\mu\left(\frac{\partial u}{\partial y}\right)_{y=0} = \frac{\mu g_0 \beta \theta_{\max}\delta}{\nu}\left(\frac{\partial U}{\partial Y}\right)_{Y=0} \tag{8}$$

Differentiating the velocity profile given by equation (7) we have the dimensionless wall shear stress

$$\left(\frac{\partial U}{\partial Y}\right)_{Y=0} = -\tfrac{1}{3}g - \tfrac{1}{2}f \tag{9}$$

The function g is known whereas f is unknown because of the undetermined pressure gradient $\frac{\partial p'}{\partial X}$. We eliminate f by performing two definite integrations on equation (6); first with respect to Y, then with respect to X; that is

$$\int_0^1 \frac{\partial^2 U}{\partial Y^2}\, dY = [f + g] \int_0^1 dY - g \int_0^1 Y dY$$

or

$$\left(\frac{\partial U}{\partial Y}\right)_{Y=1} - \left(\frac{\partial U}{\partial Y}\right)_{Y=0} = f + \tfrac{1}{2}g \tag{10}$$

Next, we insert the definition of f into equation (10) and integrate with respect to X.

$$\int_0^{2\pi R'} [f + \tfrac{1}{2}g]dX = \int_0^{2\pi R'} Gr \frac{\partial p'}{\partial X}\, dX + 2\int_0^{\pi R'} \left[\frac{X}{\pi R'} - 1\right] \cos\frac{X}{R'}\, dX + \tfrac{1}{2}\int_0^{2\pi R'} g dX \tag{11}$$

where symmetry about the 1-2 plane has been used in writing the second integral on the right.

We may show that the constant average velocity $\bar{U}$, obtained by integrating equation (7) with respect to Y between the limits 0 and 1, is equal to $-\frac{1}{12}[f + \frac{1}{2}g]$. Therefore, the bracketed integrand on the left side of equation (11) is a constant and may be removed from the integral sign. Furthermore, since the first integral on the right is zero, we can perform the integration and solve equation (11) for f. Thus,

$$f = -\tfrac{1}{2}g - \frac{2}{\pi^2} + \frac{1}{2\pi R'}\int_0^{\pi R'} g dX \tag{12}$$

If we substitute equation (12) into equation (9) and integrate around the circumference between the limits 0 and $2\pi R'$, and note that the definite integral in equation (12) is a constant during this integration, we obtain the following expression for the dimensionless circumferential shear force per unit length of float

$$-\frac{2}{3}\int_0^{\pi R'} g dX + \frac{2R'}{\pi}$$

By substituting the expression for $g(X)$ into the above equation and utilizing equation (8), we may express the shear force per unit length of float as

$$\mu\left(\frac{\partial u}{\partial y}\right)_{y=0} = \rho_r g_0 \beta \theta_{\max}\delta \times \left[\frac{2R'}{\pi} - \frac{2}{3}\int_0^{\pi R'} C(X, t)\cos\frac{X}{R'}\, dX\right] \tag{13}$$

Notice that when there is no temperature gradient across the gap, $C(X, t) = 0$ and the equation reduces to a steady state relation.

The integral in equation (13) can be numerically evaluated at a given instant of time by computing $C(X, t)$ at a number of discrete points along one-half the fluid circumference ($0 \rightarrow \pi R'$) with temperature data obtained from the phase II thermal analysis. The product in the integrand is then computed at these points and the integration performed by a numerical integration procedure such as Simpson's rule.

Results

The foregoing analysis allows one to compute the circumferential viscous drag on a floated inertial reference device as a function of time. For example, this analysis was used to compute the viscous force on a 0.890-in-dia gyro float with a 0.005-in. gap using Fluro-Chem 3000/130/2.0750 (viscosity, centipoise/temperature, deg F/density, g per cc) at 0.6 sec after the application of a 1 deg F temperature difference across the outer diameter of the fluid annulus with a nominal temperature of 130 deg F. The results showed a value of 0.007 dyne/in. which was approximately 80 percent of the final steady state value of 0.009 dyne/in. It is noteworthy that the final steady state value and the phase II response time are dependent upon the "heat sink characteristics" of the float. The foregoing numerical results were for a particular float design and should not necessarily be regarded as typical of all floated inertial reference devices.

References

1 Goodman, L. E., and Robinson, A. R., "Thermal Drift of Floated Gyroscopes," TRANS. ASME, Vol. 79, Dec. 1957, pp. 506–508.

2 Moore, F. K., "High Speed Aerodynamics and Jet Propulsion," *Theory of Laminar Flows*, Vol. IV, Princeton University Press, 1964, pp. 530–560.

3 Grover, J. H., and Holter, W. H., "Solution of the Transient Heat Conduction Equation for an Insulated, Infinite Metal Slab," *Jet Propulsion*, Vol. 27, Dec. 1957, pp. 1249–1252.

4 Seigel, Robert, "Transient Free Convection From a Vertical Flat Plate," TRANS. ASME, Vol. 80, Feb. 1958, pp. 347–359.

Nonuniform Temperature Distribution Analysis for Long Coaxial Cylinders

R. D. CASAGRANDE[1] and C. N. SHEN[2]

Nomenclature

A = surface area, Fourier coefficients
a = radius ratio
B, C, D, L, M = constants defined in the text
E = emissive power
F = geometric factor, constant defined in the text
K = kernel in the integral expression
J = radiosity
n = zero or positive integer
q = net heat flux from the surface per unit area
r = separation distance between points
R = radius of the cylinder
S = general coordinate
T = absolute temperature
U = absorbed heat flux distribution on the convex surface of the outer cylinder
α = surface absorptivity
γ = angle defined by the radius ratio
ϵ = surface hemispherical emissivity
ϕ, λ = dummy angular coordinate variable
θ = angular coordinate of the cylinders
σ = Stephan-Boltzmann constant

[1] General Electric Company, Space Division, King of Prussia, Pennsylvania

[2] Professor of Mechanical Engineering, Rensselaer Polytechnic Institute, Troy, New York.

Contributed by the Heat Transfer Division of THE AMERICAN SOCIETY OF MECHANICAL ENGINEERS. Manuscript received by the Heat Transfer Division, May 1, 1970.

Differentiating the velocity profile given by equation (7) we have the dimensionless wall shear stress

$$\left(\frac{\partial U}{\partial Y}\right)_{Y=0} = -\tfrac{1}{3}g - \tfrac{1}{2}f \tag{9}$$

The function g is known whereas f is unknown because of the undetermined pressure gradient $\frac{\partial p'}{\partial X}$. We eliminate f by performing two definite integrations on equation (6); first with respect to Y, then with respect to X; that is

$$\int_0^1 \frac{\partial^2 U}{\partial Y^2}\, dY = [f + g] \int_0^1 dY - g \int_0^1 Y dY$$

or

$$\left(\frac{\partial U}{\partial Y}\right)_{Y=1} - \left(\frac{\partial U}{\partial Y}\right)_{Y=0} = f + \tfrac{1}{2}g \tag{10}$$

Next, we insert the definition of f into equation (10) and integrate with respect to X.

$$\int_0^{2\pi R'} [f + \tfrac{1}{2}g]dX = \int_0^{2\pi R'} Gr \frac{\partial p'}{\partial X}\, dX + 2\int_0^{\pi R'} \left[\frac{X}{\pi R'} - 1\right] \cos\frac{X}{R'}\, dX + \tfrac{1}{2}\int_0^{2\pi R'} g dX \tag{11}$$

where symmetry about the 1-2 plane has been used in writing the second integral on the right.

We may show that the constant average velocity $\bar{U}$, obtained by integrating equation (7) with respect to Y between the limits 0 and 1, is equal to $-\frac{1}{12}[f + \frac{1}{2}g]$. Therefore, the bracketed integrand on the left side of equation (11) is a constant and may be removed from the integral sign. Furthermore, since the first integral on the right is zero, we can perform the integration and solve equation (11) for f. Thus,

$$f = -\tfrac{1}{2}g - \frac{2}{\pi^2} + \frac{1}{2\pi R'}\int_0^{\pi R'} g dX \tag{12}$$

If we substitute equation (12) into equation (9) and integrate around the circumference between the limits 0 and $2\pi R'$, and note that the definite integral in equation (12) is a constant during this integration, we obtain the following expression for the dimensionless circumferential shear force per unit length of float

$$-\frac{2}{3}\int_0^{\pi R'} g dX + \frac{2R'}{\pi}$$

By substituting the expression for $g(X)$ into the above equation and utilizing equation (8), we may express the shear force per unit length of float as

$$\mu\left(\frac{\partial u}{\partial y}\right)_{y=0} = \rho_r g_0 \beta \theta_{\max}\delta \times \left[\frac{2R'}{\pi} - \frac{2}{3}\int_0^{\pi R'} C(X, t)\cos\frac{X}{R'}\, dX\right] \tag{13}$$

Notice that when there is no temperature gradient across the gap, $C(X, t) = 0$ and the equation reduces to a steady state relation.

The integral in equation (13) can be numerically evaluated at a given instant of time by computing $C(X, t)$ at a number of discrete points along one-half the fluid circumference ($0 \rightarrow \pi R'$) with temperature data obtained from the phase II thermal analysis. The product in the integrand is then computed at these points and the integration performed by a numerical integration procedure such as Simpson's rule.

Results

The foregoing analysis allows one to compute the circumferential viscous drag on a floated inertial reference device as a function of time. For example, this analysis was used to compute the viscous force on a 0.890-in-dia gyro float with a 0.005-in. gap using Fluro-Chem 3000/130/2.0750 (viscosity, centipoise/temperature, deg F/density, g per cc) at 0.6 sec after the application of a 1 deg F temperature difference across the outer diameter of the fluid annulus with a nominal temperature of 130 deg F. The results showed a value of 0.007 dyne/in. which was approximately 80 percent of the final steady state value of 0.009 dyne/in. It is noteworthy that the final steady state value and the phase II response time are dependent upon the "heat sink characteristics" of the float. The foregoing numerical results were for a particular float design and should not necessarily be regarded as typical of all floated inertial reference devices.

References

1 Goodman, L. E., and Robinson, A. R., "Thermal Drift of Floated Gyroscopes," TRANS. ASME, Vol. 79, Dec. 1957, pp. 506–508.

2 Moore, F. K., "High Speed Aerodynamics and Jet Propulsion," *Theory of Laminar Flows*, Vol. IV, Princeton University Press, 1964, pp. 530–560.

3 Grover, J. H., and Holter, W. H., "Solution of the Transient Heat Conduction Equation for an Insulated, Infinite Metal Slab," *Jet Propulsion*, Vol. 27, Dec. 1957, pp. 1249–1252.

4 Seigel, Robert, "Transient Free Convection From a Vertical Flat Plate," TRANS. ASME, Vol. 80, Feb. 1958, pp. 347–359.

Nonuniform Temperature Distribution Analysis for Long Coaxial Cylinders

R. D. CASAGRANDE[1] and C. N. SHEN[2]

Nomenclature

A = surface area, Fourier coefficients
a = radius ratio
B, C, D, L, M = constants defined in the text
E = emissive power
F = geometric factor, constant defined in the text
K = kernel in the integral expression
J = radiosity
n = zero or positive integer
q = net heat flux from the surface per unit area
r = separation distance between points
R = radius of the cylinder
S = general coordinate
T = absolute temperature
U = absorbed heat flux distribution on the convex surface of the outer cylinder
α = surface absorptivity
γ = angle defined by the radius ratio
ϵ = surface hemispherical emissivity
ϕ, λ = dummy angular coordinate variable
θ = angular coordinate of the cylinders
σ = Stephan-Boltzmann constant

[1] General Electric Company, Space Division, King of Prussia, Pennsylvania

[2] Professor of Mechanical Engineering, Rensselaer Polytechnic Institute, Troy, New York.

Contributed by the Heat Transfer Division of THE AMERICAN SOCIETY OF MECHANICAL ENGINEERS. Manuscript received by the Heat Transfer Division, May 1, 1970.

Subscripts

1 = pertains to convex side of the inner cylinder
2 = pertains to concave side of the outer cylinder
3 = pertains to a second coordinate on the outer cylinder in view of the primary outer cylinder coordinate, 2.
o = pertains to convex surface of the outer cylinder
v = viewed part of the surface
u = unseen part of the surface

Introduction

In the study of spacecraft containing two coaxial cylinders, it was found necessary to develop an analytic approach to the radiation heat transfer between the two cylinders, neither of which could be considered uniform in temperature. Analytic treatments for nonuniform radiation heat transfer for a single cylinder have been performed [1, 2, 3][3] but no work was found for the case of two coaxial cylinders with nonuniform temperatures or heat fluxes. This note presents an approach to the nonuniform radiation heat transfer between the two coaxial cylinders using a Fourier series expansion. The nonuniformity is limited to the circumferential direction, the axial direction being assumed uniform in both heat flux and temperature distribution. Another prominent assumption is that the surfaces are diffuse emitters. It should be pointed out that recent experiments [4, 5] have shown that for nonoptical surfaces, the equations of diffuse radiation produce a close correlation for real surfaces.

Analysis

The fundamental integral equations of radiant heat transfer in a general enclosure were derived in Jensen's work [6, 7] using the radiosity formulation. In the study of coaxial cylinders, subscript 1 refers to the inner cylinder and the subscript 2 refers to the outer cylinder. The integral equations are

$$J_1(S_1) = E_1(S_1) + (1 - \alpha_1)\int_{A_{2v}} J_2(S_2)K(S_1, S_2)dA_2 \quad (1)$$

$$J_2(S_2) = E(S_2) + (1 - \alpha_2)\left[\int_{A_{1v}} J_1(S_1)K(S_1, S_2)dA_1 + \int_{A_2 - A_{2u}} J_2(S_3)K(S_2, S_3)dA_{2v}\right] \quad (2)$$

where

$$K(S_i, S_j) = \frac{\cos \phi_{ij} \cos \phi_{ji}}{r_{ij}^2}, \qquad \begin{matrix}\text{for } i, j = 1, 2 \\ \text{or } i, j = 2, 3\end{matrix} \quad (3)$$

and

$$E_i = \epsilon_i \sigma T_i^4 \qquad i = 1, 2 \quad (4)$$

Utilizing Eckert's method [8] for an energy balance, the net heat fluxes leaving the surface elements are

$$q_1(S_1) = E_1(S_1) - \alpha_1 \int_{A_{2v}} J_2(S_2)K(S_1, S_2)dA_2 \quad (5)$$

$$q_2(S_2) = E_2(S_2) - \alpha_2\left[\int_{A_{1v}} J_1(S_1)K(S_1, S_2)dA_1 + \int_{A_2 - A_{2u}} J_2(S_2)K(S_2, S_3)dA_{2v}\right] \quad (6)$$

Attempts at the solution of the integral equations have led to many approximate methods. To solve the equations for an arbitrary temperature distribution, a Fourier series expansion is assumed for the radiosity. Let

$$J_i(\theta) = \sum_{n=0}^{\infty} (A_{in} \cos n\theta + B_{in} \sin n\theta), \qquad \begin{matrix}0 \le \theta \le 2\pi \\ i = 1, 2\end{matrix} \quad (7)$$

[3] Numbers in brackets designate References at end of Technical Brief.

The use of the Fourier series seems natural for cylinders and reduces the integral equations to algebraic expressions in Fourier coefficients

$$\sum_{n=0}^{\infty} (A_{1n} \cos n\theta + B_{1n} \sin n\theta) = E_1(\theta) + (1 - \alpha_1) \sum_{n=0}^{\infty} (A_{2n} \cos n\theta + B_{2n} \sin n\theta)F_n(a) \quad (8)$$

$$\sum_{n=0}^{\infty} (A_{2n} \cos n\theta + B_{2n} \sin n\theta) = E_2(\theta) + (1 - \alpha_2) \sum_{n=0}^{\infty} (A_{1n} \cos n\theta + B_{1n} \sin n\theta)aF_n(a) + (1 - \alpha_2) \sum_{n=0}^{\infty} (A_{2n} \cos n\theta + B_{2n} \sin n\theta)L_n(a) \quad (9)$$

$$q_1(\theta) = E_1(\theta) - \alpha_1 \sum_{n=0}^{\infty} (A_{2n} \cos n\theta + B_{2n} \sin n\theta)F_n(a) \quad (10)$$

$$q_2(\theta) = E_2(\theta) - \alpha_2 \sum_{n=0}^{\infty} (A_{1n} \cos n\theta + B_{1n} \sin n\theta)aF_n(a) - \alpha_2 \sum_{n=0}^{\infty} (A_{2n} \cos n\theta + B_{2n} \sin n\theta)L_n(a) \quad (11)$$

where

$$F_n(a) = \int_0^{\gamma(a)} \cos n\lambda \frac{(\cos \lambda - a)(1 - a \cos \lambda)}{(1 + a^2 - 2a \cos \lambda)^{3/2}} d\lambda \quad (12)$$

$$L_n(a) = \frac{1}{4n^2 - 1}\left\{a \cos [2n\gamma(a)] + 2n \sqrt{1 - a^2} \sin [2n\gamma(a)] - 1\right\} \quad (13)$$

$$\gamma(a) = \cos^{-1} a \quad (14)$$

and

$$a = \frac{R_1}{R_2}, \text{ the radius ratio;} \quad R_1 < R_2 \quad (15)$$

The $F_n(a)$ contains the geometric factor between the two cylinders and the $L_n(a)$ contains the geometric factor from one point on the outer cylinder to a second point on the outer cylinder visible by the first. The $F_n(a)$ and $L_n(a)$ are only dependent on the radius ratio.

The solution of the A_{in}, B_{in} depend upon what is known about the conditions around the cylinders.

Application

Consider the case of a cylindrical satellite for which $q_1(\theta)$ represents the heat flux on the inner cylinder associated with heat dissipation from electronic components. Radiation heat transfer is assumed to be the only significant mode of heat transfer between the cylinders. It is necessary to determine $E_1(\theta)$ since $T_1(\theta)$ represents the sink temperature for the electronics. An energy balance of the outer cylinder is written as

$$\epsilon_o \sigma T_2^4 = U(\theta) - q_2(\theta) \quad (16)$$

where

$U(\theta)$ represents the absorbed energy from the environment and is *known*.
$-q_2(\theta)$ represents heat addition to the outer cylinder resulting from $E_1(\theta)$ and $q_1(\theta)$.

Equation (16) can be written in terms of $E_2(\theta)$ as

$$E_2(\theta) = \frac{\epsilon_2}{\epsilon_o} U(\theta) - \frac{\epsilon_2}{\epsilon_o} q_2(\theta) \quad (17)$$

Using equation (11) for $q_2(\theta)$ results in a relation between the A_{1n}, A_{2n} and B_{1n}, B_{2n} in terms of the Fourier coefficients of $U(\theta)$. To simplify notation, let

$$M_{2n} = \left(1 + \frac{\epsilon_o}{\epsilon_2}\right)[1 - L_n(1 - \alpha_2)] - L_n\alpha_2 \quad (18)$$

$$M_{1n} = \left[\left(1 + \frac{\epsilon_o}{\epsilon_2}\right)(1 - \alpha_2) - \alpha_2\right] aF_n \quad (19)$$

With the use of equations (18) and (19) the relationships between the Fourier coefficients become

$$M_{2o}A_{2o} - M_{1o}A_{1o} = \frac{1}{2\pi}\int_0^{2\pi} U(\theta)d\theta = C_o \quad (20)$$

$$M_{2n}A_{2n} - M_{1n}A_{1n} = \frac{1}{\pi}\int_0^{2\pi} U(\theta)\cos n\theta d\theta = C_n \quad (21)$$

$$M_{2n}B_{2n} - M_{1n}B_{1n} = \frac{1}{\pi}\int_0^{2\pi} U(\theta)\sin n\theta d\theta = D_n \quad (22)$$

A second set of equations must be developed using $q_1(\theta)$. These equations can be obtained by substituting $E_1(\theta)$ defined by equation (8) into equation (10), which produces

$$q_1(\theta) = \sum_{n=0}^{\infty}\{[A_{1n} - F_n(a)A_{2n}]\cos n\theta + [B_{1n} - F_n(a)B_{2n}]\sin n\theta\} \quad (23)$$

Then, forming the Fourier coefficients,

$$A_{10} - A_{20} = \frac{1}{2\pi}\int_0^{2\pi} q_1(\theta)d\theta = P_o \quad (24)$$

$$A_{1n} - F_n(a)A_{2n} = \frac{1}{\pi}\int_0^{2\pi} q_1(\theta)\cos n\theta d\theta = P_n \quad (25)$$

$$B_{1n} - F_n(a)B_{2n} = \frac{1}{\pi}\int_0^{2\pi} q_1(\theta)\sin n\theta d\theta = Q_n \quad (26)$$

With P_n, Q_n, and C_n and D_n known, the A_{1n}, B_{1n}, A_{2n}, B_{2n} can be found by standard simultaneous algebraic expression methods of solution. The results are

$$A_{10} = A_{20} + P_0 \quad (27)$$

$$A_{1n} = A_{2n}F_n + P_n \quad (28)$$

$$B_{1n} = B_{2n}F_n + Q_n \quad (29)$$

$$A_{20} = \frac{C_0 + M_{10}P_0}{M_{20} - M_{10}} \quad (30)$$

$$A_{2n} = \frac{C_n + M_{1n}P_n}{M_{2n} - F_nM_{1n}} \quad (31)$$

$$B_{2n} = \frac{D_n + M_{1n}Q_n}{M_{2n} - F_nM_{1n}} \quad (32)$$

Having defined the Fourier coefficients, the solution to $E_1(\theta)$ is readily obtained by writing equation (8) as

$$E_1(\theta) = \sum_{n=0}^{\infty}\{[A_{1n} - (1 - \alpha_1)A_{2n}F_n(a)]\cos n\theta + [B_{1n} - (1 - \alpha_1)B_{2n}F_n(a)]\sin n\theta\} \quad (33)$$

The ready availability of time sharing computer terminals makes these series solutions practical.

Discussion

The use of the common finite element approach to the study of the radiant heat transfer between two coaxial cylinders requires a three-step procedure. First, geometric view factors between elements have to be determined for each radius ratio desired. The second step then requires the computation of the radiant exchange factors based on the ϵ_1 and ϵ_2 desired and the geometric view factors. The final step is the solution of the $n \times n$ set of simultaneous equations. In this analysis all that is required is the coding of the equations and the computation of the Fourier coefficients C_i, D_i, P_i, Q_i. The effects of changes in radius ratio and in the surface properties are easily studied as they are merely inputs to the code. While the computation of the Fourier coefficients may appear tedious, they can be obtained rapidly for any known distribution with the use of the finite Fourier coefficient formulas shown in Hildebrand [9].

References

1 Frank, I., and Gray, E. D., "Temperature Distributions in Long Cylindrical Shells," JOURNAL OF HEAT TRANSFER, TRANS. ASME, Series C, Vol. 84, 1962, pp. 190–191.

2 Usiskin, C. M., and Siegel, R., "Thermal Radiation From a Cylindrical Enclosure With Specified Wall Heat Flux," JOURNAL OF HEAT TRANSFER, TRANS. ASME, Series C, Vol. 82, 1960, pp. 369–374.

3 Sparrow, E. M., Albus, L. U., and Eckert, E. R. G., "Thermal Radiation Characteristics of Cylindrical Enclosures," JOURNAL OF HEAT TRANSFER, TRANS. ASME, Series C, Vol. 84, 1962, pp. 73–81.

4 Feldmanis, C. J., "Thermal Test of a Model Space Vehicle, Part II—Experimental Results and Comparison With Analysis," Technical Report AFFDL-TR67-42, Aug. 1968, p. 29.

5 Schornhorst, J. R., and Viskanta, R., "An Experimental Examination of the Validity of the Commonly Used Methods of Radiant Heat Transfer Analysis," ASME Paper 68-HT-42.

6 Jensen, H. H., KGL. Dansk, Videnskabernes Selskal, *Mathematish-Fysiske, Meddelser*, Vol. 24, No. 8, 1948.

7 Jakob, M., *Heat Transfer*, Vol. 2, Wiley, 1957, p. 34.

8 Eckert, and Drake, *Heat and Mass Transfer*, McGraw-Hill Publishing Co., 1959.

9 Hildebrand, F. B., *Introduction to Numerical Analysis*, McGraw-Hill Publishing Co., 1956.

Free Convection From a Two-Dimensional Finite Horizontal Plate

CHING-JEN CHEN[1]

FOR a horizontal plate when heated facing downward or cooled facing upward, were it not for edge effects from a finite plate or nonisothermal wall temperature, there would be no convection current since the fluid near the plate would be in equilibrium with the gravitational force. However, when the plate is finite there is always some fluid movement as reported by Kraus [1].[2] Kraus observed that for a heated plate facing downward, the air moves toward the plate and diverges to the edge exhibiting a stagnation-point flow. This was further confirmed by Schmidt's [2] photograph of a heated horizontal plate facing downward. Theoretically, Suriano and Yang [3] numerically solved the problem of a finite three-dimensional horizontal plate situated in an infinite fluid for small and moderate Grashof numbers. They showed that for the heated plate facing downward the fluid motion does exhibit stagnation-point flow as observed by Kraus. In this note, the free convection from a two-dimensional finite horizontal plate which is heated facing downward, for large Grashof numbers, is solved by treating the problem as a stagnation-point flow.

[1] Associate Professor of Mechanical Engineering, The University of Iowa, Iowa City, Iowa. Assoc. Mem. ASME.

[2] Numbers in brackets designate References at end of Technical Brief.

Contributed by the Heat Transfer Division of THE AMERICAN SOCIETY OF MECHANICAL ENGINEERS. Manuscript received by the Heat Transfer Division, March 31, 1969; revised manuscript received October 14, 1969.

Using equation (11) for $q_2(\theta)$ results in a relation between the A_{1n}, A_{2n} and B_{1n}, B_{2n} in terms of the Fourier coefficients of $U(\theta)$. To simplify notation, let

$$M_{2n} = \left(1 + \frac{\epsilon_o}{\epsilon_2}\right)[1 - L_n(1 - \alpha_2)] - L_n\alpha_2 \quad (18)$$

$$M_{1n} = \left[\left(1 + \frac{\epsilon_o}{\epsilon_2}\right)(1 - \alpha_2) - \alpha_2\right] aF_n \quad (19)$$

With the use of equations (18) and (19) the relationships between the Fourier coefficients become

$$M_{2o}A_{2o} - M_{1o}A_{1o} = \frac{1}{2\pi}\int_0^{2\pi} U(\theta)d\theta = C_o \quad (20)$$

$$M_{2n}A_{2n} - M_{1n}A_{1n} = \frac{1}{\pi}\int_0^{2\pi} U(\theta)\cos n\theta d\theta = C_n \quad (21)$$

$$M_{2n}B_{2n} - M_{1n}B_{1n} = \frac{1}{\pi}\int_0^{2\pi} U(\theta)\sin n\theta d\theta = D_n \quad (22)$$

A second set of equations must be developed using $q_1(\theta)$. These equations can be obtained by substituting $E_1(\theta)$ defined by equation (8) into equation (10), which produces

$$q_1(\theta) = \sum_{n=0}^{\infty}\{[A_{1n} - F_n(a)A_{2n}]\cos n\theta + [B_{1n} - F_n(a)B_{2n}]\sin n\theta\} \quad (23)$$

Then, forming the Fourier coefficients,

$$A_{10} - A_{20} = \frac{1}{2\pi}\int_0^{2\pi} q_1(\theta)d\theta = P_o \quad (24)$$

$$A_{1n} - F_n(a)A_{2n} = \frac{1}{\pi}\int_0^{2\pi} q_1(\theta)\cos n\theta d\theta = P_n \quad (25)$$

$$B_{1n} - F_n(a)B_{2n} = \frac{1}{\pi}\int_0^{2\pi} q_1(\theta)\sin n\theta d\theta = Q_n \quad (26)$$

With P_n, Q_n, and C_n and D_n known, the A_{1n}, B_{1n}, A_{2n}, B_{2n} can be found by standard simultaneous algebraic expression methods of solution. The results are

$$A_{10} = A_{20} + P_0 \quad (27)$$

$$A_{1n} = A_{2n}F_n + P_n \quad (28)$$

$$B_{1n} = B_{2n}F_n + Q_n \quad (29)$$

$$A_{20} = \frac{C_0 + M_{10}P_0}{M_{20} - M_{10}} \quad (30)$$

$$A_{2n} = \frac{C_n + M_{1n}P_n}{M_{2n} - F_nM_{1n}} \quad (31)$$

$$B_{2n} = \frac{D_n + M_{1n}Q_n}{M_{2n} - F_nM_{1n}} \quad (32)$$

Having defined the Fourier coefficients, the solution to $E_1(\theta)$ is readily obtained by writing equation (8) as

$$E_1(\theta) = \sum_{n=0}^{\infty}\{[A_{1n} - (1 - \alpha_1)A_{2n}F_n(a)]\cos n\theta + [B_{1n} - (1 - \alpha_1)B_{2n}F_n(a)]\sin n\theta\} \quad (33)$$

The ready availability of time sharing computer terminals makes these series solutions practical.

Discussion

The use of the common finite element approach to the study of the radiant heat transfer between two coaxial cylinders requires a three-step procedure. First, geometric view factors between elements have to be determined for each radius ratio desired. The second step then requires the computation of the radiant exchange factors based on the ϵ_1 and ϵ_2 desired and the geometric view factors. The final step is the solution of the $n \times n$ set of simultaneous equations. In this analysis all that is required is the coding of the equations and the computation of the Fourier coefficients C_i, D_i, P_i, Q_i. The effects of changes in radius ratio and in the surface properties are easily studied as they are merely inputs to the code. While the computation of the Fourier coefficients may appear tedious, they can be obtained rapidly for any known distribution with the use of the finite Fourier coefficient formulas shown in Hildebrand [9].

References

1 Frank, I., and Gray, E. D., "Temperature Distributions in Long Cylindrical Shells," JOURNAL OF HEAT TRANSFER, TRANS. ASME, Series C, Vol. 84, 1962, pp. 190–191.

2 Usiskin, C. M., and Siegel, R., "Thermal Radiation From a Cylindrical Enclosure With Specified Wall Heat Flux," JOURNAL OF HEAT TRANSFER, TRANS. ASME, Series C, Vol. 82, 1960, pp. 369–374.

3 Sparrow, E. M., Albus, L. U., and Eckert, E. R. G., "Thermal Radiation Characteristics of Cylindrical Enclosures," JOURNAL OF HEAT TRANSFER, TRANS. ASME, Series C, Vol. 84, 1962, pp. 73–81.

4 Feldmanis, C. J., "Thermal Test of a Model Space Vehicle, Part II—Experimental Results and Comparison With Analysis," Technical Report AFFDL-TR67-42, Aug. 1968, p. 29.

5 Schornhorst, J. R., and Viskanta, R., "An Experimental Examination of the Validity of the Commonly Used Methods of Radiant Heat Transfer Analysis," ASME Paper 68-HT-42.

6 Jensen, H. H., KGL. Dansk, Videnskabernes Selskal, *Mathematish-Fysiske, Meddelser*, Vol. 24, No. 8, 1948.

7 Jakob, M., *Heat Transfer*, Vol. 2, Wiley, 1957, p. 34.

8 Eckert, and Drake, *Heat and Mass Transfer*, McGraw-Hill Publishing Co., 1959.

9 Hildebrand, F. B., *Introduction to Numerical Analysis*, McGraw-Hill Publishing Co., 1956.

Free Convection From a Two-Dimensional Finite Horizontal Plate

CHING-JEN CHEN[1]

FOR a horizontal plate when heated facing downward or cooled facing upward, were it not for edge effects from a finite plate or nonisothermal wall temperature, there would be no convection current since the fluid near the plate would be in equilibrium with the gravitational force. However, when the plate is finite there is always some fluid movement as reported by Kraus [1].[2] Kraus observed that for a heated plate facing downward, the air moves toward the plate and diverges to the edge exhibiting a stagnation-point flow. This was further confirmed by Schmidt's [2] photograph of a heated horizontal plate facing downward. Theoretically, Suriano and Yang [3] numerically solved the problem of a finite three-dimensional horizontal plate situated in an infinite fluid for small and moderate Grashof numbers. They showed that for the heated plate facing downward the fluid motion does exhibit stagnation-point flow as observed by Kraus. In this note, the free convection from a two-dimensional finite horizontal plate which is heated facing downward, for large Grashof numbers, is solved by treating the problem as a stagnation-point flow.

[1] Associate Professor of Mechanical Engineering, The University of Iowa, Iowa City, Iowa. Assoc. Mem. ASME.

[2] Numbers in brackets designate References at end of Technical Brief.

Contributed by the Heat Transfer Division of THE AMERICAN SOCIETY OF MECHANICAL ENGINEERS. Manuscript received by the Heat Transfer Division, March 31, 1969; revised manuscript received October 14, 1969.

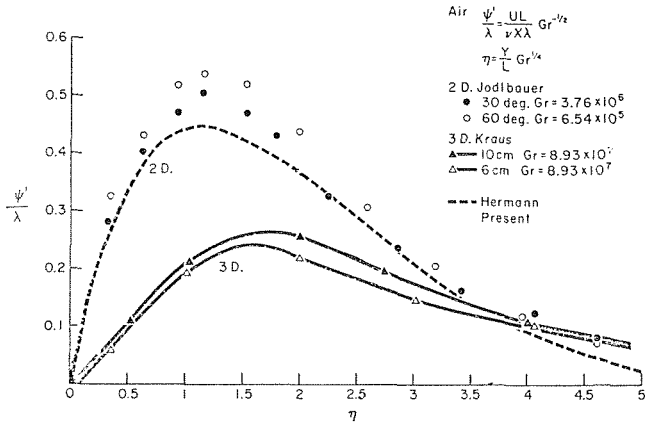

Fig. 1 **Comparison of theoretical velocity component with experimental data**

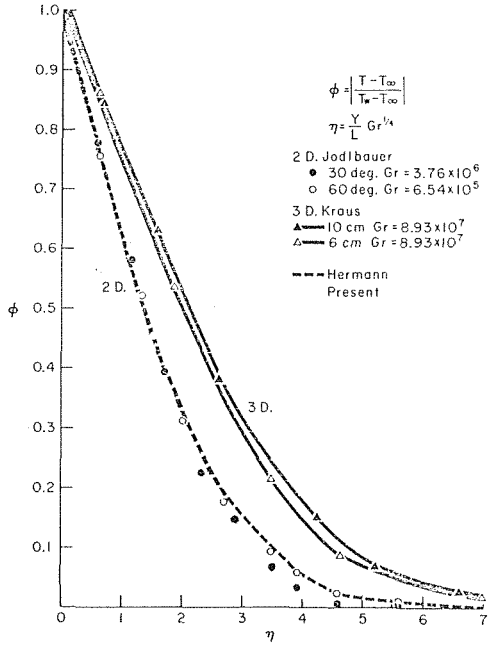

Fig. 2 Comparison of theoretical temperature distribution with experimental data

Consider the comparison between a two-dimensional blunt body of a local radius R and a horizontal flat plate with a width L. Let X and Y be the coordinates measured along and outward normal to the surface respectively. We note from Kraus' measurement that the isothermal lines near the horizontal plate are very similar to those of blunt bodies. This similarity can also be seen from photographs of Schmidt [2]. The radius of the isothermal curves, R, depends on the plate width, L, and obviously increases with it. For definiteness, the radius of the mean temperature line between the wall and ambient temperature will be taken to be R. The existence of a finite radius, R, represents the edge effect of a finite horizontal plate. For Grashof numbers of 10^5 or larger, the value of R obtained from the Schmidt's [2] photographs and from Weise's [4] measurement shows that R equals approximately 2.5 L. When the radius of the isothermal curve is identified with the radius of the blunt body, the governing equations for blunt bodies may approximately be used for the finite flat plate. The edge effect is then included through the gravity term in the X-momentum equation. Let

$$x = \frac{X}{L}, \qquad y = \frac{Y}{L}, \qquad u = \frac{U}{U_r}, \qquad v = \frac{V}{U_r},$$

$$\theta = \left|\frac{T - T_\infty}{T_w - T_\infty}\right|, \qquad U_r = \sqrt{\beta|g(T_w - T_\infty)|L} \quad (1)$$

$$p = \frac{P}{\rho U_r^2}, \qquad \lambda = \frac{L}{R}, \qquad \mathrm{G}_r = \frac{\beta|g(T_w - T_\infty)|L^3}{\nu^2}, \qquad \mathrm{Pr} = \frac{C_p\mu}{\kappa}$$

where λ is the edge factor for the two-dimensional finite horizontal plate and equals unity for the blunt body. The dimensionless governing equations are:

$$\frac{\partial u}{\partial x} + \frac{\partial v}{\partial y} = 0 \quad (2)$$

$$u\frac{\partial u}{\partial x} + v\frac{\partial u}{\partial y} = -\frac{\partial p}{\partial x} + \lambda\epsilon\theta x + \frac{1}{\sqrt{G_r}}\left(\frac{\partial^2 u}{\partial x^2} + \frac{\partial^2 u}{\partial y^2}\right) \quad (3)$$

$$u\frac{\partial v}{\partial x} + v\frac{\partial v}{\partial y} = -\frac{\partial p}{\partial y} - \epsilon\theta + \frac{1}{\sqrt{G_r}}\left(\frac{\partial^2 v}{\partial x^2} + \frac{\partial^2 v}{\partial y^2}\right) \quad (4)$$

$$u\frac{\partial \theta}{\partial x} + v\frac{\partial \theta}{\partial y} = \frac{1}{\mathrm{Pr}\sqrt{G_r}}\left(\frac{\partial^2 \theta}{\partial x^2} + \frac{\partial^2 \theta}{\partial y^2}\right) \quad (5)$$

ϵ equals one when the blunt bodies are cooled facing upward or when heated facing downward. ϵ is negative one when the blunt bodies are cooled facing downward or when heated facing upward. For large Grashof numbers, the reduction of the governing equations to the ordinary differential equations is made by the following transformation:

$$\eta = \mathrm{G}_r^{1/4}y, \qquad v = -\mathrm{G}_r^{1/4}\psi(\eta), \qquad u = x\psi'(\eta),$$
$$\theta(y) = \phi(\eta), \qquad p(y) = \mathrm{G}_r^{1/4}\pi(\eta) \quad (6)$$

where the prime denotes differentiation with respect to η. The governing equations for $\epsilon = 1$ immediately transforms to

$$\psi''' + \psi\psi'' - \psi'^2 + \lambda\phi = 0 \quad (7)$$

$$\frac{1}{\mathrm{G}_r^{1/4}}(\psi'' + \psi\psi') + \phi + \pi' = 0 \quad (8)$$

$$\phi'' + \mathrm{Pr}\psi\phi' = 0 \quad (9)$$

The boundary conditions are then

$$\psi(0) = \psi'(0) = 0, \qquad \phi(0) = 1, \qquad \phi''(0) = 0$$
$$\text{or} \quad u = v = 0, \qquad \theta = 1, \qquad y = 0 \quad (10)$$

$$\psi'(\infty) = \pi(\infty) = \phi(\infty) = 0$$
$$\text{or} \quad u = \theta = p = 0, \qquad y \to \infty \quad (11)$$

The problem may be correlated with the blunt-body solutions of Braun, Ostrach, and Heighway [5] or Hermann [6] by the following changes of variables: For low Prandtl numbers, let $F = \sqrt{\mathrm{Pr}}\,\psi$, $H = \theta$, and $\zeta = \sqrt{\mathrm{Pr}}\,\eta$. Then equations (7) and (9) are transformed into equation (46) of reference [5] when $m = \infty$. For large Prandtl numbers, let $F = \mathrm{Pr}^{-3/4}\psi$, $H = \theta$, and $\zeta = \mathrm{Pr}^{-1/4}\eta$. Equations (7) and (9) are transformed into equation (53) of reference [5]. For the two-dimensional finite flat plate, the solution is obtained by letting λ equal to one, and then substituting R equal to 2.5 L to the blunt-body solutions of references [5, 6].

In Figs. 1 and 2, the theoretical velocity and temperature profiles, converted from Hermann's [6] solution, are compared with the experimental measurements of Jodlbauer [7] for a cylindrical body. There is no experimental data available for the two-dimensional finite plate case. However, data for the three-dimensional horizontal rectangular plate, as measured by Kraus [1], are included for comparison. It is noted that the three-dimensional

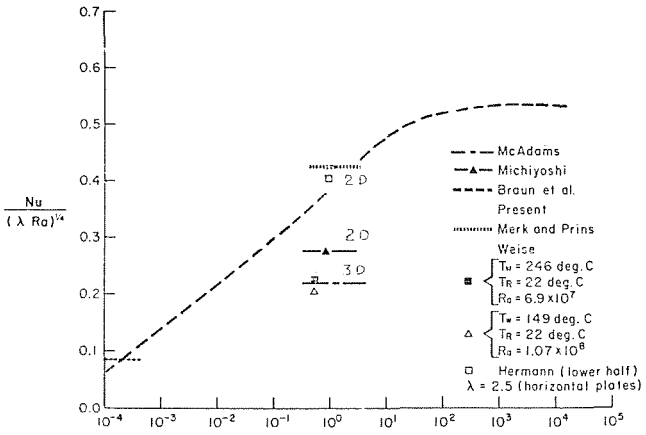

Fig. 3 Comparison of several heat-transfer calculations

case gives a smaller maximum velocity and temperature gradient near the wall, but a larger velocity and temperature boundary-layer thickness than that of the two-dimensional case. Fig. 3 shows the comparison of other related results from references [7–11] with Braun, Ostrach, and Heighway [5] and Hermann [6]. It is interesting to note that for Prandtl numbers near one, all solutions agree very well for the two-dimensional case including the lower-half average value of the horizontal cylinder [6], with the exception of the solution for an ellipsoid given by Michiyoshi [9]. Michiyoshi indicated that his two-dimensional result agrees well with Weise's experimental measurements, but it should be emphasized that Weise's experiment was three-dimensional. With λ equal to 2.5, the three-dimensional data obtained by Weise are also given in Fig. 3, which is already suggested by Fishenden and Saunders [10] and McAdams [11]. From Fig. 3, it is seen that the two-dimensional case should give a higher value of $\mathrm{Nu}/(\mathrm{Ra}\lambda)^{-1/4}$ than the three-dimensional one.

In summary, for heat-transfer calculations of the two-dimensional case with large Grashof numbers ($G_r > 10^5$) the present result or that of references [5, 6] should be used for all Prandtl numbers when λ is taken as 2.5. The formula suggested by Fishenden and Saunders [10] may be used only for the three-dimensional plate.

References

1 Kraus, von W., "Temperatur- und Geschwindigkeitsfeld bei freier Konvektion un eine wagerechte quadratische Platte," *Physik Z.*, Vol. 41, 1940, pp. 126–150.

2 Schmidt, E., *Schlierenaufnahmen des Temperaturefeldes*, Forsch. 3, Heft 4, 1932, pp. 181–189.

3 Suriano, F. J., and Yang, K. T., "Laminar Free Convection about Vertical and Horizontal Plates at Small and Moderate Grashof Numbers," *International Journal of Heat and Mass Transfer*, Vol. 11, 1968, pp. 473–490.

4 Weise, R., *Warmeubergang durch freie Konvektion*, Forsch. 6, Heft 6, 1935, pp. 281–292.

5 Braun, W. H., Ostrach, S., and Heighway, J. E., "Free-Convection Similarity Flows about Two-Dimensional and Axisymmetric Bodies with Closed Lower Ends," *International Journal of Heat and Mass Transfer*, Vol. 2, 1961, pp. 121–135.

6 Hermann, R., "Warmeubergang bei freier Stromung am wagrechten Zylinder in zweiatomigen Gasen," *VDI*, Forsch. 379, 1936, pp. 1–24.

7 Jodlbauer, K., *Das Temperatur- und Geschwindigkeitsfeld*, Forsch. 4, Heft 4, 1933, pp. 157–172.

8 Merk, H. J., and Prins, J. A., "Thermal Convection in Laminar Boundary Layer," Appl. Aci. Res. A 4, pt. 1, 11; 11, 195; 11, 207, 1953–54.

9 Michiyoshi, I., "Heat Transfer from an Inclined Thin Flat Plate by Natural Convection," *Bulletin of JSME*, Vol. 7, No. 28, 1964, pp. 745–750.

10 Fishenden, M., and Saunders, O. A., *An Introduction to Heat Transfer*, Oxford Univ. Press, 1950, p. 95.

11 McAdams, W. H., *Heat Transmission*, McGraw-Hill, New York, 1954, p. 180.

Wall Recombination Heat Transfer in a Dissociated Slip Flow

D. M. COGAN[1]

Introduction

THE heat transfer to a body traveling in a dissociated or ionized gas depends on the amount of recombination occurring in the vicinity of the body as well as the normal fluid dynamic heating. Fay and Riddell [1][2] have shown that over a wide range of conditions recombination occurs only at the surface, in which case, the recombination heat transfer depends on the diffusion controlled concentration of dissociated species close to the wall and the remainder of the flow field is chemically frozen. Analytic solutions of the diffusion equations have been obtained by several authors including Chambré and Acrivos [2], who considered the case of a flat plate, and Freeman and Simpkins [3], who extended this to flow over a wedge. In obtaining these solutions it was assumed that the layer in which diffusion occurs is thin compared with the boundary layer, and thus the analysis is strictly valid in the limit of Schmitt number (Sc) tending to infinity. Consistent with this assumption a Fage and Falkner velocity distribution without slip was used to determine the flow within the diffusion layer.

In rarefied flows considerable velocity slip can occur in the vicinity of a leading edge, and under these circumstances an alternative to the linear Fage and Falkner variation of velocity can be used. Provided the Schmitt number and the slip velocity at the wall are both large, the velocity within the diffusion region will be approximately constant. Using this model the wall recombination heat transfer has been calculated and presented in this paper.

Analysis

The equation for the conservation of species, in a two-dimensional flow, of an ideal dissociating gas comprised of a binary mixture is

$$\rho u \frac{\partial \alpha}{\partial x} + \rho v \frac{\partial \alpha}{\partial y} = \frac{\partial}{\partial y}\left(\rho D_{12} \frac{\partial \alpha}{\partial y}\right) + \dot{w}_A \tag{1}$$

where α is the mass fraction of the dissociated constituent [4]. As explained in the Introduction it is a valid assumption to consider the gas to be chemically frozen. There is then no production of species and $\dot{w}_A$ is identically zero.

The recombination rate at the wall will be assumed to be proportional to the concentration, and the concentration gradient at the wall will be given by Fick's law as

$$D_w \left.\frac{\partial \alpha}{\partial y}\right|_w = k_w \alpha_w, \tag{2}$$

k_w being the wall catalytic rate constant.

Freeman [3] solved equation (1) together with those for momentum and energy by using the Illingworth transformations and the streamwise coordinate transformation

$$\zeta = \frac{k_w \,\mathrm{Sc}\, (2\xi)^{1/2}}{\mu_w u_e} \tag{3}$$

for the case of a "cold wall" when $\frac{\rho\mu}{\rho_e \mu_e}$ and Sc can reasonably be

---

[1] Department of Aeronautics, Imperial College of Science and Technology, London, England.

[2] Numbers in brackets designate References at end of Technical Brief.

Contributed by the Heat Transfer Division of THE AMERICAN SOCIETY OF MECHANICAL ENGINEERS. Manuscript received by the Heat Transfer Division, December 3, 1969; revised manuscript received, May 19, 1970.

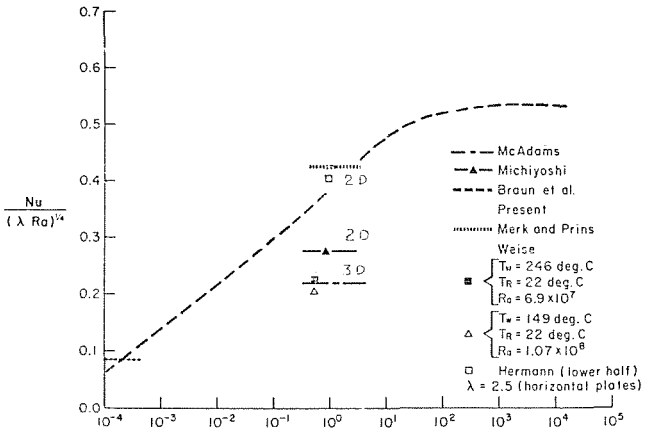

Fig. 3 Comparison of several heat-transfer calculations

case gives a smaller maximum velocity and temperature gradient near the wall, but a larger velocity and temperature boundary-layer thickness than that of the two-dimensional case. Fig. 3 shows the comparison of other related results from references [7–11] with Braun, Ostrach, and Heighway [5] and Hermann [6]. It is interesting to note that for Prandtl numbers near one, all solutions agree very well for the two-dimensional case including the lower-half average value of the horizontal cylinder [6], with the exception of the solution for an ellipsoid given by Michiyoshi [9]. Michiyoshi indicated that his two-dimensional result agrees well with Weise's experimental measurements, but it should be emphasized that Weise's experiment was three-dimensional. With λ equal to 2.5, the three-dimensional data obtained by Weise are also given in Fig. 3, which is already suggested by Fishenden and Saunders [10] and McAdams [11]. From Fig. 3, it is seen that the two-dimensional case should give a higher value of $\mathrm{Nu}/(\mathrm{Ra}\lambda)^{-1/4}$ than the three-dimensional one.

In summary, for heat-transfer calculations of the two-dimensional case with large Grashof numbers ($G_r > 10^5$) the present result or that of references [5, 6] should be used for all Prandtl numbers when λ is taken as 2.5. The formula suggested by Fishenden and Saunders [10] may be used only for the three-dimensional plate.

References

1 Kraus, von W., "Temperatur- und Geschwindigkeitsfeld bei freier Konvektion un eine wagerechte quadratische Platte," *Physik Z.*, Vol. 41, 1940, pp. 126–150.

2 Schmidt, E., *Schlierenaufnahmen des Temperaturefeldes*, Forsch. 3, Heft 4, 1932, pp. 181–189.

3 Suriano, F. J., and Yang, K. T., "Laminar Free Convection about Vertical and Horizontal Plates at Small and Moderate Grashof Numbers," *International Journal of Heat and Mass Transfer*, Vol. 11, 1968, pp. 473–490.

4 Weise, R., *Warmeubergang durch freie Konvektion*, Forsch. 6, Heft 6, 1935, pp. 281–292.

5 Braun, W. H., Ostrach, S., and Heighway, J. E., "Free-Convection Similarity Flows about Two-Dimensional and Axisymmetric Bodies with Closed Lower Ends," *International Journal of Heat and Mass Transfer*, Vol. 2, 1961, pp. 121–135.

6 Hermann, R., "Warmeubergang bei freier Stromung am wagrechten Zylinder in zweiatomigen Gasen," *VDI*, Forsch. 379, 1936, pp. 1–24.

7 Jodlbauer, K., *Das Temperatur- und Geschwindigkeitsfeld*, Forsch. 4, Heft 4, 1933, pp. 157–172.

8 Merk, H. J., and Prins, J. A., "Thermal Convection in Laminar Boundary Layer," Appl. Aci. Res. A 4, pt. 1, 11; 11, 195; 11, 207, 1953–54.

9 Michiyoshi, I., "Heat Transfer from an Inclined Thin Flat Plate by Natural Convection," *Bulletin of JSME*, Vol. 7, No. 28, 1964, pp. 745–750.

10 Fishenden, M., and Saunders, O. A., *An Introduction to Heat Transfer*, Oxford Univ. Press, 1950, p. 95.

11 McAdams, W. H., *Heat Transmission*, McGraw-Hill, New York, 1954, p. 180.

Wall Recombination Heat Transfer in a Dissociated Slip Flow

D. M. COGAN[1]

Introduction

THE heat transfer to a body traveling in a dissociated or ionized gas depends on the amount of recombination occurring in the vicinity of the body as well as the normal fluid dynamic heating. Fay and Riddell [1][2] have shown that over a wide range of conditions recombination occurs only at the surface, in which case, the recombination heat transfer depends on the diffusion controlled concentration of dissociated species close to the wall and the remainder of the flow field is chemically frozen. Analytic solutions of the diffusion equations have been obtained by several authors including Chambré and Acrivos [2], who considered the case of a flat plate, and Freeman and Simpkins [3], who extended this to flow over a wedge. In obtaining these solutions it was assumed that the layer in which diffusion occurs is thin compared with the boundary layer, and thus the analysis is strictly valid in the limit of Schmitt number (Sc) tending to infinity. Consistent with this assumption a Fage and Falkner velocity distribution without slip was used to determine the flow within the diffusion layer.

In rarefied flows considerable velocity slip can occur in the vicinity of a leading edge, and under these circumstances an alternative to the linear Fage and Falkner variation of velocity can be used. Provided the Schmitt number and the slip velocity at the wall are both large, the velocity within the diffusion region will be approximately constant. Using this model the wall recombination heat transfer has been calculated and presented in this paper.

Analysis

The equation for the conservation of species, in a two-dimensional flow, of an ideal dissociating gas comprised of a binary mixture is

$$\rho u \frac{\partial \alpha}{\partial x} + \rho v \frac{\partial \alpha}{\partial y} = \frac{\partial}{\partial y}\left(\rho D_{12} \frac{\partial \alpha}{\partial y}\right) + \dot{w}_A \tag{1}$$

where α is the mass fraction of the dissociated constituent [4]. As explained in the Introduction it is a valid assumption to consider the gas to be chemically frozen. There is then no production of species and $\dot{w}_A$ is identically zero.

The recombination rate at the wall will be assumed to be proportional to the concentration, and the concentration gradient at the wall will be given by Fick's law as

$$D_w \left.\frac{\partial \alpha}{\partial y}\right|_w = k_w \alpha_w, \tag{2}$$

k_w being the wall catalytic rate constant.

Freeman [3] solved equation (1) together with those for momentum and energy by using the Illingworth transformations and the streamwise coordinate transformation

$$\zeta = \frac{k_w \,\mathrm{Sc}\, (2\xi)^{1/2}}{\mu_w u_e} \tag{3}$$

for the case of a "cold wall" when $\frac{\rho\mu}{\rho_e \mu_e}$ and Sc can reasonably be

---

[1] Department of Aeronautics, Imperial College of Science and Technology, London, England.

[2] Numbers in brackets designate References at end of Technical Brief.

Contributed by the Heat Transfer Division of THE AMERICAN SOCIETY OF MECHANICAL ENGINEERS. Manuscript received by the Heat Transfer Division, December 3, 1969; revised manuscript received, May 19, 1970.

taken to be constant and $\frac{\rho_e}{\rho_w} \ll 1$. Under these conditions the momentum and energy equations are those of a chemically inert gas and are decoupled from the concentration equation (1) which can be rewritten as

$$\frac{\partial^2 Z}{\partial \eta^2} + \mathrm{Sc}\, f \frac{\partial Z}{\partial \eta} - \mathrm{Sc}\, \zeta \frac{\partial f}{\partial \eta} \frac{\partial Z}{\partial \zeta} = 0, \tag{4}$$

with the boundary conditions

$$\frac{\partial Z}{\partial \eta}(\zeta, 0) = \zeta Z(\zeta, 0),$$

$$Z(\zeta, \infty) = 1.$$

Z is the reduced mass fraction $\frac{\alpha}{\alpha_e}$ which for the frozen flow is $\frac{\alpha}{\alpha_\infty}$.

Equation (4) can be solved if we specify the velocity distribution within the diffusion layer, i.e., we feed in a solution to the decoupled momentum and energy equations. Adopting the Fage and Falkner approximation and including slip

$$f(\eta) = \frac{u_w}{u_e}\eta + \frac{1}{2}\eta^2 f''(0). \tag{5}$$

This assumption implies that the diffusion layer is thin compared with the viscous layer, i.e., $\mathrm{Sc} \gg 1$.[3] For the present analysis we will consider a boundary layer in which significant slip occurs, i.e., $\frac{u_w}{u_e} = 0(1)$ and as $f''(0)$ is also $0(1)$, the first term on the right-hand side of (5) dominates as η is small in the diffusion layer.

In physical terms the present assumption implies that within the thin diffusion layer adjacent to the wall, the velocity is essentially constant and equal to the slip velocity. This requires the slip velocity to be large, and thus the solution is asymptotically valid as the leading edge is approached.

The value of u_w is needed for the calculation and is obtained from the boundary layer equation assuming Maxwellian slip, i.e.,

$$u_w = \bar{\sigma}\left(\frac{\pi}{2}\right)^{1/2} \frac{\mu}{\sqrt{P\rho}} \left.\frac{\partial u}{\partial y}\right|_w \tag{6}$$

where $\bar{\sigma} = \frac{2-\sigma}{\sigma}$; σ being the tangential momentum accommodation coefficient.

Substitution of $\frac{u_w}{u_e}\eta$ for $f(\eta)$ in equation (3), using equation (6) to eliminate $\frac{u_w}{u_e}$ yields

$$Z_{\eta\eta} + \frac{1}{a}\left(\frac{\eta}{\zeta} Z_\eta - Z_\zeta\right) = 0, \tag{7}$$

where $\frac{1}{a} = \left(\frac{\pi}{2}\right)^{1/2} \mathrm{Sc}^2 \bar{\sigma} \left(\frac{k_w^2}{RT_w}\right)^{1/2} f''(0)$ and is assumed to be constant.

The problem may be simplified by a further change of variables. If $\epsilon = \eta\zeta$, equation (7) may be reduced to

$$\zeta^2 \frac{\partial^2 Z}{\partial \epsilon^2} = \frac{1}{a}\frac{\partial Z}{\partial \zeta}. \tag{8}$$

Finally, the streamwise coordinate may be rescaled such that $\theta = \frac{\zeta^3}{3}$, and equation (8) becomes

$$\frac{\partial^2 Z}{\partial \epsilon^2} = \frac{1}{a}\frac{\partial Z}{\partial \theta}. \tag{9}$$

This is subject to the boundary conditions

$$\frac{\partial Z}{\partial \epsilon} = Z_w \tag{10}$$

when $\epsilon = 0$ from equation (4) and $Z \to 1$ at the leading edge. (11)

The problem is now formally identical to that of time-dependent diffusion in a half space and hence may be solved by the application of Laplace transforms.

If $\bar{Z}(P, \epsilon)$ is the Laplace transform of $Z(\theta, \epsilon)$, then the transform of equation (9), with equation (11) substituted, is

$$a\frac{\delta^2 \bar{Z}}{\delta \epsilon^2} = P\bar{Z} - 1,$$

the solution of which is

$$\bar{Z} = \frac{1}{P} + C\exp\left(-\left[\frac{P}{a}\right]^{1/2}\epsilon\right). \tag{12}$$

The constant C is eliminated by differentiating equation (12) and substituting the result into the transform of equation (10), and this yields

$$\bar{Z} = \frac{1}{P} - \frac{Z_w}{P}\left(\frac{a}{P}\right)^{1/2}\exp\left(-\left[\frac{P}{a}\right]^{1/2}\epsilon\right).$$

Inverting this, with the aid of the table of transforms edited by Erdelyi [6], gives

$$Z = 1 - Z_w\left\{2\left[\frac{a\theta}{\pi}\right]^{1/2}\exp\left[\frac{-\epsilon^2}{4a\theta}\right] - \epsilon\,\mathrm{erfc}\left[\frac{\epsilon}{2(a\theta)^{1/2}}\right]\right\}. \tag{13}$$

It will be seen that at large values of ϵ, with θ finite, corresponding to large distances from the wall, the solution is invalid, since equation (13) reduces to $Z \simeq 1 + \epsilon Z_w$, which is impossible as $Z \leqslant 1$. This failure is not surprising since the assumption that the velocity is constant, at its wall value, is obviously violated far from the wall.

No such difficulty exists at the wall as $\epsilon = 0$; then equation (13) reduces to

$$Z_w = \frac{1}{1 + \left(\frac{4a\theta}{\pi}\right)^{1/2}}. \tag{14}$$

Discussion

As the formulation of the present work is different from that preceding it, a direct comparison in terms of ζ or θ is not possible. However, as the present analysis is concerned with wall concentration in a rarefied flow, it is appropriate to compare the solutions in terms of the viscous interaction parameter, $\bar{V}_\infty$.

Equation (14) may be expressed as

$$Z_w = \left\{1 + \left[\frac{16}{3}\frac{\mathrm{Sc}}{f''(0)\bar{\sigma}}\frac{k_w^2}{RT_w}\right]^{1/2} \times \left[\frac{1}{\pi\gamma}\frac{C_\infty \mu_e}{A^2\mu_w}\frac{\rho_e u_e}{\rho_\infty u_\infty}\right]^{3/4}\frac{1}{\bar{V}_\infty^{3/2}}\right\}^{-1}, \tag{15}$$

where

$$\bar{V}_\infty = \frac{C_\infty M_\infty}{(R_{e_{x_\infty}})^{1/2}},$$

[3] For the case of no slip, Freeman [5] has compared this result with a more detailed analysis for $\mathrm{Sc} = 0(1)$ and shown that no serious error is introduced by using the Fage and Falkner approximation even when $\mathrm{Sc} \simeq 0.5$. It would appear that the method is insensitive to the requirement of $\mathrm{Sc} \gg 1$.

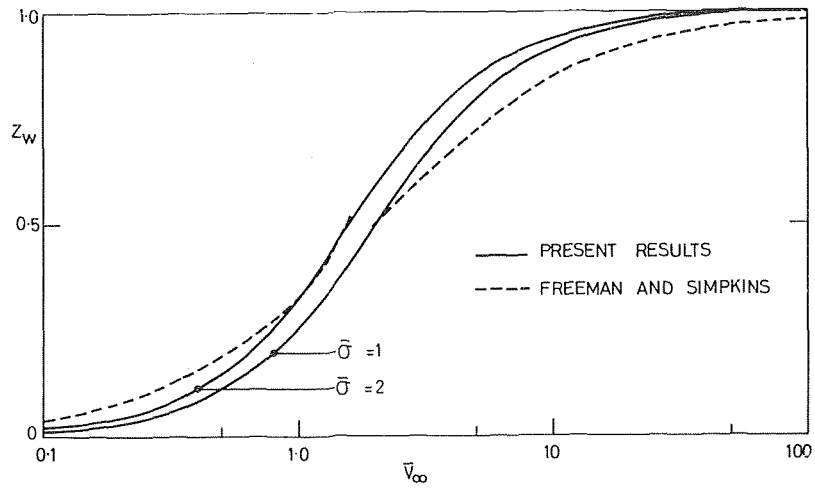

Fig. 1 Species concentration at a cold, highly catalytic wall

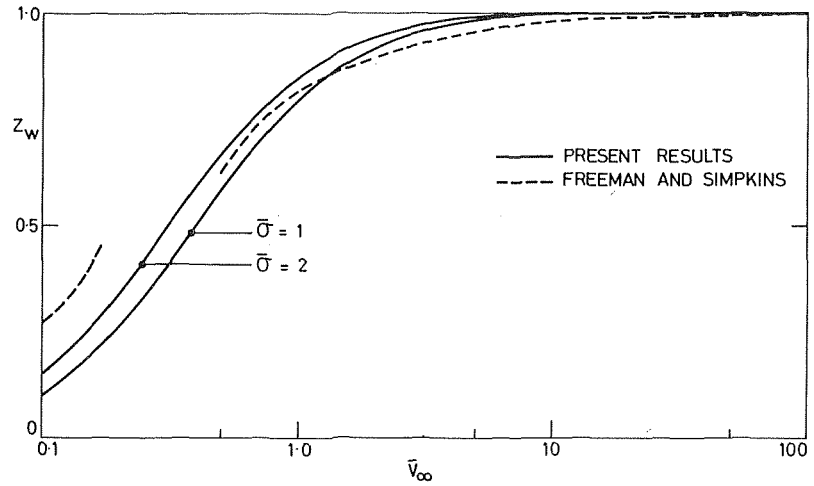

Fig. 2 Species concentration at a hot, weakly catalytic wall

$$C_\infty = \frac{T_\infty \mu_w}{T_w \mu_\infty},$$

and

$$A = \frac{u_e}{u_\infty}.$$

Freeman's results for a flat plate are presented as series solutions in terms of $\frac{\zeta}{K}$ and $\frac{K}{\zeta}$ where

$$K = \frac{2}{3}\left[\frac{1}{6}\,\mathrm{Sc}\, f''(0)\right]^{1/3} \frac{\Gamma\left(\frac{2}{3}\right)}{\Gamma\left(\frac{4}{3}\right)}.$$

The streamwise coordinate may be expressed in terms of the viscous interaction parameter as

$$\frac{\zeta}{K} = \frac{3}{2}\,\frac{\Gamma\left(\frac{4}{3}\right)}{\Gamma\left(\frac{2}{3}\right)}\left(\frac{6\,\mathrm{Sc}^2}{f''(0)}\right)^{1/3}\left(\frac{2C_\infty \mu_e}{A^2\gamma\mu_w}\,\frac{\rho_e u_e}{\rho_\infty u_\infty}\,\frac{k_w^2}{RT_w}\right)^{1/2}\frac{1}{\bar{V}_\infty}. \quad (16)$$

In order to compare the various solutions, it is necessary to assign suitable values to the quantities in equations (15) and (16). In the case of a cold, highly catalytic wall, these might have the values

$$\frac{C_\infty \mu_e \rho_e u_e}{A^2 \gamma \mu_w \rho_\infty u_\infty} = 1 \quad \text{and} \quad \frac{k_w}{(RT_w)^{1/2}} = 1.$$

An adiabatic, weakly catalytic wall may be represented by

$$\frac{C_\infty \mu_e \rho_e u_e}{A^2 \gamma \mu_w \rho_\infty u_\infty} = \frac{1}{4} \quad \text{and} \quad \frac{k_w}{(RT_w)^{1/2}} = \frac{1}{4}.$$

The results for these two representative cases are compared in Figs. 1 and 2 where the effect of different accommodation coefficients is also shown. If the reflection of incident molecules at the wall is completely diffuse $\bar{\sigma} \simeq 1$, and if 30 percent of the molecules undergo specular reflection $\bar{\sigma} \simeq 2$. It will be seen that close to the leading edge ($\bar{V}_\infty$ large), the wall concentration predicted by the present theory is higher than that indicated in the earlier work, which is reasonable since one would expect the increased bulk motion produced by wall slip to enhance the concentration. Downstream ($\bar{V}_\infty$ small) the wall velocity becomes small and ceases to be representative of the velocity in the diffusion region. Thus the neglect of those dissociated species trans-

ported at the higher velocities which occur away from the wall causes the prediction of wall concentration to be too low. The present theory and that of Freeman are likely to be correct in the upstream and downstream limits, respectively, but both underestimate the wall concentration in the intermediate region.

The effect of slip appears to be significant mainly in the rarefied regime corresponding to fairly large values of $\bar{V}_\infty$. In this regime the present theory should be valid, since equation (1) in a fundamental gas dynamic conservation equation, and although boundary-layer-type transformations are employed to solve it, the boundary layer assumptions are not made.

In the weakly catalytic wall case, neglect of slip is not serious as the wall concentration does not fall much below its free stream value until $\bar{V}_\infty < 0(1)$, which is the lower limit of applicability of the present theory. However, in the highly catalytic wall case, the difference is significant as the present theory provides estimates of wall concentration which are 20 percent greater than those obtained from continuum theory. The heat transfer arising from the recombination of the dissociated species at the wall in rarefied slip flow will be increased correspondingly and may be calculated from

$$\dot{q} = \rho_w k_w h_R \alpha_\infty Z_w, \tag{17}$$

where h_R is the energy of recombination, and Z_w is evaluated from equation (15).

References

1 Fay, J. A., and Riddell, F. R., *Journal of Aeronautical Sciences*, Vol. 25, 1958, pp. 73–85.

2 Chambré, P. L., and Acrivos, A., *Journal of Applied Physics*, Vol. 27, 1956, pp. 1322–28.

3 Freeman, N. C., and Simpkins, P. G., *Quarterly Journal of Mechanics and Applied Mathematics*, Vol. 18, 1965, pp. 213–229.

4 Dorrance, W. H., *Viscous Hypersonic Flow*, McGraw-Hill, 1962.

5 Freeman, N. C., Int. Symposium Fundamental Hypersonic Flow, 1964.

6 Erdelyi, A., ed., *Tables of Integral Transforms*, McGraw-Hill, 1954.

Gas Film Cooling—Effects of Coolant Flow Conditions

GEORGE W. HAERING[1]

Gas film cooling is the process of injecting a gas through discrete holes or slots along a wall, to insulate that wall from a high-temperature gas flow. This film persists for a distance downstream of the slot, its cooling effect gradually eroded by turbulent mixing with the high-temperature stream. The process finds application chiefly in localized high heat flux areas such as rocket nozzle throats, arcjets, hypersonic airbreathing engines, and stagnation regions.

Since the problem is very complex, analytical prediction of even subsonic gas film cooling is in a primitive state. The same is true of experimental prediction. A number of investigators have experimentally studied film cooling (or the related problem of film heating) of an adiabatic wall at negligible pressure gradient. References [1][2] and [2] give reviews of these studies. Each experimenter could find acceptable correlation for his own data, but one investigator's correlation generally fails when applied to other than his own data. This situation suggests important factors omitted in each.

Reference [2] suggests that one such factor involves the geometry of the injection slot. It notes, as a result of examining data from several sources, that the effectiveness of film cooling is higher in those geometries with a large contraction ratio in the secondary fluid passage, prior to injection at the slot. The geometry of an injection slot is one of the simpler items to control in a design situation, and such an improvement would be valuable.

A short series of tests to verify this geometry effect was undertaken in an apparatus whose description follows. Ambient air of velocity about 117 ft/sec flows through a 1-ft²-cross-section plexiglass duct. One wall of the square-cross-section duct contains both a slot, facing the downstream direction and of uniform height 0.21 in. and of length the entire 1 ft available, and thermocouples, mounted 0.03 in. from the smooth wall surface temperature. The backface of this wall is insulated to provide a uniform adiabatic surface. Fig. 1 clarifies the geometry involved. Secondary air, of variable flow rate, heated approximately 40 deg F above ambient, first enters a plenum area and then flows through the slot and along the wall which is being shielded from the cooler mainstream. Reference [3] presents more complete details of the equipment, procedures and the resultant data.

The width of the passage for the secondary gas immediately prior to injection through the slot is a prime variable in these tests, and the test equipment allowed the width of this passage to be set at 0.109, 0.465, or 2.5 in. (see Fig. 1) for a distance of $2^1/_2$ in. upstream of the slot in the secondary passage.

Fig. 2 shows the experimental results as the difference of wall and mainstream air temperature, nondimensionalized, with the ratio X/MS. Here X is the distance downstream from the slot, S is the slot height (0.21 in.), and M is the ratio of the mass velocity (density times velocity) of the secondary flow to that of the mainstream. At each of four M's (nominally 0.3, 0.5, 0.7, and 0.95), data for the three secondary passage widths (0.109, 0.465, and 2.50 in.) are presented.

The data are in general accord with those of other experimenters. It has become customary to correlate film protection data, in the first approximation, as the temperature ratio (presented in Fig. 2) set equal to $A(X/MS)^{-0.8}$. A is a complicated function of turbulence, geometry, etc., which lies between 15 and 25, according to various experimenters. The data of this study indicate the value for A of about 17.

The experiments reveal the effect of passage width is negligible at $M = 0.3$, small at $M = 0.5$, larger at $M = 0.7$, and can be very significant at $M = 0.95$. However, excluding the case of the narrow passage, smaller than the slot, the effect is nowhere very great.

A possible explanation for these trends follows. Gas film cooling is basically a turbulent mixing problem. Reference [4] indicates that eddy viscosity in the outer "wake" portion of a boundary layer scales as the boundary-layer thickness and as the outer-edge velocity in the constant-pressure case. The turbulent Prandtl number does not vary greatly across a boundary layer, so this is also true of the eddy thermal conductivity. At least approximately this will be true in the boundary layers of the main and secondary streams. Neglecting other sources, which in any event are the same at constant M in these tests, the mainstream boundary layer will control the mixing process, since it is thicker (0.42 in.) and of higher outer-edge velocity. The boundary layers in the secondary stream should influence the mixing process only at high secondary velocity (large M) and at thick secondary boundary layers (produced by lack of acceleration in the secondary stream, or small passage width). These are exactly the trends in Fig. 2.

This is surely an oversimplification. Also important may be the overall turbulence levels of both streams (as is shown in an introductory way in references [3] and [5]), the manner in which

[1] Visiting Research Professor, Department of Mechanics, Escola de Engenharia de São Carlos, Universidade de São Paulo, São Carlos, São Paulo, Brazil.

[2] Numbers in brackets designate References at end of Technical Brief.

Contributed by the Heat Transfer Division of The American Society of Mechanical Engineers. Manuscript received by the Heat Transfer Division, July 2, 1969.

ported at the higher velocities which occur away from the wall causes the prediction of wall concentration to be too low. The present theory and that of Freeman are likely to be correct in the upstream and downstream limits, respectively, but both underestimate the wall concentration in the intermediate region.

The effect of slip appears to be significant mainly in the rarefied regime corresponding to fairly large values of $\bar{V}_\infty$. In this regime the present theory should be valid, since equation (1) in a fundamental gas dynamic conservation equation, and although boundary-layer-type transformations are employed to solve it, the boundary layer assumptions are not made.

In the weakly catalytic wall case, neglect of slip is not serious as the wall concentration does not fall much below its free stream value until $\bar{V}_\infty < 0(1)$, which is the lower limit of applicability of the present theory. However, in the highly catalytic wall case, the difference is significant as the present theory provides estimates of wall concentration which are 20 percent greater than those obtained from continuum theory. The heat transfer arising from the recombination of the dissociated species at the wall in rarefied slip flow will be increased correspondingly and may be calculated from

$$\dot{q} = \rho_w k_w h_R \alpha_\infty Z_w, \tag{17}$$

where h_R is the energy of recombination, and Z_w is evaluated from equation (15).

References

1 Fay, J. A., and Riddell, F. R., *Journal of Aeronautical Sciences*, Vol. 25, 1958, pp. 73–85.

2 Chambré, P. L., and Acrivos, A., *Journal of Applied Physics*, Vol. 27, 1956, pp. 1322–28.

3 Freeman, N. C., and Simpkins, P. G., *Quarterly Journal of Mechanics and Applied Mathematics*, Vol. 18, 1965, pp. 213–229.

4 Dorrance, W. H., *Viscous Hypersonic Flow*, McGraw-Hill, 1962.

5 Freeman, N. C., Int. Symposium Fundamental Hypersonic Flow, 1964.

6 Erdelyi, A., ed., *Tables of Integral Transforms*, McGraw-Hill, 1954.

Gas Film Cooling—Effects of Coolant Flow Conditions

GEORGE W. HAERING[1]

Gas film cooling is the process of injecting a gas through discrete holes or slots along a wall, to insulate that wall from a high-temperature gas flow. This film persists for a distance downstream of the slot, its cooling effect gradually eroded by turbulent mixing with the high-temperature stream. The process finds application chiefly in localized high heat flux areas such as rocket nozzle throats, arcjets, hypersonic airbreathing engines, and stagnation regions.

Since the problem is very complex, analytical prediction of even subsonic gas film cooling is in a primitive state. The same is true of experimental prediction. A number of investigators have experimentally studied film cooling (or the related problem of film heating) of an adiabatic wall at negligible pressure gradient. References [1][2] and [2] give reviews of these studies. Each experimenter could find acceptable correlation for his own data, but one investigator's correlation generally fails when applied to other than his own data. This situation suggests important factors omitted in each.

Reference [2] suggests that one such factor involves the geometry of the injection slot. It notes, as a result of examining data from several sources, that the effectiveness of film cooling is higher in those geometries with a large contraction ratio in the secondary fluid passage, prior to injection at the slot. The geometry of an injection slot is one of the simpler items to control in a design situation, and such an improvement would be valuable.

A short series of tests to verify this geometry effect was undertaken in an apparatus whose description follows. Ambient air of velocity about 117 ft/sec flows through a 1-ft²-cross-section plexiglass duct. One wall of the square-cross-section duct contains both a slot, facing the downstream direction and of uniform height 0.21 in. and of length the entire 1 ft available, and thermocouples, mounted 0.03 in. from the smooth wall surface temperature. The backface of this wall is insulated to provide a uniform adiabatic surface. Fig. 1 clarifies the geometry involved. Secondary air, of variable flow rate, heated approximately 40 deg F above ambient, first enters a plenum area and then flows through the slot and along the wall which is being shielded from the cooler mainstream. Reference [3] presents more complete details of the equipment, procedures and the resultant data.

The width of the passage for the secondary gas immediately prior to injection through the slot is a prime variable in these tests, and the test equipment allowed the width of this passage to be set at 0.109, 0.465, or 2.5 in. (see Fig. 1) for a distance of $2^1/_2$ in. upstream of the slot in the secondary passage.

Fig. 2 shows the experimental results as the difference of wall and mainstream air temperature, nondimensionalized, with the ratio X/MS. Here X is the distance downstream from the slot, S is the slot height (0.21 in.), and M is the ratio of the mass velocity (density times velocity) of the secondary flow to that of the mainstream. At each of four M's (nominally 0.3, 0.5, 0.7, and 0.95), data for the three secondary passage widths (0.109, 0.465, and 2.50 in.) are presented.

The data are in general accord with those of other experimenters. It has become customary to correlate film protection data, in the first approximation, as the temperature ratio (presented in Fig. 2) set equal to $A(X/MS)^{-0.8}$. A is a complicated function of turbulence, geometry, etc., which lies between 15 and 25, according to various experimenters. The data of this study indicate the value for A of about 17.

The experiments reveal the effect of passage width is negligible at $M = 0.3$, small at $M = 0.5$, larger at $M = 0.7$, and can be very significant at $M = 0.95$. However, excluding the case of the narrow passage, smaller than the slot, the effect is nowhere very great.

A possible explanation for these trends follows. Gas film cooling is basically a turbulent mixing problem. Reference [4] indicates that eddy viscosity in the outer "wake" portion of a boundary layer scales as the boundary-layer thickness and as the outer-edge velocity in the constant-pressure case. The turbulent Prandtl number does not vary greatly across a boundary layer, so this is also true of the eddy thermal conductivity. At least approximately this will be true in the boundary layers of the main and secondary streams. Neglecting other sources, which in any event are the same at constant M in these tests, the mainstream boundary layer will control the mixing process, since it is thicker (0.42 in.) and of higher outer-edge velocity. The boundary layers in the secondary stream should influence the mixing process only at high secondary velocity (large M) and at thick secondary boundary layers (produced by lack of acceleration in the secondary stream, or small passage width). These are exactly the trends in Fig. 2.

This is surely an oversimplification. Also important may be the overall turbulence levels of both streams (as is shown in an introductory way in references [3] and [5]), the manner in which

[1] Visiting Research Professor, Department of Mechanics, Escola de Engenharia de São Carlos, Universidade de São Paulo, São Carlos, São Paulo, Brazil.

[2] Numbers in brackets designate References at end of Technical Brief.

Contributed by the Heat Transfer Division of The American Society of Mechanical Engineers. Manuscript received by the Heat Transfer Division, July 2, 1969.

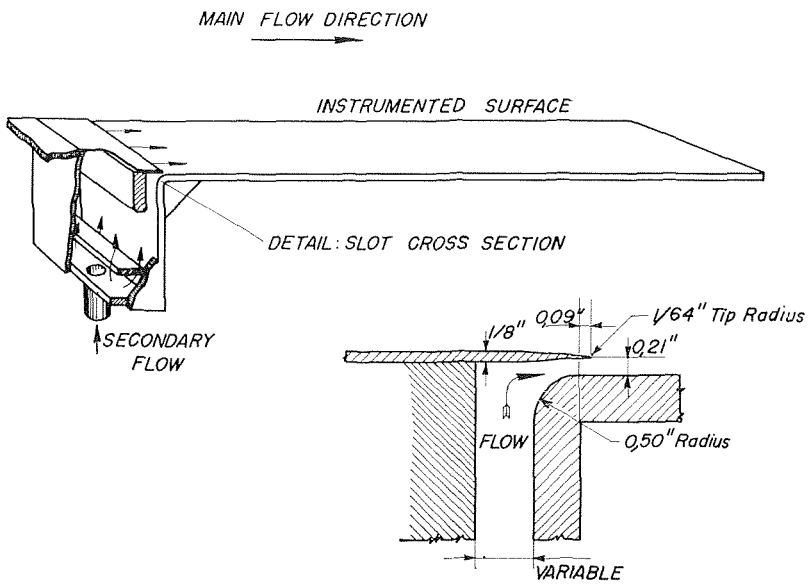

Fig. 1 Cutaway view of test apparatus

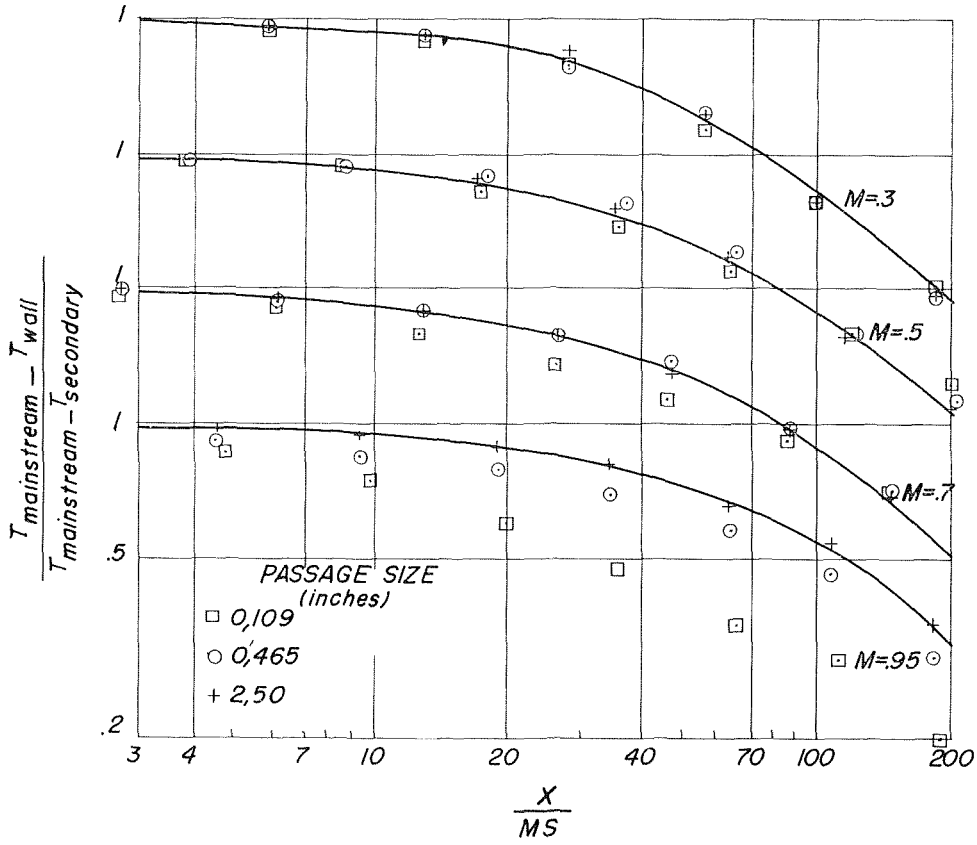

Fig. 2 Effects of coolant flow conditions (for clarity, the ordinate is a logarithmic scale, shifted upward a distance corresponding to a factor of 2 with each injection ratio)

the acceleration affects their scale and intensity, and the general shape of the secondary-velocity profile, although in these tests this profile did not vary greatly. We may conclude, albeit qualitatively, that acceleration of the secondary stream can improve film cooling, especially as slot velocity increases.

References

1 Samuel, A. E., "Film Cooling of an Adiabatic Flat Plate at Zero Pressure Gradient in the Presence of a Hot Mainstream and Cold Tangential Secondary Injection," JOURNAL OF HEAT TRANSFER, TRANS. ASME, Vol. 85, No. 3, Aug. 1965, pp. 409–418.

2 Haering, G. W., "A Proposed Correlation Scheme for Gas Film Cooling Data," AFAPL-TR-66-56, Wright-Patterson AFB, Ohio, August 1966.
3 Haering, G. W., "Boundary Layer Separation Control and Wall Temperature Control by Tangential Fluid Injection," dissertation, The Ohio State University, Aug. 1968, pp. 21–29.
4 Kovasznay, L. S. G., "Structure of the Turbulent Boundary Layer," *Physics of Fluids*, Part 2, Vol. 10, No. 9, Sept. 1967, pp. S25–S30.
5 "Exploratory Research Program for Turbo-Propulsion Exhaust Systems, Phase I–Final Report," for contract AF 33(615)-3128, United Aircraft Corporation, July 1966 (classified report, but sections concerning film cooling, pp. 3–13 to 3–53, are unclassified).

Formulation of an Irradiation Factor Method for Surface Radiation Problems

JAMES E. HITCHCOCK[1]

Nomenclature

A = area
E_b = blackbody emissive power
f = ratio of specular reflectivity to total reflectivity
F_{ki} = diffuse view factor from surface k to surface i
$F_{ski}{}^{j}$ = diffuse-specular view factor from surface k to surface i with surface j emitting
H_{ji} = irradiation factor for surface i with surface j emitting
I_{ji} = irradiation on surface i with surface j emitting
J_{ji} = radiosity factor for surface i with surface j emitting
Q = heat transfer
R = radiosity
T = absolute temperature
α_{ji} = absorptivity of surface i with surface j emitting
ϵ = emissivity
λ = wavelength
ρ_{ji} = reflectivity of surface i with surface j emitting

Subscripts

d = diffuse
s = specular
λ = monochromatic

Introduction

An irradiation factor method is formulated herein for an enclosure of surfaces separated by a radiatively nonparticipating medium. It is assumed that the enclosure is subdivided into N surfaces such that the radiosity is uniform over each surface. In general, the surfaces are nongray, diffuse emitters and partially diffuse/partially specular reflectors. For nongray analyses, the temperature of each surface is assumed to be known, whereas, for gray analyses, either the temperature or the heat transfer at each surface may be specified.

In previous analyses of problems in this class, the methods of solution were centered on radiosities [1–3],[2] absorption factors [4], and dimensionless heat fluxes [5]. The present method of solution is centered on irradiations and utilizes irradiation factors.

Formulation

The equation for the total energy per unit time incident on surface i is borrowed from the literature; e.g., [1]

$$I_i A_i = \sum_{k=1}^{N} R_{dk} A_k F_{ski}; \quad i = 1, 2, 3, \ldots, N \tag{1}$$

where the diffuse radiosity of surface k is given by

$$R_{dk} = \epsilon_k E_{bk} + \rho_{dk} I_k \tag{2}$$

and F_{ski}, the diffuse-specular view factor,[3] is the fraction of the diffuse energy leaving surface k which is incident on surface i directly and by specular reflections. Substituting R_{dk} from equation (2) into equations (1)

$$I_i A_i = \sum_{k=1}^{N} [\epsilon_k E_{bk} A_k F_{ski} + \rho_{dk} I_k A_k F_{ski}] \tag{3}$$

Now assume, as was done in [2], that only the jth surface of the enclosure is emitting; i.e., $E_{bk} = 0$ for $k \neq j$. Equations (3) become

$$I_{ji} A_i = \epsilon_j E_{bj} A_j F_{sji}{}^{i} + \sum_{k=1}^{N} I_{jk} A_k \rho_{djk} F_{ski}{}^{j} \tag{4}$$

Observe that the energy incident on surface i with surface j emitting, $I_{ji}A_i$, consists of energy emitted by surface j which goes directly and by specular reflections to surface i plus energy emitted by surface j which is incident on surfaces k, is reflected, and then goes directly and by specular reflections from surfaces k to surface i. Next, an irradiation factor is defined by

$$H_{ji} \equiv \frac{I_{ji} A_i}{E_{bj} A_j} \tag{5}$$

In words, the irradiation factor, H_{ji}, is the ratio of the energy actually emitted by surface j which is eventually incident on surface i to the energy surface j would emit if it were a blackbody. Dividing equations (4) through by $E_{bj}A_j$ and introducing the irradiation factor, equations (4) become

$$H_{ji} = \epsilon_i F_{sji}{}^{j} + \sum_{k=1}^{N} H_{jk} \rho_{djk} F_{ski}{}^{j} \tag{6}$$

Equations (6) are solved simultaneously for the irradiation factors by any of a number of available methods; e.g., gaussian elimination, determinants, matrix inversion, or any iteration technique. Then, the heat transfer at surface i is given by the difference between the energy absorbed by surface i (sum of contributions with surfaces j emitting one at a time) and the energy emitted by surface i.

$$Q_i = \sum_{j=1}^{N} E_{bj} A_j H_{ji} \alpha_{ji} - \epsilon_i E_{bi} A_i \tag{7}$$

The diffuse-specular view factors, $F_{ski}{}^{j}$, in equations (6) are functions of geometry and specular reflectivities [1]. For an enclosure of all diffuse surfaces, $F_{ski}{}^{j}$ reduce to ordinary diffuse view factors, F_{ki}. The total surface properties required in equations (6) and (7) are determined from monochromatic surface property data:

$$\epsilon_k = \frac{\int_0^\infty \epsilon_{\lambda k} E_{b\lambda k} d\lambda}{\int_0^\infty E_{b\lambda k} d\lambda} \tag{8}$$

[1] Associate Professor of Mechanical Engineering, Air Force Institute of Technology, Wright-Patterson Air Force Base, Ohio Assoc. Mem. ASME.
[2] Numbers in brackets designate References at end of Technical Brief.
[3] Exchange factor, E_{Ak-Ai}, in reference [1].

Contributed by the Heat Transfer Division of The American Society of Mechanical Engineers. Manuscript received by the Heat Transfer Division, August 28, 1969; revised manuscript received January 16, 1970.

2 Haering, G. W., "A Proposed Correlation Scheme for Gas Film Cooling Data," AFAPL-TR-66-56, Wright-Patterson AFB, Ohio, August 1966.
3 Haering, G. W., "Boundary Layer Separation Control and Wall Temperature Control by Tangential Fluid Injection," dissertation, The Ohio State University, Aug. 1968, pp. 21–29.
4 Kovasznay, L. S. G., "Structure of the Turbulent Boundary Layer," *Physics of Fluids*, Part 2, Vol. 10, No. 9, Sept. 1967, pp. S25–S30.
5 "Exploratory Research Program for Turbo-Propulsion Exhaust Systems, Phase I–Final Report," for contract AF 33(615)-3128, United Aircraft Corporation, July 1966 (classified report, but sections concerning film cooling, pp. 3–13 to 3–53, are unclassified).

Formulation of an Irradiation Factor Method for Surface Radiation Problems

JAMES E. HITCHCOCK[1]

Nomenclature

A = area
E_b = blackbody emissive power
f = ratio of specular reflectivity to total reflectivity
F_{ki} = diffuse view factor from surface k to surface i
$F_{ski}{}^{j}$ = diffuse-specular view factor from surface k to surface i with surface j emitting
H_{ji} = irradiation factor for surface i with surface j emitting
I_{ji} = irradiation on surface i with surface j emitting
J_{ji} = radiosity factor for surface i with surface j emitting
Q = heat transfer
R = radiosity
T = absolute temperature
α_{ji} = absorptivity of surface i with surface j emitting
ϵ = emissivity
λ = wavelength
ρ_{ji} = reflectivity of surface i with surface j emitting

Subscripts

d = diffuse
s = specular
λ = monochromatic

Introduction

An irradiation factor method is formulated herein for an enclosure of surfaces separated by a radiatively nonparticipating medium. It is assumed that the enclosure is subdivided into N surfaces such that the radiosity is uniform over each surface. In general, the surfaces are nongray, diffuse emitters and partially diffuse/partially specular reflectors. For nongray analyses, the temperature of each surface is assumed to be known, whereas, for gray analyses, either the temperature or the heat transfer at each surface may be specified.

In previous analyses of problems in this class, the methods of solution were centered on radiosities [1–3],[2] absorption factors [4], and dimensionless heat fluxes [5]. The present method of solution is centered on irradiations and utilizes irradiation factors.

Formulation

The equation for the total energy per unit time incident on surface i is borrowed from the literature; e.g., [1]

$$I_i A_i = \sum_{k=1}^{N} R_{dk} A_k F_{ski}; \quad i = 1, 2, 3, \ldots, N \tag{1}$$

where the diffuse radiosity of surface k is given by

$$R_{dk} = \epsilon_k E_{bk} + \rho_{dk} I_k \tag{2}$$

and F_{ski}, the diffuse-specular view factor,[3] is the fraction of the diffuse energy leaving surface k which is incident on surface i directly and by specular reflections. Substituting R_{dk} from equation (2) into equations (1)

$$I_i A_i = \sum_{k=1}^{N} [\epsilon_k E_{bk} A_k F_{ski} + \rho_{dk} I_k A_k F_{ski}] \tag{3}$$

Now assume, as was done in [2], that only the jth surface of the enclosure is emitting; i.e., $E_{bk} = 0$ for $k \neq j$. Equations (3) become

$$I_{ji} A_i = \epsilon_j E_{bj} A_j F_{sji}{}^{i} + \sum_{k=1}^{N} I_{jk} A_k \rho_{djk} F_{ski}{}^{j} \tag{4}$$

Observe that the energy incident on surface i with surface j emitting, $I_{ji}A_i$, consists of energy emitted by surface j which goes directly and by specular reflections to surface i plus energy emitted by surface j which is incident on surfaces k, is reflected, and then goes directly and by specular reflections from surfaces k to surface i. Next, an irradiation factor is defined by

$$H_{ji} \equiv \frac{I_{ji} A_i}{E_{bj} A_j} \tag{5}$$

In words, the irradiation factor, H_{ji}, is the ratio of the energy actually emitted by surface j which is eventually incident on surface i to the energy surface j would emit if it were a blackbody. Dividing equations (4) through by $E_{bj}A_j$ and introducing the irradiation factor, equations (4) become

$$H_{ji} = \epsilon_i F_{sji}{}^{j} + \sum_{k=1}^{N} H_{jk} \rho_{djk} F_{ski}{}^{j} \tag{6}$$

Equations (6) are solved simultaneously for the irradiation factors by any of a number of available methods; e.g., gaussian elimination, determinants, matrix inversion, or any iteration technique. Then, the heat transfer at surface i is given by the difference between the energy absorbed by surface i (sum of contributions with surfaces j emitting one at a time) and the energy emitted by surface i.

$$Q_i = \sum_{j=1}^{N} E_{bj} A_j H_{ji} \alpha_{ji} - \epsilon_i E_{bi} A_i \tag{7}$$

The diffuse-specular view factors, $F_{ski}{}^{j}$, in equations (6) are functions of geometry and specular reflectivities [1]. For an enclosure of all diffuse surfaces, $F_{ski}{}^{j}$ reduce to ordinary diffuse view factors, F_{ki}. The total surface properties required in equations (6) and (7) are determined from monochromatic surface property data:

$$\epsilon_k = \frac{\int_0^\infty \epsilon_{\lambda k} E_{b\lambda k} d\lambda}{\int_0^\infty E_{b\lambda k} d\lambda} \tag{8}$$

[1] Associate Professor of Mechanical Engineering, Air Force Institute of Technology, Wright-Patterson Air Force Base, Ohio Assoc. Mem. ASME.
[2] Numbers in brackets designate References at end of Technical Brief.
[3] Exchange factor, E_{Ak-Ai}, in reference [1].

Contributed by the Heat Transfer Division of The American Society of Mechanical Engineers. Manuscript received by the Heat Transfer Division, August 28, 1969; revised manuscript received January 16, 1970.

$$\alpha_{jk} = \frac{\int_0^\infty \alpha_{\lambda k} I_{\lambda jk} d\lambda}{\int_0^\infty I_{\lambda jk} d\lambda} \tag{9}$$

$$\rho_{jk} = 1 - \alpha_{jk} \tag{10}$$

$$\rho_{sjk} = f\rho_{jk}, \qquad 0 \leq f \leq 1 \tag{11}$$

and

$$\rho_{djk} = (1 - f)\rho_{jk} \tag{12}$$

where f is assumed here to be independent of wavelength.

Various approximate methods can be used to determine the absorptivities defined by equations (9), which can be rewritten as

$$\alpha_{jk} = \frac{\int_0^\infty \alpha_{\lambda k} H_{\lambda jk} E_{b\lambda j} d\lambda}{\int_0^\infty H_{\lambda jk} E_{b\lambda j} d\lambda} \tag{13}$$

In the gray analysis, $\alpha_{\lambda k}$ is assumed to be independent of wavelength. Consequently, $\alpha_{jk} = \epsilon_k(T_k)$. In the semi-gray analysis [6], $H_{\lambda jk}$ is assumed to be independent of wavelength; i.e., the irradiation on surface k is assumed to have the blackbody distribution evaluated at the temperature of surface j. Consequently, $\alpha_{jk} = \epsilon_k(T_j)$. A better approximation is to assume that $H_{\lambda jk}$ is proportional to $\epsilon_{\lambda j}$; i.e., the irradiation on surface k is assumed to have the actual emissive power distribution of surface j. Of course, a multiple-band analysis can also be used, where the surfaces are assumed to be gray within each band. In this method equations (6) and (7) are solved for each band (E_{bj} in equation (7) would be the blackbody emissive power of surface j in a band), and the total heat transfer at surface i would be the sum of the contributions of each band.

In gray analyses, either the temperature or the heat transfer at each surface may be specified with minor modifications to the foregoing equations. Assume that in an enclosure the temperature is known for surfaces 1 through M and the heat transfer is known for surfaces $M + 1$ through N. Equations (6) remain the same, but the surfaces k, $M + 1 \leq k \leq N$, are treated as perfect reflectors except when they are emitting. Specifically, the actual specular reflectivity, ρ_{sjk}, is used, but the diffuse reflectivity is given by $\rho_{djk} = 1 - \rho_{sjk}(\alpha_{jk} = \epsilon_k = 0)$, except when $k = j$. Thus, there is heat transfer at surfaces k, $M + 1 \leq k \leq N$, only when they are emitting. The unknown values of Q_i, $1 \leq i \leq M$, are given by

$$Q_i = \sum_{j=1}^{M} E_{bj} A_j H_{ji} \epsilon_i + \sum_{j=M+1}^{N} \frac{H_{ji}\epsilon_i}{(H_{jj} - 1)\epsilon_j} Q_j - \epsilon_i E_{bi} A_i \tag{14}$$

The terms in the first summation of equation (14) are the same as those in equation (7) ($\alpha_{ji} = \epsilon_i$ for this gray analysis). $H_{ji}\epsilon_i/(H_{jj} - 1)\epsilon_j$ in the second summation of equation (14) is the ratio of the energy absorbed by surface i to the heat transfer at surface j when surface j is emitting. Thus, the terms in the second summation are the contributions of the known heat-transfer surfaces to the energy absorbed by surface i. For $1 \leq i \leq M$ and $1 \leq j \leq M$

$$\sum_{i=1}^{M} H_{ji}\epsilon_i = \epsilon_j \tag{15}$$

and

$$A_j H_{ji} \epsilon_i = A_i H_{ij} \epsilon_j \tag{16}$$

Using equations (16), equation (14) can be written in a more convenient form as

$$Q_i = \sum_{j=1}^{M} E_{bj} A_i H_{ij} \epsilon_j + \sum_{j=M+1}^{N} \frac{H_{ji}\epsilon_i}{(H_{jj} - 1)\epsilon_j} Q_j - \epsilon_i E_{bi} A_i \tag{17}$$

The unknown values of E_{bi}, $M + 1 \leq i \leq N$, can also be determined using equation (14). Solving equation (14) explicitly for E_{bi}

$$E_{bi} = \frac{1}{A_i}\left[\sum_{j=1}^{M} E_{bj} A_j H_{ji} + \sum_{j=M+1}^{N} \frac{H_{ji}}{(H_{jj} - 1)\epsilon_j} Q_j\right] - \frac{Q_i}{\epsilon_i A_i} \tag{18}$$

The bracketed quantity in equation (18) is the total energy incident on surface i, $I_i A_i$. In equations (17) and (18), omit the terms representing the contributions of surfaces j when $\epsilon_j = 0$.

Observations

All methods which have been presented for the solution of problems in this class are, of course, related. However, upon close examination, there are practical differences.

1 The principal equations in the present formulation, equations (6) and (7), are easily remembered because they have a simple physical interpretation. The same can be said for the absorption-factor method [4], but it cannot be used in nongray analyses. The dimensionless heat flux equations [5], corresponding to equations (6), have no simple physical interpretation. The principal equations in the radiosity method [1–3], written in forms similar to equations (6) and (7), appear as follows:

$$J_{dji} = \delta_{ij}\epsilon_j + \rho_{dji} \sum_{k=1}^{N} J_{djk} F_{ski} \tag{19}$$

and

$$Q_i = \sum_{j=1}^{N} \frac{E_{bj} A_j J_{dji} \alpha_{ji}}{\rho_{dji}} - \frac{(\rho_{dii} + \alpha_{ii})\epsilon_i E_{bi} A_i}{\rho_{dii}} \tag{20}$$

where a radiosity factor, J_{dji}, is defined by

$$J_{dji} \equiv \frac{R_{dji} A_i}{E_{bj} A_j} \tag{21}$$

Equations (19) are comparable to equations (6), but equation (20) is not quite as simple as equation (7).

2 In the present method, no special provisions need to be made for the limiting case of $\alpha = 1$ for one or more surfaces, which makes it convenient to investigate this limit. If $\alpha_i = 1(\rho_{dji} = 0)$ in the radiosity method, equation (20) is indeterminate, and one must resort again to calculating the irradiation on surface i, which involves an additional summation.

3 The present method readily incorporates diffuse-specular surfaces, approximate nongray methods of determining absorptivities, and known heat-transfer boundary conditions in gray surface problems.

4 The irradiation factors, H_{ji}, are related to the total-exchange areas, $\overline{S_j S_i}$ [2] (formerly $A_j \bar{s}_{ji}$), by

$$\overline{S_j S_i} = A_j \bar{s}_{ji} = A_j H_{ji} \alpha_{ji} \tag{22}$$

References

1 Sparrow, E. M., and Cess, R. D., *Radiation Heat Transfer*, Brooks-Cole, Belmont, Calif., 1966.

2 Hottel, H. C., and Sarofim, A. F., *Radiative Transfer*, McGraw-Hill, New York, N. Y., 1967.

3 Love, T. J., *Radiative Heat Transfer*, Merrill, Columbus, Ohio, 1968.

4 Gebhart, B., *Heat Transfer*, McGraw-Hill, New York, N. Y., 1961.

5 Sparrow, E. M., *Radiation Heat Transfer Between Surfaces*, *Advances in Heat Transfer*, Vol. 2, Academic Press, New York, N. Y., 1965.

6 Wiebelt, J. A., *Engineering Radiation Heat Transfer*, Holt, Rinehart and Winston, New York, N. Y., 1966.

Non-Newtonian Boundary Layer Separation Induced by Mass Injection

K. H. KIM,[1] J. C. MULLIGAN,[2] and M. N. ÖZIŞIK[3]

Nomenclature

C = dimensionless injection velocity for Newtonian flow
C^* = dimensionless injection velocity for non-Newtonian flow
C_D = dimensionless drag coefficient
f = dimensionless stream function
L = length of flat plate
N = non-Newtonian power-law exponent
Re = $U_\infty^{2-N}L^N/\nu_0$, Reynolds number
u = velocity component in x direction
U_∞ = mainstream velocity
v = velocity component in y direction
v_w = injection velocity
x = coordinate along the surface
y = coordinate normal to the surface
η = dimensionless similarity variable
ψ = stream function
ν = kinematic viscosity
ν_0 = non-Newtonian viscosity coefficient
τ_{xy} = local shear stress

Introduction

One of the most interesting and recondite considerations of boundary layer flow is the separation singularity which results with mass injection at the surface. The boundary layer equations fail, mathematically, when the rate of fluid injection is sufficiently large. Physically, this represents a separation of the boundary layer from the surface. Numerical investigations have generally been successful in showing this separation on a porous flat surface oriented parallel with the flow, even though the mainstream flow is uniform.

The classical work of Schlichting and Bussmann [1][4] showed that it is possible to generalize the Blasius solution for uniform Newtonian flow past a semi-infinite plate to account for certain distributions of suction and injection. This was done by representing the boundary condition at the surface as

$$f(0) = C \tag{1}$$

instead of $f(0) = 0$, where f is the Blasius stream function. The normal component of the velocity at the surface is then given by the relation

$$v_w = -C(\nu U_\infty/2x)^{1/2} \tag{2}$$

where a positive value of C corresponds to suction and a negative value to injection. The numerical solutions of Schlichting and Bussmann [1], Iglisch [2], Thwaites [3], Lessen [4], and Lock [5] all demonstrate the separation singularity which develops in the boundary layer equation at a certain negative value of C. Emmons and Leigh [6] presented extensive numerical calculations and found that separation occurs when $C = -0.87574$. Gross et al. [7] report, essentially, this same value of C.

Many fluids cannot be represented by the classical Newtonian constitutive equation but can, however, be approximately described by a power-law of the form

$$\tau_{xy} = \nu_0\left(\frac{\partial u}{\partial y}\right)^N \tag{3}$$

The flow characteristics of these fluids are important because it has been shown that significant reductions in drag occur. The studies of Thompson and Snyder [8], Kim and Eraslan [9], and Scott and Krall [10] all demonstrate a further reduction in drag obtained by fluid injection. None of these investigations, however, demonstrates the separation singularity for non-Newtonian fluids.

The present work is concerned with the determination of the dimensionless injection velocity, C^*, which is required for the boundary layer separation of an incompressible power-law fluid flowing across the surface of a porous flat plate, defined in cartesian coordinates as the plane $x \geq 0$, $y = 0$.

Analysis

The equations which describe the two-dimensional, steady, boundary layer flow of an incompressible power-law fluid with constant properties are

$$\frac{\partial u}{\partial x} + \frac{\partial u}{\partial y} = 0 \tag{4}$$

$$u\left(\frac{\partial u}{\partial x}\right) + v\left(\frac{\partial u}{\partial y}\right) = \nu_0 N\left(\frac{\partial^2 u}{\partial y^2}\right)\left(\frac{\partial u}{\partial y}\right)^{N-1} \tag{5}$$

with the boundary conditions

$$u(x, 0) = 0 \tag{6a}$$

$$v(x, 0) = v_w(x) \tag{6b}$$

$$\lim_{y\to\infty} u(x, y) = U_\infty = \text{constant} \tag{6c}$$

A similarity reduction of these equations yields

$$f''' + \left[\frac{1}{N(N+1)}\right] f(f'')^{2-N} = 0 \tag{7}$$

with

$$f(0) = C^* \tag{8a}$$

$$f'(0) = 0 \tag{8b}$$

$$\lim_{\eta\to\infty} f'(\eta) = 1 \tag{8c}$$

where the similarity variables are defined as

$$\eta = \left(\frac{y}{L}\right)\text{Re}^{\frac{1}{1+N}}\left(\frac{x}{L}\right)^{-\frac{1}{1+N}} \tag{9}$$

and

$$f(\eta) = \psi(x, y)\left[\text{Re}\,\frac{L}{x}\right]^{\frac{1}{1+N}}\Big/ U_\infty L \tag{10}$$

The velocity components u and v are given in terms of the similarity variables as

$$\frac{u}{U_\infty} = f'(\eta) \tag{11}$$

and

$$\frac{v}{U_\infty} = \text{Re}^{-\frac{1}{1+N}}\cdot\left(\frac{x}{L}\right)^{-\frac{N}{N+1}}\cdot\frac{1}{N+1}\left[\eta f'(\eta) - f(\eta)\right] \tag{12}$$

The injection velocity is then described by the relation

---

[1] Graduate Assistant.
[2] Assistant Professor of Mechanical and Aerospace Engineering.
[3] Professor of Mechanical and Aerospace Engineering, North Carolina State University, Raleigh, North Carolina.
[4] Numbers in brackets designate References at end of Technical Brief.

Contributed by the Heat Transfer Division of THE AMERICAN SOCIETY OF MECHANICAL ENGINEERS. Manuscript received by the Heat Transfer Division, November 29, 1969.

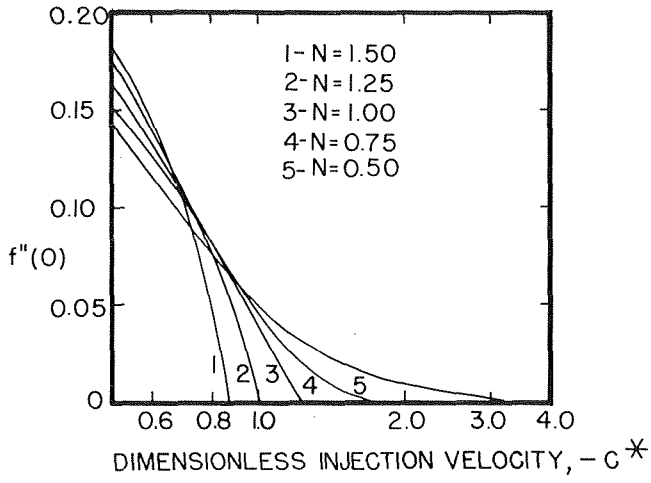

Fig. 1 Behavior of $f''(0)$ near separation

$$v_w = \frac{-C^* U_\infty}{N+1}\left[\mathrm{Re}\left(\frac{x}{L}\right)^N\right]^{-\frac{1}{1+N}} \tag{13}$$

For Newtonian flow, the power-law exponent is unity and the similarity injection velocity C^* reduces to $C\sqrt{2}$.

The dimensionless drag coefficient for the plate is defined as

$$C_D = \frac{1}{LU_\infty^2}\int_0^L (\tau_{xy})_w dx \tag{14}$$

Carrying out the integration gives

$$C_D = (1+N)\mathrm{Re}^{-\frac{1}{1+N}}[f''(0)]^N \tag{15}$$

Here we note that the drag coefficient C_D becomes zero when $f''(0)$ becomes zero provided that the power-law exponent, N, is different from zero.

Equation (7), with the boundary conditions (8), was solved numerically using a fourth-order Runge-Kutta method with particular attention to computations of the injection velocity, C^*, for which $f''(0)$ vanishes for N less than and greater than unity.

Results and Discussion

The quantity $f''(0)$ is shown plotted versus $-C^*$ in Fig. 1. It can be seen that the drag reduces to zero very abruptly with an increase in $-C^*$ for values of $N > 1$. For values of $N < 1$, however, it takes a significantly greater injection rate to cause separation. The variation of the critical injection rate with the power-law exponent, N, is shown in Fig. 2. The results are seen to be in good agreement with those of Emmons and Leigh [6] and Gross, et al. [7], for $N = 1$.

The accuracy of the computations is difficult to evaluate since the critical injection rate appears as an excluded singularity and can only be approached numerically. The critical injection rates reported here correspond to a value of $f''(0)$ generally less than 10^{-6}, with a boundary condition mismatch of less than 1 percent. Thus it is believed the above results are accurate to within ± 0.0001 for $N \leq 1$ and ± 0.001 for $N > 1$.

References

1 Schlichting, H., and Bussmann, K., "Exakte losungen fur die laminare grenzschicht mit absaugung und ausblasen," *Schr. dtsch. Akad. Luftfahrtf.*, 7B, 1943, pp. 25–69.

2 Iglisch, R., "Elementarer existenzbeweis fur die stromung in der laminaren grenzschicht zur potentials tromung $U = u_1 x^m$ mit $m > 0$ bei absaugen und ausblasen," *Z. angew. Math. Mech.*, 33, 1953, pp. 143–147.

3 Thwaites, B., "An Exact Solution of the Boundary Layer Equations Under Particular Conditions of Porous Surface Suction," Rep. Memor. A.R.C. No. 2241, London, 1946.

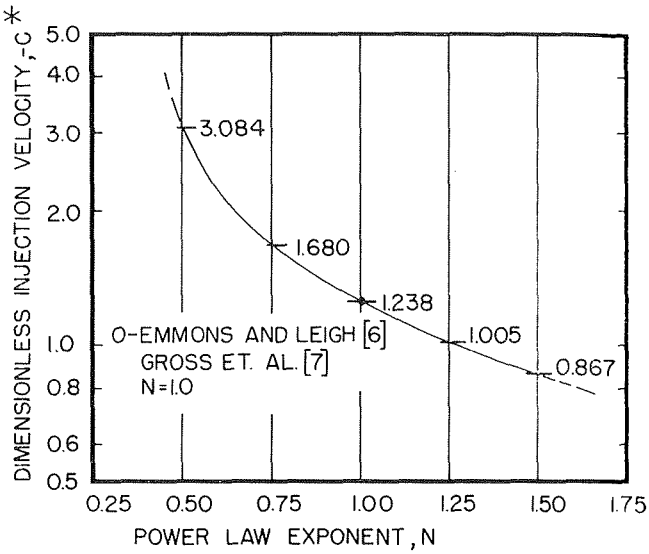

Fig. 2 Effect of N on the critical injection velocity

4 Lessen, M., "On the Stability of the Free Laminar Boundary Layer Between Parallel Streams," N.A.C.A. Rep. No. 979, 1949.

5 Lock, R. C., "The Velocity Distribution in the Laminar Boundary Layer Between Parallel Streams," *Quarterly Journal of Mechanics and Applied Mathematics*, 4, 1951, pp. 42–63.

6 Emmons, H. W., and Leigh, D. C., "Tabulation of the Blasius Function With Blowing and Suction," A.R.C. Rep. No. 157, London, 1953.

7 Gross, J. F., Hartnett, J. P., Masson, D. J., and Gasley, Carl, Jr., "A Review of Binary Laminar Boundary Layer Characteristics," *International Journal of Heat and Mass Transfer*, 3, 1961, pp. 198–221.

8 Thompson, E. R., and Snyder, W. T., "Drag Reduction of a Non-Newtonian Fluid by Fluid Injection at the Wall," *Journal of Hydronautics*, 2 (10), 1968, pp. 177–180.

9 Kim, K. H., and Eraslan, A. H., "Flow of a Non-Newtonian Fluid Past Wedges With Wall Mass Injection," *Journal of Hydronautics*, 3 (1), 1969, pp. 57–59.

10 Scott, C. J., and Krall, K. M., "Surface Effusion Drag Reduction Using Non-Newtonian Fluids," JOURNAL OF HEAT TRANSFER, TRANS. ASME, Series C, Vol. 90, No. 2, 1968, pp. 277–279.

A Short Table of Maximum Slopes for Transient Matrix Heat-Transfer Testing

G. F. KOHLMAYR[1] and D. LOMBARI[1]

LOCKE's [1][2] maximum-slope method for the reduction of test data in transient matrix heat-transfer testing has been extended by one of the present authors [2] from the case of a step change to that of an "arbitrary" upstream fluid-temperature change. Wheeler [3] has recently found and reported that a heater-flow system has a temperature rise which is approximately exponential. Denoting as in reference [2] the normalized upstream fluid-temperature change by $g(\mu)$, where μ stands for the "free time"

[1] Pratt & Whitney Aircraft Division, United Aircraft Corp., East Hartford, Conn.

[2] Numbers in brackets designate References at end of Technical Brief.

Contributed by the Heat Transfer Division of THE AMERICAN SOCIETY OF MECHANICAL ENGINEERS. Manuscript received by the Heat Transfer Division, January 12, 1970.

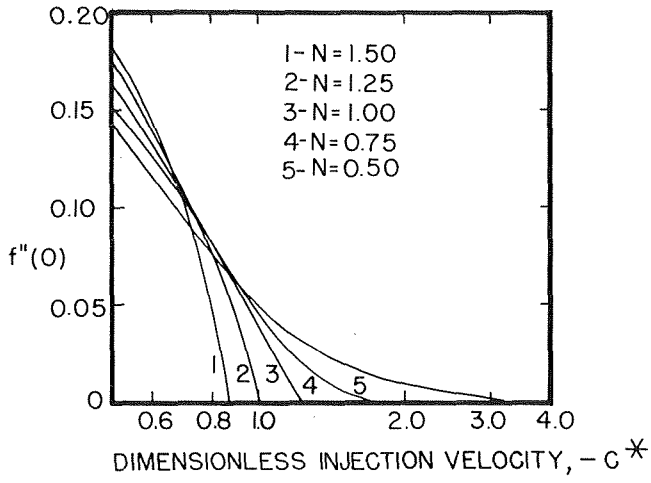

Fig. 1 Behavior of $f''(0)$ near separation

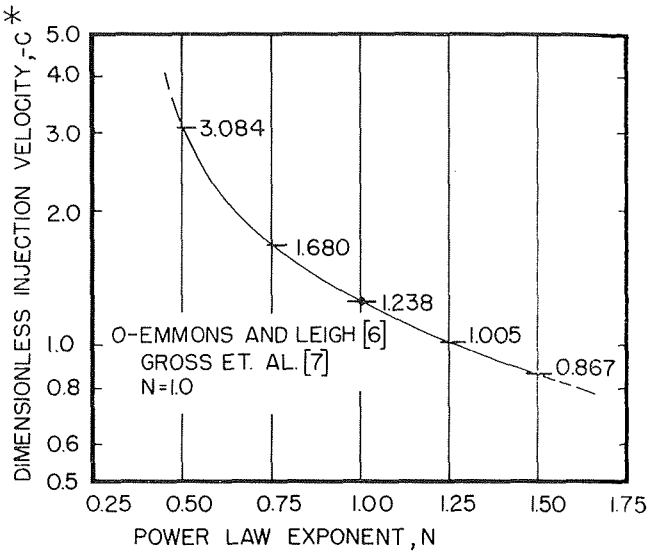

Fig. 2 Effect of N on the critical injection velocity

$$v_w = \frac{-C^* U_\infty}{N+1}\left[\mathrm{Re}\left(\frac{x}{L}\right)^N\right]^{-\frac{1}{1+N}} \tag{13}$$

For Newtonian flow, the power-law exponent is unity and the similarity injection velocity C^* reduces to $C\sqrt{2}$.

The dimensionless drag coefficient for the plate is defined as

$$C_D = \frac{1}{LU_\infty^2}\int_0^L (\tau_{xy})_w dx \tag{14}$$

Carrying out the integration gives

$$C_D = (1+N)\mathrm{Re}^{-\frac{1}{1+N}}[f''(0)]^N \tag{15}$$

Here we note that the drag coefficient C_D becomes zero when $f''(0)$ becomes zero provided that the power-law exponent, N, is different from zero.

Equation (7), with the boundary conditions (8), was solved numerically using a fourth-order Runge-Kutta method with particular attention to computations of the injection velocity, C^*, for which $f''(0)$ vanishes for N less than and greater than unity.

Results and Discussion

The quantity $f''(0)$ is shown plotted versus $-C^*$ in Fig. 1. It can be seen that the drag reduces to zero very abruptly with an increase in $-C^*$ for values of $N > 1$. For values of $N < 1$, however, it takes a significantly greater injection rate to cause separation. The variation of the critical injection rate with the power-law exponent, N, is shown in Fig. 2. The results are seen to be in good agreement with those of Emmons and Leigh [6] and Gross, et al. [7], for $N = 1$.

The accuracy of the computations is difficult to evaluate since the critical injection rate appears as an excluded singularity and can only be approached numerically. The critical injection rates reported here correspond to a value of $f''(0)$ generally less than 10^{-6}, with a boundary condition mismatch of less than 1 percent. Thus it is believed the above results are accurate to within ± 0.0001 for $N \leq 1$ and ± 0.001 for $N > 1$.

References

1 Schlichting, H., and Bussmann, K., "Exakte losungen fur die laminare grenzschicht mit absaugung und ausblasen," *Schr. dtsch. Akad. Luftfahrtf.*, 7B, 1943, pp. 25–69.

2 Iglisch, R., "Elementarer existenzbeweis fur die stromung in der laminaren grenzschicht zur potentials tromung $U = u_1 x^m$ mit $m > 0$ bei absaugen und ausblasen," *Z. angew. Math. Mech.*, 33, 1953, pp. 143–147.

3 Thwaites, B., "An Exact Solution of the Boundary Layer Equations Under Particular Conditions of Porous Surface Suction," Rep. Memor. A.R.C. No. 2241, London, 1946.

4 Lessen, M., "On the Stability of the Free Laminar Boundary Layer Between Parallel Streams," N.A.C.A. Rep. No. 979, 1949.

5 Lock, R. C., "The Velocity Distribution in the Laminar Boundary Layer Between Parallel Streams," *Quarterly Journal of Mechanics and Applied Mathematics*, 4, 1951, pp. 42–63.

6 Emmons, H. W., and Leigh, D. C., "Tabulation of the Blasius Function With Blowing and Suction," A.R.C. Rep. No. 157, London, 1953.

7 Gross, J. F., Hartnett, J. P., Masson, D. J., and Gasley, Carl, Jr., "A Review of Binary Laminar Boundary Layer Characteristics," *International Journal of Heat and Mass Transfer*, 3, 1961, pp. 198–221.

8 Thompson, E. R., and Snyder, W. T., "Drag Reduction of a Non-Newtonian Fluid by Fluid Injection at the Wall," *Journal of Hydronautics*, 2 (10), 1968, pp. 177–180.

9 Kim, K. H., and Eraslan, A. H., "Flow of a Non-Newtonian Fluid Past Wedges With Wall Mass Injection," *Journal of Hydronautics*, 3 (1), 1969, pp. 57–59.

10 Scott, C. J., and Krall, K. M., "Surface Effusion Drag Reduction Using Non-Newtonian Fluids," JOURNAL OF HEAT TRANSFER, TRANS. ASME, Series C, Vol. 90, No. 2, 1968, pp. 277–279.

A Short Table of Maximum Slopes for Transient Matrix Heat-Transfer Testing

G. F. KOHLMAYR[1] and D. LOMBARI[1]

LOCKE's [1][2] maximum-slope method for the reduction of test data in transient matrix heat-transfer testing has been extended by one of the present authors [2] from the case of a step change to that of an "arbitrary" upstream fluid-temperature change. Wheeler [3] has recently found and reported that a heater-flow system has a temperature rise which is approximately exponential. Denoting as in reference [2] the normalized upstream fluid-temperature change by $g(\mu)$, where μ stands for the "free time"

[1] Pratt & Whitney Aircraft Division, United Aircraft Corp., East Hartford, Conn.

[2] Numbers in brackets designate References at end of Technical Brief.

Contributed by the Heat Transfer Division of THE AMERICAN SOCIETY OF MECHANICAL ENGINEERS. Manuscript received by the Heat Transfer Division, January 12, 1970.

Table 1 Maximum slopes for various heater time constants in dependence of N_{tu}

N_{tu} \ μ_H	0.00	0.02	0.04	0.06	0.08	0.10	0.20	0.30	0.40	0.50
3.0	.5766	.5764	.5757	.5746	.5731	.5711	.5506	.5225	.4942	.4676
3.5	.6039	.6036	.6028	.6013	.5993	.5966	.5745	.5453	.5155	.4875
4.0	.6321	.6318	.6309	.6292	.6268	.6237	.5995	.5682	.5366	.5068
4.5	.6603	.6600	.6589	.6569	.6542	.6508	.6242	.5906	.5568	.5251
5.0	.6880	.6876	.6864	.6842	.6811	.6773	.6482	.6121	.5760	.5424
5.5	.7151	.7146	.7132	.7108	.7074	.7030	.6714	.6327	.5944	.5588
6.0	.7414	.7409	.7393	.7366	.7328	.7281	.6937	.6524	.6118	.5743
6.5	.7670	.7664	.7646	.7617	.7575	.7523	.7153	.6713	.6284	.5890
7.0	.7919	.7912	.7893	.7860	.7815	.7759	.7361	.6894	.6442	.6029
7.5	.8161	.8154	.8133	.8097	.8048	.7987	.7561	.7068	.6593	.6162
8.0	.8397	.8390	.8366	.8328	.8275	.8209	.7755	.7235	.6738	.6288
8.5	.8627	.8619	.8594	.8552	.8495	.8424	.7942	.7396	.6877	.6409
9.0	.8852	.8843	.8816	.8771	.8710	.8634	.8123	.7551	.7010	.6525
9.5	.9072	.9062	.9033	.8985	.8919	.8838	.8299	.7700	.7138	.6636
10.0	.9286	.9276	.9245	.9193	.9123	.9037	.8470	.7845	.7262	.6743
15.0	1.1215	1.1197	1.1143	1.1055	1.0939	1.0800	.9944	.9071	.8294	.7623
20.0	1.2862	1.2836	1.2755	1.2627	1.2460	1.2265	1.1126	1.0025	.9079	.8281
30.0	1.5649	1.5602	1.5460	1.5241	1.4966	1.4655	1.2971	1.1470	1.0240	.9237
35.0	1.6872	1.6812	1.6636	1.6369	1.6037	1.5668	1.3725	1.2046	1.0694	.9605

(see equation (8) of reference [2]) one has, according to Wheeler

$$g(\mu) = 1 - \exp(-\mu/\mu_H) \tag{1}$$

for the case that the test matrix is heated. In equation (1) μ_H denotes (in free-time units) the heater time constant. The present authors have used an existing computer program which is described in reference [4] to compute a table of maximum-slope values, for N_{tu} values from 3.0 to 35.0, and for heater time constants from 0.0 to 0.50. It is believed that Table 1 may be of use in transient heat-transfer test data reduction.

References

1 Locke, G. L., "Heat Transfer and Flow Friction Characteristics of Porous Solids," TR No. 10, Department of Mechanical Engineering, Stanford University, Stanford, Calif., 1950.

2 Kohlmayr, G. F., "Extension of the Maximum-Slope Method to Arbitrary Upstream Fluid Temperature Changes," JOURNAL OF HEAT TRANSFER, TRANS. ASME, Series C, Vol. 90, No. 1, Feb. 1968, p. 176.

3 Wheeler, A. J., "Single-Blow Transient Testing of Matrix-Type Heat Exchanger Surfaces at Low Values of N_{tu}," TR No. 68, Department of Mechanical Engineering, Stanford University, Stanford, Calif., 1968.

4 Kohlmayr, G. F., and Lombari, D., "Reduction of Transient Matrix Heat-Transfer Test Data—Computer Program Manual," Pratt & Whitney Aircraft Report No. 2950, 1966.

Combined Free and Forced Laminar Convection in a Vertical Tube With Constant Wall Temperature

W. J. MARNER[1] and H. K. McMILLAN[2]

[1] Assistant Professor of Mechanical Engineering, South Dakota School of Mines and Technology, Rapid City, S. D. Assoc. Mem. ASME.

[2] Associate Professor of Engineering, University of South Carolina, Columbia, S. C.

Contributed by the Heat Transfer Division of THE AMERICAN SOCIETY OF MECHANICAL ENGINEERS. Manuscript received by the Heat Transfer Division, November 24, 1969; revised manuscript received, February 13, 1970.

Nomenclature

A = cross-sectional area of tube
c_p = constant-pressure specific heat
D = tube diameter
Gr = Grashof number, $\rho^2 g\beta_w(T_w - T_i)R^3/\mu^2$
g = acceleration of gravity
k = thermal conductivity
Nu_{am} = arithmetic mean Nusselt number, $\dfrac{2(1-\theta_m)}{\bar{z}(1+\theta_m)}$
Nu_z = local Nusselt number, $-2\left(\dfrac{\partial\theta}{\partial\bar{r}}\right)_w \Big/ \theta_m$
p = pressure
P = dimensionless pressure, $\dfrac{1}{\mathrm{Pr}}\left(\dfrac{p+\rho_w gz}{\rho v_m{}^2}\right)$
Pr = Prandtl number, $c_p\mu/k$
r = radial coordinate
$\bar{r}$ = dimensionless radial coordinate, r/R
R = tube radius
Re = Reynolds number, $\rho v_m R/\mu$
T = temperature
U = dimensionless axial velocity, v_z/v_m
v_m = mean axial velocity
v_r = radial velocity
v_z = axial velocity
V = dimensionless radial velocity, Re Pr v_r/v_m
w = mass flow rate
z = axial coordinate
$\bar{z}$ = dimensionless axial coordinate, $\dfrac{z/R}{\mathrm{Re\,Pr}}$
β = coefficient of volumetric expansion
θ = dimensionless temperature, $(T - T_w)/(T_i - T_w)$
μ = viscosity
ρ = density

Subscripts

i = inlet
m = mean
w = wall

THE problem of combined free and forced laminar convection in a vertical tube with constant wall temperature has been the subject of investigation for a number of years. Of interest here is the case where the fluid enters the heat-transfer section with a fully developed velocity profile and is heated in upflow (or cooled in downflow) due to a sudden change in wall temperature from one fixed value to another fixed value (i.e., the wall temperature profile is a step function).

Martinelli and Boelter [1][3] initially attacked this problem in 1942 and Pigford [2] and Rosen and Hanratty [3] followed later with solutions which also included a temperature-dependent viscosity. However, all of these analyses are approximate and none of the methods can accurately predict velocity and temperature profiles or local Nusselt numbers. The purpose of this note is to present some results for the problem with constant viscosity which were obtained from a numerical solution.

For steady-state flow and heat transfer, negligible axial diffusion of heat and momentum, constant properties except for density in the body force term in the momentum equation, pressure a function of axial distance only, and no viscous dissipation, the continuity, momentum, and energy equations become

$$\frac{\partial v_r}{\partial r} + \frac{v_r}{r} + \frac{\partial v_z}{\partial z} = 0 \tag{1}$$

$$\rho\left(v_r\frac{\partial v_z}{\partial r} + v_z\frac{\partial v_z}{\partial z}\right) = -\frac{dp}{dz} + \mu\left(\frac{1}{r}\frac{\partial v_z}{\partial r} + \frac{\partial^2 v_z}{\partial r^2}\right) - \rho g \tag{2}$$

[3] Numbers in brackets designate References at end of Technical Brief.

Table 1 Maximum slopes for various heater time constants in dependence of N_{tu}

N_{tu} \ μ_H	0.00	0.02	0.04	0.06	0.08	0.10	0.20	0.30	0.40	0.50
3.0	.5766	.5764	.5757	.5746	.5731	.5711	.5506	.5225	.4942	.4676
3.5	.6039	.6036	.6028	.6013	.5993	.5966	.5745	.5453	.5155	.4875
4.0	.6321	.6318	.6309	.6292	.6268	.6237	.5995	.5682	.5366	.5068
4.5	.6603	.6600	.6589	.6569	.6542	.6508	.6242	.5906	.5568	.5251
5.0	.6880	.6876	.6864	.6842	.6811	.6773	.6482	.6121	.5760	.5424
5.5	.7151	.7146	.7132	.7108	.7074	.7030	.6714	.6327	.5944	.5588
6.0	.7414	.7409	.7393	.7366	.7328	.7281	.6937	.6524	.6118	.5743
6.5	.7670	.7664	.7646	.7617	.7575	.7523	.7153	.6713	.6284	.5890
7.0	.7919	.7912	.7893	.7860	.7815	.7759	.7361	.6894	.6442	.6029
7.5	.8161	.8154	.8133	.8097	.8048	.7987	.7561	.7068	.6593	.6162
8.0	.8397	.8390	.8366	.8328	.8275	.8209	.7755	.7235	.6738	.6288
8.5	.8627	.8619	.8594	.8552	.8495	.8424	.7942	.7396	.6877	.6409
9.0	.8852	.8843	.8816	.8771	.8710	.8634	.8123	.7551	.7010	.6525
9.5	.9072	.9062	.9033	.8985	.8919	.8838	.8299	.7700	.7138	.6636
10.0	.9286	.9276	.9245	.9193	.9123	.9037	.8470	.7845	.7262	.6743
15.0	1.1215	1.1197	1.1143	1.1055	1.0939	1.0800	.9944	.9071	.8294	.7623
20.0	1.2862	1.2836	1.2755	1.2627	1.2460	1.2265	1.1126	1.0025	.9079	.8281
30.0	1.5649	1.5602	1.5460	1.5241	1.4966	1.4655	1.2971	1.1470	1.0240	.9237
35.0	1.6872	1.6812	1.6636	1.6369	1.6037	1.5668	1.3725	1.2046	1.0694	.9605

(see equation (8) of reference [2]) one has, according to Wheeler

$$g(\mu) = 1 - \exp(-\mu/\mu_H) \tag{1}$$

for the case that the test matrix is heated. In equation (1) μ_H denotes (in free-time units) the heater time constant. The present authors have used an existing computer program which is described in reference [4] to compute a table of maximum-slope values, for N_{tu} values from 3.0 to 35.0, and for heater time constants from 0.0 to 0.50. It is believed that Table 1 may be of use in transient heat-transfer test data reduction.

References

1 Locke, G. L., "Heat Transfer and Flow Friction Characteristics of Porous Solids," TR No. 10, Department of Mechanical Engineering, Stanford University, Stanford, Calif., 1950.

2 Kohlmayr, G. F., "Extension of the Maximum-Slope Method to Arbitrary Upstream Fluid Temperature Changes," JOURNAL OF HEAT TRANSFER, TRANS. ASME, Series C, Vol. 90, No. 1, Feb. 1968, p. 176.

3 Wheeler, A. J., "Single-Blow Transient Testing of Matrix-Type Heat Exchanger Surfaces at Low Values of N_{tu}," TR No. 68, Department of Mechanical Engineering, Stanford University, Stanford, Calif., 1968.

4 Kohlmayr, G. F., and Lombari, D., "Reduction of Transient Matrix Heat-Transfer Test Data—Computer Program Manual," Pratt & Whitney Aircraft Report No. 2950, 1966.

Combined Free and Forced Laminar Convection in a Vertical Tube With Constant Wall Temperature

W. J. MARNER[1] and H. K. McMILLAN[2]

[1] Assistant Professor of Mechanical Engineering, South Dakota School of Mines and Technology, Rapid City, S. D. Assoc. Mem. ASME.

[2] Associate Professor of Engineering, University of South Carolina, Columbia, S. C.

Contributed by the Heat Transfer Division of THE AMERICAN SOCIETY OF MECHANICAL ENGINEERS. Manuscript received by the Heat Transfer Division, November 24, 1969; revised manuscript received, February 13, 1970.

Nomenclature

A = cross-sectional area of tube
c_p = constant-pressure specific heat
D = tube diameter
Gr = Grashof number, $\rho^2 g\beta_w(T_w - T_i)R^3/\mu^2$
g = acceleration of gravity
k = thermal conductivity
Nu_{am} = arithmetic mean Nusselt number, $\dfrac{2(1-\theta_m)}{\bar{z}(1+\theta_m)}$
Nu_z = local Nusselt number, $-2\left(\dfrac{\partial\theta}{\partial\bar{r}}\right)_w \Big/ \theta_m$
p = pressure
P = dimensionless pressure, $\dfrac{1}{\mathrm{Pr}}\left(\dfrac{p+\rho_w gz}{\rho v_m{}^2}\right)$
Pr = Prandtl number, $c_p\mu/k$
r = radial coordinate
$\bar{r}$ = dimensionless radial coordinate, r/R
R = tube radius
Re = Reynolds number, $\rho v_m R/\mu$
T = temperature
U = dimensionless axial velocity, v_z/v_m
v_m = mean axial velocity
v_r = radial velocity
v_z = axial velocity
V = dimensionless radial velocity, Re Pr v_r/v_m
w = mass flow rate
z = axial coordinate
$\bar{z}$ = dimensionless axial coordinate, $\dfrac{z/R}{\mathrm{Re\,Pr}}$
β = coefficient of volumetric expansion
θ = dimensionless temperature, $(T - T_w)/(T_i - T_w)$
μ = viscosity
ρ = density

Subscripts

i = inlet
m = mean
w = wall

THE problem of combined free and forced laminar convection in a vertical tube with constant wall temperature has been the subject of investigation for a number of years. Of interest here is the case where the fluid enters the heat-transfer section with a fully developed velocity profile and is heated in upflow (or cooled in downflow) due to a sudden change in wall temperature from one fixed value to another fixed value (i.e., the wall temperature profile is a step function).

Martinelli and Boelter [1][3] initially attacked this problem in 1942 and Pigford [2] and Rosen and Hanratty [3] followed later with solutions which also included a temperature-dependent viscosity. However, all of these analyses are approximate and none of the methods can accurately predict velocity and temperature profiles or local Nusselt numbers. The purpose of this note is to present some results for the problem with constant viscosity which were obtained from a numerical solution.

For steady-state flow and heat transfer, negligible axial diffusion of heat and momentum, constant properties except for density in the body force term in the momentum equation, pressure a function of axial distance only, and no viscous dissipation, the continuity, momentum, and energy equations become

$$\frac{\partial v_r}{\partial r} + \frac{v_r}{r} + \frac{\partial v_z}{\partial z} = 0 \tag{1}$$

$$\rho\left(v_r\frac{\partial v_z}{\partial r} + v_z\frac{\partial v_z}{\partial z}\right) = -\frac{dp}{dz} + \mu\left(\frac{1}{r}\frac{\partial v_z}{\partial r} + \frac{\partial^2 v_z}{\partial r^2}\right) - \rho g \tag{2}$$

[3] Numbers in brackets designate References at end of Technical Brief.

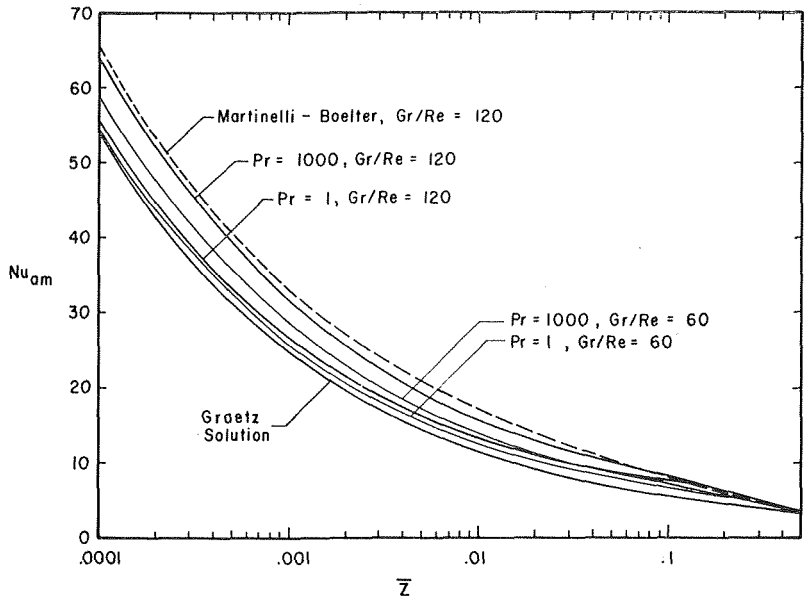

Fig. 1 Comparison of arithmetic mean Nusselt numbers with the results of Martinelli and Boelter [1]

$$\rho c_p \left(v_r \frac{\partial T}{\partial r} + v_z \frac{\partial T}{\partial z} \right) = k \left(\frac{1}{r} \frac{\partial T}{\partial r} + \frac{\partial^2 T}{\partial r^2} \right) \tag{3}$$

In addition, since there are 3 equations with 4 unknowns, the continuity integral

$$w = \int_A \rho v_z dA \tag{4}$$

is necessary to obtain a solution. Noting symmetry about the tube axis, the boundary conditions are

$$\left.\begin{aligned} v_z(r, 0) &= 2v_m[1 - (r/R)^2] \\ v_z(R, z) &= v_r(R, z) = 0 \\ T(r, 0) &= T_i \\ T(R, z) &= T_w \qquad (z > 0) \\ \frac{\partial v_z}{\partial r}(0, z) &= \frac{\partial T}{\partial r}(0, z) = 0 \\ p(0) &= 0 \end{aligned}\right\} \tag{5}$$

Assuming a linear variation of density with temperature in the body force term in equation (2), and expressing equations (1)–(4) in nondimensional form, yields

$$\frac{\partial V}{\partial \bar{r}} + \frac{V}{\bar{r}} + \frac{\partial U}{\partial \bar{z}} = 0 \tag{6}$$

$$\frac{1}{\mathrm{Pr}} \left(V \frac{\partial U}{\partial \bar{r}} + U \frac{\partial U}{\partial \bar{z}} \right) = -\frac{dP}{d\bar{z}} + \frac{1}{\bar{r}} \frac{\partial U}{\partial \bar{r}} + \frac{\partial^2 U}{\partial \bar{r}^2} - \frac{\mathrm{Gr}}{\mathrm{Re}} \theta \tag{7}$$

$$V \frac{\partial \theta}{\partial \bar{r}} + U \frac{\partial \theta}{\partial \bar{z}} = \frac{1}{\bar{r}} \frac{\partial \theta}{\partial \bar{r}} + \frac{\partial^2 \theta}{\partial \bar{r}^2} \tag{8}$$

$$\frac{1}{2} = \int_0^1 \bar{r} U d\bar{r} \tag{9}$$

with the boundary conditions

$$\left.\begin{aligned} U(\bar{r}, 0) &= 2[1 - \bar{r}^2] \\ U(1, \bar{z}) &= V(1, \bar{z}) = 0 \\ \theta(\bar{r}, 0) &= 1 \\ \theta(1, \bar{z}) &= 0 \quad (\bar{z} > 0) \\ \frac{\partial U}{\partial \bar{r}}(0, \bar{z}) &= \frac{\partial \theta}{\partial \bar{r}}(0, \bar{z}) = 0 \\ P(0) &= 0 \end{aligned}\right\} \tag{10}$$

From equations (6)–(9) it is apparent that the dependent variables—U, V, θ, and P— are functions of $\bar{r}$ and $\bar{z}$ with Gr/Re and Pr as parameters. This coupled system of equations was solved numerically using a modification of the numerical procedure of Osterle and Bodoia [4, 5]. Additional details of the solution are available elsewhere [6].

A comparison of the arithmetic mean Nusselt number Nu_{am} of Martinelli and Boelter with the present investigation for Gr/Re = 120 is given in Fig. 1. Since Martinelli and Boelter neglected the inertia terms in the momentum equation, their results should compare most favorably with large Prandtl-number solutions. As may be seen in Fig. 1, the agreement between their results for Gr/Re = 120 and the present investigation for Pr = 1000 and Gr/Re = 120 is good with a maximum difference in Nu_{am} of less than 10 percent. However, for Pr = 1 and Gr/Re = 120 the agreement is poor with differences of up to 30 percent.

In order to show the effect of the parameter Gr/Re on Nu_{am}, two additional solutions are presented in Fig. 1: Pr = 1, Gr/Re = 60 and Pr = 1000, Gr/Re = 60. Comparing these curves with the corresponding Gr/Re = 120 values, it will be noted that, for given Pr, an increase in Gr/Re results in an increase in Nu_{am}. The Graetz solution is also given in Fig. 1 which, for Pr = 1000 and Gr/Re = 120, shows that free convection increases Nu_{am} by as much as 52 percent.

Typical developing dimensionless axial-velocity profiles for Pr = 1 and Gr/Re = 120 are shown in Fig. 2. The fluid enters the heat-transfer section with a fully developed velocity profile. As the fluid is heated, a decrease in density near the wall

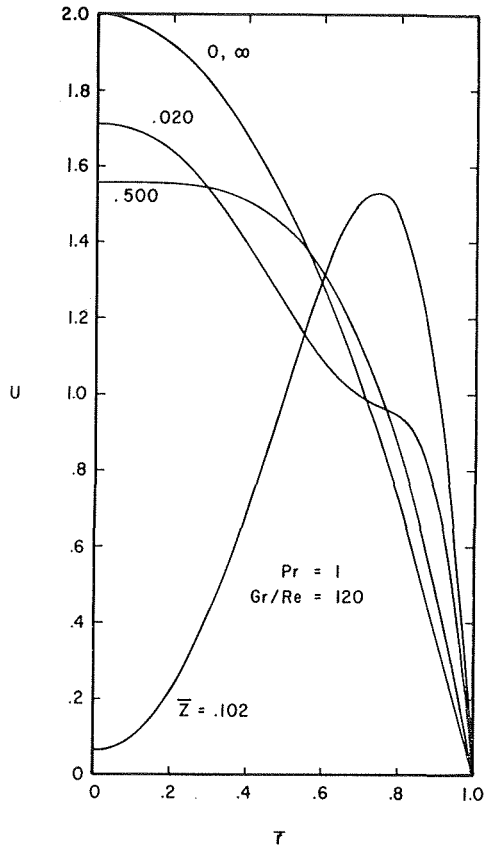

Fig. 2 Typical developing dimensionless axial-velocity profiles

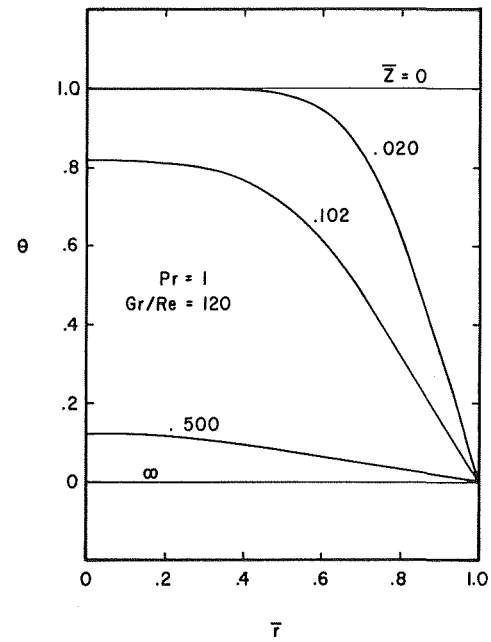

Fig. 3 Typical developing dimensionless temperature profiles

is accompanied by a corresponding increase in the buoyant force, and the velocity near the wall increases, e.g., compare the curves for $\bar{z} = 0$ and $\bar{z} = 0.020$. The velocity profiles continue to deviate from the originally parabolic profile until, at $\bar{z} = 0.102$, the deviation is a maximum, and the centerline velocity at this point is a minimum. As $\bar{z}$ continues to increase, the velocity distribution reapproaches a fully developed profile as the fluid temperature asymptotically approaches the wall temperature. For example, at $\bar{z} = 0.5$, the centerline velocity has reached a value of 1.56 compared to the fully developed value of 2.0. Numerical calculations showed that the degree of velocity profile distortion increases with increasing Gr/Re. The velocity profile which shows maximum deviation from a parabolic distribution, as evidenced by a minimum centerline velocity, will be referred to as the condition of maximum velocity profile distortion.

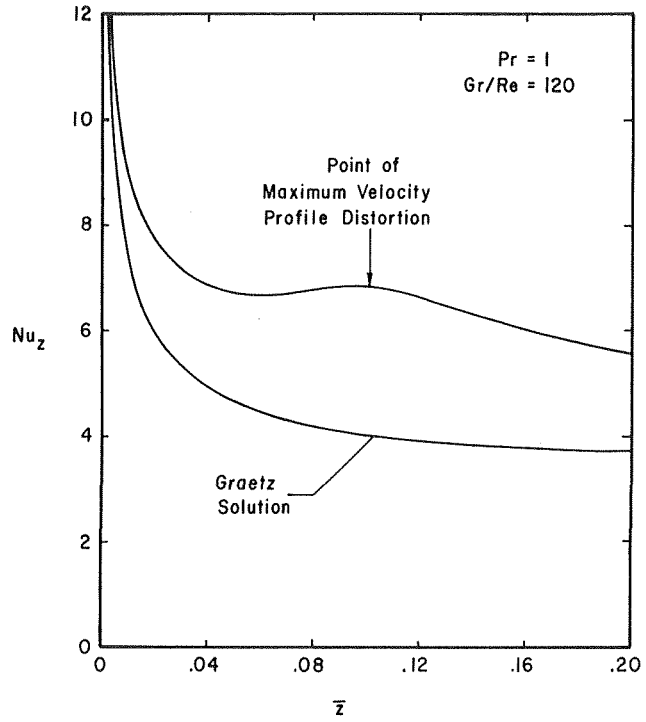

Fig. 4 Typical behavior of the local Nusselt number near the point of maximum velocity-profile distortion

Typical developing dimensionless temperature profiles, corresponding to the velocity profiles given in Fig. 2, are shown in Fig. 3. Starting from an initial value of 1.0, θ asymptotically approaches a value of zero as the fluid temperature approaches the wall temperature. For $\bar{z} = 0.5$, the centerline dimensionless temperature has been reduced to a value of 0.119.

A very interesting result which was obtained is shown in Fig. 4. Near the point of maximum velocity profile distortion, the local Nusselt number Nu_z shows an increase with increasing axial distance. This unusual behavior may be explained by noting that the slope of the velocity profile at the wall, which significantly influences the heat transfer, continually increases until the point of maximum profile distortion is reached (compare the slopes in Fig. 2). Numerical calculations indicated that this increase in Nu_z becomes more pronounced with increasing Gr/Re but appears to decrease with increasing Pr.

References

1 Martinelli, R. C., and Boelter, L. M. K., "The Analytical Prediction of Superposed Free and Forced Viscous Convection in a Vertical Pipe," *University of California Publications in Engineering*, Vol. 5, 1942, pp. 23–58.

2 Pigford, R. L., "Nonisothermal Flow and Heat Transfer Inside Vertical Tubes," *Chemical Engineering Progress Symposium Series*, Vol. 51, 1955, pp. 79–92.

3 Rosen, E. M., and Hanratty, T. J., "Use of Boundary-Layer Theory to Predict the Effect of Heat Transfer on the Laminar-Flow Field in a Vertical Tube With a Constant-Temperature Wall," *AIChE Journal*, Vol. 7, 1961, pp. 112–123.

4 Bodoia, J. R., and Osterle, J. F., "Finite Difference Analysis of Plane Poiseuille and Couette Flow Developments," *Applied Scientific Research*, Sec. A, Vol. 10, 1961, pp. 165–176.

5 Bodoia, J. R., and Osterle, J. F., "The Development of Free Convection Between Heated Vertical Plates," JOURNAL OF HEAT TRANSFER, TRANS. ASME, Series C, Vol. 84, 1962, pp. 40–44.
6 Marner, W. J., "Combined Free and Forced Laminar Non-Newtonian Convection in a Vertical Tube," PhD dissertation, University of South Carolina, 1969.

Temperature Charts for Simple Shapes in a Linearly Changing Environment

A. M. POINDEXTER[1]

Nomenclature

Bi	=	dimensionless conductance, Biot number	$h\delta/k$
Fo	=	dimensionless time, Fourier modulus	$\alpha\theta/\delta^2$
c	=	specific heat of solid	(Btu/lb, °F)
g	=	rate of increase of environment temperature	(°F/hr)
h	=	surface convection coefficient	(Btu/hr-ft², °F)
k	=	thermal conductivity of solid	(Btu/hr-ft, °F)
t_e	=	environmental temperature at time θ	(°F)
t_δ	=	surface temperature of solid at time θ	(°F)
t_0	=	central temperature of solid at time θ	(°F)
α	=	thermal diffusivity of solid	$k/\rho c$
δ	=	plate half-thickness, radius of cylinder or radius of sphere	(ft)
ρ	=	density of solid	(lb/ft³)
θ	=	time after start of transient	(hr)

[1] Westinghouse Electric Corp., Astronuclear Laboratory, Pittsburgh, Pa.

Contributed by the Heat Transfer Division of THE AMERICAN SOCIETY OF MECHANICAL ENGINEERS. Manuscript received by the Heat Transfer Division, October 13, 1969; revised manuscript received January 6, 1970.

Introduction

IT IS necessary at times to predict transient temperature of infinite plates, infinite cylinders, or spheres which are convectively gaining heat at their surface from an environment whose temperature is changing linearly with time.

$$t_e = g\theta \tag{1}$$

A solution of this boundary-value problem exists [1–3][2] and it has been plotted. This note presents the solution charted in a different way which has the following advantages:

1 Because the parameters plotted in Figs. 1, 2, and 3 represent the difference between points in the solid and the rising environment, they reach asymptotically constant values after a sufficient period of time. Thus the transient, completed in time for all practical purposes, can be shown. The dimensionless time parameter chosen (following the lead of Heisler [4]) for the abscissa compresses the transient time scale for the complete range of relative boundary conductance, Bi, into a single chart.

2 The influence on the transient of environment ramp rate, relative boundary conductance, thermal properties and size of the solid are clearly shown. Both the internal- and surface-environment temperature differences are shown to be directly proportional to the environment ramp rate, g, the square of the characteristic dimension, δ, and inversely proportional to the thermal diffusivity of the solid, α. The surface temperature difference is, in addition, inversely proportional to the relative boundary conductance, Bi.

3 The internal temperature difference is shown directly without the necessity for taking the difference between separate plots of center and surface temperature. This makes the curves more convenient for estimating transient thermal stress.

The dimensionless temperature parameters plotted in Figs. 1, 2, and 3 are asymptotic at infinite time to the values given in Table 1.

Note that the limiting case Bi = 0 is shown on the curves. There is a nontrivial case in which internal thermal resistance is negligible compared to finite surface resistance. In this case, the dimensionless abscissa parameter for a slab becomes:

[2] Numbers in brackets designate References at end of Technical Brief.

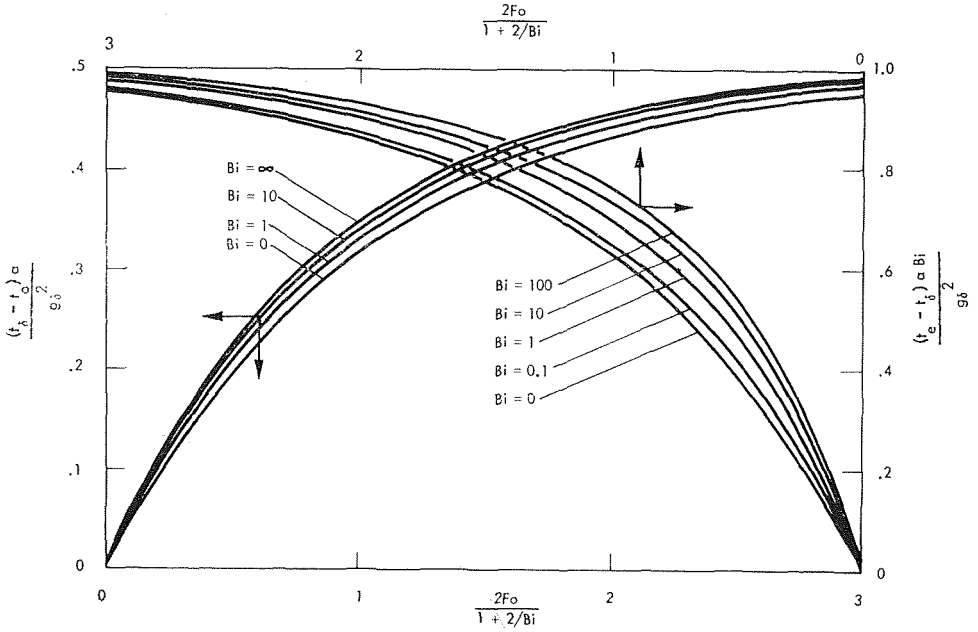

Fig. 1 Transient temperature response of a slab convectively coupled to a linearly changing environment

5 Bodoia, J. R., and Osterle, J. F., "The Development of Free Convection Between Heated Vertical Plates," JOURNAL OF HEAT TRANSFER, TRANS. ASME, Series C, Vol. 84, 1962, pp. 40–44.
6 Marner, W. J., "Combined Free and Forced Laminar Non-Newtonian Convection in a Vertical Tube," PhD dissertation, University of South Carolina, 1969.

Temperature Charts for Simple Shapes in a Linearly Changing Environment

A. M. POINDEXTER[1]

Nomenclature

Bi	=	dimensionless conductance, Biot number	$h\delta/k$
Fo	=	dimensionless time, Fourier modulus	$\alpha\theta/\delta^2$
c	=	specific heat of solid	(Btu/lb, °F)
g	=	rate of increase of environment temperature	(°F/hr)
h	=	surface convection coefficient	(Btu/hr-ft², °F)
k	=	thermal conductivity of solid	(Btu/hr-ft, °F)
t_e	=	environmental temperature at time θ	(°F)
t_δ	=	surface temperature of solid at time θ	(°F)
t_0	=	central temperature of solid at time θ	(°F)
α	=	thermal diffusivity of solid	$k/\rho c$
δ	=	plate half-thickness, radius of cylinder or radius of sphere	(ft)
ρ	=	density of solid	(lb/ft³)
θ	=	time after start of transient	(hr)

[1] Westinghouse Electric Corp., Astronuclear Laboratory, Pittsburgh, Pa.
Contributed by the Heat Transfer Division of THE AMERICAN SOCIETY OF MECHANICAL ENGINEERS. Manuscript received by the Heat Transfer Division, October 13, 1969; revised manuscript received January 6, 1970.

Introduction

IT IS necessary at times to predict transient temperature of infinite plates, infinite cylinders, or spheres which are convectively gaining heat at their surface from an environment whose temperature is changing linearly with time.

$$t_e = g\theta \tag{1}$$

A solution of this boundary-value problem exists [1–3][2] and it has been plotted. This note presents the solution charted in a different way which has the following advantages:

1 Because the parameters plotted in Figs. 1, 2, and 3 represent the difference between points in the solid and the rising environment, they reach asymptotically constant values after a sufficient period of time. Thus the transient, completed in time for all practical purposes, can be shown. The dimensionless time parameter chosen (following the lead of Heisler [4]) for the abscissa compresses the transient time scale for the complete range of relative boundary conductance, Bi, into a single chart.

2 The influence on the transient of environment ramp rate, relative boundary conductance, thermal properties and size of the solid are clearly shown. Both the internal- and surface-environment temperature differences are shown to be directly proportional to the environment ramp rate, g, the square of the characteristic dimension, δ, and inversely proportional to the thermal diffusivity of the solid, α. The surface temperature difference is, in addition, inversely proportional to the relative boundary conductance, Bi.

3 The internal temperature difference is shown directly without the necessity for taking the difference between separate plots of center and surface temperature. This makes the curves more convenient for estimating transient thermal stress.

The dimensionless temperature parameters plotted in Figs. 1, 2, and 3 are asymptotic at infinite time to the values given in Table 1.

Note that the limiting case Bi = 0 is shown on the curves. There is a nontrivial case in which internal thermal resistance is negligible compared to finite surface resistance. In this case, the dimensionless abscissa parameter for a slab becomes:

[2] Numbers in brackets designate References at end of Technical Brief.

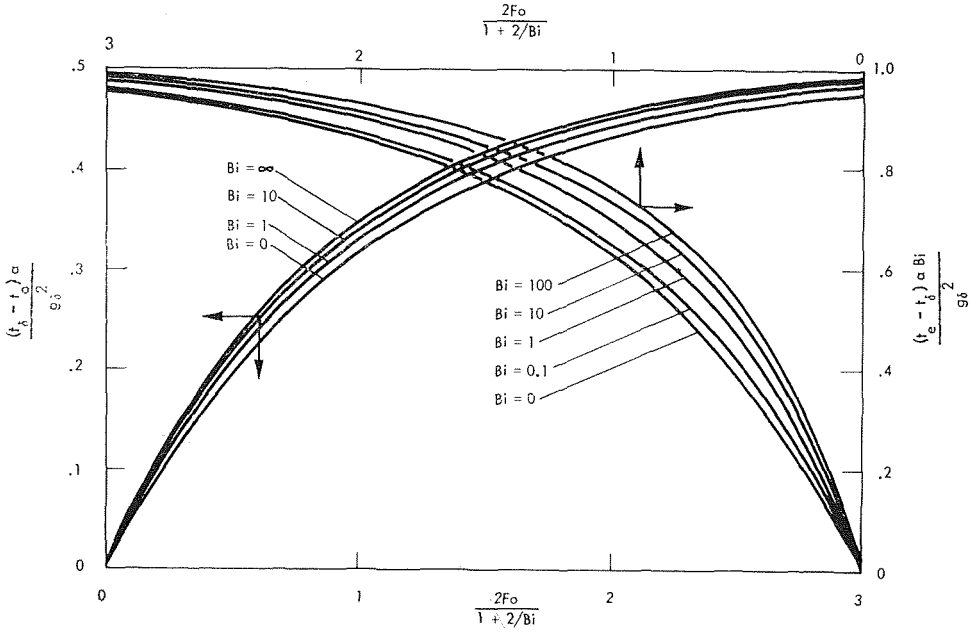

Fig. 1 Transient temperature response of a slab convectively coupled to a linearly changing environment

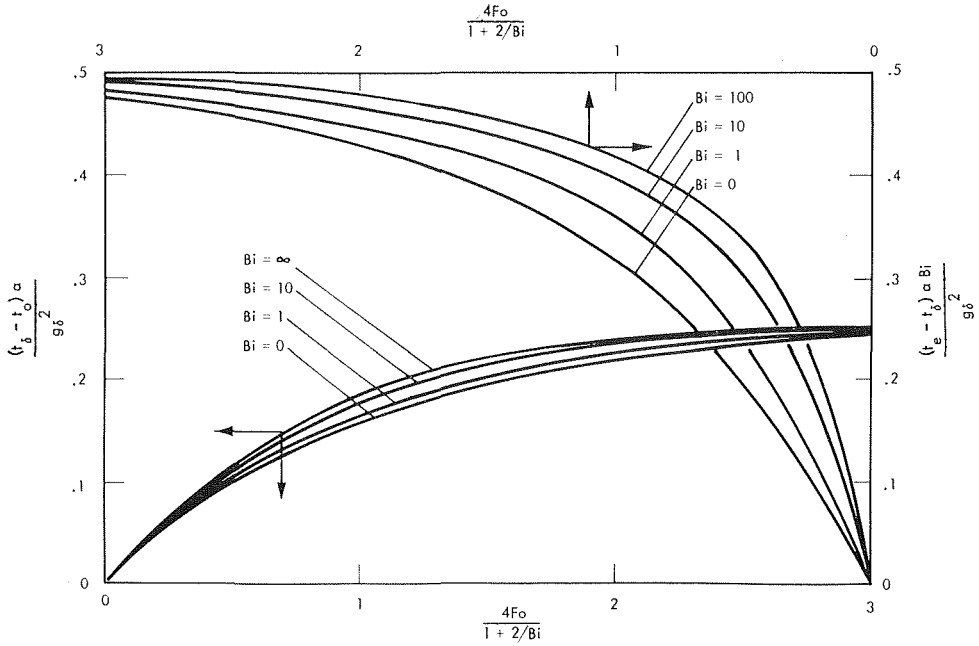

Fig. 2 Transient temperature response of a cylinder convectively coupled to a linearly changing environment

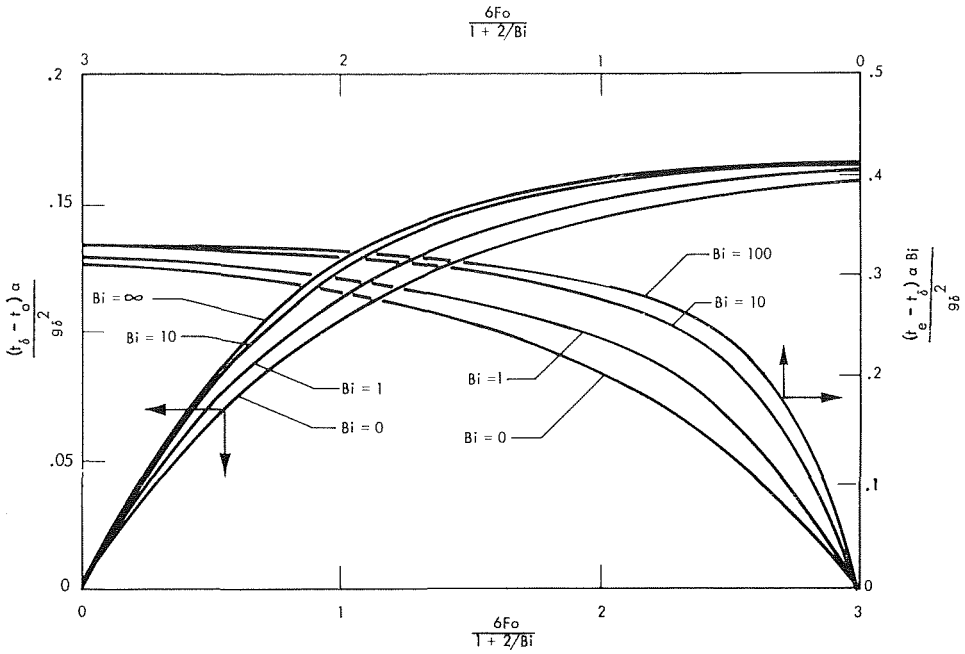

Fig. 3 Transient temperature response of a sphere convectively coupled to a linearly changing environment

$$\frac{2\mathrm{Fo}}{1+2/\mathrm{Bi}} = \mathrm{FoBi} = \frac{h\theta}{\rho c\delta}$$

The values for a cylinder and sphere will be twice and three times the above value. The ordinate parameter for surface-environment temperature difference becomes:

$$(t_e - t_\delta)\frac{\alpha \mathrm{Bi}}{g\delta^2} = (t_e - t_\delta)\frac{h}{g\rho c\delta}$$

Use of these parameters allows transient evaluation of the difference between surface and environment temperature.

For the nontrivial case of $\mathrm{Bi} = \infty$ (finite internal resistance and negligible surface thermal resistance) the slab abscissa parameter becomes:

$$\frac{2\mathrm{Fo}}{1+2/\mathrm{Bi}} = 2\mathrm{Fo}$$

The cylinder and sphere parameter will be twice and three times this value. This allows evaluation of the internal temperature difference.

Table 1 Asymptotic values of dimensionless temperature parameters

	Slab	Cylinder	Sphere
$(t_\delta - t_0)\frac{\alpha}{g\delta^2}$	1/2	1/4	1/6
$(t_e - t_\delta)\frac{\alpha \mathrm{Bi}}{g\delta^2}$	1	1/2	1/3

References

1 Carslaw, H. S., and Jaeger, J. C., *Conduction of Heat in Solids*, Oxford University Press, 2nd ed., 1959, p. 127.
2 Ibid., p. 202.
3 Ibid., p. 238.
4 Heisler, M. P., "Temperature Charts for Internal Heat Generation," ASME Paper 54-SA-44, June 1954.

The Use of Extrapolation for the Solution of Heat Transfer Problems by Finite-Difference Methods

ROMAN U. SCHOENHERR[1] and STUART W. CHURCHILL[2]

For many problems in transient heat conduction in bounded regions a solution can be developed formally in terms of an infinite series of the form

$$U(x, y, z, t) = \sum_{n=1}^{\infty} f_n(x, y, z)e^{-\alpha_n{}^2 t} + U(x, y, z, \infty) \quad (1)$$

where α_n increases with n. For sufficiently long times the series may then be approximated by the first term only, i.e.,

$$U \sim f_1(x, y, z)e^{-\alpha_1{}^2 t} + U(x, y, z, \infty) \quad (2)$$

Taking the partial derivative of U with respect to time,

$$\partial U/\partial t \sim -\alpha_1{}^2 f_1(x, y, z)e^{-\alpha_1{}^2 t} \quad (3)$$

Combining equations (2) and (3) to eliminate $f_1(x, y, z)$,

$$U \sim (-\partial U/\partial t)\alpha_1{}^2 + U(x, y, z, \infty) \quad (4)$$

Hence a plot of U versus $\partial U/\partial t$ at any point should become linear for long times, with slope $-1/\alpha_1{}^2$ and intercept $U(x, y, z, \infty)$, the steady-state value of U.

This relationship suggests the following technique for the reduction of the time and number of calculations required to carry out a transient, numerical integration by finite-difference methods. The relationship between U and dU/dt is examined periodically as the calculations proceed. As soon as linearity is attained to some specified approximation, the calculation may be terminated. Since the remaining stepwise calculations which would be required to attain a close approach to the steady state are ordinarily a significant fraction of the total calculation, a great saving may be accomplished.

Alternatively, differentiating equation (3) permits elimination of α_1, giving an expression from which $U(x, y, z, \infty)$ can be calculated directly:

$$U(x, y, z, \infty) \sim U - \frac{(\partial U/\partial t)^2}{\partial^2 U/\partial t} \quad (5)$$

[1] Engineering Research Department, 3M Company, St. Paul, Minn.
[2] Carl V. S. Patterson Professor of Chemical Engineering, University of Pennsylvania, Philadelphia, Pa.

Contributed by the Heat Transfer Division of The American Society of Mechanical Engineers. Manuscript received by the Heat Transfer Division, September 29, 1969; revised manuscript received, January 26, 1970.

Application to Steady-State Problems

The solution of a steady-state problem by first converting it to an unsteady-state problem has often been proposed or attempted in the hope that iteration in real time will be faster or better-behaved than other iteration procedures or direct matrix inversion. The above extrapolation technique provides a strong weighting factor in favor of the unsteady-state procedure.

Details of Application

The extrapolation technique may be applied as follows to either an unsteady-state problem or to a steady-state problem which has been converted to an unsteady-state problem:

1 The equation is expressed in finite-difference form.
2 The iterative solution in real time is carried out for some arbitrary number of time steps.
3 The last three successive values of U are used to extrapolate numerically U versus $\Delta U/\Delta t$ to $\Delta U/\Delta t = 0$ for every spatial point.
4 After some arbitrary number of additional time steps the extrapolation is repeated and the values of $U(x, y, z, \infty)$ are compared with the previously extrapolated values.
5 If the extrapolated values at any point do not agree within some specified tolerance the procedure is continued.
6 If the extrapolated values at all points do agree within the specified tolerance the solution has been tentatively completed.
7 This tentative steady-state solution is then tested by a further time step in which a negligible change is demanded.
8 If the unsteady-state solution is of intrinsic interest the values of $\alpha_1{}^2$ are determined from the final extrapolation. These final calculated values of $\alpha_1{}^2$ may differ from position to position in contrast to the implication of equations (1)–(4).
9 If the simple, explicit, finite-difference representation is utilized, the maximum allowable time step is limited by stability considerations. For example, for one-dimensional calculations with the temperature specified at the boundaries, the time step must be less than $(\Delta x_i)^2/2K_i$ where Δx_i is the grid size and K_i is the thermal diffusivity at the ith nodal point. The allowable time step is thus controlled by the smallest space increment. This limitation can be relaxed in steady-state problems by choosing pseudo values for K_i such that $(\Delta x_i)^2/2K_i$ is the same at all points. The transient behavior then becomes non-real but the steady-state solution is unchanged. Analogous constructions can be readily developed for more complicated situations.
10 After some experience with a particular type of problem it may be possible to restrict the trial extrapolations to only a few critical space points.

Illustrative Example

Calculations were carried out and the computer times compared using the conventional explicit, unsteady-state formulation with and without extrapolation and using matrix inversion of the steady-state formulation for conduction in a square region with the following combinations of heat transfer coefficient and external temperature on the four consecutive sides of the square: $h = 2$, $T = 1$; $h = 2$, $T = 0$; $h = 1$, $T = 1$; and $h = 1$, $T = 0$. The calculations were carried out for a series of grid divisions ranging from 9 to 49 nodal points. The temperatures at the nodal points were calculated to within ± 0.1 percent by extrapolation. These values agreed to at least four significant figures with those obtained by matrix inversion. The unsteady-state calculations without extrapolation were carried out until an equivalent error was attained.

The required time on a CDC3300 computer increased approximately linearly, as the square, and as the cube of the number of nodal points for extrapolation, no extrapolation, and matrix inversion, respectively. For 64 nodal points the actual times were 2.7, 7.8, and 37.5 seconds, respectively. The advantage of

Table 1 Asymptotic values of dimensionless temperature parameters

	Slab	Cylinder	Sphere
$(t_\delta - t_0)\frac{\alpha}{g\delta^2}$	1/2	1/4	1/6
$(t_e - t_\delta)\frac{\alpha \mathrm{Bi}}{g\delta^2}$	1	1/2	1/3

References

1 Carslaw, H. S., and Jaeger, J. C., *Conduction of Heat in Solids*, Oxford University Press, 2nd ed., 1959, p. 127.
2 Ibid., p. 202.
3 Ibid., p. 238.
4 Heisler, M. P., "Temperature Charts for Internal Heat Generation," ASME Paper 54-SA-44, June 1954.

The Use of Extrapolation for the Solution of Heat Transfer Problems by Finite-Difference Methods

ROMAN U. SCHOENHERR[1] and STUART W. CHURCHILL[2]

For many problems in transient heat conduction in bounded regions a solution can be developed formally in terms of an infinite series of the form

$$U(x, y, z, t) = \sum_{n=1}^{\infty} f_n(x, y, z)e^{-\alpha_n{}^2 t} + U(x, y, z, \infty) \quad (1)$$

where α_n increases with n. For sufficiently long times the series may then be approximated by the first term only, i.e.,

$$U \sim f_1(x, y, z)e^{-\alpha_1{}^2 t} + U(x, y, z, \infty) \quad (2)$$

Taking the partial derivative of U with respect to time,

$$\partial U/\partial t \sim -\alpha_1{}^2 f_1(x, y, z)e^{-\alpha_1{}^2 t} \quad (3)$$

Combining equations (2) and (3) to eliminate $f_1(x, y, z)$,

$$U \sim (-\partial U/\partial t)\alpha_1{}^2 + U(x, y, z, \infty) \quad (4)$$

Hence a plot of U versus $\partial U/\partial t$ at any point should become linear for long times, with slope $-1/\alpha_1{}^2$ and intercept $U(x, y, z, \infty)$, the steady-state value of U.

This relationship suggests the following technique for the reduction of the time and number of calculations required to carry out a transient, numerical integration by finite-difference methods. The relationship between U and dU/dt is examined periodically as the calculations proceed. As soon as linearity is attained to some specified approximation, the calculation may be terminated. Since the remaining stepwise calculations which would be required to attain a close approach to the steady state are ordinarily a significant fraction of the total calculation, a great saving may be accomplished.

Alternatively, differentiating equation (3) permits elimination of α_1, giving an expression from which $U(x, y, z, \infty)$ can be calculated directly:

$$U(x, y, z, \infty) \sim U - \frac{(\partial U/\partial t)^2}{\partial^2 U/\partial t} \quad (5)$$

[1] Engineering Research Department, 3M Company, St. Paul, Minn.
[2] Carl V. S. Patterson Professor of Chemical Engineering, University of Pennsylvania, Philadelphia, Pa.

Contributed by the Heat Transfer Division of The American Society of Mechanical Engineers. Manuscript received by the Heat Transfer Division, September 29, 1969; revised manuscript received, January 26, 1970.

Application to Steady-State Problems

The solution of a steady-state problem by first converting it to an unsteady-state problem has often been proposed or attempted in the hope that iteration in real time will be faster or better-behaved than other iteration procedures or direct matrix inversion. The above extrapolation technique provides a strong weighting factor in favor of the unsteady-state procedure.

Details of Application

The extrapolation technique may be applied as follows to either an unsteady-state problem or to a steady-state problem which has been converted to an unsteady-state problem:

1 The equation is expressed in finite-difference form.
2 The iterative solution in real time is carried out for some arbitrary number of time steps.
3 The last three successive values of U are used to extrapolate numerically U versus $\Delta U/\Delta t$ to $\Delta U/\Delta t = 0$ for every spatial point.
4 After some arbitrary number of additional time steps the extrapolation is repeated and the values of $U(x, y, z, \infty)$ are compared with the previously extrapolated values.
5 If the extrapolated values at any point do not agree within some specified tolerance the procedure is continued.
6 If the extrapolated values at all points do agree within the specified tolerance the solution has been tentatively completed.
7 This tentative steady-state solution is then tested by a further time step in which a negligible change is demanded.
8 If the unsteady-state solution is of intrinsic interest the values of $\alpha_1{}^2$ are determined from the final extrapolation. These final calculated values of $\alpha_1{}^2$ may differ from position to position in contrast to the implication of equations (1)–(4).
9 If the simple, explicit, finite-difference representation is utilized, the maximum allowable time step is limited by stability considerations. For example, for one-dimensional calculations with the temperature specified at the boundaries, the time step must be less than $(\Delta x_i)^2/2K_i$ where Δx_i is the grid size and K_i is the thermal diffusivity at the ith nodal point. The allowable time step is thus controlled by the smallest space increment. This limitation can be relaxed in steady-state problems by choosing pseudo values for K_i such that $(\Delta x_i)^2/2K_i$ is the same at all points. The transient behavior then becomes non-real but the steady-state solution is unchanged. Analogous constructions can be readily developed for more complicated situations.
10 After some experience with a particular type of problem it may be possible to restrict the trial extrapolations to only a few critical space points.

Illustrative Example

Calculations were carried out and the computer times compared using the conventional explicit, unsteady-state formulation with and without extrapolation and using matrix inversion of the steady-state formulation for conduction in a square region with the following combinations of heat transfer coefficient and external temperature on the four consecutive sides of the square: $h = 2$, $T = 1$; $h = 2$, $T = 0$; $h = 1$, $T = 1$; and $h = 1$, $T = 0$. The calculations were carried out for a series of grid divisions ranging from 9 to 49 nodal points. The temperatures at the nodal points were calculated to within ± 0.1 percent by extrapolation. These values agreed to at least four significant figures with those obtained by matrix inversion. The unsteady-state calculations without extrapolation were carried out until an equivalent error was attained.

The required time on a CDC3300 computer increased approximately linearly, as the square, and as the cube of the number of nodal points for extrapolation, no extrapolation, and matrix inversion, respectively. For 64 nodal points the actual times were 2.7, 7.8, and 37.5 seconds, respectively. The advantage of

extrapolation would be even greater for a three-dimensional problem.

Extension to Other Problems

The extrapolation method has been used with comparable success for a wide range of problems beyond those of conduction and beyond those in which it can be justified formally. These problems include unstable natural convection in an enclosed region, freezing in an enclosed region, cyclic heating and cooling, and the deflection and moment distribution of concrete slabs.

One obvious requirement for successful use of the extrapolation method is that the calculations approach the steady state in an exponential manner rather than by decreasing oscillations. If oscillations are due to numerical instability, it may be possible to eliminate them by the use of some alternative, finite-difference representation. Even if the oscillations are due to the physics of the problem it may be possible to eliminate them and determine the steady-state solution by modifying the coefficients of the transient terms.

Temperature Profiles for Liquid Metals and Moderate-Prandtl-Number Fluids

LINDON C. THOMAS[1]

LITTLE success has been achieved to date in the formulation of a turbulent transport model for both liquid metals and fluids with moderate values of the Prandtl number. Generally analyses have been based upon the classical mixing length concept where various assumptions have been made for the ratio ϵ_H/ϵ_m. Feeling that a fresh approach to the problem is needed, the fairly elementary renewal-penetration model will now be employed in the analysis of the temperature profiles associated with turbulent heat transfer to low- and moderate-Prandtl-number fluids. Interestingly, Einstein and Li [5][2] were fairly successful in adapting a similar intermittent flow model to the prediction of the temperature distributions for turbulent air flow.

The elementary renewal-penetration model is based on the hypothesis that eddies intermittently move from the turbulent core to the close vicinity of the wall. It is hypothesized that molecular transport is the predominant mechanism of energy transport during the residency of a fluid element in the vicinity of the wall. Accordingly, the energy equation may be written for individual elements at the wall as (in terms of the instantaneous contact time, θ) [10]

$$\frac{\partial t}{\partial \theta} = \alpha \frac{\partial^2 t}{\partial y^2} \tag{1}$$

with boundary conditions

$$t = T_i \quad \text{at} \quad \theta = 0 \tag{2}$$

$$t = T_i \quad \text{at} \quad y = \infty \tag{3}$$

and

$$t = T_0 \quad \text{at} \quad y = 0 \tag{4a}$$

for a uniform wall-temperature boundary condition, or

$$\frac{\partial t}{\partial y} = -\frac{q_0}{k} \quad \text{at} \quad y = 0 \tag{4b}$$

for a uniform wall-heat-flux boundary condition, where T_i represents the temperature of eddies at the first instant of renewal and T_0 is the wall temperature.

The solutions to the previous equations give rise to expressions for the instantaneous temperature t within fluid elements at the wall of the form

$$t - T_i = (T_0 - T_i)\,\text{erfc}\left(\frac{y}{2\sqrt{\alpha\theta}}\right) \tag{5a}$$

for uniform wall temperature, and

$$t - T_i = \frac{q_0}{\sqrt{\rho ck}}\left[2\sqrt{\frac{\theta}{\pi}}\exp\left(\frac{-Y^2}{4\theta}\right) - Y\,\text{erfc}\left(\frac{Y}{2\sqrt{\theta}}\right)\right] \tag{5b}$$

for uniform wall heat flux, where $Y = y/\sqrt{\alpha}$. The effect on the mean temperature profile, T, of eddies continually moving to and from the surface may be accounted for by use of the age distribution principle. That is, an expression for mean temperature profile may be written as

$$T = \int_0^\infty t\phi(\theta)d\theta \tag{6}$$

where $\phi(\theta)$ is defined such that $\phi(\theta)d\theta$ represents the fraction of fluid elements in contact with the surface with contact time between θ and $\theta + d\theta$. Danckwerts [2] suggested a useful distribution of the form

$$\phi(\theta) = \frac{\exp(-\theta/\tau)}{\tau} \tag{7}$$

where τ is the mean residence time. Based on equations (5*a*), (5*b*), (6), and (7), expressions for the local mean temperature profile within the wall region may be written as

$$T - T_i = (T_0 - T_i)\exp\left(\frac{-y}{\sqrt{\alpha\tau}}\right) \tag{8a}$$

for uniform wall temperature, and

$$T - T_i = q_0\left(\frac{\tau}{\rho ck}\right)^{1/2}\exp\left(\frac{-y}{\sqrt{\alpha\tau}}\right) \tag{8b}$$

for uniform wall heat flux. (The use of Laplace transformation facilitates the required integration.) An expression for the local mean coefficient of heat transfer may be obtained on the basis of either equation (8*a*) or (8*b*) of the form

$$h = \frac{q_0}{T_0 - T_b} = \frac{T_i - T_0}{T_b - T_0}\left(\frac{\rho ck}{\tau}\right)^{1/2} \tag{9}$$

It should be observed that the foregoing analysis gives rise to expressions for the local heat transfer and temperature profile. Accordingly, the use of these relationships must be restricted to thermally fully developed flow. For moderate-Prandtl-number fluids T_i may merely be replaced by T_b. However, T_i may not be set equal to T_b for low-Prandtl-number fluids due to the significance of energy transfer during the flight of eddies from the bulk stream to the wall region. The use of equation (9) in correlating experimental heat-transfer data, especially for liquid metals, requires the formulation of an expression for T_i. The lack of knowledge concerning this important parameter has been, in part, responsible for the failure to adapt the renewal-penetration model to liquid metal heat transfer.

Another difficulty encountered in the use of the renewal-penetration model is in the evaluation of the mean frequency of renewal, $1/\tau$. Significantly, a realistic formulation for τ may be

---

[1] Assistant Professor, Department of Mechanical Engineering, The University of Akron, Akron, Ohio. Assoc. Mem. ASME.

[2] Numbers in brackets designate References at end of Technical Brief.

Contributed by the Heat Transfer Division of THE AMERICAN SOCIETY OF MECHANICAL ENGINEERS. Manuscript received by the Heat Transfer Division, December 1, 1969; revised manuscript received December 10, 1969.

extrapolation would be even greater for a three-dimensional problem.

Extension to Other Problems

The extrapolation method has been used with comparable success for a wide range of problems beyond those of conduction and beyond those in which it can be justified formally. These problems include unstable natural convection in an enclosed region, freezing in an enclosed region, cyclic heating and cooling, and the deflection and moment distribution of concrete slabs.

One obvious requirement for successful use of the extrapolation method is that the calculations approach the steady state in an exponential manner rather than by decreasing oscillations. If oscillations are due to numerical instability, it may be possible to eliminate them by the use of some alternative, finite-difference representation. Even if the oscillations are due to the physics of the problem it may be possible to eliminate them and determine the steady-state solution by modifying the coefficients of the transient terms.

Temperature Profiles for Liquid Metals and Moderate-Prandtl-Number Fluids

LINDON C. THOMAS[1]

Little success has been achieved to date in the formulation of a turbulent transport model for both liquid metals and fluids with moderate values of the Prandtl number. Generally analyses have been based upon the classical mixing length concept where various assumptions have been made for the ratio ϵ_H/ϵ_m. Feeling that a fresh approach to the problem is needed, the fairly elementary renewal-penetration model will now be employed in the analysis of the temperature profiles associated with turbulent heat transfer to low- and moderate-Prandtl-number fluids. Interestingly, Einstein and Li [5][2] were fairly successful in adapting a similar intermittent flow model to the prediction of the temperature distributions for turbulent air flow.

The elementary renewal-penetration model is based on the hypothesis that eddies intermittently move from the turbulent core to the close vicinity of the wall. It is hypothesized that molecular transport is the predominant mechanism of energy transport during the residency of a fluid element in the vicinity of the wall. Accordingly, the energy equation may be written for individual elements at the wall as (in terms of the instantaneous contact time, θ) [10]

$$\frac{\partial t}{\partial \theta} = \alpha \frac{\partial^2 t}{\partial y^2} \tag{1}$$

with boundary conditions

$$t = T_i \quad \text{at} \quad \theta = 0 \tag{2}$$

$$t = T_i \quad \text{at} \quad y = \infty \tag{3}$$

and

$$t = T_0 \quad \text{at} \quad y = 0 \tag{4a}$$

for a uniform wall-temperature boundary condition, or

$$\frac{\partial t}{\partial y} = -\frac{q_0}{k} \quad \text{at} \quad y = 0 \tag{4b}$$

for a uniform wall-heat-flux boundary condition, where T_i represents the temperature of eddies at the first instant of renewal and T_0 is the wall temperature.

The solutions to the previous equations give rise to expressions for the instantaneous temperature t within fluid elements at the wall of the form

$$t - T_i = (T_0 - T_i) \operatorname{erfc}\left(\frac{y}{2\sqrt{\alpha\theta}}\right) \tag{5a}$$

for uniform wall temperature, and

$$t - T_i = \frac{q_0}{\sqrt{\rho c k}}\left[2\sqrt{\frac{\theta}{\pi}} \exp\left(\frac{-Y^2}{4\theta}\right) - Y \operatorname{erfc}\left(\frac{Y}{2\sqrt{\theta}}\right)\right] \tag{5b}$$

for uniform wall heat flux, where $Y = y/\sqrt{\alpha}$. The effect on the mean temperature profile, T, of eddies continually moving to and from the surface may be accounted for by use of the age distribution principle. That is, an expression for mean temperature profile may be written as

$$T = \int_0^\infty t\phi(\theta)d\theta \tag{6}$$

where $\phi(\theta)$ is defined such that $\phi(\theta)d\theta$ represents the fraction of fluid elements in contact with the surface with contact time between θ and $\theta + d\theta$. Danckwerts [2] suggested a useful distribution of the form

$$\phi(\theta) = \frac{\exp(-\theta/\tau)}{\tau} \tag{7}$$

where τ is the mean residence time. Based on equations (5*a*), (5*b*), (6), and (7), expressions for the local mean temperature profile within the wall region may be written as

$$T - T_i = (T_0 - T_i) \exp\left(\frac{-y}{\sqrt{\alpha\tau}}\right) \tag{8a}$$

for uniform wall temperature, and

$$T - T_i = q_0\left(\frac{\tau}{\rho c k}\right)^{1/2} \exp\left(\frac{-y}{\sqrt{\alpha\tau}}\right) \tag{8b}$$

for uniform wall heat flux. (The use of Laplace transformation facilitates the required integration.) An expression for the local mean coefficient of heat transfer may be obtained on the basis of either equation (8*a*) or (8*b*) of the form

$$h = \frac{q_0}{T_0 - T_b} = \frac{T_i - T_0}{T_b - T_0}\left(\frac{\rho c k}{\tau}\right)^{1/2} \tag{9}$$

It should be observed that the foregoing analysis gives rise to expressions for the local heat transfer and temperature profile. Accordingly, the use of these relationships must be restricted to thermally fully developed flow. For moderate-Prandtl-number fluids T_i may merely be replaced by T_b. However, T_i may not be set equal to T_b for low-Prandtl-number fluids due to the significance of energy transfer during the flight of eddies from the bulk stream to the wall region. The use of equation (9) in correlating experimental heat-transfer data, especially for liquid metals, requires the formulation of an expression for T_i. The lack of knowledge concerning this important parameter has been, in part, responsible for the failure to adapt the renewal-penetration model to liquid metal heat transfer.

Another difficulty encountered in the use of the renewal-penetration model is in the evaluation of the mean frequency of renewal, $1/\tau$. Significantly, a realistic formulation for τ may be

[1] Assistant Professor, Department of Mechanical Engineering, The University of Akron, Akron, Ohio. Assoc. Mem. ASME.

[2] Numbers in brackets designate References at end of Technical Brief.

Contributed by the Heat Transfer Division of The American Society of Mechanical Engineers. Manuscript received by the Heat Transfer Division, December 1, 1969; revised manuscript received December 10, 1969.

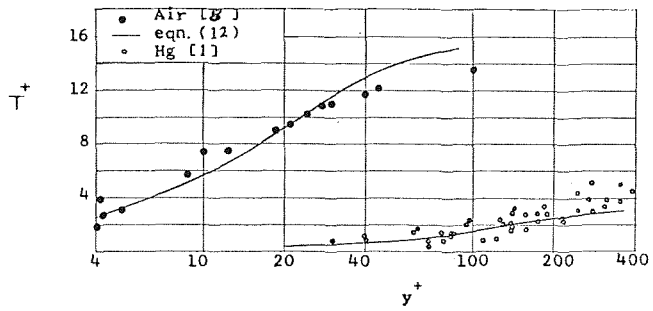

Fig. 1 Comparison of equation (12) with data for air and mercury

obtained by applying the renewal-penetration model to momentum transfer. Analogous to the heat-transfer analysis presented herein, Einstein and Li [4] and Hanratty [7] obtained an expression for the local mean wall shear stress similar to

$$\sigma_0 = \rho U_i \sqrt{\frac{\nu}{\tau}} \tag{10}$$

where U_i represents the axial velocity of eddies at the first instant of renewal. Einstein and Li and Hanratty merely set U_i/U^* equal to an arbitrary constant. However, it appears that U_i may be better represented by the bulk velocity, U. Hence, equation (10) may be written in the form

$$U^* \sqrt{\frac{\tau}{\nu}} = \sqrt{\frac{2}{f}} \tag{11}$$

Experimental temperature-profile data are generally presented in dimensionless form in terms of the friction temperature, T^*, as $T^+ = (T_0 - T)/T^*$ where $T^* = (q_0''/(\rho c U^*)$. Accordingly, the present analysis gives rise to an expression for the dimensionless temperature profile for both uniform-wall-temperature and uniform-wall-heat-flux boundary conditions of the form (from the coupling of equation (8*a*) or (8*b*) and equations (9) and (11))

$$T^+ = \sqrt{\frac{\mathrm{Pr}}{f/2}} \left[1 - \exp\left(-y^+ \sqrt{\mathrm{Pr}\,\frac{f}{2}} \right) \right] \tag{12}$$

Significantly, equation (12) does not involve the parameter T_i. Hence, it appears that a comparison of this expression with experimental data for both low- and moderate-Prandtl-number fluids should provide some measure of applicability of the renewal-penetration model, particularly to liquid metals.

The present analysis suggests that h and T are independent of the axial boundary condition. However, this result must be interpreted in light of the assumption of simple one-dimensional transfer (equation (1)) and the boundary condition given by equation (3). These underlying assumptions appear to be appropriate for high-turbulence-intensity heat transfer to liquid metals but become questionable for low values of the Peclet number. In this regard, experimental heat-transfer data are known to be essentially independent of the form of the axial boundary condition for values of the Peclet number above approximately 5×10^3 [9].

Equation (12) is compared in Figs. 1 and 2 with experimental temperature-profile data for fully developed turbulent pipe flow of mercury, air, and water for uniform wall heat flux. The data for mercury (Pr = 0.02) were taken for values of the Reynolds number ranging from 2.5×10^5 to 7.3 to 10^5 such that Pe $> 5 \times 10^3$. Equation (12) is seen to correlate these data extremely well. (Equation (12) suggests a weak dependence of T^+ on the Reynolds number which is well within the scatter of the data.)

Due to the nature of the renewal-penetration model, equation (12) is expected to be applicable to the wall region only. Accordingly, this expression is seen to diverge from the data for air

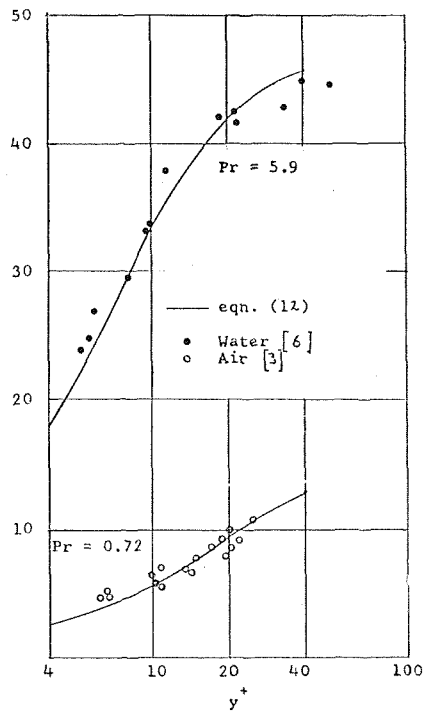

Fig. 2 Comparison of equation (12) with experimental data for air and water

at y^+ approximately equal to 30.0 (i.e., just outside the wall region). In somewhat surprising contrast, equation (12) is found to adequately correlate the mercury data for values of y^+ as large as 300.0. It may be concluded that the thermal influence of the wall region extends a considerable distance into the turbulent core for liquid metals. Although measurements were not reported by Brown, et al. [1] for values of y^+ less than 30.0, it appears that the mean temperature profile in the wall region may be predicted by equation (12).

Concluding Remarks

It has been demonstrated that the elementary renewal-penetration model gives rise to an expression for the dimensionless temperature profile which correlates experimental data in the wall region for turbulent pipe flow of mercury, air, and water for uniform wall heat flux and for Pe $> 5 \times 10^3$. It therefore appears that the renewal-penetration model may be adapted to turbulent heat transfer to liquid metals for high turbulence intensities. Due to the lack of knowledge concerning the parameter T_i, the model has not been used to predict the mean Nusselt number for liquid metals. However, it is felt that direction has been provided for further studies regarding the application of this model to the study of turbulent heat transfer to liquid metals.

Acknowledgment

Financial support for this study was received from NSF-GK 3048.

References

1 Brown, H. E., Amstead, B. H., Short, B. E., "Temperature and Velocity Distribution and Transfer of Heat in a Liquid Metal," TRANS. ASME, Vol. 79, 1957, pp. 279–285.

2 Danckwerts, P. V., "Significance of Liquid-Film Coefficients in Gas Absorption," *AIChE Journal*, Vol. 43, 1951, p. 1460.

3 Deissler, R. G., and Eien, C. S., "Analysis of Turbulent Heat Transfer, Mass Transfer and Friction in Smooth Tubes at High Prandtl and Schmidt Numbers," NACA TN 2629, 1952.

4 Einstein, H. A., and Li, H., "The Viscous Sublayer Along a Smooth Boundary," *Proc. ASCE, J. Eng. Mech. Div.*, Vol. 82, No. E.M., 1956, p. 1–27.

5 Einstein, H. A., and Li, H., "Shear Transmission From a Tur-

bulent Flow to Its Viscous Boundary Sub-layer," *Heat Transfer and Fluid Mechanics Institute Proceedings*, Vol. 13, 1955, p. 1–16.

6 Gowen, R. A., and Smith, J. W., "The Effect of the Prandtl Number on Temperature Profiles for Heat Transfer in Turbulent Pipe Flow," *Chemical Engineering Science*, Vol. 22, 1967, pp. 1701–1711.

7 Hanratty, T. J., "Turbulent Exchange of Mass and Momentum with a Boundary," *AIChE Journal*, Vol. 2, Sept. 1956, pp. 359–362.

8 Johnk, R. E., and Hanratty, T. J., "Temperature Profiles for Turbulent Flow of Air in a Pipe—II," *Chemical Engineering Science*, Vol. 17, 1962, pp. 881–892.

9 Siegel, R., and Sparrow, E. M., "Comparison of Turbulent Heat Transfer Results for Uniform Wall Heat Flux and Uniform Wall Temperature," JOURNAL OF HEAT TRANSFER, TRANS. ASME, Series C, Vol. 82, 1960, p. 152.

10 Thomas, L. C., "The Applicability of the Renewal-Penetration Model to Transport Processes Associated with Axial Flow and Flow Past Submerged Bodies," PhD thesis, Kansas State University, 1968.